

UNIVERSIDAD NACIONAL DE MAR DEL PLATA
FACULTAD DE INGENIERÍA
DEPARTAMENTO DE INGENIERÍA EN MATERIALES

Diseño y comportamiento mecánico de núcleos ultralivianos basados en CFRP para uso en estructuras sándwich

(Design and mechanical behavior of ultralight cores based on CFRP for use in
sandwich structures)

Tesis presentada por

Juan Pablo Raúl Vitale

para optar por el grado académico de

Doctor en Ciencias de los Materiales

Trabajo desarrollado en el

Instituto de Investigaciones en Ciencia y Tecnología de Materiales,
INTEMA (UNMdP-CONICET), Mar del Plata, Buenos Aires, Argentina

en conjunto con el

Institut für Leichtbau, Universität der Bundeswehr München, Múnich, Alemania

Supervisores académicos:

- Director: Dr. Ing. Ariel Stocchi (Universidad Nacional de Mar del Plata, Argentina)
- Co-director: Dr. Ing. Gaston Francucci (Universidad Nacional de Mar del Plata, Argentina)
- Co-director: Univ. Prof. Dr.-Ing. Helmut Rapp (Universität der Bundeswehr München, Alemania)

Abril de 2022



RINFI se desarrolla en forma conjunta entre el INTEMA y la Biblioteca de la Facultad de Ingeniería de la Universidad Nacional de Mar del Plata.

Tiene como objetivo recopilar, organizar, gestionar, difundir y preservar documentos digitales en Ingeniería, Ciencia y Tecnología de Materiales y Ciencias Afines.

A través del Acceso Abierto, se pretende aumentar la visibilidad y el impacto de los resultados de la investigación, asumiendo las políticas y cumpliendo con los protocolos y estándares internacionales para la interoperabilidad entre repositorios



Esta obra está bajo una [Licencia Creative Commons Atribución-
NoComercial-CompartirIgual 4.0 Internacional](https://creativecommons.org/licenses/by-nc-sa/4.0/).

UNIVERSIDAD NACIONAL DE MAR DEL PLATA
FACULTAD DE INGENIERÍA
DEPARTAMENTO DE INGENIERÍA EN MATERIALES

Diseño y comportamiento mecánico de núcleos ultralivianos basados en CFRP para uso en estructuras sándwich

(Design and mechanical behavior of ultralight cores based on CFRP for use in
sandwich structures)

Tesis presentada por

Juan Pablo Raúl Vitale

para optar por el grado académico de

Doctor en Ciencias de los Materiales

Trabajo desarrollado en el

Instituto de Investigaciones en Ciencia y Tecnología de Materiales,
INTEMA (UNMdP-CONICET), Mar del Plata, Buenos Aires, Argentina

en conjunto con el

Institut für Leichtbau, Universität der Bundeswehr München, Múnich, Alemania

Supervisores académicos:

- Director: Dr. Ing. Ariel Stocchi (Universidad Nacional de Mar del Plata, Argentina)
- Co-director: Dr. Ing. Gaston Francucci (Universidad Nacional de Mar del Plata, Argentina)
- Co-director: Univ. Prof. Dr.-Ing. Helmut Rapp (Universität der Bundeswehr München, Alemania)

Abril de 2022

“De nuestros miedos nacen nuestros corajes, y en nuestras dudas viven nuestras certezas. Los sueños anuncian otra realidad posible, y los delirios otra razón. En los extravíos nos esperan los hallazgos porque es preciso perderse para volver a encontrarse”

Eduardo Galeano

Foreword

This work has been developed over several years, going through different formats and approaches, having started at the former Composite Materials Group (now CET) belonging to INTEMA in Argentina, and culminated at the Institut für Leichtbau (ILB) of the Universität der Bundeswehr München, in Germany.

First of all, I would like to thank my directors Dr. Ing. Ariel Stocchi and Dr. Ing. Gaston Francucci in Argentina for giving me the opportunity to work under their tutelage and develop as a researcher. Dr. Stocchi had previously been the director of my degree thesis, so we have been working together for many years. I emphasise the predisposition of both of them for my academic and professional progress in an area that has been of great interest to me, such as composite materials, providing me with fundamental knowledge in materials processing and characterisation. I would like to emphasise their "open door" culture, where every new idea was welcomed and perfected to be successful, which has led to long constructive discussions, shaping the research work. I take away from them countless experiences and advice. I would like to thank the entire team of the Composite Materials Group during my time there for the space provided, the use of equipment, the collaboration, and the nice experiences we had together.

Thus arose the opportunity to work together with the ILB to investigate ultralight sandwich structures based on CFRP under the co-supervision of Univ.-Prof. Dr.-Ing. Helmut Rapp, to whom I am deeply grateful for having trusted me from the beginning and for opening the doors for me to continue my research training in Germany. Prof. Rapp has given me countless times his support and advice, always available for consultations and giving his valuable input, backed up by his many years of scientific experience. I am grateful to Univ.-Prof. Dr.-Ing. Philipp Höfer for providing the necessary space and support to continue working at the institute. Also, to all my colleagues at the institute for the enriching discussions and nice moments in and outside of work, especially with my colleague and friend M.Sc. Felix Brandmayr, since my first research stay in Germany in 2015.

A special recognition I would like to give to the Mechanical Technology Group during my time as a teacher at UNMdP, under the direction of Prof. Dolores Echeverría and Prof. Daniel Sosa, both of them predisposed to cooperative work, always helping

to extend my knowledge in manufacturing and quality control, fostering my academic growth. In particular I thank Prof. Sosa for having literally taught me how to be a university teacher, always giving his best regardless of the time invested and seeking professional excellence. To Prof. Reutemann for the countless professional anecdotes that lightened the hours of teaching. I would like to thank them and all their team for the beautiful moments we shared.

I acknowledge the following institutions for their financial support: at the beginning, the ANPCyT project FSNano 004; during its development and completion, the Bayerisches Hochschulzentrums für Lateinamerika (BAYLAT) and the Deutsche Akademische Austauschdienst (DAAD). Thanks to the Universidad Nacional de Mar del Plata and the Universität der Bundeswehr München for their cooperation, and to their respective International Secretariats. I would like to thank INTEMA and ILB for the use of equipment and resources that promoted the realisation and completion of this thesis. A special mention goes to Prof. Dr. Aldo Boccaccini (FAU), through BAYLAT, for giving me the opportunity to participate in the Network of Argentinean Scientists in Germany (RCAA).

My greatest gratitude is always to my family for their unconditional support. To my wife Julieta for having been by my side for so many years, listening to me and advising me as the best life partner you can have, having gone through so many things together and starting to be a family with the arrival of little Giovanni, who has brought light and joy to all our environment. To my parents, my sister, my parents-in-law, and brothers-in-law, for their emotional support, their life advice and for looking after our wellbeing. To my friends, who even today, after almost 20 years, are still best friends regardless of the distance, and continue to celebrate my achievements.

Resumen

El uso de materiales base ligeros, como los compuestos reforzados con fibra de carbono (CFRP), puede mejorar la eficiencia energética de los vehículos de pasajeros entre un 6% y un 8% por cada 10% de reducción de peso, lo que aplicado a vehículos eléctricos e híbridos fomentaría una mayor competitividad y atracción hacia la nueva generación del transporte. Dentro del grupo de estructuras más eficientes que ofrecen muy bajo peso y buenas propiedades mecánicas, se destacan las estructuras tipo sándwich. Normalmente éstos se componen de un par de placas de cubierta, llamadas pieles, de polímeros reforzados con fibras o de aluminio, y núcleos celulares de muy baja densidad (por ejemplo, espumas, Nomex® o núcleos tipo panal de abeja o *honeycomb* de aluminio). En la actualidad, el uso de materiales de tipo celular para núcleos ha ganado mayor atención y es tendencia en el área de los diseñadores de materiales. En este contexto, las estructuras celulares ultraligeras de diseño utilizan los principios de carga orientada con el material base, aprovechando su anisotropía, como es el caso de los núcleos honeycomb 3D y los reticulados o *lattices* basados en CFRP.

El objetivo principal de este trabajo fue contribuir a la investigación en diseño y estudio del comportamiento mecánico de nuevos materiales de tipo núcleo celular, a través de diferentes enfoques. El trabajo se centra en núcleos de muy baja densidad para aplicaciones sándwich ($\rho_c < 48 \text{ kgm}^{-3}$), basados en CFRP, presentando mayor rigidez y resistencia en comparación con sus contrapartes comerciales. En estos términos, el alcance de este trabajo se dirigió a tratar tres puntos focales:

1. Explorar el diseño y la fabricación de nuevos tipos de núcleos sándwich ultraligeros: se propusieron enfoques originales de diseño: (a) *núcleos honeycomb 3D*, desarrollando el método fabricación por enclavamiento mecánico; (b) *núcleos reticulados*, con foco en su diseño a partir de materiales prefabricados. En ambos casos, la función objetivo fue lograr núcleos de ultrabajo peso y, a su vez, obtener un panel sándwich completo, alcanzándose buena calidad de terminación y repetibilidad.
2. Estudiar el comportamiento de los núcleos propuestos por casos de carga típicos, identificando y prediciendo sus modos principales de falla: Se estudió la relación morfológica de los núcleos y sus propiedades mecánicas, a partir de las geometrías de las celdas unitarias que los componen y de las propiedades mecánicas del material

base, con el fin de desarrollar modelos analíticos para predecir y estudiar los modos de falla de las estructuras obtenidas. Estos modelos fueron complementados por simulaciones por elementos finitos (FE) con buena correlación. Así, se perfilaron los modos principales de falla para evaluar el comportamiento del material previo a los ensayos. Como primera etapa, el trabajo se centra en el estudio de los núcleos en compresión fuera del plano y cizallamiento de placa, para luego complementarse con una investigación en flexión en 4 puntos, evaluando el panel sándwich como conjunto, siendo la rigidez de los núcleos y los espesores de piel las variables.

3. Caracterizar el comportamiento mecánico de los núcleos y de los paneles sándwich, propuestos para la retroalimentación de modelos: se llevaron a cabo una serie de ensayos mecánicos cuasiestáticos, en base a los estados de carga previamente establecidos. Se correlacionaron los datos experimentales y las predicciones de los modelos, proporcionando una retroalimentación para su validación. Los datos experimentales se encuentran en buena correspondencia con los modelos de predicciones.

Los núcleos honeycomb 3D presentaron densidades de $38,67 - 47,64 \text{ kgm}^{-3}$; mientras que los núcleos reticulados, densidades de $8,66 - 49,7 \text{ kgm}^{-3}$. El rango menor de densidad representa un tipo de núcleos que aun no ha sido explotado. Ambos núcleos exhibieron avances en el desempeño mecánico específico en comparación con otros materiales de núcleos conocidos, por ejemplo, en algunos casos superando en compresión en 35,5 % en términos de resistencia y en 124,6 % en términos de rigidez al mejor material competidor; y en cizallamiento, con módulos de corte de 5 a 6 veces, e índices de resistencia de 2,7 a 4,5 veces mayores que los núcleos competidores de arquitectura cuadrada.

Esta disertación brinda nuevos enfoques para la obtención de núcleos celulares de ultrabajo peso, cuyas características de celda abierta, además ofrece potenciales aplicaciones multifuncionales (por ejemplo, transferencia de calor, capacidad de refuerzo con espumas, o la incorporación de cables o electrónica). Los núcleos de estudio representan una alternativa atractiva a los núcleos celulares tradicionales metálicos y/o poliméricos y, al mismo tiempo, siendo materiales sencillos de fabricar. Los modos de falla predichos por los resultados analíticos brindan una herramienta de interés para diseñadores de materiales en diferentes aplicaciones, pudiéndose conocer las propiedades mecánicas del panel sándwich antes de su fabricación.

Abstract

The use of lightweight base materials, such as carbon fibre reinforced composites (CFRP), can improve the energy efficiency of passenger vehicles by 6-8% for every 10% reduction in weight, which, when applied to electric and hybrid vehicles, would make them more competitive and attractive to the new generation of transport. Within the group of more efficient structures offering very low weight and good mechanical properties, sandwich structures stand out. These typically consist of a pair of cover plates, called skins, made of fibre-reinforced polymers or aluminium, and very low-density cellular cores (e.g., foams, Nomex® or aluminium honeycomb cores). Nowadays, the use of cell-type materials for cores has gained increased attention and is a trend in the area of material designers. In this context, ultra-lightweight cellular design structures use the principles of oriented loading with the base material, taking advantage of its anisotropy, as in the case of CFRP-based 3D honeycomb cores and lattices.

The main objective of this work was to contribute to the research in design and study of the mechanical behaviour of new cellular core-type materials, through different approaches. The work focuses on very low-density cores for sandwich applications ($\rho_c < 48 \text{ kgm}^{-3}$), based on CFRP, presenting higher stiffness and higher strength compared to their commercial counterparts. In these terms, the scope of this work aimed to address three focal points:

1. To explore the design and fabrication of new types of ultra-lightweight sandwich cores: original design approaches were proposed: (a) *3D honeycomb cores*, developing the fabrication method by mechanical interlocking; (b) *lattices* cores, with focus on their design from prefabricated materials. In both cases, the objective function was to achieve ultra-low weight cores and, at the same time, to obtain a complete sandwich panel, achieving good finish quality and repeatability.
2. To study the behaviour of the cores proposed for typical load cases, identifying, and predicting their main failure modes: The morphological relationship of the cores and their mechanical properties was studied, based on the geometries of the unit cells that create them and the mechanical properties of the base material, in order to develop analytical models to predict and study the failure modes of the structures obtained. These models were complemented by finite element (FE) simulations with good

correlation. Thus, the main failure modes were profiled to evaluate the behaviour of the material prior to testing. As a first stage, the work focuses on the study of the cores in out-of-plane compression and plate shear, and then complemented by a 4-point bending investigation, evaluating the sandwich panel as a whole, with core stiffness and skin thicknesses as variables.

3. To characterise the mechanical behaviour of the cores and sandwich panels, proposed as model feedback: a series of quasi-static mechanical tests were carried out, based on previously established loading states. Experimental data and model predictions were correlated, providing feedback for validation. The experimental data are in good correspondence with the model predictions.

The 3D honeycomb cores presented densities of 38.67 - 47.64 kgm⁻³; while the lattices cores showed densities of 8.66 - 49.7 kgm⁻³. The latter lower density range represents a type of core that has not yet been exploited. Both cores' cases exhibited advances in specific mechanical performances compared to other known core materials, for example, in some cases outperforming the best competing material in compression by 35.5 % in terms of strength and 124.6 % in terms of stiffness; and in shear, with shear moduli 5 to 6 times, and shear strengths 2.7 to 4.5 times higher than competing cores with square architecture.

This dissertation provides new approaches to obtain ultra-lightweight cell cores, whose open cell characteristics also offer potential multifunctional applications (e.g., heat transfer, foam reinforcement capability, or the incorporation of wires or electronics). The studied cores represent an attractive alternative to traditional metallic and/or polymeric cell cores while being simple to fabricate. The failure modes predicted by the analytical results provide a tool of interest for material designers in different applications, being able to know the mechanical properties of the sandwich panel before its fabrication.

Contents

- Foreword 3
- Resumen 5
- Abstract 7
- Contents 9
- 1 Introduction 14
 - 1.1 Background 14
 - 1.2 Dissertation hypothesis 16
 - 1.3 Dissertation goals 17
 - 1.3.1 Primary goals 17
 - 1.3.2 Specific goals 17
 - 1.4 Dissertation outline 18
- 2 Composite materials: general aspects 20
 - 2.1 Fibre reinforced polymers (FRP): main concepts 20
 - 2.1.1 Fibres 21
 - 2.1.2 Thermoset polymer matrix 25
 - 2.2 Properties and analytical approaches of FRP 28
 - 2.2.1 Micromechanics 29
 - 2.2.2 Macromechanics 33
 - 2.2.3 Failure cases 39
 - 2.3 FRP manufacturing processes 49
- 3 Sandwich construction: state of the art 55
 - 3.1 Sandwich structures concepts 55
 - 3.1.1 Lightweight construction 55
 - 3.1.2 Periodic cellular materials 58
 - 3.2 Failure modes 62
 - 3.2.1 Load introduction 62
 - 3.2.2 Base calculations 62
 - 3.2.3 Failure modes 65
 - 3.2.4 Failure load surfaces 68
- 4 Ultra-lightweight 3D-honeycomb cores 70
 - 4.1 Literature review 70
 - 4.2 Design and construction 73

4.2.1	Materials	73
4.2.2	Square-honeycomb design	75
4.2.3	Manufacturing method	79
4.3	Core out-of-plane compression	81
4.3.1	Compressive stiffness	83
4.3.2	Compressive strength	87
4.4	Core plate shear	98
4.4.1	Shear stiffness	100
4.4.2	Shear strength	107
4.5	Experimental tests	118
4.5.1	Compressive tests	118
4.5.2	Shear test	127
4.6	Concluding remarks.....	133
5	Ultra-lightweight lattices made from CFRP rods	135
5.1	Literature review	135
5.2	Materials and design	138
5.2.1	Materials	138
5.2.2	Lattice core design.....	139
5.2.3	Core relative density estimation	143
5.3	Core out-of-plane compression	144
5.3.1	Compressive stiffness	145
5.3.2	Compressive strength	152
5.4	Core plate shear	161
5.4.1	Shear stiffness	162
5.4.2	Shear strength	165
5.5	Experimental tests	174
5.5.1	Compressive tests	174
5.5.2	Shear tests.....	181
5.6	Concluding remarks.....	190
6	Ultra-lightweight sandwich panels: a case of study by four-point bending	192
6.1	Literature review	192
6.2	Materials and design	194
6.2.1	Materials	194
6.2.2	Bending sample design.....	195
6.3	Theoretical approach.....	197

6.3.1	Loading case.....	198
6.3.2	Maximum displacement	200
6.3.3	Failure modes, loads and stresses	201
6.4	FE approach.....	213
6.4.1	Model	213
6.4.2	Analysed cases.....	215
6.5	Experimental tests.....	225
6.5.1	Bending test set up	226
6.5.2	Bending tests results.....	227
6.5.3	Discussion	234
6.6	Extrapolation to ultra-lightweight 3D-honeycomb cores.....	237
6.6.1	Sample design	238
6.6.2	FE model	238
6.6.3	Analysed cases.....	240
6.6.4	Partial conclusions.....	247
6.7	Concluding remarks.....	248
7	Discussion and conclusions	251
7.1	Discussion	251
7.1.1	Compressive response	251
7.1.2	Shear response.....	255
7.1.3	Ashby-style charts.....	258
7.2	Difficulties found	264
7.3	Conclusions.....	266
8	Resume and outlook	269
8.1	Resume	269
8.2	Outlook	272
Annexes.....		274
A	Complementary information: polymer composite materials reinforced with fibres	275
A.1	Global demand of polymer composite materials reinforced with fibres.....	275
B	Base material properties	278
B.1	Ultra-lightweight 3D-honeycomb cores.....	278
B.1.1	Elastic properties	278
B.1.2	Strength	279
B.2	Ultra-lightweight lattice-cores made from CFRP rods.....	280

B.2.1	Elastic properties. Skin I ($t_f = 0.8$ mm)	280
B.2.2	Elastic properties. Skin II ($t_f = 1.21$ mm)	281
B.2.3	Strength	283
C	Core and skin densities	284
C.1	Ultra-lightweight 3D-honeycomb cores	284
C.1.1	Composite plate	284
C.1.2	Core densities	284
C.2	Ultra-lightweight lattice-cores made from CFRP rods	286
C.2.1	Composite skins I ($t_f = 0.8$ mm)	286
C.2.2	Composite skins II ($t_f = 1.21$ mm)	286
C.2.3	Core densities	287
D	Complementary analyses for Chapter 5	288
D.1	Loads over mid-plane node	288
D.1.1	Comparison between two kind of mid-plane node shapes	288
D.2	Variation of rod orientation according to angle ω and its effect on Euler buckling behaviour by compressive loads	291
D.3	Variation of rod orientation according to angle α and its effect on Euler buckling behaviour by shear loads	293
D.3.1	Resultant shear loads over the mid-plane node due to external compressive loads	295
D.4	Potentially additional failure mode in compressive loading	298
E	Complementary studies for Chapter 6 and buckling diagrams	300
E.1	Maximum displacement while bending	300
E.2	Coordinates system transformation for the use of homogeneous anisotropic faces into face buckling analyses	302
E.3	Buckling coefficients for different plates sizes, boundary conditions and load cases	304
E.3.1	Compression	305
E.3.2	Shear	306
	Nomenclature	308
	List of figures	311
	List of tables	318
	List of publications	320
	Refereed Journal Articles related to the research	320
	Congresses, Conferences and Symposiums	320
	Bibliography	321

1 Introduction

1.1 Background

Human activities have an impact on the environment around us. Materials and energy resources consumption while releasing dangerous waste products into the environment are threatening the well-being of future generations [1]. After the 21st Paris Conference, the 175 signatory parties (174 plus the European Union, EU) pledged to invest and intensify the necessary actions to combat climate change, while reducing greenhouse gases [2]. In this matter, the EU has established, by 2021, new regulations for exhaust gases in new transport vehicles, in which car manufacturers must provide a fleet of vehicles capable of generating an average of less than 95 g/km of CO₂. According to Nikowitz [3], only combustion engine powered vehicles capable of achieving this goal are sub-compact vehicles that weigh less than 1200 kg. In order to reach CO₂ emissions requirements while responding to increasing demands in comfort, further hybridization and electrification of the automotive fleet turns out to be inevitable.

Besides improved aerodynamics and rolling friction, the production of lightweight vehicles is the main strategy of automotive and transport related industries to increase fuel efficiency, reduce emissions, or improve energy economy [4]. The use of lightweight materials, such as carbon fibre reinforced polymers (CFRP), can improve the energy efficiency of passenger vehicles by between 6% and 8% for every 10% weight reduction, while making electric and hybrid vehicles more competitive [5]. In other words, a reduction of 100 kg can reduce CO₂ emissions by almost 10 g per driven kilometre [6].

Today's manufacturers are employing new material-based concepts into passenger series vehicles. Low-weight metal alloys, composites materials and hybrid structures have been implemented for many years. For example, Audi AG has incorporated the CFRP materials directly as a part of high-performance body structure (Figure 1.1). In particular, CFRP based materials offer the greatest potential for weight savings (40 – 60%) but costs 2 to 10 times compared to its metal counterparts [7].

Once developed for aerospace applications and then transferred to high-performance race cars, fibre reinforced polymers (FRP) have been established as base raw materials for construction of lightweight sensitive structures, due to their high specific

mechanical properties as stiffness and strength [8,9]. The actual trends indicate that raw materials with more lightweight potential (i.e. lower weight for assembly groups) as FRP are in focus of development and will gradually replace various components in transport industries as automotive, aerospace, naval and railroad [5,10–14]. Thus, the global demand of CFRP components has been growing in the last few years and the prognosis shows a sustained growth (see Annex A).

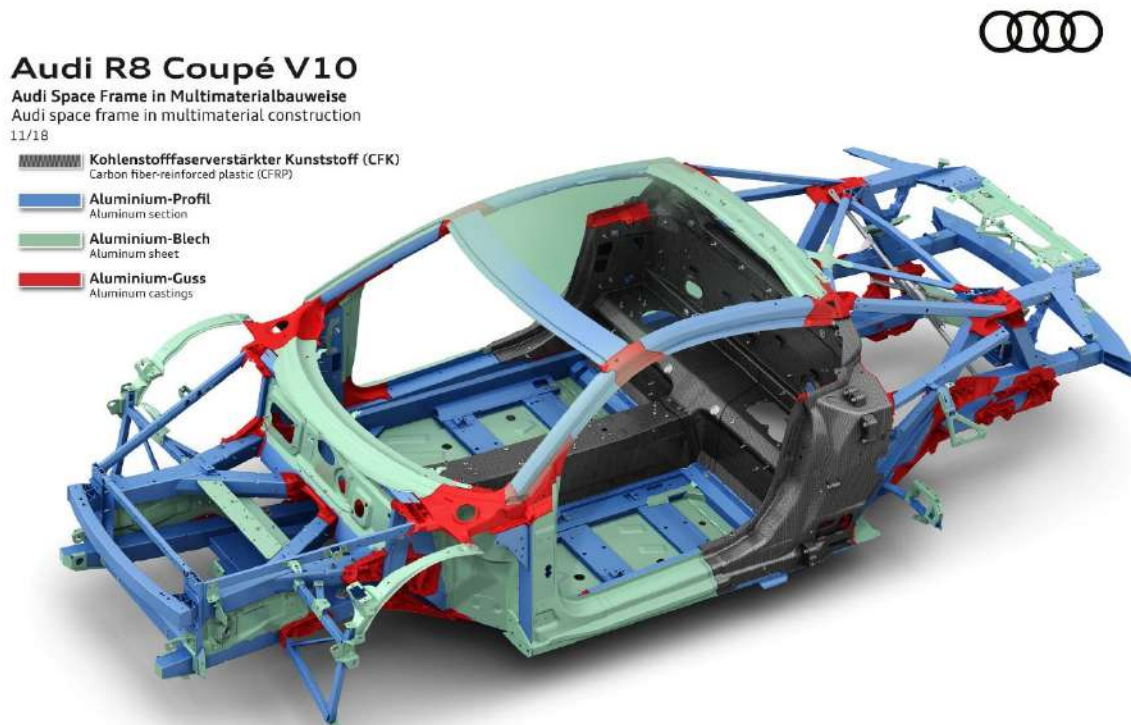


Figure 1.1. Audi Space Frame [Source: Audi AG]

Within the group of structures that offer a highly lightweight potential, sandwich-type structures stand out [15]. They are typically made-up of pairs of FRP (or aluminium) faces and a low density cellular cores (e. g., foams, Nomex®, aluminium honeycombs), as is the case in modern airliners for many components (Figure 1.2) and are now established as secondary structures for business aircraft considering their great cost-reliability/weight ratio [16,17]. Typically use of sandwich panels is found in helicopters [18] or aerospace [19,20] applications. In this context, the use of cellular-type materials has now gained greater attention and is the trend among material designers in the field. As an example of the trend in research, CFRP square-honeycombs cores [21] or lattice-based cores i.e., an array of interconnected bars [22,23], are being targeted.

Construction methods based on cellular structures applied to ultra-lightweight sandwich cores, (i.e., in this case, as cores with less than 48 kgm^{-3} [24]), not only offer advantages in terms of weight [24,25], but are also synonymous of efficient use of materials and principles of oriented loading, as is the case of lattice-based materials. Currently, lattice-based materials are mainly made from titanium and other metal alloys [26,27], which leaves room for the exploitation of other parent materials such as FRP, given their outstanding specific mechanical properties [22].

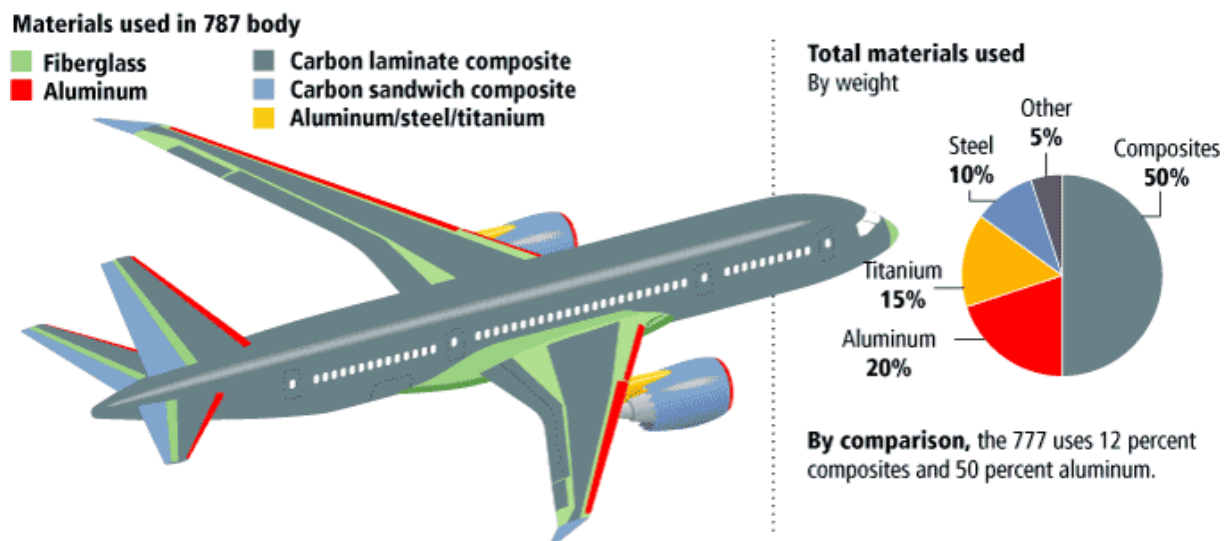


Figure 1.2. Boeing 787 Dreamliner materials airframe [28]

In these terms, the scope of this work essentially targets three focal points:

- I. To explore the design of new-kind of ultra-lightweight sandwich cores based on CFRP, with focus on the manufacturing of square-honeycomb cores.
- II. To characterise the designed core materials by typical loading cases, identifying their principal failure modes.
- III. To study the overall sandwich panel mechanical behaviour by bending.

1.2 Dissertation hypothesis

In theory, it would be possible to manufacture ultra-lightweight cores with complex geometries into a 3D square-honeycomb pattern based on CFRP, by combining cutting-edge designs and different out-of-autoclave (OOA) processing techniques.

The development of CFRP-based ultra-lightweight materials from 3D square-honeycomb or lattice-based cores for sandwich applications, would be mechanically superior and competitive with most commercially known materials.

By analysing typical loading cases such as compression, shear or bending, it would be possible to predict the properties of a sandwich core and/or a sandwich structure such as its stiffness and strength, by developing theoretical and numerical models, based on a representative unit repetitive cell, and employing the parent material's elastic properties.

Additionally, theoretical failure prediction models in a form of failure maps, can be contrasted by numerical models and then verified throughout series of quasi-static experimental tests, regarding to the typical loading cases.

The results of the experimental tests could be used as feedback for the analytical and numerical models for validation and further improvements through an iterative procedure.

1.3 Dissertation goals

1.3.1 Primary goals

The main objective of this work is to contribute to the research in the studies of design and the mechanical behavior of new cellular core materials for sandwich applications, by considering two different core approaches. The work focuses on the study of very low-density cores for sandwich applications, employing CFRP as base material, showing higher stiffnesses and strengths in contrast to their commercial counterparts.

1.3.2 Specific goals

The expansion of the state of knowledge which is intended with this dissertation is based on specific goals resumed in three main working packages:

1. Development of sandwich cores based on CFRP materials, as an alternative to the already known core-materials. Two approaches are studied as (i) 3D honeycombs cores based on CFRP plates; (ii) Lattices-cores based on CFRP rods. The main feature is to reach an ultra-lightweight core density. For case (i), also the manufacturing aspects are presented, including several known advanced

composite materials processing techniques such as the vacuum assisted resin infusion (VARI or VI) or the hot press method.

2. Investigation of the structural behaviour of the sandwich cores under typical loading cases. Study the relationship between the morphology of the cores and their mechanical properties, based on the unit cell's topologies and the elastic properties of the base material, for developing analytical and numerical models to predict the elastic properties and the failure modes of the structures obtained. In this sense, outlining the so-called "failure maps" to evaluate the failure behaviour of the material in advance. As a first stage, the work focuses on the study of cores' behaviour under out-of-plane compression and plate shear, and it is complemented with a four-point bending investigation, where eventually the whole sandwich assembly is evaluated. For bending evaluation, models based on lattice-cores are presented as case of study, later transferred to other core cases.
3. Experimental determination of the proposed materials properties by a series of quasi-static tests, based on the previously considered loading cases. The experimental data and the models' predictions are contrasted and correlated, providing feedback to validate and improve the models. A comparison to concurrent materials is provided and discussed, and final conclusions are promoted to consolidate the results.

1.4 Dissertation outline

The work is outlined in 8 chapters as follows:

Chapter 1 discusses the motivation, the hypothesis, the objectives and establishes the background of the dissertation.

Chapter 2 reviews the general aspects concerning fibre reinforced polymers, the materials processing methods of interest and the theoretical mechanical background issued to these materials.

Chapter 3 presents the state of the art of sandwich structures including concepts and types. In addition, the main loading cases are addressed with the different likely failure modes.

Chapter 4 describes the concept, design, and fabrication of novel ultra-light-weight sandwich cores such as the 3D-honeycomb cores based on CFRP laminates.

Micro and macro-mechanical models are presented for predicting the cores' stiffness and strength (including failure modes), while studying out-of-plane compression and plate-shear loading cases. The theoretical models are complemented by finite element simulations (FE) developed via commercial software FEMAP™ 10.3 with NX™ NASTRAN® [29], and later validated favourably by experimental tests.

Chapter 5 describes the concept and the design of ultra-lightweight BCC-like lattice cores based on CFRP rods. Analogously to Chapter 4, theoretical and numerical models for predicting the cores' elastic properties are provided for out-of-plane compression and plate-shear loading cases. Experimental tests are carried out for validating the models with very good correspondence.

Chapter 6 focuses on four-point bending studies of sandwich panels taking as case of study the lattice-based cores. The studies include theoretical models for predicting sandwich failure behaviour when increasing the skin thickness or varying core stiffness. FE simulations complement and give support to the theory. Experimental tests contrast and validate satisfactorily the models.

Chapter 7 analyses the competitiveness of the proposed materials, contrasting the work upon other research and commercial materials typically employed in sandwich cores. A summary of the conclusions gathered along the work is provided.

Chapter 8 summarizes the dissertation and suggests several enhancements for future work.

2 Composite materials: general aspects

The term "composite" (as a compound) in composite materials refers to the fact that two or more materials are combined on a macroscopic scale (visible to the naked eye) to form a third material with properties sought for a specific application [8]. The bonding between the matrix and the fibres occurs during the manufacturing process, with the creation of the interface that will have a fundamental influence on the mechanical properties of the material produced [9]. Fundamental features of composite materials are high strength, high stiffness, high elastic modulus, resistance to corrosion, impact, fatigue, wear, low weight, etc. Composites can be classified into four main types according to their morphology [8]:

- Composite materials reinforced with fibres, consisting in fibres within a matrix.
- Laminate composite materials, obtained from layers of one or more materials.
- Particulate composite materials, where particles are distributed in a matrix.
- Combinations of any or all the previous three.

In particular, Ashby [1] classified composite materials according to three broad categories: metallic, ceramic, or polymeric compounds, according to the base material of the matrix. The focus of this dissertation is set on those thermoset polymer matrix composite materials reinforced with synthetic fibres as carbon fibre reinforced polymers (CFRP), with an overlook to a potential application in passenger transportation, aerospace or other high performance uses.

2.1 Fibre reinforced polymers (FRP): main concepts

Fibre reinforced polymers (FRP) consist of continuous or discontinuous fibres, natural or synthetic, of high strength and high elastic modulus, embedded in and bonded to a matrix through an interface, which will determine the final behaviour of the composite under the acting stresses. The combination of both main components generates properties that could not be obtained with either of them acting separately. Generally speaking, the fibres carry the major portion of the loads, while the surrounding matrix keeps them in the desired location and orientation, acting as a load-transferring medium between the two and protecting them from environmental damage. Focusing

on long fibres, the basic building block of a compound fibre-matrix is the layer (or *lamina*) being a flat arrange of fibres in the matrix. The FRP are made from an assembly of layers to form a composite laminate. Commonly, the two typical flat layers are presented as shown in Figure 2.1, and the principal axes are exhibited parallel and perpendicular to the fibre directions [8]. Woven layers are made of fibres oriented along two perpendicular directions: the warp and the fill (or weft). In woven cloths, the fill yarns pass over and under the warp yarns, following different fixed patterns such as a plain weave (as in Figure 2.1.b), twill (each fil yarn pass over two warp yarns) or satin pattern (each fill yarn pass over four warp yarns). Due to their low density, fibre-reinforced polymers offer comparable or better mechanical properties to traditional metallic materials, exhibiting outstanding strength-to-density and modulus-to-density ratios and nowadays are in an increasing demand [8].

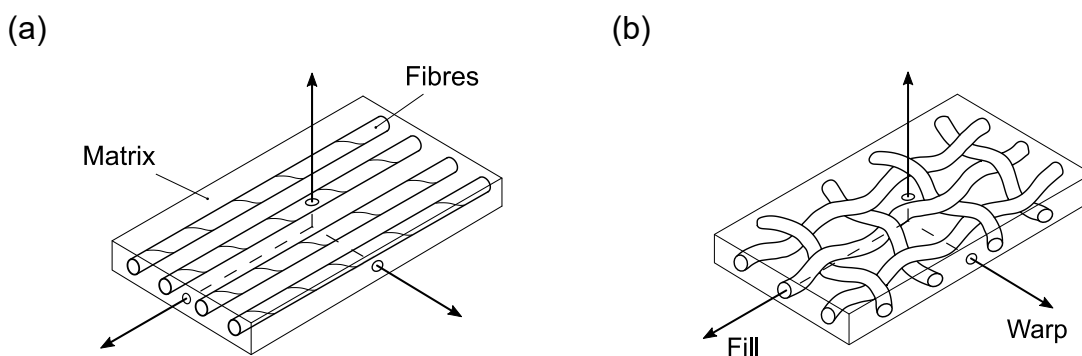


Figure 2.1. Two basic building blocks of a laminate. (a) Unidirectional. (b) Woven. [30]

2.1.1 Fibres

Fibres (synthetic or natural) are used as reinforcement for polymers because they present high mechanical properties as strength and stiffness, and low weight. Fibres yarns consist of thousands of filaments with diameters ranging from 5 to 15 microns and can be produced using textile machines. They are available as short or long fibres, depending on the production process. In addition, fabrics with long fibre arrangements can take the following forms: unidirectional (yarns, ribbons, or linear arrangements in fabric), bidirectional (woven or non-woven fabrics with fibres following two directions), three-dimensional or multidirectional (fabrics with fibres following more than two directions).

The main materials available as synthetic fibres are glass, aramid (polymeric), carbon, boron, and silicon carbide [9]. While the most common natural plant fibre base materials include one or more of the following: jute, sisal, hemp, coconut, oil palm, date palm, kenaf, ramie, pineapple leaf, cotton, flax, curagua, bamboo and rapeseed [31]. Synthetic fibres are the most widespread fibres such as glass fibres and those for high performance use such as carbon or aramid fibres [9,30,32–34], and a brief comparison example is made among a few type of fibres in the following section.

Since this work focuses on the use of carbon fibre fabrics, a general description of this reinforcement is provided in section 2.1.1.2.

2.1.1.1 Comparison of fibre properties

The main interest of the present dissertation is the development of high performance lightweight structures. Thus, the specific properties of the reinforcing materials are compared within this section, i.e., the tensile strength over density ratio as σ/ρ , and the Young's modulus over density ratio as E/ρ . The specific mechanical properties act as indicator of the effectiveness of the reinforcement fibre in weight-sensitive applications (material performance index, PI).

Table 2.1. Properties and indices of commonly used fibre reinforcements.

Type of fibre	Density (kgm ⁻³)	σ/ρ (MPa/kgm ⁻³)	E/ρ (MPa/kgm ⁻³)	Elongation at break (%)	Fibre diameter (µm)
E-glass	2500	1.36	29	4.8	10
S-glass	2440	1.97	35	5	10
Carbon T300	1760	2.07	140	1.4	7
Aramid Kevlar49	1440	2.49	90	2.8	11.9
Jute	1300 – 1450	0.30 – 0.53	10 – 18.9	1.16 – 1.5	25.2
Sisal	1450	0.32 – 0.44	6.4 – 15.1	3 – 7	50 - 200

Note: adapted from [8,9,32,35]

Table 2.1 summarises the mechanical behaviour of the fibres commonly used in polymer composites, for comparative purposes. In order to evaluate the performance of materials for a given application, materials selection indices are of high interest [1]. It can be seen that carbon fibres present the best material index for stiffness, almost five times the E-glass value. The lowest material indices are shown by the natural fibres

presenting, for instance, about one tenth the carbon fibres' stiffness value, although still having comparable specific strength indices to the others.

The mechanical properties are not only relevant from the point of view of load-bearing capacity, but also its ability to maintain its shape when used as reinforcement. The proper selection of fibre type, volume fraction, length and orientation should be considered as characteristics that will influence the resulting composite laminate. Some of the most relevant properties are density, strength and modulus (in tension or compression), fatigue, cost, etc. [32].

2.1.1.2 Carbon fibres

The exploration for alternatives to glass fibres began in the late 1950s, to fulfill the need of parts and components having high stiffness and low weight, the search for new materials, to obtain high strength and rigidity, strong atomic bonds such as covalent (even superior to metallic ones) was needed. Since 1971, poly-acrylonitrile (PAN) textile fibre has been used as a precursor of fibre and has become so popular that more than 90% of the market is based on it. The advantages of the raw material PAN are that it has a carbon yield of 55% by weight and very high modulus of elasticity and tensile strengths, which are adjustable depending on the processing variables.

The process of obtaining PAN fibres generally consists of oxidizing these base materials at 300°C and then carbonizing them at 1500°C in an inert atmosphere during another stage. Structurally, with the removal of oxygen and nitrogen, the filaments contain mostly carbon following an aromatic ring-like arrangement of parallel planes (graphite-like). The high longitudinal mechanical properties are derived from the graphitic shape (e. g. exhibiting an elastic modulus of 1050 GPa in parallel direction). The crystalline structure of an elementary carbon cell is shown schematically in Figure 2.2.a. On the same plane, each vertex of a hexagon has one carbon bonded to three others by a covalent bond; whereas on parallel planes there are only (weak) van der Waals forces, being carbon fibres highly anisotropic. Figure 2.2.b shows a growing fibre also presenting the arrangement of hexagon chains arrangements. The resulting filaments are of glossy black colour.

There is a wide variety of available fibres that, according to the manufacturing process, temperature, time and spinning tension, it is possible to vary the tensile modulus ranging from 207 GPa to 1035GPa. The same is valid for the tensile strength

since the high processing temperature causes a higher ordering of the crystallographic planes (Figure 2.3).

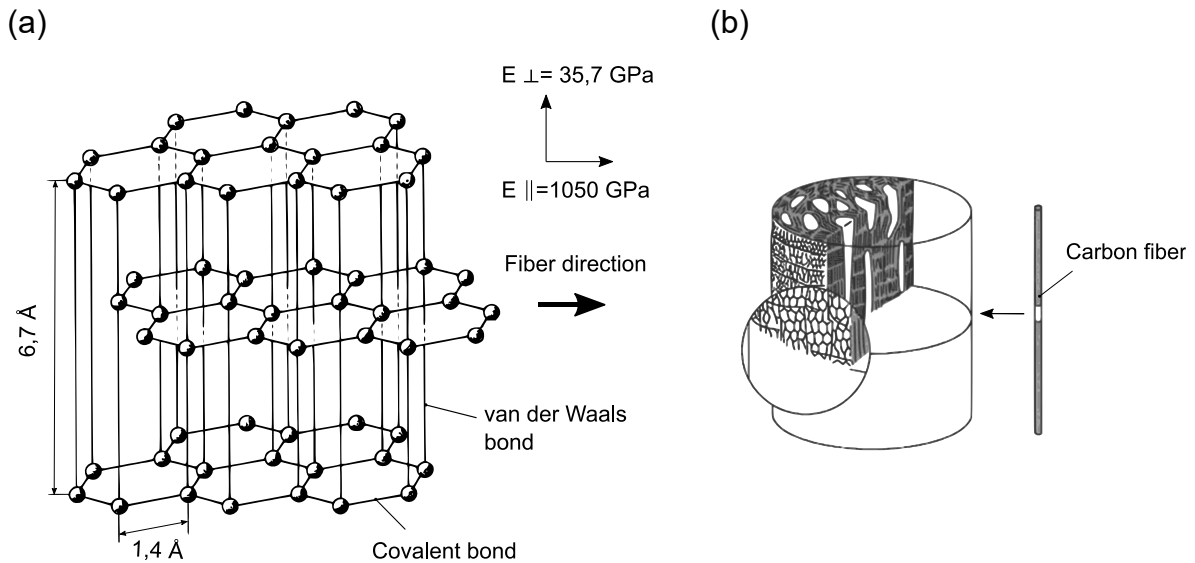


Figure 2.2. Carbon fibre inner structures. (a) Elementary cell of a graphite lattice [33]. (b) Example of a carbon fibre yarn structure [9]

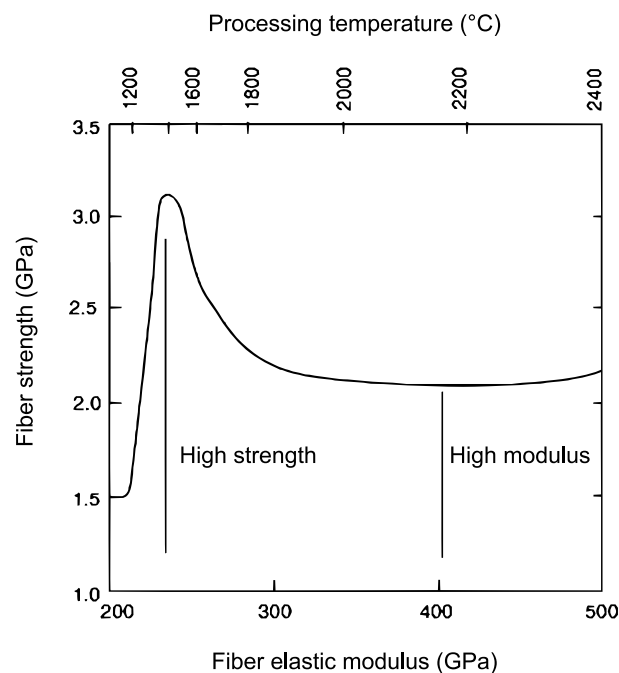


Figure 2.3. The elastic modulus and tensile strength of PAN carbon fibres [36]

Therefore, carbon fibre properties can be adjusted by controlling the processing variables which, at the same time, affects the fibres final cost. With PAN as a precursor, it is possible to categorise the resulting carbon fibres into four broad groups as: high

tensile strength (HT) one of the most widespread fibre types, intermediate modulus (IM), high elastic modulus (HM) and ultra-high elastic modulus (UHM). Table 2.2 summarizes the most significant properties of the four mentioned standard PAN-based carbon fibre types.

Table 2.2. Properties of standard PAN-based carbon fibres [33]

<i>Type of carbon fibres</i>	Fibre density gcm ⁻³	Tensile strength GPa	Tensile module GPa	Compressive strength GPa	Elongation at break %	Fibre diameter µm
HT	1.74	3.60	240	2.50	1.50	7
IM	1.80	5.60	290	4.20	1.93	5
HM	1.83	2.30	400	1.50	0.57	6.5
UMS	1.85	3.60	550	1.80	0.65	5

The advantages of carbon fibres are, as previous mentioned, their very high strength-to-weight ratios, as well as the elastic modulus-to-weight ratios, very low coefficient of thermal expansion (which provides good dimensional stability), high resistance to fatigue and high thermal. The disadvantages are its low deformation at break, low resistance to impact and high electrical conductivity, which could cause short circuits in non-insulated electrical machinery. Their high cost has conditioned them mostly to high performance applications, mainly in the aerospace sector, but also in passenger and competition vehicles, boats and certain sporting goods, where low weight plays a significant role.

2.1.2 Thermoset polymer matrix

There are many matrix materials that can be used in combination with fibres to produce a composite material with desired features such as very high strength and stiffness and still present a low density [8]. As previously introduced, the common matrix materials can be polymers, metals, or ceramics, and within the polymers two broad categories emerge as thermoplastic or thermoset based [1,8,32]. Here, the thermoset matrices are addressed.

The primary roles of a matrix in a composite material can be mentioned as follows: (1) to hold the fibres in place, (2) to transfer stresses between the fibres, (3) to provide a barrier against an adverse environment, such as chemicals and moisture; (4) to protect the fibre surface from mechanical degradation (e.g., by abrasion, erosion,

etc.). The matrix plays a secondary role if the material is subjected to tensile stresses, because the fibres act as "wires" and bear most of the loads. On the other hand, if the stresses are applied in compression, the matrix provides the material with lateral support against the possibility of fibre buckling, greatly influencing the compressive strength of the composite. They also have an influence on interlaminar loads (i.e., between layers of the material if it is multi-layered), which is relevant when the material is subjected to bending or shear loads. In-plane shear strength (e.g., in a pure shear loading case such as torsion of a beam or plate shear) is also influenced by the characteristics of the matrix. In addition, the manufacturing of the component directly affects its final mechanical performance and this will strongly depend on the processing variables used when incorporating the matrix into the fibrous reinforcement (for example: initial temperature of the resin (that controls its viscosity and cure kinetics) and curing cycle configuration, are common variables that must be reported when manufacturing components, e.g., for the aerospace industry) [32].

The most used polymeric matrices in combination with long continuous fibres are epoxy, vinylester and polyester resins (ranked in order of highest to lowest cost and according to their mechanical properties, the most expensive being the best performing). The former is implemented in aeronautical and aerospace applications where low shrinkage, excellent adhesion, better mechanical properties and chemical resistance are required [37], while the latter two are mostly used in automotive, marine and electrical applications. The interest of this thesis lies in producing high mechanical performance and low weight materials, and therefore, the incorporation of continuous and long carbon fibres for reinforcement of epoxy thermoset-based polymeric matrix has been selected.

Among the polymeric structures, three main forms are recognized: linear, branched, or cross-linked (Figure 2.4). A linear polymer is classified as long-chain molecules containing one or more repeating unit of atoms joined together by strong covalent bond along the chain (such as in thermoplastic polymers [32]). The individual long molecules are not chemically joined, but they are held together by secondary bonds such as van der Waals bonds and hydrogen bonds. They present much lower overall strength and stiffness than the other two structures exhibited. Branched polymers have a primary polymer chain with other polymer chains attached to it like branches in a tree. Cross-linked polymers have a long number of three-dimensional polymer chains strongly interconnected by chemical bonds (primary covalent bonds), presenting the

highest mechanical strength and stiffness, compared to linear or branched polymers [30]. With a few exceptions, thermoplastics are usually linear or branched polymers; while thermosets are cross-linked polymers [38].

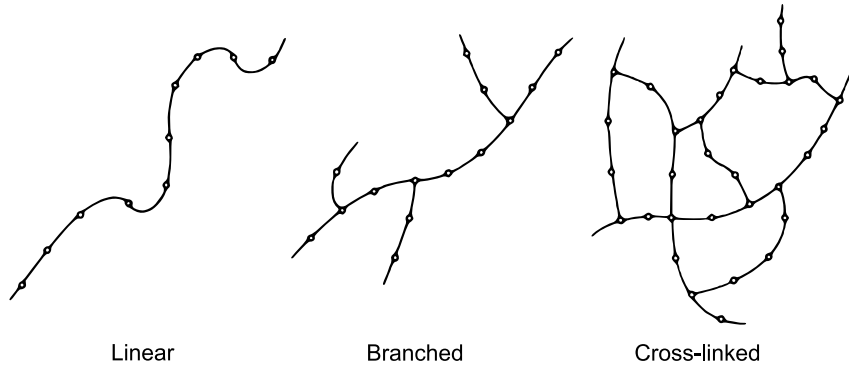


Figure 2.4. Schematic representation of polymeric structures [30]

Thermoset polymers are obtained from temperature-favoured chemical reactions, which will bring the system to a certain percentage of cure (conversion). The longer and more branching the polymer has in its main chains, the higher the probability is that the branches will connect [38]. During the curing process, the polymer is initially a low viscosity liquid (comprised of linear independent polymer chains), and it is transformed into a solid material comprised of a large, cross-linked molecule (as a network). Although these materials exhibit rigid-rubber behaviour, they cannot flow as thermoplastics do above their glass transition temperature (thermoplastics have secondary bonding forces between molecules). Therefore, they cannot be remoulded as a fluid, even if heated sufficiently, since this will only degrade the polymer by breaking the covalent bonds. Thus, crosslinking reactions can be initiated in two ways: (1) starting the reaction with highly-functional monomers, (2) creating the crosslinks between already formed linear or branched monomers (through reaction and curing after) as for example, curing reactions in epoxy or polyester resins [38]. Due to their low initial viscosity, thermoset matrices allow moulding to be done at room temperature during the processing of the composite material.

In the selection of a matrix for high-performance composite materials based on FRP, the primary consideration lies on its basic mechanical properties such as its elastic modulus, strength and toughness once cured. A list of resins' properties commonly used in the material processing of fibre-reinforced polymers (such in *liquid composite moulding techniques*) is presented in Table 2.3.

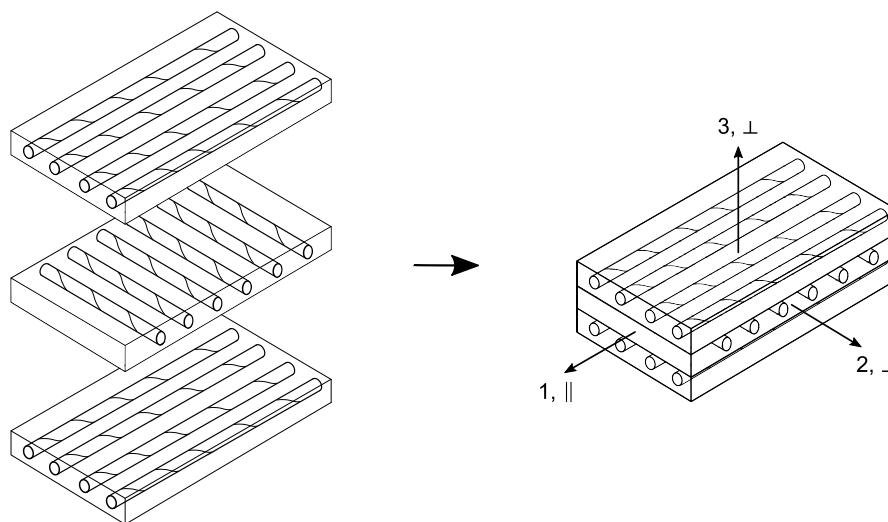
Table 2.3. Properties of commonly used thermoset matrices [9,39,40]

Type of resin	Density kgm ⁻³	E MPa	G MPa	σ MPa	ν	Elongation at break %	Heat distortion / limit °C
Epoxy	1200	3300	1600	130	0.4	2	90 – 200
Phenolic	1300	3000	1100	70	0.4	2,5	120 – 200
Polyester	1200	3300	1400	80	0.4	2,5	60 – 200
Vinylester	1150	3300	1410	75	0.36	7	≈ 100

2.2 Properties and analytical approaches of FRP

In this section, the general concepts for the mechanical study of the properties of FRPs will be established. In the corresponding sections, more in-depth analyses will be carried out according to the case of study.

In practice, the macroscopic description of the structural-mechanical behaviour of an FRP-laminate (Figure 2.5) is based on the study of individual unidirectional layers (or woven layers, then individualized) and, at the same time, the individual layer depends on the interaction between the base components.

**Figure 2.5.** Multi-layer composite consisting of individual layers. (Adapted from [30])

The fibre-matrix interactions are evaluated following different aspects based on the component proportion and distribution over the cross-sectional area within the composite (see *fibre packing models* [30,34]).

The mechanics of fibre-reinforced composite materials [30,32] are studied on two levels:

1. *Micromechanical* approaches: evaluates the interaction of components on a microscopic scale. In general, the equations that describe the elastic and thermal characteristics of a layer are based on micromechanical approaches.
2. *Macromechanical* approaches: where the response of a fibre-reinforced composite material to mechanical and thermal loads is studied, considering the material as homogeneous on a macroscopic scale, in particular its cross-section and fibre distribution [41]. Here, orthotropic elasticity equations are used to calculate stresses, strains, and deflections.

2.2.1 Micromechanics

To evaluate the fibre-matrix interactions, the following assumptions are considered [32]:

- a. The fibres are evenly distributed.
- b. There is a perfect bonding between the fibres and the matrix.
- c. The matrix has no voids.
- d. The applied force is only parallel or normal to the direction of the fibre.
- e. The sheet has no residual stresses
- f. Fibres and matrix behave as linearly elastic materials.

The aim of the micromechanical approaches deals with the determination of the elastic moduli or the stiffnesses or compliances of a FRP in terms of the properties of the constituent materials [30]. Furthermore, as stated at the beginning of this chapter, the objective of the composite material is to obtain a new material with the advantages of each individual component to generate a better one. Therefore, the proportions of each component are of vital importance for the final properties of our composite material, in this case taken as a unidirectional (UD) layer (or UD-laminate of one layer).

In particular, the proportion of fibres has a direct impact on the strength and stiffness of the material. Thus, the fibre volume fraction φ_f is one of the most important design parameters and it can be calculated by the fibre volume, the relative weight (fibre or matrix over total laminate weight), the relative area or the relative thickness, (relative to the property of the total composite). The fibre volume fraction can be estimated with Equation (2.1), where factor n is the number of layers (here as UD-laminate is equal to the unit), M_f is the areal density of the dry fibres layer (also textile weight), ρ_f is the fibre density and t_{comp} is the composite thickness.

$$\varphi_f = n \frac{M_f}{\rho_f t_{comp}} \quad (2.1)$$

Regarding fibre volume fraction of FRP in the aerospace industry, a standard value is 60%, with an upper limit of 65% (a higher volume would imply a lack of fibre impregnation with the matrix). This percentage by volume varies according to the manufacturing method of the part and the subsequent application [32,34].

The fibre volume fraction and the fibre orientation influence the UD-layer behaviour. To study the UD-layer elastic properties it is necessary first to identify whether the external forces are applied normal (2-direction or 3-direction) or parallel (1-direction) to fibre orientation (Figure 2.6).

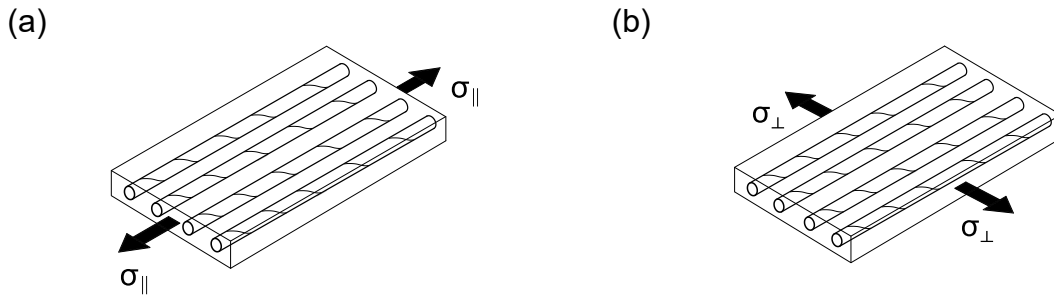


Figure 2.6. UD-layer loading. (a) Longitudinal. (b) Transverse.

Then, the main properties are defined according to the parallel and perpendicular directions as follows [34].

2.2.1.1 Stresses applied to a UD-layer in parallel orientation

If the forces are applied over the parallel orientation of the fibres in a UD-layer (commonly identify as the 1-direction, as in Figure 2.6.a) considering previous assumptions, the following balance of forces, stresses and strains are valid [34]:

$$F_{\parallel} = F_f + F_m \Rightarrow \sigma_{\parallel} A_{comp} = \sigma_f A_f + \sigma_m A_m \quad (2.2)$$

$$\frac{\Delta l_{comp}}{l_{comp}} = \varepsilon_{\parallel} = \varepsilon_f = \varepsilon_m \quad (2.3)$$

$$\sigma_f = E_f \varepsilon_f \quad ; \quad \sigma_m = E_m \varepsilon_m \quad (2.4)$$

The above stresses and strains (subscript *m*: represent the matrix; *f*: the fibres; and *comp*: the composite) are then replaced and equated into Eq. (2.5). Parameter l_{comp} represents the length of the composite and Δl_{comp} the length of the deformed composite after applying the parallel stress. Moreover, if the parameters are specified in

terms of the fibre volume fraction φ_f , the elastic modulus of the UD-layer composite E_{\parallel} is given by Eq. (2.6), by means of a *rule of mixture*.

$$E_{\parallel} \varepsilon_{\parallel} A_{comp} = (E_{f\parallel} A_f + E_m A_m) \varepsilon_{\parallel} \quad (2.5)$$

$$E_{\parallel} = E_{f\parallel} \varphi_f + E_m (1 - \varphi_f) \quad (2.6)$$

Eq. (2.6) shows that the parallel modulus of a composite UD-layer is in an intermediate value between the modulus of the parallel fibre and the matrix modulus [32].

2.2.1.2 Stresses applied to a UD-layer in perpendicular orientation

Similarly, the study can be carried out in the transverse direction (i.e., perpendicular to the fibres). Assuming that the width of the UD-laminate is W_{comp} and after applying the perpendicular stress, the composite deformation ΔW_{comp} is reached as the sum of the deformation of its constituents, the following equations can be resumed [32]:

$$\sigma_{\perp} = \sigma_m = \sigma_f \quad (2.7)$$

$$\Delta W_{comp} = \Delta W_f + \Delta W_m \quad (2.8)$$

$$\varepsilon_{\perp} W_{comp} = \varepsilon_{f\perp} W_f + \varepsilon_m W_m \quad (2.9)$$

Dividing by W_{comp} , it is possible to rewrite Eq.(2.9) in terms of the fibres and matrix fractions as

$$\varepsilon_{\perp} = \varepsilon_{f\perp} \varphi_f + \varepsilon_m \varphi_m \quad (2.10)$$

Then, specifying Eq. in terms of the stresses as

$$\frac{\sigma_{\perp}}{E_{\perp}} = \frac{\sigma_f}{E_{f\perp}} \varphi_f + \frac{\sigma_m}{E_m} \varphi_m \quad (2.11)$$

Rearranging Eq. (2.11), while assuming $\sigma_f = \sigma_m = \sigma_{\perp}$, the transverse modulus of the UD-laminate composite E_{\perp} (obtained also by a rule of mixtures) is written as

$$E_{\perp} = \frac{E_{f\perp} E_m}{E_{f\perp} (1 - \varphi_f) + E_m \varphi_f} \quad (2.12)$$

The last equation is obtained while assuming many simplifications (e. g., no lateral contractions, no imperfections, sufficient and homogeneous adhesion) and in practice the E_{\perp} may vary from the theoretical approach given by Eq. (2.12). Hence, many authors have proposed many more complex approaches (for example, while

employing different fibre packing models) to achieve more accurate values [42,43]. As an example, by using empirical and theoretical models and considering the contraction of the matrix as the Poisson's modulus ν_m , the transverse elastic modulus E_{\perp} according to Puck [44] is presented in Eq. (2.13).

$$E_{\perp} = \frac{E_m}{1 - \nu_m^2} \frac{1 + 0.85 \varphi_f^2}{(1 - \varphi_f)^{1.25} + \frac{E_m}{(1 - \nu_m^2)E_{f\perp}} \varphi_f} \quad (2.13)$$

2.2.1.3 Properties of the UD-layer in perpendicular – parallel orientation

Considering Figure 2.7 as the layer coordinate system, the transverse-longitudinal shear modulus $G_{\perp\parallel}$ can be determined analogously to the modulus of elasticity E_{\perp} [9], as

$$G_{\perp\parallel} = G_m \frac{1}{(1 - \varphi_f) + \frac{G_m}{G_{f\perp}} \varphi_f} \quad (2.14)$$

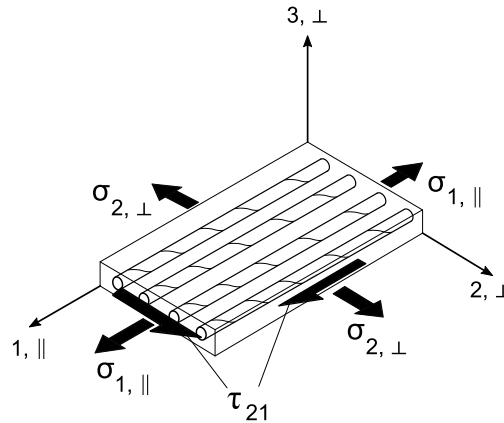


Figure 2.7. UD-layer coordinate system in the directions of its orthotropic axes

Furthermore, the above equation was also improved by many authors using semi-empirical approaches. Förster [43], published a semi-empirical equation for the transverse longitudinal shear modulus as Eq. (2.15).

$$G_{\perp\parallel} = G_m \frac{1 + 0.4 \varphi_f^{0.5}}{(1 - \varphi_f)^{1.45} + \frac{G_m}{G_{f\perp}} \varphi_f} \quad (2.15)$$

By using the rule of mixtures, the longitudinal and transverse expansions of the UD-layer material (i.e., Poisson's ratio in parallel and perpendicular orientations) is given by Eq. (2.16) considering the Poisson's ratio of the fiber f and the matrix m [30,34].

$$v_{\perp\parallel} = \varphi_f v_{f\perp\parallel} + (1 - \varphi_f) v_m \quad (2.16)$$

It is important to note that the Poisson's moduli in the perpendicular – parallel and, parallel – perpendicular directions are not independent [34]. Both are coupled by Eq. (2.17).

$$\frac{v_{\perp\parallel}}{E_{\perp}} = \frac{v_{\parallel\perp}}{E_{\parallel}} \quad (2.17)$$

This work is focused on multi-laminate composites, which are still thin-walled materials having in average, less than 1.25 mm thickness. Therefore, the micromechanically derived basic elastic quantities obtained in this section are sufficient to determine the elastic law for the plane state of stresses, i.e., when $\sigma_3 = 0$. The influence of thermal, humidity (so-called *hygrothermal effects*) or contractions effects of the matrix volume exceed the aims of this project and are not considered.

2.2.2 Macromechanics

Macromechanical approaches are used to study the behaviour of a multi-layer laminate with different orientations (Figure 2.5). Besides the direct experimental tests for determining the characteristic values of the laminate, another verified way consists of composing the material mathematically from materials laws of the individual layers knowing in advance the behaviour of each layer in different orientation regarding to the principal material directions [8,9,34,41].

As a result, the UD-laminate is idealized macroscopically as a very thin homogeneous anisotropic element allowing the study as a plane stress state ($\sigma_3 = 0$; additionally, the shear stresses $\tau_{23} = \tau_{32} = 0$).

The following assumptions are required for the studies [8,41]:

- a. The fibre orientation is exact.
- b. Fibres and matrix behave as linearly elastic materials (i.e., superposition principle does apply).
- c. Deformation hypothesis according to Kirchhoff's plate theory ($\gamma_{23} = \gamma_{32} = 0$; and the normal vector to the layers remain normal after deformation).
- d. The layers are perfectly bonded.
- e. The displacements are small.

2.2.2.1 Classical lamination theory

For studying the mechanics of a structural multi-laminate, the classical lamination theory (CLT) is implemented and consists of mechanical studies of stresses and deformations applied to a two-dimensional body problem. On the one hand, the stress-strain behaviour of an individual sheet is analysed, and it is extended to the other sheets, considering the orientation angles of the fibres. On the other hand, the laminate stiffnesses are related to the strains and curvatures [8].

2.2.2.1.1 Material elastic law for a UD-layer

Considering an orthotropic layer material (there are three orthogonally oriented planes of symmetry), the stress and strains relations under plane stresses according to the principal material coordinates are given by Eq. (2.18) [8,41].

$$\begin{bmatrix} \sigma_{11} \\ \sigma_{22} \\ \tau_{21} \end{bmatrix} = \begin{bmatrix} Q_{11} & Q_{12} & 0 \\ Q_{21} & Q_{22} & 0 \\ 0 & 0 & Q_{66} \end{bmatrix} \cdot \begin{bmatrix} \varepsilon_{11} \\ \varepsilon_{22} \\ \gamma_{21} \end{bmatrix} \quad (2.18)$$

In which

$$Q_{ii} = \frac{E_{ii}}{1 - \nu_{ij}\nu_{ji}} \quad \dots \quad i = 1, 2 \quad (2.19)$$

$$Q_{66} = G_{12} \quad (2.20)$$

$$Q_{ij} = \frac{\nu_{ji}E_{ii}}{1 - \nu_{ij}\nu_{ji}} \quad \dots \quad i = 1, 2 \quad (2.21)$$

$$\{\sigma\}_{1,2} = [Q]_{1,2} \cdot \{\varepsilon\}_{1,2} \quad (2.22)$$

Eq. (2.22) is the reduced form of Eq. (2.18) the term $[Q]$ is also known as the “reduced” stiffness matrix of the material. Since there is no deformation restriction in the thickness direction in the plane stress state, the stiffness in the plane is then called reduced stiffness [8,34].

If the coordinates are not the principal coordinates in the plane of the layer, its necessary to convert one coordinate system as the local coordinate system (lamina) by 1-, 2- and 3-directions, into another global coordinate system defined by x-, y-, z- direction, via a polar transformation which graphically is represented by the Mohr's circle [8,34]. Then, the stresses are defined by Eq. (2.23). The term $[\bar{Q}]$ denotes the transformed reduced stiffnesses. This case normally occurs when the individual UD-

layers in a multi-laminate are arranged at different fibre angles α to those defined as principal for obtaining desired material properties (for example, required stiffnesses or strengths). To be able to convert stresses and strains from one coordinate system to other, the transformation relationships are obtained by using the Mohr's circle geometry, from which a transformation matrix is created. For further details about the transformation graphical approach, see references [8,41].

$$\begin{bmatrix} \sigma_x \\ \sigma_y \\ \tau_{xy} \end{bmatrix} = \begin{bmatrix} \bar{Q}_{11} & \bar{Q}_{12} & \bar{Q}_{16} \\ \bar{Q}_{12} & \bar{Q}_{22} & \bar{Q}_{26} \\ \bar{Q}_{16} & \bar{Q}_{26} & \bar{Q}_{66} \end{bmatrix} \cdot \begin{bmatrix} \varepsilon_x \\ \varepsilon_y \\ \gamma_{xy} \end{bmatrix} \quad (2.23)$$

In which

$$\bar{Q}_{11} = Q_{11} \cos^4 \alpha + 2(Q_{12} + 2Q_{66}) \sin^2 \alpha \cos^2 \alpha + Q_{22} \sin^4 \alpha \quad (2.24)$$

$$\bar{Q}_{12} = Q_{11} + Q_{22} - 4Q_{66} \sin^2 \alpha \cos^2 \alpha + Q_{12}(\sin^4 \alpha + \cos^4 \alpha) \quad (2.25)$$

$$\bar{Q}_{22} = Q_{11} \sin^4 \alpha + (Q_{12} - 2Q_{66}) \sin^2 \alpha \cos^2 \alpha + Q_{22} \cos^4 \alpha \quad (2.26)$$

$$\bar{Q}_{16} = (Q_{11} + Q_{12} - 2Q_{66}) \sin \alpha \cos^3 \alpha + (Q_{12} - Q_{22} + 2Q_{66}) \sin^3 \alpha \cos \alpha \quad (2.27)$$

$$\bar{Q}_{26} = (Q_{11} + Q_{12} - 2Q_{66}) \sin^3 \alpha \cos \alpha + (Q_{12} - Q_{22} + 2Q_{66}) \sin \alpha \cos^3 \alpha \quad (2.28)$$

$$\bar{Q}_{66} = (Q_{11} + Q_{12} - 2Q_{12} - 2Q_{66}) \sin^2 \alpha \cos^2 \alpha + Q_{66}(\sin^4 \alpha + \cos^4 \alpha) \quad (2.29)$$

It is important to remark that the above cases considered the material as a single plane orthotropic layer in two-dimensions. The case for three-dimensions deals with nine independent constants (note the subscript of each $[\bar{Q}]$ terms above).

2.2.2.1.2 Material elastic law for a multi-layer material

Fibre composite structures typically require supporting loads in different directions, so different fibre directions are often used to optimize the material properties. The CLT is used to predict the mechanical behaviour of a multilayer material by building its material elasticity law from the elasticity laws of the individual layers. Additionally, it determines the distortions and stresses of the individual layers through a layer-by-layer stress analysis. As previously presented, the laminate is assembled by stacking oriented laminas into a form of a plate or a shell. In contrast to the lamina, the laminate has a finite thickness and therefore a flexural rigidity.

Then, the laminate can be studied as wall elements, for the normal and shear loads applied (\hat{N}) over the laminate width b_l as $\{\hat{n}\} = \hat{N}/b_l$ (Figure 2.8.a); and as plate elements, for the moments applied (\hat{M}) over the laminate width $\{\hat{m}\} = \hat{M}/b_l$ (Figure 2.8.b) [34]. The superscript “^” denotes the entire laminate.

A reference plane of an n -layered laminate is selected to describe the strains (Figure 2.8.c). The laminate's total thickness is $t = 2Z_0$.

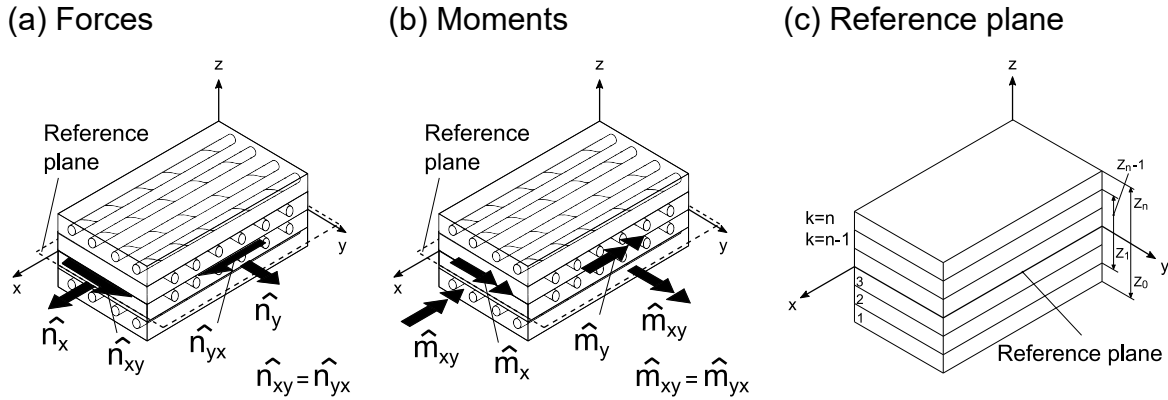


Figure 2.8. Scheme of forces and moments acting on a laminate, and reference plane

For each layer a force-moment equilibrium can be considered. Since the thickness of the laminate is inhomogeneous, the integration of internal forces can only take place over the thickness of the respective individual layer. Then, the internal forces or stresses added up in layers, considering as reference scheme. For the laminate, the equilibrium of forces and moments are given in Eq. (2.30) and Eq. (2.31).

$$\{\hat{n}\} = \sum_{k=1}^n \int_{Z_{k-1}}^{Z_k} \{\sigma\}_k \cdot dz \quad (2.30)$$

$$\{\hat{m}\} = \sum_{k=1}^n \int_{Z_{k-1}}^{Z_k} \{\sigma\}_k \cdot z \cdot dz \quad (2.31)$$

Then Eq. (2.22) is written as Eq. (2.32) for each “k” layer and employing the reduced transformed stiffness.

$$\{\sigma\}_k = [\bar{Q}]_k \cdot \{\varepsilon\}_k \quad (2.32)$$

The straining over the cross-section is resumed by Eq. (2.33), considering the distance z to the reference plane (subscript “0”) and the curvature κ . Its reduced form is shown in Eq. (2.34). Usually, laminates are laid-up symmetrically to the reference

plane to avoid undesired distortions, for example, due to internal hygrothermal stresses.

$$\begin{Bmatrix} \hat{\varepsilon}_x(z) \\ \hat{\varepsilon}_y(z) \\ \hat{\gamma}_{xy}(z) \end{Bmatrix} = \begin{Bmatrix} \varepsilon_x \\ \varepsilon_y \\ \gamma_{xy} \end{Bmatrix}_0 + z \cdot \begin{Bmatrix} \kappa_x \\ \kappa_y \\ \kappa_{xy} \end{Bmatrix}_0 \quad (2.33)$$

$$\{\hat{\varepsilon}\} = \{\varepsilon\}_0 + z \cdot \{\kappa\}_0 \quad (2.34)$$

Combining Eq. (2.32) and (2.34) into Eq. (2.30) and Eq. (2.31), the relation between forces and moments with the strains and stresses are given in Eq. (2.35) and Eq. (2.36).

$$\{\hat{n}\} = \sum_{k=1}^n [\bar{Q}]_k \cdot \left[\int_{Z_{k-1}}^{Z_k} \{\varepsilon\}_0 \cdot dz + \int_{Z_{k-1}}^{Z_k} \{\kappa\}_0 \cdot z \cdot dz \right] \quad (2.35)$$

$$\{\hat{m}\} = \sum_{k=1}^n [\bar{Q}]_k \cdot \left[\int_{Z_{k-1}}^{Z_k} \{\varepsilon\}_0 \cdot dz + \int_{Z_{k-1}}^{Z_k} \{\kappa\}_0 \cdot z^2 \cdot dz \right] \quad (2.36)$$

Then, the integrals for the forces and moments can be solved over the thickness of the individual layers, and thus, Eq. (2.35) and Eq. (2.36) can also be written as Eq. (2.37) and Eq. (2.38), respectively.

$$\{\hat{n}\} = \sum_{k=1}^n \left[[\bar{Q}]_k \cdot (Z_k - Z_{k-1}) \cdot \varepsilon_0 + [\bar{Q}]_k \cdot \frac{1}{2} (Z_k^2 - Z_{k-1}^2) \cdot \kappa_0 \right] \quad (2.37)$$

$$\{\hat{m}\} = \sum_{k=1}^n \left[[\bar{Q}]_k \cdot \frac{1}{2} (Z_k^2 - Z_{k-1}^2) \cdot \varepsilon_0 + [\bar{Q}]_k \cdot \frac{1}{3} (Z_k^3 - Z_{k-1}^3) \cdot \kappa_0 \right] \quad (2.38)$$

The above equations can be expressed as Eq. (2.39), which is known as the *Material elastic law for a multi-layer material*.

$$\begin{Bmatrix} \hat{n}_x \\ \hat{n}_y \\ \hat{n}_{xy} \\ \hat{m}_x \\ \hat{m}_y \\ \hat{m}_{xy} \end{Bmatrix} = \begin{bmatrix} A_{11} & A_{12} & A_{16} & B_{11} & B_{12} & B_{16} \\ A_{12} & A_{22} & A_{26} & B_{12} & B_{22} & B_{26} \\ A_{16} & A_{26} & A_{66} & B_{16} & B_{26} & B_{66} \\ B_{11} & B_{12} & B_{16} & D_{11} & D_{12} & D_{16} \\ B_{12} & B_{22} & B_{26} & D_{12} & D_{22} & D_{26} \\ B_{16} & B_{26} & B_{66} & D_{16} & D_{26} & D_{66} \end{bmatrix} \cdot \begin{Bmatrix} \varepsilon_x \\ \varepsilon_y \\ \gamma_{xy} \\ \kappa_x \\ \kappa_y \\ \kappa_{xy} \end{Bmatrix}_0 \quad (2.39)$$

The matrixes [A], [B] and [D] are written in a resumed form as Eq.(2.40). The [A]-matrix is also known as the extensional stiffness matrix, the [B]-matrix is known as the bending-extension coupling stiffnesses, and the [D]-matrix is called the bending

stiffness. [B] and [D]-matrix are considered when bending stresses also act on the laminate.

$$[A, B, D] = \sum_{k=1}^n [\bar{Q}]_{ij,k} \cdot \left[(t_k), \left(t_k \left(z_k - \frac{t_k}{2} \right) \right), \left(\frac{t_k^3}{12} + t_k \left(z_k - \frac{t_k}{2} \right)^2 \right) \right] \quad (2.40)$$

In this work, multilayer woven composite materials oriented at $[0/90]^\circ$ are employed, and only UD-layers oriented parallel or perpendicular to the load direction are considered. Furthermore, the loading cases, only contemplate compression, tension, and shear in the plane, as it is analysed in subsequent chapters. Employing orthotropic materials means that there is no deformation-displacement coupling (that is $[B] = 0$); that is, the normal stresses σ_{11} or σ_{22} do not generate any distortion γ_{21} . Likewise shear stresses τ_{21} do not generate any strain ϵ_{11} or ϵ_{22} . This means that the respective polar transformation and the load cases evaluated according to CLT are only covered for the particular cases presented within this work.

The behaviour of woven fabric composites is studied in a similar manner with CLT, although recent studies showed improved accuracy while calculating the laminate material properties [45–48]. The main discrepancy between the traditional CLT and the improved CLT models upon woven fabrics lies in the simplifications made on the first, that considers the woven material as two balanced plies (50-50) of unidirectional reinforcement separately, regardless of the woven waviness [9]. The curvature of the fibre during the weaving operation, and the fabric thickness have an evident effect on the elastic properties such as stiffness and strength of the final manufactured material (for example, by reducing them around 5 up to 15%, depending on the employed fabric type [49]). Also the gap between the yarns depicts a negative effect on the material properties, but less significant than the waviness [50]. If the fabrics present higher account of fibres filament per yarn (tow size), the waviness effect is larger and must be considered on the calculations. For the present work, the waviness effect is dismissed due to the thinness of the laminate and the woven material tow size (3k).

2.2.2.1.3 Engineering constants of the multilayer laminate

In practice, the so-called engineering constants are of technological interest for the materials design. For the case of FRP, that means to find the elastic moduli and Poisson's ratio of the entire laminate. The constants can be determined experimentally

under uniaxial loading, for example by tensile tests, or can be calculated directly from the materials' law of elasticity by following CLT, only for normal stresses [34,51].

The law of elasticity of the multi-layer composite material while analysing the displacements field in a uniaxial loading case, is given by Eq. (2.41) obtained from Eq. (2.39) [34]. Solving Eq. (2.41) for the strain in x-direction, Eq. (2.42) is obtained.

$$\{\hat{n}\} = [A]\{\hat{\varepsilon}\} \quad (2.41)$$

$$\hat{\varepsilon}_x = (A^{-1})_{11} \cdot \hat{n}_x \quad (2.42)$$

$$\hat{\varepsilon} = \frac{\hat{\sigma}}{\hat{E}} \quad (2.43)$$

Disregarding the curvatures in Eq.(2.37) and combining it with Eq. (2.42), and employing the material law of elasticity (Hooke's law) as Eq. (2.43), then the elastic modulus of the multi-layer composite in x-direction is obtained as Eq. (2.44).

$$\hat{E}_x = \frac{1}{(A^{-1})_{11} \cdot t} \quad (2.44)$$

The other constants are also attainable with a similar procedure and are resumed as follows.

$$\hat{E}_y = \frac{1}{(A^{-1})_{11} \cdot t} \quad (2.45)$$

$$\hat{G}_{xy} = \frac{1}{(A^{-1})_{66} \cdot t} \quad (2.46)$$

$$\hat{\nu}_{xy} = \frac{(A^{-1})_{12}}{(A^{-1})_{22}} \quad (2.47)$$

$$\hat{\nu}_{yx} = \frac{(A^{-1})_{12}}{(A^{-1})_{11}} \quad (2.48)$$

2.2.3 Failure cases

Any component design analysis is normally performed by comparing stresses due to applied loads with the allowable strength of the material (strength failure) or the maximal critical load (instability failure).

2.2.3.1 Failure due to material strength

By multiaxial stress fields, a suitable failure theory must be selected for this comparison. Fibre-reinforced polymers are not isotropic and, thus many new failure

theories have been proposed for them. This section presents the main in-plane loading cases and summarizes the failure prediction in a UD-layer. Further information on this topic is found in the recommended bibliography [8,32,34,52,53].

2.2.3.1.1 Failure modes in a UD-layer

The fibres and the matrix are the basic components of a UD-layer. Hence, a distinction is made between two basic types of failure: fibre breakage or inter-fibre failure (which is associated to a matrix failure or fibre–matrix interface failure), and each failure mode is specified in compressive, tensile or shear load cases [32,34]. Fibre and matrix failure are described by failure hypothesis.

2.2.3.1.1.1 Fibre breakage

Fibre breakage is caused almost exclusively by stresses parallel to the fibres, in tension or compression (Figure 2.9). The rupture strengths are different in tension and in compression, and different theories were developed for understanding this behaviour. Under tension (Figure 2.9.a) usually failure of fibre bundles occurs under very high loads. Commonly the fibres fail successively regarding the force distribution, and individual fractures can be clearly heard. In this case, the failure mode seems to be more ductile than brittle because the gradual failure effect, although a big rumble is normally heard after the material strength is reached and fails, denoting a high release of energy. One of the parameters to consider in the calculations is the basic strength of the UD-layer, or R_{\parallel}^+ (also found as X_t). It is calculated as the only strength of the UD layer, since the fibres are the dominant component resisting tension σ_{\parallel}^+ . In general, R_{\parallel}^+ is not determined experimentally and the exact value is rarely needed, as another failure mode usually occurs firstly that requires less energy (for example, through a matrix failure or inter-fibre breakage at a lower load). Another difficulty is that experimental tests require a high clamping force that generally causes local damage. In general, R_{\parallel}^+ is determined from the rule of mixtures (or normally they are obtained from catalogues) and is used as a preliminary design parameter [8,34]. On the other hand, under compression loads (Figure 2.9.b) and assuming no global plate-buckling takes place, fibre failure normally occurs due to instability and not crushing. Thus, a micromechanical stability failure occurs, where the UD-layer present a maximum basic strength to compression R_{\parallel}^- and it does not denote a failure of the material in the strict sense. The matrix is the elastic support of the fibres and turns out to be insufficient to prevent the

fibres from buckling (case of a column on an elastic foundation model [8]). The first analytical description of shear buckling, and not the traditional Euler-buckling of columns, assumes a perfectly aligned ideal fibre arrangement. However, there is always an imperfect structure in FRPs, and the following models were developed to account for microstructural imperfections, being the most important factor the average orientation deviation angle of the existing fibre with respect to the ideal. The first models were developed by Rosen [54], and later more accurate models were obtained by Argon [55], Budiansky [56] and, Budiansky and Fleck [57].

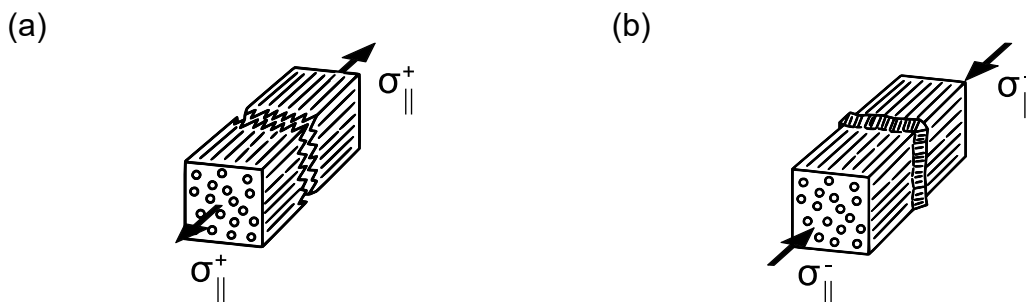


Figure 2.9. Fibre breakage schemes. (a) Parallel tensile load. (b) Parallel compression load [34]

2.2.3.1.1.2 Inter-fibre failure

The global failure of a material is generally expected to occur on the action plane of the stress. In inter-fibre failure, the effective action plane of stress does not coincide in all cases with the rupture plane since the UD-layer can support different loads in different directions. The stresses are relocated, and the failure happens gradually since the course of the breakage does not finally coincide with the direction of the load. The measured basic strength does not always correspond to the real strength under the active stresses, not necessarily conducting to a total failure of the laminate when reaching it. Puck was one of the first to study this case, assuming that inter-fibre breaks in the UD-layer are brittle, proposing three failure modes that can arise depending on the applied load mode, either individually or combined (Figure 2.10) and, introducing a new term for effective plane failure, the effective plane breaking strength R^A [34,52]. Inter-fibre breaks are initiated by stresses in which forces run over the matrix or the fibre-matrix interface. The following stresses are the failure driving force: the transverse tensile stress σ_{\perp}^+ ; the transverse compressive stress σ_{\perp}^- ; transverse-transverse shear stress $\tau_{\perp\perp}$; and the transverse-parallel shear stress $\tau_{\perp\parallel}$.

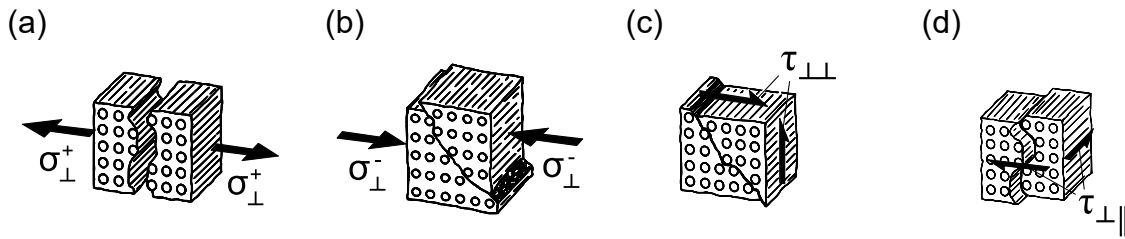


Figure 2.10. Inter-fibre failure schemes. (a) Tensile load. (b) Compressive load. (c) Transverse shear load. (d) Transverse-parallel shear load [34].

Following reference [34], the case of Figure 2.10.a represents that the action plane of the transverse normal stress σ_{\perp}^{+} and the fracture plane are coincident. Thus, the basic strength R_{\perp}^{+} of the UD-layer is considered equal to the R^A of the effective plane. If the load is applied transversely in compression σ_{\perp}^{-} of Figure 2.10.b, the action plane of the stress and the plane of failure do not coincide, denoting a failure under an oblique shear with an evident angle in the direction of the load. In other words, the failure occurs due to shear. Thus, the basic strength R_{\perp}^{-} and the effective plane strength R^A do not coincide. Since a stress σ_{\perp}^{-} cannot be the origin of a break in its plane of action, it is considered that the failure is produced by a stress $\tau_{\perp\perp}$ over the shear plane. In particular, the breakage does not occur at 45° , as is expected for cases of shear stress, but there is also a transverse stress component that causes a frictional deflection mechanism and the failure plane angle is approximately 53° ([34]). Figure 2.10.c represents the case of transverse shear load $\tau_{\perp\perp}$. The plane of action of the load and that of the break do not coincide and the break occurs in an effective plane inclined at 45° from the load plane as a result the shear-equivalent principal stress state. The last case is represented by Figure 2.10.d. In this failure mode, the shear stress $\tau_{\perp\parallel}$ is the failure cause. The break begins with microscopic cracks that run parallel to the fibres, in many cases surrounding them (fibres demand a higher energy for transverse fracture), jumping through the transverse planes of the matrix. Finally, the cracks combine, and the structure fails but gradually. The cracks jump from plane to plane at an angle of 45° . Failure occurs in the fracture plane that has the lower fracture strength, in this case, both effective action plane and fracture plane are the same and $R_{\perp\parallel} = R_{\perp\parallel}^A$.

2.2.3.1.2 Failure criterion of a UD-layer

Every structure to be designed needs to fulfil certain dimensions required for load bearing. They can only be dimensioned by comparing the expected service load

to the load that can be tolerated. In the case of FRP laminates, the design parameters are the fibre volume fraction and thicknesses of the individual layers, as well as the fibre orientations given by the layers stacking sequence. Different criteria have been developed and modified for FRP laminates, primarily upon the state of stresses of a UD-layer and for inter-fibre stresses. Generally speaking, they are distinguished as:

- *type-of-failure criteria*, an independent failure criterion is established for each of the failure types, that is, both as fibre breakage and inter-fibres criterion.

- *global failure criteria*, where all the stress-strength comparisons in a UD-layer is described by a single mathematical equation obtained through empirical methods, linking the completely different types of break, fibre break and inter-fibre failure [34].

Therefore, global failure criteria are phenomenological theories based in curve-fitting analysis. The curve stress points are not necessarily connected by a continuous curve, because of the discrepant material behaviour regarding the compression or tension response. There are many failure criteria for orthotropic materials, each designed to better predict the failure of the FRP materials based on its main components [8,9,32].

2.2.3.1.2.1 Tensile stress

One of the global failure criteria for design calculations is the Tsai-Hill [58,59] criterion interpreted as analogous to the Von Mises criterion, and it is briefly addressed as follows. For a plane stress state ($\sigma_3 = 0$; and the shear stresses $\tau_{23} = \tau_{32} = 0$), a tensile stress in the 1-2-plane of a UD-layer is set, being the fibres oriented parallel to the 1-direction. The governing failure criterion is then given by Eq. (2.49) in terms of the material principal strengths.

$$\frac{\sigma_{11}^2}{R_{\parallel}^{+2}} - \frac{\sigma_{11}\sigma_{22}}{R_{\parallel}^{+2}} + \frac{\sigma_{22}^2}{R_{\perp}^{+2}} + \frac{\tau_{12}^2}{R_{\perp\parallel}^2} = 1 \quad (2.49)$$

$$\sigma_{11} = \sigma_x \cos^2 \alpha \quad (2.50)$$

$$\sigma_{22} = \sigma_x \sin^2 \alpha \quad (2.51)$$

$$\tau_{12} = -\sigma_x \sin \alpha \cos \alpha \quad (2.52)$$

The Tsai-Hill criterion is in very good agreement, for example, when analysing experimental data of E-glass fibres/epoxy matrix, and compared to other known criteria as the maximum-stress or maximum-strain criterion in Figure 2.11 [8,32]. Nevertheless, its accuracy depends on the behaviour of the material (either ductile or brittle)

and for other pair fibre-matrix components, other global failure criteria were developed by Hashin [60] or Tsai-Wu [61] for increased curve-fitting capability.

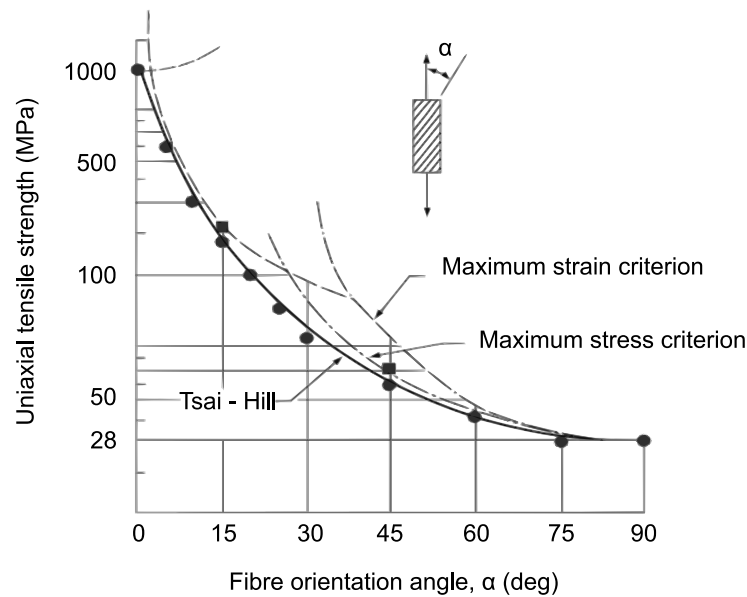


Figure 2.11. Tsai-Hill failure criterion with uniaxial strength data of a glass fibre-reinforced epoxy composite. (Adapted from [32])

2.2.3.1.2.2 Compressive stress

As presented in section 2.2.3.1.2, fibre-reinforced polymer composites under longitudinal compression loads may fail by inter-fibre breakage, either as a matrix failure or as a failure in the interphase matrix-fibre. In some cases, the FRP material may experiment failure as a localised buckling of the fibres (*micro-buckling*). Thereby, the rod-like structure of the fibres leads to a shear buckling failure rather than Euler's flexural buckling, because an insufficient shear rigidity of the matrix. By employing micro-mechanical analyses, researchers studied micro-buckling under parallel-to-fibres axial compression loading ($\sigma_{||}^-$) of aligned-fibre composites, to attain the critical compressive peak stress (σ_{crit}). Failure may occur when $\sigma_{||}^- > \sigma_{crit}$.

First analytical descriptions studied the mentioned critical load, assuming a perfectly aligned, ideal fibre arrangement. If the matrix behaves elastically, the localised buckling mode is called *elastic micro-buckling*. Applying buckling theory for columns in an elastic foundation, Rosen [54] studied two possible elastic micro-buckling modes: *extension mode*, due to extensional deformation in the matrix for low fibre volume content ($\varphi_f < 20\%$); and *shear mode*, due to shear deformation in the matrix. In failure prediction, it is more common to find shear deformation rather than extensional mode,

because most useful composites have more than 30% fibre volume content. The compressive strengths of the exposed extension and shear modes are given by Eq. (2.53) and Eq. (2.54), respectively.

$$\sigma_{\text{crit}} = 2\varphi_f \sqrt{\frac{\varphi_f E_m E_{\parallel f}}{3(1 - \varphi_f)}} \quad (2.53)$$

$$\sigma_{\text{crit}} = \frac{G_m}{1 - \varphi_f} = G_{ec} \quad (2.54)$$

Above equations depend upon the fibre volume content. Nevertheless, shear mode predicts a compressive strength lower than the extension mode. The other involved parameters are the matrix shear and elastic modulus as G_m and E_m respectively. Factor $E_{\parallel f}$, denotes the longitudinal elastic modulus of the fibres while factor G_{ec} represents the effective shear modulus of the composite. However, Rosen's models assumed perfect conditions when balancing the strain energy change to the work done by the external forces. Thus, failure prediction stated by the models shall differ from experimental data and theoretical values cannot be attained. The consequent developed models do contemplate imperfections upon the fibre arrangements, and other micro-buckling modes could be expected such as *fibre-kinking*. Rosen [54] assumed fibre-kinking as a manner of elastic shear buckling, represented as an elastic bifurcation buckling phenomenon, and could also appear in originally straight fibres.

However, other stress analysis dealt with an existing orientation deviation. Argon [55] stated that long fibres under compressive loads shall buckle due to a critical compressive load and proposed a rigid-perfectly plastic composite model (Eq. (2.55)), including a region of initial misalignment angle $\bar{\phi}$ (previous to loading) and the longitudinal shear strength k . Due to the fibre-misalignment, a compression-shear coupling occurs, and the compressive loads are in equilibrium of forces, although the fibre offset facilitates a disequilibrium of moments, and can only be balanced by an additional shear stress $\tau_{\perp\parallel}$ [34]. When the shear component equals k as $\tau_{\perp\parallel}^* = k$, it produces a local instability favoured by the misalignment angle and followed by a shear collapse band. An increasing compressive stress induces a larger fibre misorientation.

$$\sigma_{\text{crit}} = \frac{k}{\bar{\phi}} \quad (2.55)$$

Budiansky [56], Budiansky and Fleck [57] verified the stress at which fibre-kinking is initiated, joining both Rosen's and Budiansky's models, easily recognizable

when $\bar{\phi}$ is defined by small or large values. The fibre-kinking model (Figure 2.12) is described by its parameters as the kinking angle β , the kinking width W_k , and the kinking rotation angle ϕ .

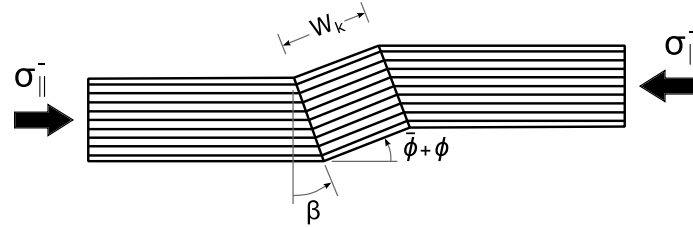


Figure 2.12. Budiansky's model for fibre kinking

Budiansky based the kinking behaviour of the fibres on an elastic-ideally plastic composite (Eq. (2.56)), including $\gamma_{\perp\parallel}$ as the shear yield strain of the composite. A concluding remark of the authors emphasized that laminates made from carbon fibres immersed into an epoxy matrix tend to fail by plastic kinking under compression loading.

$$\sigma_{\text{crit}} = \frac{G_{ec}}{1 + \frac{\bar{\phi}}{\gamma_{\perp\parallel}}} = \frac{\tau_{\perp\parallel}^*}{\gamma_{\perp\parallel} + \bar{\phi}} \quad (2.56)$$

The fibre misalignment angle $\bar{\phi}$ in Eq. (2.56) varies randomly throughout the composite [62]. The fundamental association between fibre waviness and processing methods are not intensively established, albeit primary estimations have been implemented with good experimental correlations. Following Fleck's review [62], Jelf [63] estimated an average misalignment in the range $2^\circ - 3^\circ$ while studying CFRP tubes under compression and torsion loading, with a final failure by plastic micro-buckling. Likewise, Yurgartis [64] obtained experimentally the fibre misalignment in a unidirectional carbon fibre-PEEK, resulting in fibres oriented within $\pm 3^\circ$ and 1.9° of standard deviation. Furthermore, Lankford [65] studied carbide fibres on a ceramic matrix composites under compressive loads, which failure denoted fibre-kinking. From calculations, a 4° fibre misalignment was issued. Due to the waviness inherent in the fabric manufacturing process (i.e., because of the effect of the weft upon the warp direction, see Chapter 2), woven carbon fibre cloth may have a higher fibre misalignment. Wilkinson [66] inserted brass wires into a T300/914 carbon-epoxy composite for weighting the effect of the waviness induced by the wire, starting from a minimum angle of 3° up to 17° . The misalignment effect reduced in five times the compressive strength. Moreover, the missing parameters on Eq. (2.56) are the shear yield strain and its associated

shear strength. Different graphical methods are suggested by references [24,28] for attaining the last-mentioned factors (also called the Ramberg-Osgood parameters), from shear vs. strain response of the composite.

In this work, Budiansky's model will be employed for estimating the compressive strength of the CFRP laminates. The fibre misalignment value inferred in this work is estimated in the range of $2^\circ - 5^\circ$.

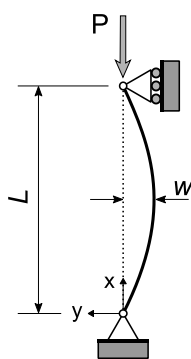
2.2.3.2 Failure due to instability

Slender or thin structures as rods or plates under compressive loads may fail by buckling, for example, when the applied compressive stress reaches the critical buckling stress, and this is also smaller than the compressive strength of the structure's base material. Therefore, stability failure must be taken into account also for slender structures made from FRP based materials, as rods and plate shapes proposed in this work. General insights are presented within this section, and more detailed descriptions are given in the correspondent chapters.

The example in Figure 2.13 serves to discuss the problem, presenting a typical case of buckling of a bar in an articulated and guided support under axial load. This case in its first mode is called the fundamental case of column buckling. Often, the buckling described in this section is called simply *Euler buckling*, who first investigated the buckling of a slender column.

The differential equation of the deflection curve is represented by Eq. (2.57) [67,68]. The equation denotes a homogeneous and linear differential equation of second order with constant coefficients.

(a)



(b)

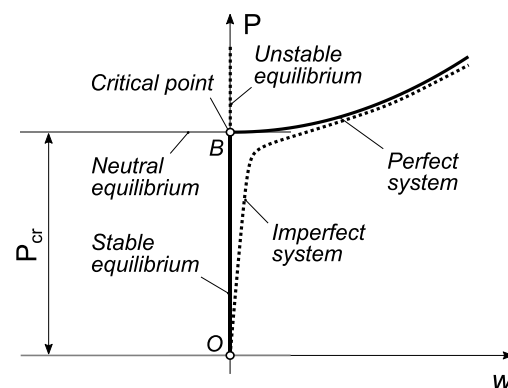


Figure 2.13. Example case for buckling topic introduction: (a) Buckling of a pinned-end column. (b) Load-deflection diagram for a linearly elastic column.

$$w(x)'' + \frac{P}{EI}w(x) = 0 \quad (2.57)$$

Then, introducing the following notation

$$\mu^2 = \frac{P}{EI} \quad (2.58)$$

Rewriting Eq. (2.57) with above notation

$$w(x)'' + \mu^2w(x) = 0 \quad (2.59)$$

The general solution of above equation is given by Eq. (2.60)

$$w(x) = C_1 \sin \mu x + C_2 \cos \mu x \quad (2.60)$$

To evaluate the constants of integration C_1 and C_2 of Eq. (2.60), the boundary conditions at the ends of the column are needed. For the case of Figure 2.13.a, the deflections are zero when $x = 0$ and $x = L$. Two cases are derived as solutions: Case 1, $C_1 = 0$, in which the column remains straight and the deflection $w = 0$ (trivial solution). Case 2 gives the so-called buckling equation as $\sin \mu L = 0$, which is satisfied when $\mu L = n\pi$ ($n = 1, 2, 3\dots$). From case 2 solution, Eq. (2.61) is attained and gives the critical load for a column with pinned ends, being the lowest when $n = 1$.

$$P = \frac{n^2 \pi^2 EI}{L^2} \quad (2.61)$$

From above evaluation, the deflection curve is given by Eq. (2.62)

$$w(x) = C_1 \sin \frac{n\pi x}{L} \quad (2.62)$$

When analysing the critical loads for columns with different support conditions, they can be associated to the critical load of a pinned-end column by introducing the concept of an effective length $L_e = kL$, in which k is called the effective length factor. Then, Eq.(2.61) is written as Eq. (2.63).

$$P_{crit} = \frac{\pi^2 EI}{(kL)^2} \quad (2.63)$$

The different values of k vary according to the boundary conditions imposed to the column. This are briefly resumed in Figure 2.14.

Moreover Figure 2.13.b denotes different states of the column while considering an ideal elastic column with large deflections (perfect system) and an elastic column

with imperfections such as small eccentricities (imperfect system). When the axial load P is of small values, between segment \overline{OB} , the column is in a state of stable equilibrium. If the system is perfect, the column remains perfectly straight under axial compression. If the system is not perfect, the column will slightly bend from the onset of loading due to the imperfections. As P reaches the critical load P_{crit} (point B), the column attains a neutral equilibrium, in which it may undergo small lateral deflections or may remain straight. When the load exceeds P_{crit} the state of the column is unstable and may undergo immediate collapse by buckling if the slightest disturbance is set. The imperfect system approaches the perfect system curve as an asymptote, and the larger the imperfections, the further the imperfect system curve moves to the right and away from the vertical. Remarkably, reaching the critical load does not mean that the structure will fail at that point. In fact, the structure is able to bear higher loads until a larger deflection is reached, failing according to an over-critical load. However, the analytical approach as Eq. (2.63) only gives an estimation of the critical load, that is, when reaching the neutral equilibrium, but no information above this value.

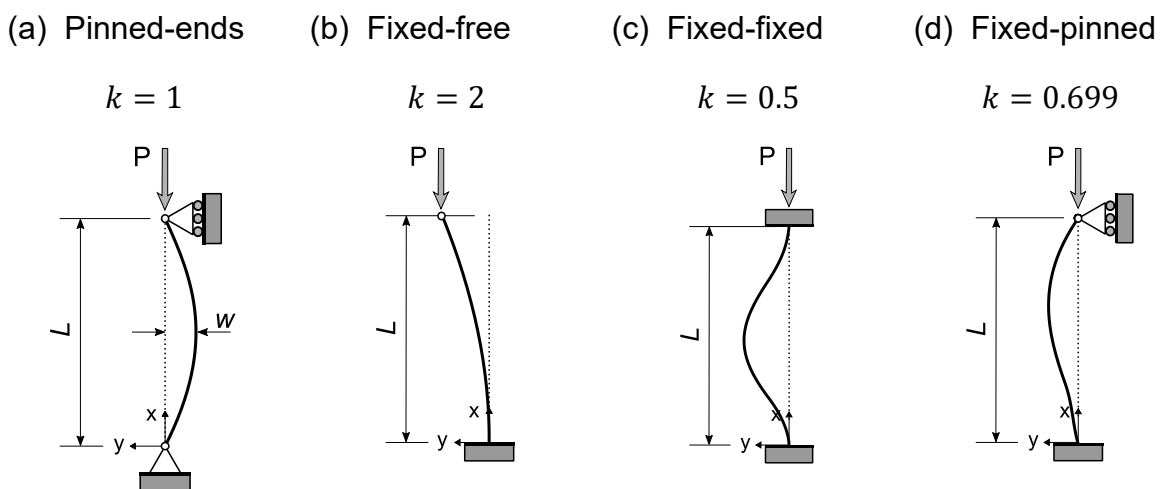


Figure 2.14. Different effective-length factors k for ideal columns [67]

2.3 FRP manufacturing processes

Material processing is the art and practice of transforming materials from one form to another. Composite materials processing involves the incorporation of two or more different components to form the final part. Composite parts subjected to significant loads require continuous fibre reinforcements. In this case, these reinforcements

play the main role in the mechanical behaviour of the composite part and the function of the matrix is to avoid relative displacements of the fibres [69]. There are different techniques for processing various types of reinforcement and polymeric matrices. The pressures and temperatures involved in composites processing are significantly lower than those needed to process metallic parts. Consequently, polymer composites are transformed into near-final parts with simple and low-cost tools, in addition to reducing the post-processing manufacturing cost. The criteria for selecting the right processing method are based on factors such as the production rate, cost, mechanical requirements, size, and shape of the designed part. An example of the production series as a function of different manufacturing process is given by Figure 2.15.

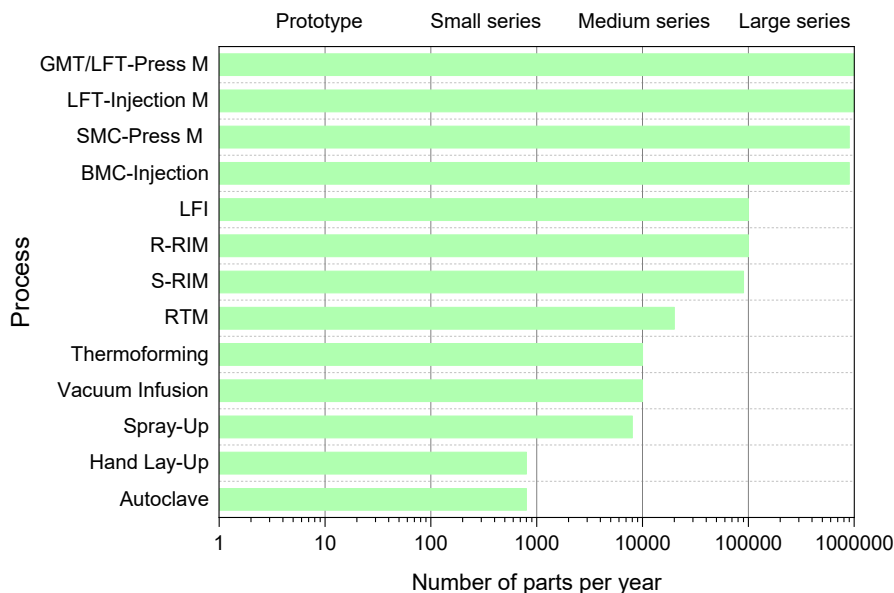


Figure 2.15. Ranking of composite part manufacturing [70]

Part manufacturing of thermosetting reinforced polymers has four basic parameters: base materials; mould or support structures (and auxiliary accessories); heat or temperature; and pressure. Depending on the manufacturing process, the base materials are selected and placed by some method into the mould. Heat and pressure are then applied to transform the components into the final shape. The heat and pressure requirements are different for different material systems [71]. A wide range of composite manufacturing processes have been developed over the years, depending on the manufacturing variables mentioned above. They could be partially summarized and divided as:

- *Conventional methods*, normally employing manual or partially automated lay-ups such as bag-moulding processes (including autoclave [72]), compression moulding [73], filament winding [74], pultrusion [75] or liquid composite moulding processes *LCM* (as hand lay-up, resin transfer moulding *RTM*, or vacuum infusion *VI*) [76–78]. The last represent the main manufacturing processes applied within this dissertation in which vacuum infusion stands-out. This point will be highlighted in this section.
- *Automated methods*, they are in current focus because they increase the flexibility of fibre placement process and allow the fabrication of more complex parts. Besides additive manufacturing *AM* with short and continuous fibres [79,80], three very popular are being used in industry as automated tape layup *ATL*, automated fibre placement *AFP*, and robotized filament winding *FW* [70,81–84]. However, their use is limited in terms of associated costs of the needed specialized machinery and constraints while fabricating complex components.

The manufacture of moulds and tools is a critical matter in manufacturing technology. The mould transforms the raw material into a certain shape, as shown in Figure 2.16 for the RTM example case. The quality and surface finishing of the processed part highly depends on the tolerances and manufacturing quality of the selected mould.



Figure 2.16. Manufacturing moulds for a helicopter tail rotor made from CFRP [71]

Essentially, four basic steps for all composite processing techniques are summarized as:

1. *Lay-up* is the arrangement of fibres and layers of material arranged in a proportion, order, and orientation according to the estimated stresses to which the component to be manufactured will be subjected.
2. *Impregnation* is the stage in which resin and fibres are mixed to form a laminate. Its purpose is to ensure that the resin flows completely between the fibres and achieves good wetting of the fibres. The parameters influencing this stage are viscosity, surface tension and capillarity, which are affected by the pressure and temperature at which the impregnation is carried out.
3. *Consolidation* is the step in which an intimate contact is created between sheets or layers of fibres, trying to remove the air trapped during processing and to increase the fibre volume fraction. Parts that do not achieve good consolidation will have trapped pores or voids, which will reduce the service load capacities of the manufactured parts. In turn, the fibres may undergo elastic deformation associated with resin flow, thus affecting their orientation, and leaving a state of residual stress in the part.
4. *Solidification* is the final stage of processing. Pressure and temperature are maintained over time. The time and degree of polymerization (in thermoset resins) will depend on the resin formulation and its curing kinetics. The shorter the solidification time, the higher the part production rate.

Currently, more than 75% of commercially manufactured parts made of composite polymers are produced from thermoset polymeric matrices such as epoxy, polyester and vinyl-ester resins [71]. Their advantages over thermoplastic matrices could be summarized as follows:

- the easier processing, since the initial state of the resin is in liquid state,
- the fibres are easily impregnated with the resin,
- continuous long-fibre, in which high performance composites can be attained,
- the processing temperature and pressure are lower,
- the elements required for processing as tooling, moulds, accessories, supplies, etc. are less expensive (apart from autoclave based FRP).

As previously mentioned, LCM are a group of techniques for out-of-autoclave (OOA) polymer composites processing, that share some common characteristic such as moulds or support structures. In a first stage, the mould is filled with dry reinforcement fibres, according to a certain stacking sequence (a preform is then assembled). In a second stage, the mould is closed and the preform is compressed inside the cavity,

increasing the fibre volume fraction. Then, a liquid resin is introduced into the mould to impregnate the preform. Once the mould is completely filled and the preform is fully saturated with resin, the cure stage begins, which is usually carried out by a suitable temperature cycle determined according to the polymer cure kinetics. Although LCM techniques have been well known since the 1970s, in recent years they are being used in mass production for the manufacture of all types of parts for automotive, transportation, marine, and aerospace vehicles [32]. This is largely due to the high capacity for mass production, the associated costs, the final part quality and the good mechanical properties achievable [85].

Among the LCM techniques, the RTM allows obtaining near finished parts of good quality composite material that will be subjected to high stresses, for example in aeronautical parts such as rotors and structural parts [69]. This process is used for small to large parts in small to medium production volumes [71]. A variant of the RTM method is the vacuum infusion *VI* as shown in Figure 2.17 (some authors refer to *VI* as vacuum assisted resin transfer moulding *VARTM* technique). In this case, mould costs are reduced as the moulds have only one rigid face. In the *VI* process, the fibres are placed in a rigid-face mould which is previously coated with a suitable release agent. Once the fibres are placed in the mould, as part of the preform assembly stage, a fabric called “peel-ply” is placed over the preform. The functions of the peel ply are to provide air evacuation paths when vacuum is applied and to peel off the disposable materials that are placed over the laminate (vacuum and resin distribution hoses, resin distribution media, etc.). Then, another layer that is called “flow-media” it is placed over the peel-ply. This technique of placing flow-media and peel ply is commonly known as Seaman's Composite Resin Infusion Moulding, *SCRIMP*. The impregnation of the fibres is relatively slow when using vacuum infusion, because of the limited pressure gradient inside the mould driven just by the atmospheric pressure (≈ 1 bar). The flow-media is a high permeable fabric that facilitates the distribution of resin inside the mould, mitigating problems like premature gelation of the resin when processing large parts. A flexible plastic film, known as the vacuum bag, is then placed over the top of the layer's assembly and it is sealed to the mould using a sealing tape. A vacuum pump is connected to the vacuum lines (which also act as vents) and generates the negative pressure necessary for the preform to be compacted, air to be evacuated and the resin to be infused. Once the vacuum is established, the catalysed resin is infused into the mould

through one or more infusion points. The infusion system is very simple and, additionally, the mould with the flexible membrane allows a visual control of the filling and impregnation. Depending on the resin used, curing can take place in a temperature-controlled chamber or at room temperature.

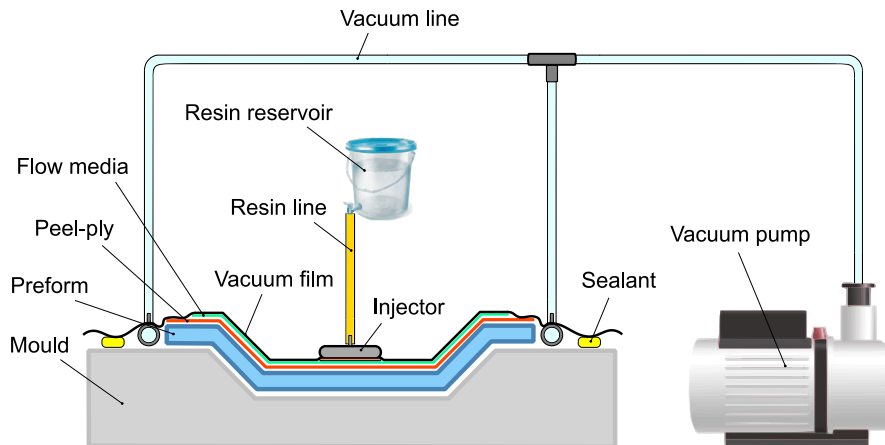


Figure 2.17. VI technique basic scheme

The VI process allows a medium-to-high fibre volume fraction, which implies good mechanical performance of the final part [71], but it should be considered that the maximum theoretical fibre compaction pressure is up to 1 bar. This means that the preform compaction behaviour will determine the maximum fibre volume fraction achievable. The present work adopted the VI technique for manufacturing sandwich panel components, such as cores and skins, and other laminates for the production of study specimens, as it consists in a very simple, versatile, and economical process, which allows good quality and high performance parts to be attained, appropriately as well for fast prototyping.

3 Sandwich construction: state of the art

The principle of a sandwich structure consists on a pair of thin, rigid faces, a lightweight core with a defined thickness and an adhesive mean capable of load transferring to and from the core [86]. Sandwich structure's concept is quite common in nature, such as the design of bird bones that feature a hollow inner cell structure (foam-like) that supports the outer bone tissue, allowing the weight of the bird to be lighter, enabling the flight [87].

Sandwich structures are very popular and can be found in numerous weight sensitive applications. Due to their efficiency and versatility, satellite and aircraft industries use them as standard structures [16,17], and the concept currently has also been extrapolated to ships [88], rail road's industries [89], wind energy systems [90], construction [91], packaging [92], and lately they are being developed for motorsport and automotive applications [93,94]. The advantages of using sandwich materials, in combination with the development of new base materials, currently focused on cellular cores, and the need for high performance weight-sensitive structures has enabled the continuous increase in their demand [32,95].

In this chapter, the concept of the sandwich structure is presented and reviewed, its common load introduction and the likely failure modes, in which preliminary work has provided experience upon the study and development of manufacturing paths and failure modes upon sandwich structures based on FRP [96,97].

3.1 Sandwich structures concepts

3.1.1 Lightweight construction

The benefits of weight reduction of transport vehicles have influenced the development of new materials based on fibre-reinforced materials, so that they have high specific strength and stiffness per unit weight. Taking advantage of the anisotropy of FRP materials, it is possible to design each component according to the acting stresses [98]. Lightweight construction is defined by Hertel [99] as "*the minimum amount of weight in an assembly that can only be achieved when each component requires only a minimum of material or contributes optimally to the minimum of a larger unit*". This

idea has gained more interest upon FRP based materials in recent years, being targeted by numerous investigations not only for its benefits over high specific properties, but as means of cost reduction. Lightweight construction for specific loading cases requires an approach that covers three fundamental aspects: design – material – manufacturing [100]. The combination of these three strategies brought a concept that consists of the "hybridization" of materials. Ashby [1], defined hybrid materials as the combination of two or more materials that allow characteristics not previously offered by their separate constituents. The concept also includes the use of a single component and empty spaces (membrane cellular concept). These materials allowed the expansion of the design scope through the conception of new materials [101], being aimed by many researchers including the authors of this project [25,102–105]. Sandwich structures represent one of the main examples of hybrid materials. A historical review in sandwich structures is recommended as in following references [95,106–109].

As presented previously, sandwich construction principle involves the layering of different materials, commonly having two rigid outer faces, a low-density core and, a bonding mean in such a configuration that provides high bending stiffness (Figure 3.1). There are three principal directions to which material properties of most honeycombs are referred; the width W , the length L and the transverse T directions [110].

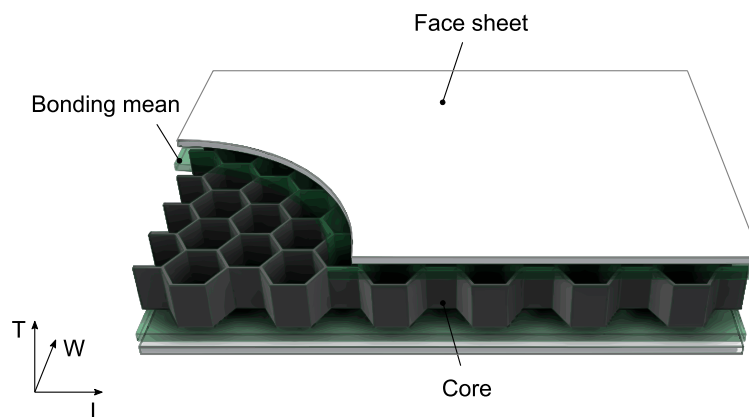
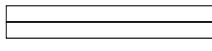

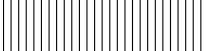


Figure 3.1. Sandwich structure basic scheme

Its configuration resembles an *I-beam* cross-section where the face sheets are comparable with the flanges, mostly bearing in-plane tensile and compression loads; while the core is like the web, typically bearing shear and out-of-plane compression loads. If the core thickness is increased, the faces are set even more apart and, thus, the Steiner component increases the second moment of area of the cross-section, obtaining a weight efficient bending structure [86,99,110].

Table 3.1 exhibits the effect of increasing core thickness upon the bending stiffness: for example, by increasing core thickness three times, the flexural rigidity increases over five times with a global weight increment of 6%.

Table 3.1. Weight efficiency of sandwich structures while bending [111]

Property			
Core thickness	0	t	$3t$
Relative flexural stiffness	1	7	37
Relative flexural strength	1	3.5	9.25
Relative weight	1	1.03	1.06

Many factors rule the choice of sandwich material components, although they may depend upon structure functionality, expected lifetime, availability and costs [112].

On the one hand, the commonly used face materials are compressed in two main groups; metallic and non-metallic. Within the metallic ones, aluminium alloys, titanium alloys and steel alloys represent the most. The latter non-metallic face materials may include plywood, plastics, resin-impregnated paper or FRP among others. The FRP based faces has brought a significant impact upon sandwich structures, because of the higher specific properties and easier manufacturing paths than the metal counterparts. The expected properties for a face sheet will depend on the functionality, but primarily are resumed as: high tensile and compressive stiffness and strength, surface finishing (fulfilling tolerances), environmental resistance and impact strength (the final impact properties of the sandwich structure is also depending on core energy absorbing features) [110,113].

On the other hand, the employed materials components and geometries for the cores are even more complex and diverse. The function of the core is not only limited to stiffen the cross-section of the panel while separating the faces. As mentioned, the core also plays a fundamental role in the shear strength and compression loads. Furthermore, the core must have sufficient Young's modulus and shear modulus to maintain the distance between faces and to give them proper support in a way that they remain flat, avoiding local buckling effects such as wrinkling. Besides the mechanical properties already presented, other primary interest properties of sandwich cores rely

upon a very low density, thermal and acoustic insulation, although the features depend on the expected applications [110,113]. In this way, an on-going effort has been set to develop new types of sandwich cores capable of achieving many of the presented features. On the following section, the main sandwich core geometries and base materials found in the literature are reviewed.

3.1.2 Periodic cellular materials

Several approaches to the development of sandwich core materials have been set over the years, and most of them are based on *cellular solids* materials [114]. Gibson [115] defined cellular solids as an assembly of cells with solid edges or faces, packed together in way that they fill volume. Within this classification, examples can be found in nature such as wood, cork, bones, or sponges, combining an effectively high modulus and collapse strength with a very low density. Moreover, man-made engineered cellular materials belong to this classification as well [116], being exploited in a variety of applications.

The above classification comprises two main core type groups ⁽¹⁾: *stochastic* cores, that may include open-cell and close-cell foams with different raw materials (e. g. polymers, metals or ceramics [115]) regarding to the intended implementation of the part [114,117]; and *periodic* cores, that introduce the concept of architected (or tailored) materials [118]. The particularity of the periodic cores is that they are composed of repeating unit cells with cell diameters ranging from tens of micrometres to tens of millimetres [119]. Periodic cellular cores can also be divided in two sub-categories ⁽²⁾: *prismatic* cores, such as two-dimensional (2D) honeycomb [78,105], corrugated cores [120,121] or three-dimensional (3D) honeycomb [25,122]; and *lattice* structures [123,124].

Some examples of the previous classification found in the literature are highlighted in Figure 3.2 [88,110,113,119,125]. The different core types primarily differ in terms of functionality, which may include different target functions such as load bearing capability, maximum tolerable weight, ease of manufacture, dimensional tolerances, costs, among others.

⁽¹⁾ The traditional core type groups only cover balsa, foams, honeycombs, and corrugated cores [110]

⁽²⁾ The periodic cellular cores' classification proposed may vary from other hierarchical descriptions [126]

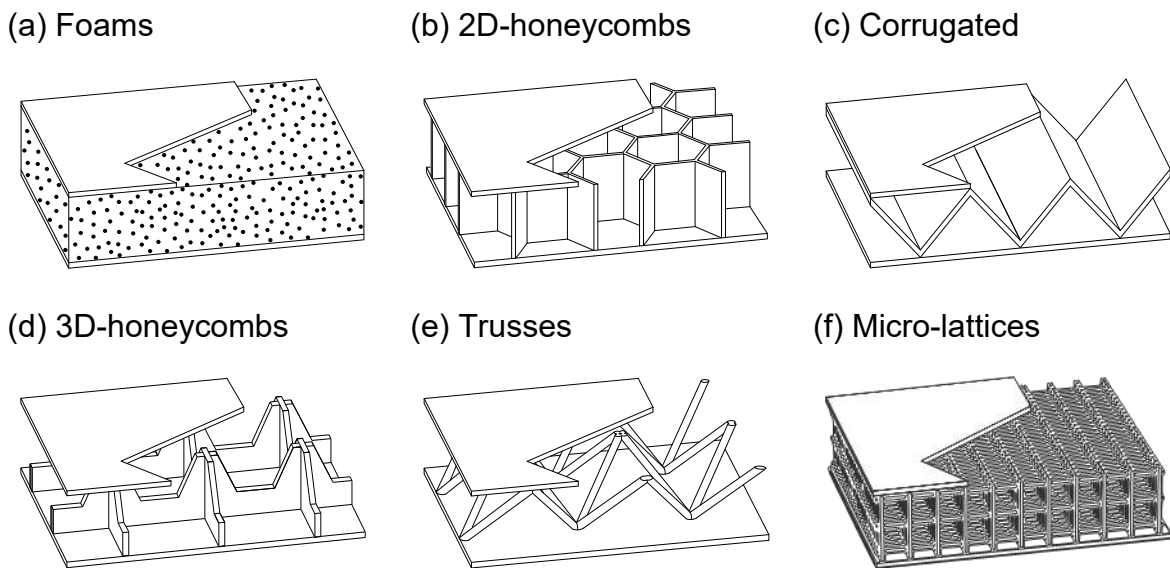


Figure 3.2. Scheme of different core topologies

Traditional sandwich cores are addressed in Figure 3.2 as follows:

- (a) Foams represent a solid on a macroscopic level, thus, sandwich manufacturing with them is commonly simple and economic (core shaping and face bonding). They offer high acoustical and thermal insulation, and good energy absorption by impact. They are widely use in marine applications.
- (b) 2D-honeycombs structures are composed of plates or sheets that form the edges of closed unit-cells, which are extruded along T -direction (thickness) and repeated in two dimensions to fill-up the space. The geometry is not limited to hexagons and, also triangular and square shapes are found. They are developed and employed mainly for aerospace purposes because of their high specific mechanical properties and versatility.
- (c) Corrugated cores are attained, for example if the 2D-honeycombs cores were rotated from one of the horizontal axes by 90° , obtaining a prismatic structure with open cells in one direction and closed in the other orthogonal directions. They represent advantages by fabricating large metal-based panels such as in railroad or marine industries.

The search of even lighter core materials (ultra-lightweight cores [25,127,128]) and basic multifunctionality concepts such as open cell configuration in order to enable applications as heat transferring, shape morphing or foam-filling [119,129–131], resulted in three of the following concepts presented in Figure 3.2:

- (d) 3D-honeycomb cores are manufactured having as basic idea the traditional square or triangular 2D-honeycomb. The core material sheets are machined according a defined pattern to have an open-cell scheme, which may have structural advantages while reaching a lowest weight design [25,132].
- (e) Trusses (or lattices) are created from different arrangements of interconnected bars patterns (firstly to imitate foams features), in order to meet certain mechanical and weight features, being competitive and even having better properties compared to traditional honeycombs [124,125].
- (f) Micro-lattices are commonly manufactured by using metal wires, casting or more recently by 3D-printing. They present repetitive unit cells also in T-direction and a size of a few millimetres. They were developed for blast resisting applications but today they are extrapolated to overall engineering applications for filling space within 3D-printed structures [119,133,134].

Current steps toward new kind of ultra-lightweight cores are being set-up. Two reasons for such advances are proposed by Evans [135] as the discovery of new manufacturing paths employing new technologies, or known methods but combined differently; and higher levels of basic knowledge about materials properties. To date, there are a vast number of techniques employed for the manufacture of lightweight cellular cores, from foam processing [136,137], batch [97] and continuous honeycomb fabrication techniques [138], slotting and bonding [139] and, more recently 3D printing techniques of FRP polymers [140]. A comprehensive review of authors and the different manufacturing techniques can be found in the work of Karlsson [141], Wadley [119] and more recently Birman [112].

Within the 3D-honeycomb category, the work of Xiong et al. [132] stands out, having studied "egg-crate" and pyramidal structures (both open-cell core types). In that work, CFRP laminates were obtained by stacking prepregs, as an electronic engraving machine cut the laminates to the desired shape and through the interlocking method they were assembled and glued to obtain the 3D-honeycomb core. By studying the different material failure modes, the authors were able to identify the failure maps (later explained in this section) for a 3-point bending load, varying the support span of the samples. Since the skin-to-core bonding area was very low, most of the specimens exhibited debonding as main failure mode, limiting the maximum achievable failure load. For example, only a 3.2 kN bending load was reached for the best sample case at 220mm span, although theoretically more than 22kN was expected when avoiding

core debonding. Regarding FRP lattices, early work presented by Finnegan and Deshpande [22] is of notable relevance. The authors fabricated pyramidal sandwich cores based on CFRP laminates. The pyramidal geometry was obtained by waterjet cutting. A small slot in the back of the lattices allows the assembly using the snap-fit technique (likewise to the interlocking method). Since the bonding area was very small, a CNC milling machine performed small machining operations on the skins to generate a suitable undercut to support the lattice structure. Once assembled, core and faces were bonded with epoxy-based adhesive. Two different types of nodes were tested to evaluate the compressive strength. They achieved core relative densities $\bar{\rho}$ in the range of 0.01 – 0.1, with $\bar{\rho} = \rho_c/\rho_s$; where ρ_c is the unit cell or core density and ρ_s represents the density of the base material. The out-of-plane compressive strength obtained was in the range of 1 – 11 MPa, where the strength increases with an increasing relative density. When compared to most known materials, including aluminium lattices and, metallic and polymeric foams, with densities below 100 kgm⁻³, the pyramidal CFRP cores showed a better compressive strength. Furthermore, George [45] obtained pyramidal CFRP lattice cores as well, with another approach. The fabrication technique involved chemically soluble polymeric moulds, previously machined with a CNC milling machine to the desired geometry. Once the moulds were machined, braided dry carbon fibre was placed in the grooves and dry carbon fabrics were sewn together using aramid rovings. When the assembly was finished, CFRP sandwich panels were obtained using vacuum infusion technique. Resin pockets were found after infusion, which can be removed mechanically, after removal of the foam support core, in another finishing step. Mechanical properties were evaluated for cores with and without support foam cores. Without the supporting foam, core densities of 44 kgm⁻³ were reached, attaining compressive and shear strengths of 1 MPa and 0.5 MPa respectively, meaning that the compression strength of already known CFRP honeycomb cores perform better, although both cores exhibited comparable shear strengths.

Further discussion among authors and research upon low density cores is addressed along this work. Nevertheless, it appears to be little research on CFRP based 3D-honeycomb cores and non-laminate-based lattices, allowing the chance of exploring new manufacturing paths and studying new materials properties. Thus, besides high mechanical performance, the target function in this dissertation is referred to attain a very low core density, while carrying-out different manufacturing approaches. At this point, the targeted core density is less than 48 kgm⁻³ and, thus, the designation ultra-

lightweight (ULW) will be endorsed [24] (the latter term regarding the core density may vary among other authors [142,143]). Therefore, to obtain ULW cores, novel methods for manufacturing 3D-honeycombs and lattice cores have been developed successfully in this work and are addressed in the corresponding chapters.

3.2 Failure modes

3.2.1 Load introduction

As outlined previously, a sandwich structure consists in a layered structure comprising thin face sheets, a low-density core, and a bonding mean that transfers load between outer and inner components: mostly, the thin faces carry the in-plane tensile and compressive loads; usually, the core bears out-of-plane compression and shear stresses; and the adhesive must transfer the shear loads between components and also must resist the out-of-plane tensile stresses, if any. An important feature of the core is that it must be stiff enough for stabilizing properly the face sheets, i. e. to maintain constant their distance and to hold them flat, avoiding face local buckling effects [86,113,144].

Mechanical studies upon cellular core materials can be founded by means of standard methods of structural mechanics by analysing the unit repetitive cell behaviour [115]. The basic theory regarding sandwich structures load analyses and design features are comprised by Allen [113], Zenkert [110] and Vinson [145].

3.2.2 Base calculations

Basic formulations concerning sandwich beam theory are briefly summarized in this section [51,113]. Commonly, the mechanical behaviour of a sandwich structure is based on cases of basic quasi-static bending, compressive or shear loading. Bending theory is based on the basic bending Bernoulli approaches (i. e. flat cross sections remains perpendicular to the longitudinal axis of the beam while bending) but usually regarding the sandwich core stiffness, the Timoshenko beam theory (i. e. transverse shear deformations are allowed) is more suitable [146,147]. When using cellular cores, the compressive and shear loads response is usually studied by identifying a unit cell. Using basic mechanical approaches related to the unit cell geometry, it is possible to predict its behaviour and to extrapolate it to the entire core panel. In some cases, such

as foams, the unit cells geometries are too complex to characterize and some approaches employ semi-empirical solutions while introducing the parameter of core relative density $\bar{\rho}$, as previously described [23,115].

The cross-sectional properties and stress introduction are established according to Figure 3.3 sign convention and dimensions.

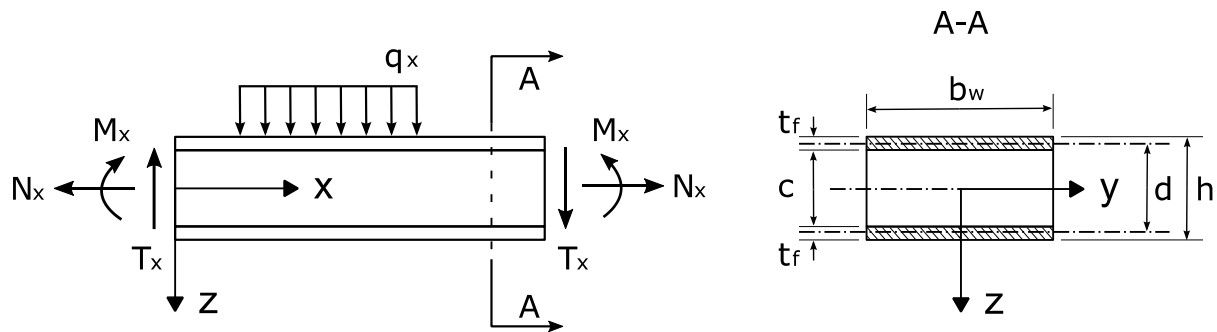


Figure 3.3. Sign convention and dimensions used for calculations [51,113]

Some assumptions are made to ease the analyses of the sandwich panels load cases as:

- the skins remain flat and parallel and present a linear elastic behaviour.
- the core is homogeneous and of elastic behaviour

3.2.2.1 Flexural rigidity

Considering a symmetrical cross-section as in section A-A in Figure 3.3 and applying Steiner's theorem according to the mid-plane and the centroid of the faces, the flexural rigidity D is then represented by Eq. (3.1). The terms E_f and E_c are the Young's moduli of the faces and core, assuming both faces identical.

$$D = E_f \frac{b_w t_f^3}{6} + E_f \frac{b_w t_f d^2}{2} + E_c \frac{b_w c^3}{12} \approx E_f \frac{b_w t_f d^2}{2} \quad (3.1)$$

Comparing each term in Eq. (3.1), some approximations are usually implemented by comparing the contribution of core and faces rigidities (e. g. having a weak core $E_f \ll E_c$; and thin faces $t_f \ll C$) to the main flexural rigidity D [68,113]. Thus, the second term represents more weight to the expression and is used as simplification.

3.2.2.2 Stresses and strains

The stresses in the faces and core due to a bending moment M are obtained by bending theory and given by Eq. (3.2) and Eq. (3.3) respectively. The maximum stresses are then obtained when z -parameter is equal to $\pm h / 2$ or $\pm c / 2$, respectively.

$$\sigma_f = \frac{M_x z}{D} E_f \quad \text{for} \quad \left(\frac{c}{2} \leq |z| \leq \frac{h}{2} \right) \quad (3.2)$$

$$\sigma_c = \frac{M_x z}{D} E_c \quad \text{for} \quad \left(|z| \leq \frac{c}{2} \right) \quad (3.3)$$

For evaluating shear stresses due to a shear load T within a sandwich beam, it must be considered the rigidity contribution of each component of the cross-section. Shear stress distribution in the faces and the core are represented by Eq. (3.4) and Eq. (3.5) respectively. The maximum shear stresses are given when z -parameter is equal to zero and exhibits a parabolic distribution in the core [51,68,113].

$$\tau_f = \frac{T_x}{D} \frac{E_f}{2} \left[\frac{c^2}{4} + c t_f + t_f^2 - z^2 \right] \quad \text{for} \quad \left(\frac{c}{2} \leq |z| \leq \frac{h}{2} \right) \quad (3.4)$$

$$\tau_c = \frac{T_x}{D} \left[\frac{E_f d t_f}{2} + \frac{E_c}{2} \left(\frac{c^2}{4} - z^2 \right) \right] \quad \text{for} \quad \left(|z| \leq \frac{c}{2} \right) \quad (3.5)$$

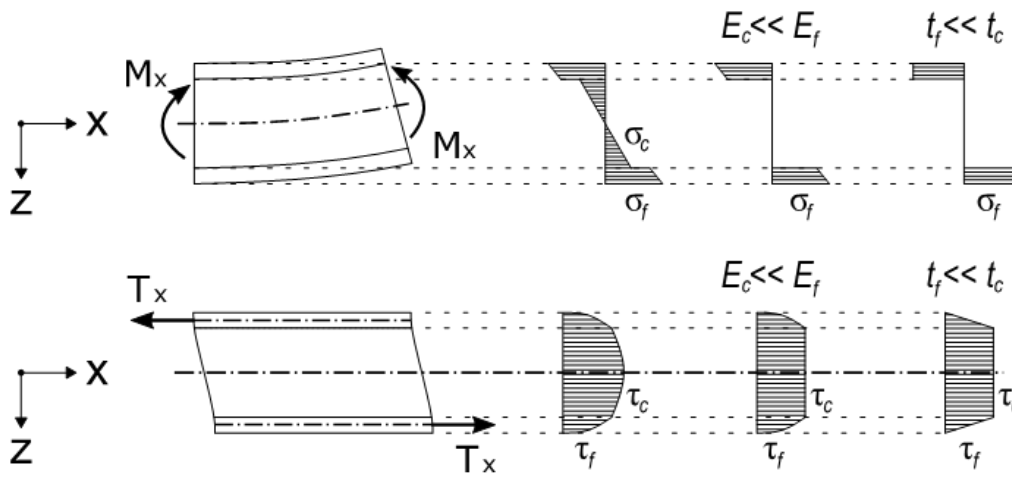


Figure 3.4. (Top). Bending stresses scheme. (Bottom). Shear stresses scheme.

Both bending and shear distribution are given schematically in Figure 3.4. As previously pointed out, when comparing core and faces, the core exhibits a smaller elastic modulus than the faces ($E_f \ll E_c$), therefore, only the bottom and top layers are considered as relevant for the bending stress studies. Moreover, commonly thin faces are employed for sandwich structures ($t_f \ll C$) and, thus, further simplifications are

allowed, such as constant bending stresses through face thicknesses despite having, in fact, a lineal stress distribution. Additionally, in the case of shear loading, the core bears the transverse loads as shear stresses, and a constant shear distribution through the core might be assumed, when flexural rigidity contribution of the core results insignificant compared to face rigidities ($E_c \approx 0$).

In practice, in-plane compression upon sandwich panels is not very common, with exception of few cases, such in pressure-loaded nozzles in aircrafts [68]. Considering equal faces, the direct strain and stresses on the core and the faces due to an in-plane N load is given by Eq.(3.6), Eq. (3.7) and Eq. (3.8) respectively [51]. Factor ε_{x0} represents the strain according to the neutral axis. The stress over the core is commonly very small compared to the faces, because faces present a larger in-plane elastic modulus than the cores, and thus, faces carry mostly the normal in-plane loads.

$$\varepsilon_{x0} = \frac{N_x}{2 E_f t_f + E_c c} \quad (3.6)$$

$$\sigma_c = E_c \varepsilon_{x0} \quad (3.7)$$

$$\sigma_f = E_f \varepsilon_{x0} \quad (3.8)$$

Specific studies regarding other basic loading upon sandwich panels, such as out-of-plane compression and lap-shear response, are carried out in corresponding chapters, while analysing each sandwich core proposed, their unit-cells geometries and their elastic behaviour, as described at the beginning of this section.

3.2.3 Failure modes

The core and the faces are commonly studied individually for failure predictions of a complete sandwich structure. Here, failure of the bonding mean is also presented for studies. The failure modes (i.e., the mechanism or the way in which the material may break or collapse) depend upon a number of factors such as the base material combination and the design variables, for instance, the geometry of faces and core (i.e., including the unit cells under study), bonding strength and the way the loads are introduced, whether in-plane, out-of-plane, tensile, compression, shear, or flexural loads, individually or combined. More information over failure modes can be found in references [111,144]. The most common failure modes of sandwich panels are presented schematically in Figure 3.5 which, in turn, will be used in this work.

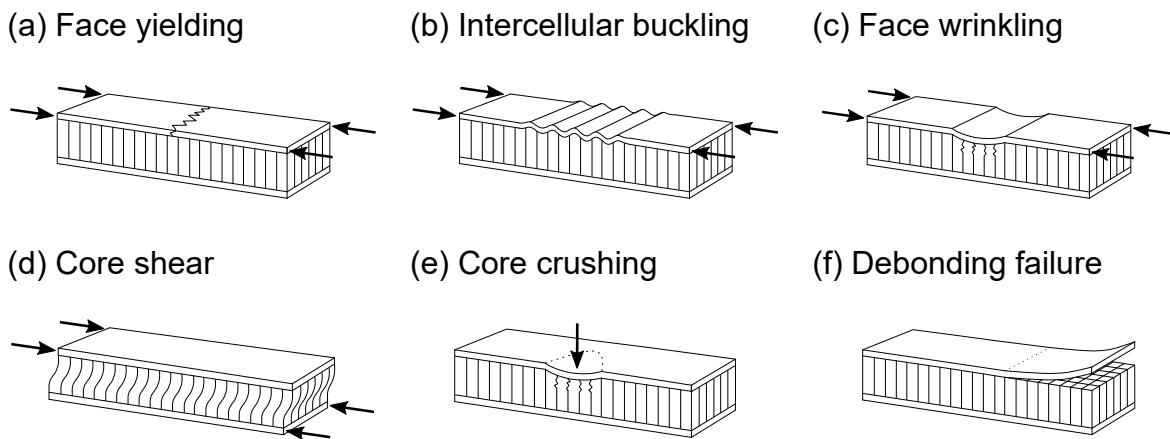


Figure 3.5. Sandwich failure modes schemes

3.2.3.1 Face failure

As presented in previous chapters, faces can be made from different base materials. In this work, FRP faces are selected in way of combining high mechanical performances with low density. Hence, as acknowledged previously, there are many failure criteria for FRP laminates, albeit two can be identified on the large scale, either as strength or stiffness failure criteria [110,111,144]:

- *Maximum stress failure* (in tensile or compression modes); also called as *face yielding* failure (Figure 3.5.a), it commonly occurs when one of the faces reaches the in-plane strength of the base material. The failure can appear due to a normal in-plane load, or bending loading, the latter considering thin faces, and a load distribution assumed as constant. Fibre reinforced polymers materials fails differently in tension than in compression loading, and the latter is commonly the critical one.
- *Elastic failure*. When the faces are submitted to in-plane loading, local plate buckling may occur. It is possible to identify two main sub-modes of skin buckling failure, regarding the core unit cells: the first sub-mode is called *face wrinkling* (Figure 3.5.b), In this case, a skin buckling mode with a wavelength greater than the width of the unit cell of the core. Assuming the face as plate on a continuous elastic foundation (the core), a critical load is calculated. Then, faces can buckle either towards inside or towards outside the panel, depending on the core elastic modulus and the adhesive strength. The second main elastic failure mode on faces is called *intercellular buckling* (Figure 3.5.c), where the wavelength of the buckling wrinkles is smaller than the size of the core unit cells. This

may occur, since a large part of the face is unsupported by the core and buckling can occur in this region locally. A critical stress for intercellular buckling can be expressed from the simple elastic plate buckling theory, suiting the parameters to FRP materials.

3.2.3.2 Core failure

Cellular cores carry mostly shear loads (for example, due to a plate-shear or three-point bending cases) and out-of-plane compressive loads. Therefore, cores may fail either by two different modes as [110,111,144]:

- *Core shear* (Figure 3.5.d). Neglecting the contribution of the skins, when shear stresses applied are higher than the shear strength of the core, the core fails in shear mode, typically denoting cracks inclined at 45° if the core is homogeneous under pure shear. When using FRP as base materials, the core shear strength depends upon the fibre orientation.
- *Core crushing* (Figure 3.5.e). If a sandwich panel is loaded by an out-of-plane force, the core may fail under the indenter (or the body transmitting the load), when the out-of-plane compressive strength of the core is exceeded. Typically, this failure arises because of a stress concentration, and thus, depends directly on the loaded area. Different works have been presented to study the behaviour of "soft" cores (flexible in the out-of-plane direction) by considering high-order effects, to predict the non-linear behaviour and to achieve a more accurate estimation upon calculations [148,149]. These studies exceed the focus of this work, and they are not considered for analyses.

3.2.3.3 Bonding failure

When using rigid and periodic cellular cores, the bonding area between the core and the skins is usually very small. If snap-fit nodes are not used, the probability of failure due to core detachment from the skin is high and the *debonding failure* mode (Figure 3.5.f) has a high probability of occurrence (so called adhesion failure of the face/core layer). It is well known that the bonded region between the faces and core members must be large enough to resist the shear stresses within the discontinuity. The bonded area must include the menisci that originate from excess glue [150]. For studying of debonding, Xiong et al. [151] proposed two simple alternative ways: firstly, considering a unit cell, when the shear stresses in the bonded area exceed the bond

strength. On the other hand, an analysis that includes the total region of the core with the number of unit cells involved, resulting in an average strength value. The latter results ever since the bonded area within a unit cell is different from one another, due to the conditions of the manufacturing process which may cause local deformations of the bonding mean (i. e. greater local bonded surfaces). Besides adhesion failure, other kind of bonding breakage can be found in the literature and specific “peeling” tests identify and quantify the failure mode, such as delamination, cohesive failure within core member [152], and consequently, exceed the aims of this work.

3.2.4 Failure load surfaces

Once the principal failure modes of a sandwich beam are defined, the govern failure modes can be easily identified as regions drawn in a 3D-chart named “failure load surfaces” by calculating failure loads for each individual failure mechanism and equating them for obtaining the failure regions’ limits. The failure mechanisms are plotted as a function of three set variables related to: the loading case, the material properties such as the core and skin elastic moduli, and the design parameters such as the core and skin thicknesses or densities [51].

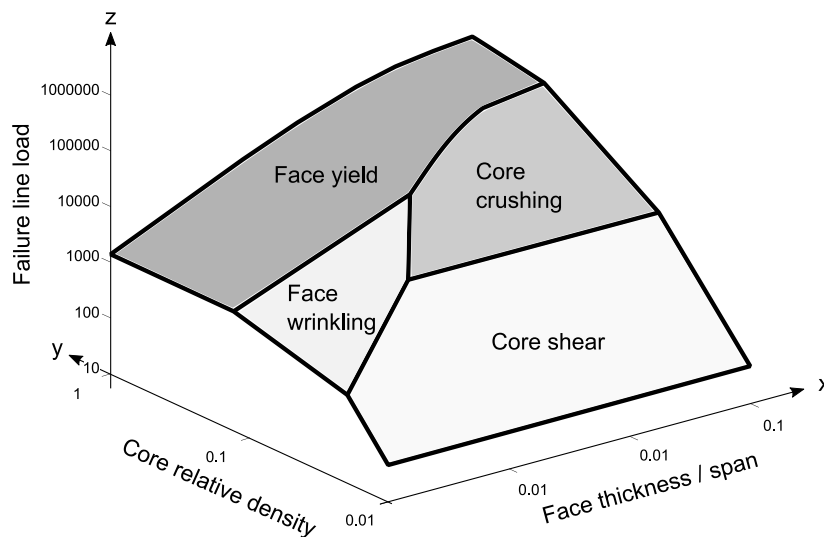


Figure 3.6. Example of failure load surfaces scheme for a sandwich beam in three-point bending. Adapted from [86]

The work of Petras [86] is presented as example to schematize the attainable failure regions for a particular GFRP-skin and aramid core case (Figure 3.6). The failure modes designations have been added to the surfaces to ease their recognition.

Besides the failure load surfaces, other graphics can be also obtained by projecting these surfaces to the orthogonal planes. Among them, the *failure mode maps* (projection over xy -plane), and the *main failure mechanism and failure loads* regarding to core or skin parameters (projection over xz -plane or yz -plane) can be found as well.

4 Ultra-lightweight 3D-honeycomb cores

As outlined in previous chapters, cellular cores for sandwich structures [1] are in focus of researchers and designers in a wide range of engineering applications. The aim is to employ a minimal number of raw materials for attaining strong and lightweight components using an open-cell topology (see section 3.1.2). Sandwich cores based on CFRP laminates have demonstrated to be competitive when their specific properties are compared to its metal counter parts either by out-of-plane compression and plate shear tests [105,139].

In this chapter, a novel manufacturing method for obtaining 3D-honeycomb cores with densities below 48 kgm^{-3} [24], based on CFRP is explored. Three different carbon fibre cores are obtained using an interlocking method [153] from CFRP composite laminates with different machined geometries. High specific compressive stiffness is the focus of the first approach. The scope of this chapter includes out-of-plane and plate shear studies. The core mechanical properties are evaluated by analytical models, supported by the finite element method. The failure modes for core strength predictions are also investigated, evaluating different failure mechanisms which derive in different failure loads, governed by buckling and maximum strength modes for compressive and shear studies, respectively. Subsequently, the predictions are in good correspondence with experiments.

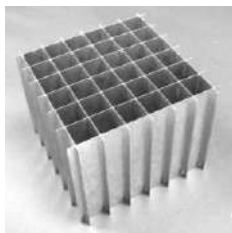
4.1 Literature review

Sandwich cores with high specific strength require a design that focuses on maximum weight savings, while still exhibiting outstanding mechanical properties. In the recent years, manufacturers and researchers put the focus on very low weight honeycombs cores with a square cell pattern (also known as *square-honeycomb* cores, Figure 4.1.a) according to different manufacturing strategies and base materials. As literature review, a selection of three of the most significant works on the topic is proposed in this section.

One of the relevant investigation found in literature upon square-honeycombs cores is the work of Côté and Evans [153]. The authors used AISI 304 steel sheets as raw material for the fabrication of square-honeycomb cores. Studies in out-of-plane

compression showed that this kind of topology exhibit higher strength and modulus compared to metallic foams and aluminium hexagonal-honeycomb based structures, if one takes as example a same core relative density ($\bar{\rho} = 0.03$) and a core cell aspect ratio of $H/L = 1$. The measured peak compressive strength of the square-honeycombs was almost 30% higher than the aluminium counterparts used as reference cores. In other work [154] they found that square-honeycomb cores under out-of-plane compression or in-plane shear loads are less susceptible to buckling than prismatic corrugated and diamond metallic cores. Additionally, Côté et al. [155] studied the effects of shear stresses on AISI 304 based square-honeycombs while varying H/L cell ratio and the core relative density. Under shear stresses, stainless steel cores of density $\bar{\rho} = 0.03$, showed 2.5 times the shear strength of aluminium 5052 honeycomb counterpart.

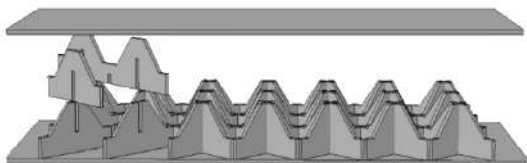
(a) Square-honeycomb core [153]



(b) Egg-boxes cores [156]



(c) Egg-honeycomb [122]



(d) Pyramidal-honeycomb [122]

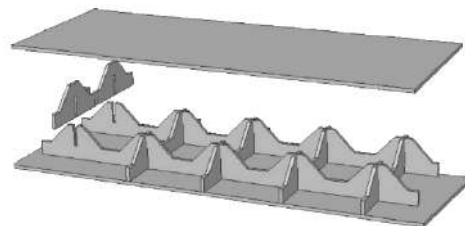


Figure 4.1. Example of the core structures mentioned

The continuous search for new base materials for increasing the specific strength and stiffness of sandwich structures led the designers to focus on CFRP composites. Consequently, CFRP-based sandwich cores are explored by Russel [21], who fabricated square-honeycomb cores by slotting woven and laminated CFRP composites with different fibre orientations. The core relative densities are attained in the range of 0.025 – 0.2, employing three different cell aspect ratios and varying the slotting relative position. Mechanical tests are performed comprising out-of-plane compressive and lap-shear tests. The observed maximum compressive strengths were 10 times higher

than those of a square-honeycomb core made of AISI 304 steel for $\rho_c \approx 250 \text{ kgm}^{-3}$ and more than 100 times compared to cellular “egg-boxes” shape cores (Figure 4.1.b) made from aluminium with a core density of $\rho_c \approx 100 \text{ kgm}^{-3}$. Regarding single-lap shear tests, the CFRP square-honeycomb cores of relative densities of $\bar{\rho} = 0.1$ reached a nominal peak shear strength of about 3.8 MPa and 6.2 MPa for laminates $[0/90]^\circ$ and woven $[\pm 45]^\circ$ CFRP-based materials, respectively. The authors confirmed that under shear stresses, the failure of laminates $[0/90]^\circ$ are governed by the deformation of the matrix (evidenced also by the larger failure strain reached), while the fibres on woven $[\pm 45]^\circ$ samples dominate the shear response of the composite.

Motivated by the wish for larger weight reductions in high-performance CFRP-based sandwich panels, Xiong et al. [122] introduced the so-called 3D-honeycomb cores (refer to Chapter 3). As pointed out by the authors, the open-cell core topology allows multifunctional benefits as active cooling systems or line embedding, among other features. The employed laminate base materials were cross plies of T700/epoxy prepregs at $[0/90]^\circ$. After finishing the CFRP-composite, a trapezoidal geometry is shaped in it with slots between unit-cells by means of an electronic engraving machine. Additionally, by varying the stacking orientation of the CFRP-sheet by 45° during the snap-fit assembly step, two different grid architectures are accomplished as: an egg-honeycomb grid (Figure 4.1.c) with core relative densities of $\bar{\rho} = 0.03$ and $\bar{\rho} = 0.06$; and a pyramidal-honeycomb grid (Figure 4.1.d) of densities $\bar{\rho} = 0.06$ and $\bar{\rho} = 0.12$. Studies upon out-of-plane compressive loading are carried-out, showing core compressive strengths of about 3 MPa and 5 MPa for the egg-honeycomb grid, and 6.5 and 11 MPa for the pyramidal-honeycomb cores. The main discrepancy between the proposed cores is established by observing the failure modes. The egg-honeycomb assembly presented fewer crossing slot-points along the CFRP-laminate, and the stability over the plate was less compared to the pyramidal-honeycomb. The latter cores were dominated by core crushing failure mode. In another study, Xiong et al. [132] evaluated the different failure modes under three-point bending of sandwich panels employing the mentioned egg and pyramidal-honeycomb cores. The authors predicted and later observed that the sandwich panels are susceptible to debonding at the core-face interface, due to the reduced bonded area at the core-face contact points, and vulnerable to face wrinkling, due to the relatively large width of unit-cells ($\approx 45 \text{ mm}$) and the resulting lack of face sheet support provided by the core.

Current research emphasizes on the development of cellular cores of relative core densities in the range of $\bar{\rho} = 0.025$ to 0.1 . As discussed previously in Chapter 3, in terms of nominal core density, cores with a density less than $\rho_c = 48 \text{ kgm}^{-3}$ ($\bar{\rho} \approx 0.035$) may be considered as an ultra-lightweight material (ULW) [24]. The aim of this chapter is to study ULW 3D-honeycomb cores proposed as an alternative for commercial sandwich cores. The core's competitiveness will be evaluated in Chapter 7.

The outline of this chapter is as follows:

1. A fabrication method based on the interlocking technique will be explored, detailing the manufacturing route to obtain ULW CFRP square honeycombs.
2. Analytical models supported by the finite element method of the core response to out-of-plane compression and plate-shear are developed for obtaining core elastic stiffnesses and strengths along with the predicted failure modes.
3. The core response is measured and described from experimental tests in compression and shear loading.
4. The results are discussed, and the theoretical models obtained are compared with the experimental data.

4.2 Design and construction

Employing different material processing techniques, square-honeycomb cores are fabricated. The base material employed is a woven CFRP plate obtained by vacuum infusion (VI). Using the computerised water jet cutting (WJC) technique, CFRP plates with three different core geometries and slots are machined. Employing the interlocking method [153], the CFRP sheets are assembled into a square pattern and bonded together with epoxy resin. The result is a hybrid structure [101] with large internal holes and densities below 48 kgm^{-3} .

4.2.1 Materials

One aim of this work is to obtain a very low density of the resulting cores. Thus, knowing in advance the density of the parent material is crucial for beginning with the first drafts of the design. The selected material processing technique for obtaining the CFRP plate is the VI. It does not allow any thickness control in the same way as RTM does, as the fibre compaction pressure is limited by atmospheric pressure. Thus, the theoretical maximum achievable pressure is 1 atm. Chen et al. [157] studied the fibre

compaction behaviour by RTM and determined the relationships between fibre volume content achieved, compression force and preform thickness reduction which allows the resin permeability to be evaluated as a function of applied pressure. Besides dry-fibre compaction analyses, scalable coupons also represent in engineering a simple manner to obtain in advance an accurate thickness overview of the plate to be manufactured. Hence, as a preliminary study for this work, different small coupons are assembled as two, three, four and five layers of base material fabric. After carrying-out the VI technique, the coupons thicknesses and weights are measured.

Therefore, the selected preform consisted of three layers of plain woven [0/90] ° *Torayca* T300-3k carbon fibre fabric. Additionally, it is interesting to remark that the susceptibility to delamination caused by machining processes is lightly reduced when woven laminates are employed, instead of unidirectional fibres [158]. The polymeric matrix applied is a DGEBA (DER 383, *Dow Chemicals*), and glycidyl aliphatic ether (*Novarchem S.A.*) is used as an epoxy reactive diluent, to decrease the resin viscosity and facilitate the vacuum infusion process. A cycloaliphatic amine (*Air Products and Chemicals Inc.*) is employed as hardener. Table 4.1 shows the properties of the fibre reinforcement and the epoxy resin selected.

Table 4.1. Carbon fibres and polymeric matrix main properties

T300 – Cloth						
Density (gcm ⁻³)	Filament diameter (µm)	Tow size number	Textile weight (gm ⁻²)	Tensile strength (GPa)	Tensile modulus (GPa)	Fracture strain (%)
1.8	7	3k	198	3.53	230	1.5
Polymeric matrix						
Epoxyde equiv. (geq ⁻¹)	Epoxyde percent. (%)	Density at 298 K (gcm ⁻³)	Viscosity at 298 K (Pa s)	Tensile strength (MPa)	Tensile modulus (GPa)	Fracture strain (%)
176 - 183	23 – 24	1.14	0.57 - 0.6	65 - 80	2.65	2 - 2.5

As a result, a CFRP composite plate with an average thickness of $t = 0.65 \pm 0.05$ mm and a mean density in the range of 1300-1350 kgm⁻³ (lab measured), and an average fibre volume content of 50.8%. The base material density is predicted of 1.475 gcm⁻³ by theory (see Annex C for further details). The difference between the values attained and the predictions is attributed to imperfections such as potential voids as a result of entrapped gas during the manufacturing process.

The base material elastic properties and its compressive strength are previously obtained based on the classical laminate theory and the Budiansky's model, respectively, and are shown in Table 4.2. Details for the calculations are given in Annex B.

Note that properties are established regarding the fibre-load orientations, considering Figure 4.7 as coordinate references, observing that unit cells are symmetrical. In this case, the local x, y, z -directions are parallel to the global 1, 2, 3-directions.

Table 4.2. Theoretical elastic properties of the woven composite material T300/epoxy.

Composite elastic modulus $E_{3s} = E_{1s}$ (GPa)	Composite elastic modulus G_{13s} (GPa)	Composite Poisson's modulus $\nu_{13s} = \nu_{31s}$ (--)	Fiber volume fraction φ_f (%)	Composite compressive strength $\sigma_{3s}^- = \sigma_{1s}^-$ (MPa)	Composite shear strength τ_{13s} (MPa)
62.6	3.56	0.03	50.8	482.3	110

Note: subscript s represents the parent material

4.2.2 Square-honeycomb design

The proposal of this chapter consists of the design of ULW hybrid structures with high strength and stiffness-to-weight ratio in an out-of-plane load case. This feature is achieved by orienting the fibres parallel to the direction of the loading (3-direction, Figure 4.7).

A further aspect to be attained is a hollow structure by virtue of the opened cell characteristic, not only for weight savings but also for allowing potential multifunctional features (e.g. heat transfer, foam filling capabilities and its benefits such as isolation or impact response, damping properties, shape morphing, among others [129,159,160]).

The hollow geometry is proposed according to three hollow designs (Figure 4.2. a-b) that deal with the loading solicitation. The catenary-like shapes have been used in civil engineering or architecture when high compressive properties are required to fulfil the mechanical demands. Ideally, catenary curves are based on inverted arches, being the locus of the points where the horizontal tensions are compensated and for that reason has no lateral stresses, and they not need lateral compensations [161].

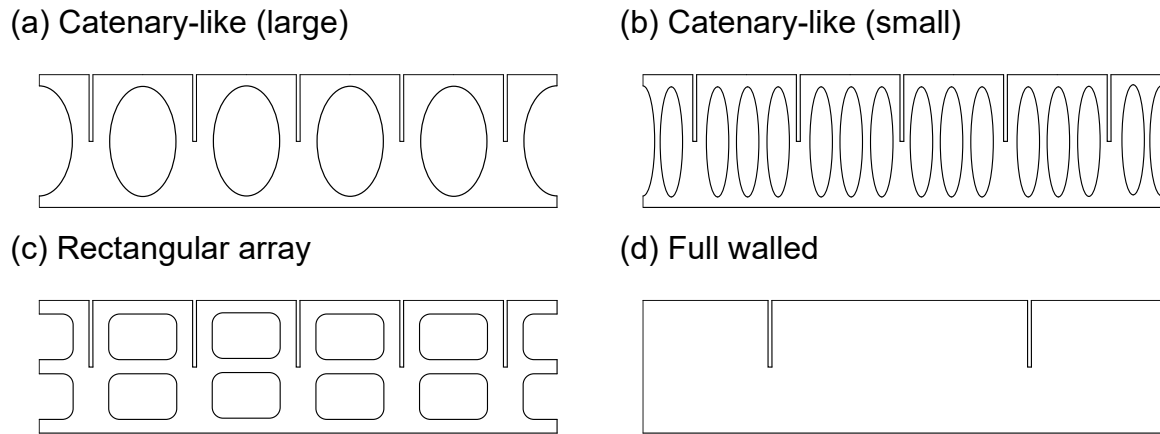


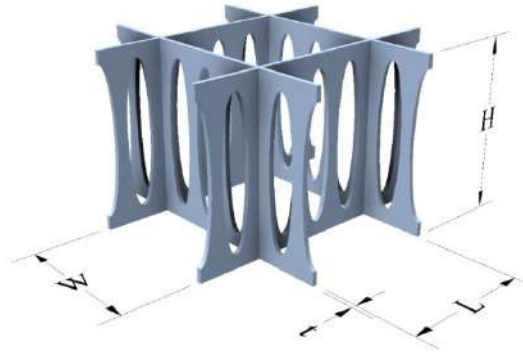
Figure 4.2. Core sheet patterns proposed

Moreover, the rectangular arrays (Figure 4.2.c) are first thought as cavities with central struts, looking forward to a more restricted system in which the load capability is enhanced by the horizontal linking (stud-link chain-like). To contrast the performance of the selected geometries, a core made from full-walled base material is taken as reference (Figure 4.2.d). A square-honeycomb core pattern is fabricated, due to its versatility and ease of manufacturing, being a competitive structure already proven compared to known sandwich cores [105,153]. The machined slotted pattern only is required over one side of the sheet, due to pattern symmetry to the horizontal mid-plane. During the sheet assembly step, one long edge of a sheet must be right side up, while the long edge from another sheet must be upside down. An additional condition that is expected in this proposal, contemplates the core symmetry along the xy -plane, i.e., considering core geometry, the number of sheets employed are equal and equidistant regarding the L and W directions. Thus, the unit cells are symmetric as $L = W$ (Figure 4.3). A higher number of cross-linked composite sheets (i.e., unit cells) enhance the out-of-plane loading strength and stiffness of the core, along with the bonding surface.

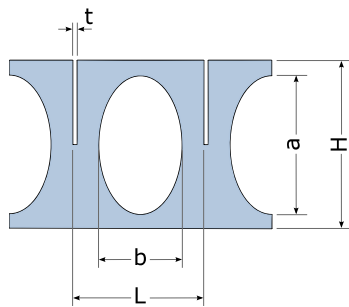
In this chapter, unit cells dimensions are of a size of 20 by 20 mm for the machined core sheets and 50 by 50 mm for the cores without cavities. The unit cells mean dimensions and core patterns are schematically given in Figure 4.3 and specified in Table 4.3. The relative density of the cores is calculated either: by the areas occupied by material within a CFRP sheet and multiplying it by its average thickness and the number of sheets; or in an analogous manner, by calculating the amount of material within a unit cell (see section 4.2.2.1). The densities of the core and unit cells are

equivalent as $\rho_{core} = \rho_{cell} = \rho_c$. The resulting densities are less than 48 kgm^{-3} , later verified by lab measurements (see Annex C).

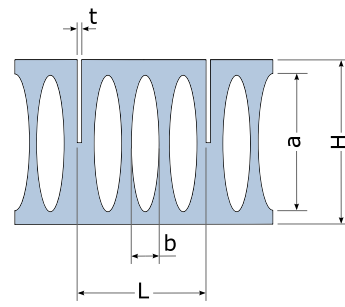
(a) Sketch example of a unit-cell



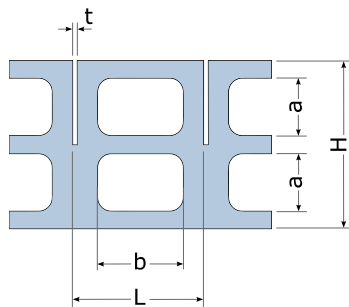
(b) Cell design 1: catenary-like (large)



(c) Cell design 2: catenary-like (small)



(d) Cell design 3: rectangular array



(e) Reference cell: full walled

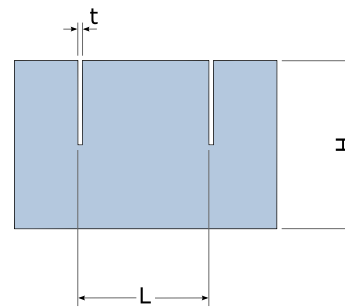


Figure 4.3. Scheme of unit repetitive cell patterns and main geometry parameters

Table 4.3. Unit-cells mean dimensions and core densities employed.

<i>Pattern</i>	<i>H</i> (mm)	<i>L = W</i> (mm)	<i>t</i> (mm)	<i>a</i> (mm)	<i>b</i> (mm)	ρ_c^* (kgm^{-3})	ρ_c^{**} (kgm^{-3})
Design 1	25.40	20	0.65	21.40	13.09	47.40	47.64
Design 2	25.40	20	0.65	21.40	4.10	47.77	46.06
Design 3	25.40	20	0.65	8.7	13.22	46.01	46.65
Reference	25.40	50	0.65	--	--	37.80	38.67

* Theoretical value. ** Lab-measured

4.2.2.1 Core relative density estimation

The calculation of the relative density of a square-honeycomb core is based on the main parameters that describe unit cells geometries (Figure 4.3) by using simple geometric considerations. Here, the core relative density of the full-walled core pattern is described.

On the one hand, the average area A_s occupied by the base material within a square unit cell as $L = W$ is given by Eq. (4.1). The unit cell area A_{cell} is shown as Eq. (4.2) and considering a relative area $A_{rel} \leq 1$ as the ratio A_s/A_{cell} , Eq. (4.3) is attained.

$$A_s = tL + tW = 2tL \quad (4.1)$$

$$A_{cell} = LW = L^2 \quad (4.2)$$

$$A_{rel} = \frac{A_s}{A_{cell}} = \frac{2t}{L} \quad (4.3)$$

On the other hand, considering the general expression of the density of the base material ρ_s as the mass of the base material m_s within a unit cell over the base material volume as

$$\rho_s = \frac{m_s}{A_s H} = \frac{m_s}{2tLH} \quad (4.4)$$

The density of the unit cell core, ergo the density of the core sample, is defined by Eq. (4.5), as the ratio of the unit-cell core mass m_{cell} and the unit cell volume V_{cell} .

$$\rho_c = \frac{m_{cell}}{V_{cell}} = \frac{m_{cell}}{L^2 H} \quad (4.5)$$

The relative density $\bar{\rho}$ of a square unit-cell honeycomb is obtained by Eq. (4.6), combining both Eq. (4.4) and Eq. (4.5), where $\rho_c/\rho_s \leq 1$. The unit-cell mass m_{cell} and the base material mass within a unit-cell m_s are equal in magnitude.

$$\bar{\rho} = \frac{\rho_c}{\rho_s} = \frac{2t}{L} = A_{rel} \quad (4.6)$$

Therefore, the relative density of a full-walled square-honeycomb core can be defined either by the relative area of the unit cell as Eq. (4.3) or by employing the ratio of the base material and core densities as Eq. (4.6).

The case of machined 3D-honeycomb cores is addressed in a similar manner, but calculating the area occupied by the base material (see Annex C for further details). From CAD models these values are also easily attained.

4.2.3 Manufacturing method

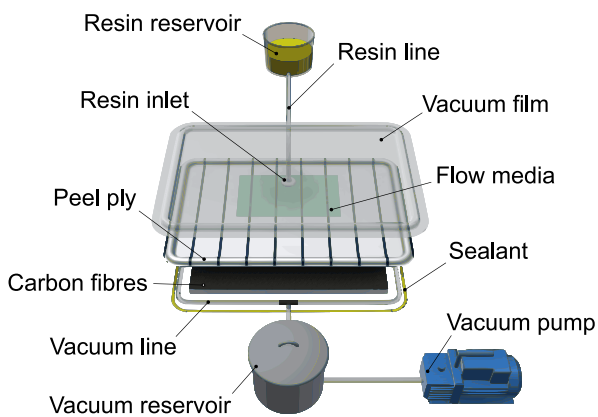
The route for manufacturing the sandwich cores is resumed as a combination of several known material processing methods, comprising the vacuum infusion (VI) technic (Figure 4.4.a), the computerized water-jet cutting phase (WJC) (Figure 4.4.b) and the slotting/interlocking method as final step for the core assembly (Figure 4.4.c). The last step contemplates the bonding between faces and core with an epoxydic gluing mean (Figure 4.4.d), to obtain a stabilized core structure. The fabrication procedure is described in further details in this section.

There are different ways to perform resin infusion in VI according to the dimensions of the plate, to fully impregnate all the fibres and to achieve a homogeneous thickness along the plate. Correia et al. [162] and Yenilmez [163] studied the thickness of the part to be manufactured at different times during the material processing stage as: before, during and after resin infusion. Prior to infusion and during the vacuum stage, the mould is ideally subjected to a pressure of 1 bar, compressed by the vacuum film. During the infusion, there is a resin flow front that counteracts the pressure exerted by the bag, as the resin makes its way through the preform, impregnating the fibres [164]. If the plate is of considerable dimensions (> 500 mm), the effect of thickness variation due to the pressure difference within the preform is much more evident, as mould filling times are extended. By placing several infusion points (inlets) or changing the infusion method, e.g., from linear to radial, it is possible to mitigate the effect of plate thickness variation, since distances travelled by the resin are shortened, giving a regular pressure distribution, and at the same time reducing processing times.

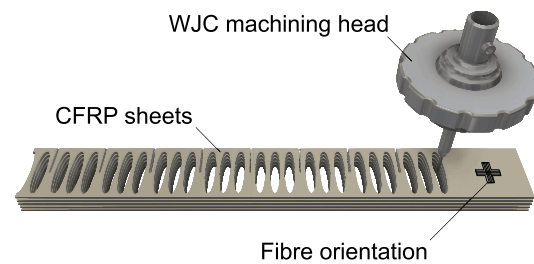
In this work, the dry assembly comprises three plain woven layers of carbon fibres fabrics, over a wax coated plain substrate to ease the releasing. The vacuum infusion transfer moulding set-up is arranged as a central-radial infusion, with lateral vacuum-lines, targeting a homogeneous final thickness of the CFRP plate after the infusion and curing stages (Figure 4.4.a). The resin is infused at room temperature. Once completed the fill, the resin line is closed, and after a few minutes, the vacuum line is closed, in a way that the pressure over the entire plate is homogenised. The mould is then put into an air circulating oven at 120 °C and cured for 2h. After curing and realising the part, the CFRP plate is cut into rectangular sheets with the desired geometries patterns employing the WJC method (Figure 4.4.b). The machined slots had a final nominal width of 0.65 mm. The clearance between sheet thickness and slot

width was less than $\pm 0.05\text{mm}$, which gives a suitable tight fit while implementing the slotting/interlocking method (Figure 4.4.c). A machined support plate is used to ensure the correct position of the CFRP sheets (the assembly-in-position method resembles reference [151]), while cross-slots are bonded together using the same base resin employed, attaining the desired square-honeycomb pattern (Figure 4.4.c). Later, the cores are put into a cabinet oven at $140\text{ }^\circ\text{C}$ for 24 h. As final step, CFRP top and bottom faces are attached to the cores using a 2-component epoxy adhesive (UHU plus End-fest 300®), to obtain stabilized core samples. Figure 4.4.d shows schematically core and face assembly with an open top-face for a better visualization of the unit cells.

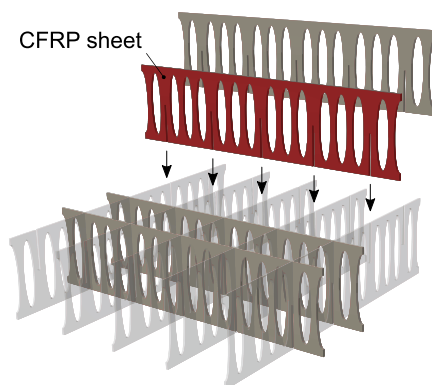
(a) Vacuum infusion setup



(b) WJC step



(c) Slotting-interlocking method



(d) Core-face assembly



Figure 4.4. The manufacturing route for obtaining ULW square honeycomb cores

Rectangular samples are cut from large core assemblies to obtain compression and shear test samples. Compression samples are made of a size of 100 by 100 mm and a height of 25.4 mm, containing an array of 4 x 4 and 1 x 1 unit cells, with 5 x 5 and 2 x 2 struts for the proposed cores and reference core, respectively (Figure 4.5).

(a) Proposed geometries

(b) Reference core

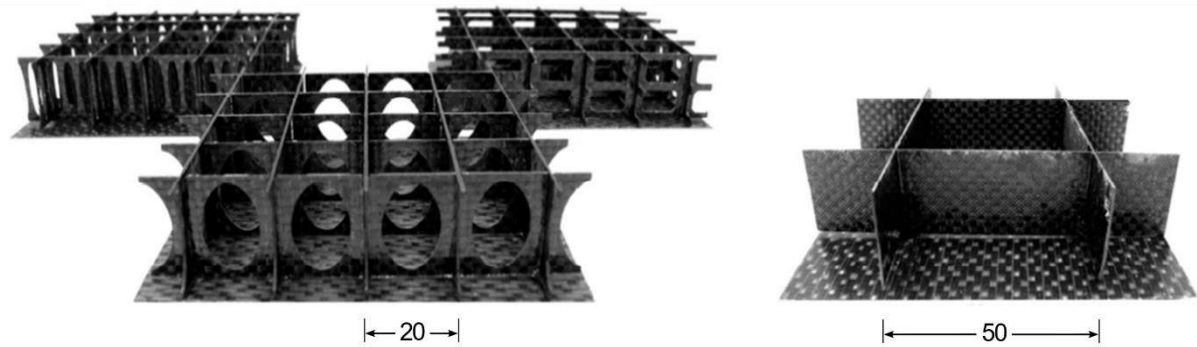


Figure 4.5. Photographs of core compression samples obtained

Shear samples are tailored to maximize pure shear stresses along the core, and sample sizes of 200 by 100 mm and 25.4 mm in height are employed. The cells arrangements are of 8 x 4 and 2 x 1 unit cells, with 10 x 5 and 4 x 2 struts for the proposed and reference cores, respectively (Figure 4.6).

(a) Reference core

(b) Proposed machined geometries

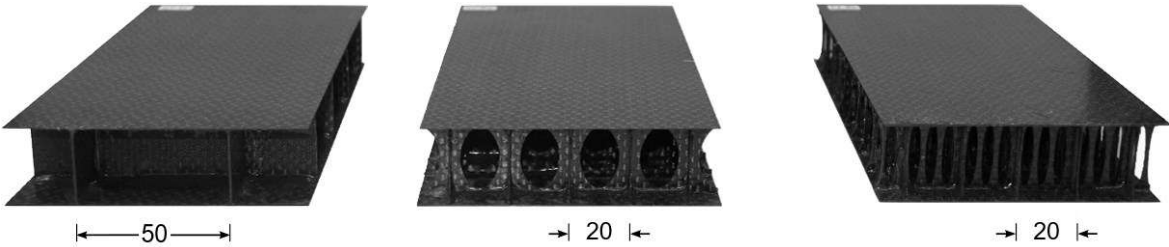


Figure 4.6. Photographs of core shear samples obtained.

4.3 Core out-of-plane compression

By analysing a single strut response to out-of-plane loading (Figure 4.7.a), the compressive stiffness and the compressive strength of the proposed square-honeycomb cores are estimated. The strut is defined as of a volume equal to the unit-cell volume $L \times W \times H$, and thus, will be identified as a representative cell element used for calculations. A nominal $t = 0.65$ mm is considered as the core wall thickness in all cases. Figure 4.7.b represents a view from top of the load case and the selected representative cell element, taking advantage of the symmetry of the model.

On one hand, analytical models are carried out by means of simple mechanical models, geometrical considerations, and displacements studies. A generic nominal

compressive load P is introduced through a top-plate and distributed along the core cells (Figure 4.8). The load is then balanced by a bottom bearing plate. The cores are considered perfectly bonded to the skins, and consequently, fixed border conditions are assumed.

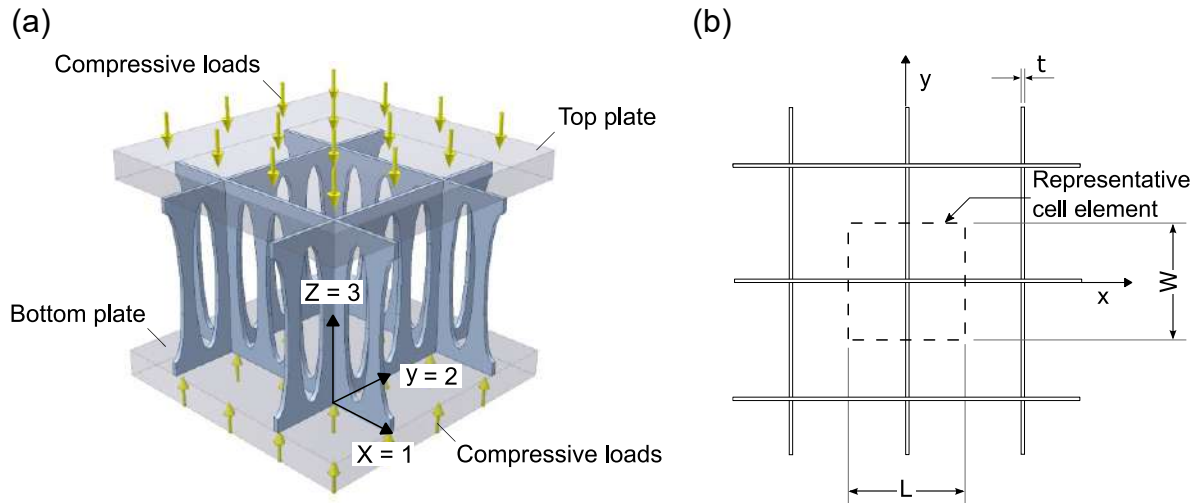


Figure 4.7. (a) A schematic compressive loading case render. (b) A top-view render with a schematic strut area used for calculations

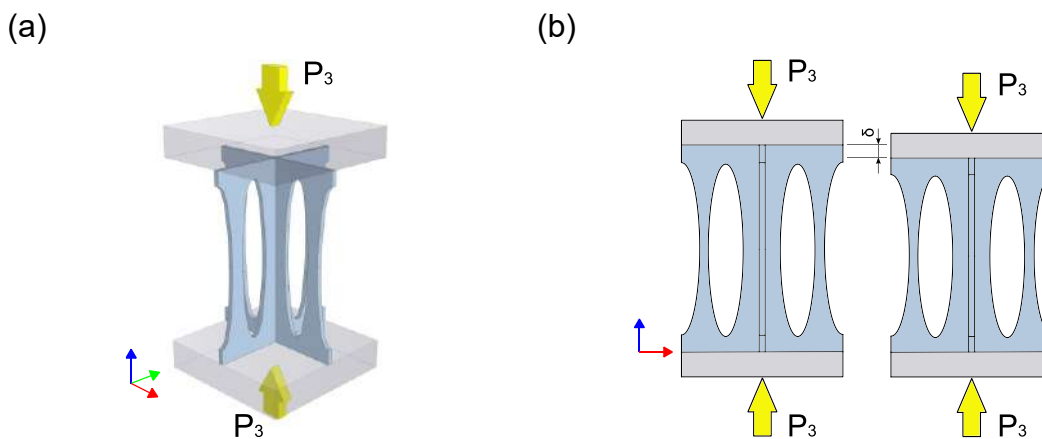


Figure 4.8. Sketches of models for calculation. (a) Representative cell element loaded. (b) Representative cell element front view: before and after straining

On the other hand, numerical models are developed by using the software FE-MAP™ 10.3 with NX™ Nastran® [29]. The simulations are carried out to have a further overview of the main structures behaviour and to validate the theoretical analyses. Finite element analyses combined with analytical calculations are used for indirectly predicting the elastic modulus, validated later by experimental tests. The evaluation of the square-honeycomb cores is resumed into a simplified case, employing unit cell

elements (Figure 4.3), which dimensions are shown in Table 4.3. The base material laminate was considered as an orthotropic material with an average thickness of $t = 0.65$ mm. The base material elastic properties are previously obtained based on classical laminate theory (see Chapter 2) and are shown in Table 4.2.

4.3.1 Compressive stiffness

A honeycomb core works as spacer between the face sheets. When the panel is loaded in compression by means of compressive plates (Figure 4.7.a), compression loads are transferred from the skins to the core. Assuming a linear behaviour and small displacements, the vertical displacement δ of the cell element assembly due to a resulting nominal load P is analysed for estimating the core compressive stiffness (Figure 4.8).

4.3.1.1 Analytical model

For determining the elastic modulus of the core E_c , a representative cell element as given in Figure 4.8.b is taken into account. The compressive load P is common to the cell element, and thus, its base material. Considering that the length L and the width W are the same ($L = W$), the compressive load P is written as Eq. (4.7) multiplying the applied stress over the cell element σ_c and the cell area given by A_{cell} in Eq.(4.2).

$$P = \sigma_c L^2 \quad (4.7)$$

The stress over the base material σ_s is attained as Eq.(4.8), incorporating the definitions of A_s (Eq. (4.1)), P (Eq.(4.7)) and $\bar{\rho}$ (Eq. (4.6)).

$$\sigma_s = \frac{P}{A_s} = \frac{\sigma_c L^2}{2tL} = \sigma_c \frac{L}{2t} = \sigma_c \frac{1}{\bar{\rho}} \quad (4.8)$$

The experienced compressive strain ε over the unit cell and base material are the same because loads and the vertical displacements are common to both. Then, the strain is written as Eq. (4.9), as the displacement over the cell height, and equated to the cell and base material stresses over the respective elastic moduli employing Hooke's law.

$$\varepsilon = \frac{\delta}{H} = \frac{\sigma_c}{E_c} = \frac{\sigma_s}{E_{3s}} \quad (4.9)$$

Incorporating Eq. (4.8) into Eq. (4.9), the elastic modulus of the core E_c is given in Eq. (4.10).

$$E_c = \frac{\sigma_c}{\sigma_s} E_{3s} = \frac{2t}{L} E_{3s} = \bar{\rho} E_{3s} \quad (4.10)$$

Eq.(4.10) shall only be applied for estimating the elastic modulus of reference cores, where the unit cells walls are made from base material without cavities, because the area of the base material A_s is considered as of a constant cross-section of length L within the area of the cell element A_{cell} . Thereupon, employing Eq. (4.10) directly for the evaluation of the Young's modulus of the machined cores would not be representative of the true material bearing the load, since the cavities in the CFRP sheet make A_s smaller compared to the reference ones.

Therefore, to evaluate the elastic moduli of the machined cores, it is necessary to set each case considering the area of material that effectively carries the payload, taken into account the pattern openings. As a first approach, it is assumed that the cruciform cross-section of the strut bears most of the compressive loads. Thus, an equivalent cruciform column of constant profile with four identical flanks of thickness t and an equivalent width $L_{eq}/2$ approximates the cell element with the pattern cavity (Figure 4.9). The size of L_{eq} is taken as the minimum width of the strut at the mid-plane.

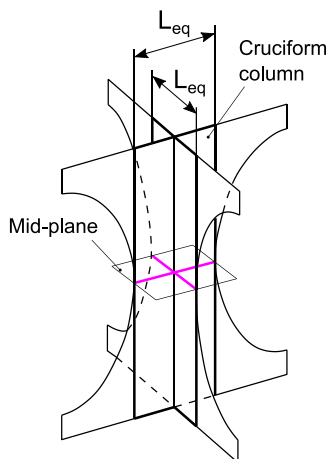


Figure 4.9. Sketch example of the structure approximation by a cruciform column

Then, recalling Eq. (4.2), Eq. (4.6) and replacing Eq. (4.1) by the area of the base material for the machined core cases as $A_s = 2tL_{eq}$ and introducing them into Eq. (4.10), the core elastic modulus of the machined cores is given by Eq.(4.11).

$$E_c = \frac{2tL_{eq}}{L^2} E_{3s} \quad (4.11)$$

The results of the analytical approached for the core compressive stiffness regarding Eq. (4.10) and Eq. (4.11) are found in Table 4.4.

Table 4.4. Core compressive elastic moduli obtained by analytical approaches

<i>Pattern</i>	L (mm)	L_{eq} (mm)	E_{3s} (GPa)	E_c (MPa)
Design 1	20	6.910	62.6	1403.50
Design 2	20	7.694	62.6	1562.84
Design 3	20	6.800	62.6	1381.25
Reference	50	50	62.6	1627.60

4.3.1.2 Numerical approach

Cells based on CFRP sheet material are discretized using a mesh of shell elements (CQUAD4, 4-node reduced integration) of size 0.4, representing the geometry of the studied cores (Figure 4.3). By using rigid elements at the top node-line, a load P of 1 kN is applied simulating a compressive load over the main set (load-controlled). The bottom node-lines are set as fully clamped while the top nodes only are able to displace according to z-direction. Considering small displacements and linear elastic behaviour (via static analyses), the elastic modulus can be derived from the vertical displacement δ obtained by the FE simulations and employing Eq. (4.12).

$$E_c = \frac{H}{\delta} \sigma_c \quad (4.12)$$

Figure 4.10 shows the distributions of the normal stress σ_z contour plots for a vertical load of 1 kN. Core design 1 and 2 denote a higher local stress concentration at the mid-plane edges as an effect of the cross-section reduction along the profile (i.e., from the top to the mid-plane and from the mid-plane to the bottom). In particular, core design 2 do exhibit higher stresses at the central strut and the small columns at each side as a result of the smaller cross-sectional area. Core design 3 shows a more uniform stress distribution in the middle cruciform column compared to design 1 and 2, as a result of the vertical lineal profile along the machined pattern from top to bottom. In this case, the local stresses are not as concentrated as in previous core patterns. As seen in the contour plots, the machined area does not contribute significantly to the overall payload capability of the cell (red contour). Moreover, the reference core exhib-

ited a regular stress distribution since no local stress concentration is attained, because the cross-sectional profile is constant along the cell. The little variation in the contour plot is attributed to numerical noise since the stress values are nearly constant.

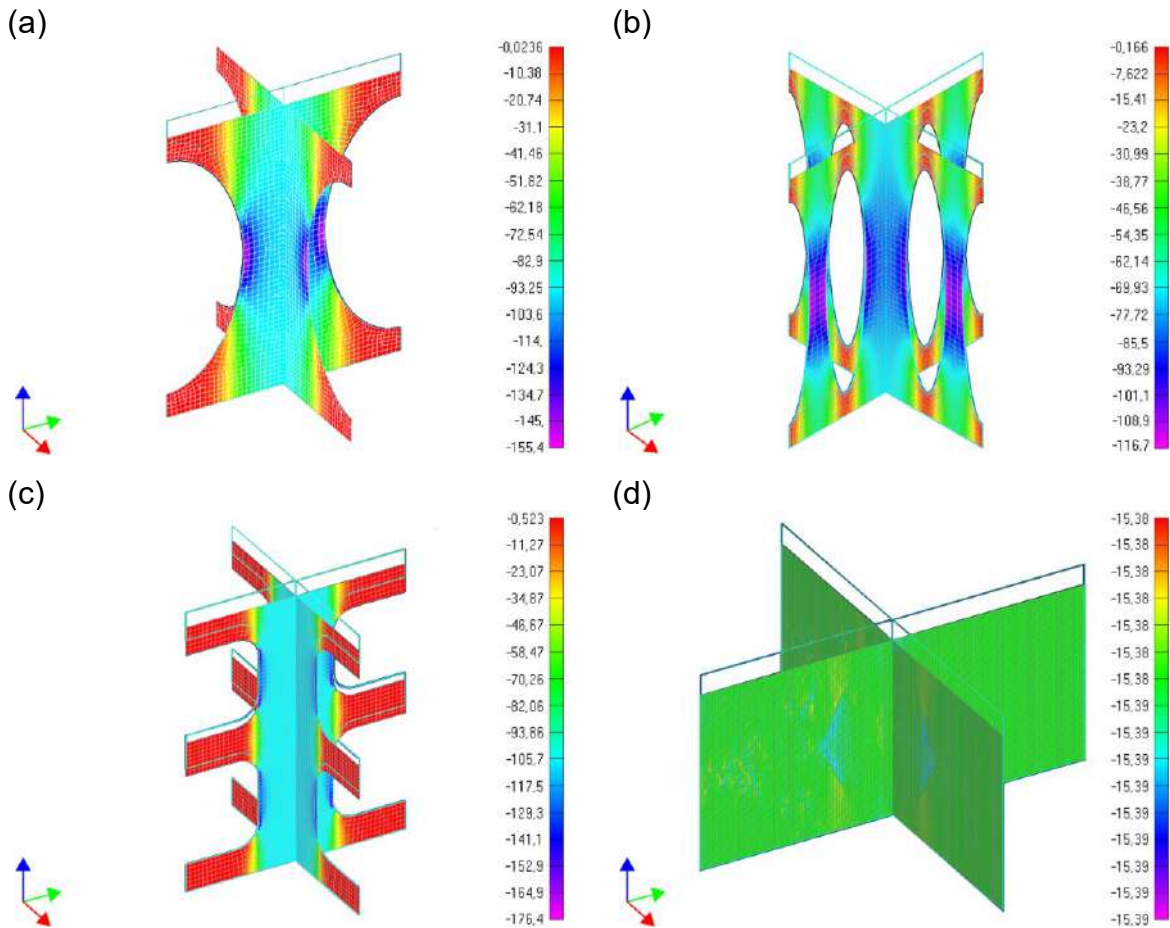


Figure 4.10. Contour plots of the normal compressive stress distribution by FE simulations: (a) core design 1, (b) core design 2, (c) core design 3, and (d) reference core

Table 4.5 comprises the relevant information regarding FEM results and a brief comparison with the theoretical ones. For a load of 1 kN, the average stresses in the mid-plane nodes of the base material σ_s are of 118.62 MPa, 104.12 MPa, and 122.76 MPa for core design 1, 2 and 3, respectively. In contrast to the machined cores, the reference cell shows a homogeneous normal stress distribution of value 15.385 MPa. For this case, considering the applied load over the cell 1 kN, and dividing it by the base material area $A_s = 2tL = 65 \text{ mm}^2$, the analytical value for the stress over the base material σ_s is 15.385 MPa, and thus, the negligible stress variations on the mesh from the simulations (numerical noise) are then disesteemed. Furthermore, the exhibited peak elastic moduli bound obtained by Eq. (4.12) of the cores is of 1392.54 MPa for

the core design 3, as the minimum; and 1935.98 MPa for the core design 2, as the maximum. Core design 1 presents an elastic modulus of 1599.5 MPa, slightly above of the reference core, which shows a compressive modulus of 1572.76 MPa according to simulations. The latter results are discussed in section 4.5.1.2.

Table 4.5. Core compressive stresses, strains and elastic moduli obtained by FE.

<i>Pattern</i>	<i>L</i> (mm)	<i>H</i> (mm)	σ_s (MPa)	δ (mm)	ϵ_c ($\mu\text{m}/\text{m}$)	E_c (MPa)	E_c^* (MPa)
Design 1	20	25.4	118.62	0.03970	1562.99	1599.50	1403.50
Design 2	20	25.4	104.12	0.03280	1291.13	1935.98	1562.84
Design 3	20	25.4	122.76	0.04560	1795.53	1392.54	1381.25
Reference	50	25.4	15.385	0.00646	254.33	1572.76	1627.60

Note: (*) Theoretical value

4.3.2 Compressive strength

Different failure mechanisms can occur during compressive loading. The mechanism that demands the lowest payload for the collapse of the structure will determine the critical compressive load P_{crit} and thereby, the core compressive strength. Thus, the core peak strength σ_{cpk} depends on the mechanism that governs the failure of the base material, either by elastic or crushing failure of the cell members (Eq. (4.13)). Considering the base material as an orthotropic composite material and assuming uniform straining under compressive loading, four failure stress mechanisms are identified as:

1. Maximum compressive strength σ_{cR} (when the base material's strength is exceeded beyond σ_{3s}^-).
2. Torsional buckling σ_{cTB} .
3. Euler flexural buckling σ_{cEu} .
4. Plate elastic buckling σ_{cB} .

$$\sigma_{cpk} = \min(\sigma_{cR}, \sigma_{cTB}, \sigma_{cEu}, \sigma_{cB}) \quad (4.13)$$

After failure modes evaluation, the mode with a higher likelihood to occur is denoted as torsional buckling, due to the laminate mechanical properties, architecture, and geometry of the cores, that leads to lower critical loads. The result is contrasted with numerical simulations with good correspondence.

4.3.2.1 Analytical approach

As previously presented in Chapter 2, FRP may fail either by strength or by stability. Since the lightweight cores proposed consist of thin-walled CFRP plates, the stability phenomenon is assumed to be the failure mode with the highest probability of occurrence in compression tests. When cores are loaded with an out-of-plane compressive load, it is assumed that all cell walls are loaded equally to ease the analysis. The different failure mechanisms are addressed as follows.

4.3.2.1.1 Maximum compressive strength

Fibre reinforced polymer composites under longitudinal compression loads, may fail by strength as a localised buckling of the fibres (*micro-buckling*). The Budiansky's failure model is employed for calculations as described in section 2.2.3.1.2.2. Then, the average composite compressive strength estimated is $\sigma_{3s}^- = 482$ MPa (see Annex B for further details).

The maximum compressive strength of the core regarding the base material compressive failure, is analysed through a representative cell element model (Figure 4.8). Thus, when the core is subjected to an out-of-plane compressive load P , failure may be attained when the base material strength is reached. The applied load is common to the base material and the cell used for analyses. Therefore, the critical load P_{cR} (i.e., when failure is attained) is written in terms of the product of composite compressive strength σ_{3s}^- and the base material area A_s , and the product of the core compressive strength σ_{cR} and the cell area A_{cell} (Eq. (4.14)).

Consequently, the core compressive strength is dependent on the core relative density as Eq. (4.15), and its valid for a full walled sheet material (reference cores). As seen in section 4.3.1.1, for the machined cores it is necessary to consider the amount of material bearing the load, and thus, a cruciform strut with flanks of $L_{eq}/2$ is implemented for approximations on the calculation. Introducing the area of the base material as $A_s = 2tL_{eq}$, Eq. (4.15) is written as Eq. (4.16) for the compressive strength of the machined core cases, disregarding the contribution to the payload of the machined curves as a first approximation.

$$P_{cR} = \sigma_{3s}^- A_s = \sigma_{cR} A_{cell} \quad (4.14)$$

$$\sigma_{cR} = \sigma_{3s}^- \frac{A_s}{A_{cell}} = \sigma_{3s}^- \bar{\rho} \quad (4.15)$$

$$\sigma_{cR} = \sigma_{3s} \frac{2tL_{eq}}{L^2} \quad (4.16)$$

4.3.2.1.2 Torsional buckling

If core members are considered as of an array of cruciform cross-section columns and of an open profile (i.e., each flank is free from constraints on the lateral vertical side), under uniform out-of-plane compressive loads and considering equally loaded core members, thin walled-columns may buckle in a torsional manner. In other words, when the structure reaches a critical load P_φ , each flank buckles by turning around the vertical axis (z-axis); while the common vertical axis remains straight (Figure 4.11). The curved arrows shown symbolize the turning direction of the flanks an angle φ .

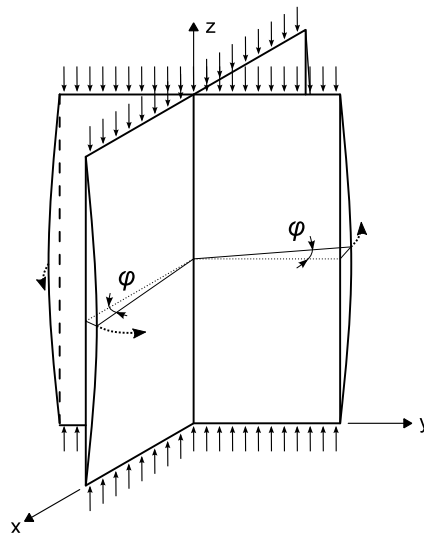


Figure 4.11. Column of cruciform cross-section showing torsional buckling [165]

The complete theory to be used in the analysis of torsional buckling is presented by Timoshenko [165], considering a column as a bar of cruciform cross-section. Regarding the proposed cores, the cruciform cross-section is made of four identical flanks (double symmetric) of thickness t and a width of L_{eq} . The symmetry associated to the core cases, eases the analyses as the shear centre coincides with the centroid. Considering the latter aspect and applying appropriate boundary conditions satisfied by sinusoidal solutions, three independent equations are attained. Two of them are discussed in the following section as the Euler critical loads for flexural buckling. The other equation is the critical load for pure torsional buckling P_φ given in Eq. (4.17)

Coefficient C_1 is called the warping rigidity, where C_w is the warping constant and equals to zero for cruciform cross-sectional shapes consisting of thin rectangular elements which intersect at a common point [165]. I_o is the polar moment of inertia of the cross-section about shear centre [0; 0; H/2] considering Figure 4.11 coordinate system. Coefficient C represents the torsional rigidity. J is the torsion constant and depends on the number of flanks m .

$$P_\varphi = \frac{A_s}{I_o} \left(C + C_1 \frac{\pi^2}{H^2} \right) \quad (4.17)$$

Where:

$$C_1 = E_{3s} C_w = 0 \quad (4.18)$$

$$C = J G_{13s} = \frac{mLt^3}{6} G_{13s} = \frac{2}{3} Lt^3 G_{13s} \quad (4.19)$$

$$I_o = I_x + I_y \approx 2 \frac{tL^3}{12} = \frac{tL^3}{6} \quad (4.20)$$

Replacing above equations into Eq. (4.17), the critical load for torsional buckling for a column like Figure 4.11 is given by Eq. (4.21). By employing $L / 2$ as size for the flanks, the last equation may be valid only for full-walled cores. As seen in previous sections, for the machined cores the amount of material bearing the load is taken into account, and the strut is approximated by a cruciform column with flanks $L_{eq} / 2$. Thus, for the machined cores Eq. (4.22) will be employed.

$$P_\varphi = \frac{8G_{13s}t^3}{L} \quad (4.21)$$

$$P_\varphi = \frac{8G_{13s}t^3}{L_{eq}} \quad (4.22)$$

Therefore, the maximum compressive strength of the core regarding torsional buckling failure mode σ_{CTB} , is evaluated based on Figure 4.8 cell model. As previously pointed out, the stress is defined by a critical load, which in this case is represented by P_φ divided by the cell area A_{cell} as given in Eq.(4.23). The contribution of the machined area is neglected, as previously stated.

$$\sigma_{CTB} = \frac{P_\varphi}{A_{cell}} \quad (4.23)$$

4.3.2.1.3 Euler flexural buckling

As introduced in previous section, column flexural buckling shall be also considered as failure mode. In this case, loads P_x Eq. (4.24) and P_y Eq. (4.25) are commonly known as the Euler critical loads for flexural buckling about x and y -axes [165], respectively (coordinate system as in Figure 4.11). Both I_x and I_y represent the second moment of area of the cross-section according to x and y -axes, in which case are equal for symmetrical cruciform sections.

$$P_x = \frac{\pi^2 E_{3s} I_x}{H^2} \approx \frac{\pi^2 E_{3s} t L^3}{12H^2} \quad (4.24)$$

$$P_y = \frac{\pi^2 E_{3s} I_y}{H^2} \approx \frac{\pi^2 E_{3s} t L^3}{12H^2} \quad (4.25)$$

As in previous cases, the above equations are valid for the reference cores for flanks $L/2$. For the machined cores Eq. (4.26) and Eq.(4.27) will be employed.

$$P_x = \frac{\pi^2 E_{3s} I_x}{H^2} \approx \frac{\pi^2 E_{3s} t L_{eq}^3}{12H^2} \quad (4.26)$$

$$P_y = \frac{\pi^2 E_{3s} I_y}{H^2} \approx \frac{\pi^2 E_{3s} t L_{eq}^3}{12H^2} \quad (4.27)$$

Hence, evaluating Euler flexural buckling failure mode the compressive strength of the core σ_{cEu} is presented in Eq. (4.28) employing Figure 4.8 as cell model. Then, the stress is represented by critical loads P_x or P_y divided by the cell area A_{cell}

$$\sigma_{cEu} = \frac{P_x}{A_{cell}} = \frac{P_y}{A_{cell}} \quad (4.28)$$

4.3.2.1.4 Plate elastic buckling

Another failure mode evaluated with a high likelihood to take place, is related to another case of elastic buckling. Therefore, noting the involved geometries under uniformly compressed loading, elastic buckling of thin-walled rectangular plates shall be found, particularly for the reference core case.

As previously stated, the columns are approximated as a bar of cruciform cross-section, made of four identical flanks of thickness t and a width $L_{eq}/2$ for the machined cores, and a width of $L/2$ for the reference core. The formula presented by Ericksen [166] is implemented for the evaluation of plate elastic buckling, made from an orthotropic base material Eq.(4.29), where coefficient D represents the bending stiffness of

a plate and shall be written as Eq. (4.30) for orthotropic composite materials. Factor λ is defined by the Poisson's moduli of the base material as $\lambda = 1 - \nu_{13s} \cdot \nu_{31s}$. Factor B represents the length of the loaded plate edge. Coefficients c_i depend on border conditions.

$$P_B = \frac{K\pi^2 D}{B^2} \quad (4.29)$$

Where:

$$D = \frac{\sqrt{E_{1s}E_{3s}}}{\lambda} \left(\frac{t^3}{12} \right) \quad (4.30)$$

$$K = \alpha c_1 + 2\beta c_2 + \frac{c_3}{\alpha} \quad (4.31)$$

$$\alpha = \sqrt{\frac{E_{1s}}{E_{3s}}} \quad (4.32)$$

$$\beta = \frac{1 - \lambda}{\sqrt{E_{1s}E_{3s}}} \left(\frac{E_{1s}\nu_{31s}}{1 - \lambda} + 2G_{13s} \right) \quad (4.33)$$

The form of the coefficients c_i (with $i = 1, 2, 3$) vary substantially from one border constraints case to another (see reference [166] for further details). For example, the case whether to be assumed as governed by plate buckling with simply supported edges, the coefficients are given by Eq. (4.34), Eq. (4.35) and Eq. (4.36).

$$c_1 = \frac{1}{n^2} \left(\frac{H}{B} \right)^2 \quad (4.34)$$

$$c_2 = 1 \quad (4.35)$$

$$c_3 = n^2 \left(\frac{B}{H} \right)^2 \quad (4.36)$$

The solutions associated to the analytical proposals are attained by applying suitable forms of sinusoidal functions, thus n represents the number of half waves into which the plate buckles. For this work, a half-wave sinus ($n=1$) and one-wave functions are considered ($n=2$), and the resulting smaller value for the critical load is later presented in the following section.

By evaluating plate buckling behaviour, the representative maximum compressive strength is given as σ_{cB} , defined by the critical load P_B divided by the unit cell area A_{cell} as given in Eq. (4.37). Figure 4.8 is implemented as unit cell model.

$$\sigma_{cB} = \frac{P_B}{A_{cell}} \quad (4.37)$$

4.3.2.1.5 Analytical results

The analytical results for the core compressive strength predictions are highlighted in Table 4.6, complemented by the bar graphic on Figure 4.11.

Table 4.6. Core compressive strength theories according to analytical approaches

<i>Pattern</i>	<i>L</i> (mm)	<i>L_{eq}</i> (mm)	σ_{cR} (MPa)	σ_{cTB} (MPa)	σ_{cEu} (MPa)	σ_{cB} (MPa)
Design 1	20	6.910	10.164	2.8297	42.710	11.840**
Design 2	20	7.694	11.579	2.7524	46.419	11.620**
Design 3	20	6.800	9.821	2.8839	40.353	12.010**
Reference	50	50	12.538	0.0625 ¹	2589 ²	2.069*

Note: minimum plate buckling stress values obtained for: (*) n=1, (**) n=2

The minimum stress values, and thus, the failure modes are predicted for the cases of torsional buckling (machined cores) and plate buckling (reference cores). Some values for reference cores, for example, they do not satisfy the specific necessary boundary conditions for pure torsional buckling behaviour (e.g., it is required to consider the flanks as a plate simply supported along three sides and completely free along the fourth side [165]) and thus, they may not give accurate results. Additionally, the width/length ratio is not considered in Eq. (4.21) and may lead to a critical load extremely low for large flanks cells. Moreover, the Euler flexural buckling is not representative of failure values in the reference cores (extremely high) compared to the other failure modes, and thus, with less probability to occur. These two values (¹) and (²) in Table 4.6 will be neglected in further comparison studies for being impractical.

The bar graphics on Figure 4.11. show the failure modes with the high likelihood to occur, comparing the theories proposed as approach. As previously said, the governing failure modes are torsional buckling and plate buckling modes. The cases of micro-buckling or the Euler column buckling model present larger predicted failure loads, and thus, less probability to come about.

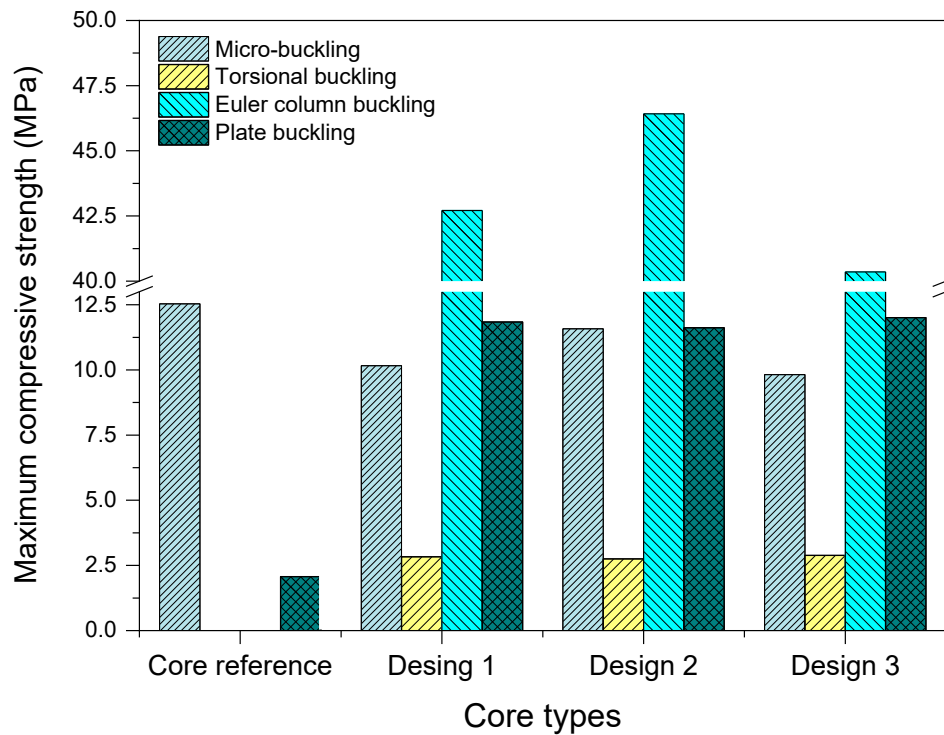


Figure 4.12. Comparison between theoretical approaches for the maximum compressive strength

4.3.2.2 Numerical approach

The failure stresses due to strength (failure of the base material without buckling) and the buckling failure stress are also via FE simulations evaluated. The stresses are analysed separately, through two different simulations:

1. Through a linear static simulation (not considering instability phenomena, it represents a strength failure), similarly as carried-out in section 4.3.1.2, then attaining the core compressive strength σ_c^* .
2. A non-linear static simulation (considering instability), as the critical stress given by the core compressive strength σ_c^{**} .

The study of the non-linear static simulation is detailed in this section. Cell element based on CFRP cell-wall are simulated by a mesh of shell elements of size 0.4 mm (CQUAD4, 4-node reduced integration), discretizing the core geometries given in Figure 4.3, and using Table 4.2 as base material properties. A non-linear static model based in a modified Newton-Raphson method is employed for the simulation. The border conditions are established in correspondence to the analytical models previously presented, in which the top and bottom-line nodes of the cell element are simulated as

simply supported, and the lateral vertical nodes are left free of constraints. For the reference case, the lateral flanks are set with no rotation in z -direction for the vertical nodes. A load P of 10 kN is applied over the top-line nodes until the simulation stops. From the tracking of displacements of representative nodes (Figure 4.13) within the discretised mesh on a cell, the instability load is then estimated from the tracking charts (Figure 4.14).

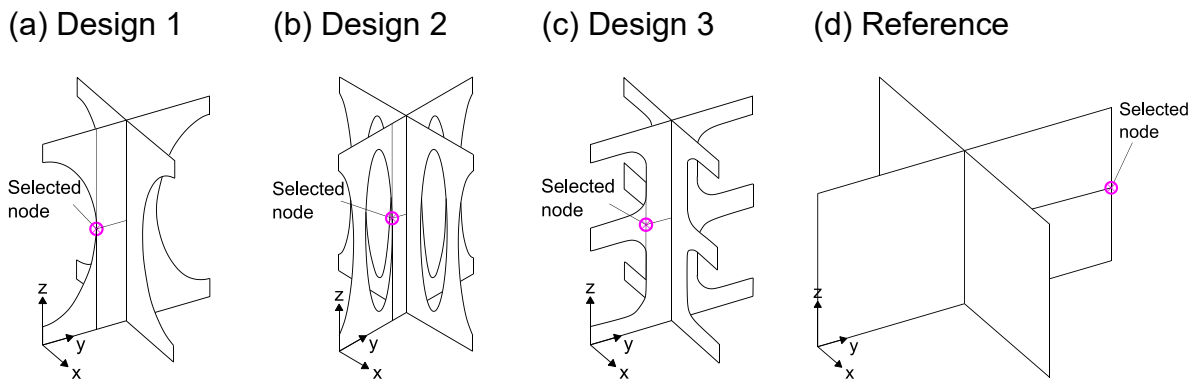
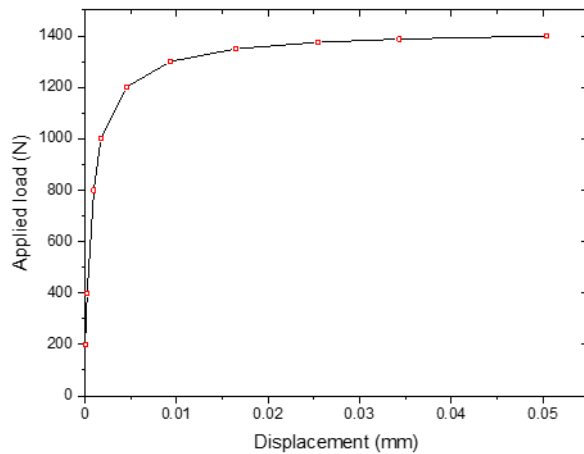


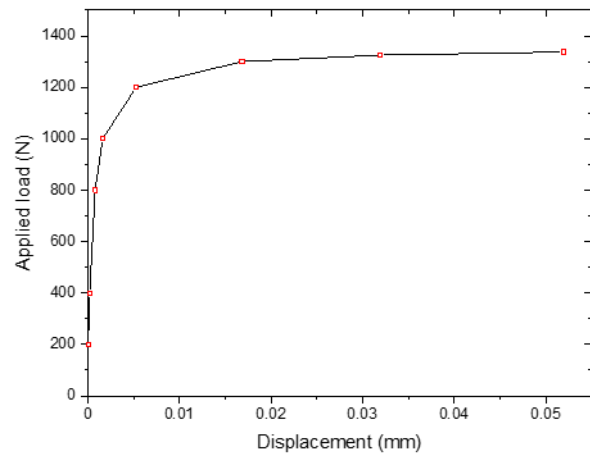
Figure 4.13. Schemes of selected nodes for displacement tracking in x -direction

Figure 4.14 exhibits the node tracking displacements due to the applied load upon the cores investigated. At the beginning, the curves lines show a stable behaviour until the inflexion point, where the curve branches in an asymptotic-like form. The behaviour of the machined cores after the inflexion point, quickly becomes unstable and the simulation stops. The inflexion point (critical load) is similar in all machined cases. Alternatively, the reference core presents a much steeper asymptotic curve than the previous mention, with a higher critical load. Also, this would mean that the structure may remain stable longer after the critical point and be able to carry further load. The substantial differences in the behaviours shown between the cores with and without cavities are mainly due to the cell size and the boundary conditions imposed. While the cell vertical flanks of the machined sheet are simulated without constraints, the reference flanks present the constraints imposed by the continuity condition given by the junction between cell members. Hence, although the behaviour of the reference cell prior to the collapse of the structure seems to be torsional buckling behaviour, it may not be possible to declare it as pure torsional buckling, since it is found as a necessary condition that the flanks of the cross-sectional columns are free of constraints [165]. Therefore, the failure of the reference cores is firstly attributable to a plate buckling failure mode.

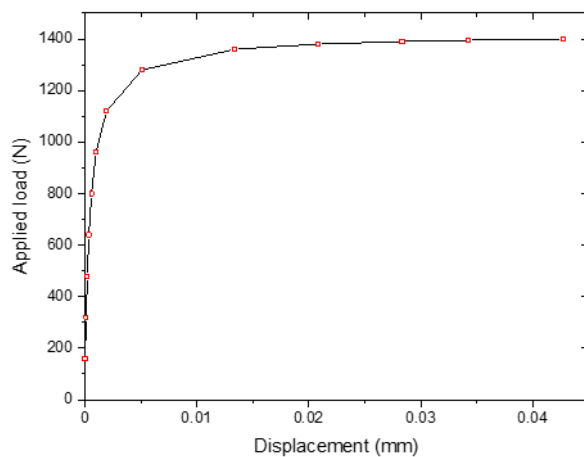
(a) Design 1



(b) Design 2



(c) Design 3



(d) Reference

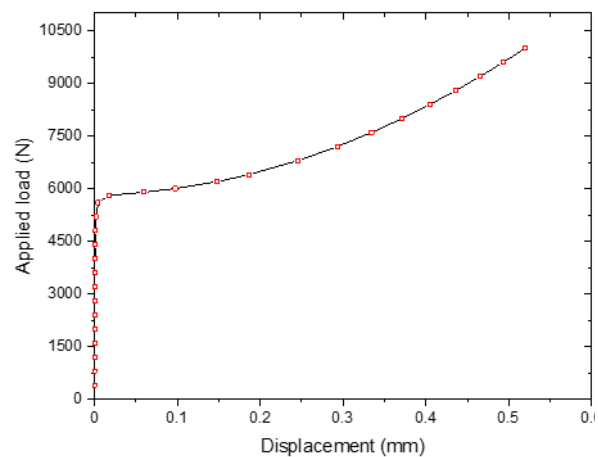


Figure 4.14. Load vs. node displacement curves obtained from the simulations

Additionally, Figure 4.15 schematically represents the renderings of the deformation of the cells predicted by the simulations at the instability step. In all cases, the cells fail by buckling as expected. The machined sheet cells resemble torsional buckling behaviour, by turning the flanks around the vertical axis as rotational vector. In particular, design 2 exhibits a large deformation of the slender narrow plates at each side of the main cruciform section, denoting a premature buckling failure. Furthermore, the reference cell fails by buckling of the plates in a co-ordinately manner that resemble torsional buckling, although the border conditions may not satisfy that end, as previously stated.

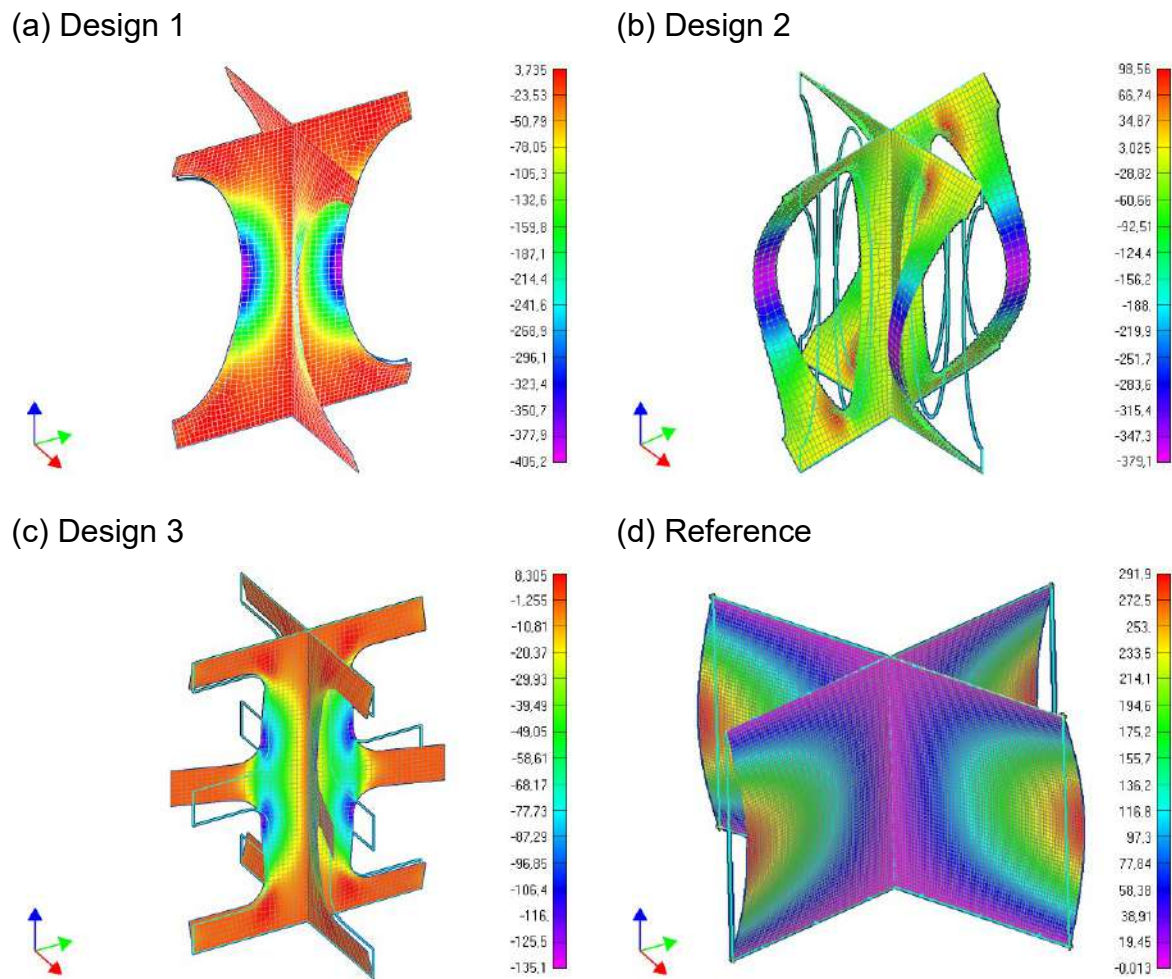


Figure 4.15. Renders obtained from the compressive loading simulations

4.3.2.2.1 Numerical approach

Table 4.7 summarizes the results obtained from simulations, and a brief comparison with the analytical approaches as shown below.

Table 4.7. Core compressive strengths got from numerical and analytical approaches

<i>Pattern</i>	<i>L</i> (mm)	P_{crit}^* (kN)	σ_c^* (MPa)	σ_c^{**} (MPa)	σ_c^{***} (MPa)	Expected failure mode
Design 1	20	1.177	2.943	10.16	2.8297	TB
Design 2	20	1.121	2.805	11.57	2.7524	TB
Design 3	20	1.192	2.981	9.82	2.8839	TB
Reference	50	5.483	2.194	12.53	2.0690	PB

Note: (*) Non-linear static simulation, (**) Linear static simulation, (***) Analytical

Factor P_{crit}^* represents the critical load of the cell element via non-linear analyses. Although the reference cell has a failure load of almost 4.6 times higher than the best of the proposed cores, the smaller number of struts within a sandwich panel limits its total load capability, and the strength of the reference cores is found smaller. No major differences are observed among the other proposed cores, having an average failure stress of around 2.9 MPa. The strengths obtained from the linear analyses are significantly higher compared to the other estimations. Nevertheless, the minimum strength analytical values are in good correspondence with the FE non-linear simulations, being the expected failure modes as of torsional buckling (TB) for the machined cores and of plate buckling (PB) for the reference one.

4.4 Core plate shear

In this section, by evaluating the response of a cell element under shear loads in the upper and lower planes (Figure 4.16), the mechanical properties of the cores of interest, comprising: the reference, design 1 and 2 cores (dimensions regarding to Table 4.3), are estimated. Figure 4.16.b represents a top view of the load case and the selected single representative cell element. The study contemplates a typical plate-shear model upon sandwich panels [167].

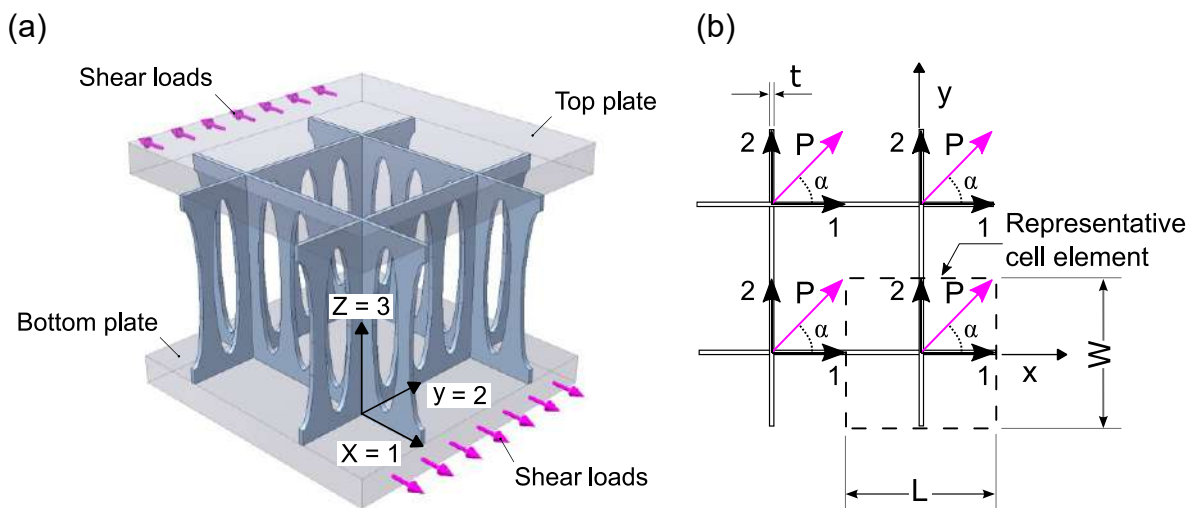


Figure 4.16. (a) A schematic shear load case over a unit cell. (b) A top-view render with a schematic cell used for calculations and generic shear loads.

Both analytical and numerical studies are included in this section. In the analytical approaches, the shear modulus is estimated analysing the displacements due to a generic shear load P , applied about the orientation angle α and distributed along the core cells. The present work studies the particular case when the shear load vectors are parallel to the x -axis ($\alpha = 0$). The failure prediction includes three different approaches from simple theoretical models, providing the necessary insights for estimating the failure behaviour of the cores. In all cases, the cell walls are assumed as thin orthotropic plates clamped at the bottom and the top, neglecting the contribution of the transverse cell walls (that is, the sheet plates parallel to the y -direction). Figure 4.17 shows the approximation model used for calculations. The model is an equivalent Timoshenko-like beam that represents the same displacement as the cell wall assembly (Figure 4.17.b and Figure 4.17.c).

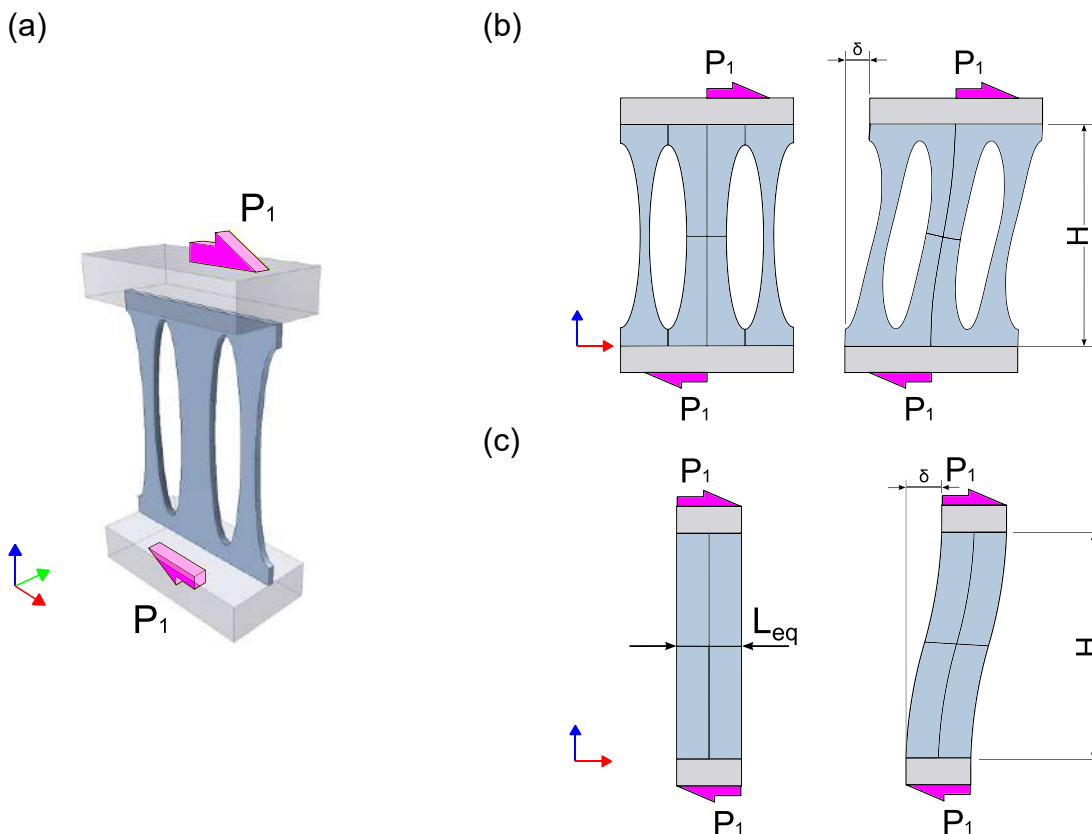


Figure 4.17. Sketches of the calculation models. (a) Cell wall sheet, neglecting transversal cell walls. (b) Cell wall loaded with a shear load before and after straining. (c) Model of an equivalent cantilever Timoshenko-like beam before and after straining.

Numerical models are developed based on commercial software FEMAP™ [29], to corroborate the theoretical analyses and to have a further overview of the proposed

core behaviour. Finite element displacement predictions and simple mechanical theory is applied for indirectly estimating the core elastic shear modulus, validated later by experimental tests. The material properties employed for the analyses are given in Table 4.2, following the coordinate system showed in Figure 4.17. Likewise, the CFRP plate is considered as an orthotropic material with an average thickness $t = 0.65$ mm.

4.4.1 Shear stiffness

The general expression of the core shear modulus can be defined by simple mechanical analyses of the behaviour of a cell subjected to shear stresses, while considering a uniform straining of the cell walls. Considering a linear behaviour and short displacements, the general expression of the displacement δ experienced by the cell assembly due to a resulting nominal load P is studied.

4.4.1.1 Analytical approach

When a shear load is applied regarding α as director angle, the shear vector P (Figure 4.16) is set by its components by Eq. (4.38).

$$\vec{P} = \vec{P}_1 + \vec{P}_2 \quad (4.38)$$

$$P_1 = |P| \cos \alpha \quad (4.39)$$

$$P_2 = |P| \sin \alpha \quad (4.40)$$

The general expression of the shear stress τ_c applied on a cell is defined by Eq. (4.41), where γ_c is the strain of the cell and G_c represents the shear modulus of the cell element.

$$\tau_c = \frac{P}{A_{cell}} = G_c \gamma_c \quad (4.41)$$

$$\tau_1 = \frac{P_1}{A_s} = G_{31s} \gamma_1 \quad (4.42)$$

$$\tau_2 = \frac{P_2}{A_s} = G_{31s} \gamma_2 \quad (4.43)$$

Similarly, the stress components depend upon the director angle following above expressions as Eq. (4.42) and Eq. (4.43), where G_{31s} is the shear modulus of

the base material, γ_1 and γ_2 are the unit-cell strains according 1-direction and 2-direction and A_s the base material area.

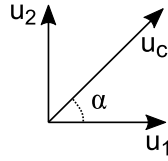


Figure 4.18. Displacement vector sketch reference for shear strain definition

The strains γ_1 and γ_2 are defined by their respective component displacements u_1 and u_2 (schematically shown in Figure 4.18) at the top plate (Figure 4.16.b). The total displacement of the cell is represented by u_c .

$$u_1 = \gamma_1 H \quad (4.44)$$

$$u_2 = \gamma_2 H \quad (4.45)$$

$$u_c = \sqrt{u_1^2 + u_2^2} \quad (4.46)$$

The total strain γ_c on the cell is given by Eq. (4.47)

$$\gamma_c = \frac{u_c}{H} = \frac{\sqrt{u_1^2 + u_2^2}}{H} \quad (4.47)$$

Recalling Eq. (4.41) and introducing Eq. (4.47), the load P turns into the expression of Eq. (4.48).

$$P = G_c \frac{\sqrt{u_1^2 + u_2^2}}{H} A_{cell} \quad (4.48)$$

Since the director angle is set in this work as $\alpha = 0$, only the component according to 1-direction will be considered ($u_2 = 0$), because the normal cell walls undergo bending and just carry an insignificant component of the shear load. Likewise, only the component of the load P_1 is considered ($P_2 = 0$). Then, the expressions in Eq. (4.38) and Eq.(4.48) are specified for the case said as Eq. (4.49).

$$P = P_1 = G_c \gamma_1 A_{cell} \quad (4.49)$$

Equating the above expression to Eq. (4.42), the expression in Eq. (4.50) is attained

$$P_1 = G_c \gamma_1 A_{cell} = G_{31s} \gamma_1 A_s \quad (4.50)$$

Consequently, solving Eq. (4.50) for G_c and introducing Eq. (4.6), the expression for the shear elastic modulus of the core is attained as Eq. (4.51), in which the elastic shear modulus of the square-honeycomb core is then related to the core relative density $\bar{\rho}$.

$$G_c = G_{31s} \frac{A_s}{A_{cell}} = G_{31s} \frac{2tL}{L^2} = G_{31s} \frac{t}{L} = G_{31s} \frac{\bar{\rho}}{2} \quad (4.51)$$

The formula given by Eq. (4.51) is assumed to be valid for full-walled cores (i.e., without machined geometries). In this work, the densities of the machined cores (i.e., with cavities) are found to be almost equal (Table 4.3). As a result, this approach cannot predict properly their mechanical properties, because it does not consider the geometrical effects of the large cavities. To overcome this difficulty, the following analyses are proposed as well for mechanical properties predictions of the machined cores.

When a beam is loaded with a load such as in Figure 4.17, the deflection at the loaded point can be determined by Castigliano's second theorem (Eq.(4.52)) [67].

$$\delta_j = \frac{\partial U_i}{\partial P_j} \quad (4.52)$$

The partial derivative of the deformation energy U_i of a structure to any load P_j is equal to the displacement δ_j corresponding to that load. This form of derivative is applicable for short displacements and linear regimes of stress-strain. This statement is fulfilled while calculating the shear modulus at the very beginning of the shear tests. As a first approach, due to the symmetry, the model (Figure 4.17.b) can be approximated as a cantilever beam with a punctual load P (Figure 4.17.c). The internal strain energy of the beam is assumed to be caused by bending and shear. In this way, the model studied is treated as a Timoshenko-like beam that includes both bending and transverse shear effect. The transverse shear effect is neglected by Euler-Bernoulli classical beam theory [146,147]. Hence, the successive planes that made the profile are not necessarily perpendicular to the bending line (Figure 4.17.c).

The total displacement is defined by the sum of both effects, U_{ib} the internal strain energy of a beam subjected just to a bending deformation and U_{is} the internal strain energy of a beam due to shear loading (Eq. (4.53)).

$$\delta_j = U_{ib} + U_{is} \quad (4.53)$$

The displacement δ_j is then obtained by tabulated results as Eq. (4.54) [168], in which, factor I_y represents the cross sectional second moment of area regarding to y -direction, and A_{k_s} represents the cross-sectional area over the form factor for shear k_s ,

$$\delta_j = \frac{PH^3}{12E_{1s}I_y} + \frac{PH}{G_{31s}A_{k_s}} \quad (4.54)$$

In which, factor I_y represents the cross sectional second moment of area regarding to y -direction, and A_{k_s} represents the cross-sectional area of the material A_s over a form correction coefficient for shear k_s ($A_{k_s} = A_s/k_s$), due to the assumption of an average shear stress acting over the entire beam cross section. Then, factor k_s is constant of a value of 6/5 for rectangular cross section beams [169].

The cross-sectional area A_s in Eq. (4.54) is valid for a beam of constant section. For the case of the machined cores, the cross-sectional area varies along the profile. Therefore, for simplifying the study, a constant value is considered while representing the behaviour of the cell element wall, with an equivalent beam that would exhibit the same displacements as the real case. The beam equivalent corrected cross-sectional area A_{keq} (Eq. (4.56)) will be approximated via numerical studies. The displacement is then attained as Eq. (4.55).

$$\delta_j = \frac{PH^3}{12E_{1s}I_y} + \frac{PH}{G_{31s}A_{keq}} \quad (4.55)$$

$$A_{keq} = A_{eq}/k_s = L_{eq} \cdot t/k_s \quad (4.56)$$

The shear modulus of the representative cell element is obtained as Eq. (4.57) by the shear stress τ_c to shear strain γ_c ratio, applying a generic shear force P according to $\alpha = 0$, then $P = P_1$ (Figure 4.17), neglecting the contribution of the perpendicular wall sheets, and introducing δ_j .

$$G_c = \frac{\tau_c}{\gamma_c} = \frac{PH}{A_{cell}\delta_j} \quad (4.57)$$

Table 4.8 shows the results obtained via analytical approaches, implementing a line load P of 10 N/mm (i.e., $P = 200$ N and $P = 500$ N for the 20x20 mm cells and 50x50 mm, respectively). For the reference cores, the core shear modulus is calculated by Eq. (4.51), attaining a theoretical value of 46.28 MPa. For the machined cores, the equivalent area of the beam A_{keq} is calculated through the estimated displacement δ_j .

As a first approach, the displacement implemented is extracted from the numerical approaches and equating it into Eq. (4.55). Then, their shear modulus is calculated by Eq. (4.57) and values of 50.55 MPa and 23.25 MPa are estimated for the core design 1 and 2, respectively. For the reference cores, the core shear modulus is calculated by Eq. (4.51), attaining a theoretical value of 46.26 MPa. For the machined cores, the equivalent area of the beam A_{keq} is calculated through the expected displacement δ_j . As a first approach, the displacement implemented is extracted from the numerical approaches and equating it into Eq. (4.55). Then, their shear modulus is calculated by Eq. (4.57) and values of 50.55 MPa and 23.25 MPa are estimated for the core design 1 and 2, respectively.

Table 4.8. Shear elastic moduli obtained by analytical approaches

<i>Pattern</i>	H (mm)	L (mm)	E_{1s} (GPa)	G_{31s} (GPa)	A_{keq} (mm ²)	I_y (mm ⁴)	δ_j (mm)	G_c (MPa)
Design 1	25.4	20	62.6	3.56	6.78	106.56	0.251	50.55
Design 2	25.4	20	62.6	3.56	4.36	28.36	0.546	23.25
Reference	25.4	50	62.6	3.56	--	--	--	46.28

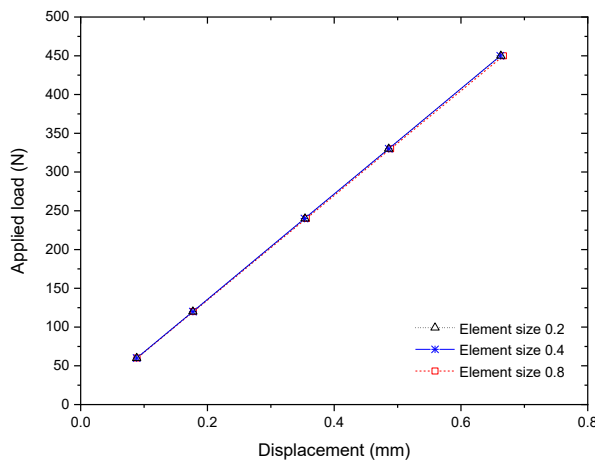
4.4.1.2 Numerical approach

In order to obtain the FE estimated shear elastic modulus of the cores G_c , load-displacement curves are calculated for three different element sizes and different loads applied (Figure 4.19). The CFRP sheet material is simulated by a mesh of shell elements (CQUAD4, 4-node reduced integration), according to design 1, 2 and reference geometries as proposed in Figure 4.3. The nodes on the plane $z = 0$ are set as constrained, while the nodes over the plane $z = H$ are constrained to move just in x -axis for simplifying the analyses, considering small displacements. For the reference core case, due to the quasi-continuity of the cells along the vertical flanks (i.e., the cells are in contact to each other all along the flanks borders), the case resembles a case of the shear flow theory [67,68], in which a plate is surrounded over the entire length with elastic pins. For this case, the vertical nodes at each flank of the studied plate are considered as simply supported, with the possibility of displacement in x -direction. A line load is applied over the top node-line, reproducing a shear load over the main set. Extrapolation of the values are carried-out in the limit as the element size tends to zero. Recalling Eq. (4.41) and Eq. (4.47), the shear modulus by the numerical approach of

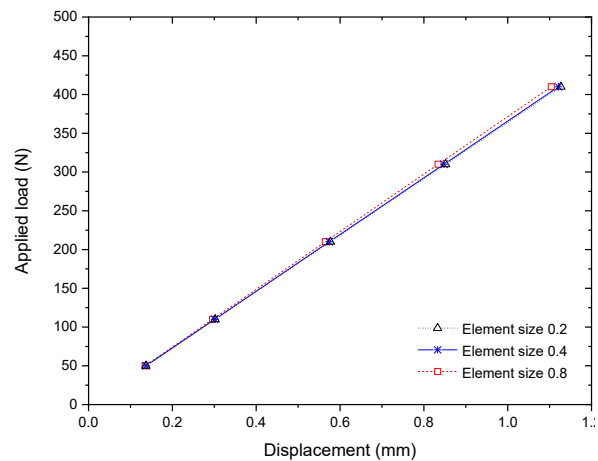
each core is calculated by Eq. (4.58) while considering the slope s from the load-displacement charts (for displacements specified in the 1-direction).

$$G_c = \frac{P}{A_{cell} \gamma_c} = \frac{PH}{A_{cell} u_c} = \frac{sH}{A_{cell}} \quad (4.58)$$

(a) Design 1



(b) Design 2



(c) Reference

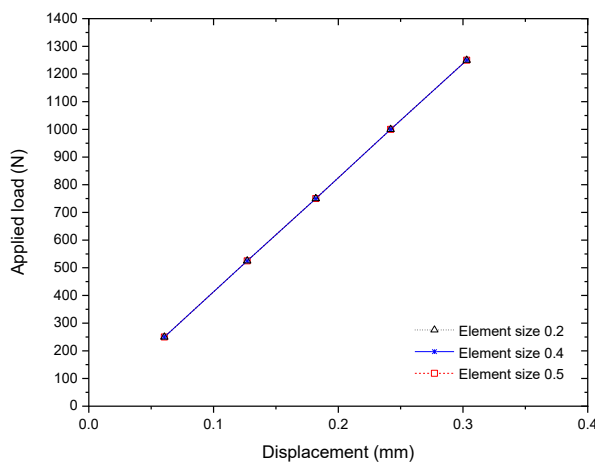


Figure 4.19. Load vs. displacement curves obtained from the FE simulations: (a) design 1, (b) design 2 and (c) reference core

Therefore, the displacement of the nodes is studied using linear static analyses. Renders of the shear response of simulated CFRP sheets also emerge from these simulations and are shown in Figure 4.20. A generic line-load of 10 N/mm is applied on the top node-line as previously mentioned. Shear stresses contours plots in xz -plane are shown and the simulated deformation as well for the cores proposed as design 1 and design 2 (Figure 4.20.a and Figure 4.20.b, respectively). The cells show a

stress concentration at the middle strut with a parabolic stress distribution over the width. Moreover, the highest shear stresses are located at the mid-plane (or neutral axis) and the middle sections. For the case 2, the struts at both sides of the centre column do not bear significant share of the main load, which is mostly concentrated in the mid-strut as a result of a higher bending rigidity compared to the slender ones. In contrast to them, Figure 4.20.c represents the case of the reference cores, showing an average shear stress distribution of value ≈ 15.38 MPa along the plate. The average shear stress over the plate can be calculated as $\tau = P/A_s = 500 / (0.65 \cdot 50) = 15.385$ MPa, agreeing with the simulation. Quasi-constant shear bands are also seen at the edges of the plate, denoting a case in correspondence with the shear flow theory [68].

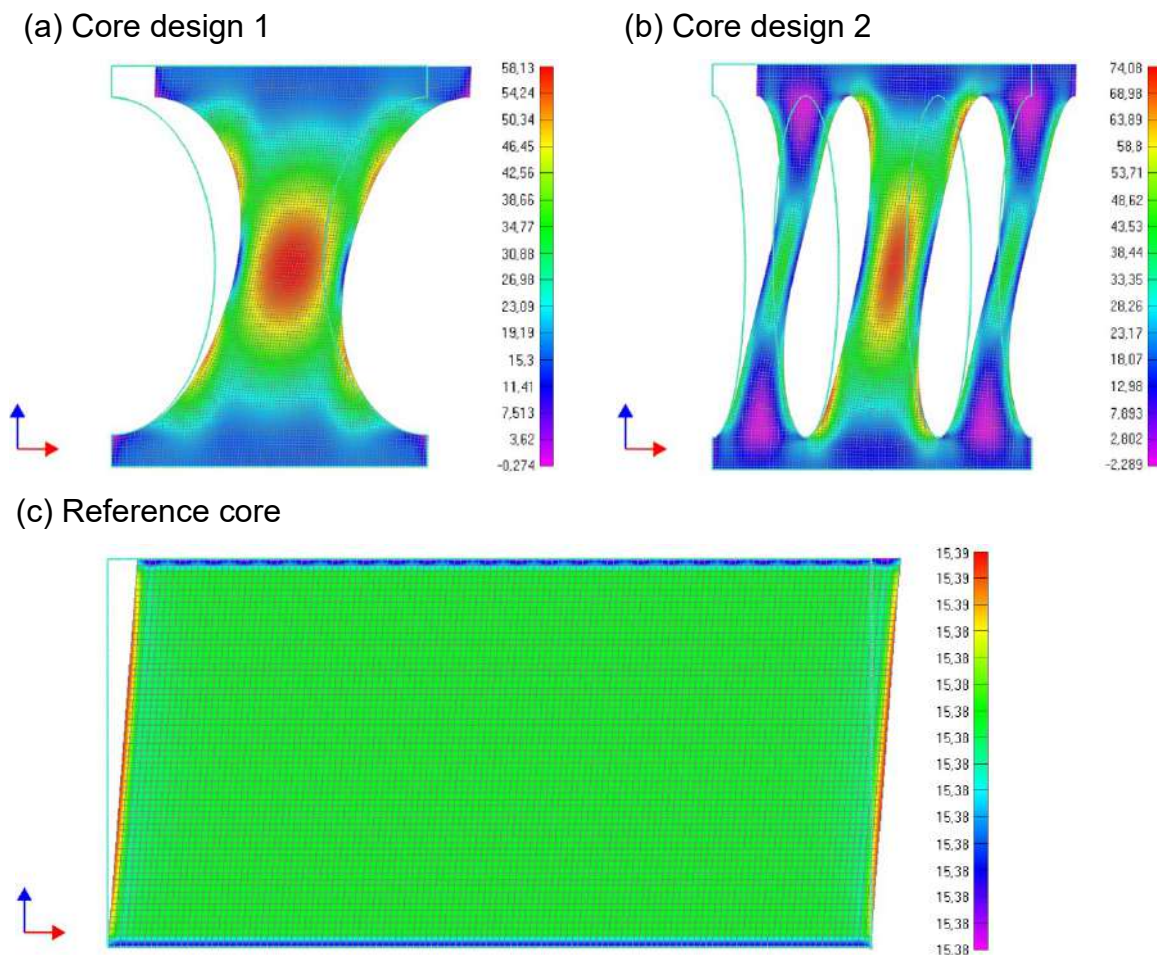


Figure 4.20. Contour plots of the shear stress distribution by FE: (a) design 1, (b) design 2, and (c) reference

Table 4.9 summarises the results obtained from linear-static simulations, comparing both shear modulus attained by theoretical approaches (Eq. (4.57) and by FE (Eq. (4.58)). The largest shear strain is shown by core design 2, mainly by the shear

and bending effect experienced by the mid-column, which is the one that bears most of the loads, exhibiting the smaller core modulus as well ($G_c = 23.26$ MPa). Although the core design 1 shows a locally larger straining (that is, within a cell) compared with the reference core, its core modulus is predicted as better than the reference one, because of the number of struts working at the same time resisting the load (50 vs. 16-struts respectively per sample of 200 by 100 mm). The table also gives information of the displacements used to calculate L_{eq} to be implemented as a part of the equivalent area $A_{eq} = L_{eq} \cdot t$ in equation (4.55).

Table 4.9. Core shear stresses, strains and elastic moduli obtained by FE.

<i>Pattern</i>	L (mm)	τ_s (MPa)	u_c (mm)	L_{eq}^* (mm)	s (N/mm)	γ_c ($\mu\text{m}/\text{m}$)	G_c (MPa)	G_c^* (MPa)
Design 1	20	58.12	0.251	12.53	796	9881	50.59	50.55
Design 2	20	74.08	0.546	8.06	366	21496	23.26	23.25
Reference	50	15.38	0.119	--	4201	4685	42.68	46.28

Note: (*) Theoretical approach

4.4.2 Shear strength

The analytical models for predicting the peak shear strength of the square honeycomb cores assuming uniform straining of the CFRP sheets, are thought as least as three governing failure modes of the cell members, including:

1. Maximum shear strength τ_{cR} (when $\tau_{cR} = \tau_{13s}$),
2. Debonding between face sheet and cell member τ_{cDB}
3. Elastic shear buckling τ_{cB} .

The failure modes proposed below consider the base material as an orthotropic composite material. The core peak shear strength τ_{cpk} is given by the collapse mechanism that exhibits the minimum value as Eq.(4.59).

$$\tau_{cpk} = \min(\tau_{cR}, \tau_{cDB}, \tau_{cB}) \quad (4.59)$$

4.4.2.1 Analytical approach

The proposed cores are made from square arrangements of thin CFRP sheet materials. Assuming that only the core walls parallel to the 1-direction bear the shear

loads (Figure 4.17), and that the loads are equally distributed along the core, the different failure modes are presented below.

4.4.2.1.1 Maximum shear strength

The cores shear strength τ_{cR} shall depend upon the failure value of the base composite material, considered as $\tau_{31s}=110$ MPa (Annex B). Considering a load P applied to the core (Figure 4.17) and neglecting the contribution of transverse sheet walls, the failure load P_{cR} applied to the unit-cell walls and thus, to the core, is the same and given as Eq. (4.60).

$$P_{cR} = \tau_{31s}A_s = \tau_{cR}A_{cell} \quad (4.60)$$

Solving Eq. (4.60) for τ_{cR} , the core failure due to peak shear strength of the CFRP cell wall is obtained by Eq. (4.61) as a function of the core relative density, observing that only the half of the total CFRP sheets bear the shear loads.

$$\tau_{cR} = \frac{A_s}{A_{cell}}\tau_{31s} = \frac{tL}{L^2}\tau_{31s} = \frac{t}{L}\tau_{31s} = \frac{\bar{\rho}}{2}\tau_{31s} \quad (4.61)$$

Hereby it should be noted that Eq. (4.61) is valid for reference cores (Figure 4.3) where the cores are made from full-walled cells.

Other cases with machined geometries required similar analyses but considering the local mid-plane cross-sectional area of the sheet material $A_s = tL_{eq}$, as previously carried-out for compression analyses (Figure 4.9). Then, applying A_s into the maximum shear stress τ_{max} on a beam of rectangular cross-section [67], Eq. (4.62) is attained.

$$\tau_{max} = \frac{3}{2} \frac{P_R}{A_s} = \frac{3}{2} \frac{P_R}{tL_{eq}} \quad (4.62)$$

The maximum shear load P_R is applied to the core and consequently to the base material. The shear stress on the core is defined as Eq. (4.41), but specifying it to the maximum load, then Eq. (4.63) is obtained.

$$\tau_{cR} = \frac{P_R}{A_{cell}} \quad (4.63)$$

Equating Eq. (4.62) and Eq. (4.63), and solving for P_R , the core shear strength is now represented by Eq. (4.64), according to the nominal composite shear strength

and leading to a shear fracture failure mode. Then, the maximum core shear stress depends directly to the shear strength of the base material.

$$\tau_{cR} = \frac{2}{3} \tau_{31s} \frac{A_s}{A_{cell}} = \frac{2}{3} \tau_{31s} \frac{tL_{eq}}{L^2} \quad (4.64)$$

The maximum shear stresses are expected in $[\pm 45]^\circ$ orientation [170]. Since the CFRP woven core base material is disposed with an orientation of $[0/90]^\circ$ (i.e. parallel to 1 and 3-direction as explained in section 4.2), the above failure mode has a high likelihood to occur, because the shear loads may be only borne by the polymeric matrix, and not the reinforcement.

4.4.2.1.2 Debonding

As stated in section 4.2, the core and skins are joined together by a bonding mean. The core made from thin-walled plates, presents a relatively small, bonded area, and thus, it also may fail by debonding failure between core and skins, due to the shear stresses. The shear distribution within the sandwich thickness is considered almost constant over the core of an average value (see Chapter 3), and thus, the bonded region between core and faces shall bear approximately the same amount of shear stress and are considered in this section for analyses.

The bonding failure occurs when the shear stresses at the interface core/face sheet, exceeds the adhesion strength or τ_{int} . The adhesion strength varies with the temperature and the time of processing. In this work, a value of $\tau_{int} \approx 20$ MPa is employed. This average value is obtained from the datasheet of the bonding mean as the UHU plus Endfest 300®.

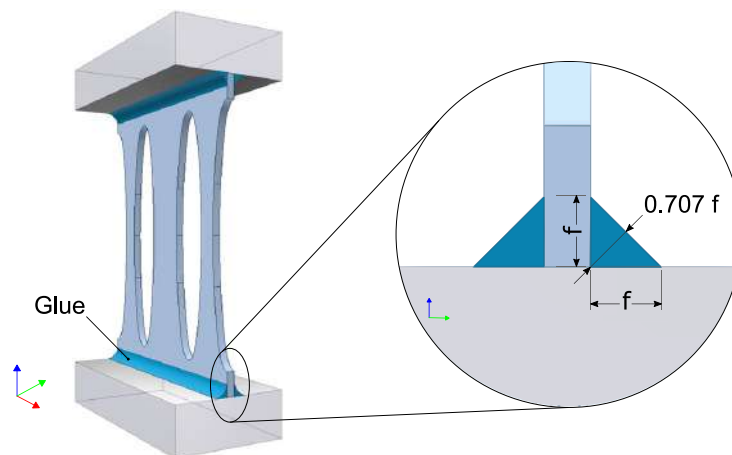


Figure 4.21. Sketches of a representative cell wall sheet showing the glued area

The mean bonded area A_{bond} of the cells is calculated considering the mean area throughout the throat of the joint (Figure 4.21), while approximating the lateral meniscus to a uniform triangle. This area depends upon the number N of CFRP sheets within a core, disregarding the transversal sheets. The triangle is thought as an isosceles of flank f . Then, the throat has a width of $\frac{\sqrt{2}}{2}f$ and a length L_{core} as the length of the core. Regarding to the size of the core, samples of 200 by 100 mm are used for the calculation (Figure 4.6). The overall bonding strength depends on the adhesion strength and the bonded surface ratio as the bonded area-to-core area or A_{bond}/A_{core} . Due to the lack of homogeneity while gluing, the amount of glued surface is variable among the cells. Therefore, an average value of glued surface in the total sample surface is estimated, and Eq. (4.65) is assumed to hold, where the F_{DB} represents the effective critical load for core-face bonding failure.

$$F_{DB} = A_{core}\tau_{DB} = A_{bond}\tau_{int}N \quad (4.65)$$

$$\tau_{cDB} = \tau_{int} \frac{\sqrt{2}fL_{core}}{A_{core}} N \quad (4.66)$$

Solving for τ_{DB} and replacing the corresponding factors, Eq. (4.66) represents the average shear strength due to core-face debonding.

4.4.2.1.3 Shear buckling

Since the core cell walls are made from thin composite plates, the shear loads applied may lead to an elastic buckling failure. Thus, stability studies are required as well. Therefore, elastic shear buckling may occur after exceeding the buckling shear limit strength τ_{cB} . The approximation method has a first fundamental assumption, in which the load-bearing capacity of the structure is exceeded above the a critical buckling point [171].

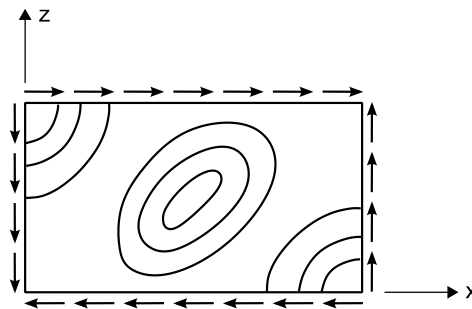


Figure 4.22. Scheme of buckling of a rectangular plate under shear loads

As for the classic approximation on isotropic materials, it may be considered for the study a rectangular plate of constant thickness, which buckles by the action of evenly distributed shear forces when reaching the instability point. After the buckling limit has been exceeded, the sheet may continue to fold together (Figure 4.22) and to break the construction [171]. In the real case, after the critical point, the structure may bear more load and break afterwards. The approach will consider an orthotropic plate, which is articulated along its edges, and is free to move in the plane of the plate.

In this work, the analytical solution to the problem will only be approached for the reference cores (full-walled cells). The behavior of core design 1 and 2 (machined cores) will only be studied via numerical analyses, because of the considerable difficulties of determining the exact effect of the machined geometries, for having a variation of the struts profile that brings more complexity into the calculations. The CFRP base material used for the core walls are thin plates ($t=0.65$ mm) obtained from woven textiles in a symmetrical lay-up of orthotropic layers, and thus, they will be considered as homogeneous plates.

Therefore, the critical elastic shear buckling stress of the CFRP sheets τ_{sB} , is defined by Eq. (4.67) according to the theory developed by Seydel [172] and expanded by Johns [173] and Leissa [174] that provided numerical approximations, considering the composite sheets as orthotropic materials.

$$\tau_{sB} = K_s \frac{\pi^2}{tL^2} \sqrt[4]{D_1 D_3^3} \quad \text{if } \theta > 1 \quad (4.67)$$

Buckling factor K_s in Eq. (4.67) is a tabulated value depending on border constraints and the relations between the orthotropic plate rigidities (D_1 , D_3 and D_{31}) represented by factor θ (Eq.(4.68)) and factor β_a (Eq. (4.69)) [173].

$$\theta = \frac{\sqrt{D_1 D_3}}{D_{31}} \quad (4.68)$$

$$\beta_a = \frac{H}{L} \sqrt[4]{\frac{D_1}{D_3}} \quad (4.69)$$

Where:

$$D_1 = E_{1s} I_x \quad (4.70)$$

$$D_3 = E_{3s} I_z \quad (4.71)$$

$$D_{31} = G_{31s}t^3/6 \quad (4.72)$$

In this work, the boundary conditions are assumed as an approximation of a plate pinned (or articulated) along the edges. In the last expression, K_s varies from $\approx 3 - 9$ for values $0 \leq \beta_a \leq 1$, specified then by the obtained value of factor θ (see Annex E, section 2.2.1).

The applied shear load over the cell becomes critical (P_{cB}) when reaching the shear buckling critical point. This load is common to the base material and the representative cell member as shown in Eq. (4.73). Then, the critical elastic shear buckling stress of core is given by Eq. (4.74).

$$P_{cB} = \tau_{sB}A_s = \tau_{cB}A_{cell} \quad (4.73)$$

$$\tau_{cB} = \tau_{sB} \frac{A_s}{A_{cell}} = \tau_{sB} \frac{tL}{L^2} = \tau_{sB} \frac{t}{L} = \tau_{sB} \frac{\bar{\rho}}{2} \quad (4.74)$$

Introducing Eq. (4.67) into the last expression, the critical elastic shear buckling stress of core is defined by Eq.(4.75), neglecting the contribution of the core walls perpendicular to the shear load.

$$\tau_{cB} = K_s \frac{t}{L} \frac{\pi^2}{tL^2} \sqrt[4]{D_1 D_3^3} = K_s \frac{\pi^2}{L^3} \sqrt[4]{D_1 D_3^3} = K_s \frac{\pi^2}{L^2} \sqrt[4]{D_1 D_3^3} \frac{\bar{\rho}}{2} \quad (4.75)$$

4.4.2.1.4 Analytical results

A comparison of the different failure modes predicted by the analytical approaches is presented within this section. Table 4.10 and Table 4.11 shows the parameters employed for the analytical calculations and the results obtained for the shear strength predictions using Eq.(4.64) for τ_{cR} , Eq.(4.66) for τ_{cDB} and Eq. (4.75) for τ_{cB} . Regarding to core design 2 and referring to Figure 4.20.b, the central strut bears most of the stresses, and thus, the approximation L_{eq} neglects the lateral struts.

Table 4.10. Core shear analytical strengths: fracture and debonding failure modes

<i>Pattern</i>	L_{eq} (mm)	f (mm)	N (--)	L_{core} (mm)	A_{core} (m ²)	τ_{int} (MPa)	τ_{31s} (MPa)	τ_{cR} (MPa)	τ_{cDB} (MPa)
Design 1	6.91	1	5	200	0.02	20	110	0.823	1.414
Design 2	4.204	1	5	200	0.02	20	110	0.501	1.414
Reference	50	1	2	200	0.02	20	110	1.430	0.565

Table 4.11. Core shear analytical strength: shear buckling failure mode

<i>Pattern</i>	D_1 (Nmm)	D_3 (Nmm)	D_{31} (Nmm)	θ (--)	β_a (--)	L (mm)	H (mm)	K_s (--)	τ_{cB} (MPa)
Design 1	--	--	--	--	--	--	--	--	1.275*
Design 2	--	--	--	--	--	--	--	--	0.875*
Reference	1433	36388	162.9	44.3	0.226	50	25.4	3.1	3.970

Note: (*) Only evaluated via numerical approaches

Figure 4.23 presents the expected failure modes comparing the different theories stated, where the failure cases due to maximum shear strength of the base material (machined cores) and debonding (reference cores) show the minimum strength value, meaning a higher probability of occurrence. It is interesting to remark that the shear buckling presented for cases 1 and 2 are only represented by numerical approaches as in section 4.4.2.2.

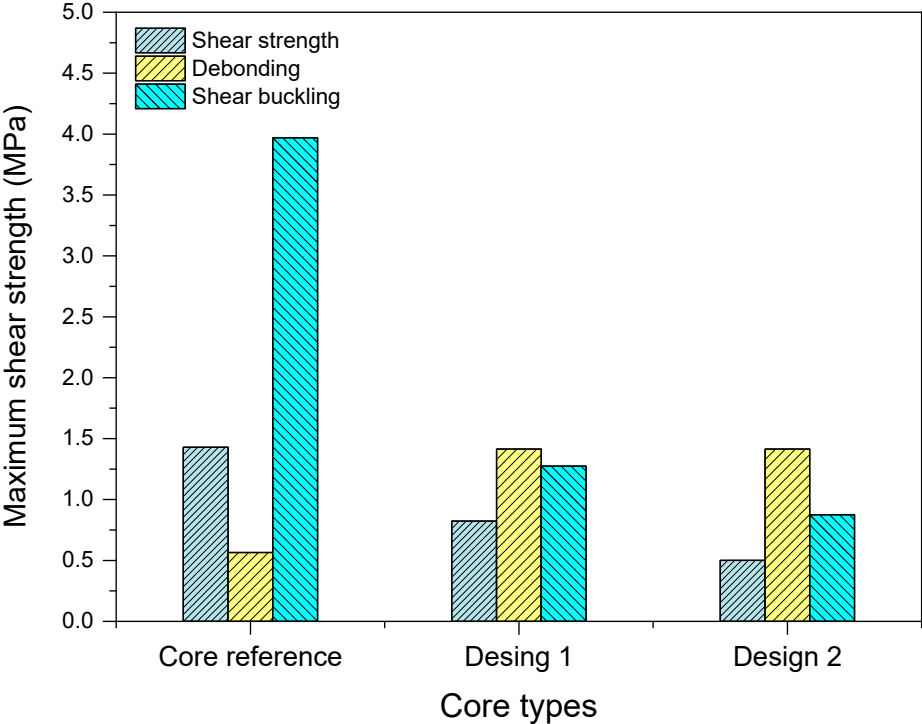


Figure 4.23. Comparative peak shear stresses among different approaches

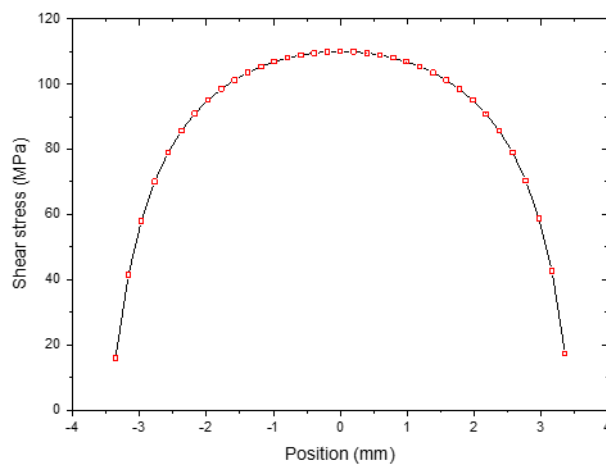
4.4.2.2 Numerical approach

As shown in section 4.3.2.2, the shear stresses shall be evaluated independently through two different simulations:

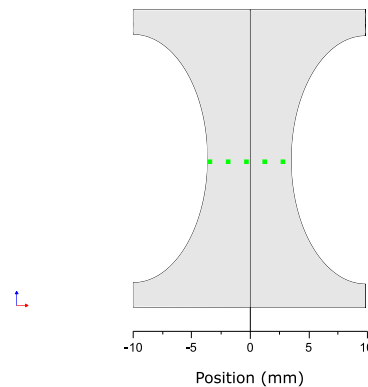
1. Through linear static simulations (without buckling behaviour)
2. Through non-linear static simulations (with buckling behaviour)

Thus, the simulation that predicts the minimum critical load, is selected as the shear failure load of the core. In both cases, cells based on CFRP sheets are discretised by a mesh of shell elements of size 0.4 mm (CQUAD4, 4-node reduced integration). Material properties are set by Table 4.2. Border conditions are established in correspondence to the analytical models previously presented, in which: for the machined cores, the top and bottom-line nodes are selected as simply supported, although the top nodes only can move in x -direction, and the nodes over the lateral flanks are set free; for the reference core, the entire plate edges are set as simply supported, and the top nodes only can move in x -direction.

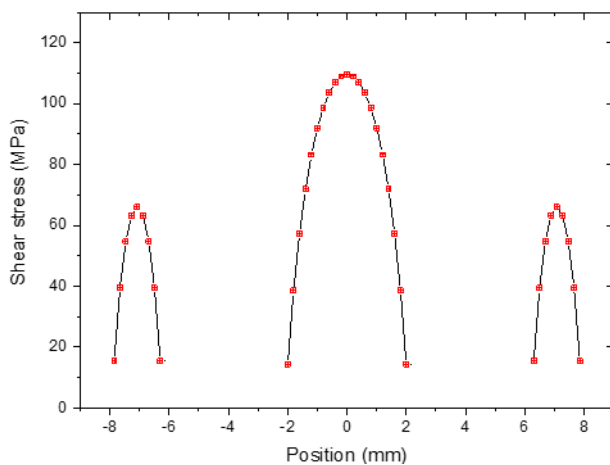
(a) Core design 1



Reference on node positioning:



(b) Core design 2



Reference on node positioning:

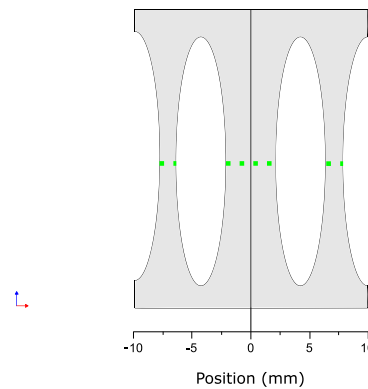


Figure 4.24. Shear stresses vs. reference nodes extracted from simulations

1. The linear static simulation is analogous to the simulations presented in previous section 4.4.1.2, for obtaining indirectly the core shear modulus. The results of the simulations are given in Figure 4.24, applying different line-loads to the top nodes until reaching the base material strength. Shear stresses vs. referenced node position curves (green horizontal mid-line) are extracted from the numerical calculations for the case of maximum shear strength of the base material. Core design 1 shows a parabolic-like curve for shear stress distribution at the mid-plane. In this case, a failure load of 16.8 N/mm is extracted, when the base material reaches 110 MPa (base material shear strength). For the case 2, the node references are obtained from the mid-plane including the centre and the two laterals' struts. The lateral struts bear significantly less load compared to the middle strut from the point of view of the stress shown, as a result of a lower bending rigidity. Thus, the highest shear stresses are observed at the centre strut, with a failure load of 14.8 N/mm, when the base material top-out 110 MPa. The full-walled reference cores present a failure shear load of 71.5 N/mm. The results charts are not plotted for being trivial, as the average load is divided by the base material area and being of a constant value along the plate as pointed out in section 4.4.1.2

2. In the non-linear static model, the top-line nodes are loaded with a 10 kN line load parallel to the x -direction, until the simulation stops. Different nodes are selected for evaluating buckling behavior of the plate sheets, as shown in Figure 4.25

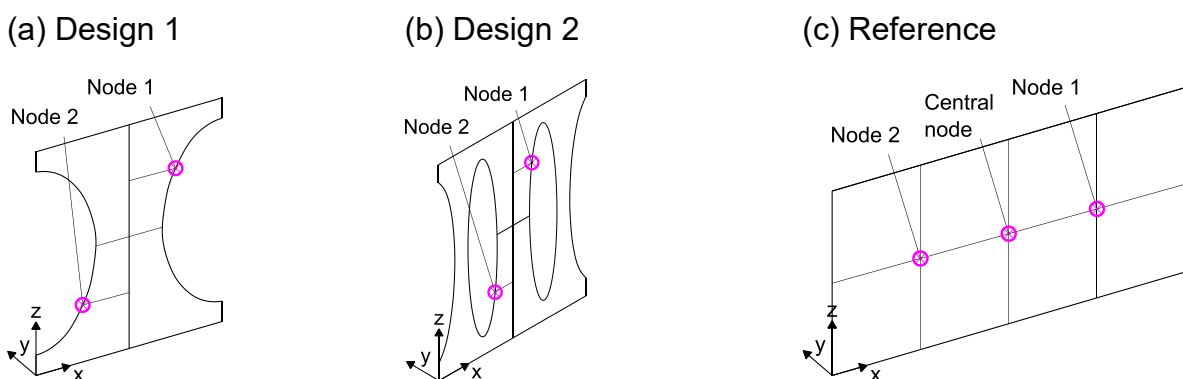


Figure 4.25. Schemes of selected nodes for displacement tracking in y -direction

Figure 4.26 shows schematically the simulated material distortion due to the applied load via an isometric rendering, and the corresponding graphs of the node displacements obtained from the FE simulations.

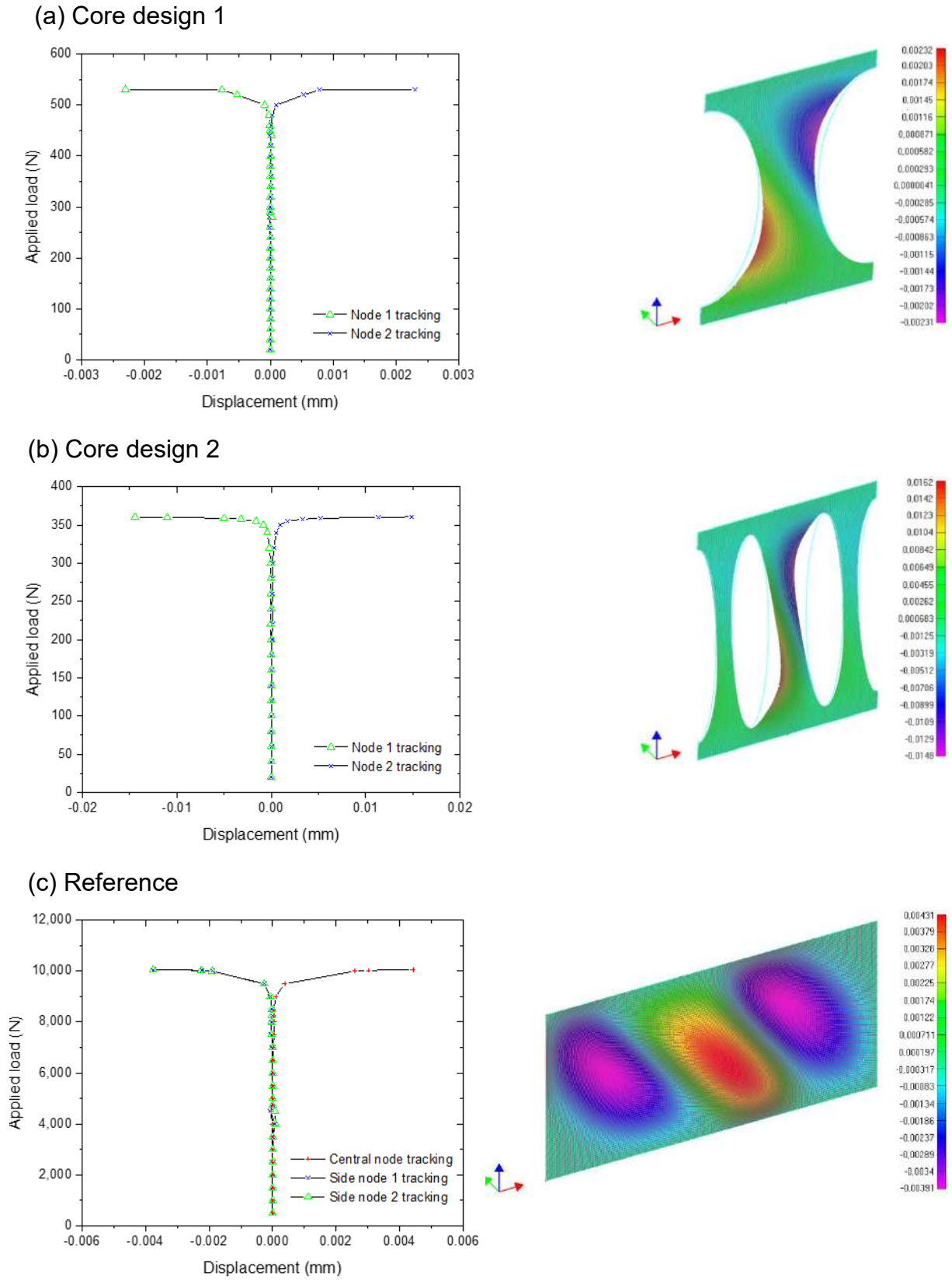


Figure 4.26. Data extracted from the non-linear simulations: *Right.* Load vs. selected node displacement curves. *Left.* Contour plots of the node displacements in *y*-direction

Employing node tracking points at opposite sides of the material sheet, Figure 4.26 represents the node displacement in y -direction for each core case. Figure 4.26.a and Figure 4.26.b show the behavior of two opposite nodes selected, both exhibiting mirrored behavior accordingly to the zero positioning. This result suggests that only one-wave wrinkle is developed in both cases. The instability regime begins at load of almost 510 N and 350 N with an estimated last-step load of 530.6 N and 360.63 N for cores design 1 and design 2, respectively. In a similar way the last case is studied as Figure 4.26.c, which represents the selected nodes tracking of reference cores. Three curves begin with zero displacement until the instability load is reached, then they behave asymptotically to positive and negative values, which indicates that the wrinkles exhibit two wave-length peaks and one dip. A load of approximately 9.875 kN is estimated as the start of the instability region; while a load of 10.046 kN sets when the instability of the model is reached.

4.4.2.2.1 Numerical approach

Table 4.12 summarizes the results obtained from the simulations, contrasting them with the analytical results for the minimum stress attained. The critical load of the cell element is given by P_{crit}^* . The minimum stresses are predicted for the case when reaching the maximum shear strength of the base material (SF: shear strength failure). Nevertheless, the analytical approaches predict that the debonding failure (DB) has also a higher probability to occur compared to the failure due to shear strength as $\tau_{cDB} < \tau_{cR}$ (Table 4.10), in particular for the reference case. Moreover, the buckling behavior obtained by non-linear static simulation is predicted of less probability to occur compared to the other failure modes.

Table 4.12. Core shear strengths according to numerical and analytical approaches

<i>Pattern</i>	L (mm)	P_{crit}^* (kN)	τ_c^* (MPa)	τ_c^{**} (MPa)	τ_c^{***} (MPa)	Expected failure mode
Design 1	20	0.51	1.275	0.84	0.823	SF
Design 2	20	0.35	0.875	0.74	0.501	SF
Reference	50	9.875	3.950	1.43	0.565 ¹	DB

Notes: (*) Non-linear static simulation, (**) Linear static simulation, (***) Analytical, (1) considering debonding failure mode

4.5 Experimental tests

To evaluate the mechanical properties as the stiffness and the strength of the proposed cores, mechanical tests are carried out following the guidelines of ASTM C365 (*Flatwise Compressive Properties of Sandwich Cores*) [175] and ASTM C273 (*Shear Properties of Sandwich Core Materials*). In both cases, a Zwick / Roell Z150 screw-driven universal testing machine is used to carry out three tests on each core sample at controlled room temperature.

4.5.1 Compressive tests

Compressive tests are carried out using the test set up shown in Figure 4.27. Two steel compression plates are used to transmit the stress to the specimen. The lower plate is placed on a spherical bearing to counteract misalignments due to lack of parallelism between the faces of the stabilized panel incorporated during the manufacturing process, and thus, promoting a better distribution of forces along the load-bearing core columns. The crosshead speed is set to 0.5 mm/min and the strain is obtained by displacement transducer HBM W2TK. Photographs of the test samples are given in Figure 4.5. Three specimens of each core case are tested, and the main sample dimensions comprise 100 x 100 x 25.4mm.

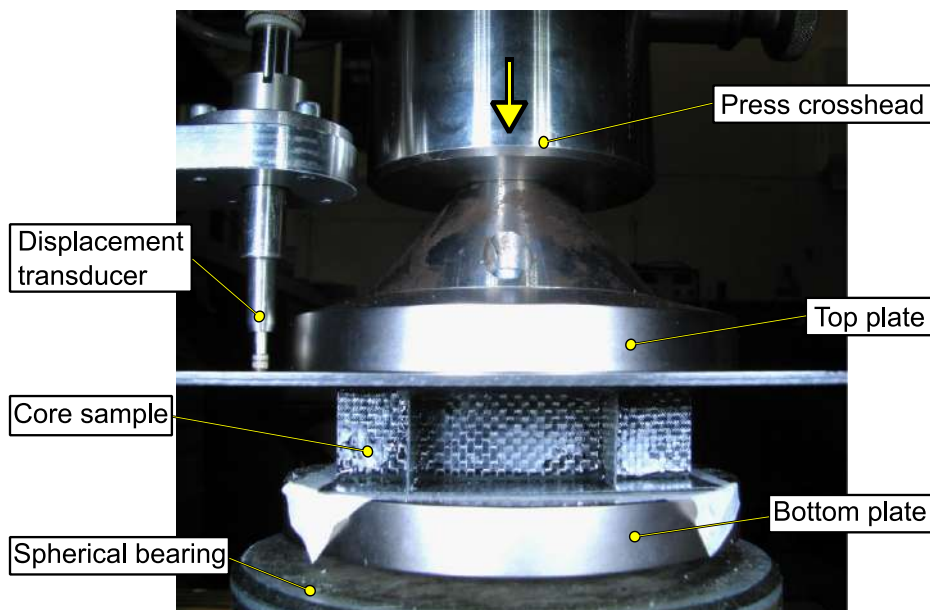


Figure 4.27. Set-up used for compression tests

4.5.1.1 Compressive test results

The compressive stress vs. strain of the design 1 cores is represented in Figure 4.28 as an example of study; while Figure 4.29 represents a matrix of photographs at selected representative values, evidencing the behaviour of the core against compressive loads.

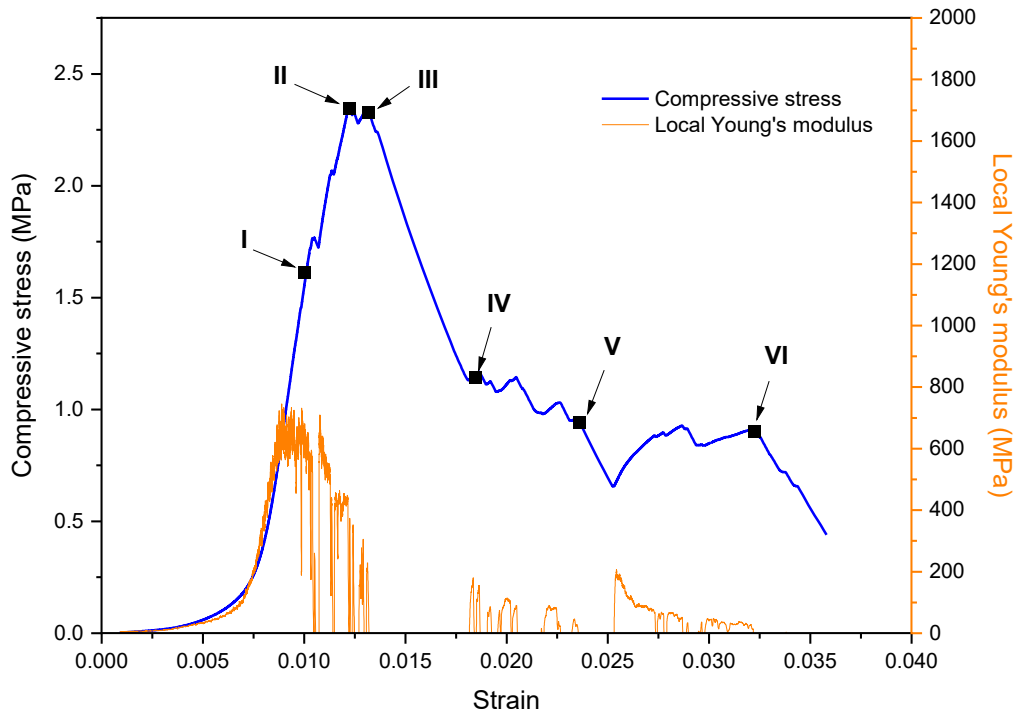
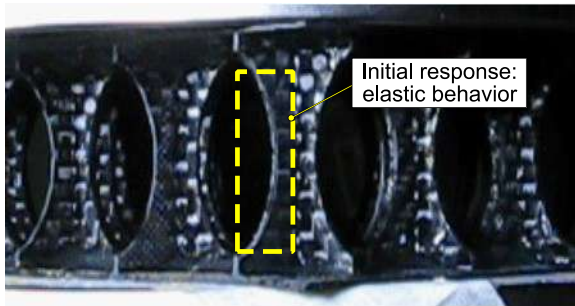


Figure 4.28. Measured compressive stress–strain response of design 1 cores

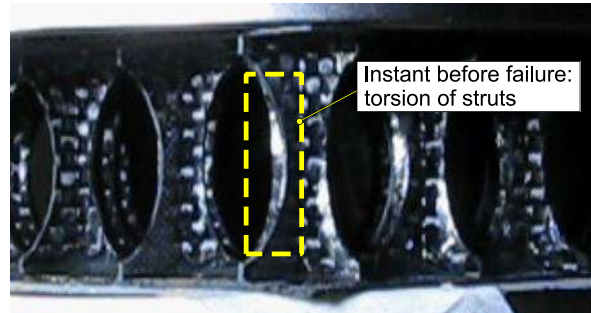
The initial response of the core is almost linear, up to the peak stress, with a small load drop after point I, suggesting a slight misalignment between the loading plates (lack of parallelism and repositioning of the patella) which causes prematurely local failure of columns due to the inhomogeneous load distribution, also evidenced by the local drop of the average young's modulus. Then, the load slope changes gradually due to the lower number of columns bearing the compressive loads before reaching the maximum compressive strength of the cores, evidencing torsional buckling failure, when observing the rotation of the column flanks as at point II in Figure 4.29. The non-linearity observable in the change of the local Young's modulus between point I and II reinforces the theory of buckling failure. Later, core collapse occurs when the maximum load capacity is reached, at point III, in which most of the remaining core columns collapse. The load drop is not sudden, but gradual, also suggesting a failure due to an

elastic buckling case. After the main drop, the stress reaches a plateau due to the local opposition of the collapsed columns and, later, the stress continues to drop with further crushing of the material (points IV-VI). Finally, local failure events occur progressively, leading to a decrease in the overall core strength, following a non-linear regime due to the subsequent collapse of the remaining strut material.

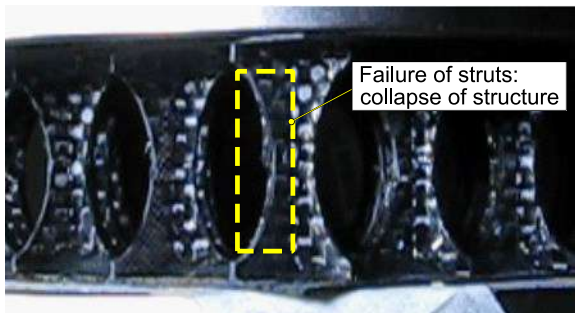
Point I = (0.0100; 1.6113)



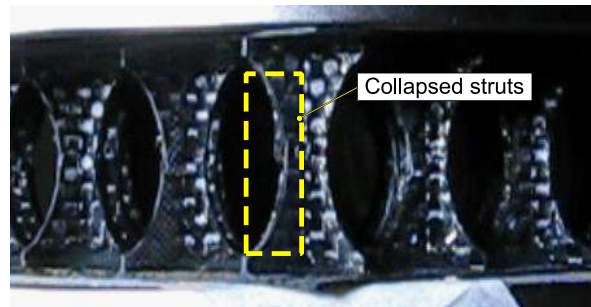
Point II = (0.0122; 2.3459).



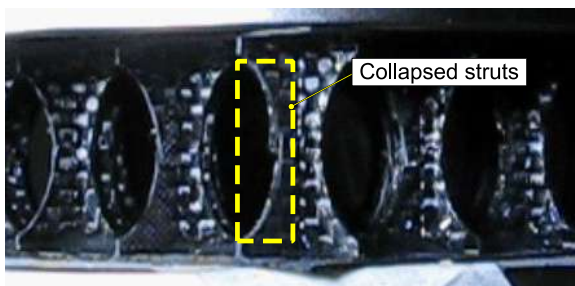
Point III = (0.0132; 2.3254)



Point IV = (0.0185; 1.1440)



Point V = (0.0236; 0.9429)



Point VI = (0.0322; 0.9007)

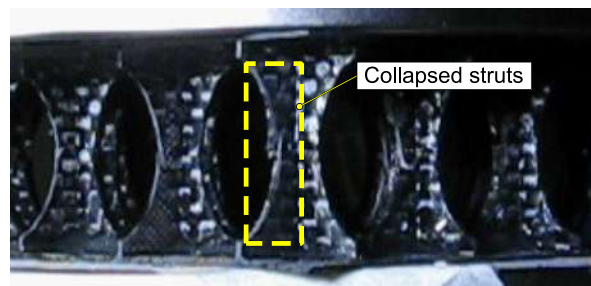


Figure 4.29. Photographs associated to selected points: compressive behaviour of design 1 cores

The obtained compressive stress σ_{33} vs. ε_{33} of the proposed cores are plotted in Figure 4.30, for the best performance samples. The curves show in all cases an elastic response at the beginning of the tests, with a small change in the load slope before the collapse of the structures, denoting the onset of elastic buckling of the CFRP structures. In most cases, premature local failures of single columns are observed due

to possible stress misdistribution along the core thickness, potentially attributable to the manufacturing process and test set-up. After the peak and collapse of the structure, in all cases the stress progressively decreases until reaching a plateau, where the already collapsed material starts to be compressed. Then, the stress decreases with further crushing and strain.

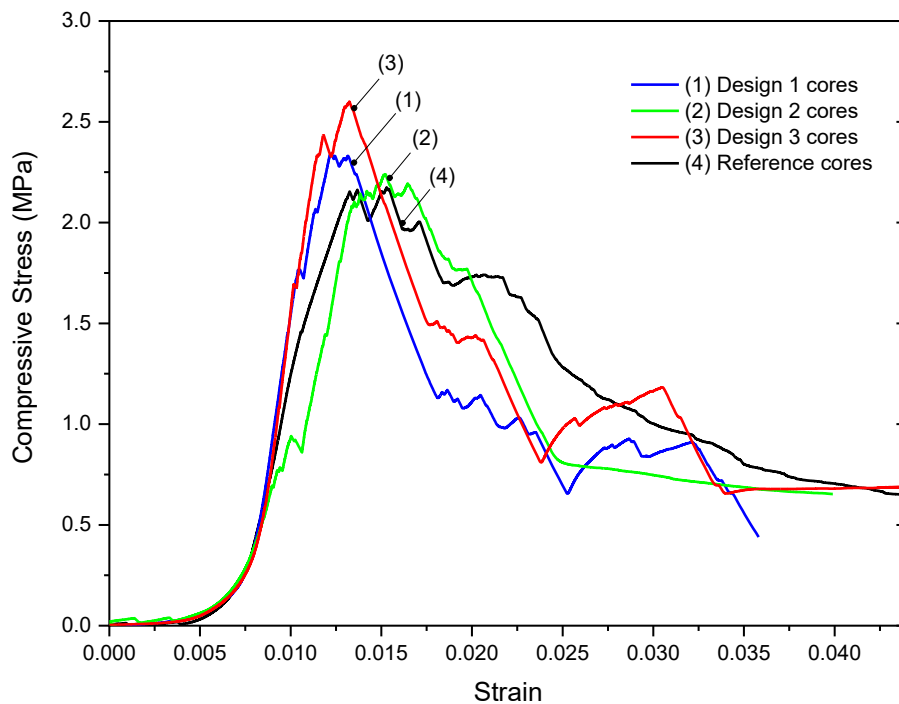


Figure 4.30. Compressive stress–strain response of square–honeycomb cores

As noticed in Figure 4.30, core design 3 showed the best compressive strength performance compared to the others, with a compressive strength of around 2.6 MPa. The worst performance is observed for both the reference core and design 2 with a peak value in the order of ≈ 2.25 MPa and 2.2 MPa, respectively. The maximum compressive strength of the proposed cores showed average peak values in the order of 2.4 MPa. The resume of the results is presented and discussed in the following section.

4.5.1.2 Discussion

Table 4.13 summarises the results obtained from the compression tests and the model predictions. The compressive strength of the cores is also exhibited in Figure 4.31 as bar graphs for comparison. The failure estimated by theoretical approaches comprised are of torsional buckling behaviour for the machined cores, and of plate buckling for the reference core.

Table 4.13. Analytical, FEM and experimental results from compressive tests

Core type	Analytical		Numerical		Experimental		Obs. mode
	σ_{cpk} (MPa)	E_c (GPa)	σ_{cpk} (MPa)	E_c (GPa)	σ_{cpk} (MPa)	E_c (GPa)	
1	2.83	1.40	2.94	1.59	2.173 ± 0.279	0.72 ± 0.02	TB
2	2.75	1.56	2.81	1.93	2.131 ± 0.151	0.61 ± 0.01	TB
3	2.88	1.38	2.98	1.39	2.514 ± 0.123	1.12 ± 0.01	TB
Ref.	2.07	1.62	2.19	1.57	2.198 ± 0.056	0.54 ± 0.02	PB

Note: TB = torsional buckling; PB = plate buckling

Although the models predict the behaviour reasonably well by the analytical and numerical results, the results are lightly overestimated. Nevertheless, in terms of the Young's modulus, the models overestimated the experimental result from two to three times, which is attributed to imperfections in the manufacturing process and test set-up, leading to a lack of parallelism between faces, perpendicular misalignments between core walls and faces, etc. Furthermore, since sandwich panel specimens are not ideally flat, compressive loads are not perfectly distributed over the panel faces, leading to local failures (small drops in load-displacement charts until reaching the main failure load) as previously seen in Figure 4.30. These premature failures may cause an overloading of the remaining struts, inducing a larger straining followed by collapse of the panel at a lower load value than the estimated load value. The discrepancy between models and experimental data is found as follows: the larger induced straining is not considered in the models, leading to a lower elastic modulus than predicted; while the predicted critical load, considered the collapse of all columns at the same time, as reaching the estimated critical load, and therefore, the predicted value is higher than the obtained in experiments. Nevertheless, good agreement is found between the numerical and analytical model predictions. It is important to highlight the ideal case, where cores could reach high load capabilities (i.e., when reaching full potential), considering a defect-free processing and assembly of the material.

Figure 4.31 compares the maximum compressive strength measured among the proposed square honeycomb cores. The limit of the experimental results agrees well with the analytical and numerical predictions. The variability between the results is attributed to several factors, mainly related to the misalignments during the manufacturing process and the configuration of the test set-up.

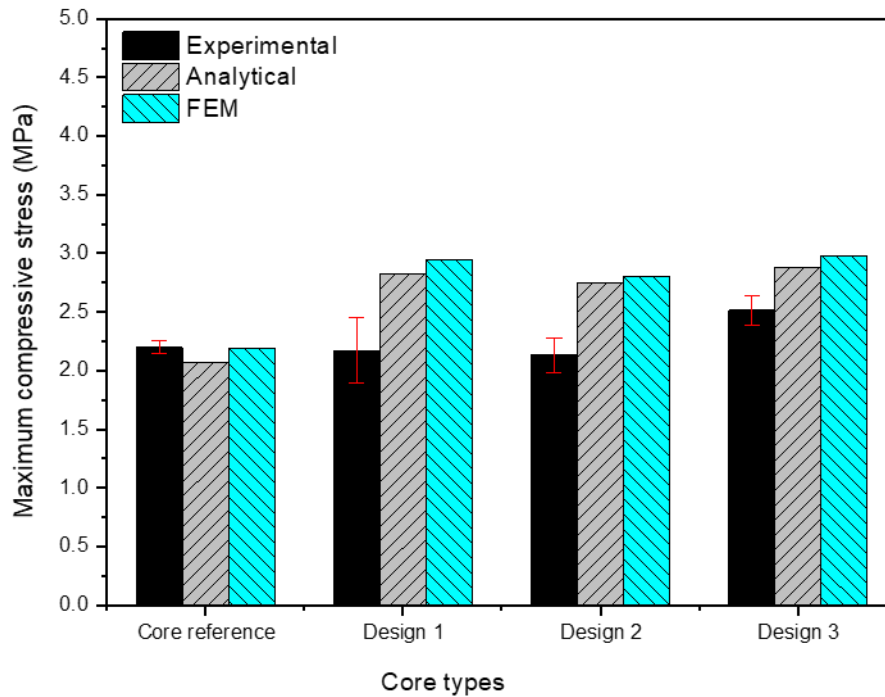


Figure 4.31. Maximum compressive stresses according to analytical, FEM and experimental

In particular, for design 2, when using the theoretical Euler buckling load (see section 2.2.3.2) applied to the slender side columns, a failure buckling load of $P_{crit} = \frac{\pi^2 EI}{(1 \cdot H)^2} = \frac{\pi^2 62600 \cdot 0.04}{(25.4)^2} = 38.24$ N is attained. Assuming that the stresses are distributed homogeneously along the cell, in terms of stresses over the base material of the slender plate, a stress of $\sigma_s = \frac{38.24}{1.745 \cdot 0.65} = 33.7$ MPa is calculated. If this stress is extrapolated to the base material within a cell, a load $P_c = 33.7 \cdot A_s = 322.6$ N is attained. Dividing the last result by the cell area A_c , the buckling stress of the slender plates in terms of stress over the cell is $\sigma_c = 0.8065$ MPa. This result means that when the loaded cell reaches the value 0.8065 MPa of stress, the narrow side plates may buckle. This estimation is in accordance with the experimental charts on Figure 4.30 (design 2 curve), where a larger drop in stress of around ≈ 0.8 MPa is shown. Then, the drop in stress is attributed to the narrow plate buckling. Furthermore, Figure 4.32 shows schematically the transition through instability of design 2 cell (Euler buckling of the narrow lateral plates, and later torsional buckling of the cross-shaped column).

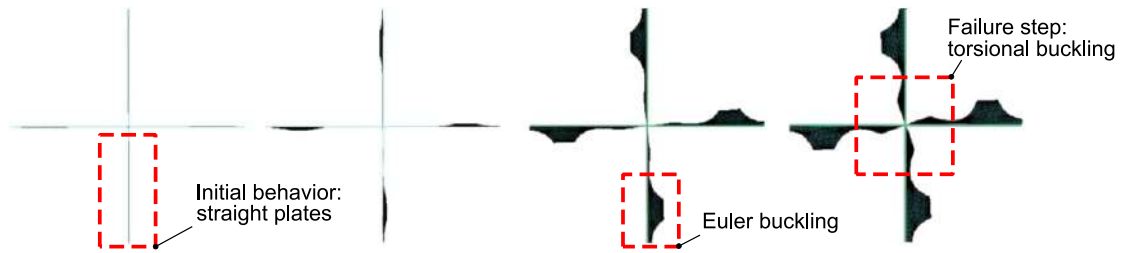


Figure 4.32. Top view of FE renders of design 2 struts in a cell member showing the transition through instability

Among the different proposals for failure models, it is clearly seen that the lowest estimated strength (in this case, also the lowest critical load) is attributed to torsional buckling, when calculations are compared with the experimental data (Table 4.13). Figure 4.33 shows a top view of the FE rendering with 4 cells working at the same time when the core is subjected to compression loads. The red arrows show the turning trend when reaching the instability load.

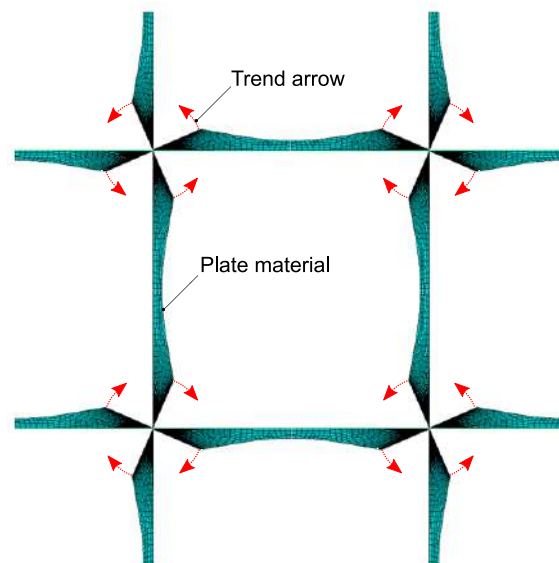


Figure 4.33. Top view of FEM renders of four struts of core design 1 showing torsional buckling

As explained in section 4.3.2.1.5, reference cores do not satisfy the border conditions for pure torsional buckling behaviour. The snapshots presented in Figure 4.34 support the hypothesis of plate buckling, showing that the buckling of the front plates is not coupled with the rest of the structure behaviour at the failure step, because the concavity of the buckled plates is oriented to the same side, contrasting the coupled and coordinated behaviour shown in torsional buckling cases.

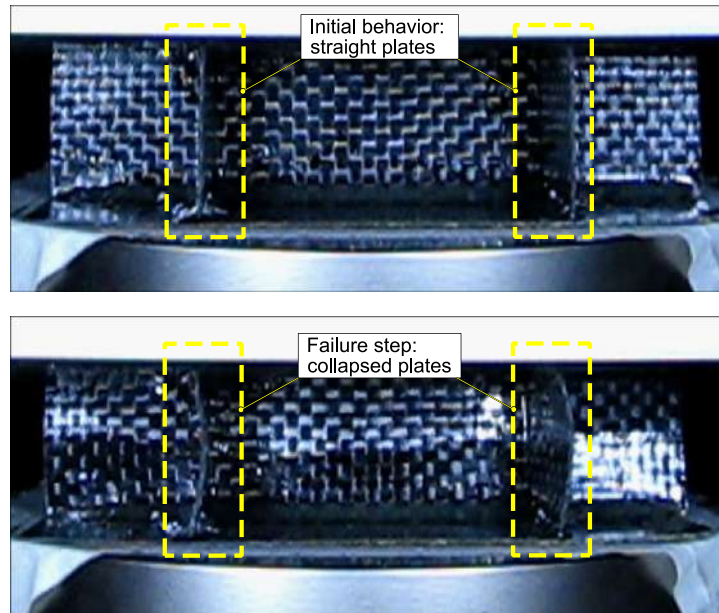
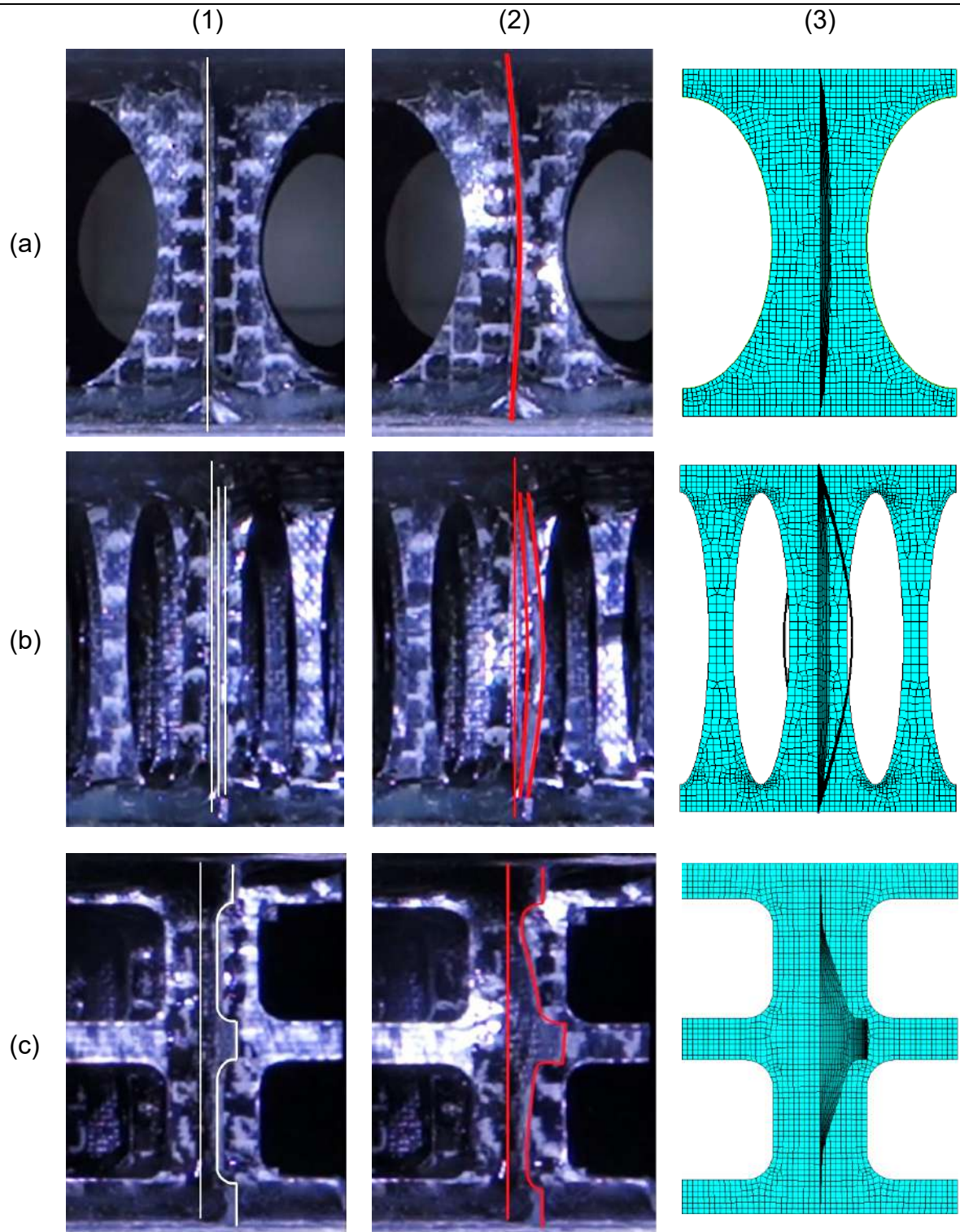


Figure 4.34. Photographs of reference core showing failure behaviour

Table 4.14 compares the experimental tests of the three proposed core and contrasts them with their respective numerical results. The first column shows the magnified photographs of the individual cells with a white straight tracking line, with focus on the initial position of the sample at the beginning of the compression test. The second column shows the instability of the columns an instant before the collapse of the structure. The red tracking lines help to define and contrast the shape of the edge laminate sheet during this stage. The difference in the light reflection upon the background material sheet allows discerning the displacement and deformation of the structure. The third column presents FEM sketches of the cell's struts showing the instability of the cells. The failure denoted a torsional buckling behaviour and, therefore, supported the proposed hypotheses.

Table 4.14. Comparison matrix of cell's struts during loading. Rows: (a) Design 1 samples. (b) Design 2 samples. (c) Design 3 samples. Columns: (1) Photographs at the beginning of compressive test. (2) Photographs before failure. (3) FEM renders at failure step



4.5.2 Shear test

Shear core samples are fixed to prismatic steel plates with a two-component epoxy glue. The standard ASTM C273 defines a minimum length-to-thickness ratio of 12:1, aiming a desired shear failure of the samples by plate shear tests. The employed ratio in this work is in average 7.9:1. Consequently, a small out-of-plane load case is led of nearly by 4.36% higher than the expected for the suggested case. Nevertheless, it has been proven that even smaller ratios led to suitable results [176]. The test set-up is schematically shown in Figure 4.35 where it can be observed that the load line is kept within the diagonal between opposite corners of the core, according to the standard recommendations.

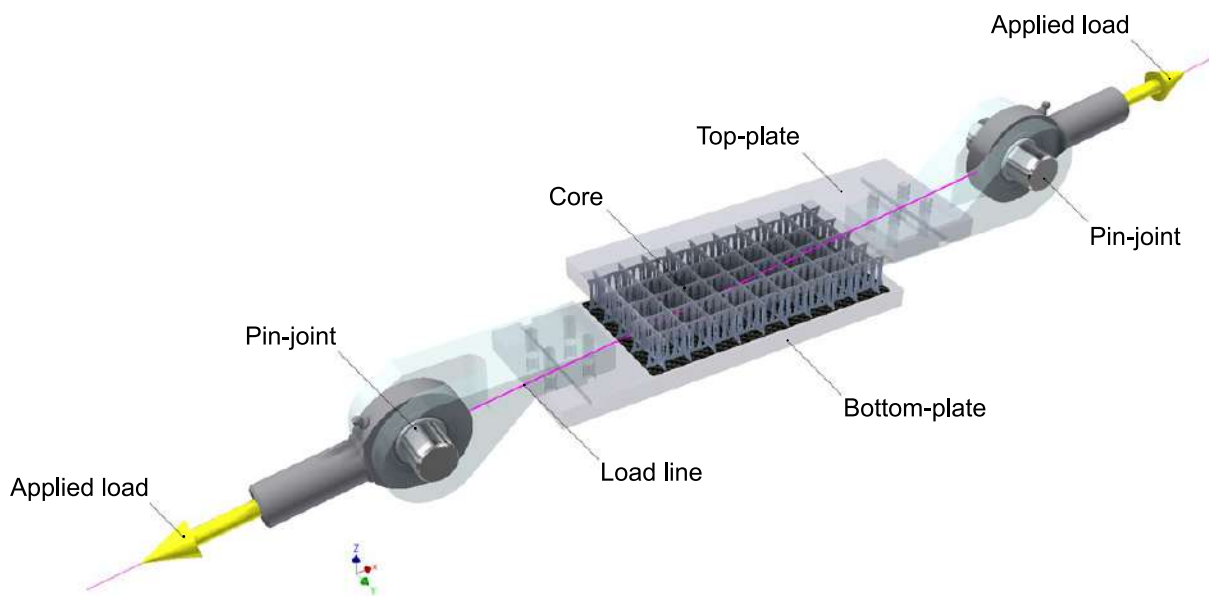


Figure 4.35. Rendering scheme of the shear test set-up

The crosshead speed employed is set by 0.5 mm/min and a displacement transducer HBM W2TK is implemented for measuring the straining. Three samples are tested, and Figure 4.6 provides photographs of the test samples, where the main sample dimensions comprise 200 x 100 x 25.4mm.

4.5.2.1 Shear test results

In-plane shear tests responses as τ_{31} vs. γ_{31} of the proposed cores are presented in Figure 4.36.

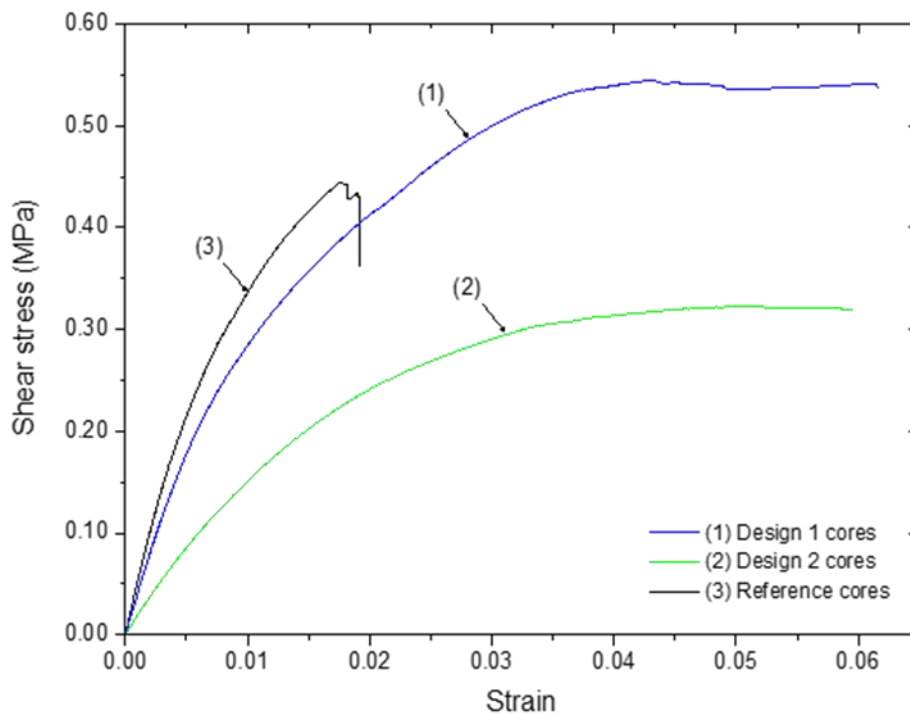


Figure 4.36. Shear stress–strain response of square–honeycomb cores

Analyzing the curves in Figure 4.36, a linear response is observed at the beginning of the curves in all the evaluated specimens, followed by a gradually change in the slope until rupture, typically expected for this kind of fiber orientation during shear loading [170]. Core design 1 and 2 presented both a significant deformation, with a decrement on the bearing of stresses and an increment of the strain, mostly occasioned by bending of the core struts. Due to the slenderness of the struts of core design 2, a larger deformation is observed. The failure of design 1 and 2 samples is attained after reaching a maximum deformation, where the cores failed in a slower and softer manner while reaching the maximum shear strength of the CFRP base material. The shear strength reached is around 0.54 MPa and 0.33 MPa, respectively. In contrast to them, reference cores exhibited catastrophic failure in all samples, dominated by debonding of the core from skins. The maximum shear strength for the reference case is of around 0.45 MPa. Despite presenting a larger number of sheets bearing the shear load, the slope exhibited by cores design 1 and 2 is smaller than the reference, evidently coming about because a larger deformation is experienced by the machined struts due to the bending effect. The latter means less shear stiffness and therefore more straining. Furthermore, the WJC manufacturing method may also bear on the overall component performance.

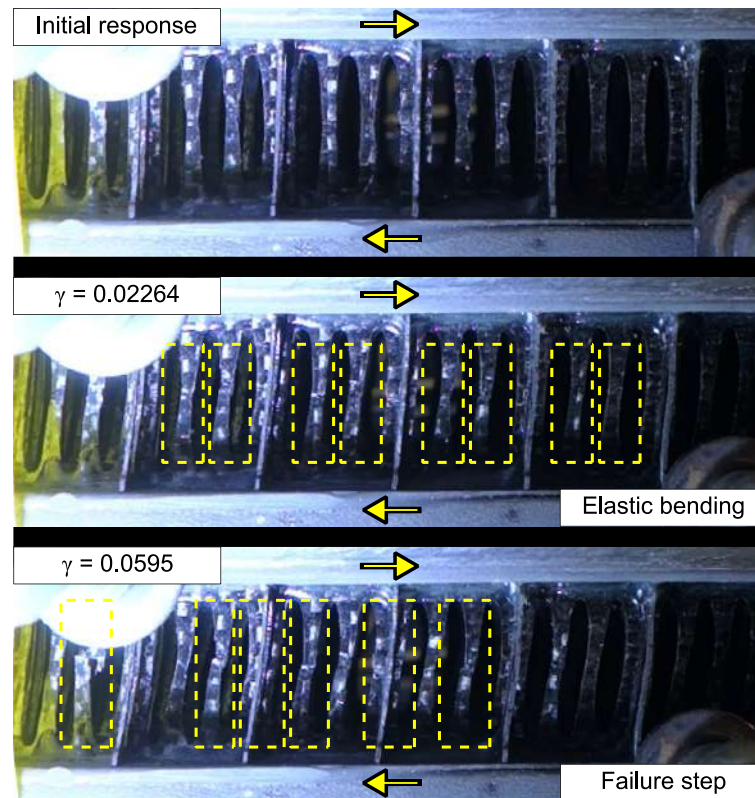


Figure 4.37. Montage of photographs showing the shear response of core design 2

A series of photographs of a core design 2 sample at different deformation levels is given by Figure 4.37, as a good example for showing the effect of bending induced by the shear loads. The snapshots show an initial elastic regime in which bending of the small columns takes place before the first signs of rupture are observed, after reaching the maximum bearable load. Remarkably, the failure does not occur at the same time on all the columns, but it happens gradually, suggesting a misalignment in the support of the loads, possibly due to the non-automated manufacturing process and test set-up.

4.5.2.2 Discussion

Table 4.15 compares the shear strength and moduli from the analytical and numerical predictions, and the experimental results. Both analytical and numerical models are reasonably in agreement, however in all cases they are moderately over estimated. The discrepancy among the experimental data and the predictions can be attributed to imperfections incorporated while manufacturing the samples or during the test set-up (e.g., misalignments of shear plates or lack of parallelism between core

sheets and shear plates), which led to not perfectly distributed loads and to local failures. These issues may considerably affect the performance of the cores, especially of the core design 2 that presented the higher number of machined geometries, and the smaller columns are more susceptible to local bending stresses. The case of reference cores exhibited debonding failure, in correspondence with the predictions. The photographs confirm this failure mode, with small cracking bands at the bottom of the sample before the sudden rupture (Figure 4.38). The smaller bonding surface influences the mechanical performance of the core, causing an abrupt premature failure (as seen in shear charts in Figure 4.36). In this case, the sample is de-attached from the support glued surface.

Table 4.15. Resume of analytical, FEM and experimental results from shear tests

Core type	Analytical		Numerical		Experimental		Obs. mode
	τ_{cpk} (MPa)	G_c (MPa)	τ_{cpk} (MPa)	G_c (MPa)	τ_{cpk} (MPa)	G_c (MPa)	
1	0.823	50.55	0.84	50.59	0.536 ± 0.008	52.52 ± 9.30	SF
2	0.501	23.25	0.74	23.26	0.334 ± 0.011	17.14 ± 2.14	SF
Ref.	0.565	46.28	1.43	42.68	0.453 ± 0.027	50.57 ± 1.14	DB

Note: DB = debonding failure; SF = shear failure

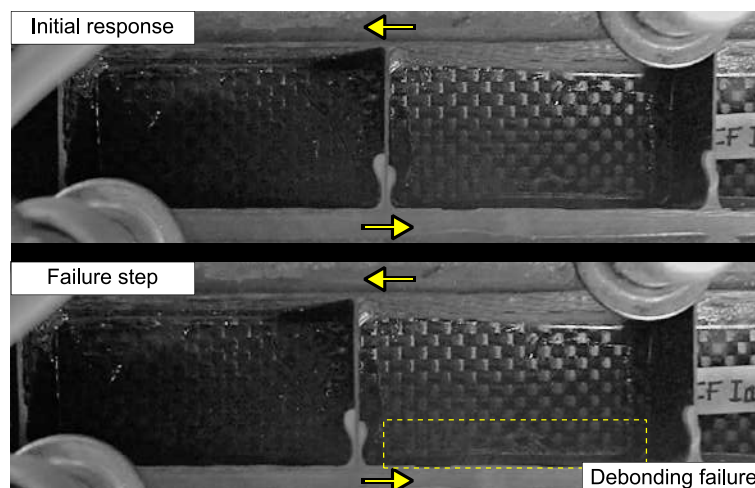


Figure 4.38. Photographs showing the debonding failure mode of reference cores

The elastic shear moduli of the cores are in good accordance with predictions (Figure 4.39). The analyses are addressed by introducing shear loads as the model

proposed in section 4.4.1. The analytical models are in good accordance with the numerical predictions, and they are validated as well by the experimental tests. The best performances are shown by reference and design 1 cores with average values of 50.57 MPa and 52.52 MPa, respectively, although reference cores showed less deviation among experimental values. Core design 1 denotes a higher rigidity, less influenced by bending in comparison with core design 2. The deviations of the experimental values are attributed to unexpected fabrications issues, less remarkable by reference cores that presented fewer machining stages during the manufacturing process. The predictions lightly underestimate the experimental results regarding to reference cores, attributed to the approximations carried out, in which the cross CFRP sheets are not considered and may influence the calculations.

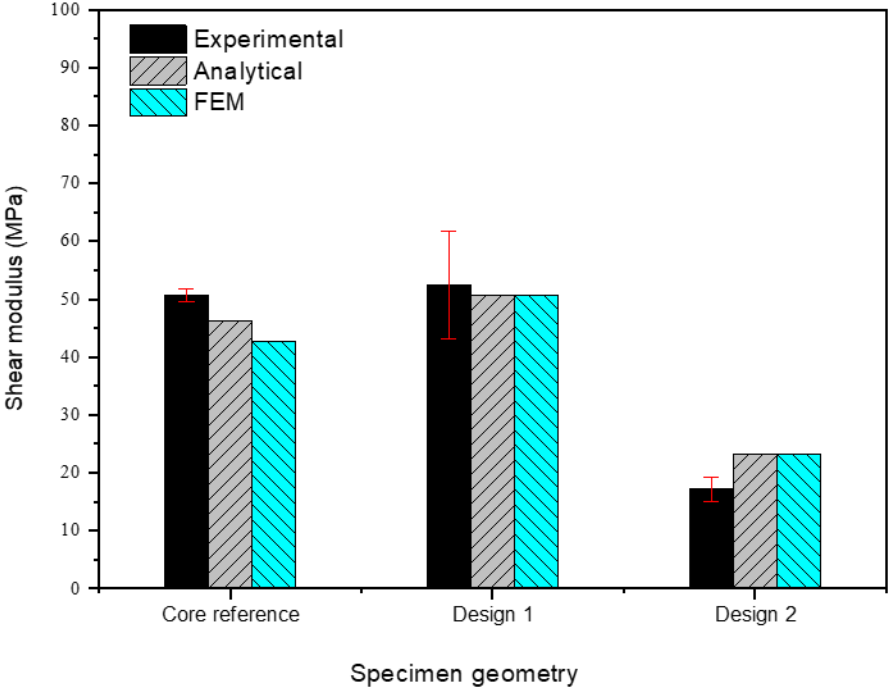
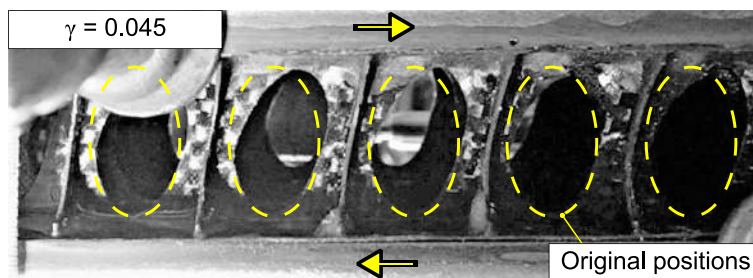


Figure 4.39. Maximum shear modulus according to experimental tests, contrasted by FEM and analytical models

Furthermore, both core design 1 and 2 showed a bending-shear deformation (Figure 4.40 and Figure 4.41) followed by a shear failure, also predicted by analytical and numerical models, despite the discrepancy contrasted by the experimental results. The failure due to buckling of the plates is considered as well in the models, but none of the specimens exhibited it. A comparison between FE predictions of the deformation of core design 1, is shown in Figure 4.40 in which the shear strain at $\gamma = 0.045$ is

observed. The original position of the struts is represented by a shadow behind the FE sheet. In this case, the deformation results from a superposition of shear and bending loads. No wrinkling of the core cell walls is predicted. Moreover, good agreement is seen between the FE predictions and core design 1 deformation at $\gamma = 0.03$ (Figure 4.41). The bending effect leads to a further distortion of the struts, also remarkable in Figure 4.37.

(a)



(b)

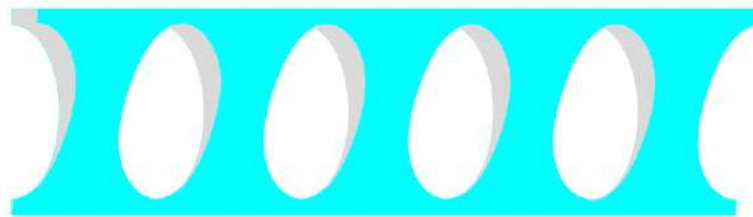
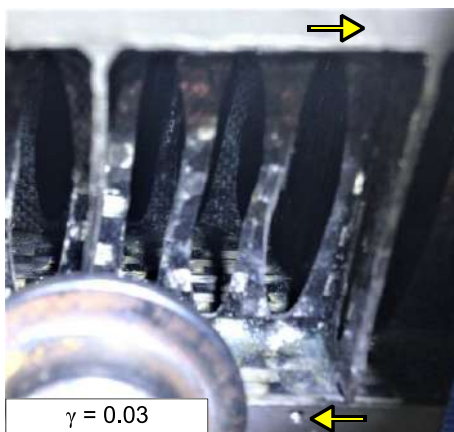


Figure 4.40. (a) Photograph and (b) FE rendering. Comparison for core design 1 deformation

(a)



(b)

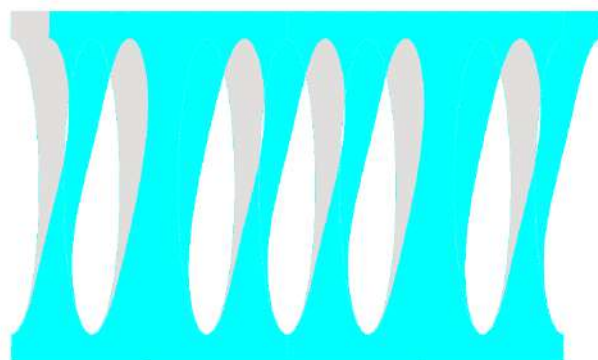


Figure 4.41. (a) Zoom-in into a photograph and (b) FE rendering. Comparison for core design 2 deformation

4.6 Concluding remarks

In this chapter, different types of ultra-lightweight cores are designed, manufactured, and tested, along with their mechanical properties' predictions, compressing theoretical and numerical approaches (elastic response and failure). The core base material is from a vacuum infused CFRP woven plate in a disposition of $[0/90]^\circ$. The proposed geometries are obtained from CAD models later used as "g-code" for the WJC technique, in which cavities are machined within the CFRP sheet. The cores are assembled using the slotting-interlocking method. The core density is maintained below 48 kgm^{-3} in all cases as a primary target.

On the one hand, the compression response of each core is evaluated and compared to that of a full-walled reference core. FE models are employed to support the theoretical approaches, which are in good agreement in all cases. The analytical and numerical approaches overestimate the core compressive strength, although the core out-of-plane stiffness is in excellent correspondence. The average compressive strength of the cores is in the range of 2.2 MPa – 2.7 MPa, while the compressive elastic modulus is in the range of 0.72 MPa – 1.12 MPa. The failure is governed by torsional buckling behavior in all machined cases, and of plate elastic buckling in reference cores. The discrepancy between experimental results and model predictions is attributed to imperfections in the manufacturing process of the main laminate composite material and the possible unequal load distribution during sample testing, that led to local premature failures.

On the other hand, the results obtained from theoretical approaches used to study the shear behavior due to the deformation of the cores, are in good agreement to the experimental tests. The FE calculations also helped to understand the displacement performed by the CFRP sheets, validating the theory of a Timoshenko-kind beams. The average shear properties of the cores are in the range of 0.33 MPa – 0.54 MPa, and of 17.14 MPa – 52.52 MPa, as core shear strength and modulus, respectively. The failure mode is dominated by shear failure of the base material for the machined cases, and of debonding of core-skin interphase for reference cores. Imperfections in the manufacturing process and/or test set-up led to unequal loading occasioning premature failures.

Remarkably, the hollow cores with interconnected holes allowed the material to be ultra-lightweight and gives the cores great potential for multifunctional applications

(e.g., heat transfer, embed foams, cables, or electronics). The number of sheets is an important point to review in structures that are made from non-monolithic parts. The glued surface ratio must be considered, not only by shear loading cases but also by flexural responses. The competitiveness of these cores will be analysed in Chapter 7 of this dissertation.

Although the catenaries-like shapes are thought firstly as an optimal shape of an arch for compressive loading, they do not have such a large influence in the overall performance of the cores, when using CFRP sheets oriented at $[0/90]^\circ$. The fibre orientation plays a fundamental role when CFRP structures are used. It should be noted that the fibre orientation employed in shear loading is better implemented when the loading case is parallel to the fibre orientation. Based on that, an improvement for this kind of material performance would be by the coupling of two layer of $[\pm 45]^\circ$ woven carbon fibre between a woven layer oriented at $[0/90]^\circ$, with a small lack of out-of-plane performance. Normally, the fibres are the component that withstand most of the load in a fibre reinforced composite material. Under pure shear loading, the maximum shear stresses are at 45° [170]. Therefore, if the orientation of the fibres is set at $[\pm 45]^\circ$, i.e., parallel to the maximum loads, this type of fibre orientation would enhance the shear performance of the proposed cores.

Nevertheless, good specific properties in terms of modulus and strength are achieved. Further improvement for minimizing the manufacturing imperfections of the material is needed in order to overcome some lack in performance. The reported manufacturing method, mechanical measurement and modeling provide a first step for developing new cores for lightweight design, attempting to expand the strength-density chart for honeycomb cores [101]. The interlocking method using reinforced polymeric materials showed to be a feasible production method to obtain light weight competing materials for sandwich applications. This method has many advantages related to the ease of material processing.

Next chapter explores an additional kind of ultra-lightweight cores as lattice materials in which the fiber orientation (i.e., throughout the CFRP rods) is set to 45° , in a way to enhance mechanical properties either by compression or shear loading, while still maintaining a very low density.

5 Ultra-lightweight lattices made from CFRP rods

For several years now, lattice-like structures have been developed as an alternative to different cellular topologies such as honeycombs cores [177], for producing lighter and stronger open-structured materials. Originally based on metals such as aluminium alloys or titanium alloys [27,125], nowadays lattice materials are gradually becoming CFRP-based materials [22,103], taking advantage of their high strength-to-weight and high stiffness-to-weight ratios.

As indicated in previous chapters, the fibre orientation plays a fundamental role in CFRP structures. The common loading cases on sandwich panels are of out-of-plane compressive loading and shear loading (see Chapter 3). Thus, it is required to find a configuration, in which both compressive and shear properties are less maximised. Hence, in this chapter the proposed lattices-based cores are manufactured from pultruded CFRP rods made from unidirectional fibres. The rods selected are of three different standard diameters for attaining core densities, ranging $5.3 - 48 \text{ kgm}^{-3}$. The investigation in this chapter comprises out-of-plane and plate shear core properties' estimations, and their failure mode predictions, in which buckling and maximum strength dominate the compressive case, while buckling and debonding failure modes govern the shear loading case. The predictions are supported by FE analyses, and then contrasted favourably with experiments.

5.1 Literature review

The search of tailored periodic materials [118] aiming the use of minimal amount of raw materials has led researchers to focus on lattices materials for attaining strong and lightweight parts. Three dimensional lattice structures take advantage of positioning the base material where it is needed and its open-cell characteristic as well. They are defined as materials with a connected network of struts, in a similar manner as how foams are interconnected. Thus, two forms of structures are found within this kind, whether bending-dominated or stretch-dominated (i.e., tension or compression-dominated) structures. The first mentioned are typified as lattices with very low-connectivity, where cell edges easily bend against loading, which leads to a very low core modulus

or strength. In contrast to them, stretch-dominated structures present a different structural configuration (as fully triangulated lattices) that leads the struts to be pulled or pushed rather than bended, which results in a structure with a higher modulus or strength compared to bending-dominated structures [23].

Low-weight 3D-lattices structures with high mechanical performance represent a manufacturing challenge, mainly due to the necessary trusses interconnections to obtain stretch-dominated structures and its complexity for accessing the part. Traditionally, metal-based sandwich lattices were commonly achieved by different techniques based on drilling, folding and welding [178–180]. Other methods implied different arrangements of metal wires, based on several fabrication steps as weaving or bending, welding, and later a heat treatment [181,182].

Recent approaches on manufacturing 3D-lattices materials for sandwich panels applications, explored the implementation of additive manufacturing (AM) as a suitable way to use metallic-based or polymeric-based base materials for obtaining lightweight cores. In this context, a commonly used unit cell for lattice structures is implemented as Body-Centered Cubic (BCC), due to its simplicity and similar or better mechanical properties compared to conventional honeycomb cores [183]. Smith [133,184] studied the compressive behavior of BCC and BCC-Z, the latter present also vertical pillars on the vertical direction. By means of Selective Laser Melting (SLM) of 316L stainless-steel, different 3D cores were obtained with relative densities $\bar{\rho}$ ranging from 3.5 to 13.9 % (i.e., 280 – 1112 kgm⁻³, if one employs 8000 kgm⁻³ as stainless-steel density) for the BCC and from 4 to 15.9 % (i.e., 320 – 1275 kgm⁻³ in absolute values) for BCC-Z, presenting elastic moduli ranging from 10.6 to 207.5 MPa and from 84.6 to 2273.2 MPa, respectively. Furthermore, polymeric structures such as 3D-printed BCC made by Fused Deposition Modeling (FDM) have been studied by Tahseen [185]. Several models using Neural Network (NN) algorithm and Finite Element Analyses (FEA) were carried out in a way to predict the compressive elastic properties of the BCC unit cells based on Acrylonitrile Butadiene Styrene (ABS), with different aspect ratios. Liu [186] investigated the mechanical properties of 3D-printed BCC unit cells, based on Polylactic Acid (PLA) while changing the printing angle for different aspect ratios. The peak compressive strength and Young's modulus of the printed lattice which printing path was parallel to the applied load, were 37.6 % – 65.3 % and 11.4% – 39.6% higher compared to the integrated structured, where the filament has an angle of 45° with

respect to the applied load, concluding the importance of taking advantage of the anisotropy of the base material.

Regarding fibre-reinforced composite materials, several studies incorporated carbon fibre reinforced polymers as from machined laminates as base material for manufacturing pyramidal lattice structures (i.e., considering only the half of a BCC unit cell) [22]. Consequently, lattice cores were also studied by Xiong and Vaziri [103,151], who obtained pyramidal truss structures from unidirectional carbon/epoxy prepregs oriented at $[0/90]^\circ$ and processed by hot-press compression moulding, with 45° mould angles. Relative core densities ranging 1.25 – 4.7 % or $19.37 - 72.85 \text{ kgm}^{-3}$ in absolute values (employing $\rho_s = 1550 \text{ kgm}^{-3}$) were obtained for different numbers of prepreg plies through thickness and evaluated in out-of-plane compressive tests. The core compressive moduli were obtained in the range 45.8 – 241 MPa. Concerning plate shear tests, the relative core densities were evaluated in the range of 0.64 – 2.83 % or $9.92 - 43.86 \text{ kgm}^{-3}$ in absolute values (employing $\rho_s = 1550 \text{ kgm}^{-3}$), attaining core shear moduli in the range from 9.53 to 58.93 MPa. Moreover, different failure modes were observed during tests depending on core densities, in which buckling of the struts, fracture of the base material and delamination-debonding governed the strength of the cores. Similar failure mode behavior was noticed either by out-of-plane and plate shear tests. Other significant works have been carried out focusing on CFRP octet-truss structures (i.e., considering the unit cell as two opposite pyramidal lattice structures connected by its bases and not by its tops as in BCC). By using snap-fit nodes, Dong [187] manufactured CFRP octet-truss lattices with relative core densities of 1.7 – 16 % or $24.48 - 230.4 \text{ kgm}^{-3}$ in absolute values (employing $\rho_s = 1440 \text{ kgm}^{-3}$) reaching peak out-of-plane elastic modulus in the range of 75 – 983 MPa. The dominant failure mode was delamination of the struts, although Euler buckling and plastic fiber-micro buckling were also identified, reaching out-of-plane compressive strengths of 0.6 – 9.89 MPa.

Only little research can be found in the field of non-laminate-based lattices, particularly for exploding BCC-like CFRP-based structures, which provides suitable space for further investigations, and this will be the focus of this chapter. The scope for the upcoming sections is set on ultra-lightweight cores based on CFRP rods, employing BCC-like unit cells as lattice structures, and targeting core densities below 48 kgm^{-3} [24]. The investigation comprises:

1. Base material selection and features description.
2. Analytical core cell design.

3. Analytical and numerical approaches for mechanical properties predictions according to out-of-plane compressive and plate shear loading cases, including failure modes studies.
4. Experimental tests and the respective model validation.

5.2 Materials and design

Sandwich panels are provided from the UniBwM labs based on BCC-like lattice structures. The base materials are prefabricated CFRP rods and multi-laminate woven carbon fibre cloth. The core densities are in the range from 8.6 to 49 kgm⁻³.

5.2.1 Materials

The base material employed for manufacturing the lattice cores consists in an array of CFRP rods type T300 fibres/epoxy of density 1.55 gcm⁻³ (corroborated by lab measures), comprising three different diameters: 0.5 mm, 1 mm, and 1.5 mm. Table 4.1 shows the composite rods mechanical properties employed for calculations [188]. Figure 5.1.a is taken as local coordinate references for the rods.

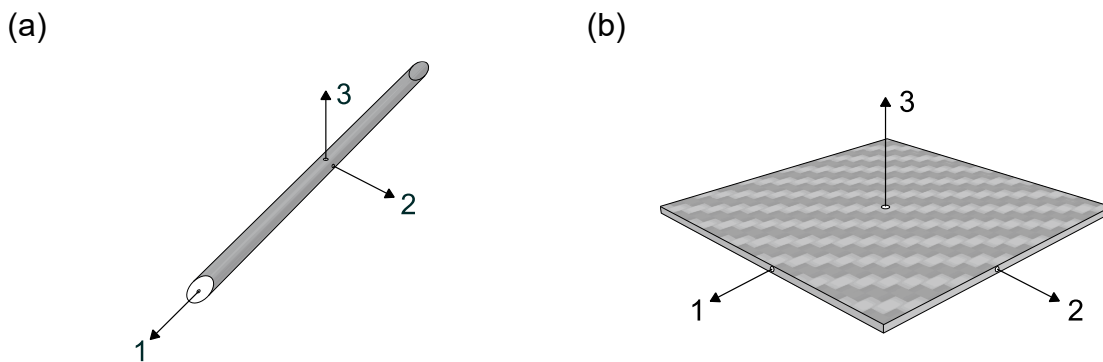


Figure 5.1. Local coordinate systems for (a) rods and (b) skins

Table 5.1. Mechanical properties of the CFRP rods employed for calculations

Rod elastic modulus	Fiber volume fraction	Rod shear modulus*	Rod Poisson's Modulus*	Rod compressive strength	Rod shear strength
E_{1s}	φ_f	G_{12s}	$\nu_{21s} = \nu_{12s}$	$\sigma_{1s}^- = R_{1s}^-$	τ_{12s}
(GPa)	(%)	(GPa)	(--)	(MPa)	(MPa)
115	65	5.8	0.016 – 0.25	450	90

Note: subscript s represents the parent material. (*) Approximated via Eq. [2.15 – 2.17]

The preform of the sandwich skins consists in four layers of woven T300-3k (*Torayca*) carbon fibre 2/2 twill fabrics, combined with epoxy resin and hardener “type L” (*R&G Faserverbundwerkstoffe GmbH*). The resulting CFRP base material for the skins has an average thickness of $t = 0.8 \pm 0.05$ mm (lab measured), and an average fibre volume content of 55%. Although the base material density is predicted of 1.485 gcm^{-3} by theory (see Annex C for further details), it was measured in the laboratory a resulting average density of 1.422 gcm^{-3} , inferring manufacturing deviations such as possible voids due to entrapped gas incorporated during the manufacturing process. The CFRP skins’ mechanical properties are pre-estimated based on the classical laminate theory (see Chapter 2) and shown in Table 4.2 (see Annex B for further details). Figure 5.1.b is taken as local coordinate references for the face sheets.

Table 5.2. Theoretical elastic properties of the woven composite material T300/epoxy.

Composite elastic modulus $E_{2s} = E_{1s}$ (GPa)	Composite shear modulus G_{12s} (GPa)	Composite Poisson’s modulus $\nu_{12s} = \nu_{21s}$ (--)	Fiber volume fraction φ_f (%)	Composite compressive strength $R_{2s}^- = R_{1s}^-$ (MPa)	Composite shear strength R_{12s} (MPa)
67.78	4.06	0.028	55	527.44	110

Note: subscript s represents the parent material

5.2.2 Lattice core design

Lattice properties depend upon three main factors: the raw materials, the grade of connectivity and shape of the truss (e.g., bars, beams, or sheets), and its relative density $\bar{\rho}$. The unit cell defines the minimal periodic unit that describes the main structure and determinates the mechanical and physical properties of the main structure. In BCC lattices structures (Figure 5.2.a), the rods have a connection node at the middle of the unit cell similar to 3D-Kagomé structure [189], but with four trusses. Normally, if the lattice structure is fabricated using a 3D-printer and based in metallic raw material as titanium alloys [190], the connection node is made as a part of the main structure. Whether the lattice architecture is fabricated using metal wires [181] or expanded metal [177], the cross-points between the trusses (or the trusses and the skins depending on the case) is by brazing. Usually, wire-woven bulk structures present slender wire

trusses that are not straight parallel to the line load despite of having a minimum deflection, making the structure even more susceptible to Euler buckling failure mode. On the other hand, CFRP braided stitched lattice cores have a large nodal connectivity and greater debonding strength, although a fibre volume content of about 52% [191]. As seen previously, the fibre volume content defines the material mechanical properties while bearing the load [8]. In this work, BCC-like lattice core materials (Figure 5.2.b) made from CFRP pre-fabricated pultruded trusses with 65% fibre volume content are studied. The connection node is designed in a way that all the trusses meet to each other at the mid-plane of the unit cell, avoiding the common point of the formal BCC structures, while displacing the trusses from the common centre. The BCC-like design also allows a higher densification of the unit cell for smaller cell sizes and 45° orientation angles, a clear difference when compared to pyramid-like cells that present bigger unit cells to set the trusses at the same angles [22].

(a) BCC unit cell

(b) BCC-like unit cell

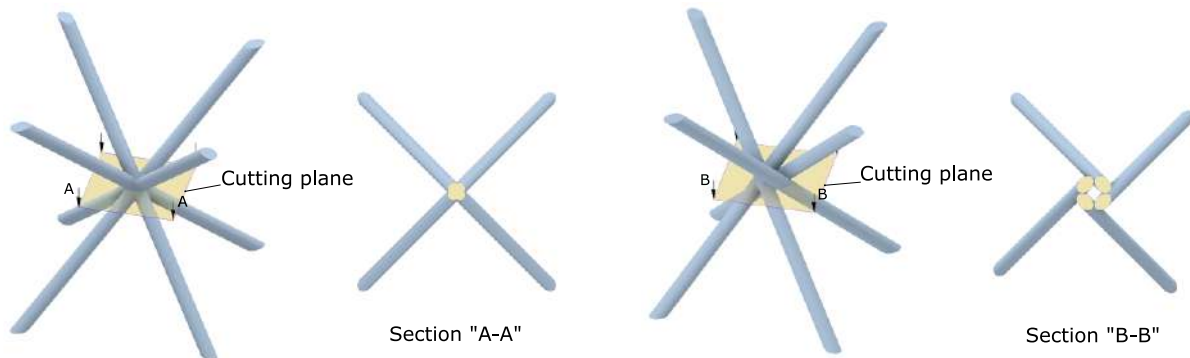
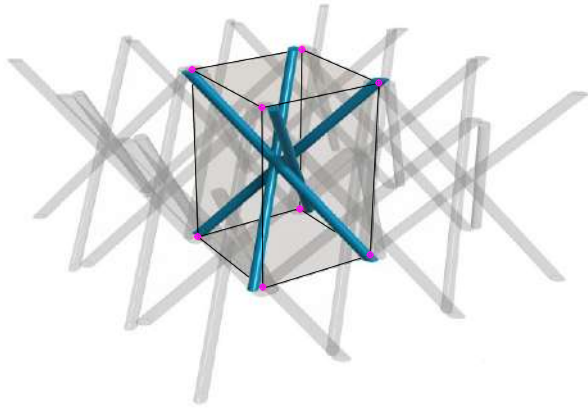


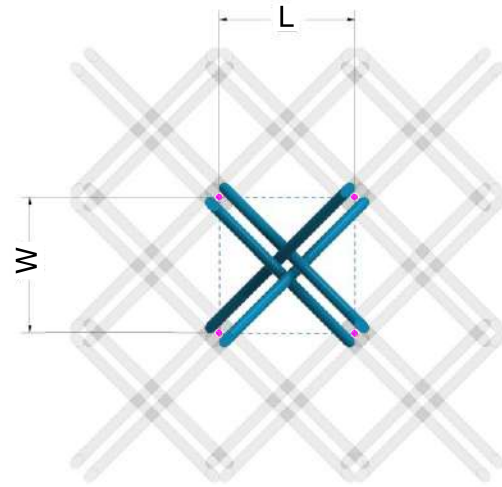
Figure 5.2. Sketches examples of lattice unit cells

In order to have a better visualization of the defined unit cell and the lattice core proposed, Figure 5.3 represents sketches of an array of 3×3 lattice core. The repetitive unit cell is defined as the one that has dimensions repeated periodically throughout the length and width of the core. In this work, it has been considered an equivalent unit cell that coincides with the midpoint of the distance between the center of the rods in projection to the lower and upper planes of the core (Figure 5.3.b and Figure 5.3.c).

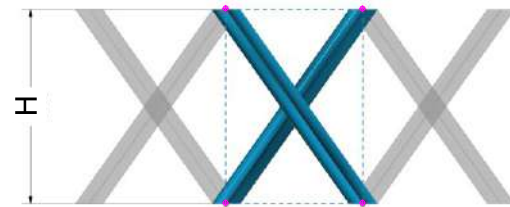
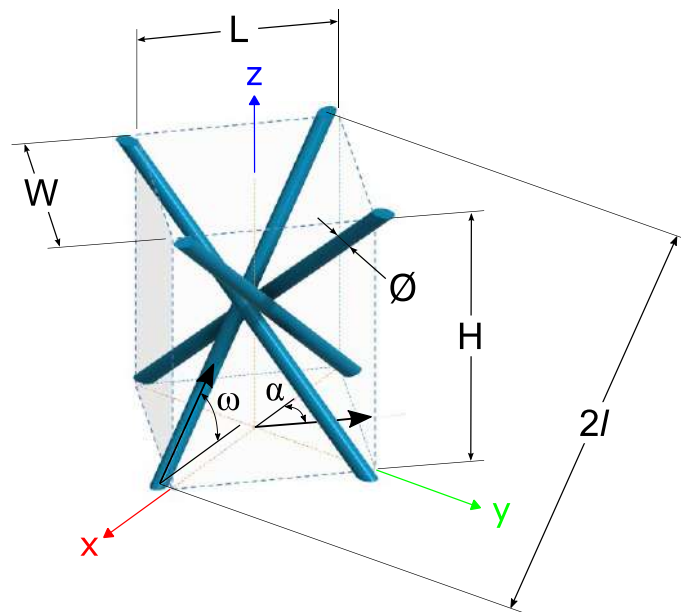
(a) Perspective view



(b) Top view



(c) Front view

**Figure 5.3.** Sketches of proposed lattice core in an array of 3 x 3**Figure 5.4.** Sketch of unit cell parameters

The unit cell design parameterization for truss positioning is defined by variables as: the rod diameters \emptyset (also noted as d), the director angle ω and the cell height H

(Figure 5.4). Furthermore, three different rod diameters as 0.5 mm, 1 mm, and 1.5 mm are used for studying the behavior of different core densities as the unit cell size is maintained constant. The relative density $\bar{\rho}$ of the cores is previously calculated using the average weight of the CFRP rods (with circular cross sections) and the unit cell volume. The expected core relative density $\bar{\rho}$ is below 0.03 kgm^{-3} or $\rho_c = 48 \text{ kgm}^{-3}$. According to lab-measurements (Table 5.3), the real core density presents little discrepancies from the analytical prediction, attributed to the added weight incorporated by the glued connections between the rods, and rods to skins (see Annex C). The cores with 0.5 mm rods show a larger glue residual as a result of the finishing process.

Table 5.3 summarizes the unit cell's main dimensions and core densities attained. The orientation angles α and ω are proposed in this work to be 45° . The cell height H is fixed to 25.4 mm, while the width W and the length L are proposed to be equal and dependent on the core height H as $L = W = \frac{\sqrt{2}}{2}H$, resulting in a unit cell size of 17.96 mm.

Table 5.3. Unit cells mean dimensions and core densities employed for analyses

\emptyset	L	W	H	α	ω	ρ_c^*	ρ_c^{**}
(mm)	(mm)	(mm)	(mm)	($^\circ$)	($^\circ$)	(kgm^{-3})	(kgm^{-3})
0.5	17.96	17.96	25.40	45	45	5.34	8.66
1	17.96	17.96	25.40	45	45	21.34	22.92
1.5	17.96	17.96	25.40	45	45	48.03	49.76

Notes: (*) Theoretical value. (**) Lab-measured

The lattice-based CFRP sandwich panels exhibited the designed architecture. Arrays of 3 x 3 cells are shaped into square samples for the compressive tests with a size of 65 mm by 65 mm and 25.4 mm in height (Figure 5.5).

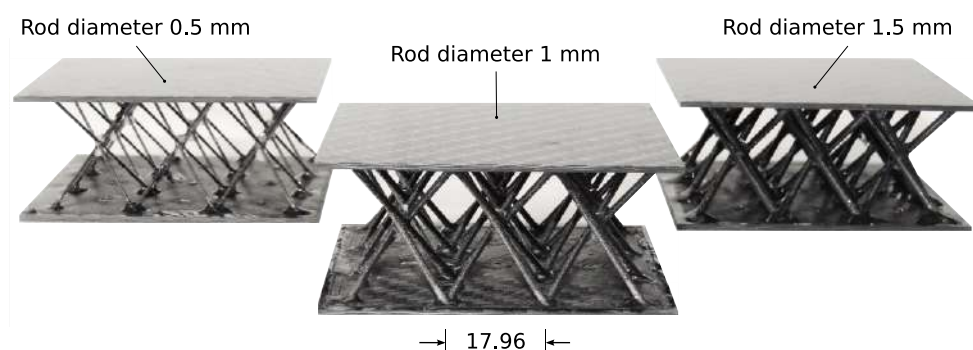


Figure 5.5. Compressive samples with different rod diameters

Moreover, rectangular samples having arrays of 10 x 3 cells are employed for the shear tests with a size of 180 mm by 65 mm and 25.4mm in height (Figure 5.6).

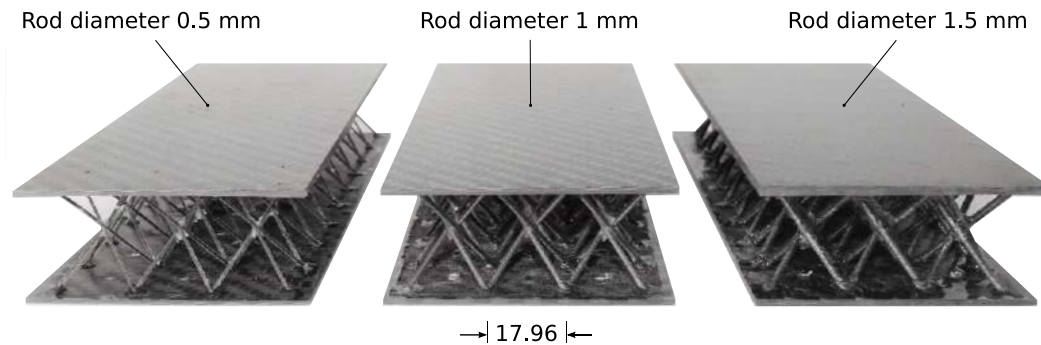


Figure 5.6. Shear samples with different rod diameters

5.2.3 Core relative density estimation

The main parameters that influence the geometry of the unit cell include: the director angles α and ω , and the strut length l as sketched in Figure 5.4. The strut length could be also indirectly obtained by the cell height (i.e., core thickness). The general expression for the cross-sectional area of the unit cell A_{cell} is given by multiplying both sizes L and W of the cell as Eq. (5.1). The height H of the unit cell is defined as Eq. (5.2) while the cell volume V_{cell} is obtained as Eq.(5.3) .

$$A_{cell} = LW = (2l \cos \omega)^2 \cos \alpha \sin \alpha \quad (5.1)$$

$$H = 2l \sin \omega \quad (5.2)$$

$$V_{cell} = 4l^3 \cos^2 \omega \sin \omega \sin 2\alpha \quad (5.3)$$

Furthermore, considering that the CFRP rods have a circular cross-section of an average diameter d , it is possible to obtain the average volume of the rods V_{rod} while multiplying its cross-area and the length $2l$ within a cell. Then, the relative density of the cell $\bar{\rho}_c$ and thus, the core, is obtained as Eq. (5.4).

$$\bar{\rho}_c = \frac{4V_{rod}}{V_{cell}} = \frac{\pi d^2}{2l^2 \cos^2 \omega \sin \omega \sin 2\alpha} = \frac{2\pi d^2 \sin \omega}{H^2 \cos^2 \omega \sin 2\alpha} \quad (5.4)$$

The variation of the relative density (Eq. (5.4)) as a function of the diameter of the rods is shown graphically in Figure 5.7, in which a quadratic polynomial curve is represented. By multiplying the relative density of the core $\bar{\rho}_c$ by the density of the rods $\rho_s = 1550 \text{ kgm}^{-3}$ (i.e., the base material from which they are made), the core density is

attained as $\rho_c = \bar{\rho}_c \cdot \rho_s$. Then, the theoretical core densities are obtained and exhibited in Table 5.3 as well.

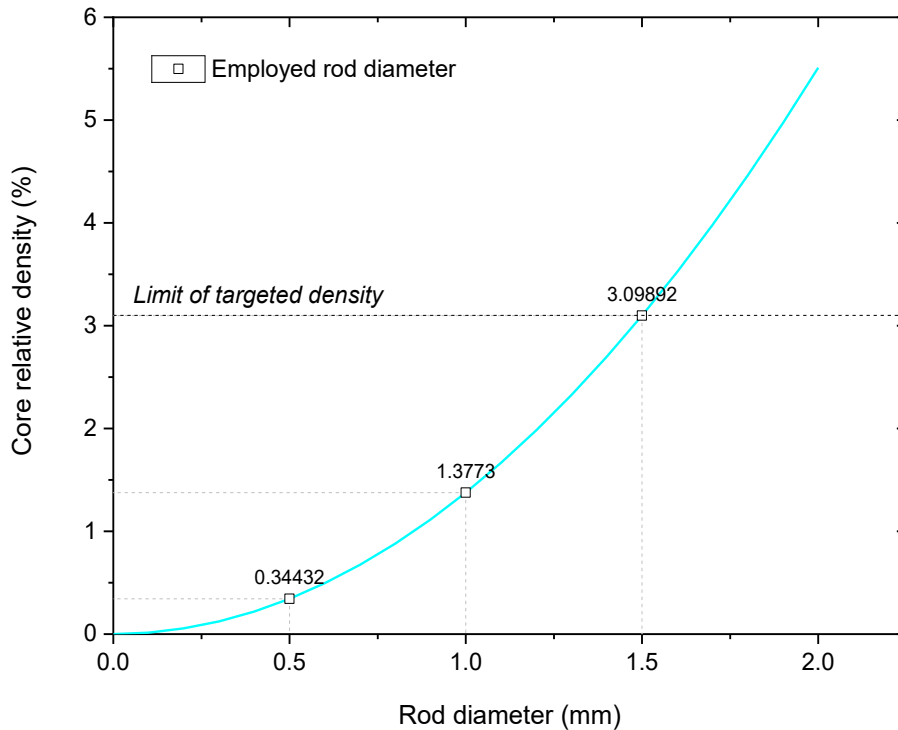


Figure 5.7. Core relative density variation as a function of the rod's diameter

5.3 Core out-of-plane compression

The analytical and FE models for the core mechanical response as the core compressive elastic modulus and strength are presented in this section. The single unit cell model from Figure 5.8 is taken as basis for the analyses. A generic compressive load is applied according to the z-direction, in order to study the displacements experienced by the rods, modelled as built-in trusses at both ends. Analytical models are based on the load's decomposition into its perpendicular components upon a single rod, following a local coordinate system (Figure 5.8.c). the displacements are evaluated at the middle of the unit cell, taking advantage of its symmetry. Moreover, linear and non-linear simulations using FEMAP™ 10.3 with NX™ Nastran® [29] are carried out in order to further complement the analytical studies for predicting core behaviour under the applied stresses using Figure 5.8 as the coordinate reference and modelling the base material employing Table 4.1 properties. The CFRP rods are simulated by discretization using 1D-bar elements (CBAR) and 48 elements per rod.

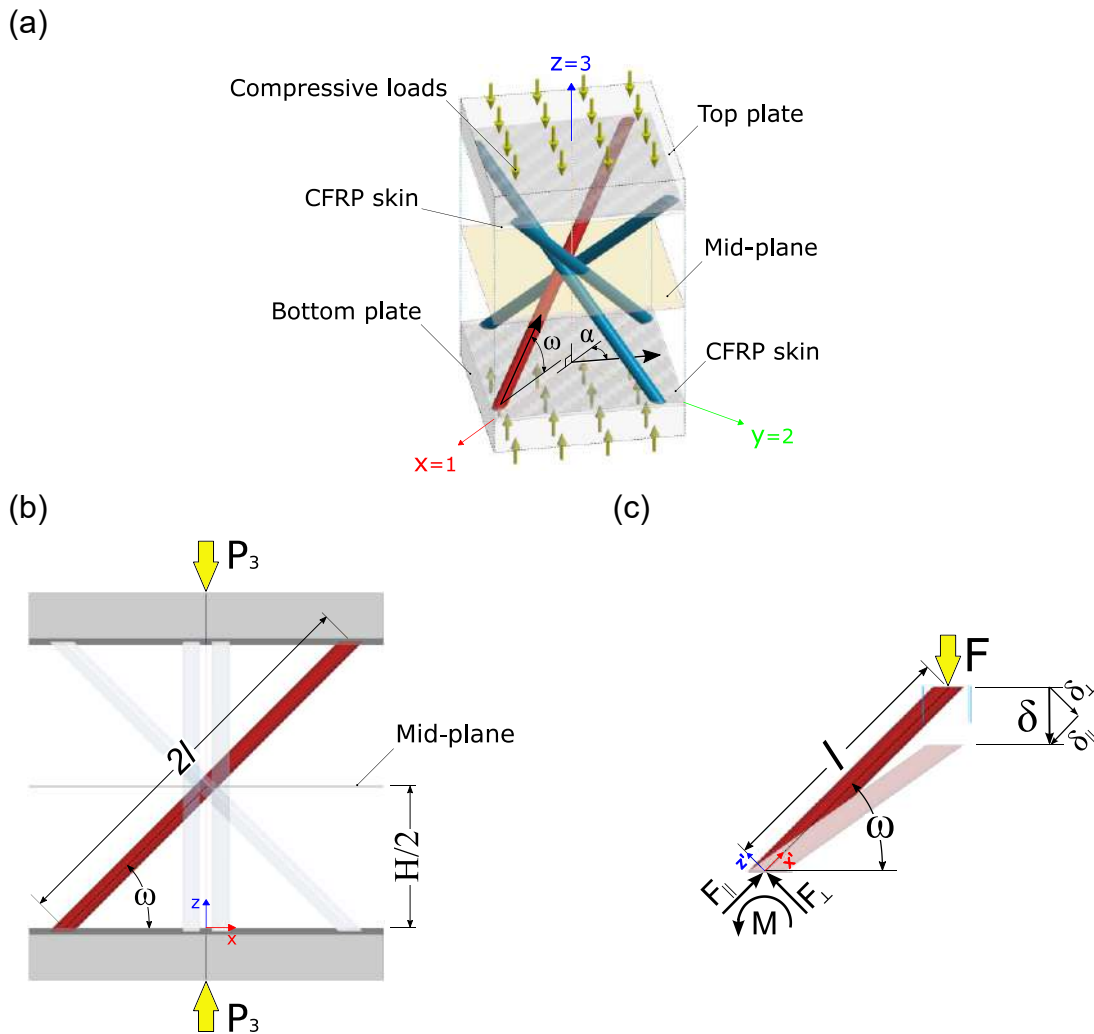


Figure 5.8. (a) A schematic BCC-like lattice render with a compression loading case. (b) Sketch of the load case. (c) Free body diagram of a CFRP half truss.

5.3.1 Compressive stiffness

The analyses for obtaining the compressive elastic modulus E_c of the CFRP lattice core contemplates the elastic straining of a single truss within the half of the studied unit cell (Figure 5.8.c). Such deformations are obtained by simple beam theory while considering the displacement δ experimented by a pultruded CFRP truss due to $\frac{1}{4}$ of the total applied compressive load P , as $P = 4F$.

5.3.1.1 Analytical approach

Considering small displacements, when a beam is loaded by a concentrated load, the deflection δ_j at the loading point can be determined by calculating the partial derivative of the strain energy of the beam U with respect to the acting forces F_j as

Castigliano's second theorem as Eq. (5.5) [67].

$$\delta_j = \frac{\partial U}{\partial F_j} \quad (5.5)$$

In this way, based on the symmetry of the cell (Figure 5.8.b and Figure 5.8.c) the model is sketched as a cantilever beam with a punctual load F at the core mid-plane. The displacement δ due to the load F is then defined by its perpendicular displacement components in parallel (δ_{\parallel}) and perpendicular (δ_{\perp}) directions according to the rod orientation as Eq. (5.6) and Eq. (5.7).

$$\delta_{\parallel} = \delta \sin \omega \quad (5.6)$$

$$\delta_{\perp} = \delta \cos \omega \quad (5.7)$$

Considering the displacement on each perpendicular directions, the internal strain energy of the beam in parallel direction U_{\parallel} is caused by the parallel component of the force F , equal in modulus to the reaction F_{\parallel} , and depends on the cross-sectional area of the rod as $A_{rod} = \frac{\pi d^2}{4}$.

$$U_{\parallel} = \int_0^l \frac{N^2 dx'}{2E_{rod1s}A_{rod}} \quad (5.8)$$

Eq. (5.8) shows the internal strain energy due to the parallel load component. Factor N represents the general expression of the applied axial forces while E_{rod1s} is the Young's modulus of the base material of the rod in parallel direction. Then solving Eq. (5.8) deriving with respect to F , the displacement in parallel direction is shown as Eq. (5.9). In this case, N is equal to F_{\parallel} .

$$\delta_{\parallel} = \frac{\partial U_{\parallel}}{\partial F_j} = \sum_{j=1}^m \left(\int_0^l \frac{N_j}{E_{rod1s}A_{rod}} \frac{\partial N_j}{\partial F_i} dx' \right) = \frac{F_{\parallel} l}{E_{rod1s}A_{rod}} \quad (5.9)$$

Furthermore, the internal strain energy of the rod in perpendicular direction U_{\perp} is dependent on the perpendicular component of the force F as F_{\perp} , and the flexural rigidity $E_{rod1s}I_{x'}$ of the truss (Eq. (5.10)). Factor M represents the general expression of the acting bending moment. The transverse shear effect upon the shear strain energy is neglected in this formulation due to the slenderness of the truss ($L \gg d$) [169] and the truss is assumed as an Euler-Bernoulli beam.

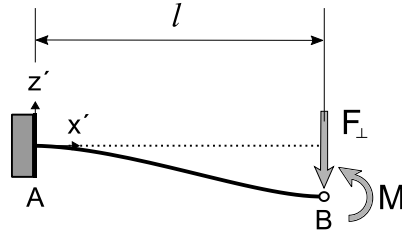


Figure 5.9. Scheme of a cantilever beam with a guided end (lateral displacement with no rotation)

The case is schematically represented in Figure 5.9 as a cantilever beam with a guided end, at which the angle of the cross-section does not change (rotation restricted). This effect is represented by a concentrated moment $M_{(x')}$ at the end of the beam acting in an opposite way to the displacement due to F_{\perp} .

$$U_{\perp} = \int_0^l \frac{M^2 dx'}{2E_{rod1s}I_{x'}} \quad (5.10)$$

Deriving Eq. (5.10) with respect to F the component of the displacement in perpendicular direction is presented as Eq. (5.11). Component $I_{x'}$ represents the cross-sectional second moment of area, where $I_{x'} = \frac{\pi d^4}{64}$.

$$\delta_{\perp} = \frac{\partial U_{\perp}}{\partial F_j} = \sum_{j=1}^m \left(\int_0^l \frac{M_j}{E_{rod1s}I_{x'}} \frac{\partial M_j}{\partial F_i} dx' \right) = \frac{F_{\perp} l^3}{3E_{rod1s}I_{x'}} - \frac{M_{(x')} l^2}{2E_{rod1s}I_{x'}} \quad (5.11)$$

Since the angle at point B does not change at the end of the beam where $M_{(x')}$ and F_{\perp} act, the sum of the rotations must be zero. Therefore, the angles at point B are calculated via Eq. (5.12) applying Castigliano's second theorem for rotations at the location of the concentrated force and moment.

$$\theta = \frac{\partial U_{\perp}}{\partial M_j} = \sum_{j=1}^m \left(\int_0^l \frac{M_j}{E_{rod1s}I_{x'}} \frac{\partial M_j}{\partial M_i} dx' \right) = \frac{F_{\perp} l^2}{2E_{rod1s}I_{x'}} - \frac{M_{(x')} l}{E_{rod1s}I_{x'}} = 0 \quad (5.12)$$

From Eq. (5.12) and solving for the moment $M_{(x')}$, Eq. (5.13) defined the relations between the force and the opposite moment.

$$M_{(x')} = \frac{F_{\perp} l}{2} \quad (5.13)$$

Replacing Eq. (5.13) in Eq. (5.11), the total displacement at point B is then defined by Eq. (5.14).

$$\delta_{\perp} = \frac{F_{\perp} l^3}{3E_{rod1s} I_{x'}} - \frac{F_{\perp} l^3}{4E_{rod1s} I_{x'}} = \frac{F_{\perp} l^3}{12E_{rod1s} I_{x'}} \quad (5.14)$$

The core effective out-of-plane compressive modulus E_c is defined by the unit cell modulus as Eq. (5.15), as the ratio of the compressive stress σ_c to the compressive strain ε_c of the unit cell.

$$E_c = \frac{\sigma_c}{\varepsilon_c} \quad (5.15)$$

According with Figure 5.8.b coordinate system, ε_c is then defined by Eq. (5.16).

$$\varepsilon_c = \frac{(\delta_{\parallel}^2 + \delta_{\perp}^2)^{\frac{1}{2}}}{l \sin \omega} = \frac{\delta}{l \sin \omega} \quad (5.16)$$

Moreover, since each unit cell has four trusses, the total compressive stress over a unit cell is given as Eq. (5.17), specifying force P by its components according to z-direction (Figure 5.8).

$$\begin{aligned} \sigma_c &= \frac{P}{A_{cell}} \equiv \frac{2(|F_{\parallel}| \sin \omega + |F_{\perp}| \cos \omega)}{(l \cos \omega)^2 \sin 2\alpha} = \\ &= E_{rod1s} \frac{\pi d^2 \delta}{2l^3 \cos^2 \omega \sin 2\alpha} \left[\sin^2 \omega + \frac{3}{4} \left(\frac{d}{l} \right)^2 \cos^2 \omega \right] \end{aligned} \quad (5.17)$$

Substituting Eq. (5.16) and Eq.(5.17) into Eq. (5.15) and solving for E_c , the core modulus is given by Eq. (5.18).

$$E_c = E_{rod1s} \frac{\pi d^2 \sin \omega}{2l^2 \cos^2 \omega \sin 2\alpha} \left[\sin^2 \omega + \underbrace{\frac{3}{4} \left(\frac{d}{l} \right)^2 \cos^2 \omega}_{\text{transversal term}} \right] \quad (5.18)$$

The component called as ‘‘transversal term’’ in Eq. (5.18), it only contributes from 0.02906 to 0.26 % to the expression in parentheses for the cases analyzed in this work, so it will be neglected to ease calculations, and thus, Eq. (5.19) is assumed to hold as the core compressive modulus. The contribution of the transverse force, will be then addressed indirectly via FE-simulations as the bending moment attained (section 4.3.2.2)

$$E_c \approx E_{rod1s} \frac{\pi d^2 \sin^3 \omega}{2l^2 \cos^2 \omega \sin 2\alpha} \quad (5.19)$$

The variation of the compressive modulus dependent on the diameter is shown in Figure 5.10. The curve denotes a function of fourth grade in which the larger the diameter, the greater the elastic modulus of the core. It should be borne in mind that the elastic moduli values are obtained for a core geometrical configuration, in which most of the unit cell is empty, and only a small part of the cell volume bears the load (i.e., the rods).

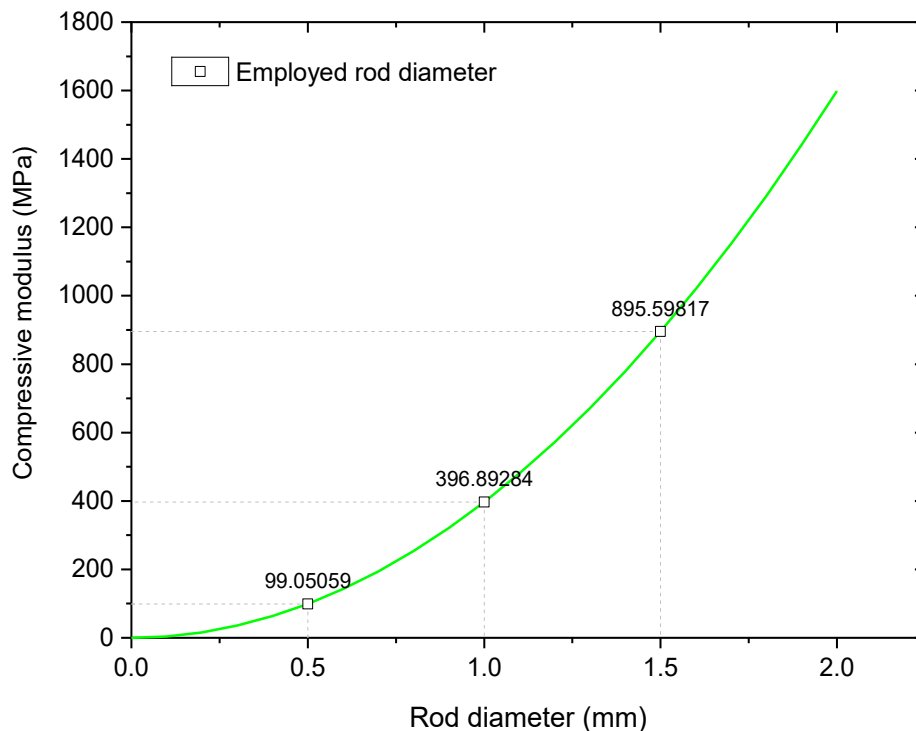


Figure 5.10. Curve of core compressive modulus predicted by the analytical model

5.3.1.2 Numerical approach

Different linear static FE-simulations are carried out to have better insights on the structure behavior: firstly, the unit cell lattice structure is simulated as a BCC-like structure (simulating the effect of mid-plane connecting points as an array of bars as in Figure 5.11.a and Figure 5.12), and then, the unit cell is plot as an equivalent BCC structure, in which the rods have a common node in the mid-plane as in Figure 5.11.b). The latter simulation is addressed via two different boundary conditions set at the mid-plane as a pinned node or as a node with rotational constrains, albeit it is free to displace only over z-direction. In both cases, the ends of the rods are fully constrained. The structures sketched in Figure 5.11 with rod diameter $d = 0.5$ mm are taken as example for analyses. The results of the strains obtained from the simulations for a

total generic load of 1 kN in the vertical z-direction at the top-end nodes were 3.1306% for the case of Figure 5.11.a and 3.1312% for the case of Figure 5.11.b, representing a difference of 0.019%, which is acceptable for further numerical studies either as BCC or BCC-like unit cell models. No substantial differences are observed in the displacements of the Figure 5.11.b case in terms of rotational constraints at the central node. Additionally, simple load FE linear analyses over the mid-plane node (Figure 5.12) are carried out for evaluating the loads within the node's region to complement the study, and are provided in Annex D.

a) Unit cell as BCC-like lattice structure (b) Unit cell as BCC lattice structure

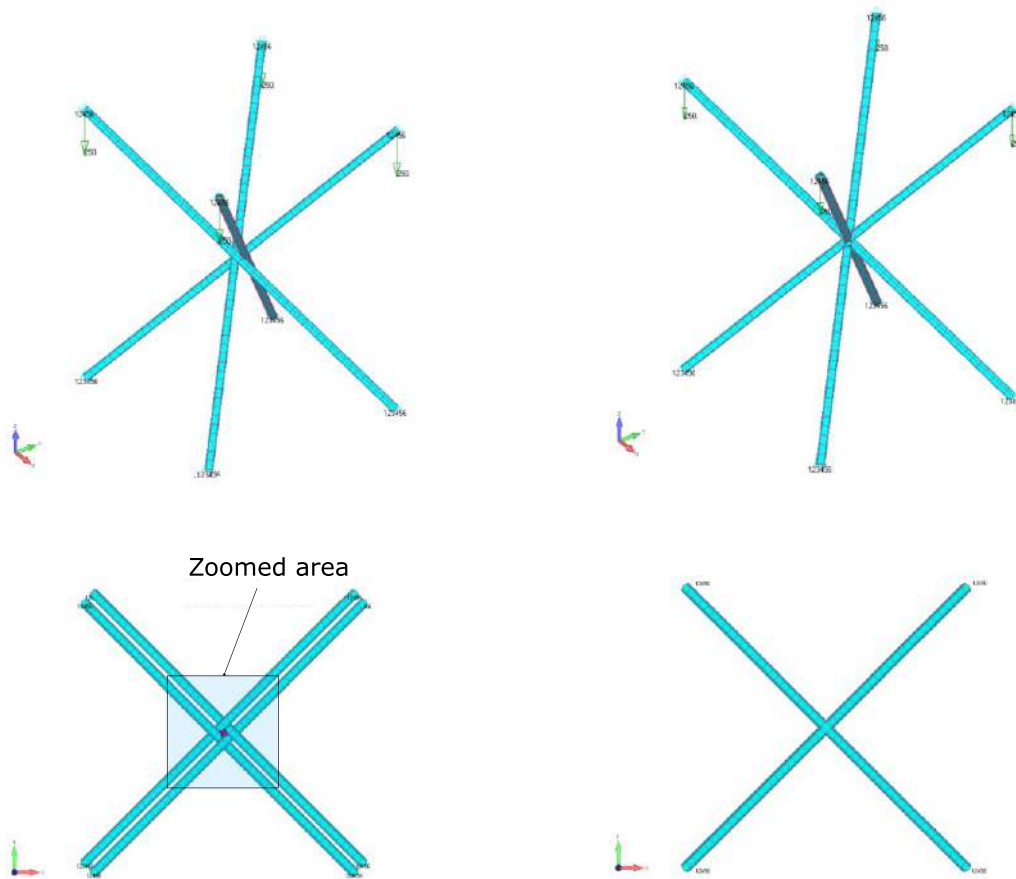


Figure 5.11. Bar-array FE renders of the unit cells employed for simulations comparisons

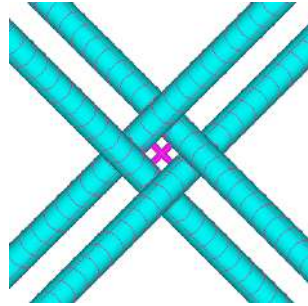


Figure 5.12. Zoomed central node as an array of bars

In order to validate the analytical compressive modelling, linear static finite element (FE) simulations are implemented for indirectly predicting the elastic compressive modulus of the core E_c , considering the three different rod diameters proposed, while analyzing the unit cell response to load cases.

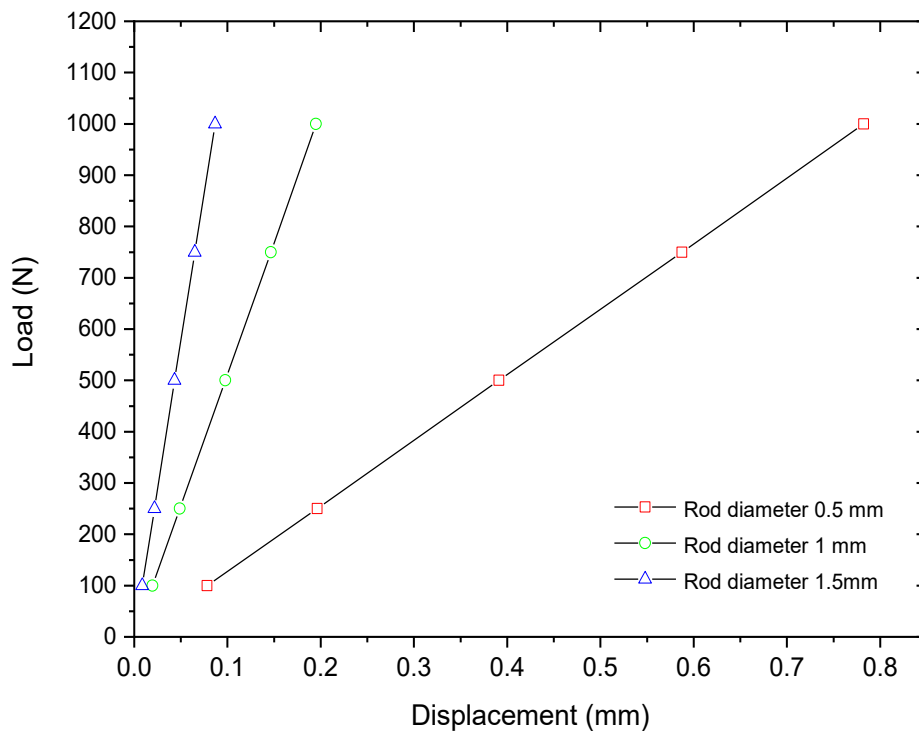


Figure 5.13. Compressive load vs. displacement obtained from linear simulations

The compressive modulus E_c of the BCC-like cores are obtained indirectly from the load vs. displacement curves (Figure 5.13), based on the slope $s = \frac{P}{\delta}$ and calculated applying Eq. (5.20), regarding to the core thickness H and the vertical displacement δ .

$$E_c = \frac{H}{\delta} \sigma_c = \frac{H}{\delta} \frac{P}{A_{cell}} = \frac{sH}{A_{cell}} \quad (5.20)$$

Therefore, by obtaining the displacements of the top-nodes, the behaviour of the unit cell is studied. Table 4.5 shows a summary of the linear static results for the different rods size proposed and a briefly comparison with the theoretical results, applying a total generic load of 1 kN in the vertical z-direction. The predicted strain results to be larger for the smaller diameters and thus, the core moduli vary directly proportional to the rod size. Then, the core compressive moduli are predicted as 100.65 MPa, 403.95 MPa and 909.2 MPa, for the 0.5 mm, 1mm and 1.5 mm rod's diameter, respectively. The values are in good correspondence with the theoretical approaches.

Table 5.4. Core compressive elastic moduli predicted by FE

\emptyset (mm)	L (mm)	H (mm)	δ (mm)	s (N/mm)	ϵ_c ($\mu\text{m/m}$)	E_c (MPa)	E_c^* (MPa)
0.5	17.96	25.4	0.7822	1274.064	3079.82	100.65	99.05
1	17.96	25.4	0.1949	5123.580	767.38	403.95	396.89
1.5	17.96	25.4	0.0866	11547.370	340.94	909.19	895.59

Note: (*) Theoretical value

5.3.2 Compressive strength

In this section, the analytical and FE studies of BCC-like lattice cores under compressive loads are employed for obtaining the main core failure loads and mechanisms. The failure modes are considered when unit cell members collapse. Several failure mechanisms are investigated including ⁽³⁾:

5. Elastic buckling of a truss σ_{cB}
6. Compressive fracture of a truss σ_{cR} (when σ_{1s}^- exceeds R_{1s}^-).

The governing failure mode is then associated to the one in which the core peak compressive strength σ_{cpk} is the lowest and is given by Eq. (4.13).

$$\sigma_{cpk} = \min(\sigma_{cB}, \sigma_{cR}) \quad (5.21)$$

⁽³⁾ Another failure mode as truss push-out, or the entry of the rod through the skins, is proposed as a potential failure mode under other study conditions in Annex D

The influence of the director angle ω (Figure 5.8) on the compressive strength is addressed by exemplifying its effect over the Euler buckling load in compression. The description is presented in Annex D, by analyzing a particular case of a constant cell area.

5.3.2.1 Analytical approach

The analytical approaches are modelled following the line-up of Figure 5.8. Considering the failure of a core member as the rods, the failure modes addressed are the ones proposed the beginning of this section and described as follows. The transversal load is neglected to ease the analyses as its contribution is almost negligible as detailed in section 5.3.1.1.

5.3.2.1.1 Elastic buckling of a truss

Slender CFRP rods under compressive loads might undergo Euler buckling. Assuming that the trusses are thought as beams with two ends built-in between the core and face sheets. Only the half of the unit cell is employed to ease the analyses (Figure 5.8.c), in order to study the buckling behavior of the rods with length l .

Therefore, Euler's critical load is given as Eq. (5.22) [67] (see section 2.2.3.2). Factor k presents different values according to the established boundary conditions. It shall be noted that $k = 1$ represents a truss with one end clamped and the other free, while $k = 0.5$ if the truss present two ends fixed. Then, the k values can be found between these two values ($0.5 \leq k \leq 1$) since the connections in the real case between rods and rod-skins are elastic links. In this work, as starting point for studies is assumed that the trusses are pinned but guided at the mid-plane considering the connecting node effect. This leads to a k value of $0.699 \approx 0.7$. This value will be later confirmed by numerical simulations.

$$F_{rodEu} = \frac{\pi^2 E_{rod1s} I_{x'}}{(kl)^2} \geq F_{\parallel} \quad (5.22)$$

The compressive load applied to the unit cell is decomposed to its rod members by means of the director angles ω and α (Figure 5.8). When the critical buckling load is attained, the parallel load F_{\parallel} is equal in modulus to F_{rodEu} . Thus, replacing Eq. (5.22) into Eq. (5.17) and considering four trusses within a unit cell, the nominal compressive strength of the core due to Euler buckling failure of the trusses is given by Eq. (5.23).

$$\sigma_{cB} \approx \frac{E_{rod1s} \pi^3 d^4}{32k^2 l^4 \cos^2 \omega \sin 2\alpha} \sin \omega \quad (5.23)$$

The influence of the director angle ω on the buckling load is shown in Annex D, by analyzing a particular case of a constant cell area.

5.3.2.1.2 Compressive fracture of a truss

The nominal out-of-plane compressive strength of the BCC-like CFRP core (σ_{cR}) depends upon the failure compressive strength value of the employed rod members (R_{1s}^-). The load is decomposed to the rods as a local axial stress to rods as σ_{1s}^- . Then, the fracture of the rod is attained when $\sigma_{1s}^- \geq R_{1s}^-$, and as a result, the collapse of the core. The failure load of the CFRP rods is set by Eq. (5.24).

$$F_{rodR} = R_{1s}^- A_{rod} \geq F_{\parallel} \quad (5.24)$$

Recalling previous outcome and considering also co-linear compressive loads to the trusses according to director angles (Figure 5.8), the parallel load F_{\parallel} is equal in modulus to F_{rodR} when the collapse strength of the base material is reached. Consequently, combining Eq. (5.24) and Eq. (5.17), the core compressive strength considering unit cell member fracture, is obtained by Eq. (5.25) .

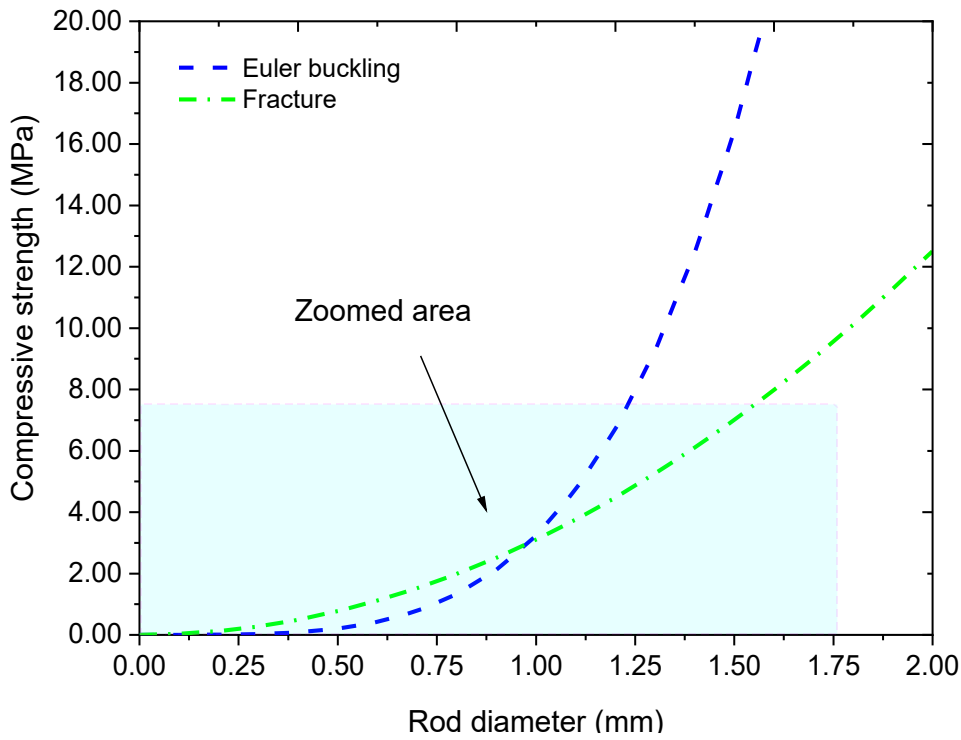
$$\sigma_{cR} \approx \frac{R_{1s}^- \pi d^2}{2 l^2 \cos^2 \omega \sin 2\alpha} \sin \omega \quad (5.25)$$

5.3.2.1.3 Analytical results

The analytical predictions of the failure modes are plotted in Figure 5.14, identifying: Euler buckling failure mode (σ_{cB}), as the blue-dashed curve (calculated using Eq. (5.23)) and rod fracture (σ_{cR}), as the green-dotted-dashed curve (Eq. (5.25)). The dominant modes are plotted as the grey region, as the area below the failure.

The strengths predictions for the analyzed cases are exhibited in Table 4.6. The failure modes are predicted as the minimum stress for each core case. The modes with a higher probability to occur are Euler buckling failure for the cores made from 0.5 mm rods, and core Euler buckling regarding to the 1 mm rods (although they are found also close to the fracture region), and fracture regarding to the 1.5 mm.

(a) Curve plotting for predicted failure modes



(b) Zoomed area for identifying failure regions

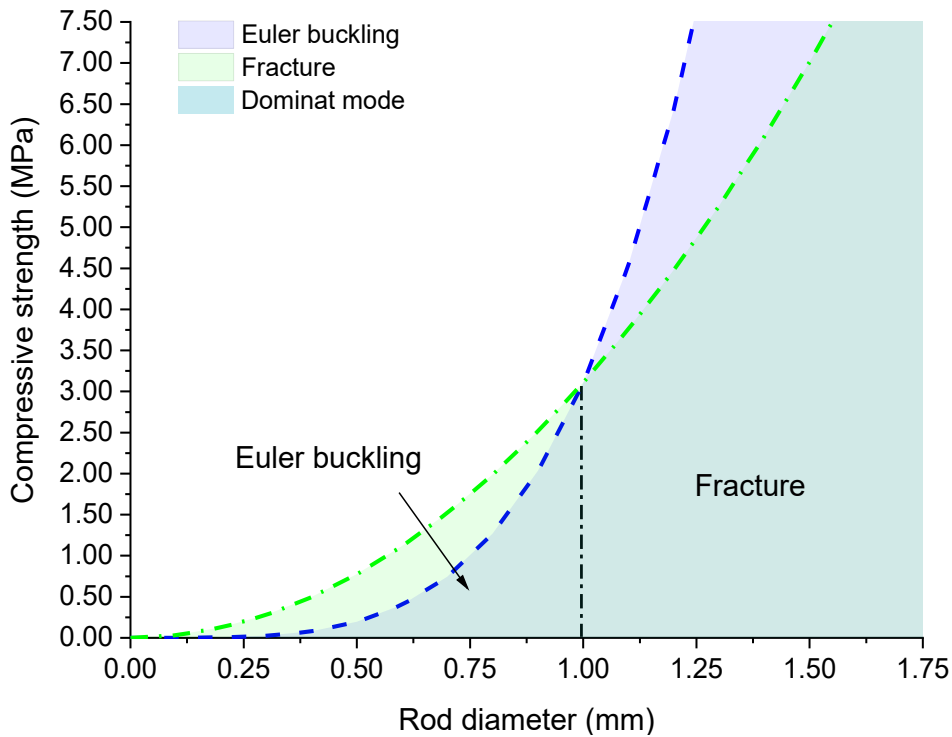


Figure 5.14. Failure maps according to analytical predictions for compressive loads

Table 5.5. Core compressive strengths according to analytical approaches

\emptyset (mm)	L (mm)	f (mm)	t_1 (mm)	α (°)	ω (°)	R_{1s}^- (MPa)	E_{rod1s} (MPa)	σ_{cB}^* (MPa)	σ_{cR} (MPa)
0.5	17.96	2	0.4	45	45	450	115	0.193	0.775
1	17.96	2	0.4	45	45	450	115	3.098	3.106
1.5	17.96	2	0.4	45	45	450	115	15.72	7.009

Note: (*) the values are obtained for a buckling k factor of 0.7

As previously presented, a seed value $k = 0.7$ is employed for the base theoretical buckling calculations in Eq. (5.23). Nevertheless, different attainable strengths while varying k coefficient (section 5.3.2.1.1) are presented in Table 5.6 as an example of the attainable strength values for the core cases analysed, The k coefficients will also be attained via numerical analyses and experimental tests.

Table 5.6. Core compressive strength due to Euler buckling for different k coefficients

\emptyset (mm)	$k = 0.5$	$k = 0.6$	$k = 0.7$	$k = 0.8$	$k = 0.9$	$k = 1$
	σ_{cB} (MPa)	σ_{cB} (MPa)	σ_{cB} (MPa)	σ_{cB} (MPa)	σ_{cB} (MPa)	σ_{cB} (MPa)
0.5	0.379	0.263	0.193	0.148	0.117	0.095
1	6.072	4.216	3.098	2.372	1.874	1.518
1.5	30.827	21.407	15.728	12.042	9.514	7.707

5.3.2.2 Numerical approach

The FE simulations give support to the analytical models by evaluating the failure independently according to two different simulations. This section presents two different FE predictions:

1. The linear static simulations, in which the core elastic modulus is indirectly predicted (as in section 4.3.1.2), and the local stresses of the rods, when buckling is not considered. Static FE simulations evaluated each lattice-based core design proposed. However, the case of 0.5 mm is presented as a study example for the procedure, although the results are then given for each rod case. Therefore, a generic load of 1 kN is applied according to z-direction, taking Figure 5.8 as coordinate reference.

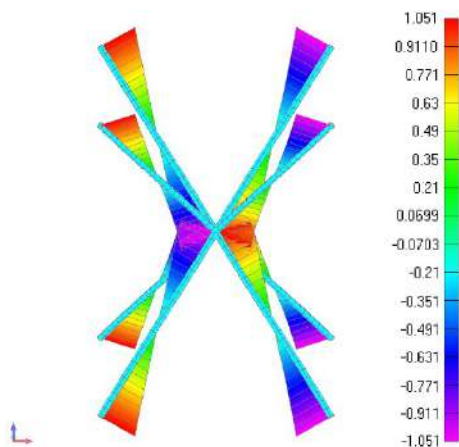
Figure 5.15 presents renderings of the bending moments and combined stresses distribution. The force is then mostly transferred as axial compressive loads to the rods, throughout the director angles ω and α . The load axial has a value of

353.35 N per rod and represents more than 99% of the stress components. The theoretical value is on average $\sigma_s = \frac{1}{4} \frac{1000}{\sin 45} / \pi \frac{0.5^2}{4} = 1800.63$ MPa for the proposed case, having good correspondence with the simulations.

The bending moment, although almost negligible, results on a linear distribution with a maximum at both rod's ends and at the mid-plane due the applied constraints. Recalling section 5.3.1.1. of the analytical approach, the neglect of the transverse term in the calculations is supported as well considering the small value of the bending moments attained, and the predominance of the axial load observed on the simulations.

The missing core cases for 1 mm and 1.5 mm presented similar results as the slender case of 0.5 mm (they present the same axial loads along the rods), only having on average axial stresses of 449.89 MPa and 199.95 MPa, respectively for a total simulated load of 1 kN.

(a) Bending moments



(b) Combined stresses

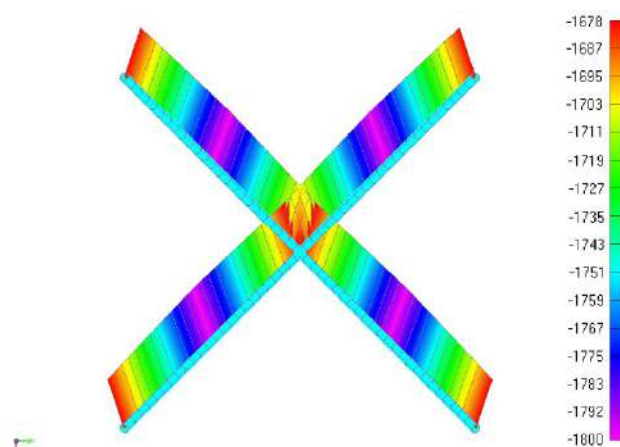
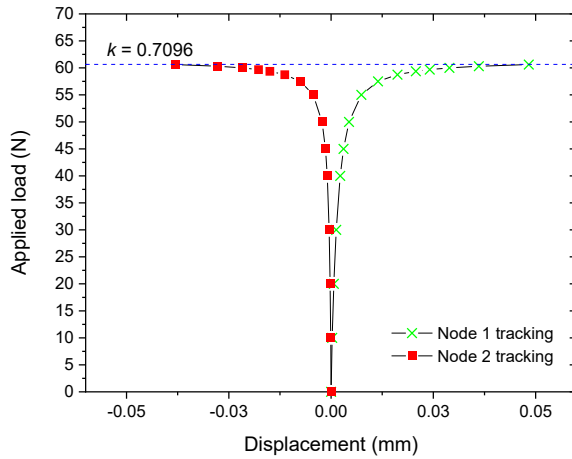


Figure 5.15. Renders of the bending moment and combined stress distribution due to compressive loads for the 0.5 mm rod diameter lattice unit cell

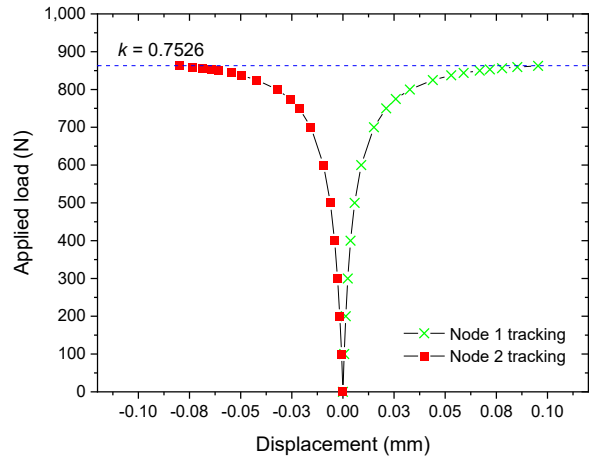
2. The non-linear simulations show insights upon the critical load attainable for each core case are addressed. They present the buckling behaviour of rods during compressive loading. The instability load is established by employing a modified Newton-Raphson method as solver. The simulation is carried out applying vertical loads over the top nodes, at the same time acquiring the displacements performed by the rest of the nodes, until the model becomes unstable, and the simulation stops. Thus, tracking points on selected nodes are extracted and their trajectory curves are given

in Figure 5.16, starting from zero displacement up to instability, while reaching the critical load. The maximum displacement of the nodes denotes an asymptote to which is possible to identify the critical applied load and indirectly obtain the critical Euler's factor k given by Eq. (5.22). The critical loads P_{crit}^* are found of 60.6 N, 862.5 N and 3865.6 N for diameters 0.5 mm, 1 mm, and 1.5 mm, respectively.

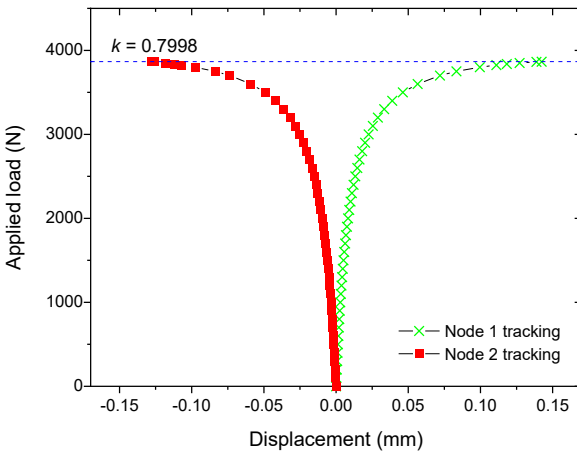
(a) Rod diameter 0.5 mm



(b) Rod diameter 1 mm



(c) Rod diameter 1.5 mm



Reference on node tracking

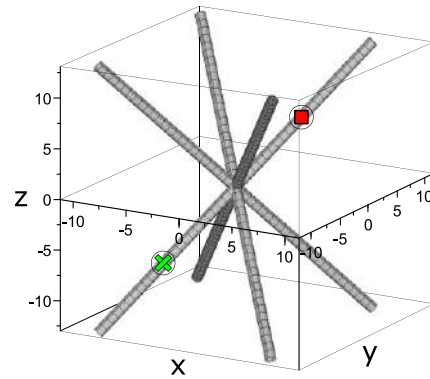


Figure 5.16. Load vs. node displacement curves obtained from the non-linear simulations

Furthermore, the material distortion due to the applied load on the failure step is provided in Figure 5.17. Remarkably, the figures present a change in the orientation of the mid-node at the mid-section, denoting a rotation at the inflexion point as the effect of buckling of the rods. It could be inferred that the constraint of the rotating mid-node does not have an effect on the displacements according to the linear simulations (as stated in the section 4.3.1.2), but it can play a fundamental role when evaluating

buckling of bars. In practical terms, as an example, Euler's critical factor k would change from ≈ 0.7 to 0.5 and would underestimate the critical load of the proposed real case.

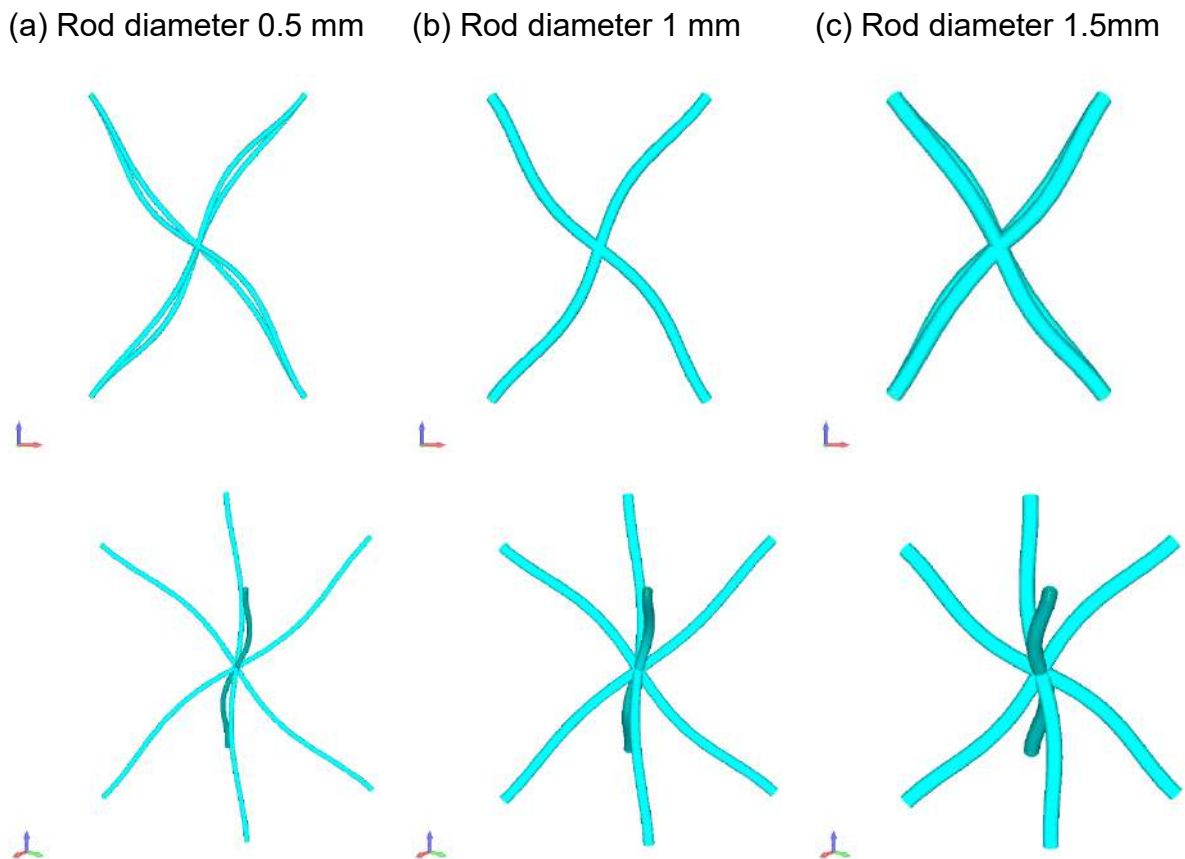


Figure 5.17. Renders obtained from FE buckling simulations at the failure step for different rod diameters, while compression loading

5.3.2.2.1 Numerical results

In order to get a better overview of the results of the linear static and non-linear simulations, Figure 5.18 shows a summary of the predicted strength results for each core case. The core strength predictions exhibit a direct dependence upon the rod's size, i.e., the larger the rod size, the higher the core strength. Thus, the expected core strengths are of 0.187 MPa, 2.67 MPa and 6.981 MPa (the smaller value of the bar graph for each case), for rods varying as 0.5 mm, 1 mm, and 1.5 mm, respectively. From the simulations, buckling failure is predicted for rods diameter 0.5 mm and 1 mm, while failure by fracture for the 1.5 mm.

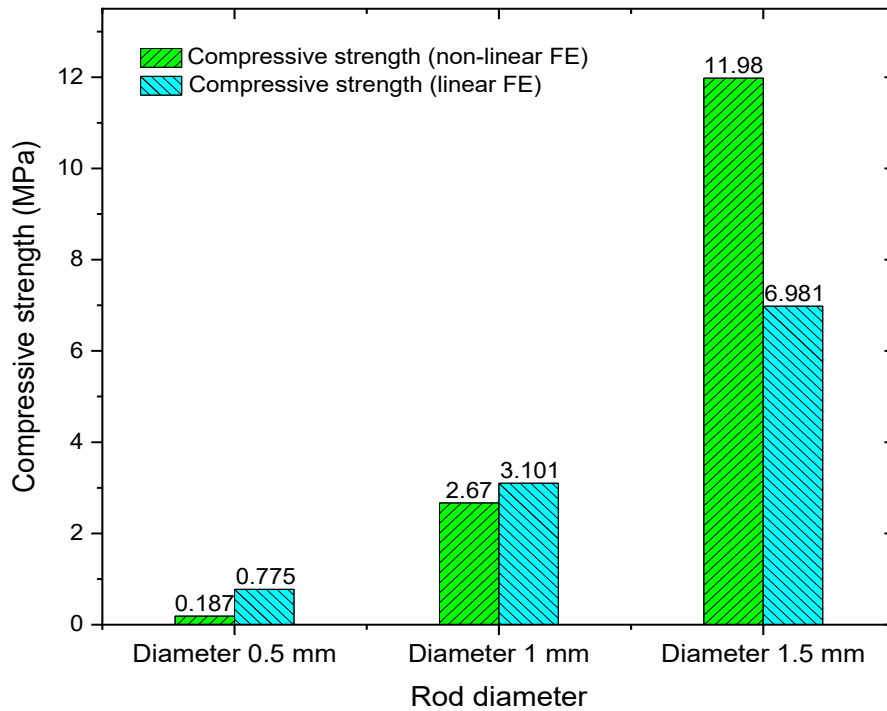


Figure 5.18. Summary of FE simulations for core compressive strength predictions

Table 5.7. Core compressive strengths from numerical and analytical approaches

\emptyset (mm)	L (mm)	P_{crit}^* (kN)	σ_c^* (MPa)	σ_c^{**} (MPa)	σ_c^{***} (MPa)	Expected failure mode
0.5	17.96	60.6	0.187	0.775	0.193 ¹	Euler buckling
1	17.96	862.5	2.670	3.101	3.098 ¹	Euler buckling
1.5	17.96	3865.6	11.98	6.981	7.009	Fracture

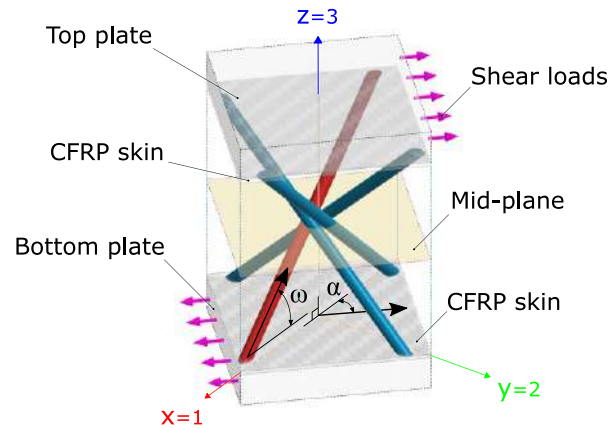
Notes: (*) Non-linear static simulation, (**) Linear static simulation, (***) Analytical. (1) calculated using $k = 0.7$

The results are complemented by Table 4.7, in which the numerical and analytical approaches are compared. The minimum strength is attributed to buckling failure for the slender rods as 0.5 mm and 1 mm, predicting values of 0.187 MPa and 2.67 MPa. In contrast, the predictions for the rod diameter 1.5 mm show a failure due to rod fracture because of its larger rigidity as $E_{15}I_{x'}$, in which the buckling behaviour may be avoided and thus, a core compressive strength of 6.98 MPa would be attained. These numerical results are in correspondence with the theoretical values attained, as 0.193 MPa, 3.098 MPa, and 7.009 MPa for rods diameters of 0.5 mm, 1 mm, and 1.5 mm, respectively.

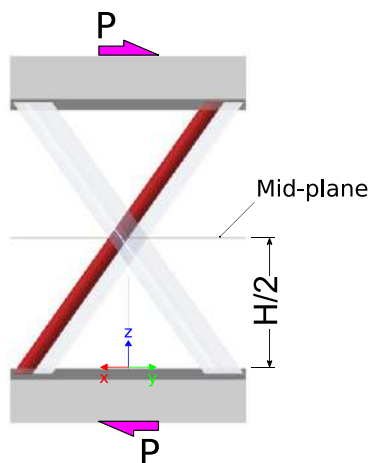
5.4 Core plate shear

This section presents the mechanical properties' prediction by shear loading.

(a) Scheme of a representative unit cell with a plate-shear loading case



(b) From view of the loading case



(c) Sketch of displacement components

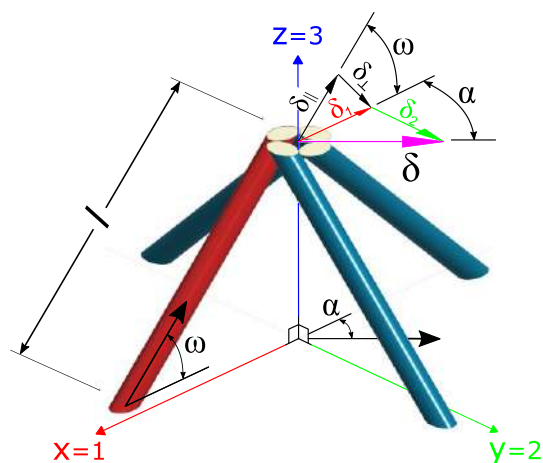


Figure 5.19. Schematic BCC-like lattice render with a shear loading case.

The shear load is transferred by the load plates as shown in Figure 5.19, while assuming that the rods within the unit cell are fixed at their ends to the CFRP skins. Employing Figure 5.19.c as model reference for theoretical calculations, the displacement δ due to a total force applied P is studied while considering the diagram of displacements over the mid-plane at a distance $H/2$, observing that only the half of the total displacement would be attained when comparing the relative displacement of the bottom and to plates. In addition, numerical approaches are provided for supporting the analytical models, likewise as set out in section 5.3, employing rod's mechanical properties from Table 4.1 and the coordinate references as Figure 5.19.

5.4.1 Shear stiffness

The director angles ω and α (Figure 5.19) have an effect on the shear load transferred, influencing the rods' response. In this work, the displacement according to the director angles is taken as base for calculations of the core shear modulus by studying a single unit cell.

5.4.1.1 Analytical approach

The displacement δ has been decomposed not only into its components according to 1-direction (δ_1) and 2-direction (δ_2), but also into its components on xz-plane as parallel (δ_{\parallel}) and perpendicular (δ_{\perp}) directions regarding the rod under study.

Hence, the displacement δ due to the load P is defined by its perpendicular displacement components as Eq. (5.26) and Eq. (5.27).

$$\delta_1 = \delta \cos \alpha \quad (5.26)$$

$$\delta_2 = \delta \sin \alpha \quad (5.27)$$

Moreover, the displacement components are defined according to rod orientation as Eq.(5.28) and Eq. (5.29) in order to study the rod strain.

$$\delta_{\parallel} = \delta_1 \cos \omega \quad (5.28)$$

$$\delta_{\perp} = \delta_1 \sin \omega \quad (5.29)$$

Recalling previous analyses, concerning internal strain energy of a beam, the displacement in parallel and perpendicular directions are given by Eq. (5.9) and Eq. (5.14), respectively. To simplify the studies, it is assumed that the elastic response of the rods to tensile and compressive loads is the same. Then, the total force component in 1-direction P_1 is defined by the response of two rods within a unit cell (one in tension and the other in compression) as Eq. (5.30).

$$\begin{aligned} |P_1| &= 2(F_{\parallel} \cos \omega + F_{\perp} \sin \omega) = \\ &= \frac{\pi d^2}{2l} E_{rod1s} \delta_1 \left[\cos^2 \omega + \frac{3}{4} \left(\frac{d}{l} \right)^2 \sin^2 \omega \right] \end{aligned} \quad (5.30)$$

An analogous analysis is done concerning 2-direction and thus, Eq. (5.31) defines the total force component P_2 .

$$|P_2| = \frac{\pi d^2}{2l} E_{rod1s} \delta_2 \left[\cos^2 \omega + \frac{3}{4} \left(\frac{d}{l} \right)^2 \sin^2 \omega \right] \quad (5.31)$$

The total applied load P is given in terms of the displacement as Eq. (5.32)

$$|P|^2 = |P_1|^2 + |P_2|^2 = \frac{\pi d^2}{2l} E_{rod1s} \delta \left[\cos^2 \omega + \frac{3}{4} \left(\frac{d}{l} \right)^2 \sin^2 \omega \right] \quad (5.32)$$

The overall shear stress τ_c applied on a unit cell is given by Eq.(5.33), where γ_c denotes the strain caused by the generic load P and G_c represents the shear modulus of the unit cell.

$$\tau_c = \frac{P}{A_{cell}} = G_c \gamma_c \quad (5.33)$$

The strain γ_c is defined as Eq. (5.34) in terms of the displacement over the half-cell height ratio.

$$\gamma = \frac{\delta}{l \sin \omega} \quad (5.34)$$

Substituting Eq. (5.34) and Eq. (5.32) into Eq. (5.33) and solving for G_c , the core effective in-plane shear modulus is defined as Eq. (5.35).

$$G_c = \frac{E_{rod1s} \pi d^2 \sin \omega}{4 l^2 \cos^2 \omega \sin 2\alpha} \left[\cos^2 \omega + \underbrace{\frac{3}{4} \left(\frac{d}{l} \right)^2 \sin^2 \omega}_{\text{transverse term}} \right] \quad (5.35)$$

Analogously to section 5.3.1.1, the component “transversal term” in the last expression, it only contributes from 0.02906 to 0.26 % to the expression in parentheses for the cases analyzed in this work, so it will be neglected to ease calculations. Then, the core shear modulus varies regarding the rod’s diameter following a polynomic curve of second grade (Figure 5.20), and it is directly dependent on the rod’s elastic modulus (Eq. (5.36))

$$G_c \approx \frac{E_{rod1s} \pi d^2 \sin \omega}{4 l^2 \sin 2\alpha} \quad (5.36)$$

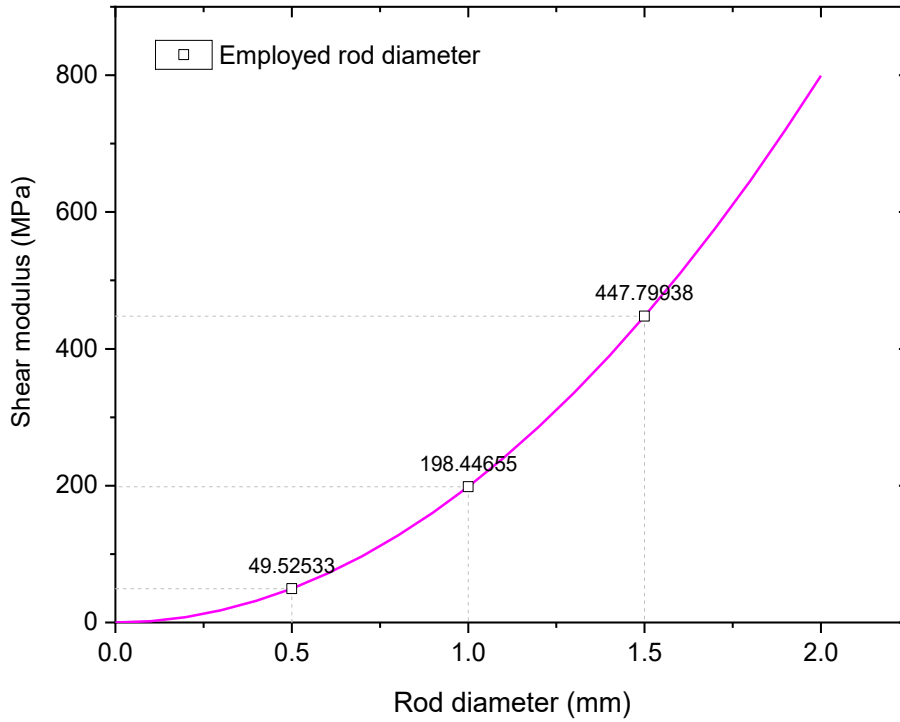


Figure 5.20. Curve of core shear modulus predicted by the analytical model

5.4.1.2 Numerical approach

Linear static FE simulation complement the analytical studies. The elastic shear modulus of the core G_c , is studied through a unit cell considering the three different rod diameters proposed. As outlined in section 4.3.1.2, here the shear modulus G_c of the BCC-like cores is obtained also indirectly from the displacement of the top nodes of the cell regarding to the load applied (Figure 5.21). Using the slope $s = \frac{P}{\gamma_c}$, and employing Eq. (5.37), the shear modulus is calculated.

$$G_c = \frac{P}{A_{cell} \gamma_c} = \frac{PH}{A_{cell} \delta} = \frac{sH}{A_{cell}} \quad (5.37)$$

The core shear moduli obtained from the linear simulations are resumed in Table 5.8. The predicted shear moduli are of 49.52 MPa, 198.32 MPa and 447.36 MPa for the rod's diameter varying 0.5 mm, 1 mm, and 1.5 mm, respectively. The straining depends directly on the rod's size (its flexural rigidity), being the largest value found for the smallest rod's diameter. The displacement and straining are presented for the case of a total shear load of 1 kN. Good correspondences are found between theory and simulations.

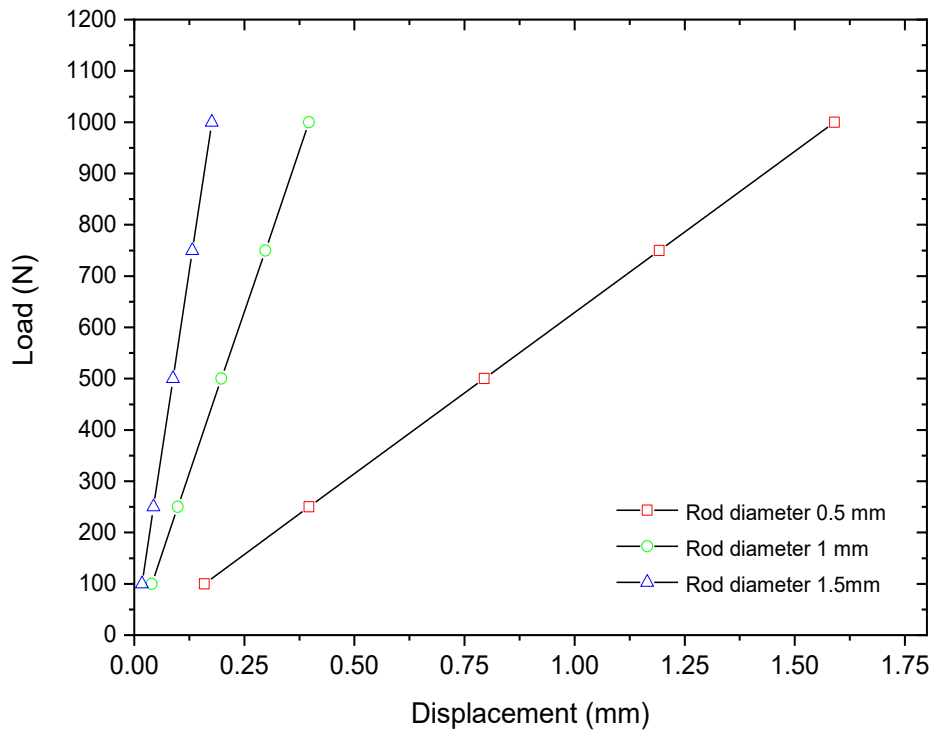


Figure 5.21. Shear load vs. displacement curves obtained from the simulations

Table 5.8. Core shear elastic moduli predicted by FE

\emptyset (mm)	L (mm)	H (mm)	δ (mm)	s (N/mm)	γ_c ($\mu\text{m}/\text{m}$)	G_c (MPa)	G_c^* (MPa)
0.5	17.96	25.4	4.033	629.72	0.1588	49.58	49.53
1	17.96	25.4	1.008	2517.91	0.0397	198.27	198.44
1.5	17.96	25.4	0.446	5683.13	0.0176	447.52	447.46

Note: (*) Theoretical value

5.4.2 Shear strength

The analytical models developed for core shear failure predictions focused on the collapse of unit cell members, considering that the shear load applied is transferred mostly as axial loads to the rods. The shear strength of the core is governed either by:

1. Elastic buckling of a truss τ_{cB}
2. Compressive fracture of a truss τ_{cR} (when σ_{1s}^- exceeds R_{1s}^-).
3. Truss pull-out τ_{cP}

The dominant failure mode results as the one where the shear strength τ_{cpk} is a minimum (Eq. (4.59)). The failure regions are presented in section 5.4.2.1.4, where the dominant modes are plotted as the grey region, as the area below the failure curve.

$$\tau_{cpk} = \min(\tau_{cB}, \tau_{cR}, \tau_{cP}) \quad (5.38)$$

Furthermore, FE models are presented in this section for evaluating the stresses from two independent points of view: considering buckling and not considering it.

The influence of the director angle α (Figure 5.19) on the shear strength is addressed by exemplifying its effect over a buckling load due to a plate-shear case and is described in Annex D, by analyzing a particular case of a constant cell area.

5.4.2.1 Analytical approach

The core shear strength depends on the failure value of the lattice core members, and the description is presented as follows. As previously stated in section 4.4.1.1, the transversal term is neglected to ease the analyses.

5.4.2.1.1 Elastic buckling of a truss

Recalling previous analyses, slender CFRP rods under axial loads can fail by elastic buckling while reaching a critical load as Eq. (5.22). Assuming that the rod boundary conditions as clamped at both ends and considering the mid-plane as pinned but guided constraint (factor $k \approx 0.7$), the core nominal shear strength due to core member buckling τ_{cB} is given by Eq. (5.39) while substituting Euler's critical load Eq. (5.22) as F_{\parallel} in Eq. (5.32) (i.e., first incorporating the terms in Eq. (5.30) and Eq. (5.31)) and replacing the correspondent terms in Eq. (5.33).

$$\tau_{cB} \approx \frac{E_{rod1s} \pi d^4}{64 k^2 l^4 \cos \omega \cos \alpha \sin 2\alpha} \quad (5.39)$$

The influence of the director angle α on the buckling load due to shear is shown in Annex D, by analyzing a particular case of a constant cell area.

5.4.2.1.2 Fracture of a truss

Core member crushing is also expected when the parallel load F_{\parallel} is equal to the failure load of the CFRP rods (Eq. (5.24)) during a shear loading case. Then, substituting Eq. (5.24) and Eq. (5.32) into Eq. (5.33), the nominal core shear strength τ_{cR} is given by Eq. (5.40).

$$\tau_{cR} \approx \frac{R_{1S}^- \pi d^2}{4 l^2 \cos \omega \cos \alpha \sin 2\alpha} \quad (5.40)$$

5.4.2.1.3 Truss pull-out

The detachment between the rods and the core skins, thought as a debonding failure, is evaluated as well for the case of shear loading. As simplification for the analyses, it is assumed that two similar failure modes can occur either as truss push-out (similarly as shown in Annex D) or as truss pull-out, since in the case of shear loads two rods within a unit cell are in tension, and the other two in compression (Figure 5.19). Local axial stresses are considered to be equal in modulus (i.e., in tension or compression).

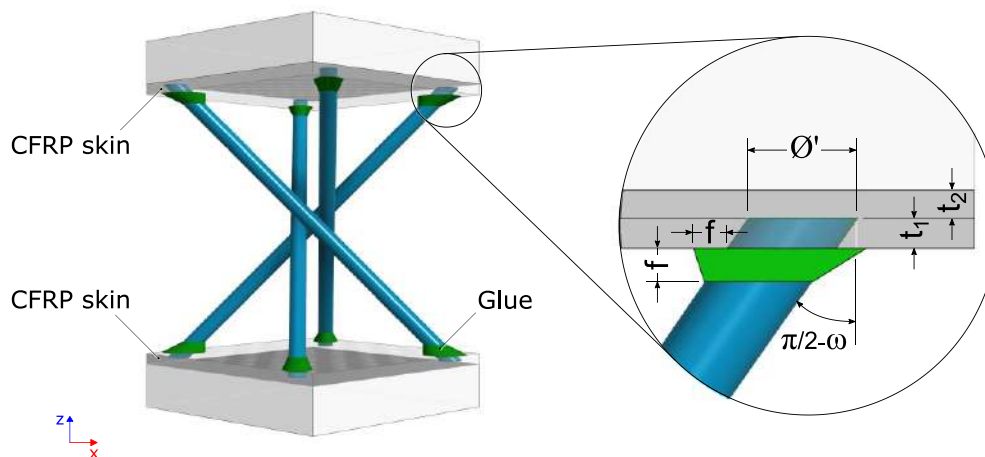


Figure 5.22. A BCC-like lattice sketch showing the connection rods-skins

Since cover layers of thickness t_2 are set out over the rods' ends (Figure 5.22) and steel plates are given for transferring the shear loads to the sample, the expected dominant debonding mode will be truss pull-out from the skins, while bearing tensile loads. The truss pull-out failure is simplified as a debonding failure between the CFRP rods and the skins. The adhesion strength between the rod and the faces is assumed as $\tau_{int} = 20$ MPa [150]. The bonded area is given by Eq. (5.41), where t_1 represents the thickness of the skin in which the rods go through. The glued meniscus between rod and skin with an estimated average flank size f are also taken into account [150]. The flanks sizes are measured in the lab, having a nominal value of 2 mm (in average $f = 2 \pm 0.5$ mm) for each rod size. The size of the flank is pre-designed in the manufacturing process.

$$A_{bond} = \frac{\pi dt_1}{\sin \omega} + \frac{\sqrt{2}f\pi d}{2 \sin \omega} \quad (5.41)$$

Consequently, considering that the number of involved trusses that bear the shear loads is four within each unit cell, ($N = 4$), the global bonding strength concerning the adhesion strength and the bonded surface between rod-skin is F_{rodP} (Eq. (5.42)).

$$F_{rodP} = A_{bond}\tau_{int}N \quad (5.42)$$

As seen in previous failure formulations, the parallel load F_{\parallel} is equal in modulus to F_{rodP} when the adhesion strength is reached. Combining Eq. (5.32), Eq. (5.33) and Eq. (5.42), the estimated core shear strength by evaluating truss pull-out from the skins is given by Eq. (5.43).

$$\tau_{cP} \approx \frac{\tau_{int}\pi d}{l^2 \cos \omega \sin \omega \cos \alpha \sin 2\alpha} \left(t_1 + \frac{\sqrt{2}}{2} f \right) \quad (5.43)$$

5.4.2.1.4 Analytical results

Table 5.9 shows the shear strengths according to the analytical results. For the 0.5 mm rod case, a Euler buckling failure mode is predicted, having a strength of 0.136 MPa; while rod pull-out failure mode is expected for the cores made from 1 mm and 1.5 mm rods, attaining strengths of 1.001 MPa and 1.507 MPa, respectively.

Table 5.9. Core compressive strengths according to analytical approaches

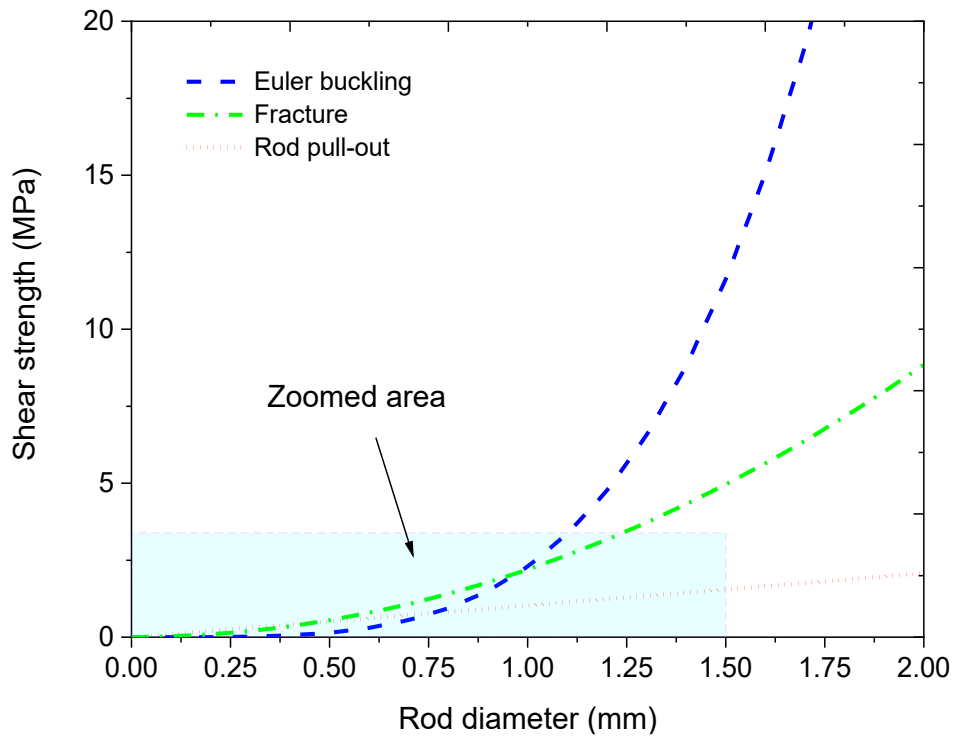
\emptyset (mm)	L (mm)	f (mm)	t_1 (mm)	α (°)	ω (°)	R_{1s}^- (MPa)	E_{rod1s} (MPa)	τ_{cB}^* (MPa)	τ_{cR} (MPa)	τ_{cP} (MPa)
0.5	17.96	2	0.4	45	45	450	115	0.136	0.548	0.500
1	17.96	2	0.4	45	45	450	115	2.190	2.196	1.001
1.5	17.96	2	0.4	45	45	450	115	11.12	4.956	1.507

Note: (*) the values are obtained for a buckling k factor of 0.7

Figure 5.23 represents the main failure modes regarding to the analytical predictions. The blue-dashed line corresponds to Euler buckling failure τ_{cB} drawn by Eq. (5.39), the green-dotted-dashed curve represents the failure due to fracture τ_{cR} using Eq. (5.40), and the red-dotted curve represents the rod pull-out τ_{cP} employing Eq. (5.43). The grey area below the curves represents the dominant modes, and the

change in the failure regions is predicted approximately for rods of diameter ≈ 0.75 mm, from Euler buckling mode to rod pull-out.

(a) Curve plotting for predicted failure modes



(b) Zoomed area for identifying failure regions

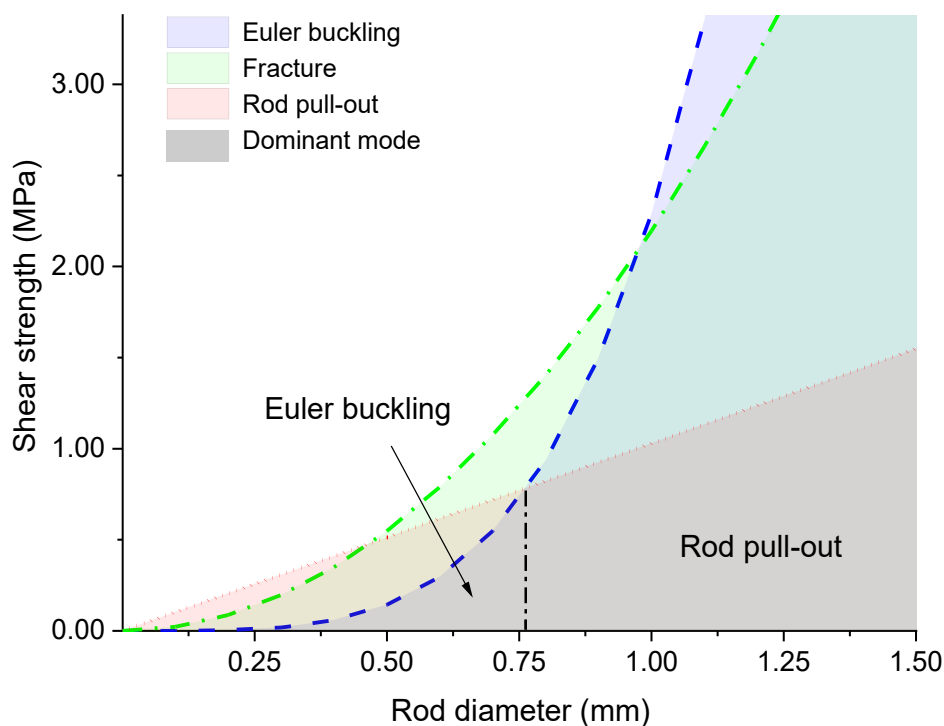


Figure 5.23. Failure maps according to analytical predictions for shear loads

A seed value $k = 0.7$ is employed in Eq. (5.39) for the base theoretical buckling calculations (τ_{cB}). Table 5.10 complement the buckling calculations, by varying k coefficient, between the attainable support cases ($0.5 \leq k \leq 1$). Different buckling strength τ_{cB} values are then presented within the table.

Table 5.10. Core shear strength due to Euler buckling for different k coefficients

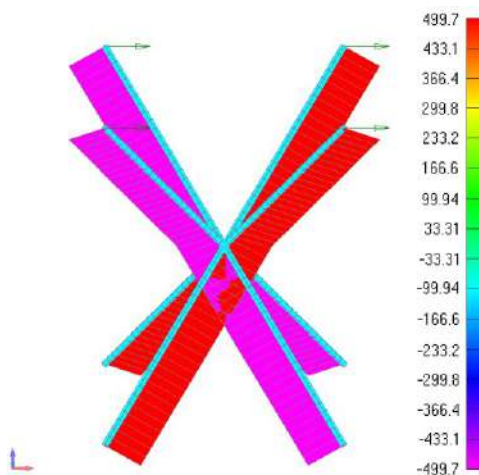
	$k = 0.5$	$k = 0.6$	$k = 0.7$	$k = 0.8$	$k = 0.9$	$k = 1$
\emptyset	τ_{cB}	τ_{cB}	τ_{cB}	τ_{cB}	τ_{cB}	τ_{cB}
(mm)	(MPa)	(MPa)	(MPa)	(MPa)	(MPa)	(MPa)
0.5	0.268	0.186	0.136	0.105	0.083	0.067
1	4.293	2.981	2.190	1.677	1.325	1.073
1.5	21.79	15.137	11.12	8.515	6.727	5.449

5.4.2.2 Numerical approach

Analogously to the compressive analysis, two independent types of simulations are carried out in this section. A total shear force $P = 1$ kN (Figure 5.19) is applied for evaluating the stresses upon the rods and for obtaining the proportional instability load factor. The description of the simulations is presented as follows.

1. The linear static simulations are similar to the ones performed in section 4.4.1.2 (no rod buckling is allowed). As example for the model, a unit cell made from trusses of 0.5 mm diameter is presented (Figure 5.24.).

(a) Axial loads



(b) Bending moments

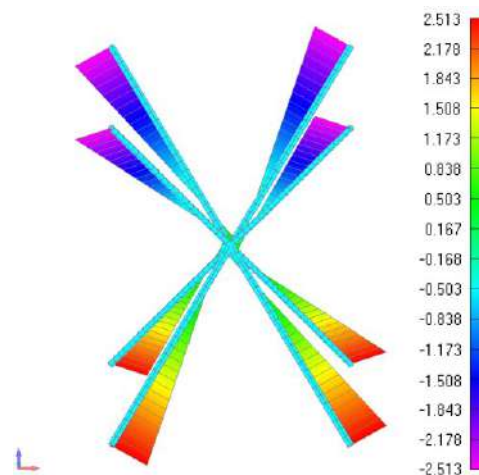
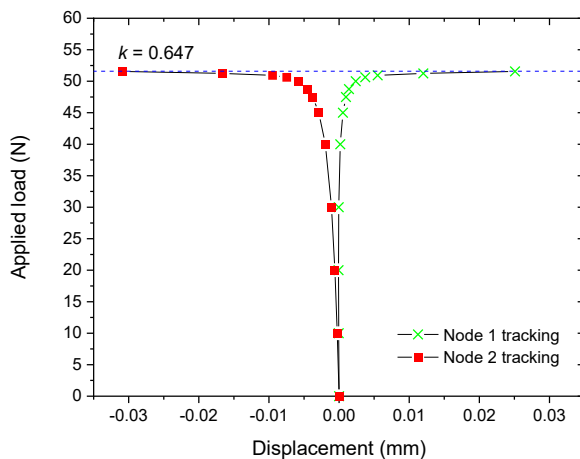


Figure 5.24. Renders of the axial loads and bending moment for the 0.5mm rod diameter lattice unit cell while shear loading

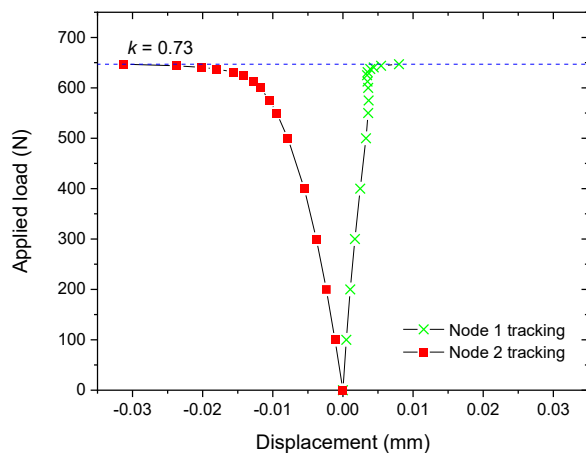
The applied load is then decomposed mostly as axial loads to the rods, where two of them are subjected to tensile loading and the other two to compressive loading. A maximum value of 499.7 N per rod is attained. Contrasting with the load employed, the resulting maximum bending moments are nearly negligible (Figure 5.24.b) and thus, the load over the rods is mostly represented by axial loads, in correspondence with stated in section 4.4.1.1. The shear loads are not exemplified schematically because of their small contribution to the maximum stresses (e.g., showing load values of almost 0.12 N and 0.9 N, for diameters of 0.5 mm and 1.5 mm, respectively).

2. The non-linear simulations evaluate the instability load throughout the load-displacement respond of selected nodes (Figure 5.25).

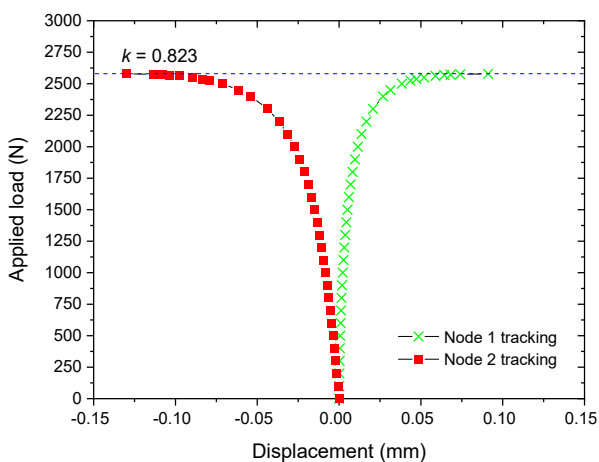
(a) Rod diameter 0.5 mm



(b) Rod diameter 1 mm



(c) Rod diameter 1.5 mm



Reference on node tracking

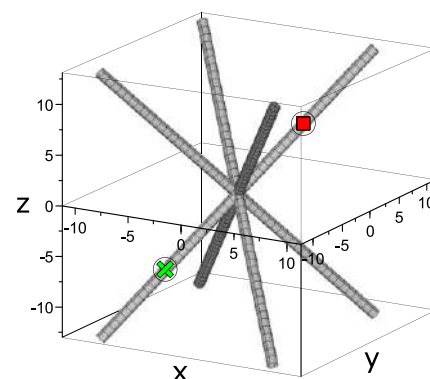


Figure 5.25. Load vs. node displacement curves obtained from the non-linear simulations

The displacements are tracked and graphically represented until the simulations stops. In all cases, the curves denote an asymptote to which the critical loads are attainable as a first approach. The k buckling coefficient factor for the mid-plane node can be extracted indirectly by equating Eq. (5.22) to the critical buckling load and solving for k . In addition, critical loads are predicted for core shear strength while evaluating buckling behaviour as 51.6 N, 649.9 N, and 2578 N for diameters varying from 0.5 mm, 1 mm, and 1.5 mm, respectively.

The core shear buckling analyses are complemented by FE renderings (Figure 5.26), where the buckling behaviour for different rod diameters are schematically represented from the simulations at the last simulated step, as top and isometric views. The material distortion is characterized by a rotation at the mid-node just as a result of the buckling of each core member.

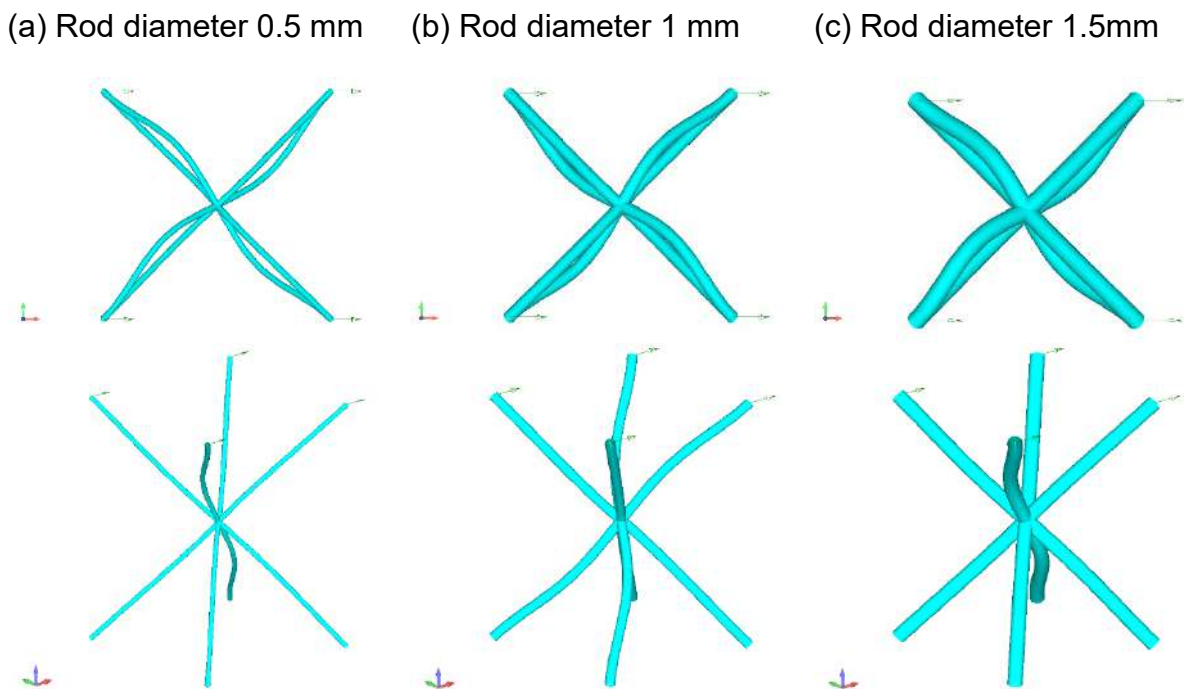


Figure 5.26. Renders obtained from FE buckling simulations at the last step for different rod diameters during shear loading

5.4.2.2.1 Numerical results

A summary of predictions according to the linear and non-linear simulations are provided in Figure 5.27. The extracted information shows that the cross-sectional area of the rods clearly influences the lattice -based shear core properties. In this way, the proposed rods diameter as 0.5 mm, 1 mm and 1.5 mm may attain different shear core

strengths as 0.548 MPa, 2.196 MPa and 4.95 MPa, respectively, when no buckling is considered, and strength as 0.159 MPa, 2.005 MPa and 7.991 MPa, respectively, when buckling is allowed in the simulations. Therefore, the expected failure modes are by Euler buckling of the 0.5 mm and 1 mm rods, and fracture of the 1.5 mm rod cores. The latter predictions did not contemplate the rod pull-out, and its average failure load will be only approximated via analytical approaches.

Table 5.11 presents a summary of the FE results and the minimum stresses calculated by analytical approaches for core shear strength prediction. In this case, factor P_{crit}^* identifies in the buckling load upon a unit cell due to shear loading. For the smallest rod diameter, it is predicted a failure mode as Euler buckling of the core members and a core shear strength of 0.159 MPa. For this case, a little difference in the analytical prediction is found, because of the buckling coefficient employed for the calculation (i.e., the theoretical seed value is $k = 0.7$ and the FE-simulation is calculated as $k = 0.64$ as seen in Figure 5.25.a). The k value is attained as an approximation from the predictions. Nevertheless, the real k value will be obtained by the experimental tests. The cores made from rods of 1 mm and 1.5 mm are predicted to experiment debonding as shown in the theoretical approaches.

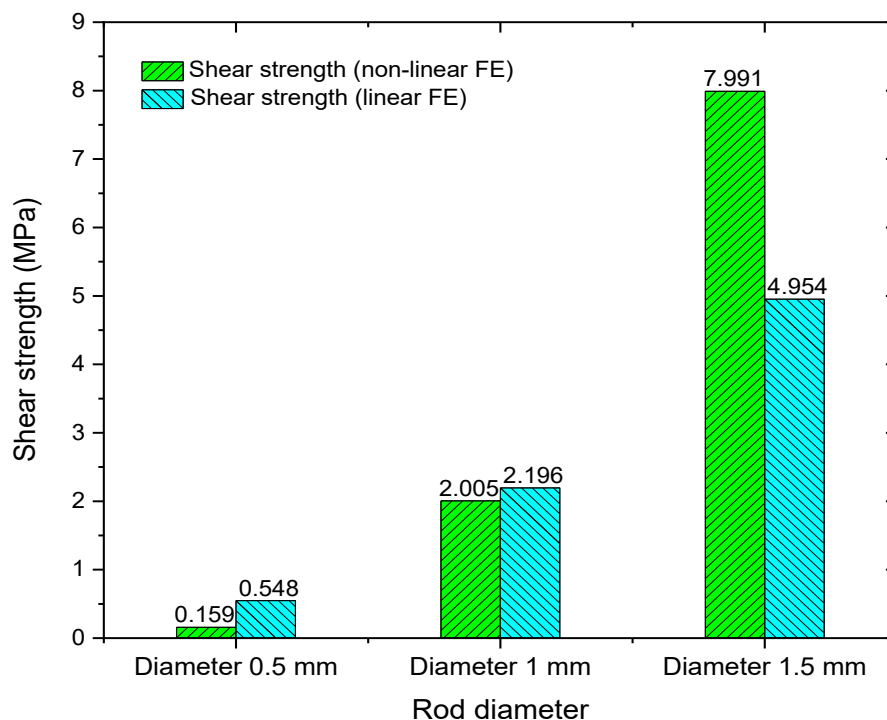


Figure 5.27. Summary of FE simulations for core shear strength predictions

Table 5.11. Core shear strengths from numerical and analytical approaches

\varnothing (mm)	L (mm)	P_{crit}^* (kN)	τ_c^* (MPa)	τ_c^{**} (MPa)	τ_c^{***} (MPa)	Expected failure mode
0.5	17.96	51.6	0.159	0.548	0.136 ¹	Euler buckling
1	17.96	649.9	2.005	2.196	1.001	Rod pull-out
1.5	17.96	2578	7.991	4.954	1.507	Rod pull-out

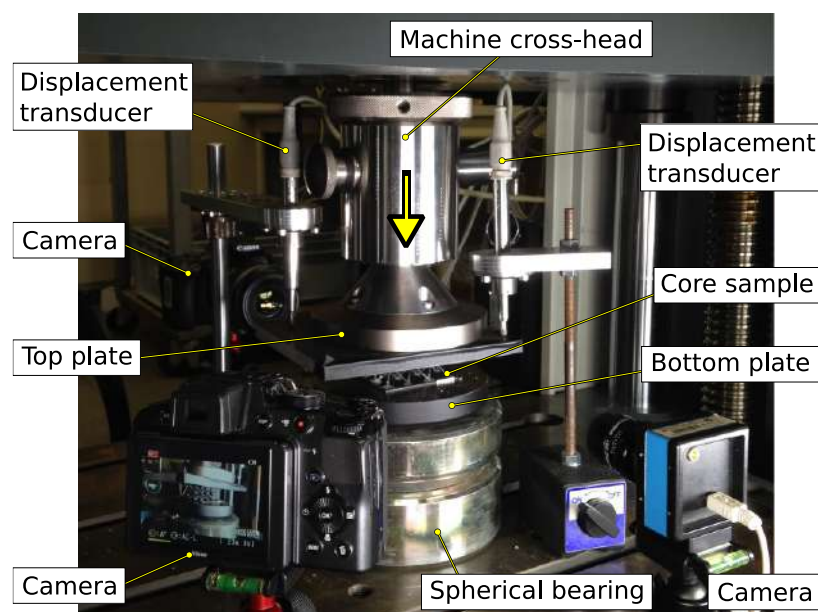
Notes: (*) Non-linear static simulation, (**) Linear static simulation, (***) Analytical. (1) calculated using $k = 0.7$

5.5 Experimental tests

Mechanical properties of the proposed lattice-based cores are evaluated by standards ASTM C365 [175] and ASTM C273 [167]. A Zwick / Roell Z150 screw-driven universal testing machine is employed for testing at controlled room temperature.

5.5.1 Compressive tests

The test set-up is similar as used in section 4.5.1, incorporating in this case two displacement transducers type HBM W5TK, for compensating potential misalignment of the sample to the compression plates (Figure 5.28). The crosshead speed is set to 0.5 mm/min. Three specimens of each core type are employed for testing (Figure 5.5), where the main sample dimensions are 65 x 65 x 25.4mm.

**Figure 5.28.** Set -up used for compression tests

5.5.1.1 Compressive test results

Representative charts showing compressive stress vs. strain and local elastic modulus vs. strain of the different cores proposed are presented in this section. The core area used for the calculations of the elastic moduli and strengths is of 3 by 3 unit-cells, employing an average core thickness of 25.4 mm for evaluating the straining. Considering that different failure behaviour is observed for each core type, descriptions of each core response are provided with support on relevant event points as follows.

The first analysed case comprises rod's diameter 0.5 mm (Figure 5.29). At the beginning of the test, the core shows a linear response followed by little changes in the slope, denoting a not uniform load distribution. Small defects on the sample are evident also like the small drops in the elastic modulus (point 2, Figure 5.30), negatively affecting the overall performance of the core, due to overloading of the remaining rods and possibly subjected to local buckling. The failure step is reached at point 3, where elastic buckling denotes the dominant failure mode. The latter observation is also supported by the fact that the load does not drop suddenly, but gradually with an evident negative slope with a large straining until reaching the ultimate strain and the structure fails.

The case for rod's diameter 1 mm is exhibited in Figure 5.31. After the take-up of slack and seating of the specimen, a linear region is seen as the load reaches point II. Local failure in form of rod's Euler buckling is observed upon this point (Figure 5.32), also detected as the evident local drop in the elastic modulus. After point II, the load continues to increase at a smaller rate until tops out at point III, where photographs give evidence of the rod's buckling and being the failure mode associated. The collapse of the structure develops subsequently going over to a negative stress slope which maintains upon the straining until reaching its maximum deformation.

The last case as rod's diameter 1.5 mm (Figure 5.33) presents an evident Hookean region at the beginning of loading, until point II. At this point, the sudden drop in the elastic modulus and the local variation of the load curve indicates local failures, and in this case, in form of rod's fracture (Figure 5.34). After point II, the increase of the stress carries over into its maximum at point III, after which the structure collapse due to rod's crushing. After failure, the stress curve steps down continuously over the strain until the end of the test.

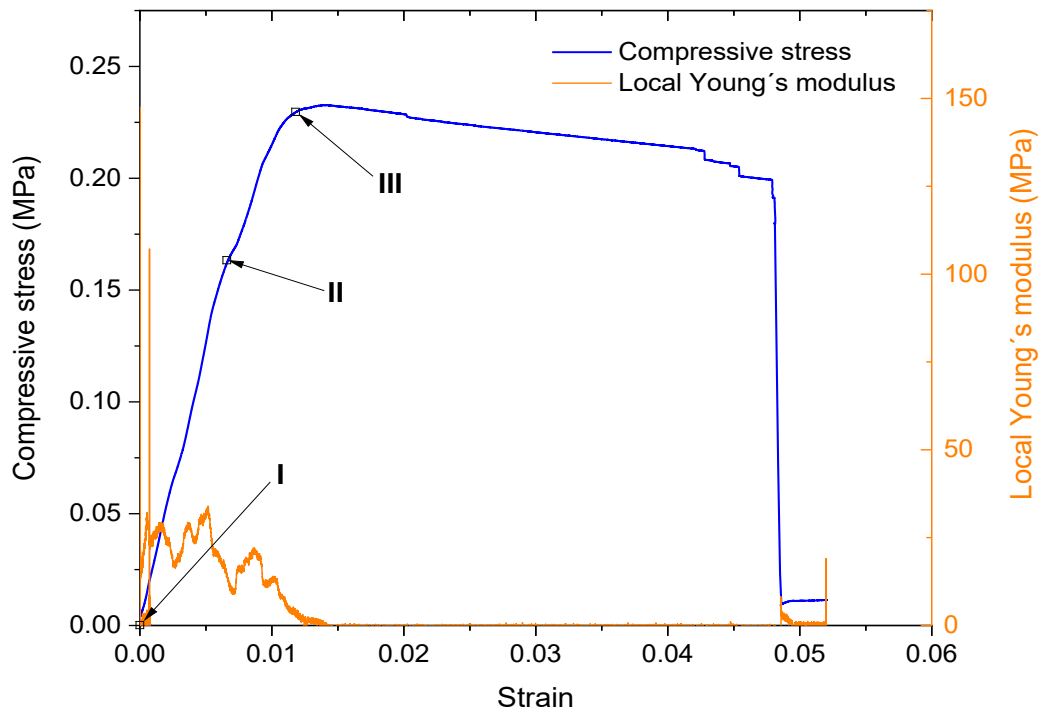


Figure 5.29. Measured compressive stress-strain response of lattice-based core with 0.5 mm rods

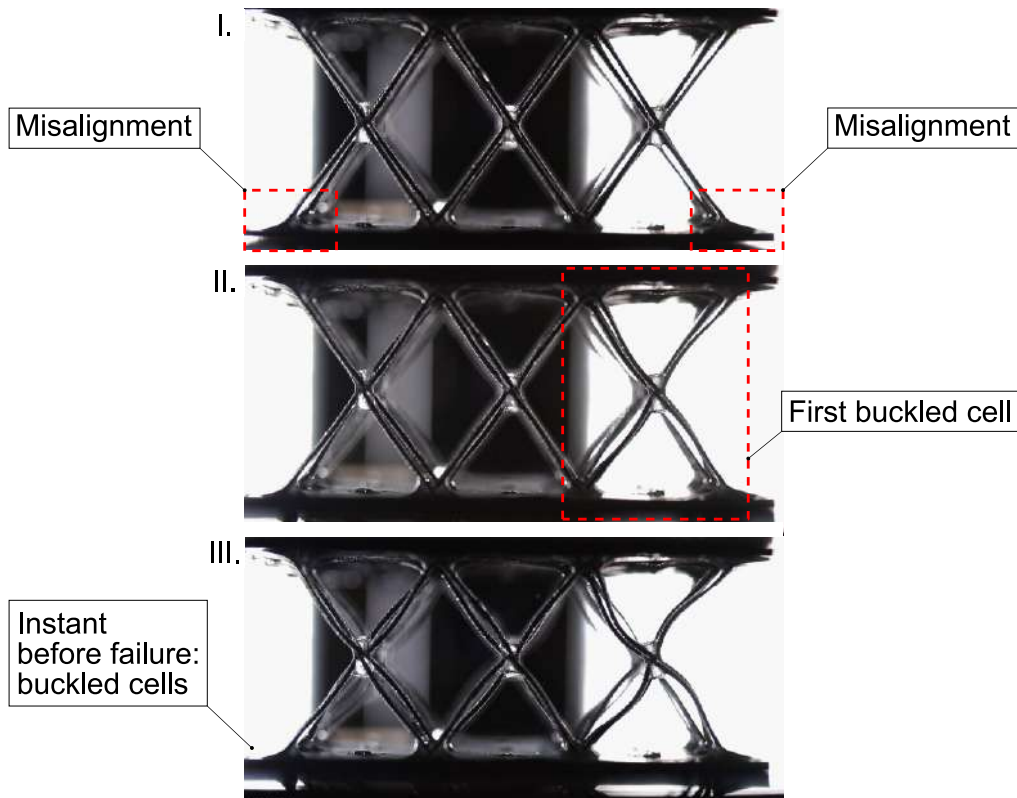


Figure 5.30. Photographs associated with selected points: compressive behaviour of lattice-based core with 0.5 mm rod

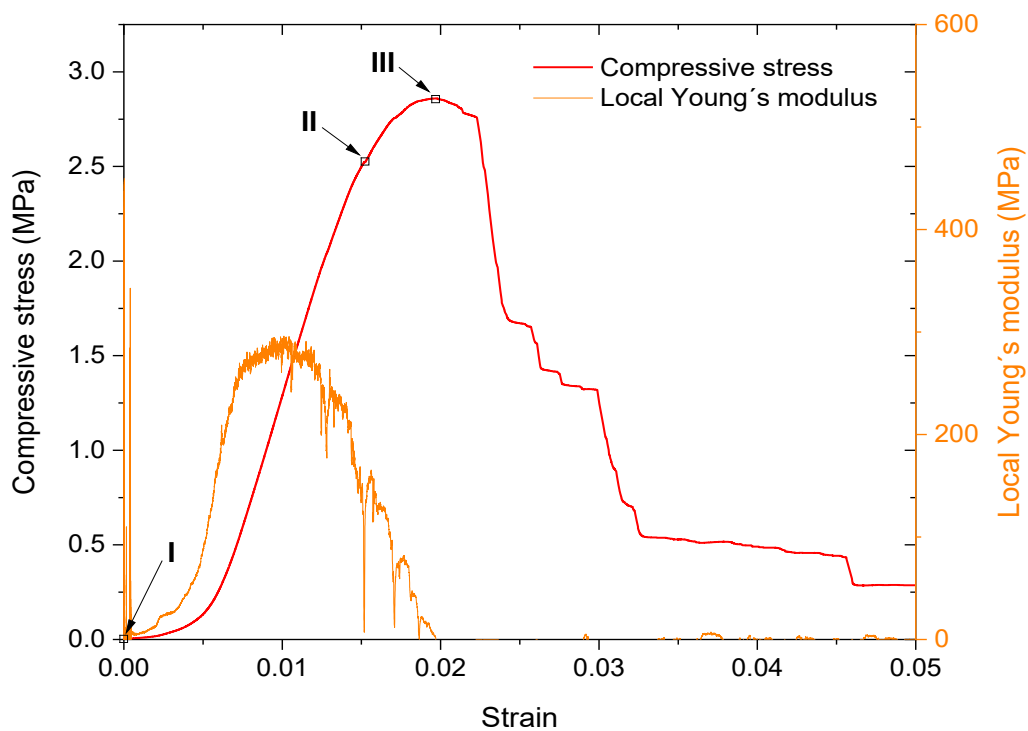


Figure 5.31. Measured compressive stress-strain response of lattice-based core with 1 mm rods

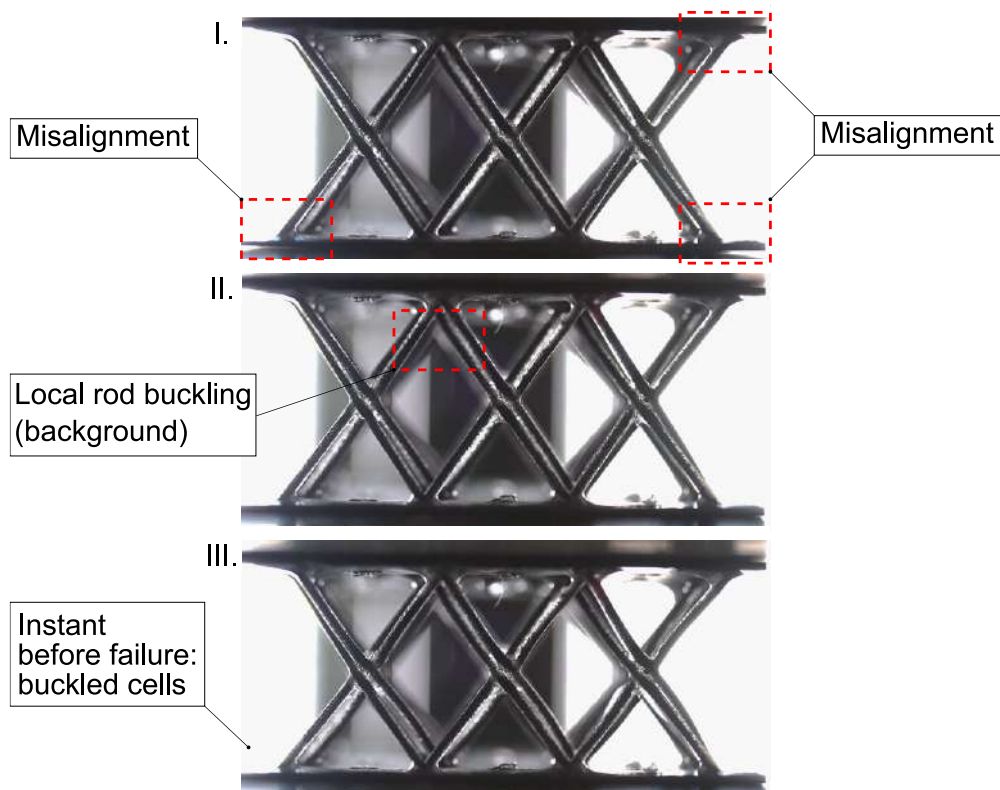


Figure 5.32. Photographs associated with selected points: compressive behaviour of lattice-based core with 1 mm rod

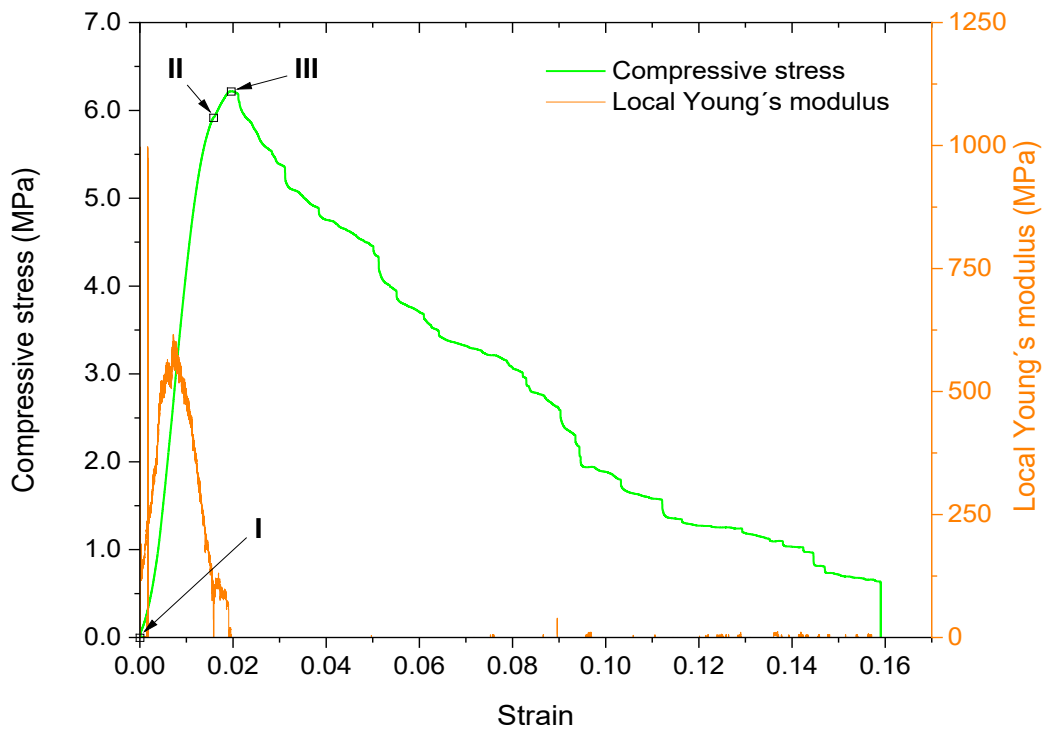


Figure 5.33. Measured compressive stress-strain response of lattice-based core with 1.5 mm rods

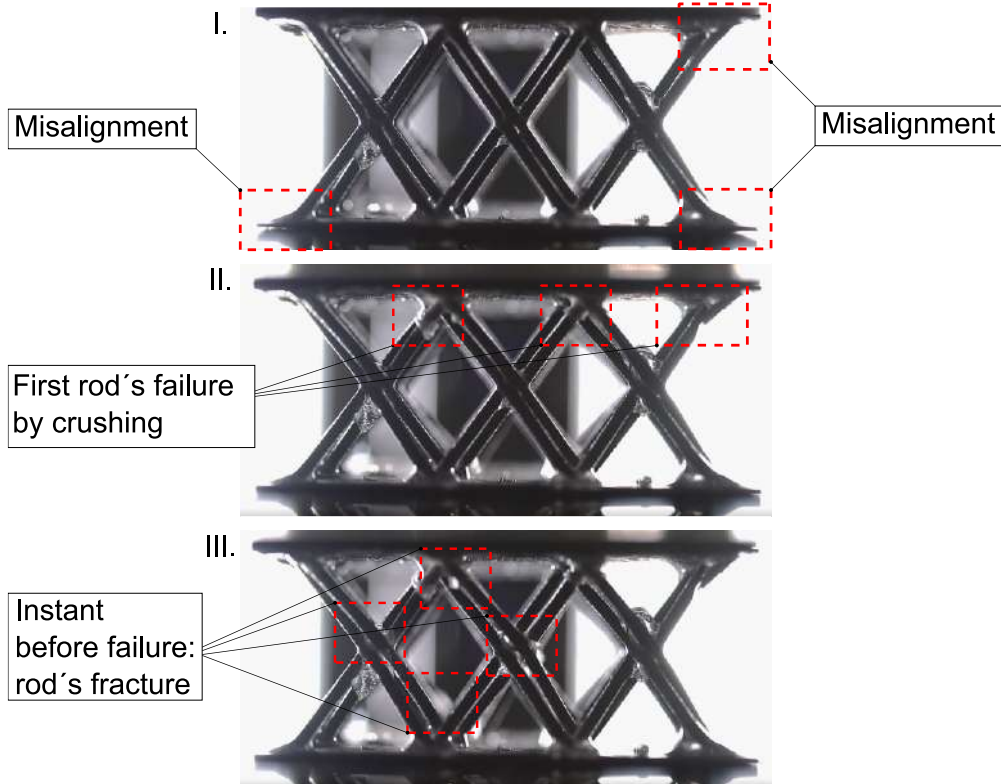


Figure 5.34. Photographs associated with selected points: compressive behaviour of lattice-based core with 1.5 mm rod

The compressive stress vs. strain charts for the best lattice-based cores response proposed are presented in Figure 5.35. The difference among the curves is evident both regarding to the strength values and the curve's form, due to the change in the cross-sectional area and the rod's rigidity. The maximum strengths obtained are of 0.24 MPa, 2.88 MPa and 6.23 MPa for rod's diameters varying 0.5 mm, 1 mm, and 1.5 mm, respectively. The smaller diameters exhibited a similar response (see also Figure 5.29 and Figure 5.31 for better details) after topping out the maximum value, both showing a sustained straining although with a negative slope, until the collapse of the structure. In contrast, the 1.5 mm case showed a sudden drop in stress after its maximum, and a continuous failure of the material as it is compressed until the end of the test is reached.

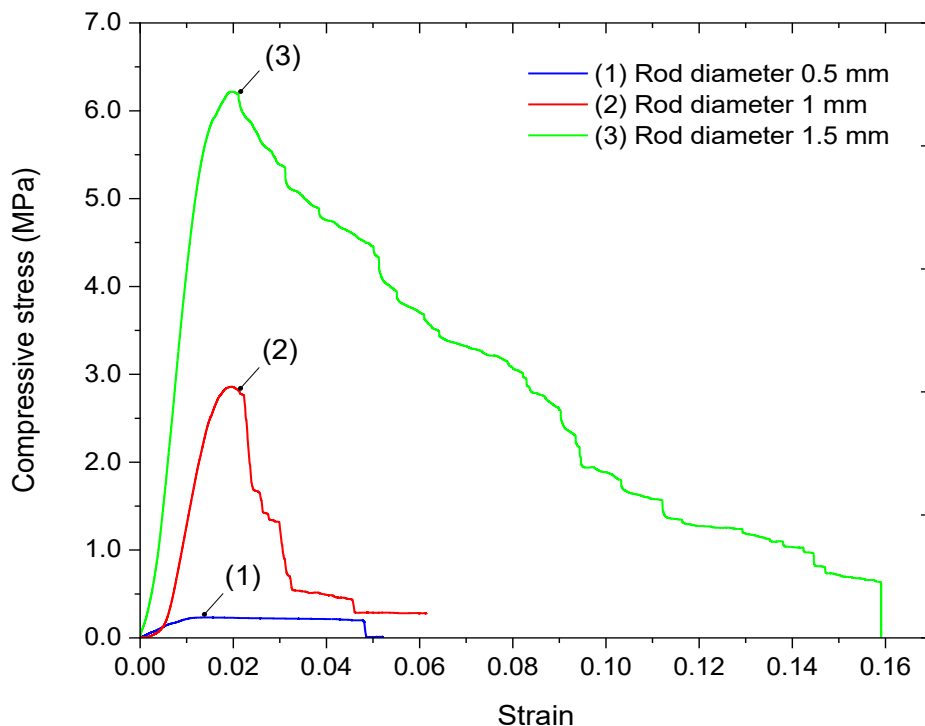


Figure 5.35. Compressive stress–strain response of lattice-based cores

5.5.1.2 Discussion

A model validation is addressed within this section for the compressive studies. The analytical and FE models presented a successful correspondence with the experimental tests, where the main governing failure mechanisms are found as: Euler buckling and rod's fracture, in correspondence with the foreseen results shown in the predictions (Table 4.7).

A comparison of the predicted values and those obtained from the compressive tests is presented in Table 5.12. The analytical models for the failure study took as a reference an average Euler factor $k = 0.7$, so that very small discrepancies from the numerical value occur. By adjusting the k -values from the FE simulations, the models could be further accurate to the results obtained. Even so, the failure values predicted by the models are in excellent correlation with the experimental values, noting the predicted failure modes as well. Looking at the elastic moduli, the standard deviations are relatively high. This suggests manufacturing defects. These may cause a misdistribution of compressive loads, causing some of the cells to be overloaded more than others, or initially only some of the cells to bear the load. This assumption is also supported by the misalignment of the skins with respect to the compression plates presented in Figure 5.30, Figure 5.32, and Figure 5.34.

Table 5.12. Resume of analytical, FEM and experimental results from compressive tests

\emptyset (mm)	Analytical		Numerical		Experimental		Obs. mode
	σ_{cpk} (MPa)	E_c (MPa)	σ_{cpk} (MPa)	E_c (MPa)	σ_{cpk} (MPa)	E_c (MPa)	
0.5	0.193	99.05	0.187	100.65	0.22 ± 0.006	33.91 ± 3.96	BF
1	3.098	396.89	2.670	403.95	2.87 ± 0.011	267.8 ± 17.83	BF
1.5	7.009	895.59	6.981	909.19	5.87 ± 0.314	472.55 ± 119.04	RF

Notes: BF = buckling failure; RF = fracture failure

Recalling the predicted failure main mode charts regarding to the compression stress as function of the rod's diameter, Figure 5.36 is presented for complementing Table 5.12 while considering only the failure mode proposed. The maps have omitted the rod's push-out (see Annex D), given the support of the external skins of thickness t_2 and the loading plates (Figure 5.22). The predicted strengths of the different lattice cores are expressed as the dots upon each rod case analyzed. In particular, according to the theoretical model represented, the case for 1 mm rods set down a point over a frontier between failure zone and thus, it could present either buckling failure, fracture failure, or mixed. Referring to its experimental and numerical data, it is concluded that

the acting failure mode is Euler buckling. The other rod cases are also exhibited in the charts, positioning the dots according to the predictions in each area assessed.

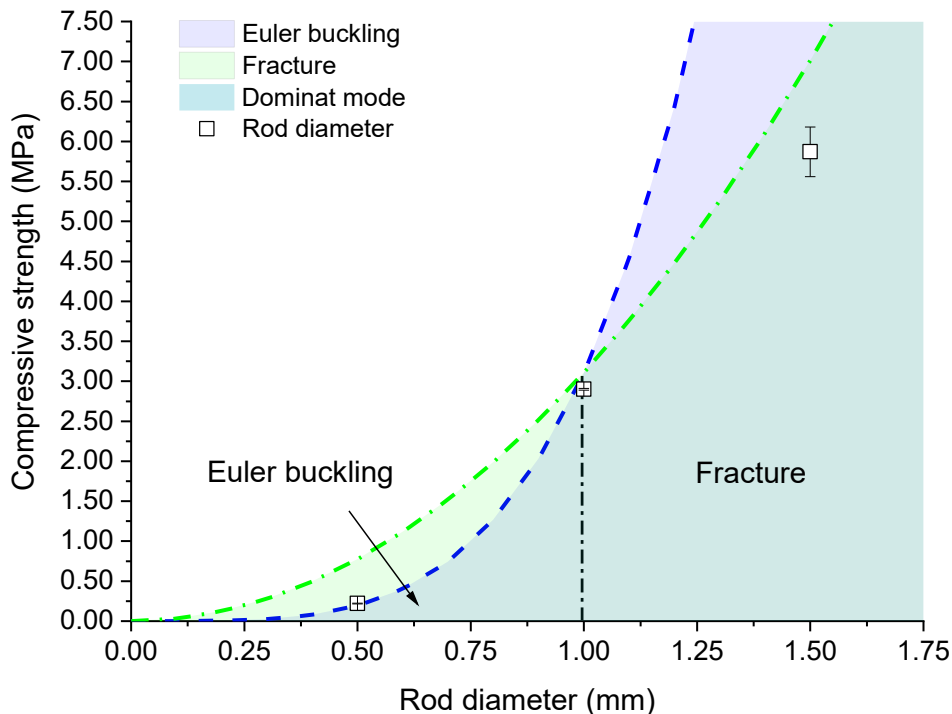


Figure 5.36. Resulting failure maps for compressive stresses and experimental data

5.5.2 Shear tests

Typical plate-shear test set-up following the line-up of the standard ASTM C273 is shown in Figure 5.37. The samples are attached to the steel-plates via adhesive and cure, assuring the main diagonal of the core parallel to the line load as pointed out in previous chapter. The employed length-to-thickness ratio is in average of 8:1. The rate of the cross-head displacement is set by 0.5 mm/min, and the core straining is measured by a displacement transducer HBM W5TK. The tests specimens are dimensioned to a size of 200 x 100 x 25.4 mm (Figure 5.6). Two specimens for each core shear sample have been provided by the UniBwM at laboratory-scale. Consequently, it is necessary the manufacturing and testing of more test specimens as future work to better satisfy the statistical analyses if required. Nevertheless, good repeatability is observed between the tests and therefore, are presented in this section.

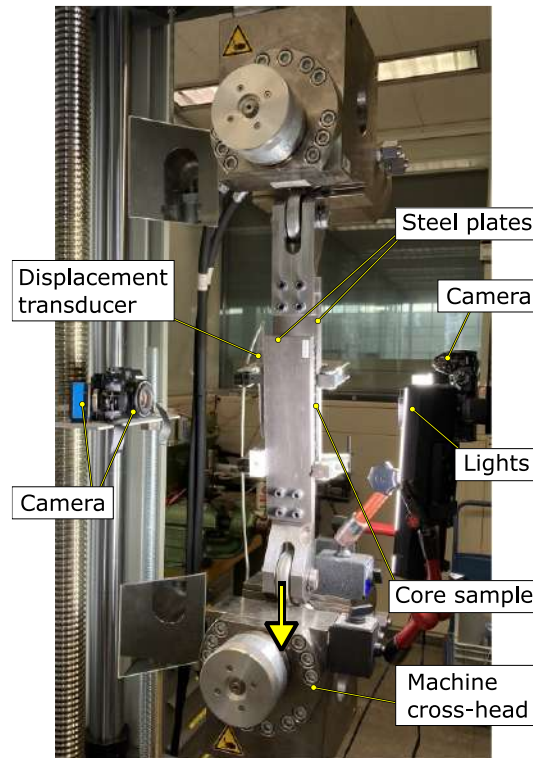


Figure 5.37. Photograph of the plate-shear test set-up

5.5.2.1 Shear test results

The shear test responses of the cores proposed identified different failure mode for each core case. In this section, a description differentiating each core case in individual charts is provided. Individual points at relevant events are set into the charts, referring to the correspondent response photographs. Additionally, a common graphic compares the behaviour of the cores. In general, local failures are observed before reaching the maximum core shear strength.

Figure 5.38 represents the shear response of a lattice core based on 0.5 mm rod's diameter. A linear behaviour is observed in the first stage of the test with a constant ratio slope, also visible by the almost constant local Young's modulus. After the maximum stress value is attained at point II, the rods reached the critical buckling load and began to buckle (Figure 5.39, point II). The bulking behaviour is also recognizable by the non-sudden change of slope on the stress and strain curve, until the maximum straining is reached and most of the cells experienced buckling failure of the rod members.

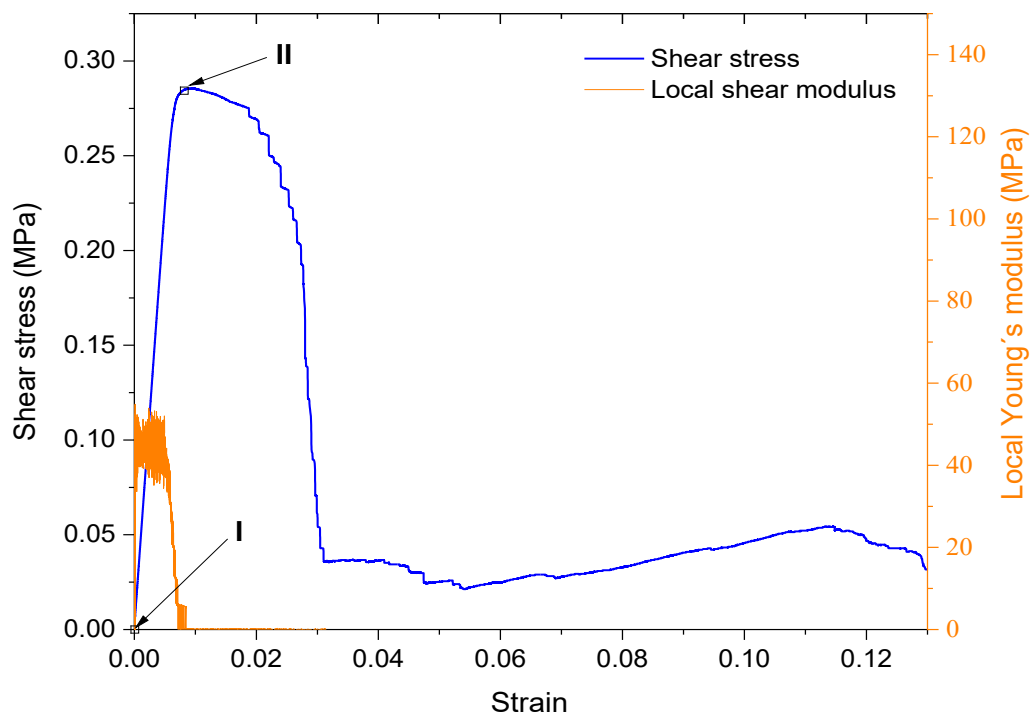


Figure 5.38. Measured shear stress–strain response of lattice-based core with rod diameter 0.5 mm

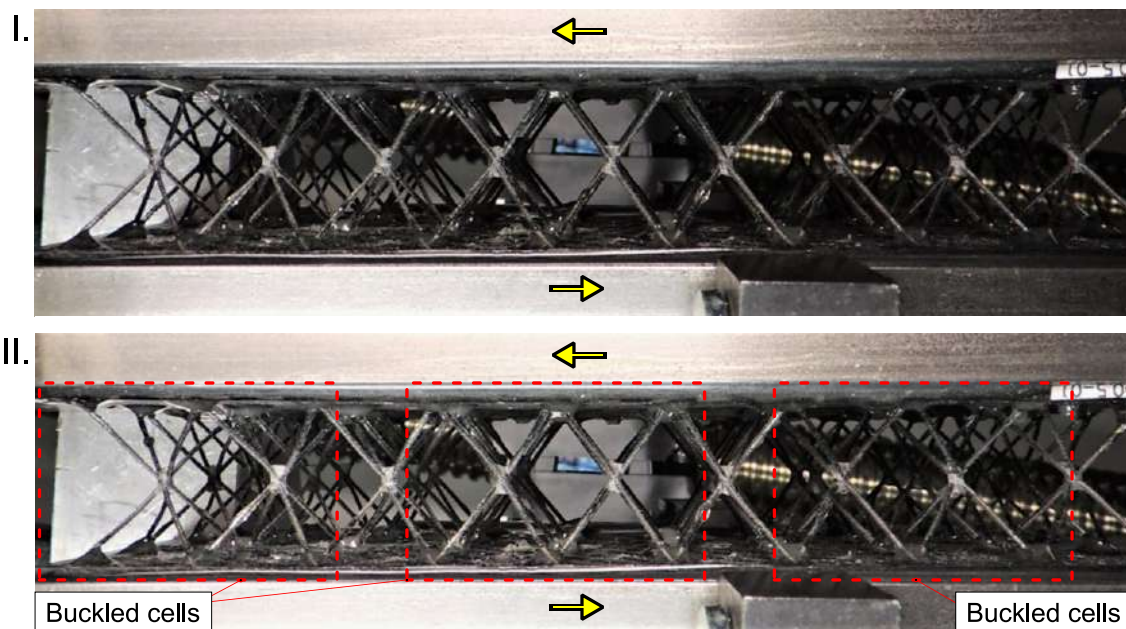


Figure 5.39. Photographs associated to selected points: shear behaviour of lattice-based core with 0.5 mm rods

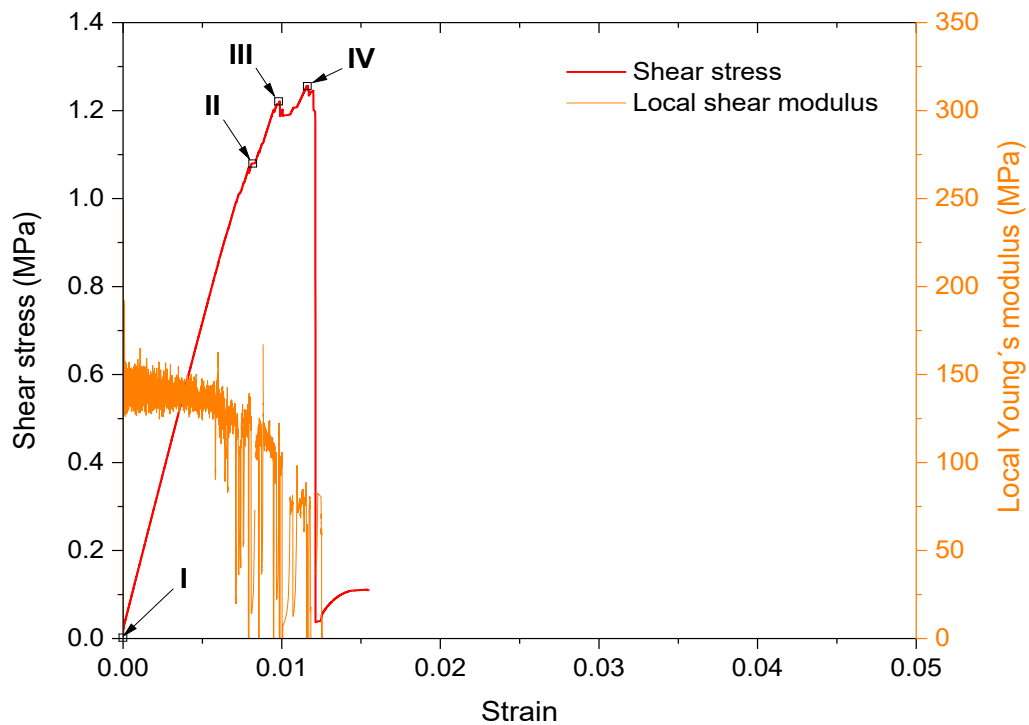


Figure 5.40. Measured shear stress–strain response of lattice-based core with rod diameter 1 mm

The case of Figure 5.40 shows the core shear behaviour of the 1 mm rod's diameter. A Hookean region is easily identified at the beginning of the test, between point I and point II, with an almost constant slope ratio. At point II, a small step in the straining is seen, meaning a local failure of one or some of the core members. Referring to Figure 5.41, point II, local rod pull-out is identified on the videos due to the tension experienced by the rods. After point II, the change in slope and change in shear elastic modulus suggests as well that less members are bearing the load. At point III, more core cells fail locally due to the tensile stress on the rods and possibly local defects. The failure is reached after point IV, where the remaining core members cannot bear more stress and fail in a sudden manner. On Figure 5.41, point IV, the failure due to truss pull-out is evident as the trusses are detached from the skins.

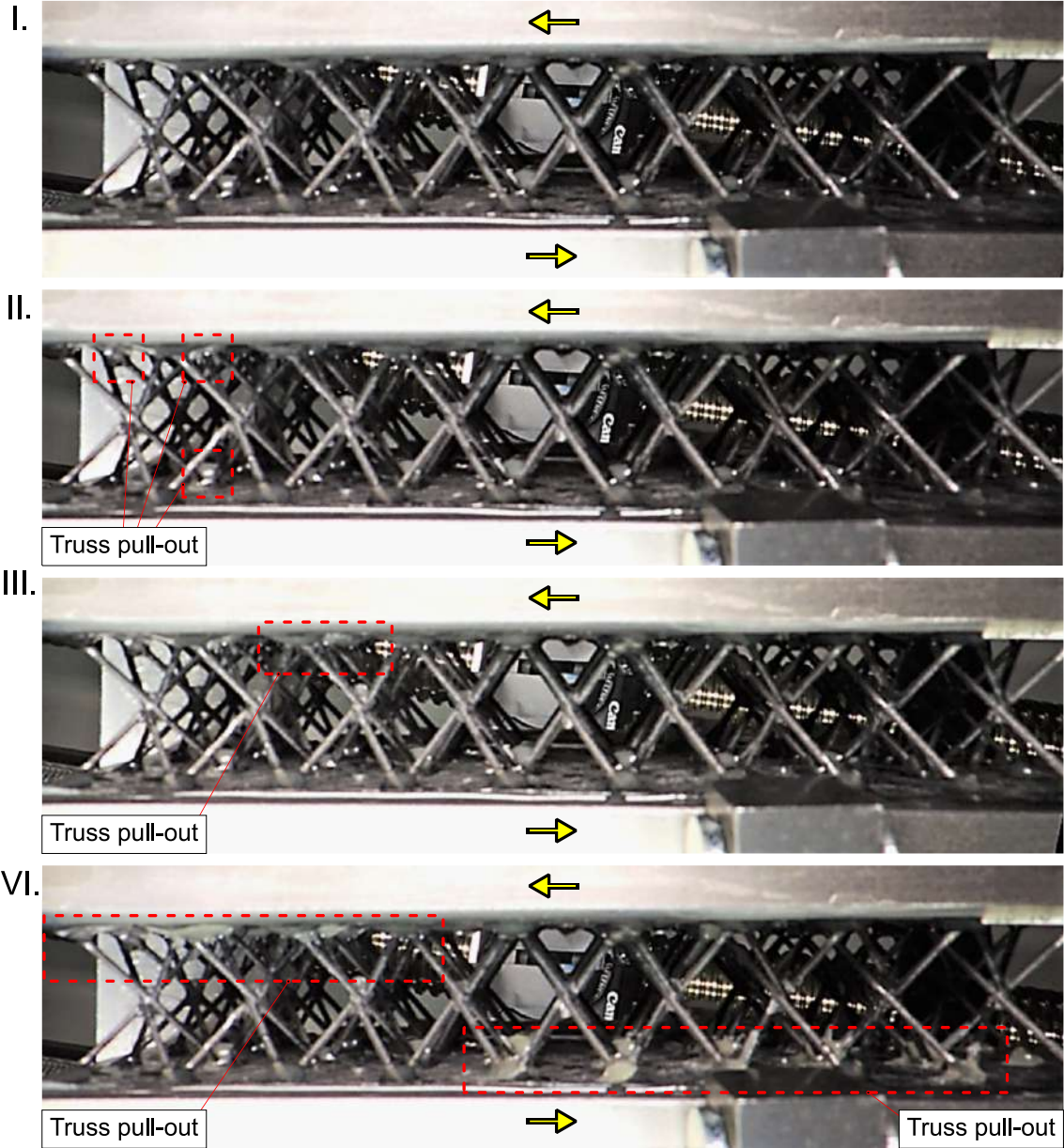


Figure 5.41. Photographs associated to selected points: shear behaviour of lattice-based core with 1 mm rods

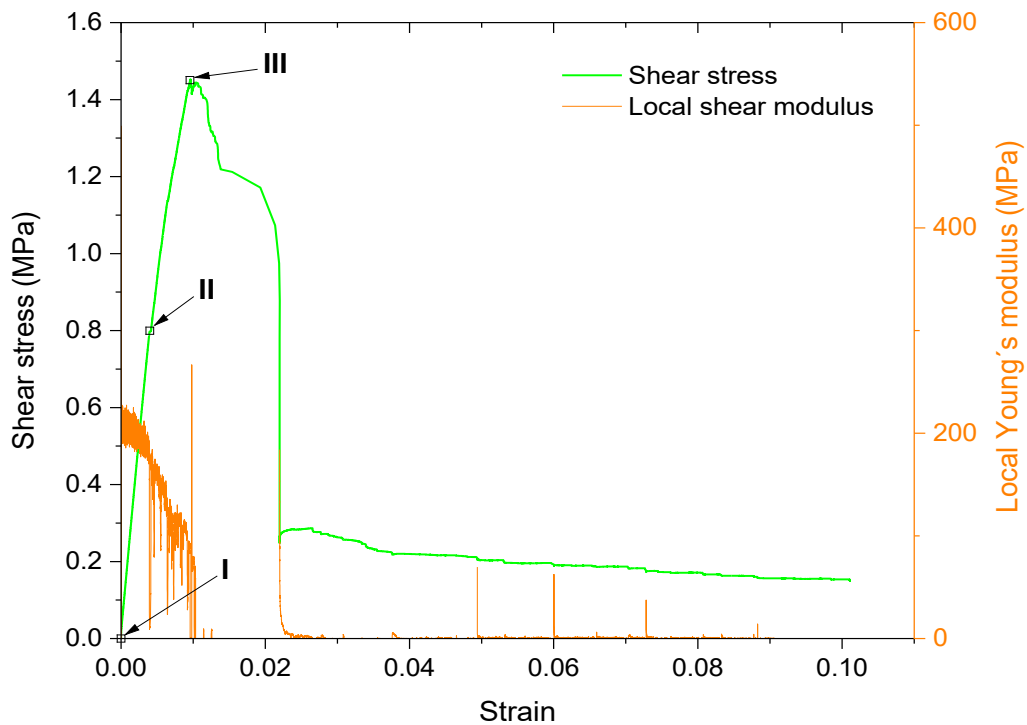


Figure 5.42. Measured shear stress–strain response of lattice-based core with rod diameter 1.5 mm

The last case is represented by Figure 5.42 and Figure 5.43 for cores made from rods of 1.5 mm. A linear response is visible at the beginning of the test, with sustained slope until point II. At point II, local failure identified as truss-pull out occurs and less core members bear the stress as the change on the Young's modulus is seen. The stress continues to increase, although with a small slope ratio and consequently a drop in the elastic modulus, until point III. When the maximum stress is reached, the structure then collapses suddenly by the detachment of core members from the skins. The truss pull-out is shown on Figure 5.43, point III.

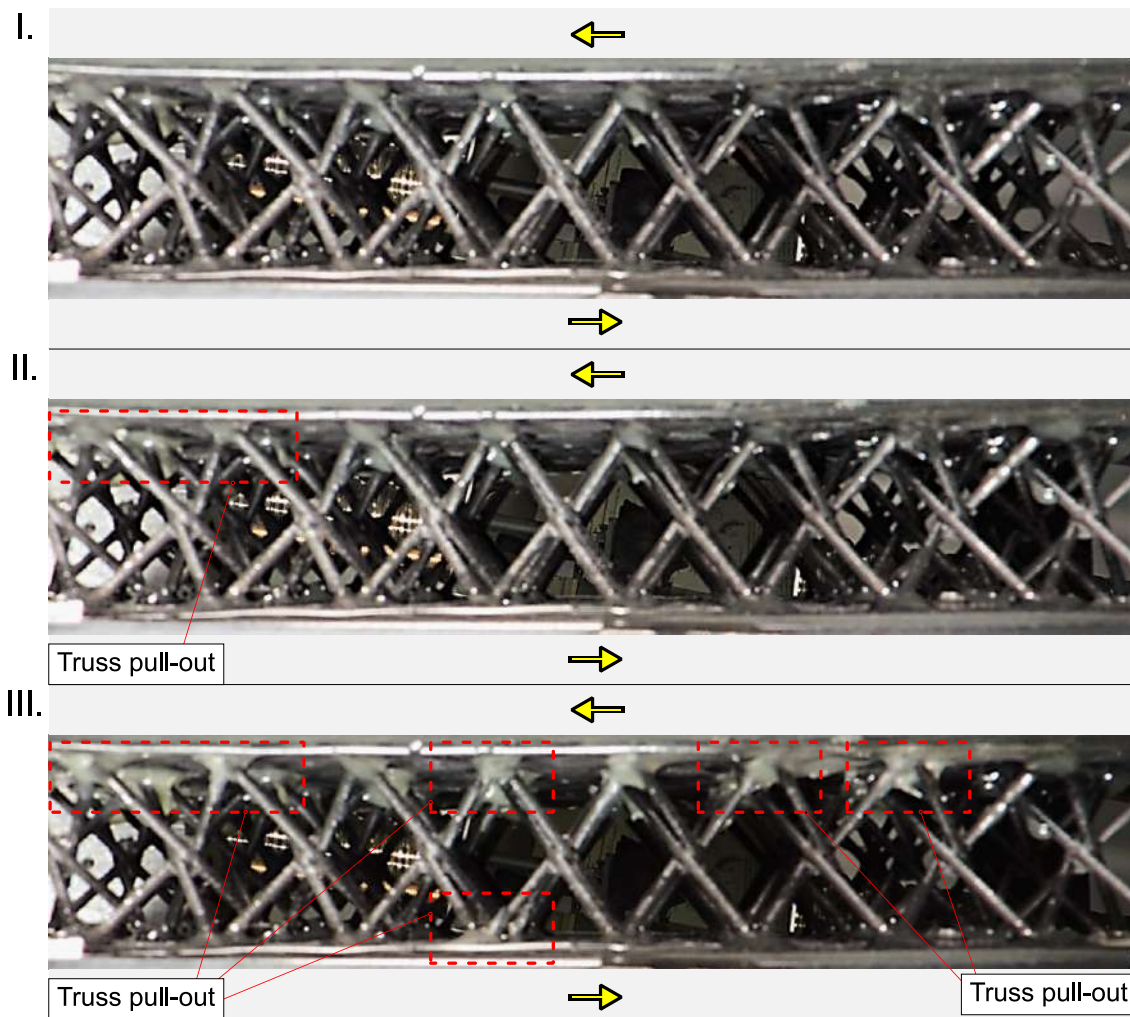


Figure 5.43. Photographs associated to selected points: shear behaviour of lattice-based core with 1.5 mm rods

A comparison chart for the best core response is given in Figure 5.44 for the shear stress tests of the lattice-based cores proposed. The maximum shear strengths are obtained in the range of 1.26 MPa – 1.45 MPa for diameters 1 mm and 1.5 mm, respectively. Although both curves are similar in behaviour, the slope of the 1.5 mm curve is the steepest, as result of its higher rigidity. After reaching the maximum strength, a sudden drop in the stress-strain response is seen as a consequence of a detachment of the rods from the skins. In contrast, the smallest rod shows a different response to the shear stress as the curve changes its slope after topping out a strength of 0.3 MPa. The stress is maintained along the straining, until the core members collapse due to buckling.

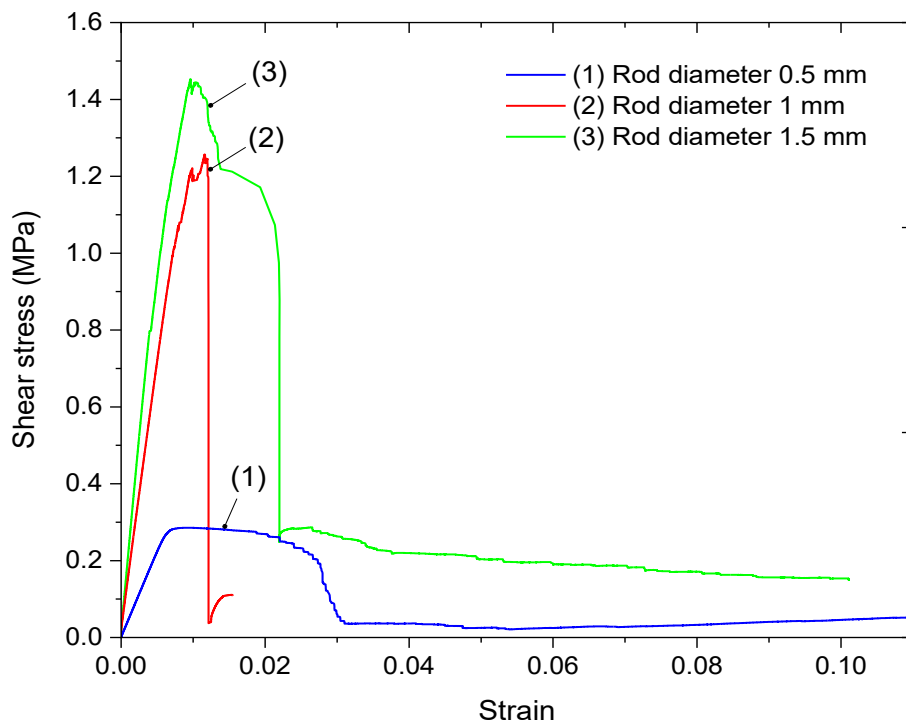


Figure 5.44. Shear stress–strain response of lattice-based cores

5.5.2.2 Discussion

After evaluating the mechanical response in shear, a model validation is carried out in this section. The dominant failure modes observed are Euler buckling and rod's pull-out as a case of debonding, both predicted successfully by the analytical and FE models with very good correspondence. Table 5.13 summarizes the shear strength and shear moduli obtained from the predictions and the experimental tests. The shear elastic moduli predictions are in very good correspondence. The main discrepancies compared to the experimental values are attributed to little manufacture imperfections. Considering the core shear strength, the predictions agree with the experimental results for the 1 mm and 1.5 mm cases.

However, a circumstantial difference between the predictions and the experimental data is observed for the 0.5 mm diameter case. The theoretical buckling models considered a base value $k = 0.7$. Looking at the numerical simulations, the k value would be closer to ≈ 0.6 (Figure 5.25.a), and it would be a hint to assume that the predictions underestimate the test results. Hence, to better accurate the models and obtain an average experimental Euler's factor k , the real failure loads are considered for the new calculations. Then, the failure loads are extracted from the experimental

data having an average failure load of ≈ 90 N per cell. Dividing it among the number of rods, employing Eq. (5.22), and equating for k , then $k \approx 0.5$.

Table 5.13. Resume of analytical, FEM and experimental results from shear tests

\emptyset (mm)	Analytical		Numerical		Experimental		Obs. mode
	τ_{cpk} (MPa)	G_c (MPa)	τ_{cpk} (MPa)	G_c (MPa)	τ_{cpk} (MPa)	G_c (MPa)	
0.5	0.136	49.58	0.159	49.52	0.29 ± 0.01	45.85 ± 1.13	BF
1	1.001	198.24	--	198.32	1.06 ± 0.19	137.015 ± 10.58	DB
1.5	1.507	447.46	--	447.36	1.36 ± 0.095	232.591 ± 29.61	DB

Notes: BF = buckling failure; DB = debonding failure

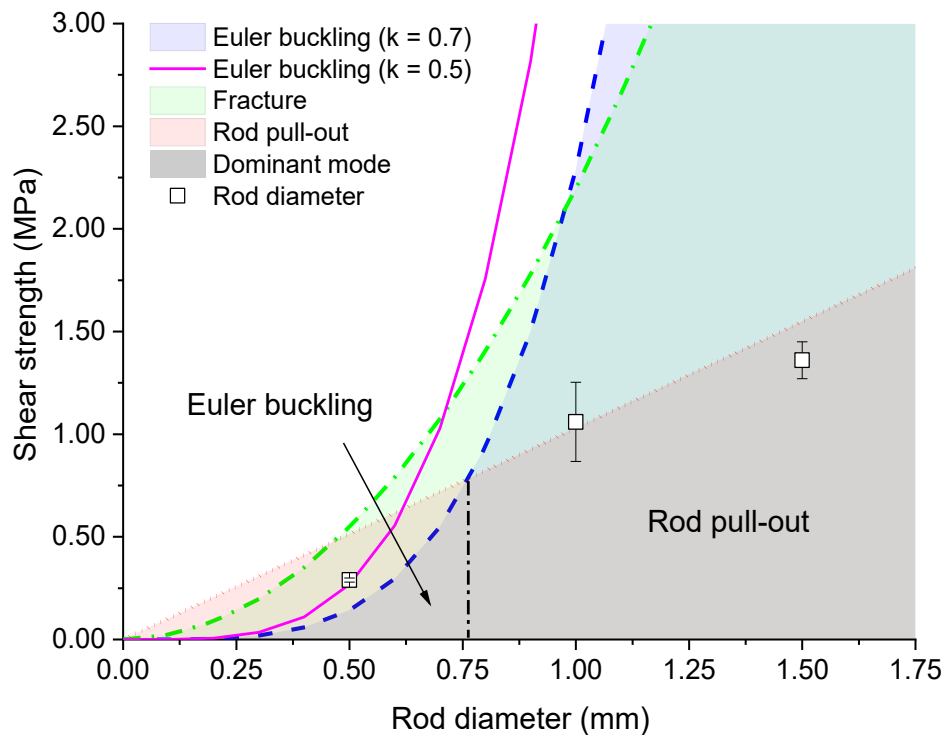


Figure 5.45. Resulting failure maps for shear stresses and experimental data

Recalling the failure maps due to shear loading (Figure 5.45), and incorporating the experimental data obtained for each rod case, the maps provide a further complement to the information presented in Table 5.13. The new curve for Eq. (5.39) but employing $k = 0.5$, is drawn as the magenta-continued line. Then, the point corresponding to rod diameter 0.5 mm, coincides with the analytical curve. Moreover, observing

the debonding strength, the models are in excellent correspondence to the experimental data, although little discrepancies are found on the top and lower values, on an average and constant gluing flank f of value 2 mm.

5.6 Concluding remarks

The design and study of different ultra-lightweight cores (core densities less than 48 kgm^{-3}) based on lattices is presented in this chapter. Three rods' diameters are taken as a basis for the study of analytical micro-mechanical models and complemented with numerical models. The peak mechanical strength to compression and shear is evaluated satisfactorily with very good correlation between the proposed models and experimental results. The little discrepancy detected is attributed to imperfections during the manufacturing of the samples, witnessed as premature local failures before the collapse of the structure. Furthermore, the failure maps for compressive and shear loading predicted satisfactorily the strength and failure mode exhibited by the cores, although further analyses shall be proposed for evaluating the entire map regions and validating more accurately the models.

As for the mechanical compression tests, average young moduli of 33.91 MPa, 267.8 MPa and 472.55 MPa, and maximum compressive strengths of 0.22 MPa, 2.87 MPa and 5.87 MPa are observed, for diameters of 0.5 mm, 1 mm, and 1.5 mm, respectively. The observed failure modes are attributed to Euler buckling for the smaller diameters and fracture of the rods for the largest.

With respect to the shear tests, an average peak shear modulus of 45.85 MPa, 137.015 MPa and 232.591 MPa, and shear strengths of 0.29 MPa, 1.06 MPa and 1.36 MPa are observed for rods' diameters of 0.5 mm, 1 mm, and 1.5 mm, respectively. In this case, the dominating failure modes are Euler buckling for the case of the 0.5 mm rods, and debonding (pull-out) between the skins and the core regarding to rods' diameters of 1 mm and 1.5 mm.

As observed in the numerical models, there is little difference in the displacement analysis either as a BCC or BCC-like structure. Actually, considering that the members in a BCC-like structure do not have a common coincident point (Fig. 5.2), this has an effect on the final stiffness of the rod's mid-plane in vertical and horizontal directions, and may differ slightly for each rod's diameter case, as predicted in the FE models. A way to adjust the k-value in the simulations is to provide torsion springs in the mid-

plane node, which constant could be obtained indirectly from the analytical results. Another way is to simulate the middle node with bars of different stiffness such that they resemble the experimentally observed behavior. However, a good starting point was to assume a Euler k -factor of ≈ 0.7 for the theoretical analysis of buckling failure. The observed values obtained indirectly by the numerical and experimental FE makes the value of k to better fit each rod and loading case, improving the analytical prediction of buckling failure, as in the case of Figure 5.45.

The next chapter explores the performance of these lattice-based core elements by incorporating them as part of a sandwich structure and analyzing them in a 4-point bending configuration to assess their suitability as a sandwich skin elastic bedding.

6 Ultra-lightweight sandwich panels: a case of study by four-point bending

As previously pointed out in Chapter 3, the interest in sandwich constructions have been risen in the past years, as a way to obtained lighter, stiffer, and stronger structures. The basic concept of a sandwich panel is presented as a lightweight core interposed between two thin, rigid skins. For the production of an efficient sandwich structure, the core must serve different purposes: resisting out-of-plane compression and shear loads, and stabilizing the thin faces against local buckling, giving the necessary support, as well as increasing the moment of inertia of the section [51,113,192]. The thinner the faces, the higher their buckling susceptibility.

The significance of this section lies in the effectiveness of the proposed cores as skin stabilizers in their application in sandwich panels, taking as an example of analysis the lattice-based cores (Chapter 5), and extrapolating the case for the 3D-honeycomb cores (Chapter 4). The loading case is selected as four-point bending, in a way to evaluate pure flexural properties of the sandwich panel, and at the same time, avoiding shear and compressive loads over the core, already evaluated in previous mentioned chapters.

Therefore, different face failure modes are presented and detailed, starting from the theory applied to the loading case and identifying failure modes as face wrinkling, intercellular buckling, and skin yielding. The agreement among the theory, FE simulations and tests turns out to be satisfactory.

6.1 Literature review

Several approaches for studying sandwich constructions appear in the literature regarding to their failure, and the most relevant are here reviewed. The theory of bending of sandwich panels is widely explained throughout different analytical models. The first models by Reissner [193] considered a homogeneous core sandwiched between two isotropic faces, both identical in thickness and properties.

Reissner assumed that the face-parallel stresses in the core and the variation of face stresses over the thickness of the faces are negligible, when the elastic moduli E and G of the core are small compared to the faces. Thus, he obtained the deflection

equations [194] and used them for solving a plate-buckling problem. Moreover, Hoff [195] made similar hypotheses and studied the buckling stress for rectangular sandwich panels subjected to edgewise compression. Hoff derived the differential equations obtained by virtual displacements and applied simply supported boundary conditions for obtaining the critical stresses for a family of curves as a function of a sandwich buckling parameter.

Plantema [196] and Allen [113] proportionated the early basic literature for understanding sandwich behaviour under bending. Sandwich panels treated as beams with different cores and faces configurations were studied to predict their most likely operative failure modes during bending, among other loading configurations. They identified the failure modes of sandwich panels, comprising different forms of elastic and plastic buckling, as local and global buckling, face yielding, and other failures attributed to the core (refer to Chapter 3). Petras [111] took the bases of Allen's theory and studied the failure modes of sandwich panels with different substrates and faces and identified three main causes of failure of faces depending on their cell size as intercellular buckling, face wrinkling and face yielding, during bending loading.

Likewise, within the framework of this thematic the author's previous publication [97] served as a prelude for determining the mechanical behaviour of traditional sandwich panels while bending, identifying the failure modes from determining in advance the failure loads of the sandwich components for different skin and core combinations. Following the insights provided by Petras and Triantafillou [144], traditional honeycomb cores made from natural fibres and polymeric foams, combined with glass and natural fibres skins were implemented. Based on this investigations, failure mode maps of the studied materials were drawn and validated for a density of 150 kgm^{-3} for different span configurations.

The purpose of this chapter is to include into the dissertation analyses the overall performance of the lattice-based cores proposed and applied to a sandwich panel, while evaluating their bending capabilities as an elastic substrate to the CFRP faces. The scope of the upcoming sections is divided according to the following aspects: the design and manufacture of the samples, the theoretical background complemented by FE models to obtain the material failure mode maps, experiments on four-point bending, and the discussion of results. The case is then extrapolated to the 3D-honeycomb cores studied, which is evaluated analytically and numerically. The buckling coefficients for the buckling failure modes are obtained from the models and compared to

the ones gained from the experimental tests. The results show the influence of the core material and faces rigidity for a skin-core combination and their expected failure modes, with very good correspondence.

6.2 Materials and design

For the validation of the proposed analytical models that describe the behaviour of sandwich materials of interest under bending, the experimental tests must be carried out. Therefore, specimens have been obtained to serve for the evaluation of flexural sandwich panels and are detailed in this section.

6.2.1 Materials

The base materials employed are the same as for the cores and faces introduced in Chapter 5. Therefore, sandwich panels are provided from the UniBwM labs having CFRP-based cores and faces.

Lattice-based cores made from three different CFRP rod diameters as 0.5 mm, 1 mm, and 1.5 mm, are employed. Additionally, faces are made from four and six layers of woven T300-3k (*Torayca*) carbon fibre 2/2 twill fabrics in a symmetrical $[0 - 90]^\circ$ setup. Epoxy resin and hardener “type L” (*R&G Faserverbundwerkstoffe GmbH*) are employed as the polymeric matrix. Furthermore, the theoretical mechanical properties of the cores and faces are resumed in Table 6.1, and Table 6.2, respectively. The coordinate reference is given in Figure 6.1.

Table 6.1. Theoretical mechanical properties of the lattice-based cores

\emptyset (mm)	ρ_c^* (kgm ⁻³)	E_{3c} (MPa)	σ_{3c} (MPa)	$G_{31c} = G_{32c}$ (MPa)	$\tau_{31c} = \tau_{32c}$ (MPa)
0.5	5.34	99.05	0.20*	49.58	0.136
1	21.34	396.89	3.09*	198.24	1.029
1.5	48.03	895.89	7.09	447.46	1.548

Note: (*) A Euler’s factor $k = 0.7$ is taken for the buckling theoretical calculations

Table 6.2. Theoretical mechanical properties of the CFRP faces

N_l (--)	t_f (mm)	ρ_f^* (gcm ⁻³)	φ_f (%)	$E_{2f} = E_{1f}$ (MPa)	G_{12f} (MPa)	$\nu_{12f} = \nu_{21f}$ (--)	$R_{2f}^- = R_{1f}^-$ (MPa)	R_{12f} (MPa)
4	0.8	1.485	55	67.78	4.06	0.028	527.44	110
6	1.21							

Note: subscript *s* represents the parent material

The faces' thicknesses are selected in a way to maintain the conditions of thin faces ($t_f \ll C$, referred to reference [110]) and still being technologically manufacturable as a quasi-monolithic structure in the form of a sandwich panel.

Therefore, the faces presented average thicknesses of $t_f = 0.8 \pm 0.05$ mm and $t_f = 1.21 \pm 0.04$ mm, while average densities of 1.422 gcm⁻³ and 1.440 gcm⁻³ both being measured in the laboratory, for a four- and six-layers' composites, respectively. The exhibited discrepancies between predictions and experimental results are attributable to imperfections as entrapped gas introduced during the manufacturing process.

In the case of the face material with four layers, an average fibre volume content of 55 % is obtained, and for the case of six layers, an average fibre volume content of 54.4 % is calculated. To lighten the theoretical and numerical calculations, it will be considered that both faces have on average ≈ 55 % of fibres, since they are found almost in the same value order. Then, the faces mechanical properties are pre-estimated based on the classical laminate theory (see Annex B for further details).

6.2.2 Bending sample design

The four-point bending sandwich specimen is designed in such a way that bending is evaluated by means of a constant flexural moment across the specimen's area of interest. The bending moment is obtained from two opposing supports located at a known distance from each other (i.e., the lever arm) and symmetrically arranged on each side of the sample (Figure 6.1).

Therefore, the shear loads are ideally placed over a reinforced core, in this case plywood, and the sample is subjected to tensile and compressive stresses on the outer facings due to the bending exerted. The objective of this section is to present the designed specimen used for the analytical and numerical calculations (Figure 6.1) to in-

investigate the failure behaviour of the sandwich configuration. The beam is simply supported on two bottom rests of diameter D_s , and the load is transmitted by two supports (or punches) of the same diameter on the top of the beam. The loads are schematically drawn as the red arrows over and under the supports.

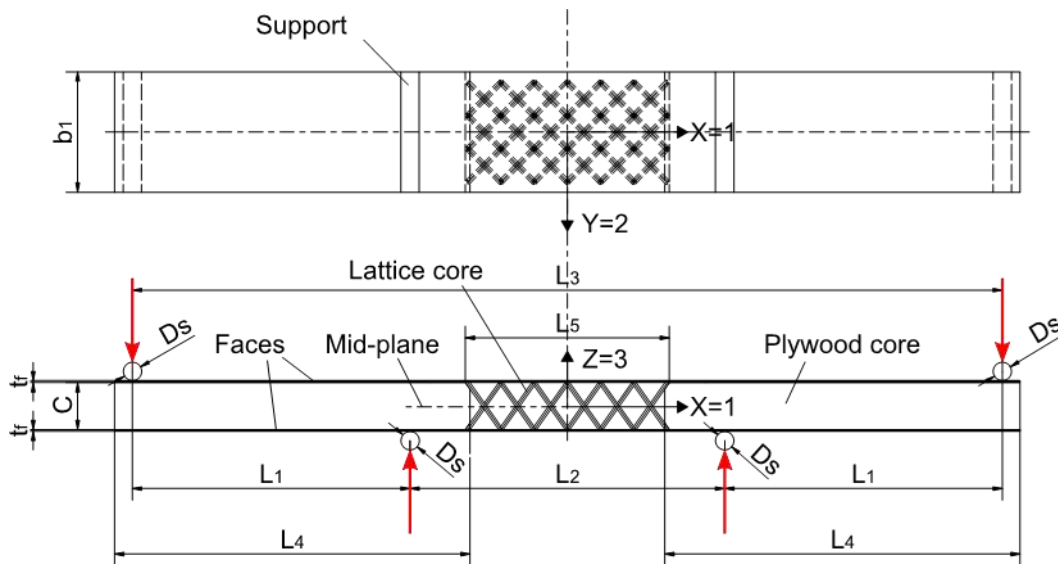
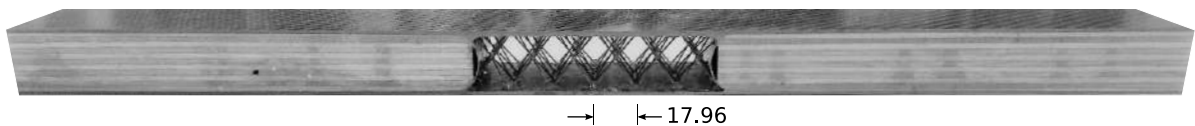
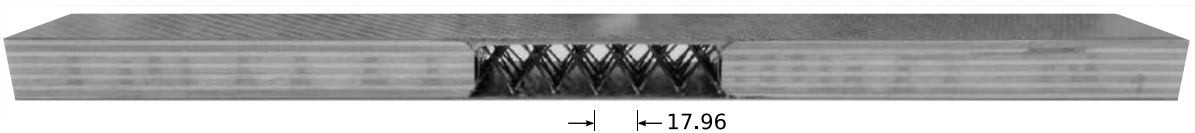


Figure 6.1. Sketch of the four-point bending sample proposed

(a) Rod diameter 0.5 mm



(b) Rod diameter 1 mm



(c) Rod diameter 1.5 mm

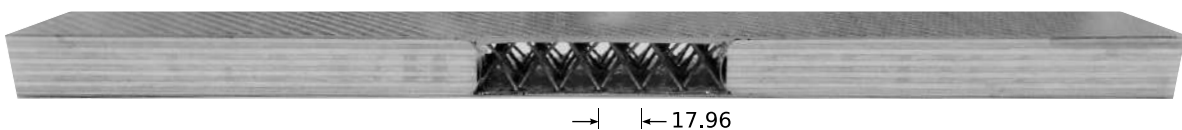


Figure 6.2. Photograph of bending samples of different lattice-cores' rod diameters

The specimen consists of a lattice-core of 25.4 mm of thickness, in an array of 6 x 3 unit cells. The faces and support plywood core are added and fixed to the assembly. The overall dimensions of the samples are of [490 x 65 x 27] mm and [490 x 65 x 27.82] mm. The samples attained for the different lattice-cores are shown in Figure 6.2.

Table 6.3. Overview of the geometric parameters and nominal dimensions employed

Rod diameter (mm)	C (mm)	t_f (mm)	L_1 (mm)	L_2 (mm)	L_3 (mm)	L_4 (mm)	L_5 (mm)	b_1 (mm)	D_s (mm)
0.5	25.4	1.21	150	170	470	192	110	65	50
1	25.4	0.8	150	170	470	192	110	65	50
1.5	25.4	0.8	150	170	470	192	110	65	50

The different parameters presented in Figure 6.1 are further examined in Table 6.3, having the core's different rods diameters as main factor. In all cases, the lever arm employed for the flexural moment is $L_1 = 150$ mm. The upper span in which the external load is applied, also known as the punch, is selected as of $L_3 = 470$ mm. The supports have a diameter of 50 mm, in order to avoid localized loads that could lead to local rupture.

6.3 Theoretical approach

Referring to Chapter 3, different are the failure modes that can occur in the faces of a sandwich structure depending on the loading case. In this section, four-point bending is analysed, it is proceeded first to interpret the state of load introduction and maximum displacement derived from geometrical studies. Such as the cases of open profile's torsional buckling stated in Chapter 4 or the Euler's rod buckling behaviour introduced in Chapter 5, other stability problems can also occur within supported plates that are subjected to compressive loads, e.g., face wrinkling or intracellular buckling.

Given the designed CFRP-based plates (Table 6.2), for calculations, faces will be considered as orthotropic plates with edges parallel to the orthotropic axes, subjected to axial stresses in tension or compression. Besides face yielding/fracture failure, other failure modes as local forms of instabilities as face wrinkling and intercellular buckling, will be introduced and described.

6.3.1 Loading case

The sketch of Figure 6.1 is simplified to a case of a beam subjected to four-point bending, and it is outlined in Figure 6.3. The straight (filled-line) and bended (dotted-curve) beam is shown, as well as the load introduction. Then, the load is applied by the testing machine as force P_z on the top of the beam and it is divided over two upper punches on points a and d . For the determination of the stresses and displacements caused by the external force over the sample, the shear and acting moment diagrams are drawn. Given the selected configuration, the shear stress does not affect the area of interest of the beam (segment \overline{bc}) where the lattice core is located. Then, the applied force is transmitted to the beam as a constant bending moment, between the supports b and c .

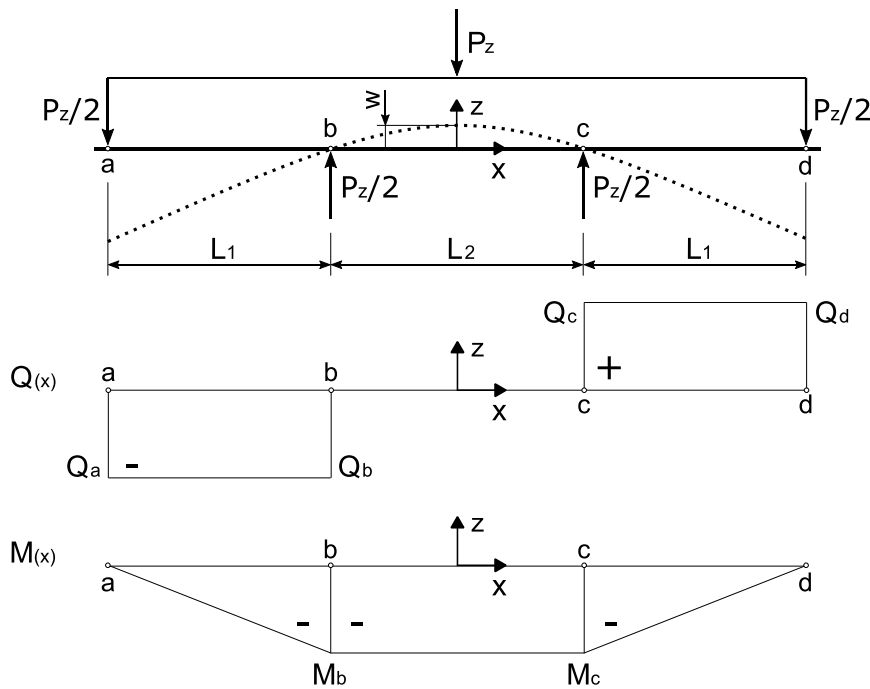


Figure 6.3. Sketch of the shear and flexural moment diagrams of a beam in a four-point bending case

The maximal shear and moment values from the diagrams are given by Eq.(5.1), Eq. (6.2) and Eq. (6.3), respectively.

$$Q_a = Q_d = -\frac{P_z}{2} \quad (6.1)$$

$$Q_b = Q_c = \frac{P_z}{2} \quad (6.2)$$

$$M_b = M_c = -\frac{P_z}{2} L_1 \quad (6.3)$$

Taking a portion of the beam between the support links as an example, the beam modelled for load analyses is sketched as the diagram given in Figure 6.4.

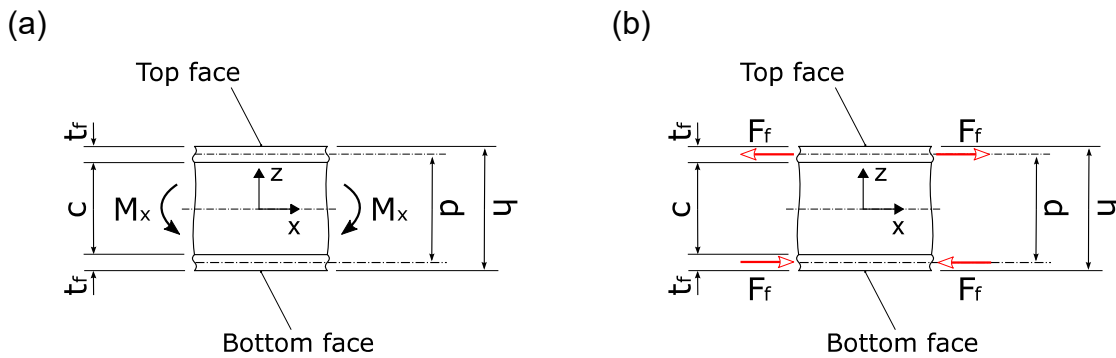


Figure 6.4. Scheme of a portion of a beam with the decomposition of the flexural moment into forces on the skins

Considering the study configuration, due to the transmission of the moment M_x , the top skin is subjected to a tensile load F_f and the lower skin to compression load F_f , both of same value, but in opposite directions. This description will then be used to analyse the different expected failure modes. Then, considering thin faces ($t_f \ll C$), simplifications such as constant stresses through the face thicknesses are also allowed (see Chapter 3). Thus, the forces are applied to the mid-planes of each top and bottom faces, as they are considered of little thickness. The relation between the load on the faces and the bending moment is given by Eq. (6.4). Then, solving for P_z , the applied load is defined in terms of load over the faces as Eq. (6.5).

$$F_f = \frac{M_x}{d} = \frac{P_z L_1}{2 d} \quad (6.4)$$

$$P_z = \frac{2dF_f}{L_1} \quad (6.5)$$

$$\sigma_{1f} = \frac{F_f}{b_1 t_f} = \frac{P_z L_1}{2 d b_1 t_f} \quad (6.6)$$

The stress on the faces σ_{1f} is defined by Eq. (6.6), as the force applied to the faces divided by the face cross-section. Analogously, Eq.(6.6) is attainable from another point of view, for the case of the beam subjected to a bending moment M_x (Figure 6.4). The bending stress σ_{xx} is then the stress applied normal to the face thickness σ_{1f} , assuming thin plates, as given in Eq.(6.7).

$$\sigma_{1f} = \sigma_{xx} = \frac{M_x E_{1f} d}{2D_x} \quad (6.7)$$

Where D_x is given by Eq. (6.8), also assuming thin faces as $t_f \ll C$ and a weak core as $E_{3c} \ll E_{1f}$ as seen in Chapter 3.

$$D_x \approx E_{1f} \frac{b_1 t_f d^2}{2} \quad (6.8)$$

Introducing Eq. (6.4) and Eq. (6.8) into Eq. (6.7), then Eq. (6.9) is attained, and confirming Eq. (6.6).

$$\sigma_{1f} = \frac{P_z L_1}{2b_1 t_f d} \quad (6.9)$$

6.3.2 Maximum displacement

The maximum displacement w between supports b and c can be quantified at the equilibrium configuration, considering a fictitious unit-load at the site and direction of interest. It is also found in the literature as the *unit-load method*, [67,169]. The method is implemented by defining the acting forces on the beam, both real (subscript “0”) and fictitious (subscript “1”) given by Eq. (6.10)

$$w = \int \frac{M_0 M_1}{EI} dx \quad (6.10)$$

Since the beam is made up of different materials such as the core and the skins, the flexural stiffness EI is replaced by its equivalent D_x given by Eq. (6.8), assuming thin faces and a weak core, as previously pointed-out.

Solving for the present case, the maximum displacement w is given by Eq. (6.11) (see Annex E for the complete procedure).

$$w = \frac{P_z L_1}{16 D_x} (L_3 - 2L_1)^2 = \frac{P_z L_1}{16 D_x} (L_2)^2 \quad (6.11)$$

6.3.3 Failure modes, loads and stresses

The sandwich panels failure under four-point bending loading is attributed to in-plane loads at the end of the faces, being one of them subjected to tensile loads and the other one to compressive loads (Figure 6.4) as a consequence of the flexural moment applied. It will be considered that the compressed face is the critical one for evaluating failure. Then, the govern failure modes are expected as: (a) face yielding, (b) face wrinkling and (c) intracellular buckling, and they are introduced within this section [51,111,113] (Figure 6.5).

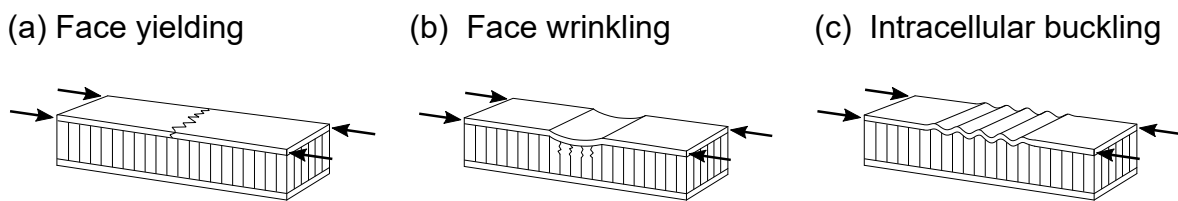


Figure 6.5. Failure modes of sandwich faces considered

Since the material properties of the constituent materials are given, the failure load can be analytically addressed, and are described within this section [51]. In this work, it is assumed a linear-elastic material behaviour and that the sandwich beams bend in a cylindrical manner [113]. The faces are loaded as consequence of the bending moment M_x due to the applied load P_z as shown in Eq. (6.4) and Eq. (6.5). Thus, the failure load will be also presented in terms of applied load P_z . Therefore, failure loads comprise the above failure modes as face yielding P_{ZY} , wrinkling P_{ZW} , and intercellular buckling P_{ZIB} . The acting failure mode is given by the lowest critical load applied P_{Zcrit} as shown in Eq. (6.12).

$$P_{Zcrit} = \min(P_{ZY}, P_{ZW}, P_{ZIB}) \quad (6.12)$$

6.3.3.1 Face yielding

Sandwich panel skins may fail due to a tensile or compressive stress. If the compressive face is considered as critical for the analysis, the failure of the plate under compressive loading could be attributed, in some cases and under certain conditions (e.g., boundary constraints, face thickness, type of support, among others) to a

strength failure and not to elastic instabilities. Then, the failure of the skin due to yielding (Figure 6.5.a) is expected when the applied stress σ_{1f} reaches the maximum allowable in-plane strength (R_{1s}^-), either as yield stress or fracture stress of the face's base material as given in Eq. (6.13) [51].

$$\sigma_{1f_{crit}} \geq R_{1s}^- \quad (6.13)$$

In this work, faces are made from composite materials based on woven carbon fibre cloth and epoxy resin. Since the composite tensile strength is considered to be larger than the compressive strength, the compressed face is then taken as the critical face. Therefore, assuming that the failure of the plate in compression is due to strength, different failure mechanisms can occur depending on the approximation criteria (chapter 2) [56]. Here, Budiansky's criteria is selected to obtain the maximum compressive strength of the base material (Annex B) [57].

Recalling Eq. (6.9) and considering the critical stress, when the maximum in-plane strength is reached (Eq. (6.13)), the critical stress on the face due to yielding is given by Eq. (6.14).

$$\sigma_{1f_{crit}} = \sigma_{1fY} = \frac{P_z L_1}{2b_1 t_f d} \geq R_{1s}^- \quad (6.14)$$

Solving the last expression for P_z , the critical applied load considering face yielding failure mode is given by Eq. (6.15).

$$P_{ZY} = \frac{R_{1s}^- 2b_1 t_f d}{L_1} \quad (6.15)$$

6.3.3.2 Face wrinkling

A long, thin, and rigid plate subjected to compression stresses may experience instability or local buckling phenomena (Figure 6.6) [197]. One of the local buckling cases on sandwich panels is attributed to wrinkling of the face sheet. This failure mode is associated with elastic buckling of faces exhibiting short buckling waves (Figure 6.5.b), although not confined to individual unit cells when using prismatic cores [198]. The wrinkles are correlated to periodic waves of a wavelength that depends upon the material properties and other geometrical parameters as core and face thicknesses [51,199].

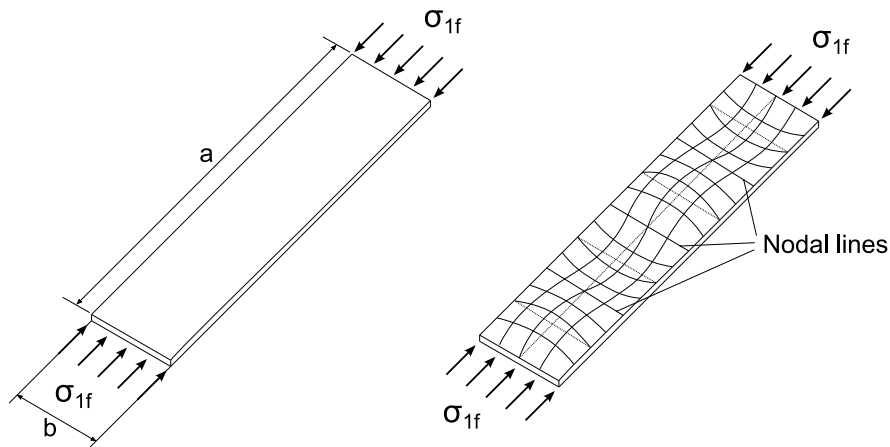
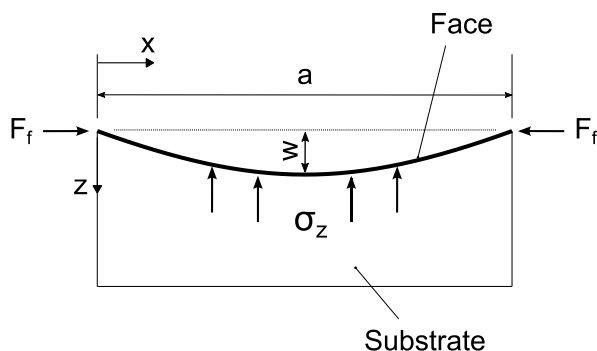


Figure 6.6. Plate under compressive in-plane stress before and after buckling

Face wrinkling on sandwich panels can be seen as the buckling of a thin column supported by a continuous elastic medium such as the core that offers a support pressure σ_z (Figure 6.7, adapted from [200]). The wrinkle occurs perpendicular to the principal acting stress.

(a) Wrinkling wave sketch



(b) Winkler foundation: rigid case

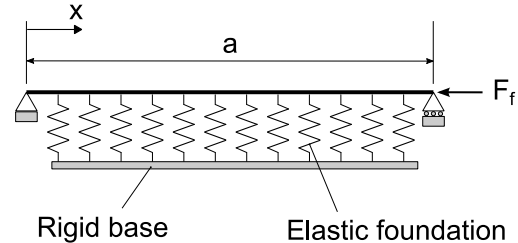


Figure 6.7. Face wrinkling wave and Winkler foundation

The simplest model is based on a Winkler's foundation model, which is established on a series of linear tension-compression springs of a known elastic constant and spaced a certain distance. Then, the foundation stiffness K_z is the ratio given in Eq. (6.16) [51].

$$K_z = \frac{2E_{3c}}{C} \quad (6.16)$$

There are different wrinkling cases depending on the geometry of the sandwich panel and base material features [200]. The rigid base wrinkling case refers to a case

in which one face is subjected to a compressive stress (Figure 6.7.b), denoting a sandwich panel loaded in bending, as in the present work. By neglecting the shear deformation in the skin and core while assuming thin faces and very low core Young's modulus in x -direction (e.g., an orthotropic core such as a honeycomb core), the expression in Eq. (6.17) represents the formulation for the critical stress on the face that results from Winkler's approach [51], where Q_b is a dimensionless buckling coefficient, in which $Q_b = 0.8165$ for this case.

$$\sigma_{1fcrit} = Q_b \sqrt{\frac{E_{3c} E_f t_f}{C}} \quad (6.17)$$

For providing better practical means for the prediction of face wrinkling, a coefficient $Q_b = 0.33$ is selected to offer a proper safer design value for practical purposes [198]. The substantial difference between above Q_b values are attributed when imperfections are considered.

If the core is assumed to be isotropic, other wrinkling models may be employed, such as the Hoff's approach [201]. Hoff takes into account the shear stress in the core, whose method calculates the strain energy stored on the core and the face. Then, the critical face stress using an isotropic cores and faces is given by Eq. (6.18), and a factor $Q_b = 0.91$ is reached for this case.

$$\sigma_{1fcrit} = \sigma_{1fW_iso} = Q_b \sqrt[3]{E_{3c} E_f G_{12c}} \quad (6.18)$$

On the other hand, Allen [113] derived a formula from calculating the differential equation of a homogeneous beam. If isotropic cores and faces are to be considered, the same formula as Eq. (6.18) was obtained, although a Q_b factor of 0.78 was attained [51]. However, as indicated in references [51,198], in the practice a safer design factor $Q_b = 0.5$ was derived to better accurate experimental tests and the theory developed taking in consideration imperfections, and the formula in Eq. (6.18) turns to be more conservative when the latter Q_b value is applied.

Therefore, the formulations for face wrinkling determination depend mainly on the type of cores, faces, and the buckling coefficient Q_b may vary from [0.33 – 0.86] and [0.5 – 0.91] for orthotropic and isotropic cores, respectively (Table 6.4). In addition, it is observed in Table 6.4 that the skins employed for analyses are isotropic in all the

cases. As noticed in the reference [202], if anisotropic faces are to be used, the orientation angles of the fibres must be considered on the failure load calculations. The procedure of the transformation of coordinates considering the orientation angles is given in Annex E.

Table 6.4. Brief literature review on different buckling coefficient values

Method/ author	Reference	Core type	Face type	Buckling coefficient Q_b	
				Eq. (6.17)	Eq. (6.18)
Winkler	[51]	Orthotropic	Isotropic	0.8165*	--
Bartelds	[203]	Orthotropic	Isotropic	0.8600*	--
Sullins	[198]	Orthotropic/ Isotropic	Isotropic	0.3300**	0.500**
Hoff	[201]	Isotropic	Isotropic	--	0.910*
Platema	[51]	Isotropic	Isotropic	--	0.825*
Allen	[113]	Isotropic	Isotropic	--	0.780*

Notes: (*) Theoretical values. (**) Estimated values considering imperfections

The failure stress under Winkler's approach is set by Eq. (6.19), when orthotropic cores and orthotropic homogeneous faces are employed. The constant factors are expressed as a part of the buckling coefficient Q_b .

$$\sigma_{1fcrit} = \sigma_{1fW} = Q_b \sqrt{\frac{E_{3c}E_{1f}t_f}{C}} \quad (6.19)$$

It is interesting to remark, that the last expression is equivalent to Eq. (6.17) for isotropic faces. In another case, if thin inhomogeneous faces are to be employed, the flexural rigidity of the laid-up laminate (i.e., stacking-up UD-laminas) shall be taken as well from the classical laminate theory as the [D]-matrix or the bending stiffness matrix (Chapter 2).

The proposed cores made of lattices resemble an orthotropic core, closer to the characteristics of a corrugated core than a foam in terms of skin foundation, when considering the free spaces where the skin lacks on support. The faces resulted in an orthotropic material with a symmetrical lay-up of woven fabrics aligned with the global coordinate system. Hence, the expression given by Eq. (6.19) for orthotropic cores and faces will be employed for face wrinkling studies. Moreover, the buckling coefficient Q_b must be also determined, and which can vary between 0.33 - 0.86 if one recalls Table

6.4. Therefore, the stress on the face as given in Eq. (6.9) is then equated to Eq. (6.19) to obtain the critical stress on the skin as Eq. (6.20).

$$\sigma_{1fcrit} = \frac{P_z L_1}{2b_1 t_f d} = Q_b \sqrt{\frac{E_{3c} E_{1f} t_f}{C}} \quad (6.20)$$

Solving Eq. (6.20) for P_z , the critical applied load considering face wrinkling failure mode is given by Eq.(6.21).

$$P_{ZW} = Q_b \sqrt{\frac{E_{3c} E_{1f} t_f}{C} \frac{2b_1 t_f d}{L_1}} \quad (6.21)$$

6.3.3.3 Intracellular buckling

When sandwich panels with corrugated or honeycomb cores are employed, the core does not constitute a continuous support, i.e., there are areas of the face where the core does not offer any foundation nor support to it. If the face buckling wavelength is equal or smaller to the cell size, another localized buckling mode may take part in the form of so-called intracellular buckling (also known as face dimpling). In this case, the facings buckle inwards or outwards the unit cell, such in a plate-like way with the cells walls acting as the edge supports [51,198].

The effect of intracellular buckling is more evident when using, for example, square-cell cores made of large cell sizes (Figure 6.8.a). In general, for honeycomb cores an empirical formula as Eq. (6.22) have been given by Norris [204] for obtaining the critical stress on the compressed isotropic face, employing a characteristic dimension as the cell size in form of the diameter of their inscribed circle S_c .

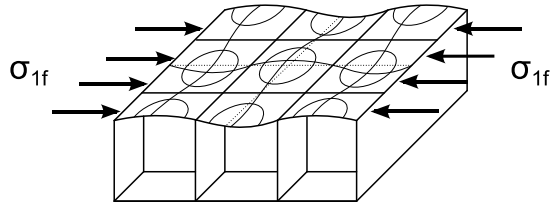
$$\sigma_{1fcrit} = \frac{2E_f}{1 - \nu_{12f}^2} \left(\frac{2t_f}{S_c} \right)^2 \quad (6.22)$$

Nevertheless, when cores with open cells are employed such as corrugated cores (Figure 6.8.b), the intracellular buckling may take place in the part of the sheet contained within the corrugation.

For orthotropic faces with edges parallel to the orthotropic axes, the case is simplified into a plate of certain dimensions under compressive line loads p_x on two ends, and subjected to edge conditions, represented by a tabulated factor K . Then, the

expression in Eq.(6.23) is employed for estimating the critical line load p_{xfcrit} on the face [68], assuming a plate that bends cylindrically.

(a) Square-cells core



(b) Corrugated core

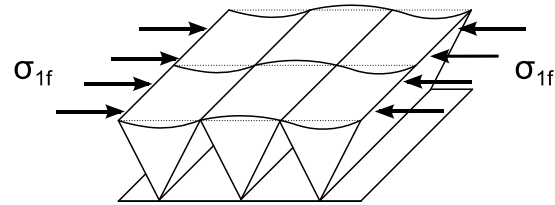


Figure 6.8. Intracellular buckling shapes on different cellular cores [205]

$$p_{xfcrit} = K\pi^2 \frac{\sqrt{B_{xf}B_{yf}}}{b^2} \quad (6.23)$$

$$B_{xf} = \frac{E_{1f}t_f^3}{12(1 - \nu_{12f}^2)} \quad (6.24)$$

$$B_{yf} = \frac{E_{2f}t_f^3}{12(1 - \nu_{12f}^2)} \quad (6.25)$$

Where B_{xf} and B_{yf} are the bending stiffnesses of the plate in x- and y-direction, respectively. The latter formulation is also expressed in terms of critical stress as Eq. (6.26).

$$\sigma_{1fcrit} = \sigma_{1fIB} = K \frac{\pi^2 \sqrt{E_{1f}E_{2f}}}{12(1 - \nu_{12f}^2)} \left(\frac{t_f}{b}\right)^2 \quad (6.26)$$

The factor K in Eq. (6.26) is presented on Annex E for different border conditions cases along plate edges, for isotropic and orthotropic plates [171,173]. For example, when using square orthotropic plates, K values are found of 2.2 ⁽⁴⁾ for all edges simple supported, and of 4.6 for loaded edges clamped and unloaded edges simply supported. As previously stated, since the composite faces are made from a woven carbon fibre cloth oriented $[0/90]^\circ$ they are treated as orthotropic. Thus, for evaluating intracellular buckling, the formula given by Eq. (6.26) will be considered for calculations.

⁽⁴⁾ The value is attained for length / width ratios $\frac{L}{W} = 1$. If infinite long plates are assumed, the K values converge to a value ≈ 2

Hence, equating Eq. (6.9) and Eq. (6.26), the critical stress on the compressed face sheet is determined by Eq. (6.27). The general expression for the cell's width b is replaced by the width W (or cell size) used in this work.

$$\sigma_{1fcrit} = \frac{P_z L_1}{2b_1 t_f d} = K \frac{\pi^2 \sqrt{E_{1f} E_{2f}}}{12(1 - \nu_{12f}^2)} \left(\frac{t_f}{W}\right)^2 \quad (6.27)$$

Solving Eq. (6.27) for the applied load P_z , the expression for evaluating intercellular buckling failure of the face sheet is given by Eq. (6.28).

$$P_{ZIB} = K \frac{\pi^2 \sqrt{E_{1f} E_{2f}}}{6(1 - \nu_{12f}^2)} \left(\frac{t_f}{W}\right)^2 \frac{b_1 t_f d}{L_1} \quad (6.28)$$

In this work, the core unit cells are square, and so is their projection on the top and bottom face planes. The faces are made from orthotropic plates. Since the face portion at the top of the unit cells are only supported at their corners by the CFRP rods as punctual supports and not along their edges (Figure 6.9), no representative tabulated K values are found in the literature. However, a seed K value of 2.2 (see Annex E) will be employed for the analytical calculations as starting point.

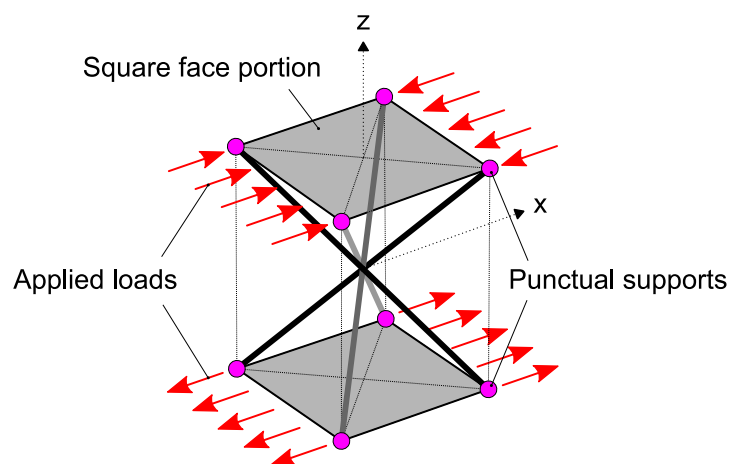


Figure 6.9. Sketch of unit cell projections to face planes and punctual supports

6.3.3.4 Analytical results

A summary of the analytical results are detailed in the Table 6.5 for failure stress predictions. The calculations are made employing Eq. (6.14) for face yielding failure mode, Eq. (6.19) for face wrinkling, and Eq. (6.26) for intracellular buckling. The parameters employed are also given, employing a core thickness $C = 25.4$ mm in all

cases. The minimum stresses and thus, the failure modes with high probability to occur are face wrinkling for core / skin combination of 0.5 mm lattices and $t_f = 1.21$ mm, and intracellular buckling for the lattice cores of 1 mm and 1.5 mm rods combined with $t_f = 0.8$ mm skins.

Table 6.5. Summary of face critical stresses from analytical predictions

\emptyset (mm)	t_f (mm)	E_{3c} (MPa)	$\frac{E_{1f}}{E_{2f}}$ (GPa)	$\frac{\nu_{1f}}{\nu_{2f}}$ (--)	b (mm)	d (mm)	K (--)	Q_b (--)	σ_{1fY} (MPa)	σ_{1fW} (MPa)	σ_{1fIB} (MPa)
0.5	1.21	99.05	67.78	0.028	17.96	26.61	--	0.33	527.4	185.2	547.9
1	0.8	396.89	67.78	0.028	17.96	26.20	2.2	--	527.4	303.7	243.1
1.5	0.8	895.89	67.78	0.028	17.96	26.20	2.2	--	527.4	456.3	243.1

6.3.3.5 Principal failure mode charts

Since there are several parameters to be evaluated for studying the failure of sandwich panels subjected to bending, the main failure modes of the different lattice cores and proposed skins are plotted within this section.

The calculations are carried out employing the formulations for each failure mode shown within this section, employing the data extracted from Table 6.1, Table 6.2 and Table 6.3. Recommended base values of $Q_b = 0.33$ for face wrinkling, and $K = 2.2$ for intercellular buckling will be considered. Later, these values will be better approximated for each case extracted from the FE simulations and then, from the experimental data in upcoming sections. The different combinations of core and faces studied are presented as follows, and the summary of results is shown in Table 6.5.

As an additional analysis also necessary for the experimental tests, it is proposed for avoiding an undesired premature shear rupture of the support part where the plywood core is located (Figure 6.1 and Figure 6.2), an average plywood shear strength value $\tau_{pw} \approx 5$ MPa is also taken into account [206].

Hence, recalling Eq. (4.62) and solving for the applied load P_Z , the maximum applied load without shear failure of the plywood support (P_{Zpw}) is calculated according to Eq. (6.29).

$$P_{Zpw} = \frac{4}{3} b_1 C \tau_{pw} \quad (6.29)$$

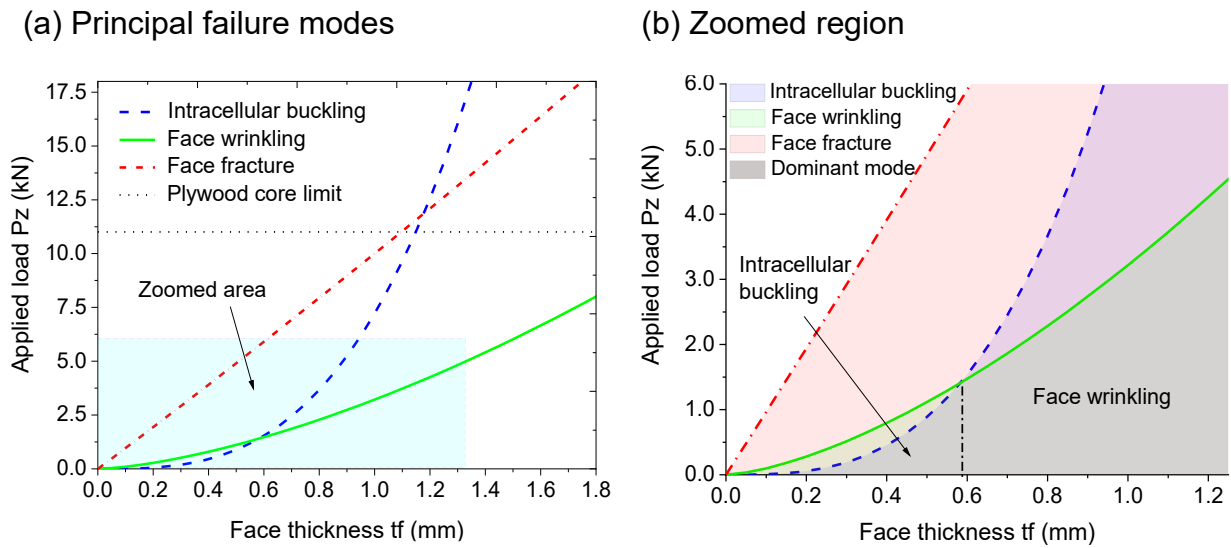


Figure 6.10. Principal failure modes for case 1: lattice-core made from 0.5 mm rods during four-point bending

The first case analysed corresponds to the core made from 0.5 mm rods (Figure 6.10). The face fracture curve shows a linear development as a function of skin thickness. In addition, the intracellular buckling failure curve presents grade 3 polynomial distribution, while face wrinkling is a potential curve to the $3/2$ power. The transition line or failure mode change occurs for skin thicknesses of about ≈ 0.6 mm, indicating that for the current case of $\tau_f = 1.21$ mm, the expected failure mode would be due to face wrinkling exhibiting an approximate theoretical value of 4.3 kN.

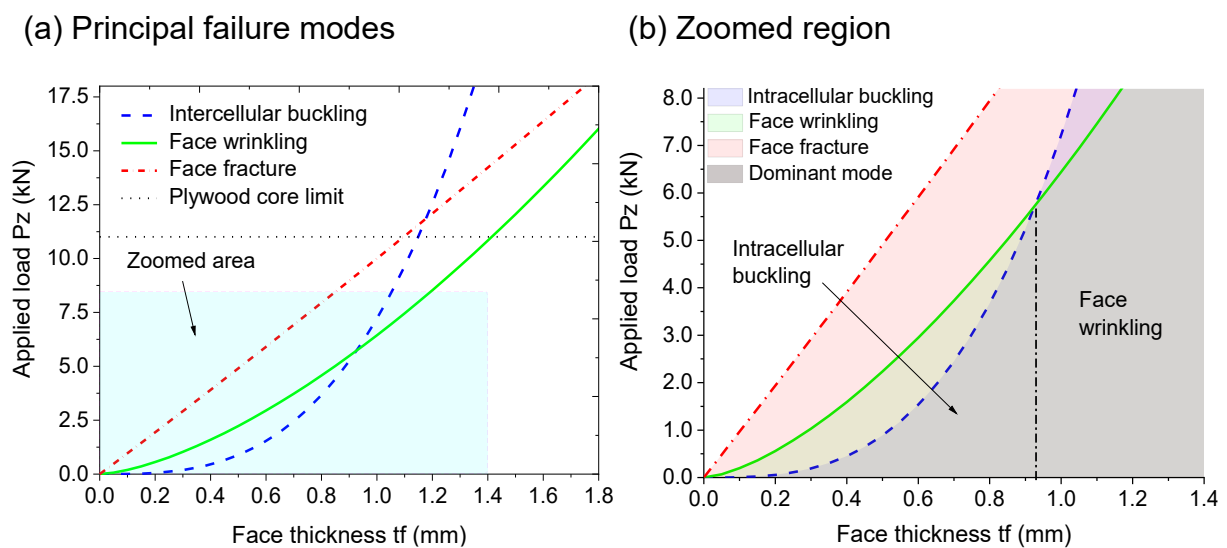


Figure 6.11. Principal failure modes for case 2: lattice-core made from 1 mm rods during four-point bending

Figure 6.11 presents a change on the failure regions compared to Figure 6.10 due to the higher out-of-plane stiffness of the core made from 1 mm rods (case 1: $E_c = 99$ MPa, while case 2, $E_c = 396$ MPa, see Table 6.1). Higher core stiffness directly affects the skin support, causing the face wrinkling behaviour to shift upwards. This effect changes the failure mode from intracellular buckling to face wrinkling, as of skin thicknesses of about 0.9 mm. Comparing the last two figures, the change in failure mode due to a stiffer core, for example, raises the maximum applied failure load from 2.75 kN to 5.25 kN, for a $\tau_f \approx 0.9$ mm. For the current proposed case of $\tau_f = 0.8$ mm, intracellular buckling failure mode is predicted at a maximum applied load of 3.6 kN.

The case presented in Figure 6.12 shows the failure mode predictions for the lattice-core made from 1.5 mm rods. As stated in previous analysis, a bigger rod diameter size influences the core out-of-plane rigidity, and regarding this case ($E_c = 895$ MPa) also influences the face wrinkling behaviour. The face wrinkling curve shifts upwards as well, and the failure mode changes by a face thickness of $\tau_f \approx 1.17$ mm, from intracellular buckling face fracture. However, the predictions also estimate that a premature shear failure of the plywood support would be attained previous to any face failure, for face thicknesses above $\tau_f \approx 1.15$ mm. The latter shall mean that a higher shear strength support core would be necessary for tests under this kind of core-skin combinations.

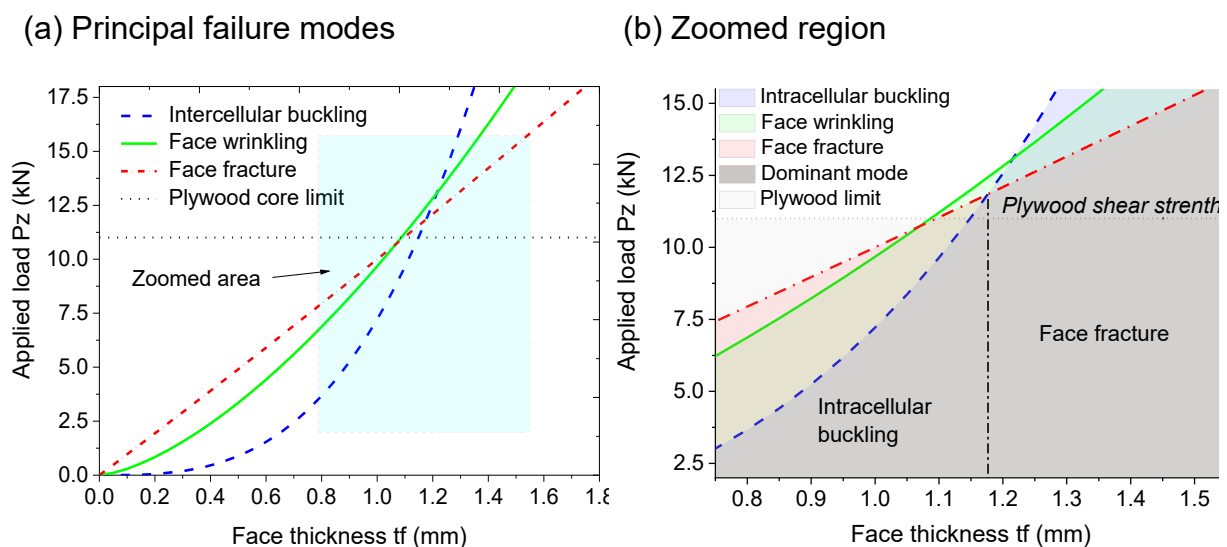


Figure 6.12. Principal failure modes for case 3: lattice-core made from 1.5 mm rods during four-point bending

Nevertheless, for the present case of $\tau_f = 0.8$ mm, intracellular buckling failure mode is predicted, and a maximum applied load of 3.6 kN, the same value as for Figure 6.11 case. Remarkably, the intracellular buckling is not affected by the rigidity of the core, under the plotted theoretical analyses (i.e., a K constant factor of 2.2) and assuming that the in-plane core rigidity is almost zero. If one refers to the real case, small local variations of skin stiffness at the contact points (Figure 6.9) can affect the overall K value of intracellular buckling, which would lead to small variations in the expected face failure load for the lattice-core cases of 1 mm and 1.5 mm rods, but with the same skin thickness. As said, this K value can be obtained indirectly from numerical models and experimental tests. As a summary of the stresses predicted on the compressed skins, the different curves according to Eq.(6.14), Eq. (6.19) and Eq. (6.26) are presented in Figure 6.13. The different lattice core employed are identified by the rod's diameters as 0.5 mm, 1 mm, and 1.5 mm. The stress curves variation is different from the latter curves expressed for the applied stresses, as a function of the skin thickness and their mathematical relations. However, the meeting points between curves are expected to be the same, indicating a change in failure mode. Thus, the meeting points remains the same as $\tau_f \approx 0.6$ mm, $\tau_f \approx 0.9$ mm and $\tau_f \approx 1.17$ mm, as previously stated.

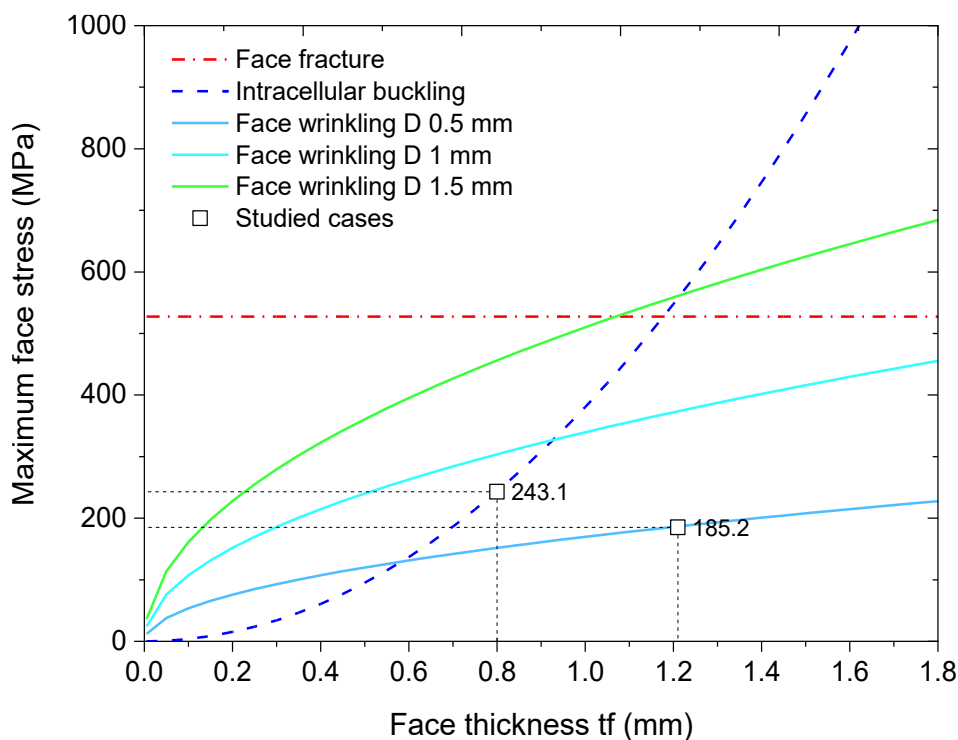


Figure 6.13. Failure stresses predictions on the face under compression

The curve representing face fracture failure (i.e., a strength failure) is common to each core case and it is represented by a constant line regarding to the face thicknesses. When buckling behaviour is considered into the calculations, the variations of the stress curves as a function of the face thickness is no longer constant. Under intracellular buckling behaviour (blue-dashed curve, in Figure 6.13), a common curve is drawn for each core case as a result of employing the same unit cell size and the same K factor for each core case as a seed value. In the reality, this may present little variations that affect the calculations. Moreover, different stress curves for face wrinkling behaviour (full-line curves, in Figure 6.13) are found for the lattice-core made from 0.5 mm, 1 mm, and 1.5 mm rod diameters, given that the core's out-of-plane rigidity increases with the rod diameter. Depending on the failure case, it is possible to observe variations on the maximum reachable stress for a determined face thickness. As an example, omitting the shear effects over the plywood supports and taking a $\tau_f = 1.2$ mm under the proposed conditions, this would represent a failure due to face wrinkling at 185 MPa, and 372 MPa for the 0.5 mm and 1 mm rod-based cores, respectively, but a failure by fracture for the 1.5 mm lattice-core reaching the face maximum strength of 527 MPa. This last example shows the influence of the core on the face failure behaviour predicted by the model. Remarkably, a failure due to face wrinkling may also be seen as a failure of the foundation.

6.4 FE approach

To complement the analytical predictions for the selected combinations of core-faces, finite element simulations were carried out. The FE simulations were performed using commercial FEMAP™ 10.3 with NX™ Nastran [29]. Employing the equations from the theoretical models (Eq. (6.19) and Eq. (6.26)) and the stresses attained at the instability step from the non-linear simulations, the buckling coefficients for face wrinkling Q_b , and for intercellular buckling K were indirectly obtained.

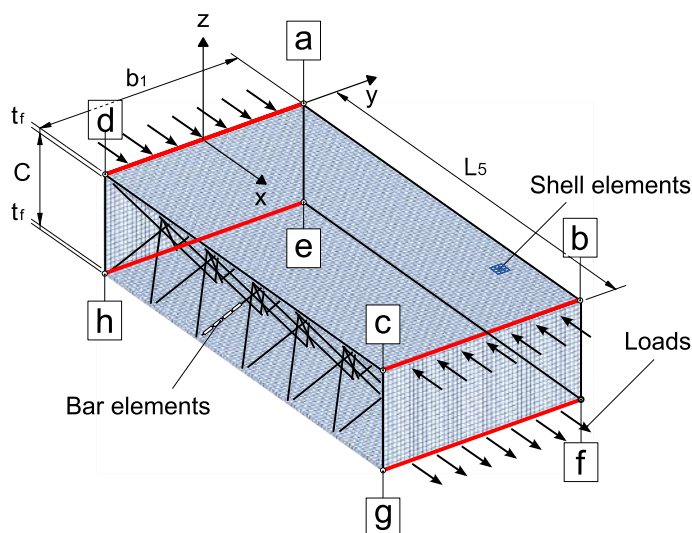
6.4.1 Model

A 3D model of the proposed sandwich panel is presented on Figure 6.14, drawn following the base sketch of Figure 6.1. The unit cell has the basic morphology as shown in Figure 5.4 (Chapter 5), and it's repeated in an array of 6 x 3 representing the

core's structure. The mid-plane node of the unit cells where the rods meet, is simulated by a connection of bars (Figure 5.11, Chapter 5). The lattice structures are discretized using 1D-bar elements (CBAR) and 48 elements per rod. The lattices are connected to the skins at each rod's end as a single node merged, assuming to be perfectly bonded. The top and bottom skins are simulated by 2D-shell elements (CQUAD4). The model takes the base material properties shown in Table 5.1 for the rods, and Table 6.2 for the web.

Linear in-plane loads of 1 kN/mm along the width of the upper and lower faces in compression and tension, respectively, are considered for the introduction of loads. For the transmission of the applied moment and to avoid local deformations such as relative displacements between plates and to maintain the cylindrical bending condition, the top and bottom skins are joined from a web of the same material and elements on each side of the panel. In addition, to avoid unwanted edge effects such as deformations induced by local displacements at the nodes of the skins where the forces are applied, linear rigid elements are placed along segments *a-d*, *b-c*, *e-h*, and *f-g* (Figure 6.14).

(a) Model



(b) Constraints references

Segment	Constraints
<i>a-b</i>	x-rotation
<i>d-c</i>	x-rotation
<i>e-h</i>	translation constrained
<i>f-g</i>	y-translation z-translation

Figure 6.14. Model sketch employed for finite element simulations

The boundary conditions were selected in a way to better represent the buckling behaviour within the sandwich panel. Normally, non-linear simulations stop when the model becomes unstable while analysing buckling behaviour and the equilibrium is not attained. Plates simulations under compression often exhibit edge effects that cause a

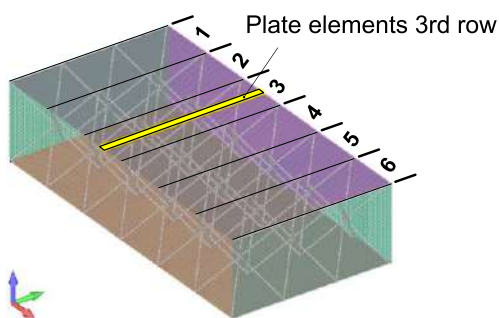
premature stop of the simulation, in many cases, before reaching the expected buckling value. To avoid undesired edge effects, the rotation, for example, in x -direction can be locked on the a - b and d - c segments. The constraints are referenced in Figure 6.14. No boundary conditions were introduced for the rest of the segments.

6.4.2 Analysed cases

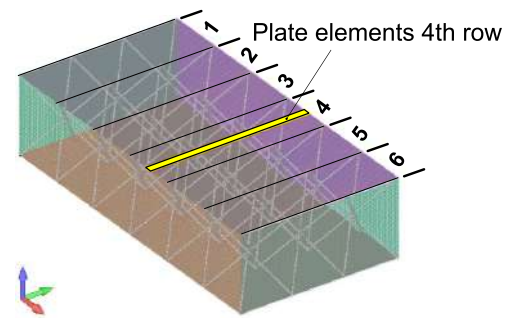
The results of the FE simulations carried out are presented in this section. The models used as basic morphology are similar to Figure 6.14, but adapting them for each lattice-core rod's diameter, and considering the face thickness for each core-face case proposed on Table 6.3. Examples on reference points for data collecting are given in Figure 6.15, in which plate-elements, rod-elements and/or nodes data are recorded.

In this section, the deformation of the renderings of each case is not the actual but scaled and enlarged to better see the contour exhibited by the strained model.

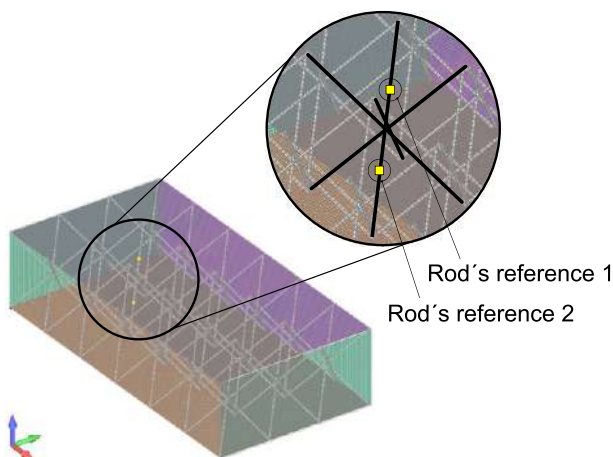
(a) Plate's reference



(b) Plate's reference



(c) Rod's reference



(d) Plate's reference

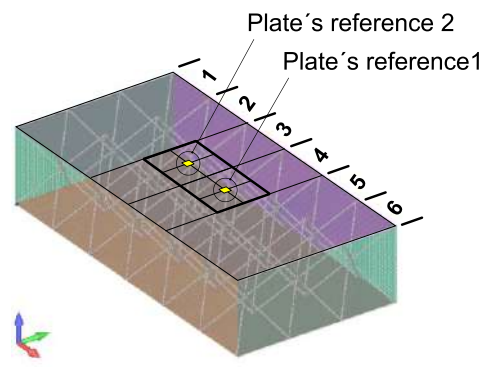


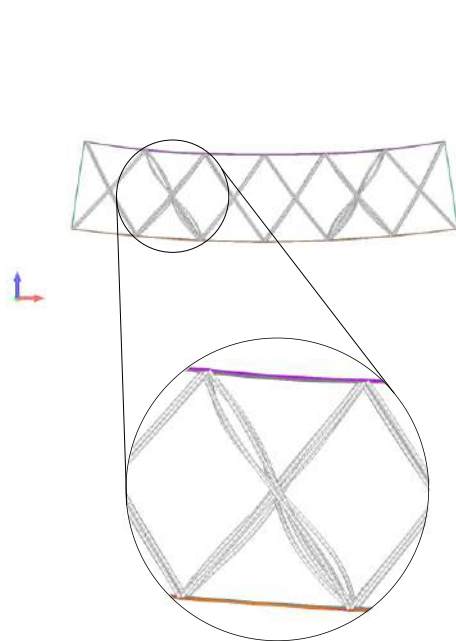
Figure 6.15. Example of benchmarks for data recording

6.4.2.1 Lattice-core made from 0.5 mm rods diameter and skins thickness of 1.2 mm

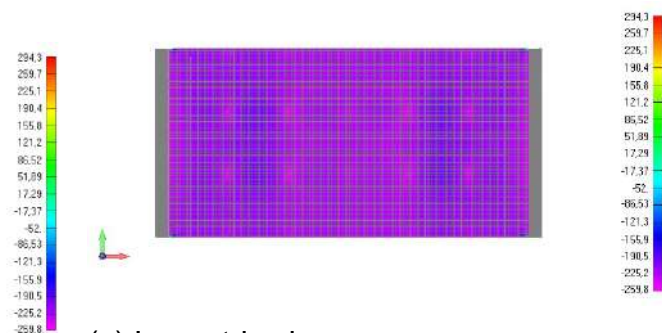
Figure 6.16 shows the results obtained from the simulation at the last step, through as the step at which the simulation stops, for the lattice-core with the 0.5 mm rods, simulating a four-point bending test. At a first instance, it is not possible to infer which buckling case is represented, whether a case of buckling due to face wrinkling or to intracellular buckling.

However, when zooming in to Figure 6.16.a, the enlarged image shows a buckled rod, and it could be inferred that actually the core is the part that fails, caused by the deformation of the skin which produced an out-of-plane load on the core, very similar to the wrinkling case presented by Figure 6.7, where the elastic foundation cannot give any further support to the plate above.

(a) Front view and zoomed area



(b) Top view



(c) Isometric view

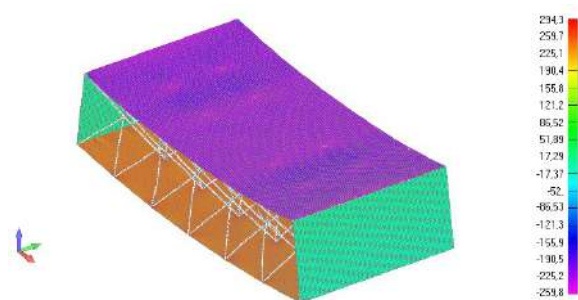
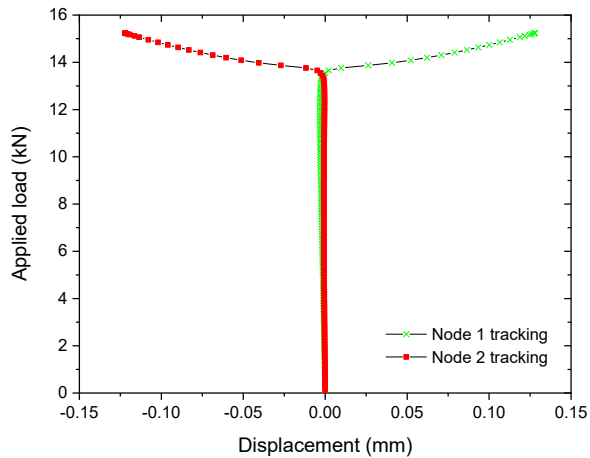


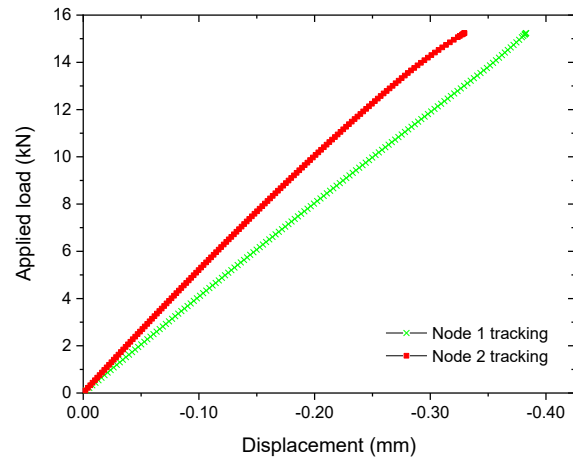
Figure 6.16. Different views obtained from the simulations for lattice-core 0.5 mm rods, and face thickness 1.2 mm. *Contour:* plate top X normal stress at last step

Nevertheless, further information also gives support to the failure mode that is observed. Thus, the displacements of the nodes are graphically characterized by node tracking, besides the load on the bar-nodes and the stresses on the plate-elements, on Figure 6.17.

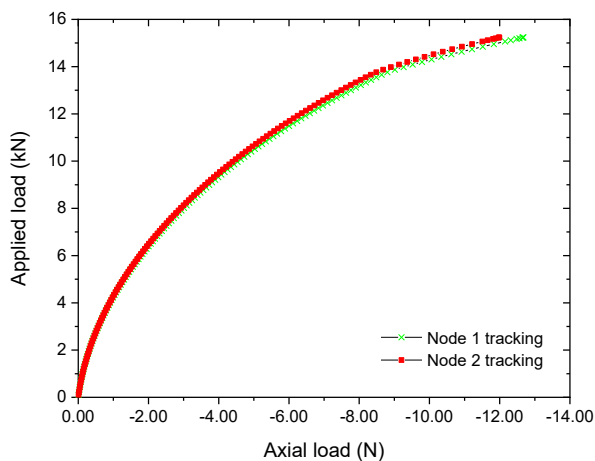
(a) Rod's node displacement tracking



(b) Plate's node displacement tracking



(c) Rod's axial load



(d) Plate X normal stress at instability step

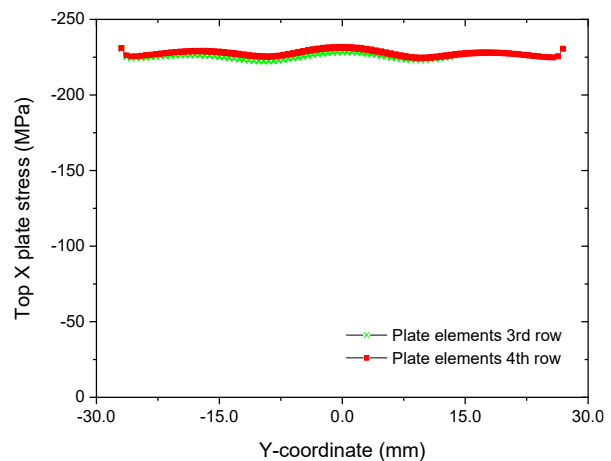


Figure 6.17. Simulation results extracted at benchmarks for lattice-core 0.5 mm rods, and face thickness 1.2 mm

Regarding to Figure 6.17a. and Figure 6.17.b, the node's displacement tracking is presented as of y-direction and of z-direction, respectively. In both cases, an instability behaviour starting from 13.68 kN and stopping at 15.23 kN of the applied load being the latter, the last step acquired. Both values are found pretty similar. The curves development shows a typical rod-buckling behaviour towards Euler's buckling (refer to Chapters 2 and 5), while the plate's nodes present a little variation from the linear behaviour. Furthermore, recalling Eq. (2.63) and employing a Euler's factor of $k \approx 1$ an axial critical load for the rods of 10.79 N is attained, which is found closer to the value witnessed on Figure 6.17.c. Although it is true that the rods are embedded in the skins at both ends, nevertheless the skins are free to move and rotate, causing the same

behaviour to be transferred to the rods at the point of linkage. Leaving aside the local stiffness of the connecting link, a $k \approx 1$ can still be assumed as a good approximation for the control calculations. However, the FE k -factor is, rigorously and indirectly calculated as $k \approx 0.95$, employing the FE failure axial load (from the last step, a rod axial load of 12 N is used for the calculation) and Eq. (2.63). Thus, taking into account the observations mentioned above, the panel failure is predicted as a face wrinkling failure mode, caused by the collapse of the foundation.

The stresses obtained from the top-plate elements at the instability step (where the buckling begins) are on average 230 MPa in compression (Figure 6.17.d), with small variations around this value, due to changes in the local stiffness of the skins caused by the influence of the rods, and boundary conditions. To have a broader view of the skin stresses obtained from the simulations, Figure 6.18 shows the x-normal stresses of the upper skin at the last step. The stress distribution is then influenced by the presence of the rods causing the stresses to decrease slightly from the average, and to increase in the intracellular zones. The stresses are found to be higher in the middle region of the plate, with points of stress concentration in the presence of the rods.

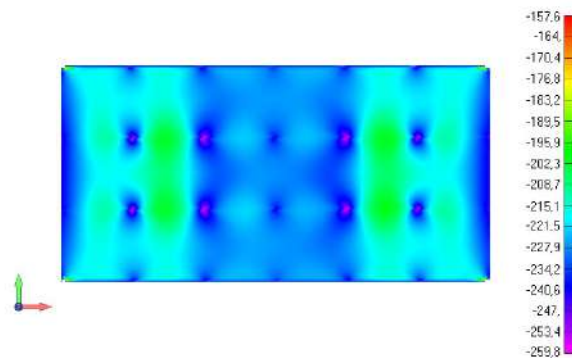


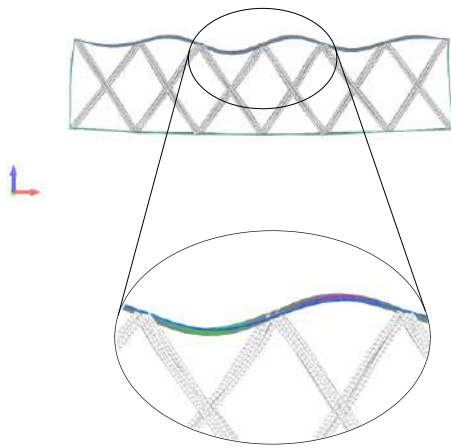
Figure 6.18. Top X normal stress of the face under compressive loads at last step

6.4.2.2 Lattice core made from 1 mm rods diameter and skins thickness of 0.8 mm

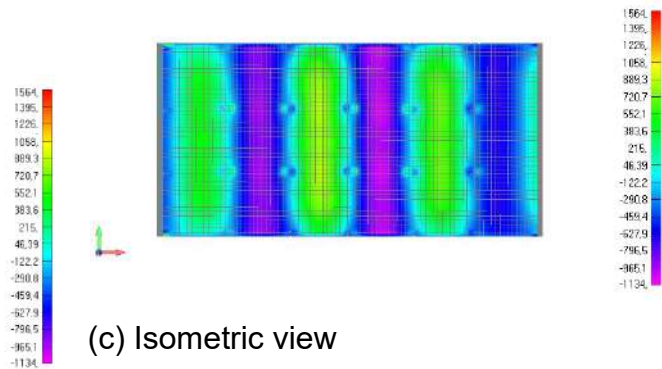
Figure 6.19 presents the results obtained for the case of cores made from 1mm diameter rods and 0.8 mm thick skins. The difference with the previous case is notorious, and directly from the images it is possible to identify the change in the failure mode, for thinner skin thicknesses. The case is evidenced as intracellular buckling, where the morphology of the skin is manifested as a wave inward and outwards of the unit cell, presenting the maximum stresses distributed in the middle of the panel. As

seen on Figure 6.20, one face's wave is stressed in compression and the other in tension.

(a) Front view and zoomed area



(b) Top view



(c) Isometric view

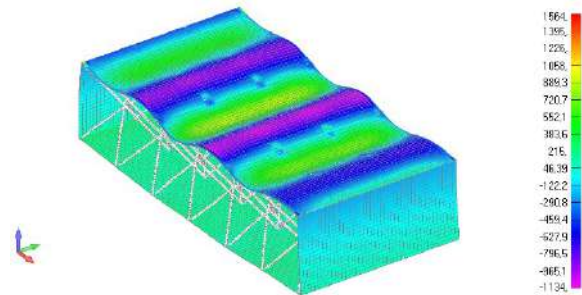
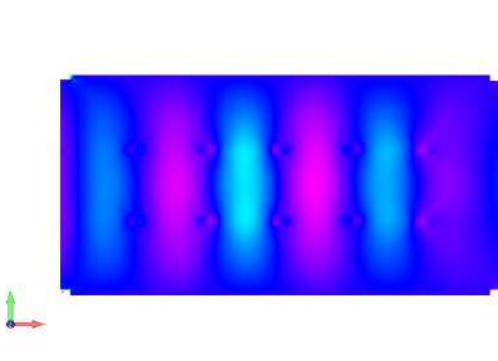


Figure 6.19. Different views obtained from the simulations for lattice-core 1 mm rods, and face thickness 0.8 mm. *Contour*: plate top X normal stress at last step

(a) Instability step



(b) Last step

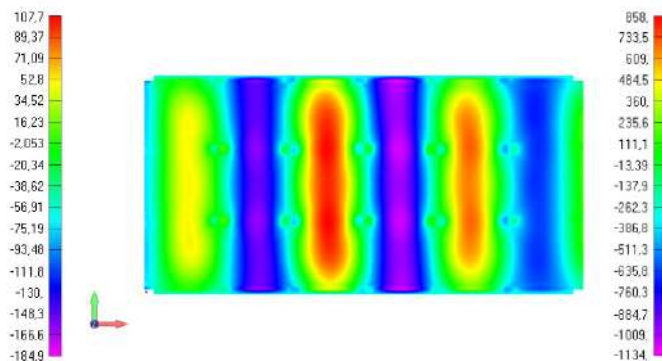


Figure 6.20. Top X normal stresses on the top face at different time steps

Additionally, the stress distribution on the third and fourth row of plate elements, previously referenced in Figure 6.15, is shown in Figure 6.21. The influence of the local stiffness provided by the rods in the connection area with the skin, makes the stress distribution to present a slight variation for each average stress, and on each side of the edges due to the imposed boundary conditions. Nonlinear simulations are set not

restricted to a maximum stress value, therefore, the stresses viewed in the last step are extremely high. In the real case, the skin, or the bond between skin-core, could be broken long before reaching these maxima. The stress representation at the last step should be taken just as an example of the stress distribution across the width of the upper skin. The compressive instability stress is of an average value of 175 MPa, considering the plate middle elements (third and fourth row).

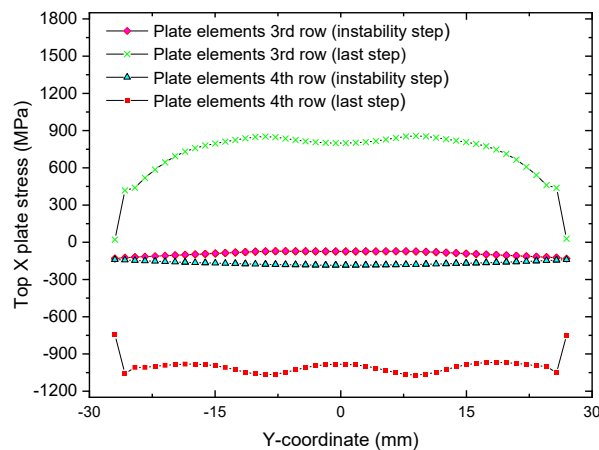
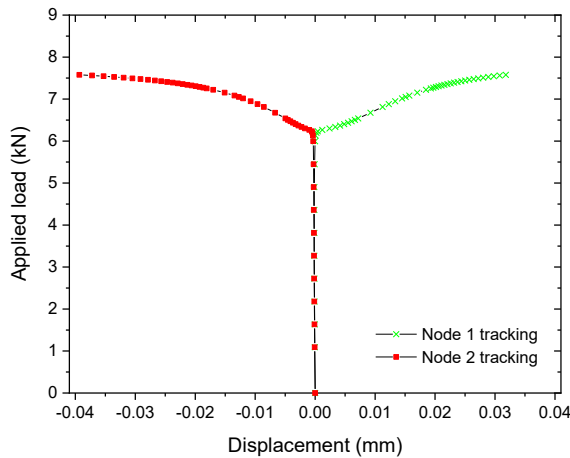


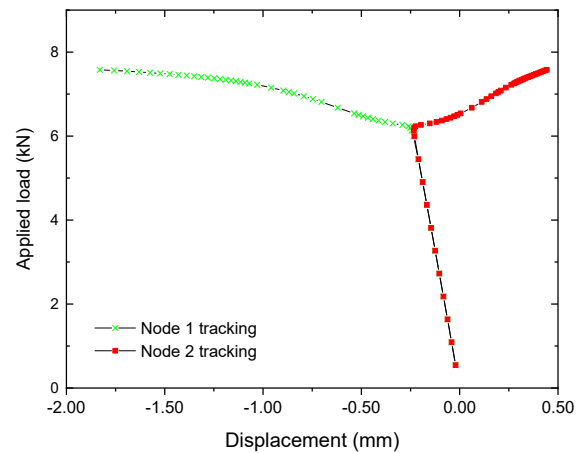
Figure 6.21. Stress distribution at reference points on the top skin at the beginning of instabilization and at the last step

From the node's displacements charts, it is difficult to infer which kind of buckling mode is attained, although the point of instability is found around 6.3 kN and continues until the simulation stops at 7.6 kN of applied load (Figure 6.22.a and Figure 6.22.b). However, referring to the scale of both tracking, the displacements are much larger at the plate-nodes than at the rod-nodes, i.e., the plate's deformation is larger and, in principle, it would drag the rods pulling or pushing them with it, explaining the small displacements of the rod-nodes that are detected (Figure 6.22.d). In terms of axial load on the bars (Figure 6.22.c), a force of 4 N in compression arises as a consequence of the load applied at the starting point of instability, close to 6.3 kN of applied load and then a bifurcation occurs, indicating a change in the direction of the axial force (compression and tension) comparing both nodes. This change in the axial loading is attributed to the effect of the plate buckling over the rods. The theoretical failure load employing Euler's buckling formula (Eq. (2.63) and $k \approx 1$) is around 172 N, indicating that the failure will not occur in the form of rod's buckling (i.e., a force of 4 N is attained while the critical load is then 172 N). Under all these statements, it can be inferred that the failure will result from buckling of the skin as intracellular buckling mode.

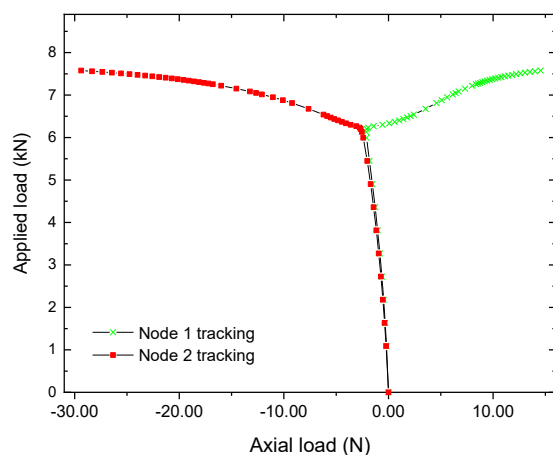
(a) Rod's node displacement tracking



(b) Plate's node displacement tracking



(c) Rod's axial load



(d) Rod and plate's node displacement tracking

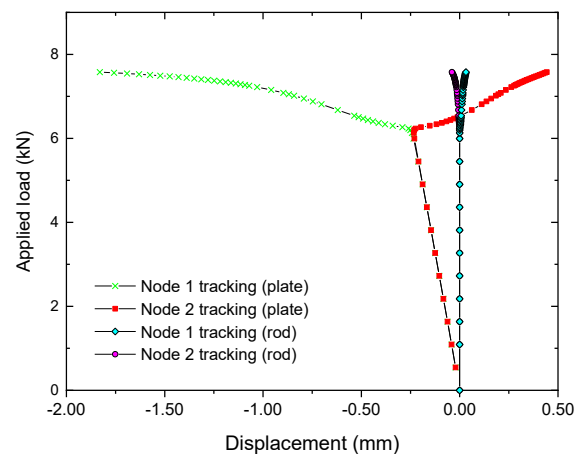


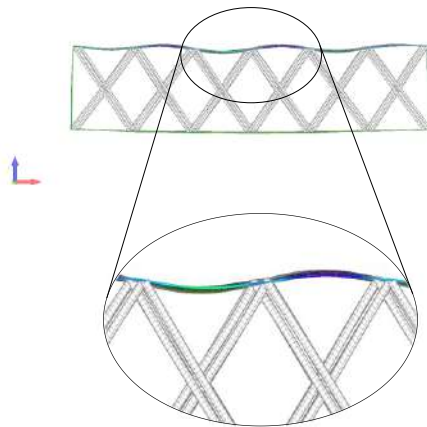
Figure 6.22. Simulation results extracted at benchmarks for lattice-core 1 mm rods, and face thickness 0.8 mm

6.4.2.3 Lattice core made from 1.5 mm rods diameter and skins thickness of 0.8 mm

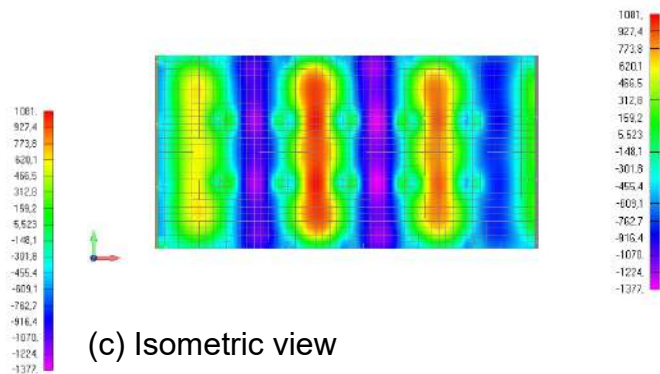
Similar to the previous study, Figure 6.23 represents a case of intracellular buckling with the naked eye. The face ripples are noticeable between cells, having the highest top X-plate stress in the middle region of the panel.

The effect of the rods on the skin is also evident, indicating a change in the distribution of stresses due to a change in the local stiffness of the connection point, as in the previous cases. Taking into account the middle array of cells along the panel ($y = 0$ region regarding to Figure 6.14), a noticeable effect is evidenced in which the stresses are higher than in the rest of the cells (Figure 6.24).

(a) Front view and zoomed area



(b) Top view



(c) Isometric view

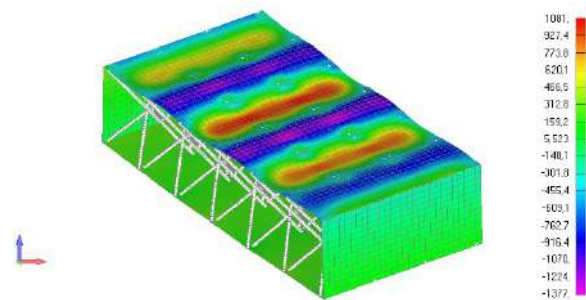
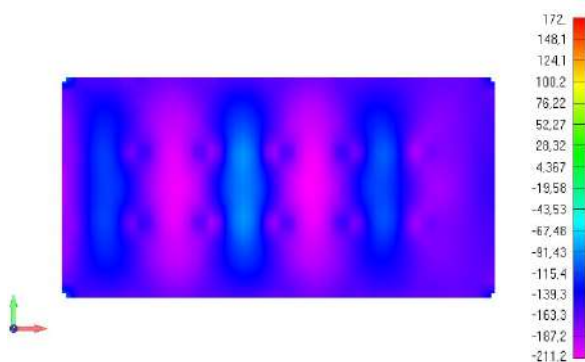


Figure 6.23. Different views obtained from the simulations for lattice-core 1.5 mm rods, and face thickness 0.8 mm. *Contour*: plate top X normal stress at last step

(a) Instability step



(b) Last step

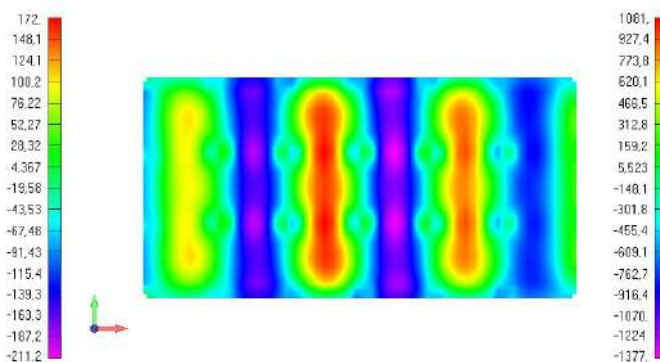
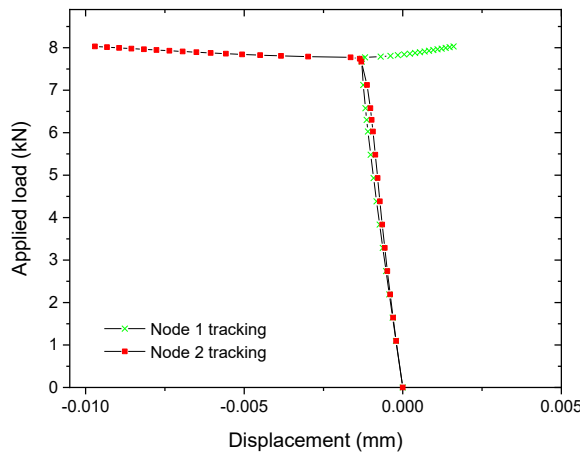


Figure 6.24. Top X normal stresses on the top face at different time steps

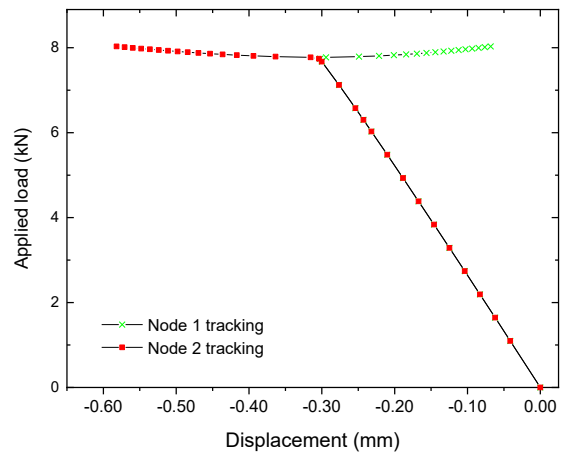
Taking as reference Figure 6.14 and Figure 6.15, the unit cells that belongs to the third and fourth rows and they are found on the region in which $y = 0$, present four rods for each core-skin linkage point (unit cell vertices), and not one or two as nearby the plate borders. On a first instance, it can be inferred that when using 1.5 mm rods, an effect of greater local stiffening is produced than in the case of 1 mm rods. This

effect may cause that the stresses are greater than in the case of the 1 mm rod lattice-core.

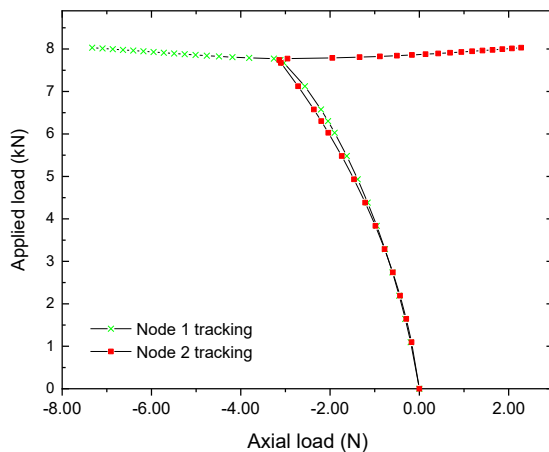
(a) Rod's node displacement tracking



(b) Plate's node displacement tracking



(c) Rod's axial load



(d) Rod and plate's node displacement tracking

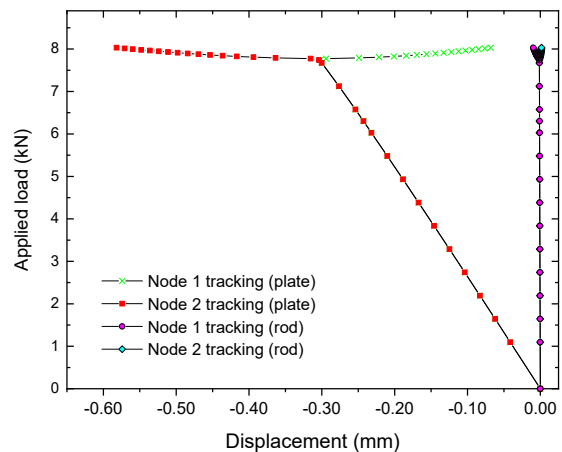


Figure 6.25. Simulation results extracted at benchmarks for lattice-core 1.5 mm rods, and face thickness 0.8 mm

Unlike the previous case (Figure 6.22), the point where the instability begins is a little higher in terms of applied load, of around 7.12 kN and the simulation continues up to an average applied load of 8 kN and then it stops (Figure 6.25.a and Figure 6.25.b). Bearing in mind that only the size of the rods has been changed but not the skin thickness, the consequence of a greater instability load is due to the local stiffening effect of the skin, which is caused by the rods at the connection points. A greater rigidity of the rods shall mean that when the skin reaches the point of instability and the buckling process begins, the rods are not pulled or pushed as easily by the skin, evidenced

by the lesser displacement above the branched point when comparing the skin-nodes and the rod-nodes (Figure 6.25.c). Then, when comparing Figure 6.22.d and Figure 6.25.d, the lattice-core made from 1 mm rods allows a greater displacement of the skins compared to the 1.5 mm core, which concentrate the stresses within the middle longitudinal cells.

As in previous studies, employing Eq. (2.63) and $k \approx 1$ the theoretical failure rod buckling load results in 874 N, meaning that foundation would not collapse due to an out-of-plane load occasioned by the skin's deformation as the axial compressive load is found of about 3 N at the instability point (Figure 6.25.c). The bifurcation seen as a change in the axial load orientation, is due to the drag effect caused by the face while buckling.

Figure 6.26 exhibits the stresses reached at the instability point at 187 MPa, and at the last step. As previously stated, this figure simulates the stress distribution at the last step, and its maximum value may not replicate what it is happening in reality, since the skin have already begun its buckling process, and may fail at a lower stress. The effect of the rods on the stresses is that of causing them to be focused in the central area of the panel, given the imposed conditions.

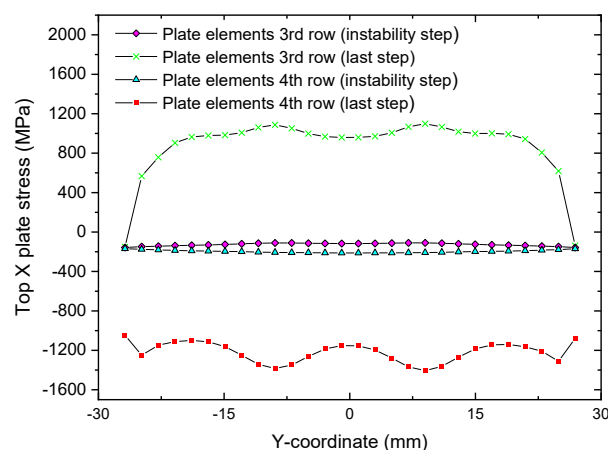


Figure 6.26. Simulation results extracted at benchmarks for lattice-core 1.5 mm rods, and face thickness 0.8 mm

6.4.2.4 Numerical results

The results obtained from the simulations are resumed Table 6.6. A nominal face thickness of 1.21 mm and 0.8 mm are taken into account. The critical stress as σ_{1fcrit} is obtained directly as an average from the stress data recorded. The FE

model's width b_1 is taken as of three unit cells. The applied load P_z is calculated from Eq. (6.21) and Eq. (6.27), employing σ_{1fcrit} attained from the simulations. The failure modes predicted are face wrinkling, for the small rod's diameter and larger face thickness, and intracellular buckling, for the bigger rod's diameters and the 0.8 mm face thickness. The discrepancies among the analytical and numerical results are given mostly by the different buckling coefficients employed for the calculations as seed values for the analytical results. The buckling coefficients will be then determined by the experimental tests, giving feedback to the models.

Comparing the cores made from 1 mm and 1.5 mm rods, the analytical results for the critical stresses predicted exhibit no differences between them, because the intracellular buckling mode is not affected by the rigidity of the core in the calculation as previously said (section 6.4.2.3). However, the FE simulations do show little differences in the critical stress estimation for intracellular buckling, inferring that the rods may affect locally the rigidity of the skin as previously seen in the stress distribution contour plots (Figure 6.20 and Figure 6.24).

Table 6.6. Summary of results taken from FE simulations

\emptyset	t_f	K^*	Q_b^*	K^{**}	Q_b^{**}	P_z^*	P_z^{**}	σ_{1fcrit}^*	σ_{1fcrit}^{**}	Failure mode predicted
(mm)	(mm)	--	--	--	--	(kN)	(kN)	(MPa)	(MPa)	--
0.5	1.21	--	0.40	--	0.33	5.3	4.3	230	185.2	FW
1	0.8	1.58	--	2.2	--	2.67	3.6	175	243.1	IB
1.5	0.8	1.66	--	2.2	--	2.82	3.6	187	243.1	IB

Notes: (*) Non-linear static simulation results/values, (**) Analytical results/values. FW: face wrinkling. IB: intracellular buckling

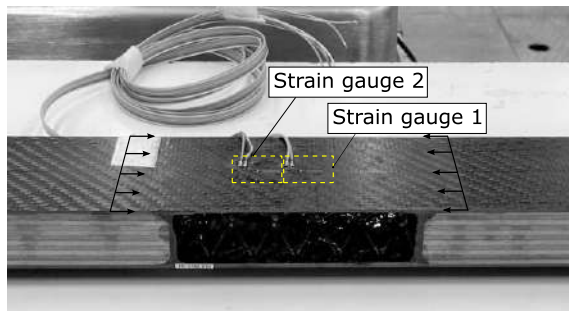
6.5 Experimental tests

For the validation of the analytical studies of sandwich panels with lattice cores based on rods and skins from CFRP under four-point bending, experimental tests are carried out. The execution of the tests and the test-rig employed is similar to those established in ASTM C393 [207].

6.5.1 Bending test set up

The bending specimens employed for testing are given in Figure 6.2, which main nominal dimensions are of 490 x 65 x 27 mm for a $t_f \approx 0.8$ mm, and 490 x 65 x 27.8 mm for a $t_f \approx 1.21$ mm. The sandwich out-of-plane straining is measured by a displacement transducer HBM W5TK. For measuring the in-plane straining of the faces, three strain gauges' type HBM 120 Ohm in a configuration of a quarter bridge with 2-wire circuit is employed. Two of them are glued to the face under compression, or in this configuration, the bottom face, and one over the face under tension, i.e., the top face (Figure 6.27). The strain gauges will also serve to determine experimentally the elastic modulus of the skins from the measured straining.

(a) Face under compression



(b) Face under tension

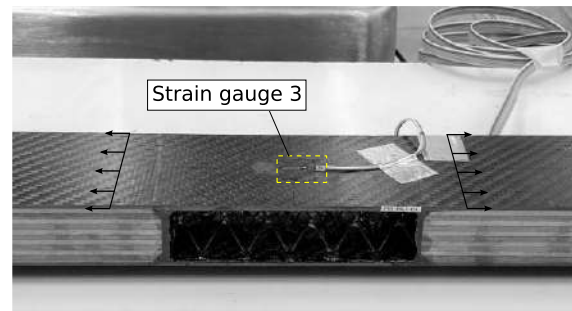


Figure 6.27. Positions of the strain gauges over the sandwich sample

The load is applied at the top of the sample at a constant rate of 1.5 mm/min throughout punches of diameter 50 mm, driven by a Zwick / Roell Z150 screw-driven universal testing machine (Figure 5.28). Two samples of each kind are tested in a controlled temperature room. As previously stated, the specimens have been obtained from the UniBwM at laboratory-scale. Therefore, for statistical interest it is highly encouraged the manufacturing and testing of more specimens as future work. However, good repeatability is gained, and thus, tests are described within this section. The sample dimensions and support/punches positioning are established in Table 6.3.

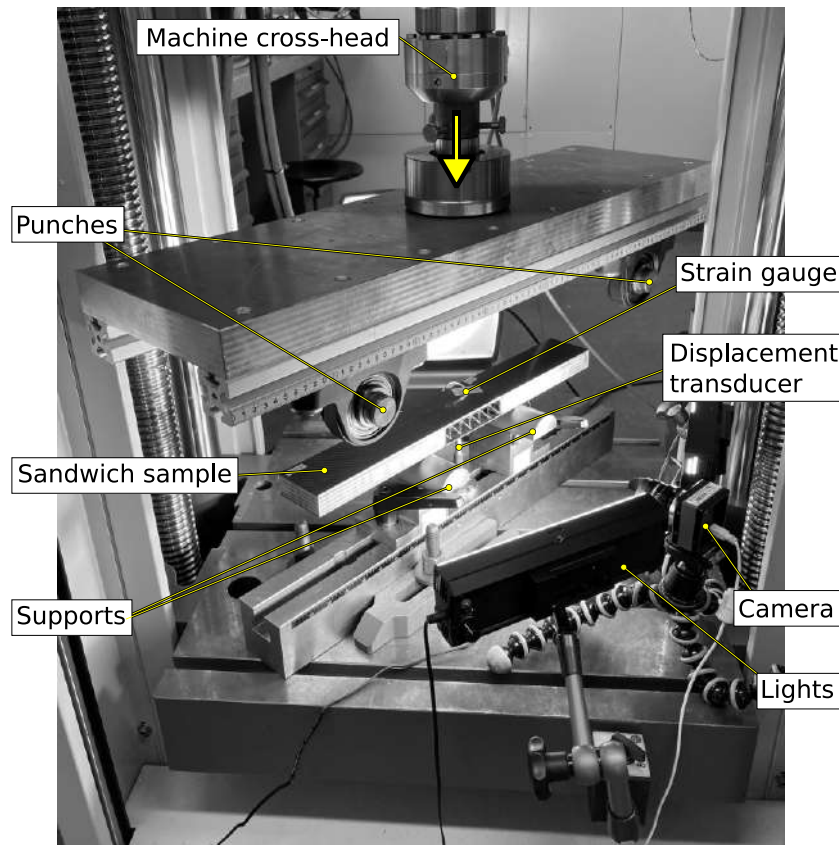


Figure 6.28. Set up used for bending tests

6.5.2 Bending tests results

The different tests for the proposed skin-core combinations are presented graphically in this section, reviewing the charts and tests in which the mechanical response turned out to be of better performance and of better representativeness. A description of the observed events on selected points is also provided.

6.5.2.1 Lattice core made from 0.5 mm rod diameter and skins thickness of 1.21 mm

The mechanical response to bending of the panel made from a lattice-core made of 0.5 mm rods and 1.21 mm nominal thickness skins, is represented in Figure 6.29. A linear zone with almost no variations is observed after the specimen seated and began to take the load up to point II, close to 4.8 kN. In the enlargement picture, reference points II and III are observed separated by a difference of approximately 0.05 mm in deflection. This would indicate that the transition between point II, at the onset of instability and point III, at the instant at which the failure occurs, is almost immediate.

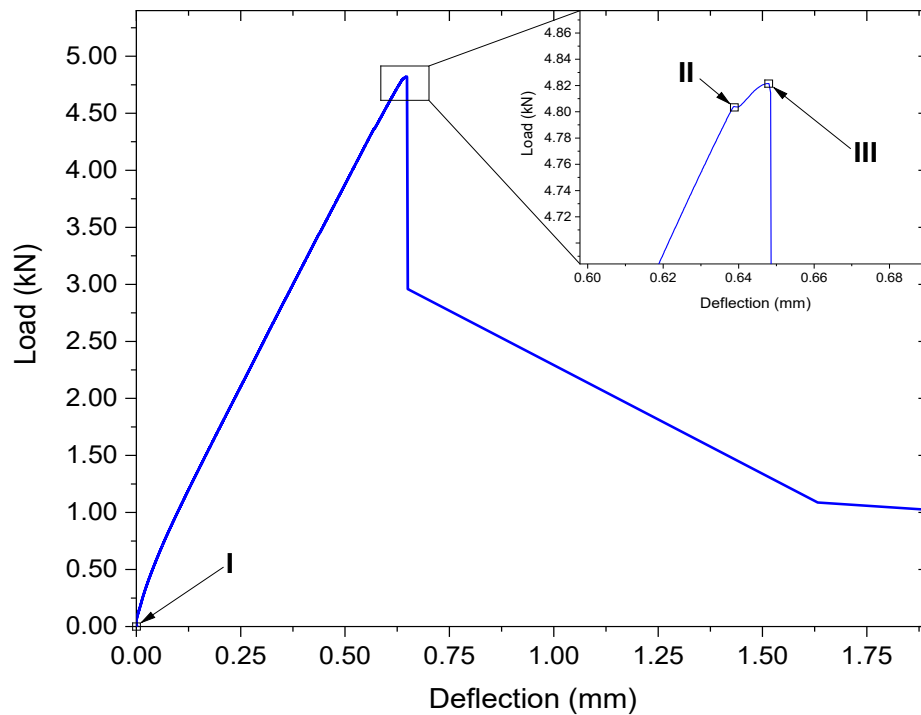


Figure 6.29. Measured load-deflection response under bending of lattice-based core with 0.5 mm rod, and nominal face thickness of 1.21 mm

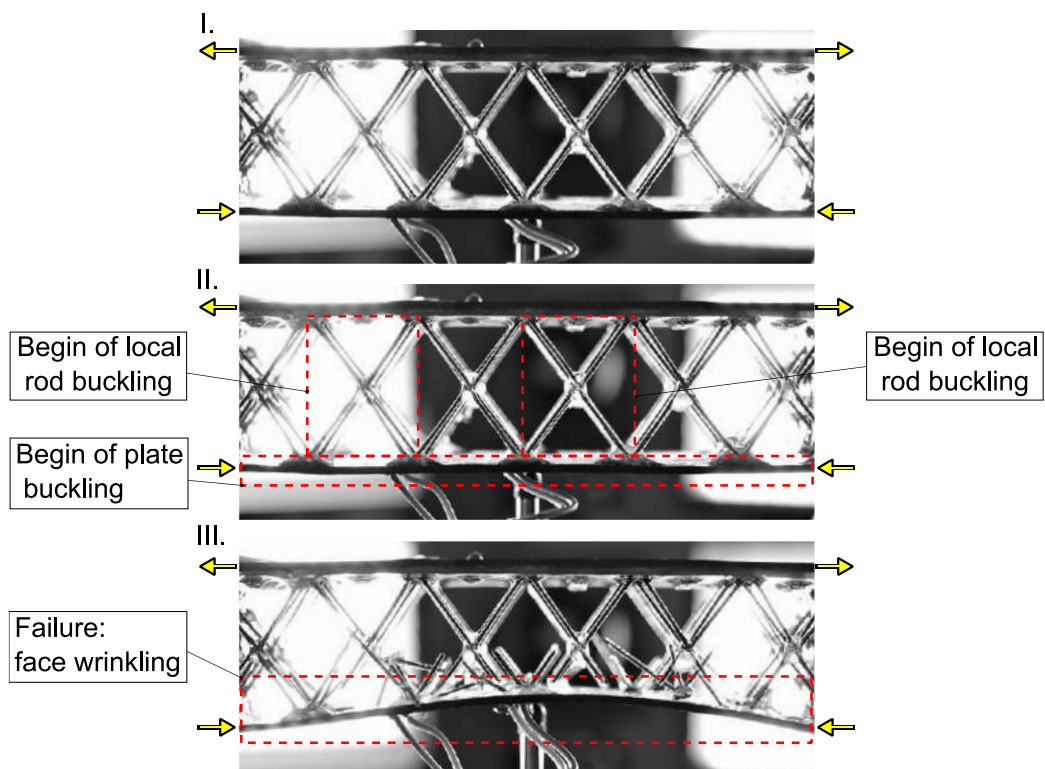


Figure 6.30. Photographs associated to selected points: bending behaviour of lattice-based core with 0.5 mm rod, and nominal face thickness of 1.21 mm

In Figure 6.30 point II, a very slight change of orientation of the rods is observed, with a slight rotation in the meeting middle node, which is perceived as a local buckling of the rods. This buckling causes a slight deviation of the lower skin under compression and favours the beginning of the face buckling. A half wavelength reaching two of the middle unit cells is seen. Then, immediately with the increase on load (up to 4.82 kN), the failure of the skin is reached, caused by the sudden collapse of the foundation.

On the other hand, Figure 6.31 shows the data collected by strain gauges in compression and tension. Both gauges 1 and 2, capture almost the same strain with a slight difference in the curve slope near the start of buckling above 200 MPa, and reaching buckling failure above 210 MPa. As expected, the maximum strength is the same in all three sensors. The response in compression shows a greater deformation than in tension due to the local elastic deformation of the core and added to the displacement of the skin evidenced in the measurement zone. According to gauge 3, the stress curve has a lineal behaviour until failure of the panel.

(a) Strain gauges 1 and 2 (compression) (b) Strain gauge 3 (tension)

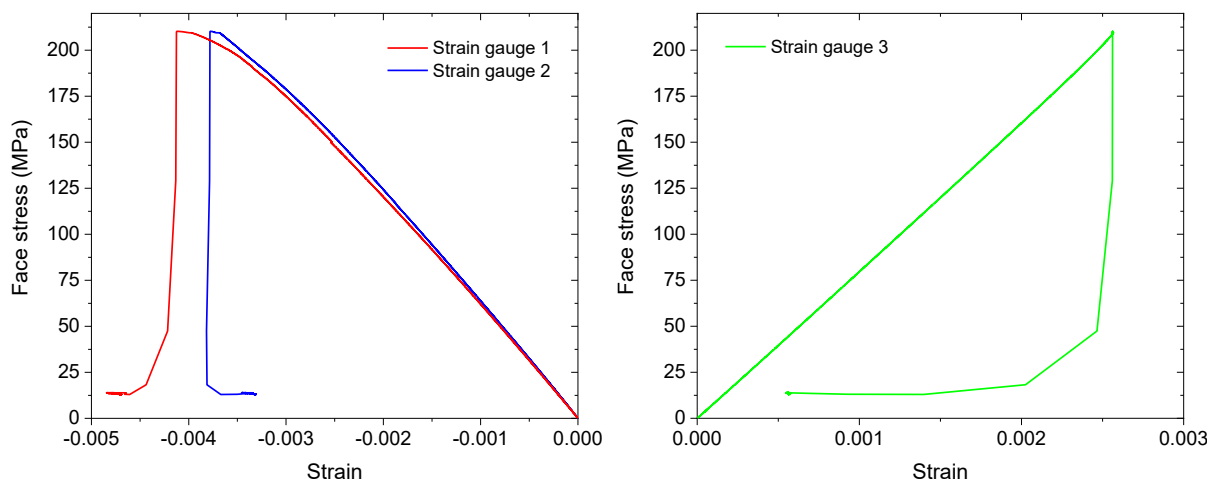


Figure 6.31. Face stress vs. strain response for lattice-based core with 0.5 mm rod, and nominal face thickness of 1.21 mm

6.5.2.2 Lattice core made from 1 mm rods diameter and skins thickness of 0.8 mm

Figure 6.32 shows the case of a panel made from a core with 1 mm rods and a face nominal thickness of 0.8 mm. After the take-up of slack and seating of the sample, a linear region continuous until point II is observed.

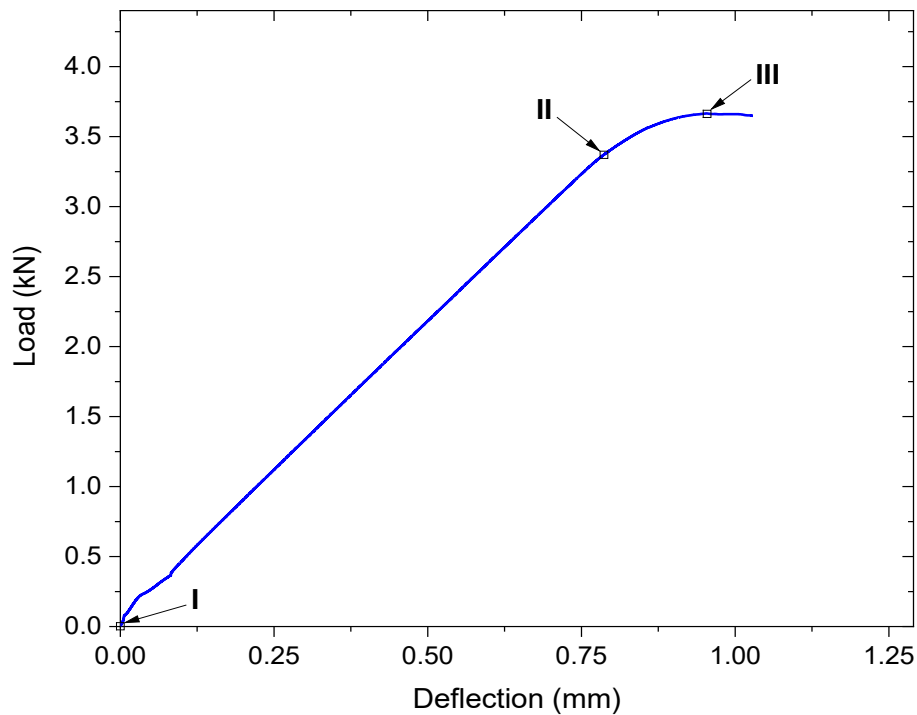


Figure 6.32. Measured load-deflection response under bending of lattice-based core with 1 mm rod, and nominal face thickness of 0.8 mm

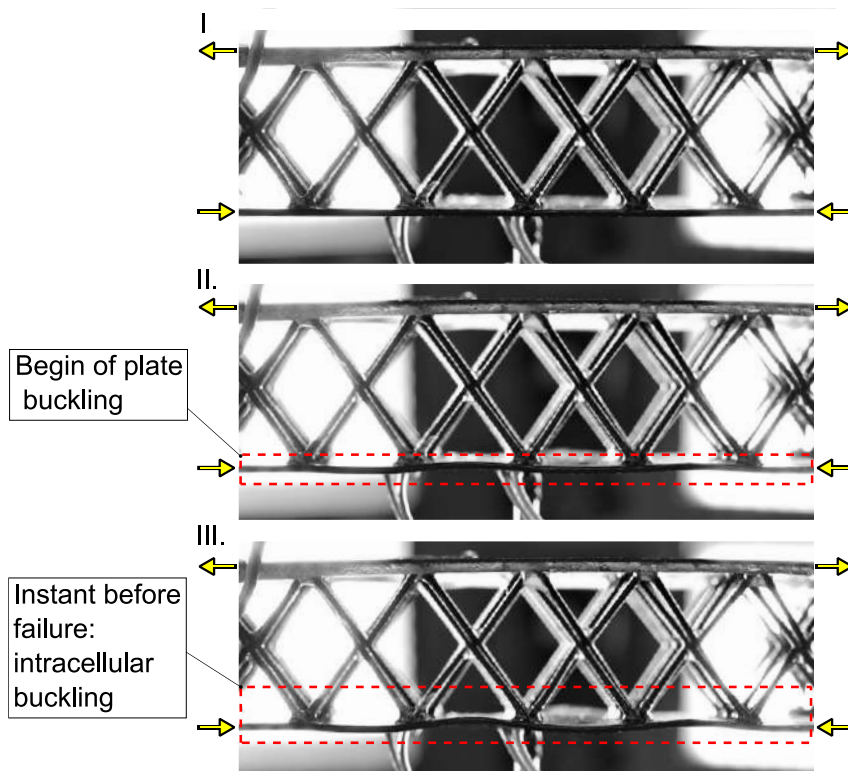


Figure 6.33. Photographs associated to selected points: bending behaviour of lattice-based core with 1 mm rod, and nominal face thickness of 0.8 mm

At point II, it is seen the beginning of the plate buckling represented in photographs in Figure 6.33. From this point, a gradual change in the load-displacement slope is evidenced up to point III where the load becomes unstable, and then the collapse of the skin under compression occurs (Figure 6.32 and Figure 6.33). The observed buckling mode is by intracellular buckling, in which half wavelength of the size of the unit cell is evidenced. Unlike the previous case, the core does not collapse, and the failure is only due to the skin.

Observing Figure 6.34, strain gauges 1 and 2 show similar response of the stress-strain curve until the instability is reached. The response above 200 MPa or what it seems like the buckling starting point, turns to be the opposite, indicating that one cell array is being tensioned while the other is being compressed until topping out 225 MPa. This evidences a typical intracellular buckling behaviour (see Section 6.3.3.3). Moreover, gauge 3 presents a linear behaviour of the face under tensile stress up to the breakage instance of the panel.

(a) Strain gauges 1 and 2 (compression) (b) Strain gauge 3 (tension)

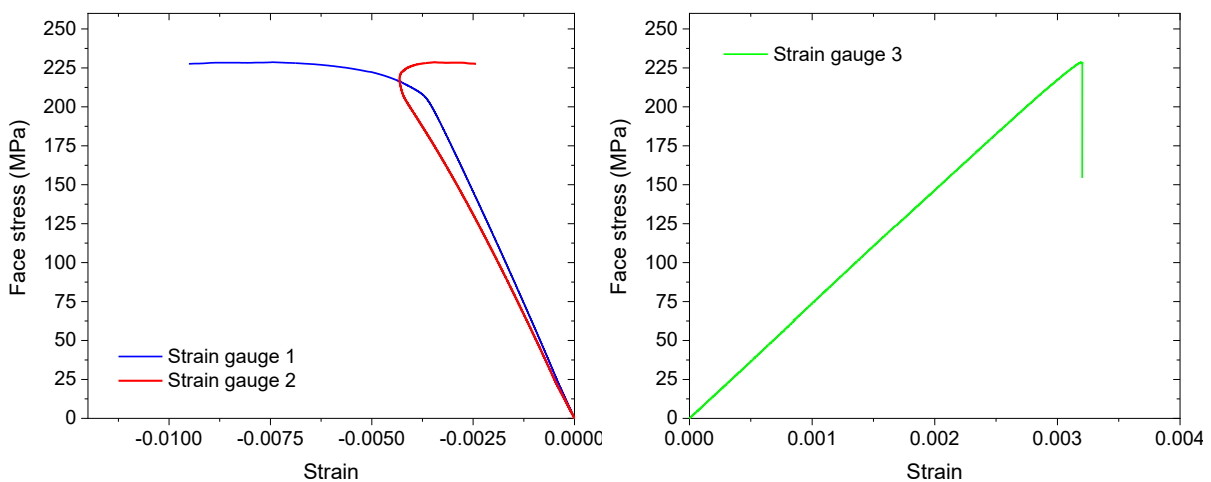


Figure 6.34. Face stress vs. strain response for lattice-based core with 1 mm rod, and nominal face thickness of 0.8 mm

6.5.2.3 Lattice core made from 1 mm rods diameter and skins thickness of 0.8 mm

The bending response of panel made from 1.5 mm rods and nominal face thickness 0.8 mm is set by Figure 6.35. At the beginning of the test, the specimen seated as a function of the load. The load-deflection response presented a linear region up to point II.

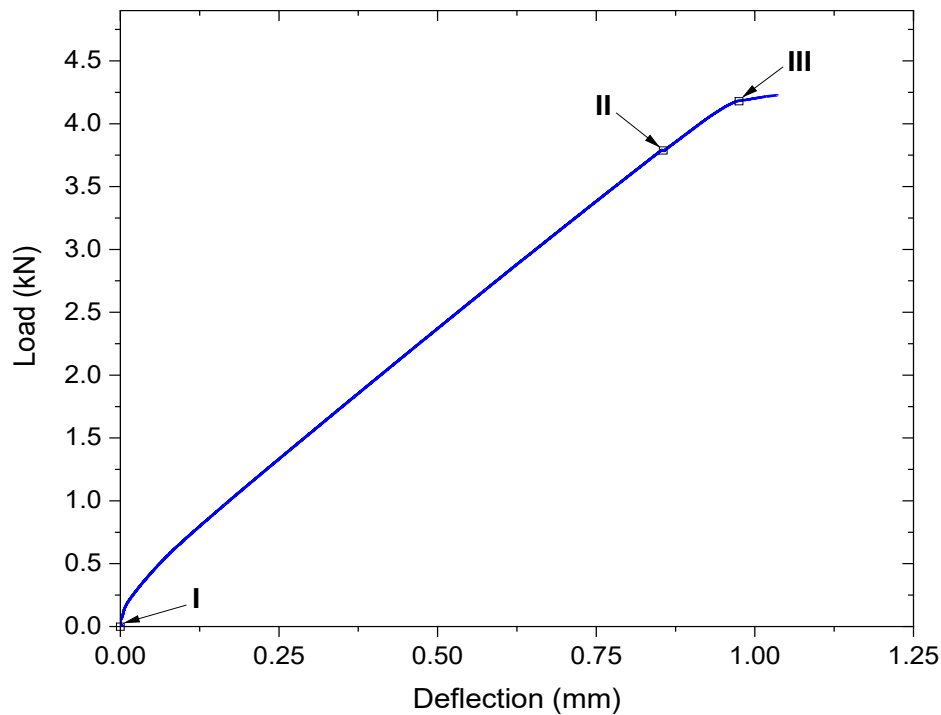


Figure 6.35. Measured load-deflection response under bending of lattice-based core with 1.5 mm rod, and nominal face thickness of 0.8 mm

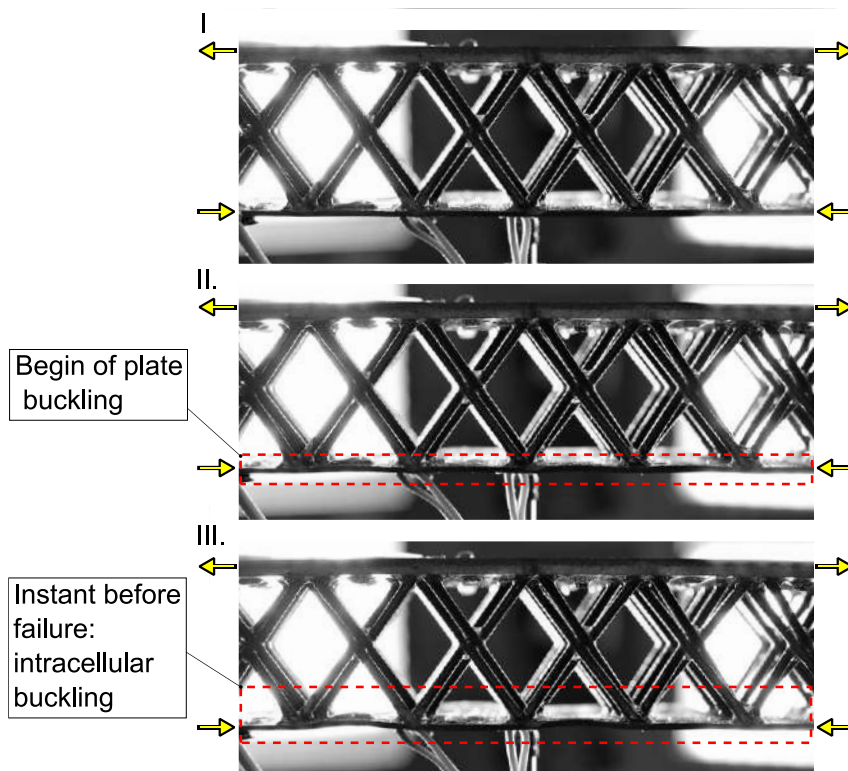


Figure 6.36. Photographs associated to selected points: bending behaviour of lattice-based core with 1.5 mm rod, and nominal face thickness of 0.8 mm

At point II, local brittle breakages of the material are seen in the tests (i.e., in form of small local drop in slope), which could originate the beginning of the plate buckling represented in photographs Figure 6.36. After stepping over the 3.8 kN load, a light change in the slop is seen until point III, meaning that the buckling has already started and continues to be in a stable regime until failure. At point three, the bottom face deformation exhibits half its wavelength within the unit cells, denoting an intracel-lular buckling behaviour (Figure 6.36).

Furthermore, strain gauges 1 and 2 exhibit a similar stress-strain behaviour, despite following different curves' slopes, attributed to the relative positioning of the sensors on the skin. The non-linearity region starts from about 220 MPa, and the stress slope becomes flatter upon 250 MPa until the stress reaches 260 MPa and the face fails. According to Figure 6.36, point III the failure is attributed to intracellular buckling, although the strain gauges do not exhibit the expected change of orientation in stresses (e.g., towards positive and negative values, respectively) as occurred in previous core case. In the present case, the cells where the sensors are glued present a buckling deformation towards the same cell side, i.e., in compression as towards the inside of the core, and these may differ from what occurs in other cells, such as those shown in the front view of Figure 6.36, point III. This implies that the face deformation after the instability stress is not symmetrical according to the midline of the skin.

(a) Strain gauges 1 and 2 (compression) (b) Strain gauge 3 (tension)

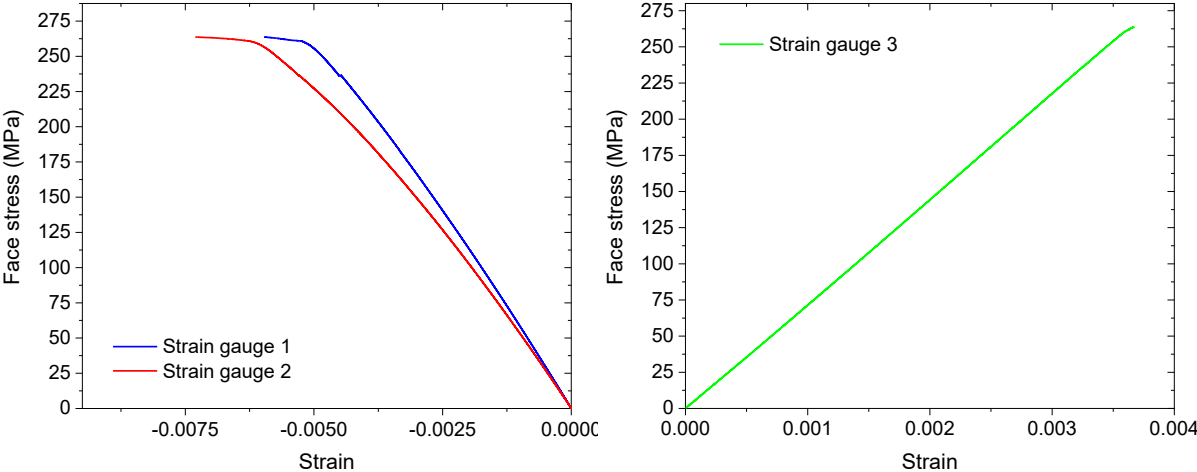
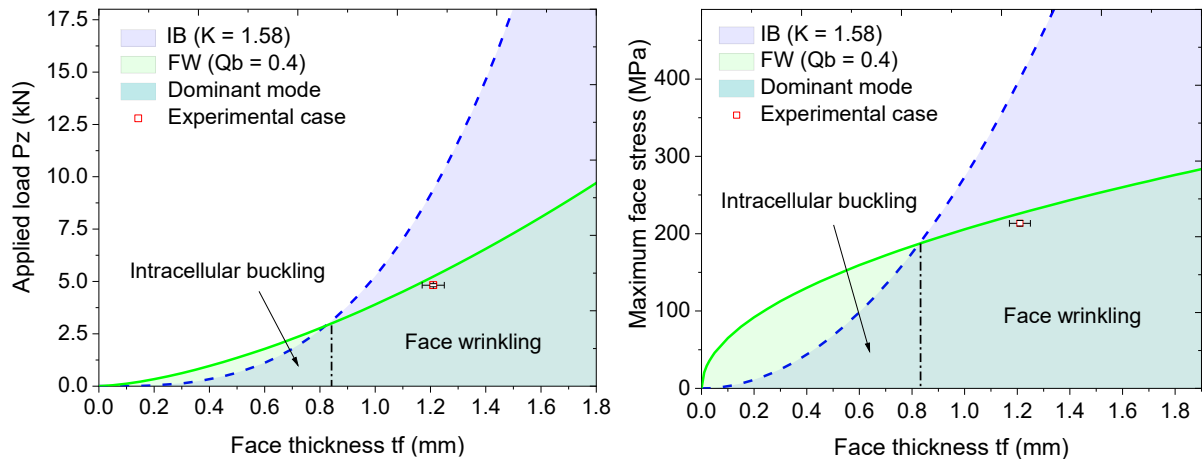


Figure 6.37. Face stress vs. strain response for lattice-based core with 0.5 mm rod, and nominal face thickness of 1.2 mm

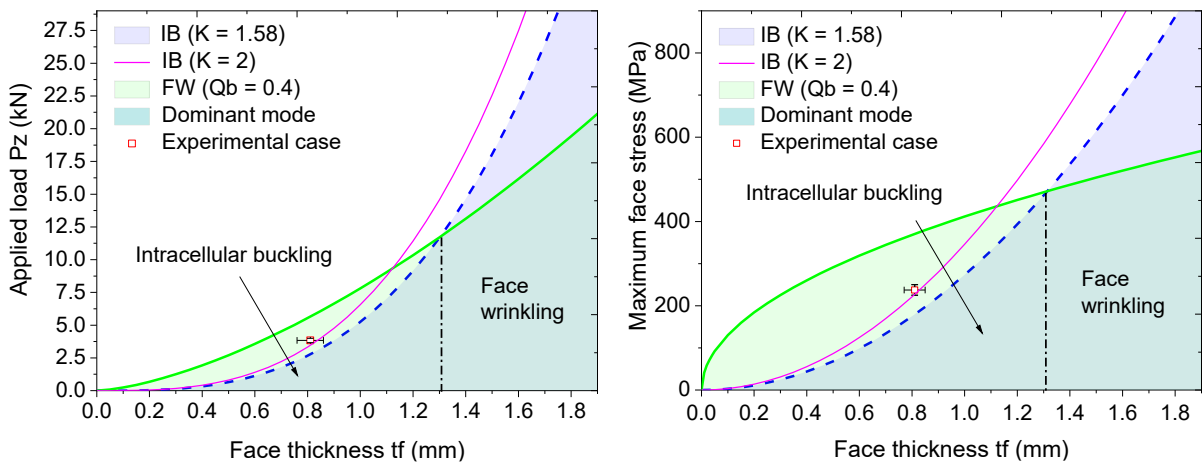
6.5.3 Discussion

In this section the obtained mechanical response results are evaluated, comparing the experimental data with the analytical and numerical approaches combined. As previously stated, regarding Table 6.6 the values of Q_b and K are obtained indirectly from the numerical results for the different cores-faces combinations proposed. Applying these factors directly into the analytical equations, charts of the applied load P_z and the maximum face stresses σ_{1fcrit} vs. the face thickness are obtained in Figure 6.38. The failure modes are in accordance with the predictions, being face wrinkling and intracellular buckling the dominant modes. Case 1, Figure 6.38, denotes a case of face wrinkling behaviour. Employing Eq. (6.19) and the experimentally obtained values, a coefficient $Q_b=0.38$ is attained. The approximate value regarding the simulations is $Q_b=0.4$, which is in excellent correlation with the experiments. Furthermore, Case 2 and Case 3 in Figure 6.38 denote cases of intracellular buckling. The FE simulations predict K values of 1.58 and 1.66, respectively, which lightly underestimates the values seen experimentally. If the criterion of maximum stress reached is employed to indirectly obtain coefficient K from the experimental values for skin-core cases and employing Eq. (6.26), K values of 2 and 2.1 are attained. The corrected curve obtained analytically (magenta-coloured curve) fits very well the experimental points acquired. Although there is a correlation between the core rod's diameter size and the local stiffness contributed to the skin, in other words, the larger the diameter, the larger the local rigidity effect on the skin (see Figure 6.18, Figure 6.20 and Figure 6.24), the values obtained by the FE simulations for the intracellular buckling coefficient K are pretty similar, and in the range 1.58 to 1.66 for core rod's diameters 1 mm and 1.5 mm, respectively. By extrapolation, the hypothetically K value for core rod's diameter 0.5 mm and face thickness 1.2 mm (Case 1 in Figure 6.38) would be less than 1.58. However, for Case 1, the failure mode is found to be as face wrinkling, whose buckling coefficient is obtained as Q_b throughout Eq. (6.19), and its K value turns out to be only theoretical, since it is not possible to obtain nor confirm the intracellular buckling behaviour for this skin-core combination. Nevertheless, a seed value of $K = 1.58$ has been established for plotting the main failure modes of case 1 in Figure 6.38. The same analogy results for cases 2 and 3 in Figure 6.38, but for face wrinkling behaviour, in which the buckling factor $Q_b = 0.4$ is set as seed theoretical value.

(a) Case 1: lattice-core with 0.5 mm rods and nominal face thickness 1.21 mm



(b) Case 2: lattice-core with 1 mm rods and nominal face thickness 0.8 mm



(c) Case 3: lattice-core with 1.5 mm rods and nominal face thickness 0.8 mm

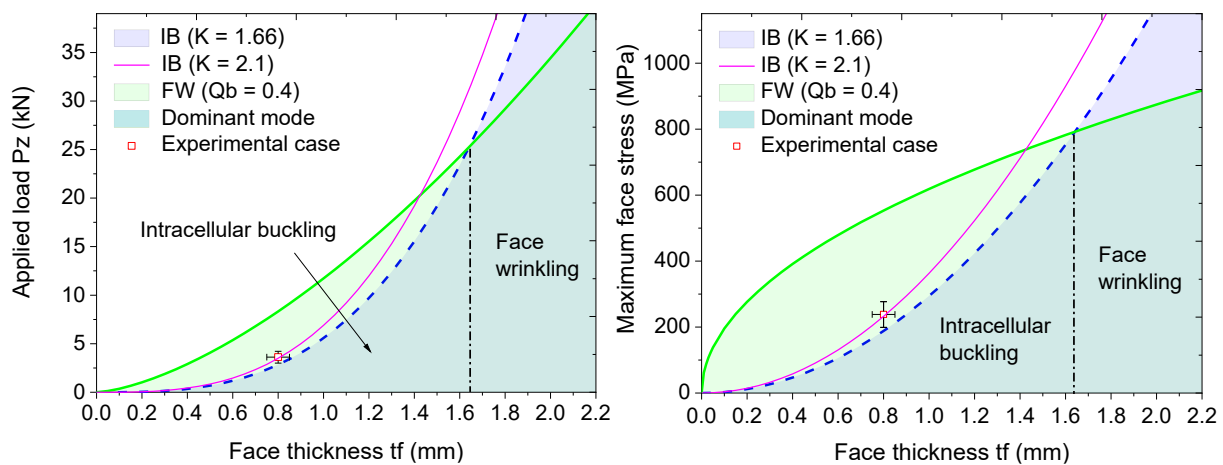


Figure 6.38. Charts obtained by analytical-numerical approaches with experimental cases. *Left column:* According to applied load. *Right column:* According to face stress. FW = Face wrinkling; IB = Intracellular buckling

Table 6.7 resumes the results previously shown in the charts. Manufacturing imperfections may influence the maximal stress failure exhibited, evidenced by the discrepancies in the standard deviations. The main differences among the failure stress values obtained are mainly as a result of the buckling factors approximations. The calculations are found to be very sensible to them. Nevertheless, good correspondence in the failure mode predictions is observed. In addition, employing accurate buckling factors attained from the experimental tests, the corrected curves approximations are in accordance with the experimental tests as seen in Figure 6.38.

Table 6.7. Resume of analytical-numerical and experimental results from bending tests

Ø (mm)	Analytical-numerical				Experimental				Obs. mode
	K (--)	Q_b (--)	P_z (kN)	σ_{1fcrit} (MPa)	K (--)	Q_b (--)	P_z (kN)	σ_{1fcrit}^* (MPa)	
0.5	--	0.4	5.3	230	--	0.38	4.82 ± 0.07	213.5 ± 3.5	FW
1	1.58	--	2.67	175	2	--	3.83 ± 0.17	237.5 ± 12.5	IB
1.5	1.66	--	2.82	187	2.1	--	3.61 ± 0.61	239.8 ± 20.2	IB

Notes: (*) maximum stress reached. FW: face wrinkling. IB: intracellular buckling

Referring to the experimental results, further information can be obtained from the experimental charts of stress and strain in terms of the elastic modulus of the faces (Figure 6.31, Figure 6.34 and Figure 6.37). If very thin faces are considered $t_f \ll C$, then the measurement of the deformation of the faces is assumed as the same throughout their thickness. However, since the measurement is made on the panel, that is, in the external layer of the beam, an effective modulus of elasticity can be obtained while employing the standard ASTM D7249 [208] applying Eq. (6.30), and the results are exhibited in Table 6.8.

$$E_{1f_eff} = \frac{(C + 2t_f) \Delta\sigma_{1f}}{(C + t_f) \Delta\epsilon_{1f}} = \frac{h \Delta\sigma_{1f}}{d \Delta\epsilon_{1f}} \quad (6.30)$$

Assuming that the mechanical response of the faces to compression and tension in the elastic range is very similar, combining the results from strain gauge 1, 2 and 3 obtained in Table 6.8, an average effective elastic modulus of 66446.8 MPa is attained. This approximation is in very good correspondence to $E_{1f} = 67782$ analytically obtained and showed in Table 6.2.

Table 6.8. Face elastic moduli obtained from sandwich bending tests via strain gauges' deformation

Face elastic modulus	Strain gauge 1 (MPa)	Strain gauge 2 (MPa)	Strain gauge 3 (MPa)
$E_{1f}^{case 1}$	61236	63335	75592
$E_{1f}^{case 2}$	60393	56926	73370
$E_{1f}^{case 3}$	60207	55364	71052
E_{1f}^{avg}	60612	58542	73338
$E_{1f_eff}^{case 1}$	63998.5	66192.2	79002.2
$E_{1f_eff}^{case 2}$	62237	58664.2	75610.3
$E_{1f_eff}^{case 3}$	62045.4	57054.5	73221.5
$E_{1f_eff}^{avg}$	62760.3	60636.9	75944.6

Note: Superscript “case 1”: lattice-core rods = 0.5 mm, $t_f = 1.2$; “case 2”: lattice-core rods = 1 mm, $t_f = 0.8$ mm; “case 3”: lattice-core rods = 1.5 mm, $t_f = 0.8$ mm. Subscript “eff”: effective

The maximum displacements obtained at the instant of failure regarding to Figure 6.29, Figure 6.32 and Figure 6.35, are presented in Table 6.9. Employing Eq. (6.11) and the maximum failure load obtained experimentally, it is possible to analytically approximate the maximum displacement, using the simplified bending stiffness as Eq. (6.8), that is, assuming thin faces as $t_f \ll C$, and a weak core as $E_{3c} \ll E_{1f}$. The analytical method is in good correspondence with the maximum displacement values attained.

Table 6.9. Maximum displacements attained by maximum load

Displacements	Theoretically (mm)	Experimentally (mm)	Difference (%)
$w_{case 1}$	0.76 ± 0.01	0.63 ± 0.05	17.83
$w_{case 2}$	0.9 ± 0.04	1.03 ± 0.08	12.62
$w_{case 3}$	0.89 ± 0.12	0.93 ± 0.1	3.806

6.6 Extrapolation to ultra-lightweight 3D-honeycomb cores

In this section, taking as reference the models proposed in section 6.3 and section 6.4, the analysis of sandwich panels under four-point-bending is extended towards the ultra-lightweight 3D-honeycomb cores presented in Chapter 4, exemplifying a case

of 0.8 mm skin thickness. Through FE models, the instability loads for the sandwich panels are attained and employed as feedback for the analytical approach. The dominant failure mode of these panels is intracellular buckling.

6.6.1 Sample design

The cores selected for studies are full-walled base material as the reference core, and the machined cores such as design 1 and 2. The specimen comprises square-honeycomb cores of 25.4 mm of thickness, in an array of 5 x 10-unit cells. The faces are identical and of a nominal thickness of 0.8 mm. The overall panels dimensions are of [200 x 100 x 27] mm (Table 6.11). The basic analytical and FE-models' characteristics for core and faces are set out in Table 4.2, Table 4.3, Table 6.2, and Table 6.10.

Table 6.10. Employed mechanical properties of the square-honeycomb cores

<i>Core type</i>	ρ_c^* (kgm ⁻³)	E_{3c} (GPa)	σ_{3c} (MPa)	$G_{31c} = G_{32c}$ (MPa)	$\tau_{31c} = \tau_{32c}$ (MPa)
Reference	37.8	1.57	2.194	51.22	1.37
Design 1	47.4	1.59	2.943	60.71	0.84
Design 2	47.77	1.93	2.805	27.91	0.74

Table 6.11. Resume of dimensions employed for FE models

<i>Core type</i>	L_5 (mm)	b_1 (mm)	C (mm)	t_f (mm)	L = W (mm)
Reference	200	100	25.4	0.80	50
Design 1	200	100	25.4	0.80	20
Design 2	200	100	25.4	0.80	20

6.6.2 FE model

The load introduction and the modelling of the basic structure is found similar to that in Section 6.4. The proposed sandwich is modelled according to the sketch in Figure 6.14. The cores are characterized by a unit cell whose topology and features are presented in Figure 4.3 and Table 4.3. On the one side, the cores are based on 2D shell elements (CQUAD4) with a mapped mesh in which the base material of a nominal thickness of 0.65 mm has the characteristics shown in Table 4.2. On the other side, the upper and lower faces are also simulated using 2D shell elements (CQUAD4)

but with a 0.8 mm thick base material and features taken from theoretical values shown in Table 6.2. Linear loads of 1 N/mm are set along the width over linear rigid elements, placed along segments *a-d*, *b-c*, *e-h*, and *f-g*.

(a) Constraints references

Segment	Constraints
<i>a-b</i>	<i>x</i> -rotation
<i>d-c</i>	<i>x</i> -rotation
<i>e-h</i>	translation constrained
<i>f-g</i>	<i>y</i> -translation <i>z</i> -translation

(b) Model

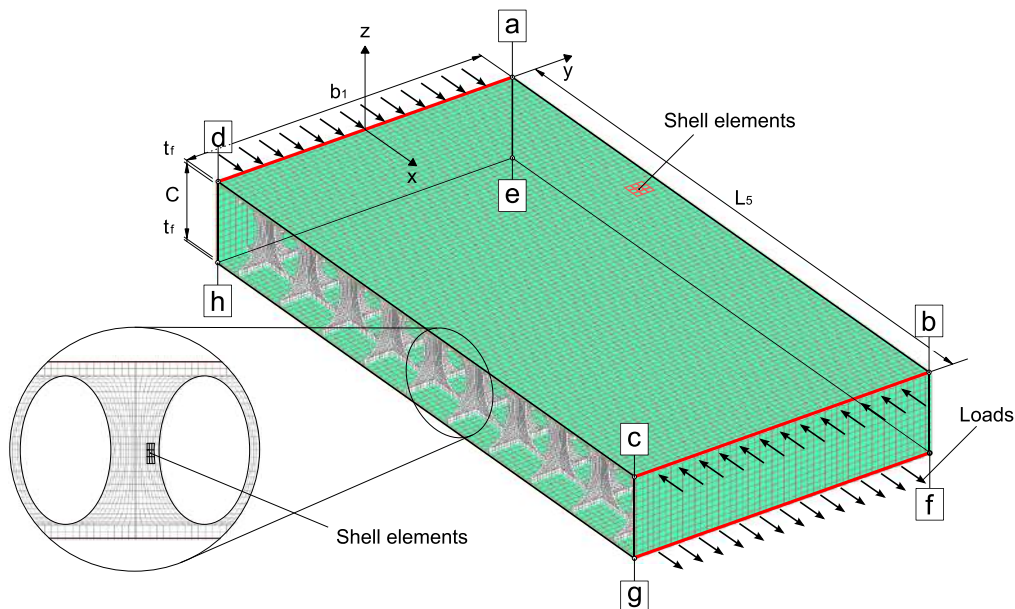


Figure 6.39. Model sketch employed for FE simulations for 3D-honeycomb cores evaluation

The panel is ideally assembled, in which the skin-to-core contacts (i.e., contact nodes) are merged. The boundary conditions are selected as follows: the rotation is locked on the *a-b* and *d-c* segments; segment *b-c* is set as pinned, while *e-h* is set as pinned but with no translation; the constraint for segment *f-g* is applied as simply supported in a way that only its nodes can translate in *x*-direction. For segments *a-d*, *e-f*, and *h-g* no constraints are set.

6.6.3 Analysed cases

Non-linear simulations using commercial FEMAP™ 10.3 with NX™ Nastran® [29] are carried out to complement the analytical studies, and their results are presented within this section. The governing failure mode is identified as intracellular buckling. The simulations are carried out using as base model the part viewed in Figure 6.39. The results obtained comprise the applied in-plane load on the faces as a function of the node tracking displacements on representative places of the model.

6.6.3.1 Reference core with 0.8 mm faces

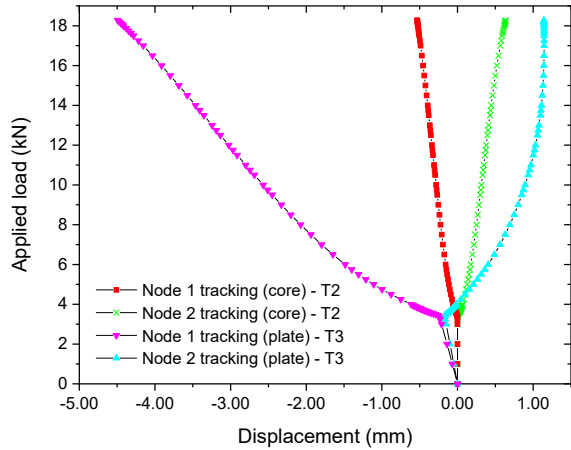
The reference case under four-point bending is seen in Figure 6.40. Node displacements present a marked bifurcation close to 3 kN. The onset of instability is considered to an average of 35 MPa (Figure 6.40.b). The magnitude of displacements is greater at the face reference nodes than at the core's nodes. Thus, the core nodes are perceived as "dragged" as a consequence of the large skin deformation, denoting an intracellular buckling behaviour. The visual evidence on intracellular buckling is also found in Figure 6.41.

Here, the deformation is not the actual but scaled and enlarged to better see the contour. The compressed skin presents half-waves of the cell size, in which the part of the face within each unit cell is compressed or pulled. Part of the applied remote stress is in turn taken up by the core and acts as a local reinforcement of the skin. This effect is observed at the inflection points on the stress curve (where the core web is found) in Figure 6.40.b. As previously mentioned, the maximum stress magnitude is just ideally treated and in fact, the real panel may fail before reaching the stresses shown at the last step.

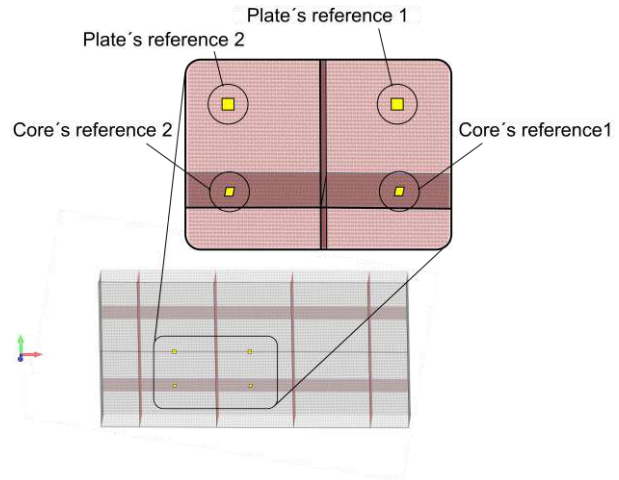
The result of the simulation also shows in Figure 6.40.a, that after the inflection point where the instability begins, the face structure does not suddenly fail, but is able to bear more load following "stably" an asymptote until the simulation stops. This may indicate that the real sandwich structure would be able to bear even more load after the critical buckling point (as explained in Chapter 2), failing according to another cause as, for example, debonding of face and core. Recalling Figure 6.22 and Figure 6.25 and comparing them to Figure 6.40.a., the sandwich panels with lattice cores are capable to bear less load after the buckling point, attributable to the smaller contact area between face and cores as they are only punctual (Figure 6.9). The larger contact area

within the unit cell of the square-honeycombs stabilizes the faces, enhancing the bearable payload after the critical point.

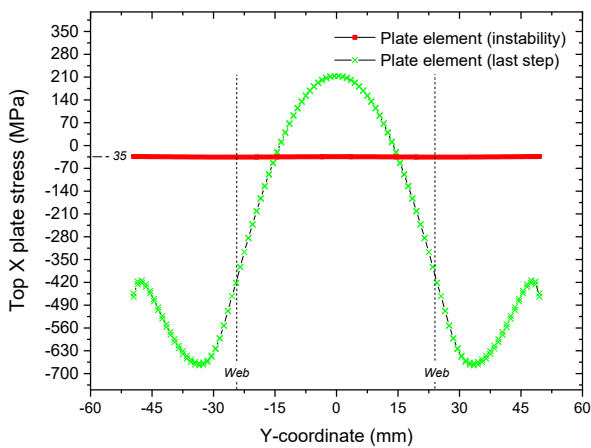
(a) Node tracking displacements



Node references for data acquisition



(b) Top face normal stresses



Element references for data acquisition

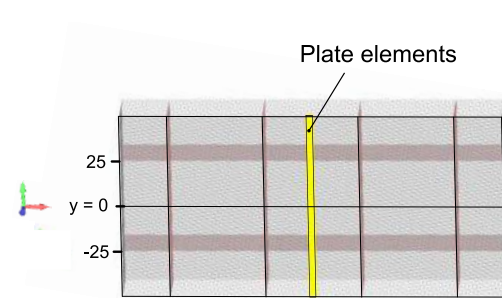


Figure 6.40. Results extracted from FE simulations for reference core case. *Note:* T2: y-direction; T3: z-direction, coordinate system as in Figure 6.39.

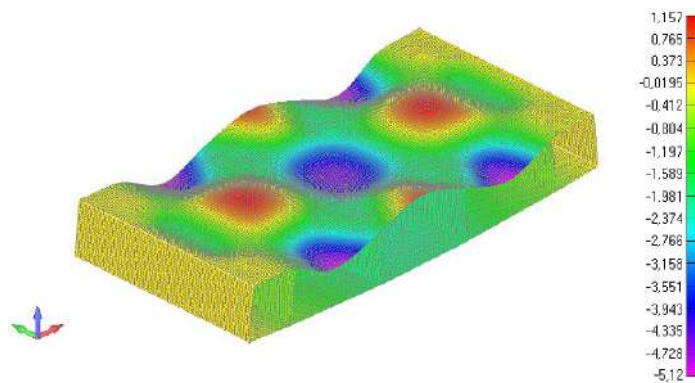
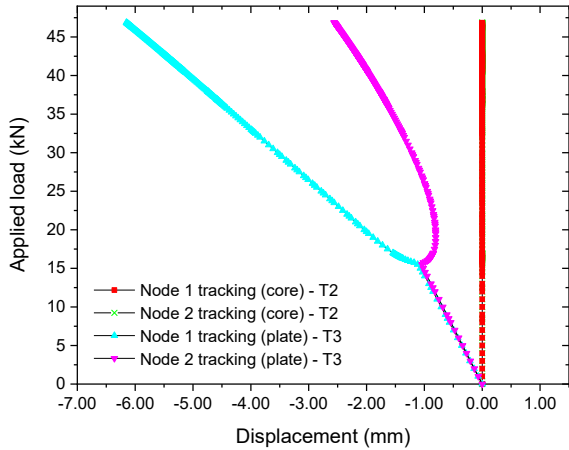


Figure 6.41. Displacements in global z-direction for reference core at last step

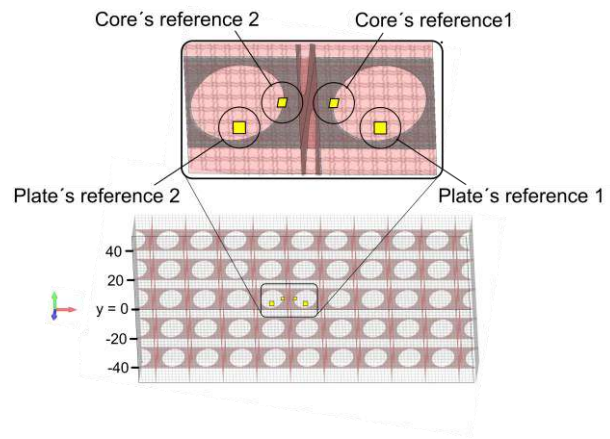
6.6.3.2 Design 1 core with 0.8 mm faces

The case of the design 1 machined cores is shown in Figure 6.42.

(a) Node tracking displacements



Node references for data acquisition



(b) Top face normal stresses

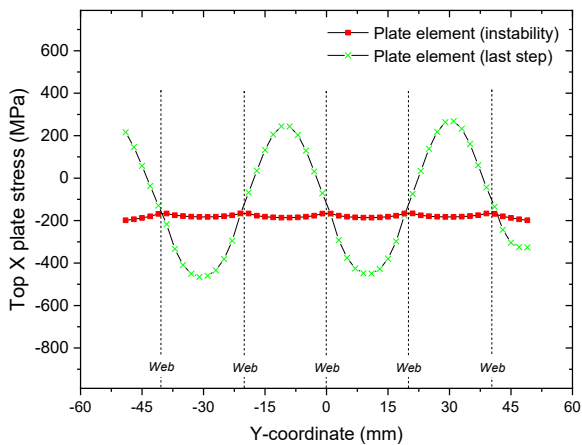


Plate references for data acquisition

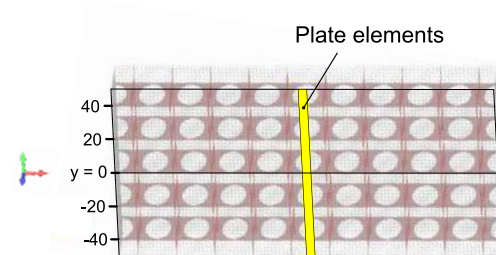


Figure 6.42. Results extracted from FE simulations for design 1 core case. *Note:* T2: y-direction; T3: z-direction, coordinate system as in Figure 6.39

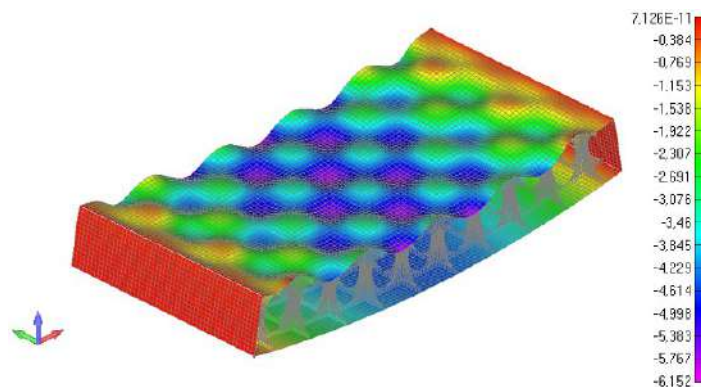


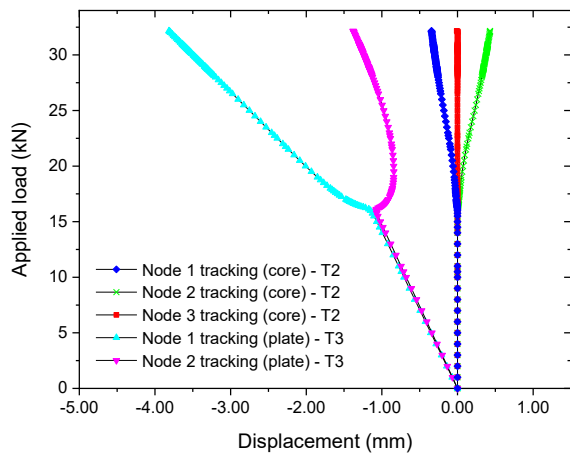
Figure 6.43. Displacements in global z-direction for design 1 core case at last step

The change in unit cell size from 50 x 50 mm for the reference core to 20 x 20 mm for the machined one has an immediate effect on the behaviour of the sandwich panel, for a same face thickness. The applied buckling load turns out to be around 16 kN, i.e., more than 5 times higher than in the previous reference case. Only the face nodes branch out from the point of instability, while the core nodes do not show any y -directional displacement. In terms of stress, the instability is close to 200 MPa in average. The small fluctuations seen around this value are due to the local effect of the core as a reinforcement of the skins. This effect is also seen at the last step of the simulations, as the inflection points of the stress curve, and at its maximum compression dip. An intracellular buckling behaviour is viewed in the simulations' images (Figure 6.43). The skin is shown buckled in turn with half-waves inwards and towards the unit-cells.

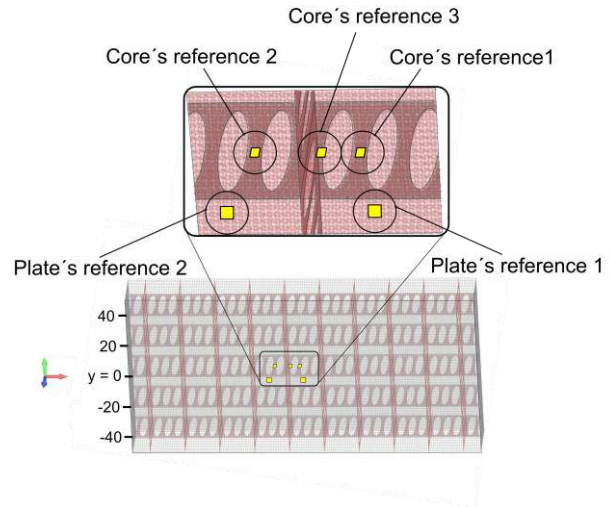
6.6.3.3 Design 2 core with 0.8 mm faces

Figure 6.44 shows the case of design 2 machined cores. Similar to design 1, an instability load of about 16 kN is attained, from which the face nodes are branched. As for the core nodes, the reference node 3, does not present displacements in y -direction, so it is not destabilised because of the skin deformation. Core node 3 belongs to a part of the column in which the cross sheet passes through. Additionally, the subjacent small columns on each side, represented by the core's reference nodes 1 and 2, do suffer a "drag" deformation due to skin buckling, because of their little stiffness as a consequence of a small thickness and width, and additionally, they are located in the vicinity of the maximum skin deformation. The instability stress of the compressed face is in average 200 MPa, as the previous case, given that the plate dimensions are the same (i.e., unit cells of 20 x 20 mm) as well as the boundary conditions. Little fluctuations in the stress values around 200 MPa are observed (Figure 6.44.b) due to the local effect of the core as reinforcement of the skins, as previously mentioned. As a corollary of this effect, the inflection points of the stress curve are observed in the last step. The peaks and dips are of lower magnitude than in design 1, presumably, due to the "drag" caused by the deformation of the skin on the small columns, represented by core's nodes 1 and 2 and makes them not to contribute to the overall support of the skins. Intracellular buckling is also identified in the images of the simulations (Figure 6.45), showing in turn half-waves between unit-cells.

(a) Node tracking displacements



Node references for data acquisition



(b) Top face normal stresses

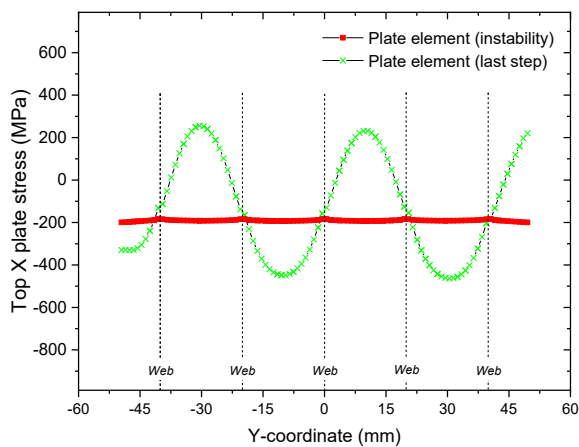


Plate references for data acquisition

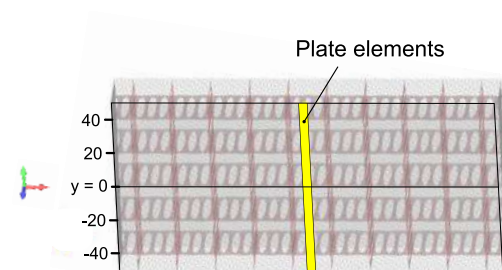


Figure 6.44. Results extracted from FE simulations for design 2 core case. *Note:* T2: y-direction; T3: z-direction, coordinate system as in Figure 6.39.

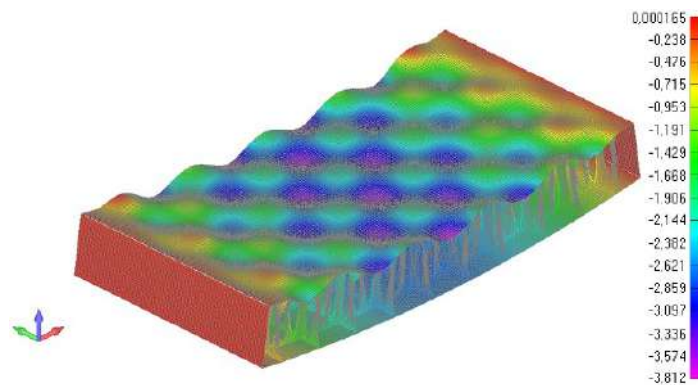


Figure 6.45. Displacements in global z-direction for design 2 core case at last step

6.6.3.4 Analytical-numerical results

Recalling the studies of section 6.3, representative graphs for the different main failure modes of a sandwich panel subjected to four-point bending are drawn within this section. The equations employed for the curves' calculations are resumed as follows: for face yielding, Eq. (6.14), and Eq. (6.15); for face wrinkling Eq. (6.19), and Eq. (6.21); and for intracellular buckling Eq. (6.26), and Eq.(6.28).

For analytical calculations, the buckling coefficient for intracellular buckling K is attained indirectly using Eq. (6.19) and employing the critical buckling point from the simulations as a seed value, for later obtaining the main failure modes curves for each core case. Nevertheless, the analytical value found in charts is given closely to $K = 2.2$ (see Annex E). Since it is not possible to obtain the value of Q_b from the simulations for the cases considered for face wrinkling, as a first approach, a buckling coefficient $Q_b = 0.33$ is taken as a minimum value (Table 6.4). The attained curves considered: the applied external load P_z , simulating the same testing rig employed as in previous sections (i.e., a lever arm of 150 mm); and the normal stresses in x-direction applied to the compressed faces. Both external load and normal stresses are set as a function of the face thickness t_f (Figure 6.46). Recalling section 6.6.3, the FE results exhibited that the dominant failure mode is intracellular buckling in all cases analysed. The average face stresses attained are of 35 MPa for the reference core, and of 200 MPa, for machined cores design 1 and 2. These stresses give buckling coefficients $K = 2.45$ and $K = 2.24$, respectively (Figure 6.46). The larger unit cells defined for the reference case as of 50 by 50 mm influence negatively the overall panel behaviour while bending, reaching in almost the entire proposed range of skin thicknesses, a failure due to intercellular buckling Figure 6.46.a. After a face thickness of 3.1 mm, the theoretical model proposes a failure due to fracture, under the established conditions, while applying a load of ≈ 60 kN. Nevertheless, it is interesting to remark that it is probable that for thicknesses greater than those of interest within this work (i.e., called as thin faces), other local effects such as debonding between the skin-core interphase may appear before a failure, for example, due to face wrinkling, but this evaluation exceeds the objectives of this work. The machined cores as design 1 and 2 (Figure 6.46.b and Figure 6.46.c) are made from unit cells of a size 20 by 20 mm. Hence, the intracellular buckling curves are found much more pronounced than those of the reference core, despite the latter having a K factor slightly higher.

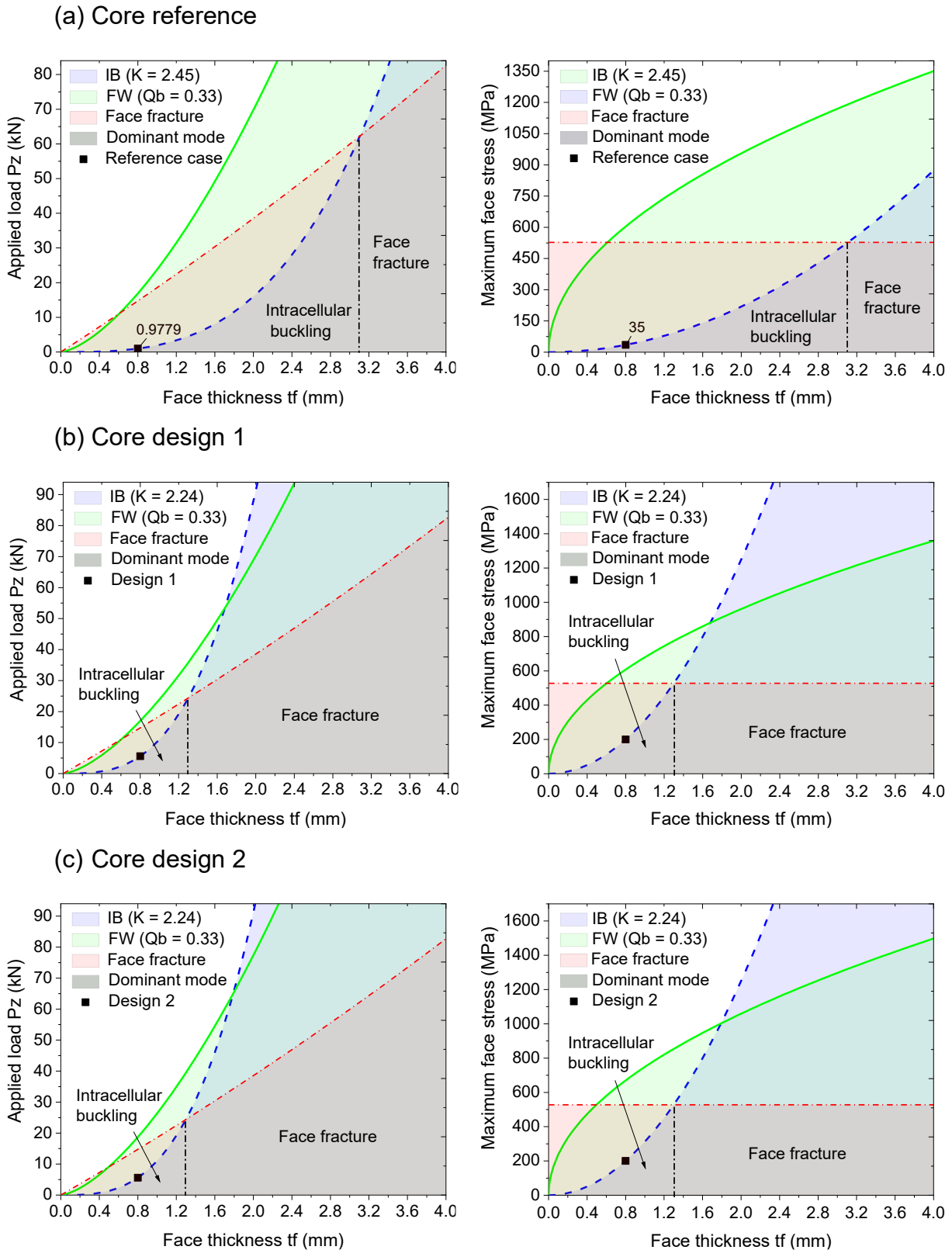


Figure 6.46. Charts obtained by analytical-numerical approaches for square-honeycomb cores. *Left:* according to applied external load P_z . *Right:* according to face stresses. *Note:* FW = Face wrinkling; IB = Intracellular buckling

Thus, a smaller unit cell would increase the face strength to intracellular buckling for the same skin thickness by approximately 5 times, according to predictions. The same K factor is attained for design 1 and design 2 cores, contemplating the same length-to-width ratio and border conditions. The other failure mode that plays a role for this core cases is face wrinkling, starting at face thickness of above 1.3 mm, under the proposed conditions. The face wrinkling curves are very similar to each other comparing the charts, lightly affected by the core out-of-plane stiffness, since they are found similar in value for all core cases proposed (table 6.3).

For the core cases studied and face thickness as $t_f = 0.8$ mm, the dominant failure mode is intracellular buckling, as predicted in the FE simulations.

6.6.4 Partial conclusions

In this section, the prediction of the behaviour of panels proposed from 3D-honeycomb cores has been carried out from numerical and analytical models. Under four-point bending and a rig similar to that proposed for the lattice-based cores, three main failure modes are identified. For the example case of a 0.8 mm skin thickness, the dominant failure mode resulted in intracellular buckling. The large unit cell size favours the occurrence of this failure mode above the others.

The change in cell size directly affects the loading behaviour of the sandwich panel, where the failure load achieves a five-fold increase for the same studied skin thickness when moving from a 50 x 50 to a 20 x 20 unit cell.

Despite maintaining a constant unit cell width-to-length ratio equal to 1, little differences can be observed in the buckling coefficient value for intracellular buckling K . However, the value of K is found very similar to the tabulated one as $K = 2.2$ (Annex E), representing a simply supported orthotropic plate along its edges. In general, analytically the tabulated values are represented for the most common cases, i.e., plates with boundary conditions as simply supported or fixed plates, on some or all edges. In practice, in sandwich panels the contact between skins and cores turns out to be an elastic bond, and the tabulated values are approximations that can be taken as a reference for the calculations.

The indirectly obtained K values are very similar, 2.45 and 2.24, for the 50 mm and 20 mm unit cell case, respectively. The slight difference is presumed to be due to the associated support type and the local stiffness obtained in each core case at the

contact nodes. That is, below the contact nodes where the skin rests on the core, there is a local elastic stiffness provided by the wall that builds the core. For example, in the case of the 50 mm cell, the wall is not machined, so the core immediately under the skin has a full-walled base material that gives support along its edges and its local stiffness is higher than in the 20 mm case, where the core has only a higher local stiffness around the columns where the sheets intersect (refer to section 4.3.1.2). For this reason, it is assumed that the value of K in the reference case is slightly higher than in the other two cases of design 1 and 2. This analysis exceeds the intention of this section, which is to exemplify the theoretical model feedback by the numerical models.

Regarding to face wrinkling failure mode, only small differences in the FW curves are observed by the change in (global) E_{3C} . The curve is directly increased by the increment in E_{3C} , so that design 2 core case shows a slightly steeper curve. In this case, the cell size does not affect the face wrinkling.

The versatility of the analytical model is remarkable, and it is important to note that other failure modes could be incorporated into the model, such as local buckling failure of the core material triggered by the distortion exerted by the skin on the core material. Also, in many cases, the failure occurs in core-to-facing bond [198]. These modes could be categorized as failure in the foundation, and therefore be incorporated as another mode of face wrinkling. This refinement of the face wrinkling failure mode requires further analysis beyond the practical purposes of this work.

As future work, it is proposed to evaluate the numerical-theoretical models and contrast them with experimental tests associated to these core types to be finally endorsed for the proposed core cases.

6.7 Concluding remarks

Starting from the establishment of a theoretical framework of analysis, the aim of this chapter was to present an analytical-numerical model for the evaluation of different cores of interest under bending tests, reviewing the particular case of four-point bending. As a study case, the lattice-based ultra-lightweight cores (Chapter 5) are taken as example, and later an extrapolation to other core cases, such as the 3D-honeycomb cores (Chapter 4) is proposed.

The design of the specimens is included as part of the work, which allowed the study of the load introduction for the development of the analytical models. In turn, this study allowed the simplification of the numerical models.

The main failure modes described by the analytical models were of intracellular buckling, face wrinkling and face yielding. The main modes are graphically detailed in terms of the external applied load or the in-plane stress over the compressed face, considered as critical for the analyses, as a function of the face thickness. For the plotting of the maps, a literature review was necessary for establishing the values of buckling coefficients K and Q_b as seed values. These values are then fed back and contrasted by the numerical and experimental values. On the one hand, the numerically attained Q_b value satisfactorily approximates what is experimentally evidenced on charts (Figure 6.38). On the other hand, the K values are also approximated adequately by the numerical simulations, although little discrepancies are evident. The model is sensitive to these discrepancies and therefore affects the critical in-plane stress value on the skin. Nevertheless, two main reasons are found to such discrepancies:

- On the one hand, the way the buckling factor are calculated. The Q_b and K values obtained from the FE simulations are set at the instability step, i.e., when the critical stress is reached, but the material does not fail yet (i.e., the failure load will be over critical as it is higher than the critical buckling point) and can keep bearing load and deformation, although critical and failure stresses are normally found close in values. For this reason, one could use another evaluation criterion such as the instant in which the non-linearity begins in the load-displacement tests. Applying this criterion, the values of Q_b and K would be lightly modified on average, which should fit better with the FE predictions.
- On the other hand, discrepancies between the experimental and the numerical results were found in the way the simulations are modelled. The numerical approach is an ideal model. It turns out to be a simplification of the observed specimen and there are deviations that are not considered such as, for example, the connections between the skin and the rods. Although the connection nodes skin-rods have been merged, the rods have an elastic linkage to the skin and its effect goes beyond the vicinity of a single node, in part due to the meniscus effect brought by the glue and the fact that rods are actually a 3D-element and not a 1D-element in which the load is transmitted punctually (this effect may be more

evident by rods with larger diameter). If necessary, as future work, improvements to the numerical models are proposed, in order to adjust the experimentally observed values. Among the enhancements, it is proposed, for example, to implement torsion springs in the FE model at the rod-face connection points whose stiffness is indirectly calculated from the experimental tests. Furthermore, the thickness value employed for the calculations is not completely homogeneous and there are local thickness deviations, mostly as a consequence of the manufacturing method. Such deviations can be detected from a 3D scanner to more approximate the FE model to the real case.

Moreover, experimental results on lattice-based cores panels validated the predictions of the analytical and numerical models. Predictions for nominal face thicknesses of 0.8 mm and 1.2 mm defined cases of intracellular buckling and face wrinkling, then satisfactorily confirmed by experimental results. Maximum average face stresses are found as 213 MPa, 237 MPa and 239 MPa for lattice-cores made from 0.5 mm, 1 mm, and 1.5 mm rod's diameters, respectively. As a corollary of the experimental tests, it is also possible to obtain the elastic modulus of the skins, whose effective experimental moduli are on average in excellent correlation with the theoretical values as 66.45 MPa and 67.78 MPa, respectively.

The interest of this chapter also lied in the extrapolation of the predictive model to the square-honeycomb cores seen on Chapter 4. A particular face thickness of 0.8 mm is studied. A large unit cell size favours the occurrence of intracellular buckling at relatively low load, and therefore, the model predicts it as the most likely to occur. In the example, from a change in cell size from a 50 x 50 to a 20 x 20 mm, the failure load was quintupled for a same skin thickness. The K values obtained indirectly were very similar for both unit cell cases, being 2.45 and 2.24, respectively.

As a final assessment, to endorse the rest of the main likely failure regions of the ultra-light weight cores, it is necessary to perform more experimental tests with specimens made from different face thicknesses. For larger thicknesses, the model can incorporate refinements to the main failure behaviour, such as the evaluation of skin-core debonding as a part of face wrinkling [198]. The latter is proposed as future work.

7 Discussion and conclusions

The focus of this chapter is on the review of results from the previous chapters. Since the work's main objective is to create sandwich panels from novel ultralight CFRP-based cores, a comparison of their competitiveness with known cores found in the literature is necessary to evaluate their performance in a sandwich structure. The results are discussed, and the conclusions obtained from the different chapters are summarised.

7.1 Discussion

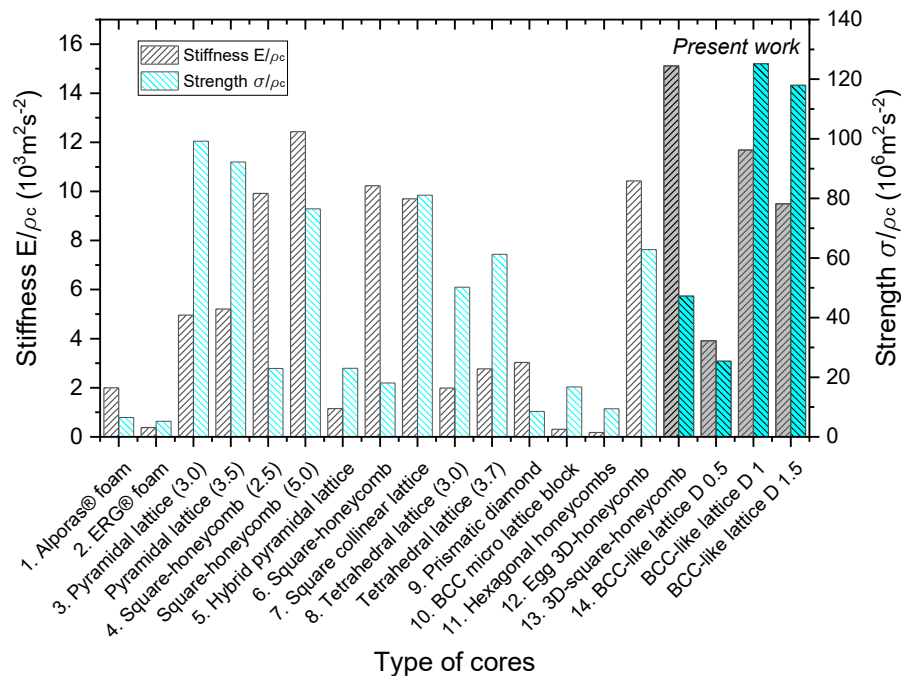
The contribution of this work to research in the field of sandwich panels is established not only in terms of the manufacturing of ultra-lightweight cores (3D-honeycomb cores), but the prediction of the mechanical properties and failure modes of the cores proposed. The loading cases are selected as the ones that characterize the cores in the usual forms such as compression and shear. The sandwich panel is evaluated then as a whole structure in bending.

To consolidate the results obtained by the mechanical characterization like the stiffnesses and strength attained, a contrast with other known materials is carried out within this section. Since the main interest lies in obtaining competitive ultra-lightweight cores, a common comparison practice is based on contrasting the specific properties of the structures obtained and their commercial counterparts, and they are highlighted as follows.

7.1.1 Compressive response

Different types of cores or geometries such as lattices, honeycombs, and foams, in combination with different base materials such as metals, polymers, composites, are contrasted to evaluate the mechanical performance in compression. The core materials are summarised in Table 7.1, which also complements Figure 7.1.

Special attention is put on relative densities of around 3% although other similar ones are presented to compare. The indexes of performance as E_{3c}/ρ_c and σ_{3c}/ρ_c , that is, the specific compression mechanical properties are taken as the basis for comparison (Figure 7.1).



Note. The numbers in parentheses next to the type of cores represent the relative density associated.

Figure 7.1. Comparison of different performance indexes in compression of similar cores

Since no larger differences are found among density and performance of the 3D square-honeycomb cores presented in this work, only the design 1 core structure (Figure 4.3) is taken as example for comparison. The present 3D square-honeycomb core has compression ratios of about 15 ($10^3 \text{m}^2 \text{s}^{-2}$) and 50 ($10^6 \text{m}^2 \text{s}^{-2}$), in terms of specific modulus and specific strength, respectively. The modulus is larger than all the cores assessed, followed closely by other square-honeycomb cores. In general, plate-based cores have a higher modulus than rod-based or foams of the same density [209]. In terms of strength, the present 3D square-honeycomb cores are superior to foams and other full-walled square-honeycomb cores, but they are outperformed by CFRP-based and metal-based lattice cores. Regarding the lattice-based cores proposed in this work, the best specific modulus is performed by the 1 mm rod lattice-based core with an index of around 11.5 ($10^3 \text{m}^2 \text{s}^{-2}$), followed by the lattices of 1.5 mm and 0.5 mm rod's diameters. Then, the specific moduli are comparable to or better than other materials presented, while the specific strength top out index values of 22.5, 125 and 119 ($10^6 \text{m}^2 \text{s}^{-2}$) for the lattice-cores made from 0.5 mm, 1 mm, and 1.5 mm rods, respectively. This represents a great advance compared to other competing core materials (e.g., proposed lattice cores of 1 mm rods outperform the best of the pyramidal lattices of $\bar{\rho} = 3.5$, by 35.5 % in terms of strength and by 124.6 % in terms of stiffness).

Table 7.1. Comparison of similar core materials (e.g., compression loading)

N°.	Type of cores (--)	Base material (--)	ρ_s (kgm ⁻³)	ρ_c (kgm ⁻³)	$\bar{\rho}$ (%)	Reference (--)
1	<i>Alporas® foam</i>	Al closed cell foam	2500	200	8.0	[117]
2	<i>ERG® foam</i>	Al open cell foam	2500	125	5.0	[117]
3	Pyramidal truss lattice	Laminate [0/90] ° CFRP	1440	43.20 50.40	3.0 3.5	[22]
4	Square-honeycomb	Woven [0/90] ° CFRP	1370	34.25 68.50	2.5 5.0	[21]
5	Hybrid pyramidal lattice	Braided CFRP	1450	43.50	3.0	[191]
6	Square-honeycomb	AISI 304	7980	239.40	3.0	[153]
7	Square collinear truss lattice	Ti-6Al-4V-coated SiC	3930	377.28	9.6	[210]
8	Tetrahedral truss lattice	Age-hardened AA 6061	2700	81 99.90	3.0 3.7	[179]
9	Prismatic diamond	AISI 304	7980	287.28	3.6	[154]
10	BCC micro lattice block	EOS Ti6Al4V	4410	246.96	5.6	[211]
11	Hexagonal honeycombs	Woven Kevlar/914	1380	57.96	4.2	[212]
12	Egg honeycomb grid panel	Laminate [0/90] ° CFRP	1550	46.50	3.0	[122]
13	3D Square-honeycomb (design 1)	Woven [0/90] ° CFRP (plates)	1350	47.64	3.52	<i>Present work:</i> Chapter 4 tests results
14	BCC-like lattice cores (D0.5, D1, D1.5)	Uni-directional CFRP (rods)	1500	8.66 22.92 49.76	0.58 1.53 3.32	<i>Present work:</i> Chapter 5 tests results

Note: the core density values shall be taken as typical values obtained from the information available in the literature

Regarding design engineering, it is useful to compare the performance of the proposed materials directly with standard commercial materials such as aluminium based honeycomb cores (Table 7.2). Aluminium honeycombs have been established for many years as an extensively used sandwich cores in the aircraft and automotive industries [213]. Their main characteristics are based on the unit cell size and the wall thickness, which also translate into the core's density. Their minimum available core density is about 16 kgm^{-3} .

Table 7.2. Comparison with a reference commercial core (e.g., compression loading)

Type of cores (--)	Base material (--)	ρ_c (kgm^{-3})	E_{3c} (MPa)	σ_{3c} (MPa)	Reference (--)
Hexagonal HexWeb (3/8", .0007 unit-cell)	Aluminium 5052	16	68.9	0.34	[214]
Hexagonal HexWeb (3/8", .001 unit-cell)	Aluminium 5052	25.6	137.89	0.65	[214]
Hexagonal HexWeb (3/8", .002 unit-cell)	Aluminium 5052	48	482	2.13	[214]
Hexagonal HexWeb (3/16", .001 unit-cell)	Aluminium 5052	49.65	517	2.31	[214]
3D Square-honey- comb (design 1)	Woven [0/90] ° CFRP (plates)	47.64	720	2.25	<i>Present work:</i> Chapter 4 tests results
BCC-like lattice cores (D0.5, D1, D1.5)	Uni-directional CFRP (rods)	8.66 22.92 49.76	33.91 267.8 472.55	0.22 2.87 5.87	<i>Present work:</i> Chapter 5 tests results

Note: the compressive values are taken from stabilized samples in all cases

The minimum achievable density in this work is limited by the technology available to manufacture the ultra-lightweight cores. The minimum presented here belongs to the lattice-cores of 0.5 mm rods, with a core density of 8.66 kgm^{-3} . This value could be even lower if thinner commercially rods were used, for example, as rods of 0.3 mm of diameter. Moreover, considering the aluminium honeycomb of density $\approx 25 \text{ kgm}^{-3}$, the lattice-cores with 1 mm rods do not only present a lighter density ($\approx 23 \text{ kgm}^{-3}$) but also, they double their compressive elastic modulus and quadruplicate their compressive strength. On the side of the core densities $\approx 48 \text{ kgm}^{-3}$, the elastic moduli are closer to each other, in which the aluminium counterparts achieve 482 MPa and 517 MPa.

The 3D square-honeycomb cores present on average 720 MPa, that is a 1.5 and 1.4 times enhancement. The lattice-core of 1.5 mm are on average in the same order of elastic modulus as their aluminium equivalent. In terms of strength, both aluminium and CFRP square-honeycomb are on the same value order. Remarkably, the lattice-core based present almost 2.6 times higher compressive strength.

7.1.2 Shear response

Analogously to the last section, the shear core's performance is assessed within this section. The average specific shear modulus and shear strength performance of the proposed cores are compared to competing sandwich structures and are briefly quoted in Table 7.3 which complements Figure 7.2.

In this work, the specific shear modulus presented by the 3D square-honeycomb core is comparable to other similar core morphologies like the full walled square-honeycomb cores, and in some cases, better than several of the lattices-truss cores as the X-type. The fibres' orientation play a critical role in plate-based cores. In shear loading the maximal loads stiffness and strength are found at $\pm 45^\circ$ [170], if the fibres longitudinal axis are not oriented parallel to this angle, the shear payload may be much lower. For instance, by adding $\pm 45^\circ$ layers into the composite lay-up, the shear performance of the laminate may be enhanced. Likewise, working with lattice structures represent certain advantages, because the trusses are oriented to a desired angle, and this translates into a higher rigidity or strength.

The lattice-based cores outperform their counterparts and dominate the scene. The lattice-core developed in this work show performance indexes of 5.3, 6, and 4.7 ($10^3\text{m}^2\text{s}^{-2}$), and of 33, 46, and 27 ($10^6\text{m}^2\text{s}^{-2}$), for the shear moduli and strengths shown by the rod's diameter 0.5 mm, 1 mm, and 1.5 mm, respectively. These values represent an enhancement in moduli from 5 to 6 times higher than the square-based honeycombs. The strength index is also better from 2.7 to 4.5 times than the square-honeycombs cores.

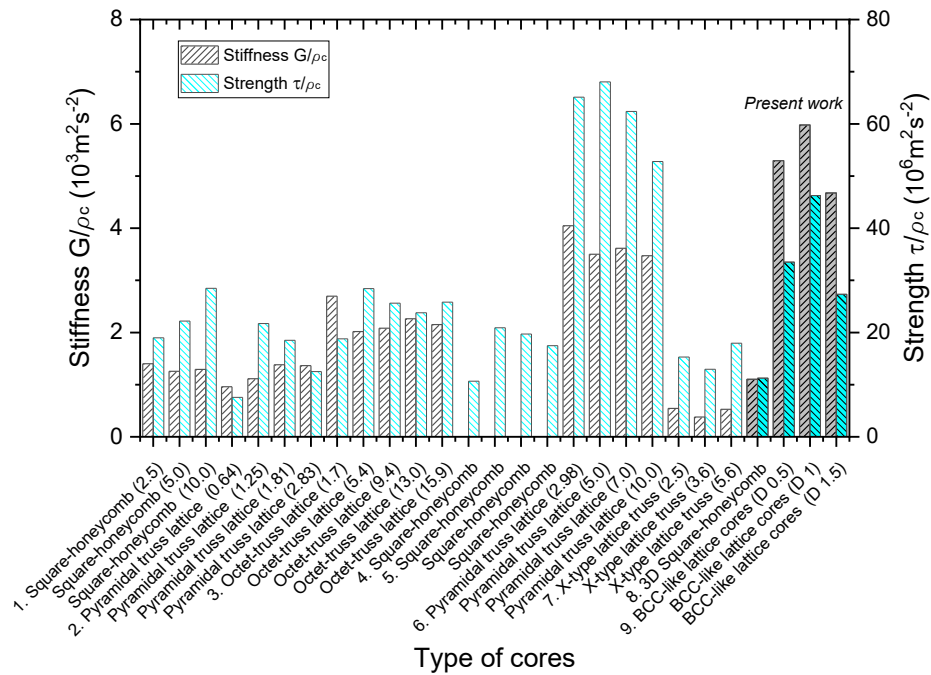
The lattice-cores proposed exhibit a higher performance in shear moduli than the other assessed cores, only outperformed in strength by the pyramidal truss lattices based on CFRP laminates. In this case, the manufacturing process would be the main focus to enhance the mechanical properties in future work. Additionally, understanding

the failure behaviour of the cores and setting out the material position and orientation is also a way to improve performance.

Table 7.3. Comparison of similar core materials (e.g., shear loading)

N°.	Type of cores (--)	Base material (--)	ρ_s (kgm ⁻³)	ρ_c (kgm ⁻³)	$\bar{\rho}$ (%)	Reference (--)
1	Square-honey-comb	Woven [0/90] ° CFRP	1370	34.25 68.5 137	2.5 5.0 10.0	[21]
2	Pyramidal truss lattice	Laminate CFRP	1550	9.92 19.38 28.06 43.87	0.64 1.25 1.81 2.83	[151]
3	Octet-truss lattice	Woven and laminate CFRP	1440	24.48 77.76 135.36 187.2 228.96	1.7 5.4 9.4 13.0 15.9	[176]
4	Square-honey-comb	Hybrid CSH/foam and woven CFRP	N/A	123	N/A	[139]
5	Square-honey-comb	Hybrid HCSH/foam and woven CFRP	N/A	78 103 150	N/A	[139]
6	Pyramidal truss lattice	Laminate CFRP	1440	43 72 101 144	2.98 5.0 7.01 10.0	[124]
7	X-type lattice truss	Laminate CFRP	1543	38.58 55.55 86.41	2.5 3.6 5.6	[215]
8	3D Square-honeycomb (design 1)	Woven [0/90] ° CFRP (plates)	1350	47.64	3.52	<i>Present work:</i> Chapter 4 tests results
9	BCC-like lattice cores (D0.5, D1, D1.5)	Uni-directional CFRP (rods)	1500	8.66 22.92 49.76	0.58 1.53 3.32	<i>Present work:</i> Chapter 5 tests results

Note: the core density values shall be taken as typical values obtained from the information available in the literature



Note. The numbers in parentheses next to the type of cores represent the relative density associated.

Figure 7.2. Comparison of different performance indexes in shear of similar cores

Furthermore, the shear performance of the designed cores with standard materials such as the aluminium honeycomb core is presented as well for comparison within this section. Traditional honeycombs cores have hexagonal cells. Thus, the cores have a remarkable anisotropy depending on the orientation of the cells, mainly due to the manufacturing process that produces double cell walls in one direction and single walls in the other (corrugation or the expansion processes [51]). This represents a drawback of the in-plane strength as a function of the load orientation [155], since the walls are not oriented parallel to it, as the two main directions L and W , which could be considered a disadvantage due to the high dependence on the geometry orientation. In this work, these negatively geometric features are saved since the cores present symmetrical unit cells oriented parallel to the global coordinates reference.

Looking at the lightest materials, the lattice-based on 0.5 mm attained almost the same strength of the aluminium counterpart, but with half of the density. The shear moduli are of the same order in W direction and about the half in L principal direction. Regarding the cores of almost 25 kgm^{-3} , the shear strength of the lattice-based materials doubles the aluminium cores, and the shear moduli are of the same value. Finally, for core densities $\approx 48 \text{ kgm}^{-3}$, the properties exhibited by the lattice-cores and the aluminium honeycomb are of the same order in terms of strength, but outperformed by the aluminium honeycomb in terms of moduli (310 MPa to 232 MPa), only in L principal

direction. By enhancing the manufacturing process of the lattice-cores, theoretically the shear modulus could achieve 447 MPa, and exceeding the modulus of the commercial core counterpart.

As previously stated, the 3D square-honeycomb cores are outperformed by the others of same density, because they fibre orientation are not adequate for shear loading, although they are comparable to other similar core materials as seen in Figure 7.2.

Table 7.4. Comparison with a reference commercial core (e.g., shear loading)

Type of cores (--)	Base material (--)	ρ_c (kgm ⁻³)	G_{31c} (MPa)		τ_{31c} (MPa)		Reference (--)
			L	W	L	W	
Hexagonal HexWeb (3/8", .0007 unit-cell)	Aluminium 5052	16	82.73	48.2	0.31	0.21	[214]
Hexagonal HexWeb (3/8", .001 unit-cell)	Aluminium 5052	25.6	144.8	75.8	0.59	0.34	[214]
Hexagonal HexWeb (3/8", .002 unit-cell)	Aluminium 5052	48	296	146	1.37	0.86	[214]
Hexagonal HexWeb (3/16", .001 unit-cell)	Aluminium 5052	49.65	310	151	1.44	0.86	[216]
3D Square-honeycomb (design 1)	Woven [0/90] ° CFRP (plates)	47.64	52.52		0.536		<i>Present work:</i> Chapter 4 tests results
BCC-like lattice cores (D0.5, D1, D1.5)	Uni-directional CFRP (rods)	8.66	45.85		0.29		<i>Present work:</i> Chapter 5 tests results
		22.92	137.02		1.06		
		49.76	232.59		1.36		

Note: the shear values are taken from stabilized samples in all cases

7.1.3 Ashby-style charts

In order to compare the mechanical properties of different base materials, Ashby and Bréchet [101] have proposed the material-property charts for engineering materials, regarding to different features of interest such as the compressive strength-density (Figure 7.3), shear strength-density (Figure 7.4) and bending strength-density charts (Figure 7.5). Many authors aimed to fill in the gaps between existing and unattainable materials from the maps by making hybrid materials, and thus, an increasing interest exists in ultra-lightweight cores for weight sensitive structures [135].

7.1.3.1 Compressive behaviour

The out-of-plane compressive behaviour is also studied in a qualitative manner by means of the Ashby-style plots. Figure 7.3 includes compressive data for CFRP honeycomb cores [21], CFRP pyramidal lattices [22,103], titanium matrix lattices [210], aluminum tetrahedral lattices [179], stainless steel honeycomb cores [153] and different metallic foams [117].

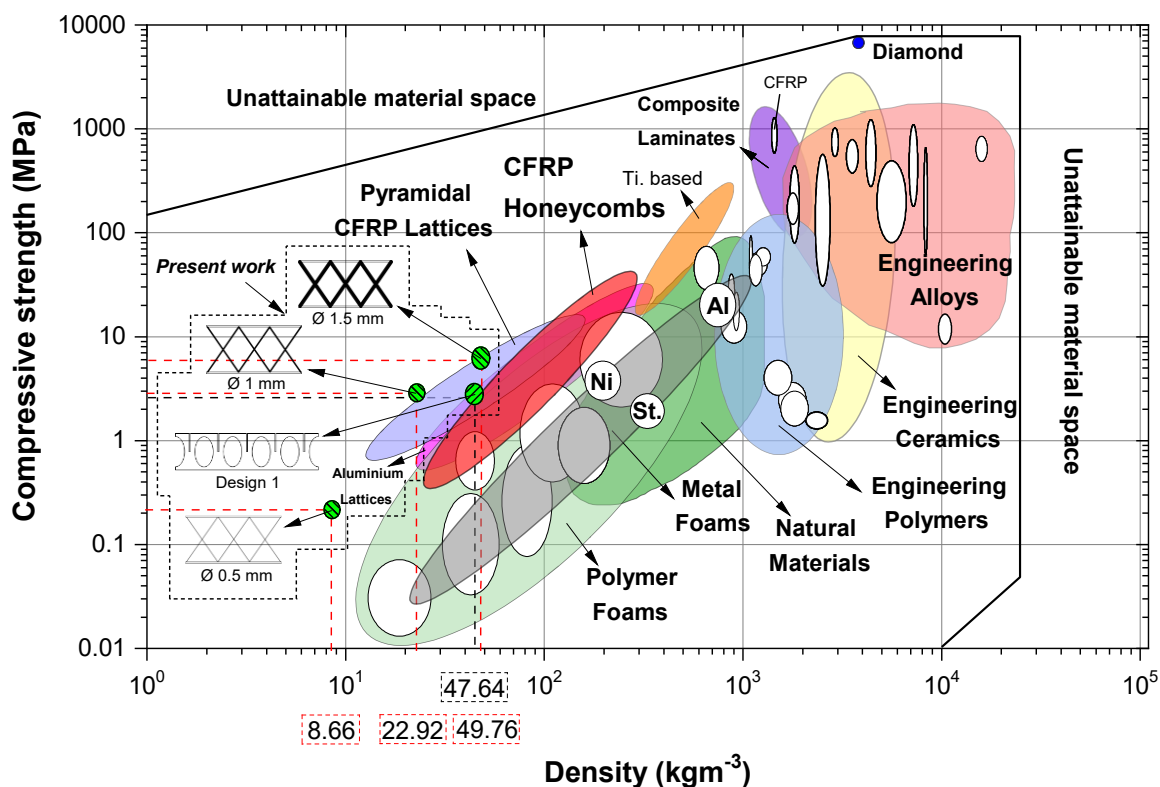


Figure 7.3. Ashby-style plot: out-of-plane compressive strength as a function of the material density.

The cores of the present work are plotted as the green-black slashed balloons on Figure 7.3. 3D square-honeycomb cores (design 1 cores) are comparable and competitive to traditional square-honeycomb CFRP-based cores with densities less than 50 kgm^{-3} . For instance, they have almost the same strength of the plotted Ni-foam but having four times less density. Also, design 1 cores outperform the metallic and polymeric foams of the same density, only exceeded by the CFRP-based lattice-cores. The proposed lattice-based cores present the best compressive performance among their same densities' counterparts. Regarding to 0.5 mm rod diameter lattice-core, no other

competing material is found in the surroundings of 8.6 kgm^{-3} , giving a chance for further material development.

7.1.3.2 Shear behaviour

As showed in previous section, features of interest are evaluated qualitatively by the Ashby-style charts. In this section, the shear behaviour as a function of the density is addressed (Figure 7.4) including data of CFRP honeycomb cores [21], CFRP pyramidal lattices [151,176], titanium matrix lattices [210], different metallic foams [117] and aluminum tetrahedral lattices [177].

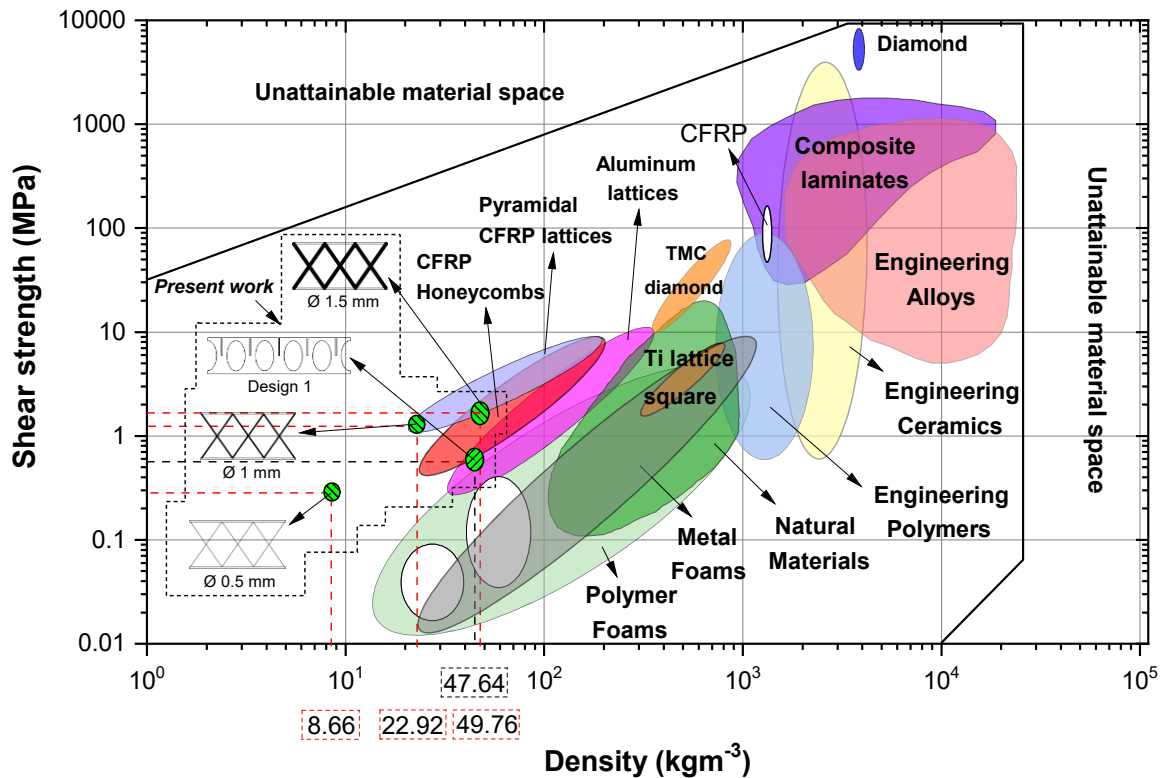


Figure 7.4. Ashby-style plot: shear strength as a function of the material density.

The cores proposed in this work present properties comparable to several same densities' counterparts. The design 1 square-honeycomb core is found on the bottom place of the red balloon corresponding to the CFRP honeycomb cores, influenced by the fibre orientation and the shear loading case. Nevertheless, they are comparable to the aluminium-based lattices and outperform the metallic and polymeric foams. Concerning to the lattice-based developed cores, they outperform the CFRP traditional

honeycomb cores and the aluminium-based materials, only comparable to the pyramidal CFRP lattices. Additionally, the lightest lattice materials as the $\approx 8.6 \text{ kgm}^{-3}$ material finds its place alone on the chart, also allowing further material developing, since it is a region still non deeply explored.

7.1.3.3 *Bending behaviour*

As explained in Chapter 3 and Chapter 6, the combination of two materials in a sandwich-type structure, thought of as two skins and a core in the middle, provides great rigidity to bending with a very small increase in weight as the core increases in thickness, as a result of the increment in the second moment of area of the entire section.

In the previous sections, the focus has been put on the comparison of the cores under study with the materials commonly used as cores in sandwich structures. In other words, only one of the components that made up the sandwich has been discussed. Since the sandwich panels are made from different components, the properties' comparison among materials demands other ways of study. Therefore, bending properties of different available sandwich materials are not easily attainable in the literature, although two different approaches are mentioned below.

On the one hand, many authors have proposed a comparison through a non-dimensional parameter called *load index*, which depends on the applied shear load, the moment generated by the shear load, geometrical variables such as the width and the total thickness of the sandwich section. This parameter is matched to the failure modes of both the skins and the cores, and is plotted as a function of another non-dimensional parameter known as the *weight index*, which depends on the weight and density of the sandwich [217–219]. On the other hand, Ashby [220] proposes treating the sandwich panel as a material with its own set of properties. Ashby simulates a monolithic homogeneous material by means of the calculation of equivalent properties. These equivalent properties include a density, a modulus, and a flexural strength of the sandwich panel. Then it would be possible to compare its properties directly with conventional materials through Ashby's style diagrams such as flexural strength vs. density. Given the practicality and simplicity of Ashby's proposal [220], this work will shortly address the sandwich flexural strength under Ashby's method guidelines as follows.

First, the equivalent density $\tilde{\rho}$ of the sandwich is defined in terms of the volume fraction occupied by the faces f_{faces} and its associations with the core density ρ_c and face density ρ_f , as of a rule of mixtures (Eq. (5.1) and Eq. (7.2)).

$$f_{faces} = \frac{2t_f}{h} \quad (7.1)$$

$$\tilde{\rho} = f_{faces}.\rho_f + (1 - f_{faces})\rho_c \quad (7.2)$$

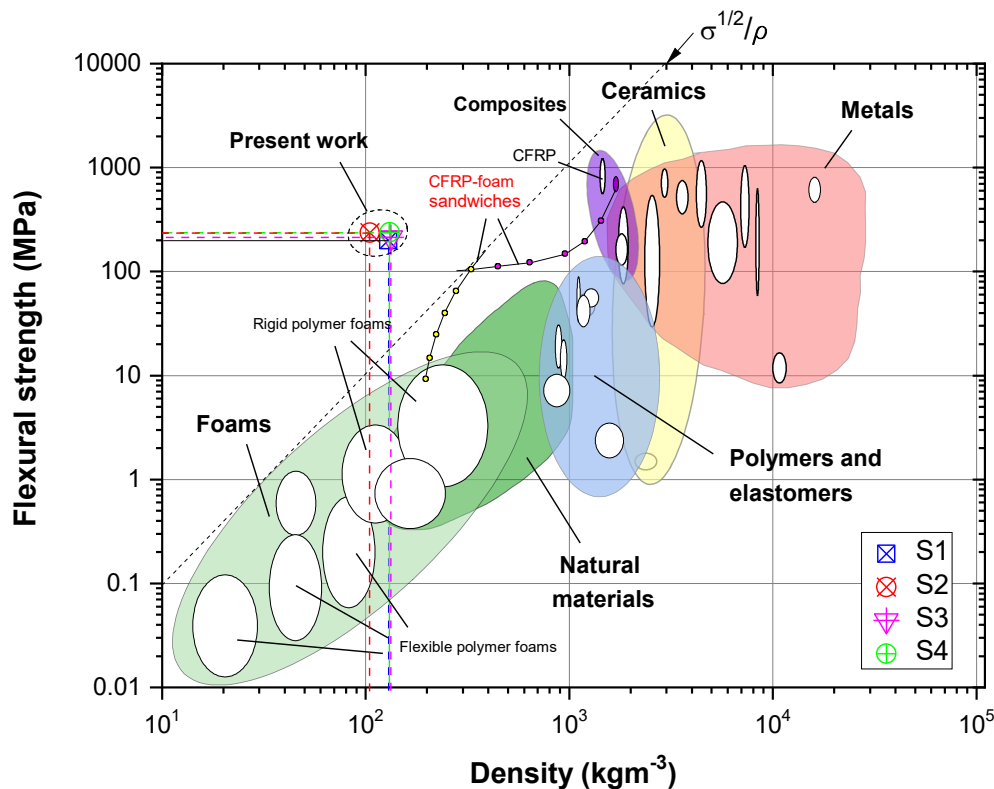
As seen in Chapter 6, the flexural strength is equal to the maximum stress in the outer fibres of the sandwich section at the instant of failure. Since thin faces are assumed, the stress is homogenized through the face thickness. In other terms, the normal stress on the faces is assumed to be equal to the bending stress due to the bending moment, as proven by the equivalency of Eq. (6.6) and Eq. (6.9). Furthermore, different failure mechanisms compete, although a core failure (i.e., a foundation failure) or a face failure are identified. The failure is then attained by the mechanism that demands the lowest load to appear. Ashby [220] defines the equivalent flexural strength $\tilde{\sigma}$ equating the flexural stress depending on the maximum moment applied to the section, to the stress that defines the failure mechanism, either as a core failure or as a face failure. In this work, the flexural strength is analogously defined as Eq. (6.33) for face yielding, Eq. (6.35) for face wrinkling, and Eq. (6.37) for intracellular buckling (see Chapter 6). The last mentioned equations are employed as the equivalent flexural strength proposed by Ashby.

Table 7.5. Sandwich data for the equivalent flexural properties analysed

Sandwich		$\tilde{\rho}$	$\tilde{\sigma}$	Failure
N°	Type of core/face thickness	(kgm ⁻³)	(MPa)	mode
S1	3D Square-honeycomb (design 1) / $t_f = 0.8$	129.08	200*	IB*
S2	BCC-like lattice cores (D 0.5) / $t_f = 1.21$	133.17	213	FW
S3	BCC-like lattice cores (D1) / $t_f = 0.8$	105.83	237	IB
S4	BCC-like lattice cores (D1.5) / $t_f = 0.8$	131.08	239	IB

Obs. * Theoretical value/mode. FW: face wrinkling; IB: intracellular buckling

Table 7.5 resumes the flexural properties homogenised to the sandwich beams. Remarkably, the sandwiches present equivalent densities of the same order in the range [105 – 133] kgm⁻³, and very similar bending strengths. The values are summarized and plotted into the Ashby-style chart shown as Figure 7.5.



Note: Adapted from [220]

Figure 7.5. Ashby-style plot: flexural strength as a function of the material density

Since a briefly comparison as example is intended within flexural properties of sandwich materials, only the materials exhibited in reference [220] are contrasted to the cores of the present work, mainly due to the lack of available information and the need to homogenized the sandwich's flexural properties. Therefore, the sandwiches materials developed in this work present higher flexural strengths for a same density material. Moreover, they outperform most of the CFRP-facesheets/polymeric foam sandwich materials, presenting one order of magnitude less density in many cases. The failure modes also influence the loading capability of the sandwich. The cores influence may be threatened as of less importance regarding bending, since the maximum bending loads are resisted by the skins on the outer fibres. Nevertheless, the cores do influence the magnitude of the skin loading capability as its foundation, when considering the failure modes. A larger core unit-cell influence the intracellular buckling behaviour of the whole sandwich, allowing larger payload in bending if the core cells are smaller. Also they influence the face wrinkling behaviour, as they increment their out-of-plane rigidity as seen Chapter 6.

The bending rigidity is also attainable, e.g., from the sample's deflection and the applied load, as $EI \approx D_x$ as seen in chapters 3 and 6. The face sheets' size and their positioning about the neutral line in bending are the main factors that govern the deflection behaviour. Nevertheless, the deflection obtained from the experiments is very sensitive to the testing rig and the test setup, as well as the manufacturing process. The deflection of the specimen obtained vertically within the supports is approximately in the range 0.63 – 1.03 mm for the lattice core cases. Taking into account that the span of the supports is $L_2 = 170$ mm, the displacement-to-length ratio is almost 0.3% and 0.6%, respectively, i.e., a small ratio between deflection and specimen dimension. Thus, under the given conditions, calculating an equivalent bending modulus from the sandwich beam as a homogeneous material as Ashby's proposal (applying ideal geometrical values combined with experimental values) would only represent an unreliable approximation of the analyzed cases within this work, due to the sensitiveness of the measure. For this purpose, the equivalent bending modulus is not represented graphically.

7.2 Difficulties found

In general terms, the difficulties encountered throughout this thesis were seen according to different aspects mainly as the manufacturing processes and the tests.

Regarding to the manufacturing process, the reproducibility of the specimens through a reliable manufacturing method was found to be an issue. In the case of the 3D- honeycomb cores, the manufacturing method is simple and relatively inexpensive (out-of-autoclave process) resulting in good quality parts. However, many steps, especially in the assembly of the cores from CFRP-sheets, are manual and this leads to imperfections, e.g., in the sheet positioning despite using grooved guides. In addition, water jet cutting method (WJC) to obtain the desired geometries has proven to be efficient, since several sheets are stacked together and cut at the same time, being the cutting quality very good at the edges. By enhancing the manufacturing process, for example, by reducing the handwork, the incorporated imperfections could be mitigated, and therefore, the core's performance would be much higher. The main disadvantage of the WJC method is that for example, when using more than 10 stacked CFRP sheets (> 6.5 mm) and a CFRP base plate size approx. 350 mm by 250 mm, there are noticeable vibrations induced by the water pressure against the material and in some cases,

delamination damage was seen in the base material mainly in the surroundings of the central area of the stack, since the table clamps of the WJC process are not able to exert sufficient clamping pressure. However, using five sheets and reducing the CFRP base plate size to approx. 250 mm by 150 mm no delamination effects were seen, but the number of sheets to be machined at the same time is limited, which increases the production time. For the case of lattice type cores, it is encouraged that the bonding area between core and skins must be optimized from the manufacturing process to better achieve the strength potential of the rods. For example, in the case of plate shear load case, the 1 mm and 1.5 mm rods are limited in its shear strength capabilities because of debonding and cannot reach the full bearable stress (for example, only 1.06 MPa instead of 2.25 MPa, for 1 mm rod as seen in Chapter 5). In general, the manufacturing time limited in some cases the production of samples (for example, regarding to the larger shear specimens), and thus, the production time must be improved.

Concerning the tests, all of them were carried-out satisfactorily, although some enhancements opportunities were found. For the compressive tests, the use of a spherical bearing as base support of the loading plates compensates substantially the manufacturing imperfections as the bearing corrects the wrong positioning of the sample under load, improving the load distribution among the struts. However, premature failure was seen in compression samples (for example in Chapter 4), because the distribution of the loads is still not ideal. For the shear tests, it was necessary to design and to machine the steel plates (both demanded more time than planned) in a way that the samples could fit properly in the test rig, targeting that the line load passes through the main diagonal of the core (Figure 4.35) as recommended in the standard [167]. In the case of bending tests, the size of the bending samples (490 x 65 x 27 mm) also represented a challenge to obtain and to test. For the bending tests, it was necessary to employ supports and punches according to the dimension of the samples, which demanded time to correctly setup and fit into the testing machine. The use of smaller redesigned samples may be useful as improvement. Regarding the shear and bending samples, a larger number of specimens may be needed to fulfil the statistical demands if required to better adjust the failure predictions, and thus, they are proposed to be obtained and tested as future work.

7.3 Conclusions

A summary of the conclusions gathered along this dissertation is presented and resumed within this section:

1. The manufacturing process detailed in Chapter 4 for 3D honeycomb cores represents an advantage for obtaining ultra-lightweight cores. The traditional metallic lattice materials such as pyramidal or tetrahedral geometries require cutting and bending punches as well as dies to build up the cores, followed by a welding step for attaching the face sheets [125]. Here, the proposed cores present an easier and faster fabrication method, having less and simpler manufacturing steps.
2. The use of pultruded CFRP-based rods for sandwich cores for BCC-like structures, allows attaining ultra-lightweight densities as seen in Chapter 5.
3. As seen in Chapters 4 and 5, the cores' elastic properties in non-conventional sandwich panels such as 3D-honeycombs or lattice-based, depend directly on:
 - (i) the properties of the base material, (ii) the amount of base material available within the unit cell, and (iii) the material positioning or the unit cell's topology, which is taken as basis for studies:
 - i. The properties of the base materials will determinate the global properties of the cores. Employing CFRP materials represents an advantage in the development of weight sensitive structures, because they provide very high specific modulus and strength, and they outperform their metallic counterparts as seen in section 7.1. The core modulus depends directly on the modulus of the parent material as seen in chapters 4 and 5. Moreover, the core strength depends also on the parent material properties, in which the CFRP materials stand-out compared to many engineering alloys (see Figure 7.3 and Figure 7.4).
 - ii. The amount of base material bearing the load within a unit cell is exemplified in different terms regarding to the analysed core as follows:
 - a. For the case of machined 3D-honeycombs, the number of CFRP-sheets, and the sheet's thickness are the factors that control the main core properties. For example, the denser the unit cell, the greater the elastic modulus and the strength of the core. The amount of material bearing the load influence the failure behaviour of the core from elastic buckling failure to fracture of the base material. The material orientation bearing the load i.e., fibre angle

- as explained in Chapter 4, also affects the final performance of part. Thus, the fibre orientation must be set according to the load case.
- b. For the case of lattice-materials, the number of CFRP-rods in a unit cell and the rod's diameter play a fundamental role in the core's properties. For instance, the larger the diameter or the rod's number, the greater the core's modulus and strength (see Chapter 5). The rod's size also influence the core's failure modes, from Euler buckling to fracture or debonding. The appropriate rod orientation influences the core's strength, as seen in Annex D.
 - iii. The cell's topology influence the core's behaviour:
 - a. For the case of machined 3D-honeycomb cores, the cell size influences the failure mode of the core, from torsional buckling to plate buckling. The core's machined geometries did not have a crucial effect on the cores' compressive behaviour since the elastic moduli and strength are found almost equal among the cores. In fact, the fibre orientation in combination with the topology may play a fundamental role in core's behaviour. In shear loading, the thinner the struts, the larger the bending term summed to the shear term, and ergo, the smaller the shear strength, as seen in design 2 cores.
 - b. For the lattice-cores, the rod's angle and positioning (could be also translated into cell's size) influence the positioning of the mid-plane linking node (Figure 5.11) as can be seen in Annex D. This effect also determinates the failure mode in compression or shear as of, for example, Euler buckling or fracture, and influences the core's strength. Moreover, the mid-plane node influences the failure behaviour of the unit cell, in compression and shear, throughout the Euler's k -factor, varying from a value 1 (two rod's end simply supported) to 0.5 (two rod's end fixed). Since the core-skin linkage is elastic, the k -factor may be found within the range above mentioned.
 4. On the other hand, the flexural properties of a sandwich structure depend mainly on the parent material of the skins, their thickness, the stiffness of the cores and the size of the unit cell. The buckling coefficients also influence the flexural strength of the sandwich beam. The above-mentioned parameters directly affect the sandwich's failure modes, from face wrinkling or face intracellular buckling to face fracture (see Chapter 6). Additionally, the use of a thick skin in combination with a core with a relatively small stiffness, results in a face wrinkling failure, in other words a foundation failure; the use of a thin skin combined with

a stiff core results in intracellular buckling failure as proposed in Chapter 6. The optimal face thickness may be given by analyzing the potential failure modes and the loading requirements. Furthermore, the unit cell size promotes the intracellular buckling failure mode at relatively low load. For example, when using 3D-honeycomb as core, switching the cell size from a 50 mm to 20 mm, the failure load is five times higher considering a same skin thickness.

5. In this work, the core's specific properties defined in terms of compressive and shear modulus and strength demonstrate the competitiveness against other core materials (see section 7.1), despite not achieving the full potential of the predicted payload capability. Remarkably, the proposed cores showed better compressive performances and comparable to better shear properties as stiffness or strength compared to traditional aluminium honeycomb cores commonly used in aerospace applications.
6. The theoretical and numerical calculations revealed the capabilities of the proposed CFRP-based cores and sandwich structures, predicting their quasi-static mechanical properties and failure behaviour, later confirmed by experimental tests. As outcome of this work, the proposed cores are promising candidates for ultra-lightweight sandwich applications.

8 Resume and outlook

The novelty of this dissertation is up to the contribution to new designs, a manufacturing path, and elastic properties predictions on novel cellular core-type materials. The loading cases for studying the mechanical behaviour of the cores are selected as out-of-plane compression, plate-shear, and bending. By means of micromechanical models from analytical and numerical approaches, the properties and failure modes are foreseen, later validated by the experimental tests with very good correspondence.

Two different core proposals are investigated as 3D-square honeycomb cores and BCC-like lattice-cores, both having CFRP as parent materials. The cores achieve the “ultra-lightweight cores” denomination, since they attained, on average, less than $\approx 48 \text{ kgm}^{-3}$ densities, also taken as primary target function. The cores present excellent mechanical performances compared to other research works, and to their commercial counterparts of the same density.

Since the cores are intended for sandwich applications, a sandwich structure is also designed, assembled, and studied under a four-point-bending loading case, identifying in advance via theoretical and numerical studies the failure modes, and corroborated later by experimental tests.

The proposed cores represent an alternative to known core materials for ultra-lightweight sandwich applications, in terms of mechanical response and specific properties.

8.1 Resume

A review of the general outcomes of this work are assembled in this section:

1. When using CFRP, the parent material's elastic properties are attainable in advance, knowing the main components' features (i.e., matrix and fibres) and applying theoretical approaches as the classical laminate theory, as seen Chapter 2, and detailed in Annex B. CFRP-based materials provide very high specific modulus and strength to the main structure, at the same time, outperforming their metallic counterparts for weight sensitive applications.
2. Sandwich structures bear the load according to different loading cases. In Chapter 3, they are resumed as: out-of-plane compression and plate-shear loading,

which are mainly borne by the core; and bending, where the skins bear in-plane tensile or compressive loads.

3. For evaluating the cores: the loading cases are established as quasi-static out-of-plane compression and plate-shear. For evaluating the sandwich as a structure: four-point-bending is considered. Micromechanical and macromechanical models are developed for predicting the elastic properties, by analysing a representative unit cell and using parent material properties. FE models give support to the theoretical approaches, establishing the most likely failure modes. Samples are manufactured according to each loading case. Good correspondence is found when predictions are contrasted to experimental results.
4. There are two cores' proposals: 3D honeycombs cores (Figure 4.2, Chapter 4); and BCC-like lattice cores (Figure 5.2, Chapter 5). The real average densities are in the range $\approx [38 - 47] \text{ kgm}^{-3}$ and $\approx [8 - 49] \text{ kgm}^{-3}$, respectively. In both cases, the cores are considered as ultra-lightweight cores.
5. There are two sandwich proposals (Chapter 6): lattice-based cores, employing 0.8 mm and 1.21 mm of face thicknesses from CFRP 2x2 twill-woven-plates in a 4- and 6-layer-up configuration, respectively, with a $[0/90]^\circ$ fibre orientation; and 3D honeycombs-based cores, using 0.8 mm of face thickness.
6. Novel manufacturing paths based on the interlocking method are achieved for fabricating ultra-lightweight 3D honeycomb cores. The cores have been manufactured from CFRP plain-woven-plates in a 3-layer-up configuration, with $[0/90]^\circ$ fibre orientation, then machined into the desired topology by a CNC water-jet cutting tool, and later assembled.
7. In 3D honeycomb cores, the failure behaviour under compression is governed by torsional buckling in all machined cases, and of plate elastic buckling in reference cores.
8. The average compressive strength of the 3D honeycomb cores is in the range of $[2.2-2.7] \text{ MPa}$, while the elastic modulus is in the range of $[0.72-1.12] \text{ MPa}$.
9. The failure mode in shear of the 3D honeycomb cores is dominated by shear failure for the machined cases, and of debonding for the reference cores. The theory of a Timoshenko-like beam is also confirmed by FE calculations.
10. The average core shear strength of 3D honeycomb cores is in the range of $[0.33-0.54] \text{ MPa}$, and the shear moduli in the range of $[17.14-52.52] \text{ MPa}$.

11. The use of uni-directional CFRP-rods with three different diameters as 0.5mm, 1 mm and 1.5 mm enables ultra-lightweight cores with BCC-like topologies.
12. The failure behaviour of the lattice-cores to compression is dominated by Euler buckling for the smaller diameters and rod's fracture for the largest.
13. The compressive elastic moduli of the lattice-cores are found as 33.91 MPa, 267.8 MPa and 472.55 MPa, while maximum compressive strengths of 0.22 MPa, 2.87 MPa and 5.87 MPa are attained for diameters of 0.5 mm, 1 mm, and 1.5 mm, respectively.
14. In shear loading, the govern failure modes of the lattice-cores are found as Euler buckling for the thinnest diameter case, and pull-out for the other rod's cases.
15. Average peak shear moduli of the lattice-cores of 45.85 MPa, 137.015 MPa and 232.591 MPa, and shear strengths of 0.29 MPa, 1.06 MPa and 1.36 MPa are observed for rods' diameters of 0.5 mm, 1 mm, and 1.5 mm, respectively.
16. With the help of support members, large samples are obtained for four-point-bending.
17. Flexural properties mainly depend on the thickness skins, the core's out-of-plane compressive stiffness and the size of the unit cell.
18. The bending failure modes attained are face wrinkling or face intracellular buckling. The thicker the skins or the weaker the cores, the higher the face wrinkling's probability. The thinner the skins, the higher the intracellular buckling's chance.
19. The maximum average face stresses or flexural strength of lattice-cores based samples are found as 213 MPa, 237 MPa and 239 MPa for lattice-cores made from 0.5 mm, 1 mm, and 1.5 mm rod's diameters, respectively.
20. From the theoretical models, the buckling coefficients Q_b and K are indirectly attainable with help of the numerical results or the experimental results.
21. As extrapolation of the models developed, the bending case for the 3D-honeycomb cores is assessed via numerical approaches.
22. The cell's size affects the sandwich's flexural strength. From a change in the cell's size from 50 mm to 20 mm, the failure load is quintupled for the same 0.8 mm skin's thickness (intracellular buckling failure mode).
23. The competitiveness of the proposed material compared to other known materials used as sandwich cores is assessed (Chapter 7).

24. The material has shown better mechanical performances in most cases compared to their commercial counterparts.

8.2 Outlook

Within the framework of this dissertation, opportunities have arisen to improve and further develop the topics discussed. These improvements are intended as a proposal for future work.

- a. **Core design improvements:** the shear properties of 3D-honeycomb cores could be possible by changing two layers of the plain woven CF-lay-up into 45° orientation. The following new lay-up is proposed: $[\pm 45, 0/90, \pm 45]^\circ$, although with a decrease in the out-of-plane compressive stiffness and strength. This improvement could be even enhanced by its combination with new machined geometries as Figure 8.1.

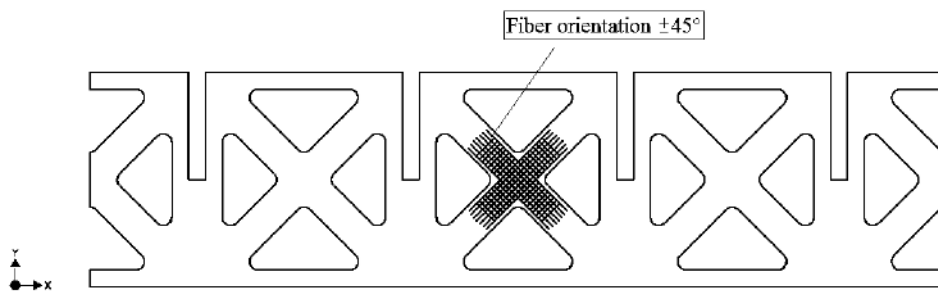


Figure 8.1. New geometries proposed for enhancing shear properties of 3D-honeycomb cores

Moreover, varying the cell size in lattice cores would give a higher buckling load, for example, in lattice-cells of 0.5 mm rods. Only by displacing half a cell in each direction would it be possible to obtain up to three contact points along a rod, ideally increasing the actual buckling failure load from 0.2 MPa to ≈ 1 MPa. The cell's size may also affect the flexural failure modes, especially when the intracellular buckling mode has preference.

- b. **Further development of FE models:** the models are sensitive to discrepancies that are not taken into account in the calculations. Unequal load distribution during sample testing, led to local premature failures. By small imperfections introductions in FE models, it could be inferred how they affect the overall loading

capability throughout the overloading on other struts. In lattice cores, the rods present an elastic linkage at the mid-plane node and to the skin. For a refinement in the FE simulations, its recommended to implement torsional springs at the rod-rod and rod-face connection points whose stiffnesses are indirectly calculated from the experimental tests. This could better approximate the Euler k -factor, and the bending buckling coefficients K and Q_b according to experimental tests.

- c. **Improvement of data and testing:** the face thicknesses on bending samples present local deviations affecting locally the face rigidity. Their dimensions could be measured using more precise instruments such as 3D-scanners to better approximate the FE model to the real case. More samples are needed to finer endorse the proposed failure models in all cases. The models could be also expanded by incorporating other cell sizes, rod's diameters or face thicknesses, possibly extended to other failure modes. Also, the experimental bending response of sandwich plates with 3D-honeycomb cores and dynamic tests are proposed to complement the theoretical and numerical investigations, and deepen the reliability analysis of the materials proposed
- d. **Potential applications and scaling manufacturing studies:** taking advantage of the hollow pattern or open cells of the cores, the multifunctional capabilities as heat transferring, fluid flowing, cables or electronics embedding, foams reinforcing for damping and stiffness efficiency, among others, may be of interest and shall be proven. The manufacturing costs are also of technological interest and shall be evaluated, also considering semi-automatized processes for quality enhancements. The potential applications of the sandwich materials are not limited to the transport industries (aerospace, automotive, railroads or ships), but also could be extended to optical branch industries (e.g., telescope support plates). Further exploration of the utility of these structures into other applications is intended as future work.

Annexes

A Complementary information: polymer composite materials reinforced with fibres

A.1 Global demand of polymer composite materials reinforced with fibres

Composite materials based on fibre-reinforced polymers are intended for commercial applications in many fields of engineering and those who belong to structural application areas are in current focus. Different industries such as: aerospace, military, automotive, marine, wind turbines, infrastructure (e.g., as construction of bridges or pillars), optics (e.g., as high precision plates [221,222]) and sporting goods, widely demand fibre reinforced polymers. Glass fibre reinforced polymers (GFRP) and carbon fibre reinforced polymers (CFRP) are highly demanded as base fibres materials. Glass fibre reinforced polymers are already standard products today. The transportation and construction industries continue to be the main customers for GFRP components, each with about a third of the total production volume. In some cases, GFRP components are already firmly established as building materials, especially in chemical plants due to the high resistant to corrosive substances [32,223]. On the other hand, the annual demand of carbon fibre reinforced composites components is mainly within commercial aviation (including defence sector) with 55,31 kt/a (being kt/a: kiloton per annum) followed by automotive sector as the second largest segment with 37,13 kt/a (Figure A.1). The annual worldwide total demand of CFRP components was ca. 154,7 kt/a , while sales were approximately US\$ 23,15 Mrd (being Mrd: thousands of millions) in 2018. In particular, the cost per kilogram of CFRP is highly conditioned upon the high quality and safety requirements as well as the subsequent certification and qualification costs in the different application areas. In contrast to the aerospace industry, standard automobile manufacturing is significantly sensitive to large-scale material processing technology, and consequently its production costs [32,224]. Between the years 2010 and 2012, only a few CFRP manufacturing methods were able to guarantee relatively large series with the expected quality, despite the fact that the total manufacturing time of the part was still high, mainly due to a low-level of automation of the process.

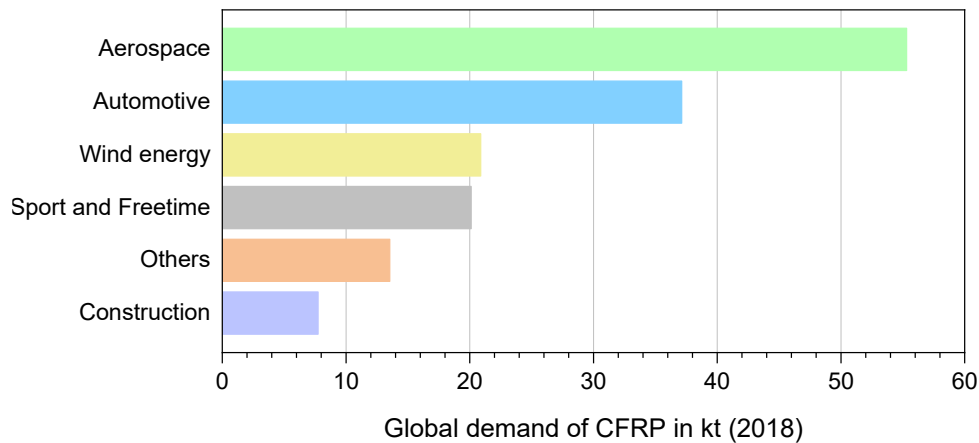


Figure A.1. Global demand of CFRP components per main sector (2018) [224]

Recent process analyses, in turn, showed that large batch production series allows significant cost reductions in the CFRP process chain. For example, in 2018 the manufacturing cost per kilogram of CFRP components was ca. 80 EUR for a batch of 5,000 articles per year; if the batch rises to 75,000 items per year, the costs could be reduced to 65 EUR. Furthermore, if it is possible to combine this effect with the processing of lower cost raw materials through new production automated technologies (for example, using RTM instead of traditional autoclave-based processes) and the reduction of finishing processes (such as off-cuts), the costs for the medium-scale manufacturing of 1 kilogram of CFRP components could be approximately reduced to 18 EUR per kg according to recent estimations [225,226].

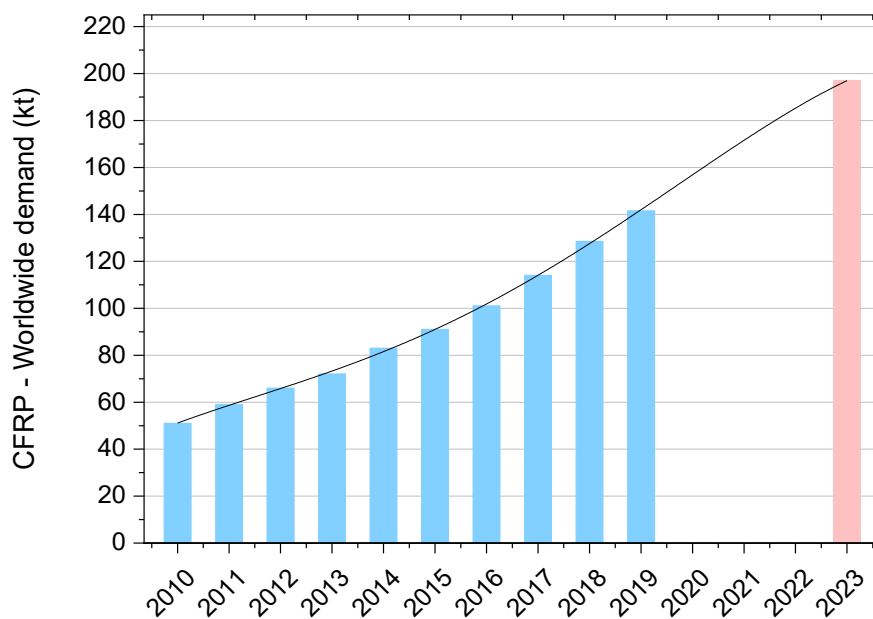


Figure A.2. Global demand of CFRP from 2010 to 2023 (estimated) [227]

Thus, an accelerated growth on the demand for composite materials is expected in the upcoming years, partly due to privatizations in the aerospace sector [224] and the development of high volume automated manufacturing techniques in the automotive sector, but which still can guarantee the expected quality and safety (e. g. RTM processes developed by AUDI AG and Voith Composites [228]). The CFRP components demand prognosis is presented on Figure A.2. Considering the historic demand along the years, an average sustained increase of almost 13% annually is expected until 2023, reaching a value of nearly 200 kt/a . Moreover, particularly the annual demand of CFRP components in the automotive sector is expected to reach the value of 72 kt/a, surpassing the aerospace sector by 7 kt/a in 2022 [223].

B Base material properties

B.1 Ultra-lightweight 3D-honeycomb cores

B.1.1 Elastic properties

The woven [0/90] ° carbon fibre fabric layer is approximated as a 50-50 laminate, with fibres a [0] ° and [90] ° and disregarding the waviness, due to the small tow size (T300-3k) and the final CFRP thickness (≈ 0.65 mm). Three woven layers are laid-up.

- Base laminate features

Single layer thickness [mm]	Total thickness (t) [mm]	Textile weight [kg/m ²]	Fibre density [kg/m ³]	Fibre volume content Eq. (2.1)	Fibre orientation [°]
0.10833333	0.65000000	0.198	1800	0.50769231	0 – 90

- Fibre and matrix elastic properties

$E_{f\parallel}$ [MPa]	$E_{f\perp}$ [MPa]	$G_{f\parallel\perp}$ [MPa]	$\nu_{f\parallel\perp}$ [-]	E_m [MPa]	ν_m [-]
<i>Toray T300</i> 230000	[34] 13000	[34] 50000	[34] 0.23	<i>Epoxy DGBA</i> 2650	0.3

- UD-layer laminate elastic properties

E_{\parallel} [MPa]	E_{\perp} [MPa]	$G_{\parallel\perp}$ [MPa]	$\nu_{\parallel\perp}$ [-]	$\nu_{\perp\parallel}$ [-]
Eq. (2.6) 118073.85	Eq. (2.13) 6747.88	Eq. (2.15) 3556.77	Eq. (2.16) 0.2645	Eq. (2.17) 0.0151

- Transformed stiffnesses

	Q_{11} Eq. (2.24)	Q_{22} Eq. (2.26)	Q_{33} Eq. (2.29)	Q_{12} Eq. (2.25)	Q_{13} Eq. (2.27)	Q_{23} Eq. (2.28)
	118547.6864	6774.963015	3556.767196	1791.717142	0	0
	6774.963015	118547.6864	3556.767196	1791.717142	1.3049E-13	6.7164E-12
	118547.6864	6774.963015	3556.767196	1791.717142	0	0
	6774.963015	118547.6864	3556.767196	1791.717142	1.3049E-13	6.71641E-12
	118547.6864	6774.963015	3556.767196	1791.717142	0	0
	6774.963015	118547.6864	3556.767196	1791.717142	1.3049E-13	6.71641E-12
$\Sigma Q_{ii} \cdot t_i =$	40729.86	40729.86	2311.90	1164.62	0.00	0.00

- Stiffness matrix [A]

40729.86 1164.616142 4.24112E-14
 1164.616142 40729.86 2.18283E-12
 4.24112E-14 2.18283E-12 2311.898677

- Compliance matrix [a] = [A⁻¹]

2.4572E-05 -7.02607E-07 2.1261E-22
 -7.026E-07 2.45721E-05 -2.319E-20
 2.1261E-22 -2.31874E-20 0.00043254

- Engineering constants

Solved for this work with Figure 4.7 as coordinate reference:

E_{1s}	=	62610.09295	[MPa]	(Eq. 2.44)
E_{3s}	=	62610.09295	[MPa]	(Eq. 2.45)
G_{13s}	=	3556.767196	[MPa]	(Eq. 2.46)
ν_{13s}	=	0.028593668	[-]	(Eq. 2.47)
ν_{31s}	=	0.028593668	[-]	(Eq. 2.48)

B.1.2 Strength

- Budianski's model (Eq. 2.56) [57]

Σ_{cs}	G_{ec}	G_m	E_m	ν_m	F_v	Φ_{nom}	Strain _{yc}	Φ_{nom}	Σ_{cs}
[MPa]	[MPa]	[MPa]	[MPa]		[%]	[°]		[°]	[MPa]
405.543	2070.97	1019.23	2650	0.300	0.508	4.000	0.017	2.000	678.266
								3.000	507.592
								4.000	405.543
								5.000	337.659

- Composite compressive strength:

$$\Sigma_{cs_avg}$$

$$(\sigma_{3s}^- = \sigma_{1s}^-)$$

$$[Mpa]$$

482.265

- Composite shear strength:

The shear strength of the UD-layer of T300/epoxy is presented as $R_{\perp\parallel} = 75$ MPa in Ref. [34]. Since the base material is based on woven T300 layers, the shear strength may be influenced by the cross-fibres, as in weft direction. The shear strength is pre-estimated as $\tau_{13s} = 110$ MPa, as presented in [139] for analogous woven T300/epoxy CFRP composite materials.

B.2 Ultra-lightweight lattice-cores made from CFRP rods

B.2.1 Elastic properties. Skin I ($t_f = 0.8$ mm)

The twill 2 x 2 [0/90] ° carbon fibre fabric layer is approximated as a 50-50 laminate, with fibres a [0] ° and [90] ° and disregarding its waviness, due to the small tow size (T300-3k) and final CFRP thickness (≈ 0.80 mm). Four woven layers are laid-up.

- Base laminate features

Single layer thickness [mm]	Total thickness (t) [mm]	Textile weight [kg/m ²]	Fibre density [kg/m ³]	Fibre volume content Eq. (2.1)	Fibre orientation [°]
0.10000000	0.80000000	0.198	1800	0.55000000	0 – 90

- Fibre and matrix elastic properties

$E_{f\parallel}$ [MPa]	$E_{f\perp}$ [MPa]	$G_{f\parallel\perp}$ [MPa]	$\nu_{f\parallel\perp}$ [-]	E_m [MPa]	ν_m [-]
<i>Toray T300</i> 230000	[34] 13000	[34] 50000	[34] 0.23	<i>Epoxy type L</i> 2650	0.3

- UD-layer laminate elastic properties

E_{\parallel} [MPa]	E_{\perp} [MPa]	$G_{\parallel\perp}$ [MPa]	$\nu_{\parallel\perp}$ [-]	$\nu_{\perp\parallel}$ [-]
Eq. (2.6) 127692.50	Eq. (2.13) 7444.25	Eq. (2.15) 4061.70	Eq. (2.16) 0.2615	Eq. (2.17) 0.0152

- Transformed stiffnesses

	Q_{11} Eq. (2.24)	Q_{22} Eq. (2.26)	Q_{33} Eq. (2.29)	Q_{12} Eq. (2.25)	Q_{13} Eq. (2.27)	Q_{23} Eq. (2.28)
	128203.592	7474.044602	4061.701775	1954.46266	0	0
	7474.044602	128203.592	4061.701775	1954.46266	1.595E-13	7.23608E-12
	128203.592	7474.044602	4061.701775	1954.46266	0	0
	7474.044602	128203.592	4061.701775	1954.46266	1.595E-13	7.23608E-12
	7474.044602	128203.592	4061.701775	1954.46266	1.595E-13	7.23608E-12
	128203.592	7474.044602	4061.701775	1954.46266	0	0
	7474.044602	128203.592	4061.701775	1954.46266	1.595E-13	7.23608E-12
$\Sigma Q_{ii} \cdot t_i =$	54271.05	54271.05	3249.36	1563.57	0.00	0.00

- Stiffness matrix [A]

54271.0546	1563.570131	6.3801E-14
1563.57013	54271.05	2.8944E-12
6.3801E-14	2.89443E-12	3249.36142

- Compliance matrix [a] = [A⁻¹]

1.8441E-05	-5.31302E-07	1.1117E-22
-5.313E-07	1.84413E-05	-1.642E-20
1.1117E-22	-1.64165E-20	0.00030775

- Engineering constants

Solved for this work with Figure 5.1 as coordinate reference:

E_{1s}	=	67782.50947	[MPa]	(Eq. 2.44)
E_{3s}	=	67782.50947	[MPa]	(Eq. 2.45)
G_{13s}	=	4061.701775	[MPa]	(Eq. 2.46)
ν_{13s}	=	0.028810388	[-]	(Eq. 2.47)
ν_{31s}	=	0.028810388	[-]	(Eq. 2.48)

B.2.2 Elastic properties. Skin II ($t_f = 1.21$ mm)

The twill 2 x 2 [0/90] ° carbon fibre fabric layer is approximated as a 50-50 laminate, with fibres a [0] ° and [90] ° and disregarding its waviness, due to the small tow size (T300-3k) and final CFRP thickness (≈ 1.21 mm). Six woven layers are laid-up.

- Base laminate features

Single layer thickness [mm]	Total thickness (t) [mm]	Textile weight [kg/m ²]	Fibre density [kg/m ³]	Fibre volume content Eq. (2.1)	Fibre orientation [°]
0.10083333	1.21000000	0.198	1800	0.54545455	0 – 90

- Fibre and matrix elastic properties

$E_{f\parallel}$	$E_{f\perp}$	$G_{f\parallel\perp}$	$\nu_{f\parallel\perp}$	E_m	ν_m
[MPa]	[MPa]	[MPa]	[-]	[MPa]	[-]
<i>Toray T300</i>	[34]	[34]	[34]	<i>Epoxy type L</i>	
230000	13000	50000	0.23	2650	0.3

- UD-layer laminate elastic properties

E_{\parallel}	E_{\perp}	$G_{\parallel\perp}$	$\nu_{\parallel\perp}$	$\nu_{\perp\parallel}$
[MPa]	[MPa]	[MPa]	[-]	[-]
Eq. (2.6)	Eq. (2.13)	Eq. (2.15)	Eq. (2.16)	Eq. (2.17)
126659.09	7364.65	4002.27	0.2618	0.0152

- Transformed stiffnesses

	Q_{11}	Q_{22}	Q_{33}	Q_{12}	Q_{13}	Q_{23}
	Eq. (2.24)	Eq. (2.26)	Eq. (2.29)	Eq. (2.25)	Eq. (2.27)	Eq. (2.28)
	127165.9491	7394.126482	4002.266098	1935.91675	0	0
	7394.126482	127165.9491	4002.266098	1935.91675	1.5598E-13	7.18093E-12
	127165.9491	7394.126482	4002.266098	1935.91675	0	0
	7394.126482	127165.9491	4002.266098	1935.91675	1.5598E-13	7.18093E-12
	127165.9491	7394.126482	4002.266098	1935.91675	0	0
	7394.126482	127165.9491	4002.266098	1935.91675	1.5598E-13	7.18093E-12
	7394.126482	127165.9491	4002.266098	1935.91675	1.5598E-13	7.18093E-12
	127165.9491	7394.126482	4002.266098	1935.91675	0	0
	7394.126482	127165.9491	4002.266098	1935.91675	1.5598E-13	7.18093E-12
	127165.9491	7394.126482	4002.266098	1935.91675	0	0
$\Sigma Q_{ii} \cdot t_i =$	81408.85	81408.85	4842.74	2342.46	0.00	0.00

- Stiffness matrix [A]

81408.85	2342.45927	9.4369E-14
2342.45927	81408.85	4.3445E-12
9.4369E-14	4.34446E-12	4842.74198

- Compliance matrix [a] = [A⁻¹]

1.2294E-05	-3.53744E-07	7.7781E-23
-3.537E-07	1.22939E-05	-1.102E-20
7.7781E-23	-1.1022E-20	0.00020649

- Engineering constants

Solved for this work using Figure 5.1 as coordinate reference:

E_{1s}	=	67224.3337	[MPa]	(Eq. 2.44)
E_{3s}	=	67224.3337	[MPa]	(Eq. 2.45)
G_{13s}	=	4002.266098	[MPa]	(Eq. 2.46)
ν_{13s}	=	0.028774014	[-]	(Eq. 2.47)
ν_{31s}	=	0.028774014	[-]	(Eq. 2.48)

Observation to “Skin I” and “Skin II”

Since the elastic properties are very similar for skins I and II of average thicknesses 0.8 mm and 1.21 mm, respectively, the characteristics of a skin of 55% of fibre volume content will be considered to ease the calculations.

B.2.3 Strength

- Budianski’s model (Eq. 2.56) [57]

Σ_{cs}	G_{cs}	G_m	E_m	ν_m	F_v	Φ_{nom}	Strain_{yc}	Φ_{nom}	Σ_{cs}
[MPa]	[MPa]	[MPa]	[MPa]		[%]	[°]		[°]	[MPa]
369.287	2264.957	1019.231	2650.000	0.300	0.550	5.000	0.017	2.000	741.799
								3.000	555.138
								4.000	443.530
								5.000	369.287

- Composite compressive strength:

Σ_{cs_avg}

$(\sigma_{3s}^- = \sigma_{1s}^-)$

[Mpa]

527.439

- Composite shear strength:

The shear strength of the UD-layer of T300/epoxy is presented as $R_{\perp\parallel} = 75$ MPa in Ref. [34]. Since the base material is based on woven T300 layers, the shear strength may be influenced by the cross-fibres, as in weft direction. The shear strength is pre-estimated as $\tau_{13s} = 110$ MPa, as presented in [139] for similar woven T300/epoxy CFRP composite materials.

C Core and skin densities

C.1 Ultra-lightweight 3D-honeycomb cores

C.1.1 Composite plate

The theoretical density expected for the composite plate made from three layers of plain woven [0/90] ° T300-3k carbon fibres fabrics and epoxy resin as the polymeric matrix, is presented below. The fibre volume content (φ_f) and the composite E-moduli were calculated using the results from Annex B.

Plain woven [0-90] °

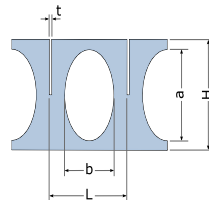
Plate_thick [mm]	n_layers [-]	Sup_dens [g/m ²]	Fibre_dens [g/cm ³]	Matrix_dens [g/cm ³]	φ_f [%]	E_max [MPa]	Comp_dens [g/cm ³]
0.6000	3	198.0000	1.8000	1.1400	55.0000	67782	1.5030
0.6500	3	198.0000	1.8000	1.1400	50.7692	62610	1.4750
0.7000	3	198.0000	1.8000	1.1400	47.1428	58214	1.4510

The experimental densities measured in the laboratory are in range \approx [1.30 – 1.35] gcm⁻³, and the plate thicknesses are of \approx [0.60 – 0.70] mm (the average is taken after three measurements).

C.1.2 Core densities

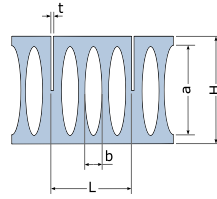
The core densities for the square honeycomb cores were estimated theoretically and validated by laboratory measurements as follows.

- Core design 1:



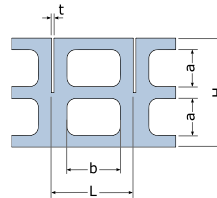
Comp_dens [kg/m ³]	Core_height [mm]	Core_length [mm]	Core_width [mm]	Core_vol [m ³]
1300	25.4	100	100	0.000254
Sheet_thick [mm]	Sheet_vol [m ³]	Sheet_area [mm ²]	Weight_sheet [kg]	Sheet_number [-]
0.65	9.2625E-07	1425	0.001204125	10
Core_weight_theory [kg]	Core_dens_theory [kg/m ³]	Core_weight_lab. [kg]	Core_dens_lab. [kg/m ³]	Core_rel_dens [-]
0.01204125	47.40649	0.0121	47.63779	0.03664

- Core design 2:



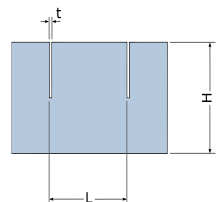
Comp_dens [kg/m ³]	Core_height [mm]	Core_length [mm]	Core_width [mm]	Core_vol [m ³]
1300	25.4	100	100	0.000254
Sheet_thick [mm]	Sheet_vol [m ³]	Sheet_area [mm ²]	Weight_sheet [kg]	Sheet_number [-]
0.65	9,334E-07	1436	0.00121342	10
Core_weight_theory [kg]	Core_dens_theory [kg/m ³]	Core_weight_lab. [kg]	Core_dens_lab. [kg/m ³]	Core_rel_dens [-]
0.0121342	47.77244	0.0117	46.06299	0.03543

- Core design 3:



Comp_density [kg/m ³]	Core_height [mm]	Core_length [mm]	Core_width [mm]	Core_vol [m ³]
1300	25.4	100	100	0.000254
Sheet_thick [mm]	Sheet_vol [m ³]	Sheet_area [mm ²]	Weight_sheet [kg]	Sheet_number [-]
0.65	8.9895E-07	1383	0.001168635	10
Core_weight_theory [kg]	Core_dens_theory [kg/m ³]	Core_weight_lab. [kg]	Core_dens_lab. [kg/m ³]	Core_rel_dens [-]
0.01168635	46.00925	0.01185	46.65354	0.03588

- Core reference:



Comp_density [kg/m ³]	Core_height [mm]	Core_length [mm]	Core_width [mm]	Core_vol [m ³]
1350	25.4	100	100	0.000254
Sheet_thick [mm]	Sheet_vol [m ³]	Sheet_area [mm ²]	Weight_sheet [kg]	Sheet_number [-]
0.7	0.000001778	2540	0.0024003	4
Core_weight_theory [kg]	Core_dens_theory [kg/m ³]	Core_weight_lab. [kg]	Core_dens_lab. [kg/m ³]	Core_rel_dens [-]
0.0096012	37.8	0.009821	38.66535433	0.0286

C.2 Ultra-lightweight lattice-cores made from CFRP rods

C.2.1 Composite skins I ($t_f = 0.8$ mm)

The theoretical density expected for the composite plate made from **four** layers of twill woven 2 x 2 [0/90] ° T300-3k carbon fibres fabrics and epoxy resin as the polymeric matrix, is presented below. The fibre volume content (φ_f) and the composite E-moduli were calculated using the results as in Annex B.

Twill woven [0-90] °

Plate_thick [mm]	n_layers [-]	Sup_dens [g/m ²]	Fibre_dens [g/cm ³]	Matrix_dens [g/cm ³]	φ_f [%]	E_max [MPa]	Comp_dens [g/cm ³]
0.7500	4	198.0000	1.8000	1.1000	58.6667	72308	1.5016
0.8000	4	198.0000	1.8000	1.1000	55.0000	67782	1.4850
0.8500	4	198.0000	1.8000	1.1000	51.7647	63822	1.4623

The experimental densities measured in the laboratory are in range \approx [**1.416** – **1.430**] gcm⁻³, and the plate thicknesses are of \approx [**0.75** – **0.85**] mm (the average value is taken after three measurements).

C.2.2 Composite skins II ($t_f = 1.21$ mm)

The theoretical density expected for the composite plate made from **six** layers of twill woven 2 x 2 [0/90] ° T300-3k carbon fibres fabrics and epoxy resin as the polymeric matrix, is presented below. The fibre volume content (φ_f) and the composite E-moduli were calculated using the results as in Annex B.

Twill woven [0-90] °

Plate_thick [mm]	n_layers [-]	Sup_dens [g/m ²]	Fibre_dens [g/cm ³]	Matrix_dens [g/cm ³]	φ_f [%]	E_max [MPa]	Comp_dens [g/cm ³]
1.18	6	198.0000	1.8000	1.1000	55.9322	68929	1.4915
1.213	6	198.0000	1.8000	1.1000	54.3971	67042	1.4807
1.26	6	198.0000	1.8000	1.1000	52.3801	64574	1.4667

The experimental densities measured in the laboratory are in range \approx [**1.386** – **1.479**] gcm⁻³, and the plate thicknesses are of \approx [**1.18** – **1.26**] mm (the average value is taken after three measurements).

C.2.3 Core densities

The core densities for the lattice-based cores are estimated theoretically from the unit cell as follows.

Cell_width [mm]	Cell_length [mm]	Cell_height [mm]	Cell_area [mm ²]	Cell_vol [mm ³]		
17.960479	17.960479	25.4	322.578815	8193.5019		
Rod_dens [g/cm ³]	Rod_diam [mm]	Rod_angle [°]	Rod_length [mm]	Rod_vol [mm ³]	Cell_mass [g]	Core_dens [kg/mm ³]
1.55	0.5	45	35.921090	7.053106	0.04372926	5.33706569
1.55	1	45	35.921090	28.212424	0.17491703	21.3482627
1.55	1.5	45	35.921090	63.477955	0.39356332	48.0335912

The laboratory results are presented as follows (the average value is taken after three measurements)

Rod_diam [mm]	Core_weight_avg [g]	Core_vol_control [mm ³]	Core_dens [kg/mm ³]
0.5	0.93	107315	8.666076504
1	2.46	107315	22.92317011
1.5	5.34	107315	49.76005218

D Complementary analyses for Chapter 5

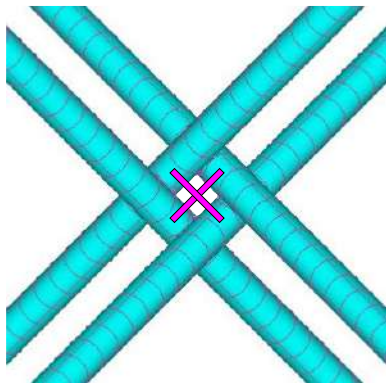
D.1 Loads over mid-plane node

The resultant force over the mid-plane node (Figure 5.11) shall be also analysed for having a first insight of the loads driven by the compression loads and the shear loads.

D.1.1 Comparison between two kind of mid-plane node shapes

The array of rods for simulating the mid-plane node that emulates the glue contact among the rods (Figure 5.12) could be seen as a cross, or as a cross circumscribed in a square array of rods (Figure D.1). The properties of the rods base materials are shown in Table 5.1. The studies are carried out by linear and non-linear FE simulations using FEMAP™ 10.3 with NX™ Nastran®.

(a) Array of rods as a cross



(b) Array of rods as a cross circumscribed

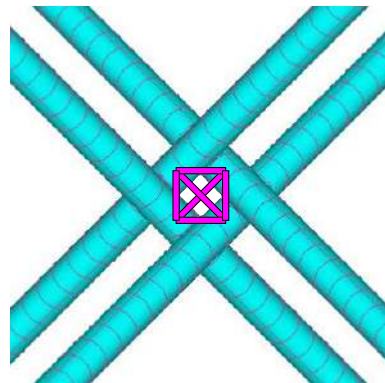







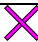
Figure D.1. Simulated array of rods for mid-plane node studies

D.1.1.1 Compression loading

The model of Figure 5.8 and Figure 5.11 are taken as basis for the simulations. Total vertical loads of 1 kN and 10 kN are applied on the top nodes. The top nodes are fixed, although they can only displace over z-direction. The boundary conditions on the bottom nodes are established as fully clamped. The end nodes of the array of rods on the mid-plane (i.e., the magenta coloured rods on Figure D.1) are merged to the appropriate nodes of the support rods (i.e., the cyan coloured rods on Figure D.1) on the mid-plane. As a first approach, the rod's diameter of the mid-plane node d_m is set as

0.5 mm, and the simulations explore through the proposed rod diameters as base materials for the lattices.

Table D.1. Results from FE simulations for load analyses upon the mid-plane node due to compressive loads and the effect of the overall unit cell behaviour regarding the shape selected.

Rod diameter d = 0.5 mm					
Simulation type	Variable	Units	Mid-plane node type		
					
Linear	Max node displacement in z	[mm]	0.810165		0.811709
Eigenvalue	Load failure factor (for a load 1 kN)	[--]	0.060933		0.060955
Non-linear	Load failure factor (for a load 1 kN)	[--]	0.060625		0.060625
Linear	Max/min axial load (mid-plane node)	[N]	1.9271	0.03351	0.01278
	Max/min shear load (mid-plane node)	[N]	4.454	0.85	0.3327
Non-linear failure step	Max/min axial load (mid-plane node)	[N]	0.2866	0.0063	0.01365
	Max/min shear load (mid-plane node)	[N]	0.2915	0.1203	2.206
Rod diameter d = 1 mm					
Simulation type	Variable	Units	Mid-plane node type		
					
Linear	Max node displacement in z	[mm]	2.019831		2.0232
Eigenvalue	Load failure factor (for a load 1 kN)	[--]	0.0905		0.09005
Non-linear	Load failure factor (for a load 1 kN)	[--]	0.0890625		0.08656
Linear	Max/min axial load (mid-plane node)	[N]	6.9069	0.2726	0.2544
	Max/min shear load (mid-plane node)	[N]	26.807	4.135	4.2274
Non-linear failure step	Max/min axial load (mid-plane node)	[N]	1.0751	0.02004	0.1211
	Max/min shear load (mid-plane node)	[N]	7.1054	0.8919	0.6368
Rod diameter d = 1.5 mm					
Simulation type	Variable	Units	Mid-plane node type		
					
Linear	Max node displacement in z	[mm]	0.883		0.898
Eigenvalue	Load failure factor (for a load 10 kN)	[--]	0.402604		0.3483
Non-linear	Load failure factor (for a load 10 kN)	[--]	0.3865		0.342813
Linear	Max/min axial load (mid-plane node)	[N]	2.1633	0.3188	0.077
	Max/min shear load (mid-plane node)	[N]	11.661	2.0714	3.167
Non-linear failure step	Max/min axial load (mid-plane node)	[N]	0.6991	0.4636	2.77051
	Max/min shear load (mid-plane node)	[N]	20.745	1.8732	9.996







No substantial differences are observed between the results obtained either by an array of rods resembling a cross or a cross circumscribed (Table D.1). The linear simulations were of a larger value than the non-linear because no instability was considered. It is important to notice, that the unit cell material shall fail before reaching the

maximum simulated load and the values showed by the mid-plane node are assumed to be smaller. However, the non-linear analyses give the first approximation on the mid-plane node loading at the failure step.

D.1.1.2 Shear loading

The model of Figure 5.19 and Figure 5.11 are taken as basis for the simulations.

Table D.2. Results from FE simulations for load analyses upon the mid-plane node due to shear loads and the effect of the overall unit cell behaviour regarding the shape selected.

Rod diameter d = 0.5 mm					
Simulation type	Variable	Units	Mid-plane node type		
					
Linear	Max node displacement ($\alpha = 45^\circ$)	[mm]	1.61974		1.6228
Eigenvalue	Load failure factor (for a load 1 kN)	[--]	0.0514487		0.0463
Non-linear	Load failure factor (for a load 1 kN)	[--]	0.0515625		0.04625
Linear	Max/min axial load (mid-plane node)	[N]	2.66	0.291	0.031
	Max/min shear load (mid-plane node)	[N]	2.14	1.44	2.94
Non-linear failure step	Max/min axial load (mid-plane node)	[N]	0.15	0.039	0.01225
	Max/min shear load (mid-plane node)	[N]	0.8081	0.1235	0.1584
Rod diameter d = 1 mm					
Simulation type	Variable	Units	Mid-plane node type		
					
Linear	Max node displacement ($\alpha = 45^\circ$)	[mm]	4.0367		4.043117
Eigenvalue	Load failure factor (for a load 1 kN)	[--]	0.0677		0.0647
Non-linear	Load failure factor (for a load 1 kN)	[--]	0.0628		0.05968
Linear	Max/min axial load (mid-plane node)	[N]	26.461	6.21	2.3528
	Max/min shear load (mid-plane node)	[N]	12.831	8.31	11.973
Non-linear failure step	Max/min axial load (mid-plane node)	[N]	5.036	1.06	1.0328
	Max/min shear load (mid-plane node)	[N]	11.09	2.3	3.01
Rod diameter d = 1.5 mm					
Simulation type	Variable	Units	Mid-plane node type		
					
Linear	Max node displacement ($\alpha = 45^\circ$)	[mm]	1.791568		1.792
Eigenvalue	Load failure factor (for a load 10 kN)	[--]	0.2955		0.2913
Non-linear	Load failure factor (for a load 10 kN)	[--]	0.2578		0.253125
Linear	Max/min axial load (mid-plane node)	[N]	15.345	6.3626	3.8169
	Max/min shear load (mid-plane node)	[N]	7.65	7.63	9.5629
Non-linear failure step	Max/min axial load (mid-plane node)	[N]	17.747	5.1082	11.146
	Max/min shear load (mid-plane node)	[N]	14.056	5.25	16.151

A total horizontal load of 1 kN is applied on the top nodes of the unit cell. The top nodes are constrained just to move on the horizontal direction parallel to vector δ and oriented by α . The bottom nodes are set as fully clamped as constraints. The end nodes of the array of rods on the mid-plane are merged to the correspondent nodes of the support rods on the mid-plane. The rod's diameter of the mid-plane node d_m is assumed as 0.5 mm. and the behaviour of the proposed rod diameters is presented.

Table D.2. shows no significant differences between the results attained either by a mid-plane node as an array of rods resembling a cross or a cross circumscribed for the shear loading case. The unit cell material might fail before reaching the maximum applied load. Nevertheless, the non-linear analyses provided a first approximation on the mid-plane node loading at the instability step.

D.2 Variation of rod orientation according to angle ω and its effect on Euler buckling behaviour by compressive loads

An example of the variation of the CFRP rods' orientation as a function of the angle ω is proposed in this section (Figure D.2). The following assumptions are established for simplifying the studies: the range of interest is limited to $[2.5 - 63]^\circ$, a maximum cell height of 25.4 mm, a constant cell area as the proposed A_{cell} in this work. Recalling equations Eq. (5.2) and Eq. (5.23), and applying the above assumptions, now the equations take the form of Eq. (D.1) and Eq. (D.2).

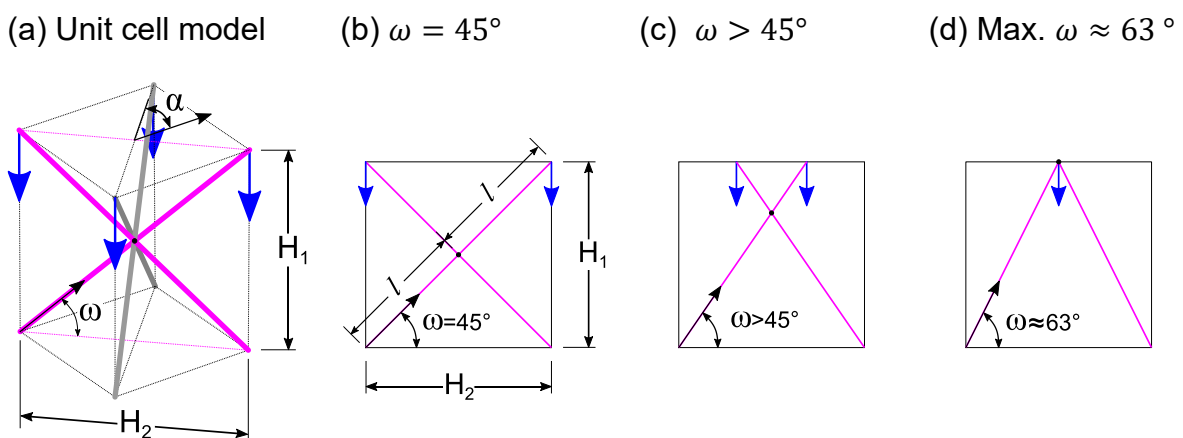


Figure D.2. Different rod orientations according to ω variation within a unit cell: unit cell model and front views of the principal diagonals

$$l = \frac{H_2}{2 \cos \omega} \quad (\text{D.1})$$

$$\sigma_{cB} = \frac{E_{rod1s} \pi^3 d^4 \cos^2 \omega}{4k^2 H_2^2 \sin \omega A_{cell}} \left[\sin^2 \omega + \underbrace{\frac{3}{4} \left(\frac{2d \cos \omega}{H_2} \right)^2 \cos^2 \omega}_{\approx 0} \right] \quad (\text{D.2})$$

Where:

d and ω are the variables

$$A_{cell} = 322.58 \text{ mm}^2$$

$$k = 0.7$$

$$H_2 = 25.4 \text{ mm}$$

$$E_{rod1s} = 115000 \text{ MPa}$$

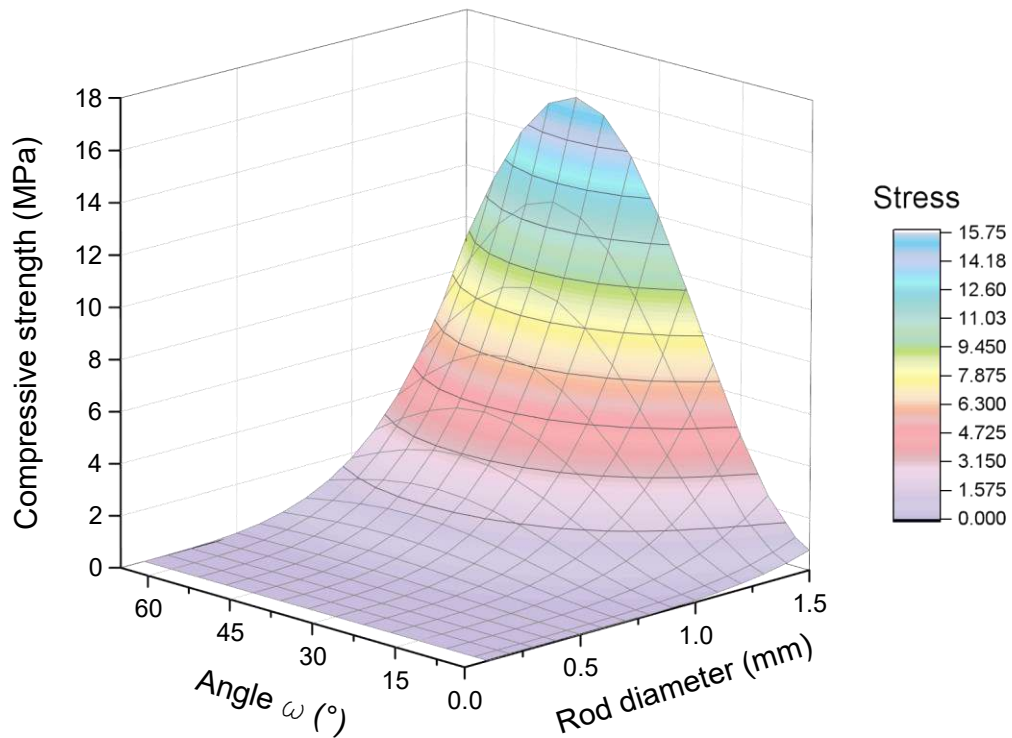


Figure D.3. Graphic 3D representation of Eq. D.2 employing d and ω as variables for the particular case analysed

The failure surface obtained while employing Eq. D.2 and above parameters is given in Figure D.3. For the particular case analysed, the maximum compressive strength for the unit cell while evaluating Euler buckling are obtained when $\omega = 45^\circ$. When the mid-node is above the half of the cell, the critical rod length is at the bottom half, and when the mid-node is below the half of the cell, the critical rod length is at the

above half. At 45° , the rods encounter each other at the mid-plane of the cell, being the suitable angle for bearing the compressive loads for the particular case analysed.

D.3 Variation of rod orientation according to angle α and its effect on Euler buckling behaviour by shear loads

A variation of the CFRP rods' orientation as a function of the angle α is proposed in this section (Figure D.4). The following assumptions are established for simplifying the studies: the range of interest is limited to $[-45 - 45]^\circ$, $\omega = 45^\circ$, a maximum cell height of 25.4 mm, a constant cell area as the proposed A_{cell} in this work. Recalling equations Eq. (D.1) and Eq. (5.39), and applying the above assumptions, now the latter equation takes the form of Eq. (D.3).

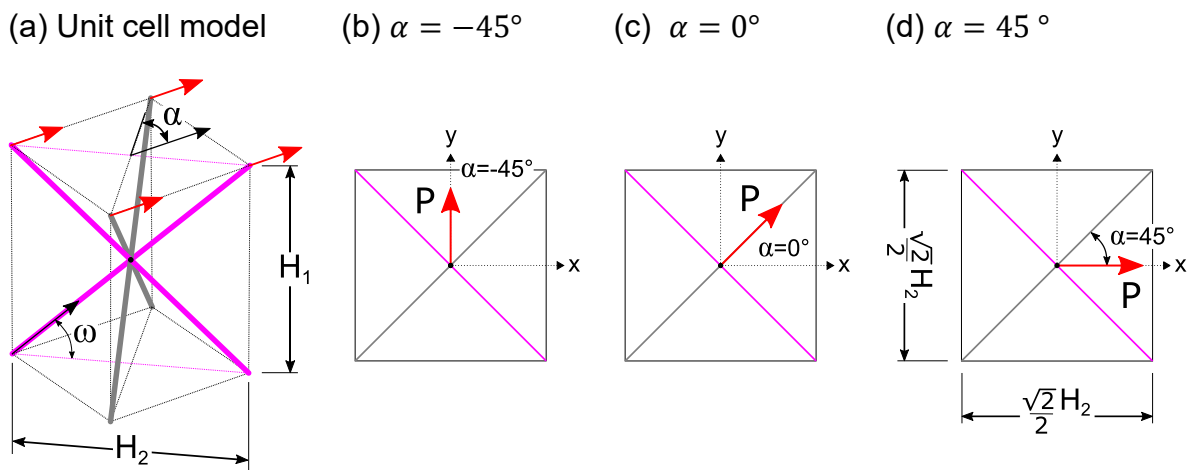


Figure D.4. Different rod orientations according to α variation within a unit cell: unit cell model and top views

$$\tau_{cB} = \frac{E_{rod1s} \pi^3 d^4 \cos \omega}{8k^2 H_2^2 \cos \alpha A_{cell}} \left[\cos^2 \omega + \underbrace{\frac{3}{4} \left(\frac{2d \cos \omega}{H_2} \right)^2 \sin^2 \omega}_{\approx 0} \right] \quad (D.3)$$

Where:

d and ω are the variables

$$A_{cell} = 322.58 \text{ mm}^2$$

$$k = 0.7$$

$$\omega = 45^\circ$$

$$H_2 = 25.4 \text{ mm}$$

$$E_{rod1s} = 115000 \text{ MPa}$$

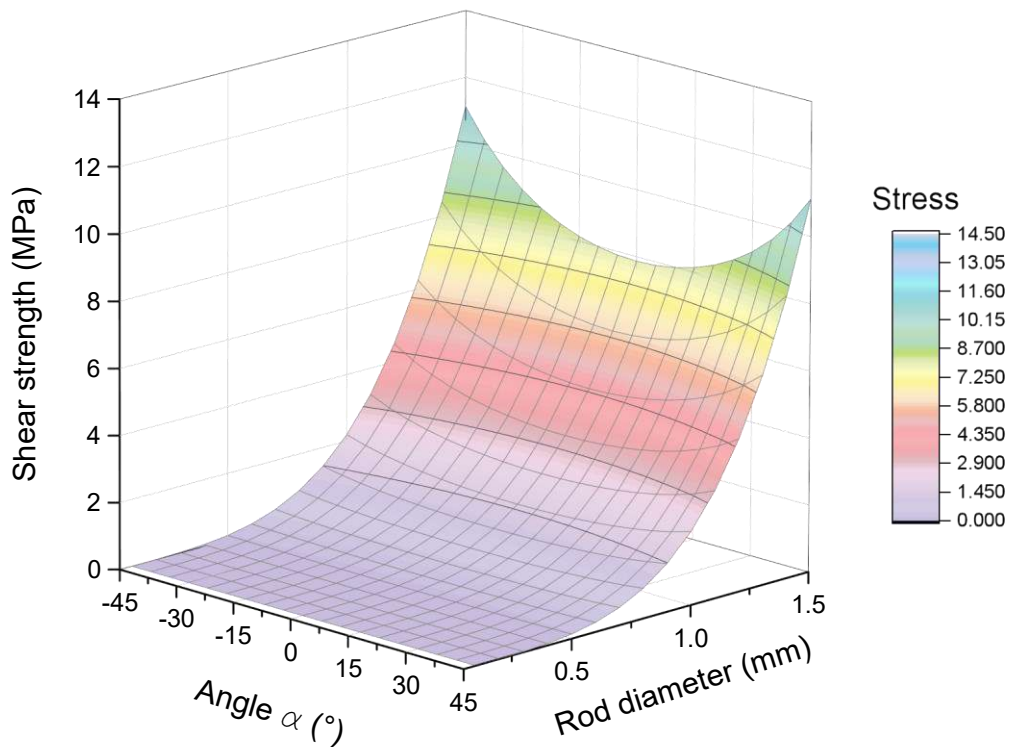


Figure D.5. Graphic 3D representation of Eq. D.3 employing d and α as variables for the particular case analysed

The failure surface obtained while employing Eq. (D.3) and above parameters is given in Figure D.5. The maximum shear strength for the unit cell while evaluating Euler buckling is obtained when $\alpha = 45^\circ$, for the case analysed.

At $\alpha = 45^\circ$, the loading case is symmetrical, and the loads are ideally equally distributed among the four rods. When $\alpha > 45^\circ$, the rods on the first and fourth quadrant bear most of the loads as the shear load is axially adequate oriented. The rods on the second and third quadrant are axially less loaded. When $\alpha = 90^\circ$, only two rods are loaded parallel in projection to the shear acting load, and the other two bear mostly shear and bending load (thus, very weak), but no axial load. This is the main reason for limiting the analysed problem to $\alpha = \pm 45^\circ$. Hence, the suitable orientation for the analysed case is $\alpha = 45^\circ$, because the buckling critical load is higher as the loads are better borne and thus, the shear strength of the cell is higher.

The above statements are also supported by FE non-linear analyses, by varying the vector load P according to angle α (Figure D.4) and observing the buckling failure load P_{Eu_FEM} (Table D.3 and Figure D.6). Rod diameter 1 mm is taken as example

for the studies and Figure D.1.5 acts as model for the simulations. A total load P of 1 kN is applied on top nodes (i.e., 250 N per rod), while bottom nodes remain constrained. The maximum buckling strength by shear loading is achieved by an angle $\alpha = 45^\circ$ between rods and the loading vector, for the particular case analysed.

Table D.3. Results from FE simulations for shear load analyses

Rod_diam [mm]	P [N]	P_x [N]	P_y [N]	alpha_rod [°]	P_Eu_FEM [N]	Tau_max [MPa]
1	1000	250	0	45	662.296	2.05312171
		246.201938	43.4120444	35	556.43	1.72515037
		226.576947	105.654565	25	498.662	1.546047
		204.788011	143.394109	10	475.864	1.4753643
		176.776695	176.776695	0	468.648	1.45299188
		143.394109	204.788011	-10	475.864	1.4753643
		105.654565	226.576947	-25	498.662	1.546047
		43.4120444	246.201938	-35	556.426	1.72513797
		0	250	-45	662.296	2.05337633

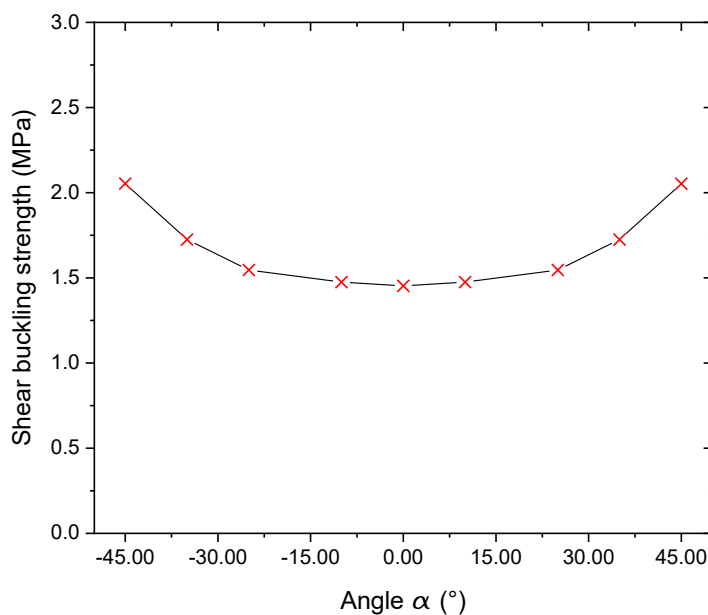
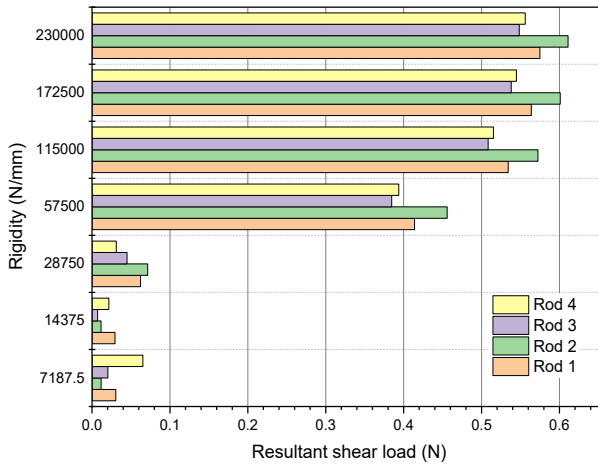


Figure D.6. Graphic representation of core shear strength varying with the load vector orientation according to angle α for a rod diameter of 1 mm

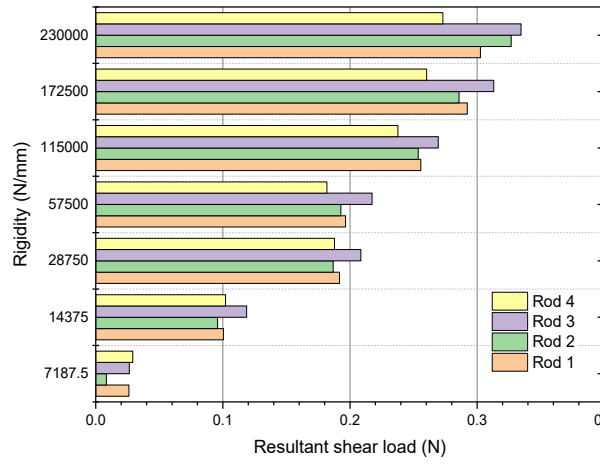
D.3.1 Resultant shear loads over the mid-plane node due to external compressive loads

In this section, shear resultant loads over the mid-plane node as consequence of the external applied forces is addressed and resumed in Figure D.7.

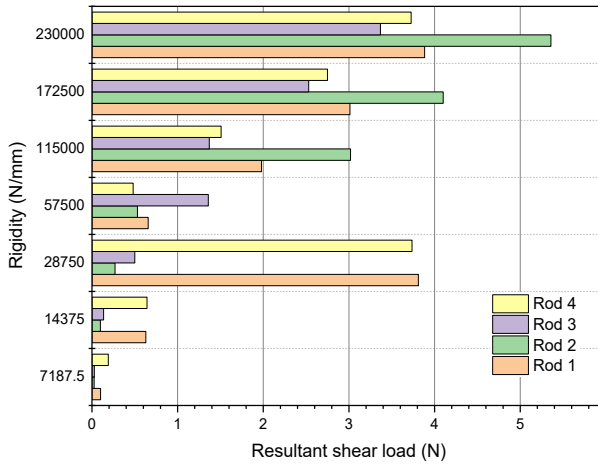
(a) Rod diameter 0.5 mm (compression)



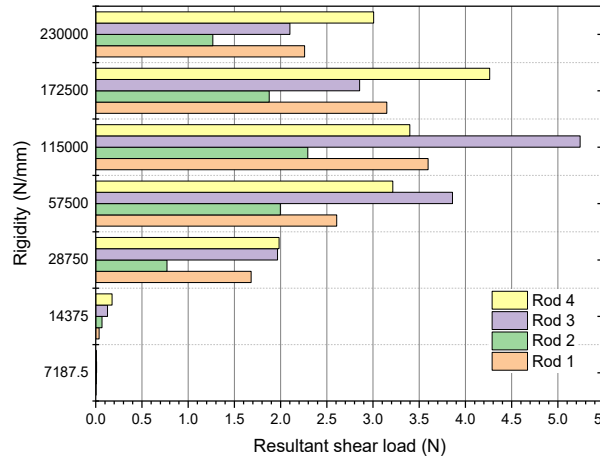
(d) Rod diameter 0.5 mm (shear)



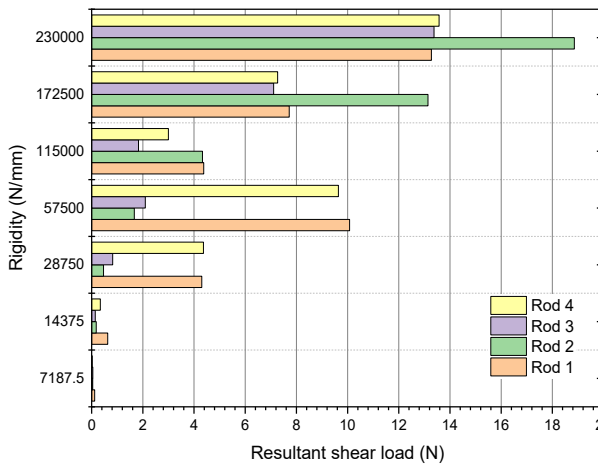
(b) Rod diameter 1 mm (compression)



(e) Rod diameter 1 mm (shear)



(c) Rod diameter 1.5 mm (compression)



(f) Rod diameter 1.5 mm (shear)

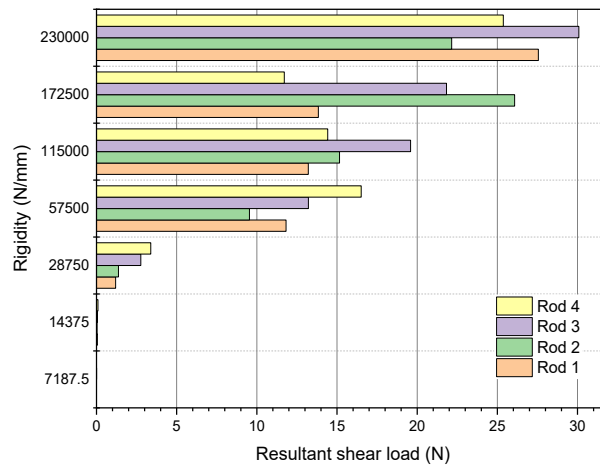


Figure D.7. Resultant shear loads for studied rod diameters at the failure step for: (left) compressive loading case, and (right) shear loading case

The adhesive joint strength is usually studied applying shear stresses or tensile (peeling) stresses. The rigidity (EI) of the mid-plane node is explored by varying the diameter of the array of rods, for each analysed rod case. The mid-plane node is simulated as Figure D.1.a and non-linear analyses provides the shear loads at the failure step. The cross-like array of rods is numbered as: top rods as 1 and 2; while the bottom rods as 3 and 4.

D.3.1.1 Compressive loading

The load is applied following the model of Figure 5.8. Total vertical loads of 1 kN and 10 kN are applied on the top nodes. The top nodes can only displace over z -direction, while the bottom nodes are set as fully clamped. The shear loads at the failure step from the non-linear simulations are presented in Figure D.7 (left) for the analysed rod cases. As the stiffness of the mid-plane node increases, the shear loads on the node also increase. The same effect is observed when increasing the diameter of the rods of the unit cell, which in a certain way, also stiffens the mid-plane. The predicted loads on the node before failure are relatively low (< 20 N). For example, for the case of 1.5 mm (Figure D.7.c), a minimum bonding area of ≈ 1 mm² is predicted to avoid failure by debonding (considering an adhesive strength of 20 MPa) for a high rigidity mid-plane nod

D.3.1.2 Shear loading

Figure 5.19 is taken as model for the simulations. Total horizontal loads of 1 kN for rod diameters 0.5 mm and 1 mm, and 10 kN for rod diameter 1.5 mm, are applied on the top nodes. The top nodes can only displace over xy -plane oriented according to $\alpha = 45^\circ$. Bottom nodes are set as fully clamped. Figure D.7 (right) shows the results resume of the resultant shear loads for the analysed rod cases. Analogously to the compression case, as the stiffness of the mid-plane node increases, the shear loads on the node also increase. The maximum predicted loads on the node before failure are below ≈ 30 N. For example, for the case of 1.5 mm (Figure D.7.f), a minimum bonding area of ≈ 1.5 mm² is predicted to avoid failure by debonding (considering an adhesive strength of 20 MPa).

D.4 Potentially additional failure mode in compressive loading

When unit cell members collapse, the failure of the structure is attained. Among the several failure mechanisms studied in Chapter 5, and additional mode such as truss push-out (or the entry of the rod through the skins) is presented within this section for compressive loading, as possible failure mode to be included, if another test setup is implemented (e.g., no flat or homogeneous plate as the steel plates shown in section 5.5.1) or outer skin layers are considered.

Typically, the experimental compressive test set-up includes two steel plates for transferring the load to the samples (Figure 5.8.a), and the truss push-out would not be attainable. However, the part as a functional component, may undergo truss push-out. The truss push-out failure is simplified as a debonding failure between the CFRP rods and the skins by depicting the contribution of the attached outer skin layers (skin layers of thickness t_2 on Figure 5.22) as a first approach and pessimistic point of view ⁽⁵⁾. This failure mode may result when the shear stresses at the link rods-faces, exceeds the adhesion strength τ_{int} , taken as $\tau_{int} = 20$ MPa [150].

$$A_{bond} = \frac{\pi d t_1}{\sin \omega} + \frac{\sqrt{2} f \pi d}{2 \sin \omega} \quad (D.4)$$

Considering the bonded surface as the contact area between the rods and the skins, the bonded area A_{bond} is set as Eq. (D.4), where t_1 represents the thickness of the skin in which the rods go through. The glued meniscus between rod and skin with an estimated average flank size f are also taken into account [150]. The flanks sizes are measured in the lab, having a nominal value of 2 mm (in average $f = 2 \pm 0.5$ mm) for each rod size. The size of the flank is pre-designed in the manufacturing process. Thus, the global bonding strength depends upon the adhesion strength, the bonded

⁽⁵⁾ The pessimistic point of view has been proposed as a simplistic alternative to the problem since it is known beforehand that this failure mode may not occur given the proposed test conditions in Chapter 5. The solution is much more complex to deal with and its analyses exceed the scope of this work. Nevertheless, if for example, the outer layers are considered and test-plates that allow the penetration of the skin are given in the test-rig, a more realistic push-out failure is presumed to occur when the glue shear strength is exceeded in combination with the delamination strength between CFRP layers (interfaces t_1 and t_2 in Figure 5.22), since penetration of the rod into the laminate t_2 is not foreseen, because they are almost the same material with similar hardness

surface between rod-skin and the number of involved trusses N . Then the effective critical load for rod-skin bonding failure is F_{rodP} (Eq. (D.5)).

$$F_{rodP} = A_{bond}\tau_{int}N \quad (D.5)$$

Analogously to previous failure formulations, the parallel load F_{\parallel} is equal in modulus to F_{rodP} , when the adhesion strength is attained. Hence, combining Eq. (D.5) and Eq. 5.17 and considering $N = 4$ within each unit cell, the core compressive strength by evaluating truss push-out through the skins is given by Eq. (D.6).

$$\sigma_{cP} \approx \frac{2\tau_{int}\pi d}{l^2 \cos^2 \omega \sin 2\alpha} \left(t_1 + \frac{\sqrt{2}}{2} f \right) \quad (D.6)$$

In this case, the main failure modes in Figure 5.14 are modified to Figure D.8, denoting rod push-out failure mode for skin thicknesses beyond 0.75 mm under the conditions established. For the cases analyses in this work, Table D.4. presents the results for the core compressive strength when rod push-out is considered (Eq. D.6.).

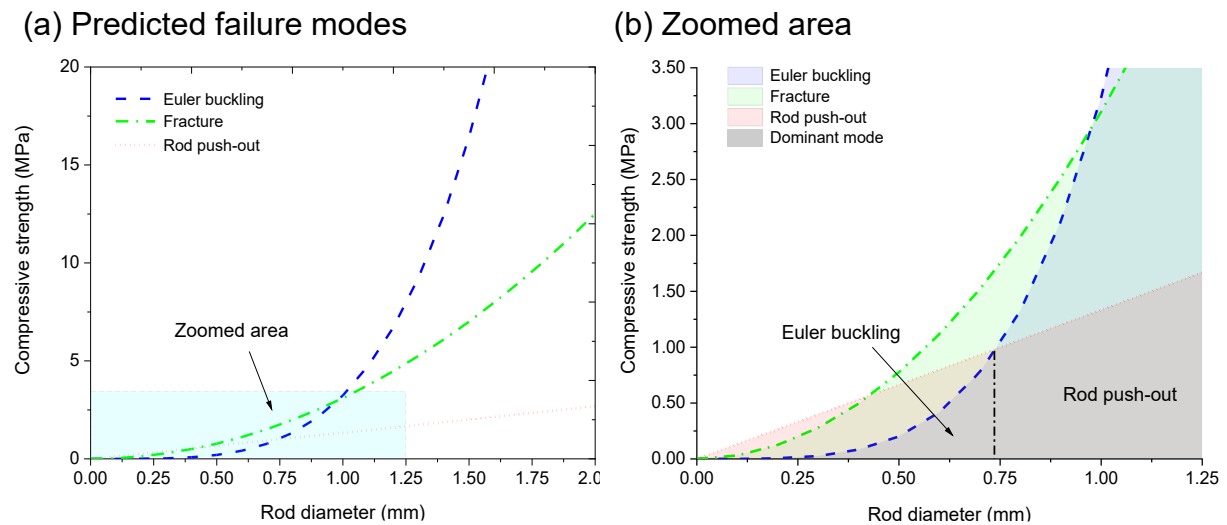


Figure D.8. Modified failure maps according to analytical predictions for compressive loads including truss push-out

Table D.4. Core compressive strengths regarding to rod push-out failure mode

\emptyset	L	f	t_1	α	ω	R_{1s}^-	E_{rod1s}	σ_{cP}
(mm)	(mm)	(mm)	(mm)	($^\circ$)	($^\circ$)	(MPa)	(MPa)	(MPa)
0.5	17.96	2	0.4	45	45	450	115	0.707
1	17.96	2	0.4	45	45	450	115	1.416
1.5	17.96	2	0.4	45	45	450	115	2.131

E Complementary studies for Chapter 6 and buckling diagrams

E.1 Maximum displacement while bending

The sketch of Figure E.1 (or the equivalent to Figure 6.1) is employed in this section for basic analyses.

- (a) System of real forces (also system “0”) (b) System of a fictitious unit load (also system “1”)

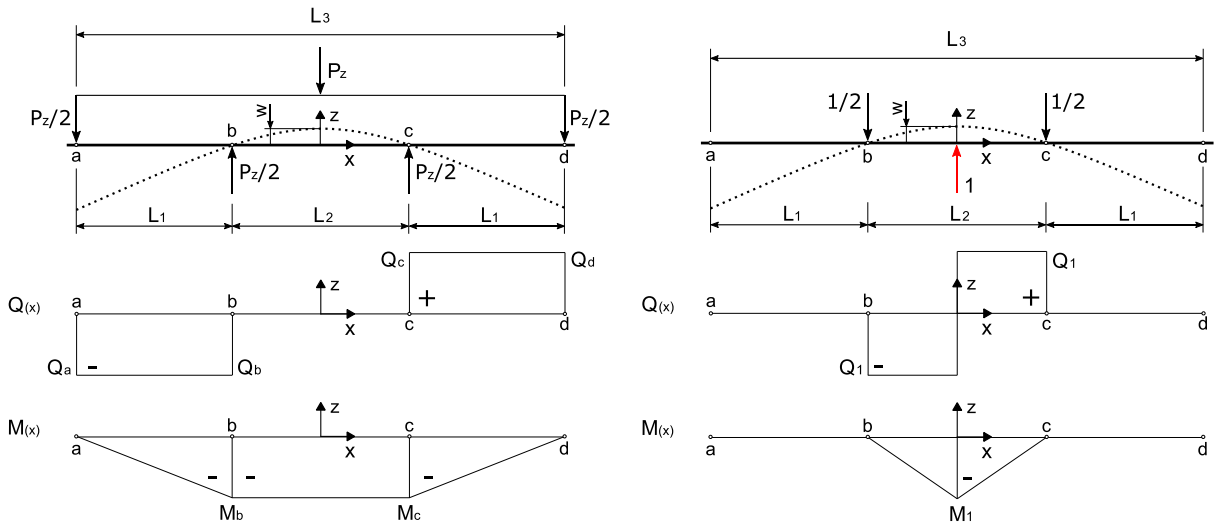


Figure E.1. Sketch of the basic beam models in a four-point bending case employed for analyses, including shear and flexural moment diagrams

The maximum displacement w between supports b and c is calculated considering the *unit-load method* [67,169]. Two system are defined as of the real forces (subscript “0”) and the fictitious unitary load (subscript “1”) given by Eq. E.1.

$$w = \int \frac{M_0 M_1}{EI} dx \quad (\text{E.1})$$

The maximal shear and moment values from the diagrams are given by Eq.(5.1), Eq. (6.2) and Eq. (6.3), respectively.

$$|Q_a| = |Q_d| = \frac{P_z}{2} \quad (\text{E.2})$$

$$|Q_b| = |Q_c| = \frac{P_z}{2} \tag{E.3}$$

$$|M_b| = |M_c| = \frac{P_z}{2} L_1 \tag{E.4}$$

$$|Q_1| = \frac{1}{2} \tag{E.5}$$

$$|M_1| = \frac{L_2}{2} \frac{1}{2} \tag{E.6}$$

Table E.1. Solution values for the integral of the product of moments given by Eq. (E.1) [229]

$M^k \backslash M^r$				
	$\frac{L}{2} M_1 M_1$	$\frac{L}{2} (M_1 + M_2) M_1$	$\frac{2L}{3} M_1 M_1$	$\frac{L}{2} M_1 M_1$
	$\frac{L}{3} M_1 M_1$	$\frac{L}{6} (M_1 + 2M_2) M_1$	$\frac{L}{3} M_1 M_1$	$\frac{L}{6} \left(1 + \frac{a}{L}\right) M_1 M_1$
	$\frac{L}{6} M_1 M_1$	$\frac{L}{6} (2M_1 + M_2) M_1$	$\frac{L}{3} M_1 M_1$	$\frac{L}{6} \left(1 + \frac{b}{L}\right) M_1 M_1$
	$\frac{L}{6} M_1 (M_1 + 2M_2)$	$\frac{L}{6} (2M_1 + M_2) M_1 + \frac{L}{6} (M_1 + 2M_2) M_1$	$\frac{L}{3} (M_1 + M_2) M_1$	$\frac{L}{6} \left(1 + \frac{b}{L}\right) M_1 M_1 + \frac{L}{6} \left(1 + \frac{a}{L}\right) M_1 M_1$
	$\frac{L}{3} M_1 M_1$	$\frac{L}{3} (M_1 + M_2) M_1$	$\frac{8L}{15} M_1 M_1$	$\frac{L}{3} \left(1 + \frac{ab}{L^2}\right) M_1 M_1$
	$\frac{L}{4} M_1 M_1$	$\frac{L}{12} (M_1 + 3M_2) M_1$	$\frac{L}{5} M_1 M_1$	$\frac{L}{12} \left(1 + \frac{a}{L} + \frac{a^2}{L^2}\right) M_1 M_1$
	$\frac{L}{6} \left(1 + \frac{c}{L}\right) M_1 M_1$	$\frac{L}{6} \left(1 + \frac{d}{L}\right) M_1 M_1 + \frac{L}{6} \left(1 + \frac{c}{L}\right) M_1 M_1$	$\frac{L}{3} \left(1 + \frac{cd}{L^2}\right) M_1 M_1$	$\frac{L}{3} M_1 M_1 - \frac{L(a-c)^2}{6ad} M_1 M_1$ $c \leq a$

To solve the integral in Eq. (E.1), a practical method is to employ tabulated values solved resolutions (Table E.1). Therefore, the displacement w is found by the sum of the displacements due to the moments applied by the real force P_z , as the constant section in L_2 at the system “0”, and the unitary load, as the triangle in L_2 at the system “1”.

$$w = \int_0^{L_2/2} \frac{M_0 M_1}{EI} dx + \int_{L_2/2}^{L_2} \frac{M_0 M_1}{EI} dx \quad (\text{E.7})$$

$$w = \frac{2}{EI} \frac{1}{2} \left[\frac{P_z L_1}{2} \frac{(L_3 - 2L_1)}{2} \frac{1}{2} \right] \frac{(L_3 - 2L_1)}{2} = \frac{P_z}{16 EI} L_1 (L_3 - 2L_1)^2 \quad (\text{E.8})$$

The beam under study is made from different materials such as the core and the skins. Thus, the flexural stiffness EI must be adequate for the case replacing it by its equivalent D_x given by Eq. (6.8), and assuming thin faces and a weak core. Then, Eq. E.8 turns into Eq. E.9, as the analytical maximum displacement predicted for the sandwich beam.

$$w = \frac{P_z}{16 D_x} L_1 (L_3 - 2L_1)^2 = \frac{P_z}{16 D_x} L_1 (L_2)^2 \quad (\text{E.9})$$

E.2 Coordinates system transformation for the use of homogeneous anisotropic faces into face buckling analyses

Analogously as reference [202], here, the case for an orthotropic core with orthotropic faces will be addressed. Recalling the insights presented in chapter 2, the stiffness matrix of each orthotropic lamina is given by Eq. (E.10). The lamina itself is thought as a very thin plate, which has in-plane stiffnesses but has no bending stiffness. Nevertheless, when laying-up a laminate (i.e., stacking-up laminas), the resulting material has a flexural rigidity since a finite thickness is given [51].

$$[Q]_{1,2} = \begin{bmatrix} \frac{E_{11}}{1 - \nu_{12}\nu_{21}} & \frac{\nu_{21}E_{11}}{1 - \nu_{12}\nu_{21}} & 0 \\ \frac{\nu_{21}E_{11}}{1 - \nu_{12}\nu_{21}} & \frac{E_{11}}{1 - \nu_{12}\nu_{21}} & 0 \\ 0 & 0 & G_{12} \end{bmatrix} \quad (\text{E.10})$$

To convert one coordinate system as the *local* coordinate system (lamina) by 1-, 2- and 3-directions, into another *global* coordinate system defined by x-, y-, z-direction, a polar transformation is needed, which graphically is represented by the Mohr's circle [8,34]. The transformation matrix is then given by Eq. (E.11) [34], where α is the fibre orientation angle presented in this case as an UD-lamina or the angle between the lay-up and the principal directions of the laminate.

$$[T]_{1,2 \rightarrow x,y} = \begin{bmatrix} \cos^2 \alpha & \sin^2 \alpha & -\sin 2\alpha \\ \sin^2 \alpha & \cos^2 \alpha & \sin 2\alpha \\ 0.5 \sin 2\alpha & -0.5 \sin 2\alpha & \cos 2\alpha \end{bmatrix} \quad (\text{E.11})$$

Then, the stiffness matrix of a lamina according to the global coordinate system is represented in Eq. (E.12).

$$[\bar{Q}]_{x,y} = [T]_{1,2 \rightarrow x,y} \cdot [Q]_{1,2} \cdot [T]_{1,2 \rightarrow x,y}^T \quad (\text{E.12})$$

Since laminates are generally made from many layers of UD-laminas, the sum of each layer properties, orientation and stacking sequence will define the final elastic characteristics of the composite. Therefore, the stiffness matrixes of the resulting laminated composite are described by Eq.(E.13), where t_k represents the k^{th} layer's thickness and z_k is the distance of each layer from the reference plane.

$$[A, B, D] = \sum_{k=1}^n [\bar{Q}]_{ij,k} \cdot \left[(t_k), \left(t_k \left(z_k - \frac{t_k}{2} \right) \right), \left(\frac{t_k^3}{12} + t_k \left(z_k - \frac{t_k}{2} \right)^2 \right) \right] \quad (\text{E.13})$$

When employing a symmetrical lay-up of orthotropic layers and considering a homogeneous plate as the laminate, the reference plane is found at $z_k = 0$ coincident with the middle surface at $t_f/2$. Therefore, the bending-extension coupling stiffness matrix $[B]$ results zero, while the $[A]$ and $[D]$ result in Eq.(E.14) and Eq.(E.15), respectively.

$$[A] = \begin{bmatrix} A_{11} & A_{21} & 0 \\ A_{22} & A_{22} & 0 \\ 0 & 0 & A_{33} \end{bmatrix} \quad (\text{E.14})$$

$$[D] = \begin{bmatrix} D_{11} & D_{21} & 0 \\ D_{22} & D_{22} & 0 \\ 0 & 0 & D_{33} \end{bmatrix} = \frac{t_f^2}{12} [A] \quad (\text{E.15})$$

If a uniaxial load is applied parallel to one of the principal orthotropic axes of the laminate such as x-direction (e.g., as seen in Figure 6.7), the failure load for Winkler's approach is defined by Eq. (E.16), for homogeneous thin plates [51].

$$P_{f \text{crit}} = 2\sqrt{D_f K_z} \quad (\text{E.16})$$

In which

$$K_z = \frac{2E_{3c}}{C} \quad (\text{E.17})$$

The last expression represents the foundation stiffness in the Winkler's model. By introducing Eq. (6.16) and replacing the local bending stiffness D_f by the first term of (D_{11}) of Eq. (E.15) into Eq.(E.16), the failure load by using orthotropic faces is given by Eq. (E.18).

$$P_{1fcrit} = 2 \sqrt{(D_{11}) \frac{2E_{cz}}{C}} = 2 \sqrt{\frac{t_f^2}{6} (A_{11}) \frac{E_{cz}}{C}} = \frac{2}{\sqrt{6}} \sqrt{t_f^2 (A_{11}) \frac{E_{cz}}{C}} \quad (\text{E.18})$$

Where the term (A_{11}) is defined by Eq. (E.19).

$$A_{11} = t_f \left[\frac{E_{xf}}{1 - \nu_{xy}\nu_{yx}} \right] \approx t_f E_{xf} \quad (\text{E.19})$$

Replacing the last expression into Eq. (E.18), then Eq. (E.20) is attained.

$$P_{1fcrit} = \frac{2}{\sqrt{6}} \sqrt{t_f^3 E_{xf} E_{cz} \frac{E_{3c}}{C}} \quad (\text{E.20})$$

For this particular case, the local and global coordinate systems are parallel and the failure stress under Winkler's approach is set by Eq. (6.19), when orthotropic homogeneous faces are employed. The constant factors are expressed as a part of the buckling coefficient Q_b .

$$\sigma_{1fcrit} = Q_b \sqrt{\frac{E_{3c} E_{1f} t_f}{C}} \quad (\text{E.21})$$

E.3 Buckling coefficients for different plates sizes, boundary conditions and load cases

The buckling coefficients K for the analysis of intracellular buckling can be obtained from tabulated values under certain conditions, such as constant sections, width-length relationships, type of boundary conditions and type of plates as isotropic or orthotropic. This section shows graphical solutions as example for estimating coefficient K .

E.3.1 Compression

When compressive loads are applied on isotropic and orthotropic plates different coefficients are attained and are presents as follows.

E.3.1.1 Isotropic plates

As a function of the width-length relations $\alpha = a / b$, and the boundary conditions, different curves are obtained for the estimation of the K buckling factor, (Figure E.2) [171].

(a) Reference for dimensions

(b) Buckling coefficients for isotropic plates

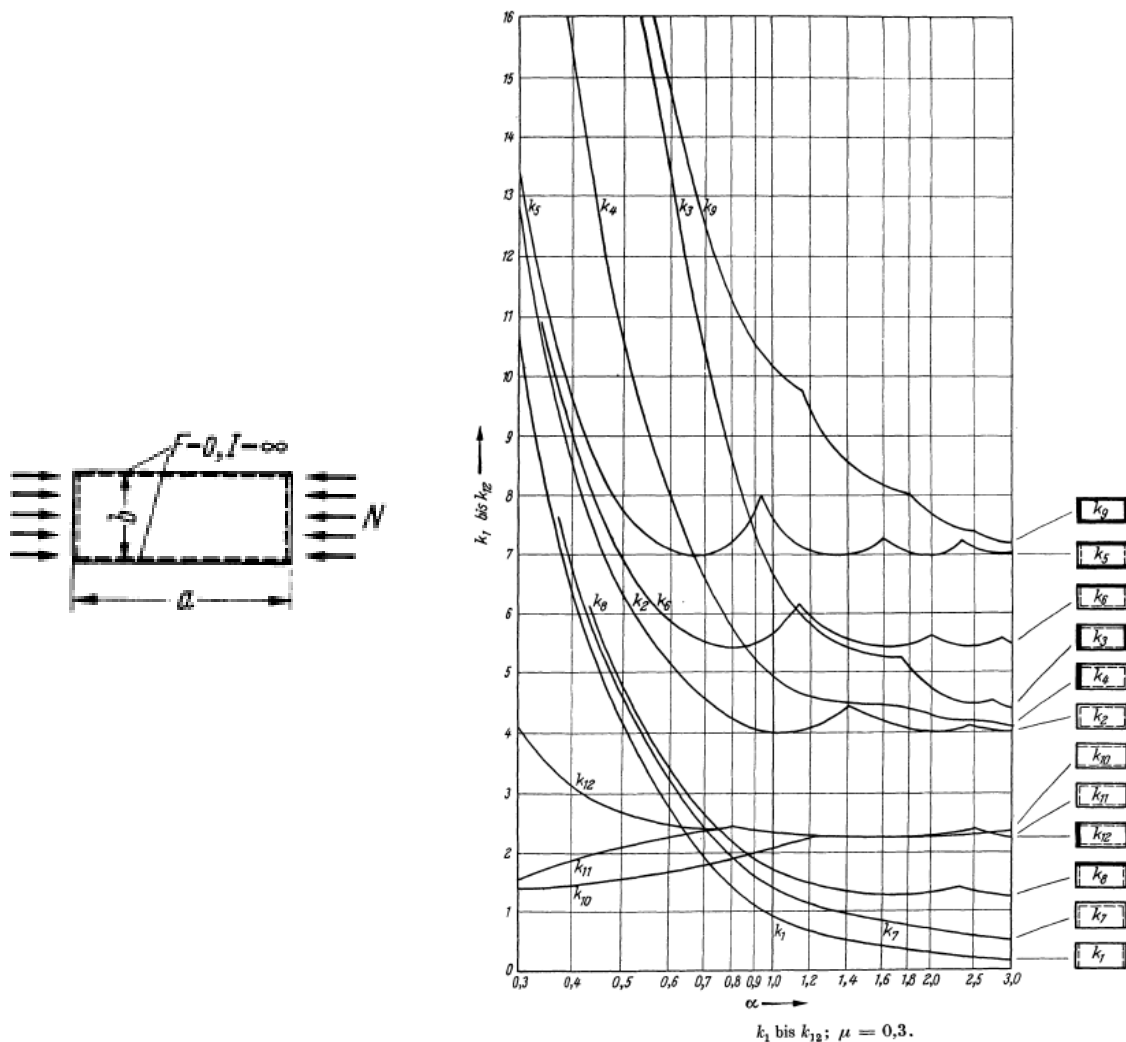


Figure E.2. Buckling coefficients for isotropic plates in compression.

E.3.1.2 Orthotropic plates

The buckling coefficients are also found in graphs like Figure E.3, where two common cases of plates are exhibited as a function of the width-length relations, the boundary conditions, and the fibre orientations [173]

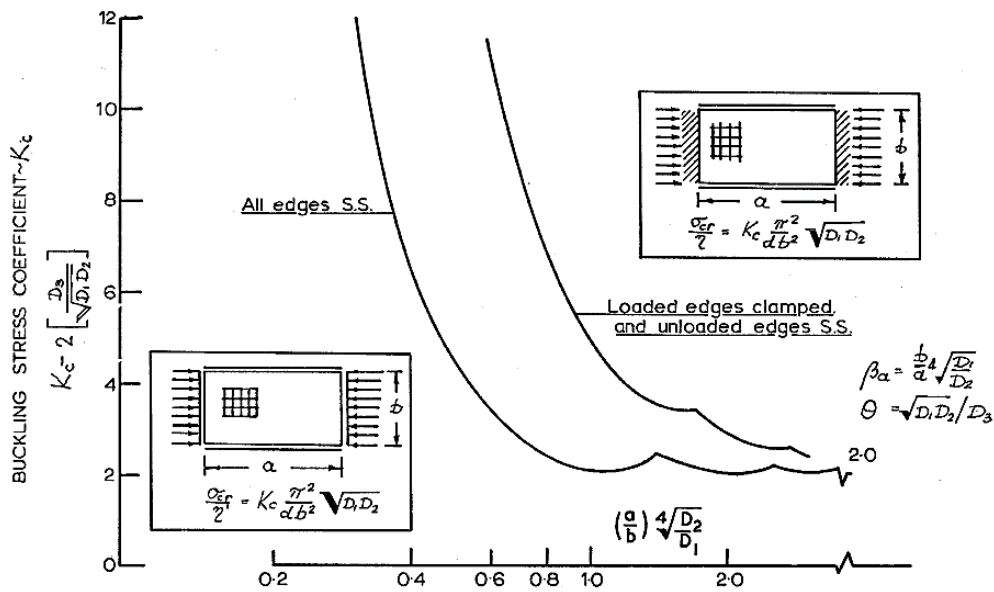


Figure E.3. Buckling coefficients for orthotropic plates in compression.

E.3.2 Shear

When shear loads are applied on orthotropic plates different coefficients are attained and are presents as follows.

E.3.2.1 Orthotropic plates

The buckling coefficients are also found in graphs like Figure E.4, where the case of a simply supported plate is exhibited as a function of the width-length relations, and the fibre orientations [173]

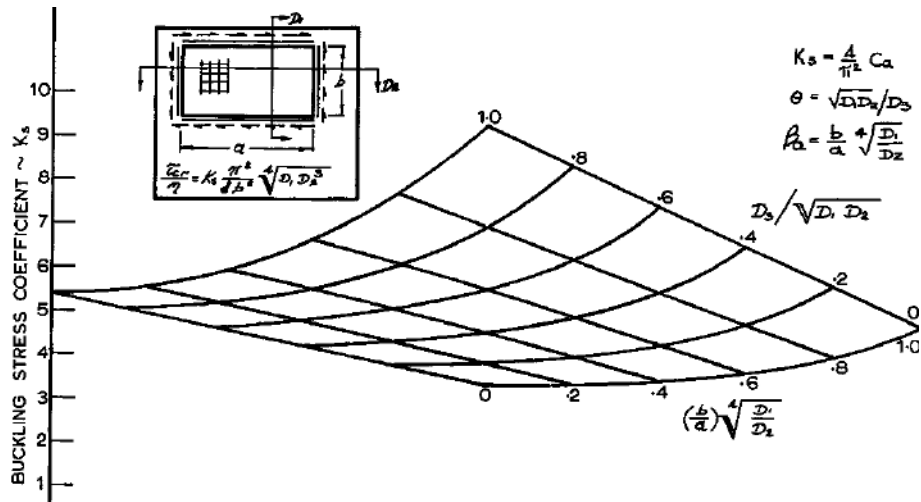


Figure E.4.. Buckling coefficients for orthotropic plates in shear

Nomenclature

Abbreviations

1D	One Dimensional
2D	Two Dimensional
3D	Three Dimensional
BCC	Body-Centered Cubic
CFRP	Carbon Fibre Reinforced Polymer
EU	European Union
FE	Finite Element Simulations
FEM	Finite Element Method
FRP	Fibre Reinforced Polymers
OOA	Out-Of-Autoclave
PAN	Poly-Acrylonitrile
PI	Performance Index
UD	Unidirectional
VARI	Vacuum Assisted Resin Infusion
VI	Vacuum Assisted Resin Infusion
CLT	Classical Lamination Theory
LCM	Liquid Composite Moulding
RTM	Resin Transfer Moulding
SCRIMP	Seaman's Composite Resin Infusion Moulding
AM	Additive Manufacturing
VARTM	Vacuum Assisted Resin Transfer Moulding
CNC	Computerised Numerical Control
ULW	Ultra-lightweight
GFRP	Glass Fibre Reinforced Polymer
WJC	Water Jet Cutting

Greek symbols

α	Fibre orientation angle
α	Director angle
δ	Displacement
ε	Strain
φ	Fibre volume fraction
ϕ	Fibre misalignment angle
γ	Shear strain
κ	Curvature
ρ	Density
σ	Normal stress
τ	Shear stress
ν	Poisson's modulus
ω	Director angle

Latin symbols

[A]	Extensional stiffness matrix
-----	------------------------------

[B]	Bending-extension coupling stiffnesses
[D]	Bending stiffness matrix
1, 2, 3	Local coordinate system
A	Area
b, b_1, b_w	Width
C	Core thickness
C	Torsional rigidity
c or C	Core thickness
d	Distance between faces neutral lines
D	Flexural rigidity
d	Rod diameter
D	Diameter
D0.5, D1, D1.5	Employed rod diameters as 0.5, 1 and 1.5 mm
F	Force
f	Flank
f_{faces}	Volume fraction occupied by faces
h	Sandwich panel thickness
H	Height
J	Torsion constant
K	Bending buckling coefficient for intracellular buckling
k	Buckling factor
l	Length
L	Length
M	Areal density
m	Mass
m	Flank
m or M	Moment
n or N	Axial load
N or N_i	Quantity of rods or layers
P	Force
q	Distributed load
R	Material maximum strength
s	Slope
t	Thickness
T, Q	Shear force
u	Displacement
U	Energy
V	Volume
W	Width
w	Beam deflection
x, y, z	Global coordinate system
C_1	Warping rigidity
C_w	Warping constant
E	Young's modulus
G	Shear elastic modulus
I	Second moment of area
I_o	Polar moment of inertia
K_s	Shear buckling factor
Q	Reduced stiffness

Q_b	Bending buckling coefficient for face wrinkling
t	Thickness
t_1, t_2	Face thicknesses
R	Material maximum strength
s	Slope
t_1, t_2	Face thicknesses
T, Q	Shear force
u	Displacement
U	Energy
V	Volume
W	Width
w	Beam deflection
x, y, z	Global coordinate system

Other symbols

∅	Rod diameter
subscript	Parallel to fibres
subscript ⊥	Perpendicular to fibres
subscript B	Plate buckling
subscript bond	Referent to the bonded area
subscript c	Referent to the core or cell
subscript <i>cell</i>	Referent to the cell
subscript <i>comp</i>	Composite
subscript <i>crit</i> or <i>cr</i>	Critical
subscript DB	Debonding
subscript <i>eff</i>	Effective
subscript <i>eq</i>	Equivalent
subscript Eu	Euler buckling
subscript f	Referent to the fibres
subscript f	Referent to the faces
subscript IB	Referent to the face intercellular buckling
subscript int	Interphase
subscript m	Referent to the matrix
subscript P	Pull-out
subscript <i>pk</i>	Peak
subscript R	Maximum strength
subscript <i>rod</i>	Referent to the rod
subscript s	Parent material
subscript TB	Torsional buckling
subscript W	Referent to the face wrinkling
subscript Y	Referent to the face yielding or fracture
subscript ∅	Torsional angle in torsional buckling
superscript -	Compressive
superscript +	Tensile

List of figures

Figure 1.1. Audi Space Frame [Source: Audi AG].....	15
Figure 1.2. Boeing 787 Dreamliner materials airframe [28].....	16
Figure 2.1. Two basic building blocks of a laminate. (a) Unidirectional. (b) Woven. [30].....	21
Figure 2.2. Carbon fibre inner structures. (a) Elementary cell of a graphite lattice [33]. (b) Example of a carbon fibre yarn structure [9]	24
Figure 2.3. The elastic modulus and tensile strength of PAN carbon fibres [36]	24
Figure 2.4. Schematic representation of polymeric structures [30]	27
Figure 2.5. Multi-layer composite consisting of individual layers. (Adapted from [30])	28
Figure 2.6. UD-layer loading. (a) Longitudinal. (b) Transverse.	30
Figure 2.7. UD-layer coordinate system in the directions of its orthotropic axes	32
Figure 2.8. Scheme of forces and moments acting on a laminate, and reference plane	36
Figure 2.9. Fibre breakage schemes. (a) Parallel tensile load. (b) Parallel compression load [34]	41
Figure 2.10. Inter-fibre failure schemes. (a) Tensile load. (b) Compressive load. (c) Transverse shear load. (d) Transverse-parallel shear load [34].....	42
Figure 2.11. Tsai-Hill failure criterion with uniaxial strength data of a glass fibre-reinforced epoxy composite. (Adapted from [32])	44
Figure 2.12. Budiansky's model for fibre kinking.....	46
Figure 2.13. Example case for buckling topic introduction: (a) Buckling of a pinned-end column. (b) Load-deflection diagram for a linearly elastic column.	47
Figure 2.14. Different effective-length factors k for ideal columns [67]	49
Figure 2.15. Ranking of composite part manufacturing [70].....	50
Figure 2.16. Manufacturing moulds for a helicopter tail rotor made from CFRP [71].....	51
Figure 2.17. VI technique basic scheme	54
Figure 3.1. Sandwich structure basic scheme.....	56
Figure 3.2. Scheme of different core topologies.....	59
Figure 3.3. Sign convention and dimensions used for calculations [51,113]	63
Figure 3.4. (Top). Bending stresses scheme. (Bottom). Shear stresses scheme.	64
Figure 3.5. Sandwich failure modes schemes.....	66
Figure 3.6. Example of failure load surfaces scheme for a sandwich beam in three-point bending. Adapted from [86]	68
Figure 4.1. Example of the core structures mentioned.....	71
Figure 4.2. Core sheet patterns proposed.....	76
Figure 4.3. Scheme of unit repetitive cell patterns and main geometry parameters	77
Figure 4.4. The manufacturing route for obtaining ULW square honeycomb cores	80
Figure 4.5. Photographs of core compression samples obtained	81
Figure 4.6. Photographs of core shear samples obtained.....	81

Figure 4.7. (a) A schematic compressive loading case render. (b) A top-view render with a schematic strut area used for calculations	82
Figure 4.8. Sketches of models for calculation. (a) Representative cell element loaded. (b) Representative cell element front view: before and after straining	82
Figure 4.9. Sketch example of the structure approximation by a cruciform column.....	84
Figure 4.10. Contour plots of the normal compressive stress distribution by FE simulations: (a) core design 1, (b) core design 2, (c) core design 3, and (d) refence core	86
Figure 4.11. Column of cruciform cross-section showing torsional buckling [165].....	89
Figure 4.12. Comparison between theoretical approaches for the maximum compressive strength ..	94
Figure 4.13. Schemes of selected nodes for displacement tracking in x-direction	95
Figure 4.14. Load vs. node displacement curves obtained from the simulations.....	96
Figure 4.15. Renders obtained from the compressive loading simulations.....	97
Figure 4.16. (a) A schematic shear load case over a unit cell. (b) A top-view render with a schematic cell used for calculations and generic shear loads.....	98
Figure 4.17. Sketches of the calculation models. (a) Cell wall sheet, neglecting transversal cell walls. (b) Cell wall loaded with a shear load before and after straining. (c) Model of an equivalent cantilever Timoshenko-like beam before and after straining	99
Figure 4.18. Displacement vector sketch reference for shear strain definition	101
Figure 4.19. Load vs. displacement curves obtained from the FE simulations: (a) design 1, (b) design 2 and (c) reference core	105
Figure 4.20. Contour plots of the shear stress distribution by FE: (a) design 1, (b) design 2, and (c) reference.....	106
Figure 4.21. Sketches of a representative cell wall sheet showing the glued area	109
Figure 4.22. Scheme of buckling of a rectangular plate under shear loads	110
Figure 4.23. Comparative peak shear stresses among different approaches.....	113
Figure 4.24. Shear stresses vs. reference nodes extracted from simulations	114
Figure 4.25. Schemes of selected nodes for displacement tracking in y-direction	115
Figure 4.26. Data extracted from the non-linear simulations: <i>Right</i> . Load vs. selected node displacement curves. <i>Left</i> . Contour plots of the node displacements in y-direction	116
Figure 4.27. Set-up used for compression tests.....	118
Figure 4.28. Measured compressive stress–strain response of design 1 cores	119
Figure 4.29. Photographs associated to selected points: compressive behaviour of design 1 cores	120
Figure 4.30. Compressive stress–strain response of square–honeycomb cores	121
Figure 4.31. Maximum compressive stresses according to analytical, FEM and experimental.....	123
Figure 4.32. Top view of FE renders of design 2 struts in a cell member showing the transition through instability	124
Figure 4.33. Top view of FEM renders of four struts of core design 1 showing torsional buckling	124
Figure 4.34. Photographs of reference core showing failure behaviour.....	125
Figure 4.35. Rendering scheme of the shear test set-up	127
Figure 4.36. Shear stress–strain response of square–honeycomb cores.....	128

Figure 4.37. Montage of photographs showing the shear response of core design 2	129
Figure 4.38. Photographs showing the debonding failure mode of reference cores	130
Figure 4.39. Maximum shear modulus according to experimental tests, contrasted by FEM and analytical models	131
Figure 4.40. (a) Photograph and (b) FE rendering. Comparison for core design 1 deformation	132
Figure 4.41. (a) Zoom-in into a photograph and (b) FE rendering. Comparison for core design 2 deformation	132
Figure 5.1. Local coordinate systems for (a) rods and (b) skins	138
Figure 5.2. Sketches examples of lattice unit cells	140
Figure 5.3. Sketches of proposed lattice core in an array of 3 x 3	141
Figure 5.4. Sketch of unit cell parameters	141
Figure 5.5. Compressive samples with different rod diameters	142
Figure 5.6. Shear samples with different rod diameters	143
Figure 5.7. Core relative density variation as a function of the rod's diameter	144
Figure 5.8. (a) A schematic BCC-like lattice render with a compression loading case. (b) Sketch of the load case. (c) Free body diagram of a CFRP half truss.	145
Figure 5.9. Scheme of a cantilever beam with a guided end (lateral displacement with no rotation)	147
Figure 5.10. Curve of core compressive modulus predicted by the analytical model	149
Figure 5.11. Bar-array FE renders of the unit cells employed for simulations comparisons	150
Figure 5.12. Zoomed central node as an array of bars	151
Figure 5.13. Compressive load vs. displacement obtained from linear simulations	151
Figure 5.14. Failure maps according to analytical predictions for compressive loads	155
Figure 5.15. Renders of the bending moment and combined stress distribution due to compressive loads for the 0.5 mm rod diameter lattice unit cell	157
Figure 5.16. Load vs. node displacement curves obtained from the non-linear simulations	158
Figure 5.17. Renders obtained from FE buckling simulations at the failure step for different rod diameters, while compression loading	159
Figure 5.18. Summary of FE simulations for core compressive strength predictions	160
Figure 5.19. Schematic BCC-like lattice render with a shear loading case	161
Figure 5.20. Curve of core shear modulus predicted by the analytical model	164
Figure 5.21. Shear load vs. displacement curves obtained from the simulations	165
Figure 5.22. A BCC-like lattice sketch showing the connection rods-skins	167
Figure 5.23. Failure maps according to analytical predictions for shear loads	169
Figure 5.24. Renders of the axial loads and bending moment for the 0.5mm rod diameter lattice unit cell while shear loading	170
Figure 5.25. Load vs. node displacement curves obtained from the non-linear simulations	171
Figure 5.26. Renders obtained from FE buckling simulations at the last step for different rod diameters during shear loading	172
Figure 5.27. Summary of FE simulations for core shear strength predictions	173
Figure 5.28. Set -up used for compression tests	174

Figure 5.29. Measured compressive stress-strain response of lattice -based core with 0.5 mm rods	176
Figure 5.30. Photographs associated with selected points: compressive behaviour of lattice-based core with 0.5 mm rod	176
Figure 5.31. Measured compressive stress-strain response of lattice -based core with 1 mm rods .	177
Figure 5.32. Photographs associated with selected points: compressive behaviour of lattice-based core with 1 mm rod	177
Figure 5.33. Measured compressive stress-strain response of lattice -based core with 1.5 mm rods	178
Figure 5.34. Photographs associated with selected points: compressive behaviour of lattice-based core with 1.5 mm rod	178
Figure 5.35. Compressive stress–strain response of lattice-based cores.....	179
Figure 5.36. Resulting failure maps for compressive stresses and experimental data	181
Figure 5.37. Photograph of the plate-shear test set-up.....	182
Figure 5.38. Measured shear stress–strain response of lattice-based core with rod diameter 0.5 mm	183
Figure 5.39. Photographs associated to selected points: shear behaviour of lattice-based core with 0.5 mm rods.....	183
Figure 5.40. Measured shear stress–strain response of lattice-based core with rod diameter 1 mm	184
Figure 5.41. Photographs associated to selected points: shear behaviour of lattice-based core with 1 mm rods.....	185
Figure 5.42. Measured shear stress–strain response of lattice-based core with rod diameter 1.5 mm	186
Figure 5.43. Photographs associated to selected points: shear behaviour of lattice-based core with 1.5 mm rods.....	187
Figure 5.44. Shear stress–strain response of lattice-based cores	188
Figure 5.45. Resulting failure maps for shear stresses and experimental data	189
Figure 6.1. Sketch of the four-point bending sample proposed.....	196
Figure 6.2. Photograph of bending samples of different lattice-cores´ rod diameters	196
Figure 6.3. Sketch of the shear and flexural moment diagrams of a beam in a four-point bending case	198
Figure 6.4. Scheme of a portion of a beam with the decomposition of the flexural moment into forces on the skins	199
Figure 6.5. Failure modes of sandwich faces considered	201
Figure 6.6. Plate under compressive in-plane stress before and after buckling	203
Figure 6.7. Face wrinkling wave and Winkler foundation	203
Figure 6.8. Intracellular buckling shapes on different cellular cores [205]	207
Figure 6.9. Sketch of unit cell projections to face planes and punctual supports.....	208
Figure 6.10. Principal failure modes for case 1: lattice-core made from 0.5 mm rods during four-point bending.....	210

Figure 6.11. Principal failure modes for case 2: lattice-core made from 1 mm rods during four-point bending.....	210
Figure 6.12. Principal failure modes for case 3: lattice-core made from 1.5 mm rods during four-point bending.....	211
Figure 6.13. Failure stresses predictions on the face under compression.....	212
Figure 6.14. Model sketch employed for finite element simulations.....	214
Figure 6.15. Example of benchmarks for data recording.....	215
Figure 6.16. Different views obtained from the simulations for lattice-core 0.5 mm rods, and face thickness 1.2 mm. <i>Contour:</i> plate top X normal stress at last step.....	216
Figure 6.17. Simulation results extracted at benchmarks for lattice-core 0.5 mm rods, and face thickness 1.2 mm.....	217
Figure 6.18. Top X normal stress of the face under compressive loads at last step.....	218
Figure 6.19. Different views obtained from the simulations for lattice-core 1 mm rods, and face thickness 0.8 mm. <i>Contour:</i> plate top X normal stress at last step.....	219
Figure 6.20. Top X normal stresses on the top face at different time steps.....	219
Figure 6.21. Stress distribution at reference points on the top skin at the beginnng of instabilization and at the last step.....	220
Figure 6.22. Simulation results extracted at benchmarks for lattice-core 1 mm rods, and face thickness 0.8 mm.....	221
Figure 6.23. Different views obtained from the simulations for lattice-core 1.5 mm rods, and face thickness 0.8 mm. <i>Contour:</i> plate top X normal stress at last step.....	222
Figure 6.24. Top X normal stresses on the top face at different time steps.....	222
Figure 6.25. Simulation results extracted at benchmarks for lattice-core 1.5 mm rods, and face thickness 0.8 mm.....	223
Figure 6.26. Simulation results extracted at benchmarks for lattice-core 1.5 mm rods, and face thickness 0.8 mm.....	224
Figure 6.27. Positions of the strain gauges over the sandwich sample.....	226
Figure 6.28. Set up used for bending tests.....	227
Figure 6.29. Measured load-deflection response under bending of lattice-based core with 0.5 mm rod, and nominal face thickness of 1.21 mm.....	228
Figure 6.30. Photographs associated to selected points: bending behaviour of lattice-based core with 0.5 mm rod, and nominal face thickness of 1.21 mm.....	228
Figure 6.31. Face stress vs. strain response for lattice-based core with 0.5 mm rod, and nominal face thickness of 1.21 mm.....	229
Figure 6.32. Measured load-deflection response under bending of lattice-based core with 1 mm rod, and nominal face thickness of 0.8 mm.....	230
Figure 6.33. Photographs associated to selected points: bending behaviour of lattice-based core with 1 mm rod, and nominal face thickness of 0.8 mm.....	230
Figure 6.34. Face stress vs. strain response for lattice-based core with 1 mm rod, and nominal face thickness of 0.8 mm.....	231

Figure 6.35. Measured load-deflection response under bending of lattice-based core with 1.5 mm rod, and nominal face thickness of 0.8 mm	232
Figure 6.36. Photographs associated to selected points: bending behaviour of lattice-based core with 1.5 mm rod, and nominal face thickness of 0.8 mm.....	232
Figure 6.37. Face stress vs. strain response for lattice-based core with 0.5 mm rod, and nominal face thickness of 1.2 mm.....	233
Figure 6.38. Charts obtained by analytical-numerical approaches with experimental cases. <i>Left column:</i> According to applied load. <i>Right column:</i> According to face stress. FW = Face wrinkling; IB = Intracellular buckling	235
Figure 6.39. Model sketch employed for FE simulations for 3D-honeycomb cores evaluation	239
Figure 6.40. Results extracted from FE simulations for reference core case. <i>Note:</i> T2: y-direction; T3: z-direction, coordinate system as in Figure 6.39.....	241
Figure 6.41. Displacements in global z-direction for reference core at last step.....	241
Figure 6.42. Results extracted from FE simulations for design 1 core case. <i>Note:</i> T2: y-direction; T3: z-direction, coordinate system as in Figure 6.39.....	242
Figure 6.43. Displacements in global z-direction for design 1 core case at last step.....	242
Figure 6.44. Results extracted from FE simulations for design 2 core case. <i>Note:</i> T2: y-direction; T3: z-direction, coordinate system as in Figure 6.39.....	244
Figure 6.45. Displacements in global z-direction for design 2 core case at last step.....	244
Figure 6.46. Charts obtained by analytical-numerical approaches for square-honeycomb cores. <i>Left:</i> according to applied external load P_z . <i>Right:</i> according to face stresses. <i>Note:</i> FW = Face wrinkling; IB = Intracellular buckling.....	246
Figure 7.1. Comparison of different performance indexes in compression of similar cores	252
Figure 7.2. Comparison of different performance indexes in shear of similar cores	257
Figure 7.3. Ashby-style plot: out-of-plane compressive strength as a function of the material density.	259
Figure 7.4. Ashby-style plot: shear strength as a function of the material density.	260
Figure 7.5. Ashby-style plot: flexural strength as a function of the material density	263
Figure 8.1. New geometries proposed for enhancing shear properties of 3D-honeycomb cores.....	272
Figure A.1. Global demand of CFRP components per main sector (2018) [224]	276
Figure A.2. Global demand of CFRP from 2010 to 2023 (estimated) [227]	276
Figure D.1. Simulated array of rods for mid-plane node studies	288
Figure D.2. Different rod orientations according to ω variation within a unit cell: unit cell model and front views of the principal diagonals	291
Figure D.3. Graphic 3D representation of Eq. D.2 employing d and ω as variables for the particular case analysed.....	292
Figure D.4. Different rod orientations according to α variation within a unit cell: unit cell model and top views.....	293
Figure D.5. Graphic 3D representation of Eq. D.3 employing d and α as variables for the particular case analysed.....	294

Figure D.6. Resultant shear loads for studied rod diameters at the failure step for: (left) compressive loading case, and (right) shear loading case..... 296

Figure D.7. Modified failure maps according to analytical predictions for compressive loads including truss push-out..... 299

Figure E.1. Sketch of the basic beam models in a four-point bending case employed for analyses, including shear and flexural moment diagrams..... 300

Figure E.2. Buckling coefficients for isotropic plates in compression..... 305

Figure E.3. Buckling coefficients for orthotropic plates in compression. 306

Figure E.4.. Buckling coefficients for orthotropic plates in shear 307

List of tables

Table 2.1. Properties and indices of commonly used fibre reinforcements	22
Table 2.2. Properties of standard PAN-based carbon fibres [33]	25
Table 2.3. Properties of commonly used thermoset matrices [9,39,40]	28
Table 3.1. Weight efficiency of sandwich structures while bending [111].....	57
Table 4.1. Carbon fibres and polymeric matrix main properties	74
Table 4.2. Theoretical elastic properties of the woven composite material T300/epoxy.	75
Table 4.3. Unit-cells mean dimensions and core densities employed.....	77
Table 4.4. Core compressive elastic moduli obtained by analytical approaches	85
Table 4.5. Core compressive stresses, strains and elastic moduli obtained by FE.	87
Table 4.6. Core compressive strength theories according to analytical approaches	93
Table 4.7. Core compressive strengths got from numerical and analytical approaches	97
Table 4.8. Shear elastic moduli obtained by analytical approaches	104
Table 4.9. Core shear stresses, strains and elastic moduli obtained by FE.....	107
Table 4.10. Core shear analytical strengths: fracture and debonding failure modes	112
Table 4.11. Core shear analytical strength: shear buckling failure mode	113
Table 4.12. Core shear strengths according to numerical and analytical approaches	117
Table 4.13. Analytical, FEM and experimental results from compressive tests	122
Table 4.14. Comparison matrix of cell's struts during loading. Rows: (a) Design 1 samples. (b) Design 2 samples. (c) Design 3 samples. Columns: (1) Photographs at the beginning of compressive test. (2) Photographs before failure. (3) FEM renders at failure step	126
Table 4.15. Resume of analytical, FEM and experimental results from shear tests.....	130
Table 5.1. Mechanical properties of the CFRP rods employed for calculations	138
Table 5.2. Theoretical elastic properties of the woven composite material T300/epoxy.	139
Table 5.3. Unit cells mean dimensions and core densities employed for analyses	142
Table 5.4. Core compressive elastic moduli predicted by FE.....	152
Table 5.5. Core compressive strengths according to analytical approaches	156
Table 5.6. Core compressive strength due to Euler buckling for different k coefficients	156
Table 5.7. Core compressive strengths from numerical and analytical approaches	160
Table 5.8. Core shear elastic moduli predicted by FE	165
Table 5.9. Core compressive strengths according to analytical approaches	168
Table 5.10. Core shear strength due to Euler buckling for different k coefficients	170
Table 5.11. Core shear strengths from numerical and analytical approaches	174
Table 5.12. Resume of analytical, FEM and experimental results from compressive tests	180
Table 5.13. Resume of analytical, FEM and experimental results from shear tests.....	189
Table 6.1. Theoretical mechanical properties of the lattice-based cores	194
Table 6.2. Theoretical mechanical properties of the CFRP faces	195
Table 6.3. Overview of the geometric parameters and nominal dimensions employed	197

Table 6.4. Brief literature review on different buckling coefficient values	205
Table 6.5. Summary of face critical stresses from analytical predictions	209
Table 6.6. Summary of results taken from FE simulations	225
Table 6.7. Resume of analytical-numerical and experimental results from bending tests	236
Table 6.8. Face elastic moduli obtained from sandwich bending tests via strain gauges' deformation	237
Table 6.9. Maximum displacements attained by maximum load	237
Table 6.10. Employed mechanical properties of the square-honeycomb cores	238
Table 6.11. Resume of dimensions employed for FE models	238
Table 7.1. Comparison of similar core materials (e.g., compression loading)	253
Table 7.2. Comparison with a reference commercial core (e.g., compression loading)	254
Table 7.3. Comparison of similar core materials (e.g., shear loading)	256
Table 7.4. Comparison with a reference commercial core (e.g., shear loading)	258
Table 7.5. Sandwich data for the equivalent flexural properties analysed	262
Table D.1. Results from FE simulations for load analyses upon the mid-plane node due to compressive loads and the effect of the overall unit cell behaviour regarding the shape selected. ...	289
Table D.2. Results from FE simulations for load analyses upon the mid-plane node due to shear loads and the effect of the overall unit cell behaviour regarding the shape selected.	290
Table D.3. Results from FE simulations for shear load analyses	295
Table E.1. Solution values for the integral of the product of moments given by Eq. (E.1) [229]	301

List of publications

Refereed Journal Articles related to the research

1. P. Vitale, G. Francucci, H. Rapp, A. Stocchi. The compressive and shear response of ultra-lightweight lattices made from CFRP rods. *Composite Structures*. *To be published, 2022*.
2. P. Vitale, G. Francucci, H. Rapp, A. Stocchi. Ultra-lightweight sandwich panels: a case of study by four-point bending. *Journal of Sandwich Structures and Materials*. *To be published, 2022*.
3. P. Vitale, G. Francucci, H. Rapp, A. Stocchi. Shear response of ultra-lightweight CFRP cores. *Composite Structures*. DOI: 10.1016/j.compstruct.2020.111879, 2020.
4. P. Vitale, G. Francucci, H. Rapp, A. Stocchi. Manufacturing and compressive response of ultra-lightweight CFRP cores. *Composite Structures*. DOI: 10.1016/j.compstruct.2018.03.065, 2018.
5. P. Vitale, G. Francucci, H. Rapp, A. Stocchi. Failure mode maps of natural and synthetic fiber reinforced composite sandwich panels. *Composites Part A*. DOI: 10.1016/j.compositesa.2016.12.021, 2016.
6. P. Vitale, G. Francucci, H. Rapp, A. Stocchi. Thermal conductivity of sandwich panels made with synthetic and vegetable fibers. *Journal of Sandwich Structures and Materials*. DOI:10.1177/1099636216635630, 2016.

Congresses, Conferences and Symposiums

1. P. Vitale, G. Francucci, H. Rapp, A. Stocchi. Development of lightweight fiber-reinforced cores for application in sandwich structures. Scientific Symposium X. Anniversary - RCAA, Argentine Embassy, Berlin, Germany, 2019.
2. P. Vitale, G. Francucci, H. Rapp, A. Stocchi. Fertigung und Strukturverhalten ultraleichter CFK-Sandwichkerne. Joint Sessions Conference of the 3er-CCeV-AG at the Universität der Bundeswehr München, Munich, Germany, 2019.
3. P. Vitale, G. Francucci, H. Rapp, A. Stocchi. Manufacturing and mechanical characterization of ultra-lightweight CFRP cores. SLAP 2018, Mar del Plata, Argentina, 2018.
4. P. Vitale, G. Francucci, H. Rapp, A. Stocchi. Fabricación y evaluación de paneles sándwich ultra-livianos de fibra de carbono. SAM-CONAMET, Cordoba, Argentina, 2016.
5. P. Vitale, G. Francucci, H. Rapp, A. Stocchi. Ultra-lightweight CFRP cores made by interlocking method: Fabrication and evaluation. ECCM17 Conference Proceedings, Munich, Germany, 2016.
6. P. Vitale, G. Francucci, H. Rapp, A. Stocchi. Failure mode maps of natural and synthetic fiber reinforced composite sandwich panels. ECCM17 Conference Proceedings, Munich, Germany, 2016.
7. P. Vitale, G. Francucci, H. Rapp, A. Stocchi. Thermal characterization of natural and synthetic fiber reinforced composite sandwich panels. COMAT 2015, Buenos Aires, Argentina, 2015.

Bibliography

- [1] Ashby MF, Cebon D. Materials selection in mechanical design. *Le J Phys IV* 1993;3:C7-1-C7-9.
- [2] UN. Paris Agreement 2016.
- [3] Nikowitz M. *Advanced Hybrid and Electric Vehicles: System Optimization and Vehicle Integration*. Springer International Publishing; 2016.
- [4] Giampieri A, Ling-Chin J, Ma Z, Smallbone A, Roskilly AP. A review of the current automotive manufacturing practice from an energy perspective. *Appl Energy* 2020;261:114074. <https://doi.org/https://doi.org/10.1016/j.apenergy.2019.114074>.
- [5] Joost WJ. Reducing vehicle weight and improving US energy efficiency using integrated computational materials engineering. *Jom* 2012;64:1032–8.
- [6] Schindler V, Sievers I. *Forschung für das Auto von morgen: Aus Tradition entsteht Zukunft*. Springer-Verlag; 2007.
- [7] Vaidya U. *Composites for automotive, truck and mass transit: materials, design, manufacturing*. DEStech Publications, Inc; 2011.
- [8] Jones RM. *Mechanics of composite materials*. vol. 193. Scripta Book Company Washington, DC; 1975.
- [9] Gay D. *Composite materials: design and applications*. CRC press; 2014.
- [10] Q. Dai A, Elgowainy JK. *Vehicle Materials: Material Composition of U.S. Light-duty Vehicles* 2016.
- [11] Mrazova M. Advanced composite materials of the future in aerospace industry. *Incas Bull* 2013;5:139.
- [12] Irving PE, Soutis C. *Polymer composites in the aerospace industry*. Woodhead Publishing; 2019.
- [13] Robinson M. Application of Composites in Rail Vehicles. *Ref. Modul. Mater. Sci. Mater. Eng.*, Elsevier; 2016. <https://doi.org/https://doi.org/10.1016/B978-0-12-803581-8.03965-5>.
- [14] Sheno RA, Dulieu-Barton JM, Quinn S, Blake JIR, Boyd SW. Composite materials for marine applications: key challenges for the future. *Compos. Mater.*, Springer; 2011, p. 69–89.
- [15] Zhang J, Ashby MF. The out-of-plane properties of honeycombs. *Int J Mech Sci* 1992;34:475–89. [https://doi.org/http://dx.doi.org/10.1016/0020-7403\(92\)90013-7](https://doi.org/http://dx.doi.org/10.1016/0020-7403(92)90013-7).
- [16] Pflug J, Verpoest I. Sandwich materials selection charts. *J Sandw Struct Mater* 2006;8:407–21.
- [17] Castanié B, Bouvet C, Ginot M. Review of composite sandwich structure in aeronautic applications. *Compos Part C Open Access* 2020:100004.
- [18] Zenker T. Automated fiber placement based manufacturing of carbon fiber reinforced sandwich helicopter sideshells. *Aerosp Eur Conf* 2020 2020:9.
- [19] Perfetto S, Schubert M, Mayer D, Dafnis A, Atzrodt H. DEVELOPMENT AND DESIGN OF MULTIFUNCTIONAL COMPOSITE STRUCTURES FOR SATELLITE APPLICATIONS n.d.
- [20] Schwingel DD, Seeliger DH-W, Vecchionacci MC, Alwes MD, Dittrich MJ. Aluminium foam sandwich structures for space applications. *57th Int. Astronaut. Congr.*, 2007, p. C2-4.
- [21] Russell B, Deshpande V, Wadley H. Quasistatic deformation and failure modes of composite square honeycombs. *J Mech Mater Struct* 2008;3:1315–40.
- [22] Finnegan K, Kooistra G, Wadley HNG, Deshpande VS. The compressive response of carbon

- fiber composite pyramidal truss sandwich cores. *Int J Mater Res* 2007;98:1264–72.
- [23] Ashby MF. The properties of foams and lattices. *Philos Trans R Soc A Math Phys Eng Sci* 2006;364:15–30. <https://doi.org/10.1098/rsta.2005.1678>.
- [24] NASA. Game changing development program, ultra-lightweightcore materials for efficient load-bearing composite sandwich structures 2014.
- [25] Vitale P, Francucci G, Rapp H, Stocchi A. Manufacturing and compressive response of ultra-lightweight CFRP cores. *Compos Struct* 2018;194. <https://doi.org/10.1016/j.compstruct.2018.03.065>.
- [26] Sypeck DJ. Cellular Truss Core Sandwich Structures. *Appl Compos Mater* 2005;12:229–46. <https://doi.org/10.1007/s10443-005-1129-z>.
- [27] Moongkhamklang P, Elzey DM, Wadley HNG. Titanium matrix composite lattice structures. *Compos Part A Appl Sci Manuf* 2008;39:176–87.
- [28] Hale J. Boeing 787 from the ground up. *Aero* 2006;4:7.
- [29] Inc SPLMS. FEMAP – Finite Element Modeling and Post processing 2011.
- [30] Jones RM. *Mechanics of composite materials*. CRC press; 1998.
- [31] Al-Oqla FM, Salit MS. 2 - Natural fiber composites. *Mater. Sel. Nat. Fiber Compos.*, Woodhead Publishing; 2017, p. 23–48. <https://doi.org/https://doi.org/10.1016/B978-0-08-100958-1.00002-5>.
- [32] Mallick PK. *Fiber-reinforced composites: materials, manufacturing, and design*. CRC press; 2007.
- [33] Flemming M, Ziegmann G, Roth S. *Faserarten. Faserverbundbauweisen Fasern und Matrices*, Berlin, Heidelberg: Springer Berlin Heidelberg; 1995, p. 6–179. https://doi.org/10.1007/978-3-642-57776-5_2.
- [34] Schürmann H. *Konstruieren mit Faser-Kunststoff-Verbunden*. Berlin: Springer; 2005.
- [35] Baillie C. *Green Composites: Polymer Composites and the Environment*. Taylor & Francis; 2005.
- [36] Watt W. Production and properties of high modulus carbon fibres. *Proc. R. Soc. Lond. A*, vol. 319, The Royal Society; 1970, p. 5–15.
- [37] Dave RS, Loos AC. *Processing of composites*. Hanser Publishers Munich; 2000.
- [38] Brazel CS, Rosen SL. *Fundamental principles of polymeric materials*. John Wiley & Sons; 2012.
- [39] Cassis FA, Talbot RC. Polyester and vinyl ester resins. *Handb. Compos.*, Springer; 1998, p. 34–47.
- [40] Sullivan JL, Kao BG, Van Oene H. Shear properties and a stress analysis obtained from vinyl-ester losipescu specimens. *Exp Mech* 1984;24:223–32.
- [41] Moser K. *Faser-Kunststoff-Verbund: Entwurfs-und Berechnungsgrundlagen*. Springer-Verlag; 2013.
- [42] Chamis CC. *Simplified composite micromechanics equations for hygral, thermal and mechanical properties* 1983.
- [43] Förster R, Knappe W. Experimentelle und theoretische Untersuchungen zur Rißbildungsgrenze an zweischichtigen Wickelrohren aus Glasfaser/Kunststoff unter Innendruck. *Kunststoffe* 1971;61:583–8.
- [44] Puck A. *Zur Beanspruchung und Verformung von GFK-Mehrschichten-Verbund-Bauelementen* 1967.

- [45] Naik NK, Shembekar PS. Elastic behavior of woven fabric composites: I—Lamina analysis. *J Compos Mater* 1992;26:2196–225.
- [46] Ishikawa T, Chou T-W. Stiffness and strength behaviour of woven fabric composites. *J Mater Sci* 1982;17:3211–20.
- [47] Raju IS, Wang JT. Classical laminate theory models for woven fabric composites. *J Compos Technol Res* 1994;16:289–303.
- [48] Naik NK, Shembekar PS, Hosur M V. Failure behavior of woven fabric composites. *J Compos Technol Res* 1991;13:107–16.
- [49] Shembekar PS, Naik NK. Elastic behavior of woven fabric composites: II—Laminate analysis. *J Compos Mater* 1992;26:2226–46.
- [50] Naik NK, Shembekar PS. Elastic behavior of woven fabric composites: III—Laminate design. *J Compos Mater* 1992;26:2522–41.
- [51] Zenkert D. *An introduction to sandwich structures* 1995.
- [52] Puck A. *Festigkeitsanalyse von Faser-Matrix-Laminaten: Modelle für die Praxis*. Hanser; 1996.
- [53] Hahn HT, Tsai SW. *Introduction to composite materials*. CRC Press; 1980.
- [54] Rosen BW. Mechanics of composite strengthening. *Fiber Comopsite Mater* 1965;72:75.
- [55] Argon AS. Fracture of Composites, *Treatise of Materials Science and Technology*, Vol. 1 1972.
- [56] Budiansky B. Micromechanics. *Comput Struct* 1983;16:3–12.
- [57] Budiansky B, Fleck N. Compressive failure of fibre composites. *J Mech Phys Solids* 1993;41:183–211.
- [58] Hill R. *The mathematical theory of plasticity*. vol. 11. Oxford university press; 1998.
- [59] Tsai SW. Strength theories of filamentary structure. *Fundam Asp Fiber Reinf Plast Compos* 1968.
- [60] Hashin Z. Failure criteria for unidirectional fiber composites 1980.
- [61] Tsai SW, Wu EM. A general theory of strength for anisotropic materials. *J Compos Mater* 1971;5:58–80.
- [62] Fleck NA. Compresssive failure of fiber composites. *Adv Appl Mech* 1997;33:7.
- [63] Jelf PM, Fleck NA. The failure of composite tubes due to combined compression and torsion. *J Mater Sci* 1994;29:3080–4.
- [64] Yurgartis SW. Measurement of small angle fiber misalignments in continuous fiber composites. *Compos Sci Technol* 1987;30:279–93.
- [65] Lankford J. Dynamic compressive fracture in fiber-reinforced ceramic matrix composites. *Mater Sci Eng A* 1989;107:261–8.
- [66] Wilkinson E, Parry T V, Wronski AS. Compressive failure in two types of carbon fibre-epoxide laminates. *Compos Sci Technol* 1986;26:17–29.
- [67] Gere J. *Mechanics of Materials (with CD-ROM and InfoTrac)*. Cengage Learning; 2003.
- [68] Klein B. *Leichtbau-Konstruktion*. Springer; 2009.
- [69] Boisse P. *Composite fiber reinforcement forming*. Wiley Encycl Compos 2012.
- [70] Frketic J, Dickens T, Ramakrishnan S. Automated manufacturing and processing of fiber-reinforced polymer (FRP) composites: An additive review of contemporary and modern techniques for advanced materials manufacturing. *Addit Manuf* 2017;14:69–86.
- [71] Mazumdar S. *Composites manufacturing: materials, product, and process engineering*. CrC

- press; 2001.
- [72] Wang Q, Wang L, Zhu W, Xu Q, Ke Y. Design optimization of molds for autoclave process of composite manufacturing. *J Reinf Plast Compos* 2017;36:1564–76.
- [73] Trauth A, Kehrer L, Pinter P, Weidenmann K, Böhlke T. On the effective elastic properties based on mean-field homogenization of sheet molding compound composites. *Compos Part C Open Access* 2021;4:100089. <https://doi.org/https://doi.org/10.1016/j.jcomc.2020.100089>.
- [74] Wang Q, Li T, Wang B, Liu C, Huang Q, Ren M. Prediction of void growth and fiber volume fraction based on filament winding process mechanics. *Compos Struct* 2020;246:112432. <https://doi.org/https://doi.org/10.1016/j.compstruct.2020.112432>.
- [75] Aranberri I, Landa M, Elorza E, Salaberria AM, Rekondo A. Thermoformable and recyclable CFRP pultruded profile manufactured from an epoxy vitrimer. *Polym Test* 2021;93:106931. <https://doi.org/https://doi.org/10.1016/j.polymertesting.2020.106931>.
- [76] Kuppusamy RRP, Rout S, Kumar K. Chapter one - Advanced manufacturing techniques for composite structures used in aerospace industries. In: Kumar K, Davim JP, editors. *Mod. Manuf. Process.*, Woodhead Publishing; 2020, p. 3–12. <https://doi.org/https://doi.org/10.1016/B978-0-12-819496-6.00001-4>.
- [77] Papargyris DA, Day RJ, Nesbitt A, Bakavos D. Comparison of the mechanical and physical properties of a carbon fibre epoxy composite manufactured by resin transfer moulding using conventional and microwave heating. *Compos Sci Technol* 2008;68:1854–61. <https://doi.org/https://doi.org/10.1016/j.compscitech.2008.01.010>.
- [78] Vitale JP, Francucci G, Xiong J, Stocchi A. Failure mode maps of natural and synthetic fiber reinforced composite sandwich panels. *Compos Part A Appl Sci Manuf* 2017;94:217–25. <https://doi.org/10.1016/j.compositesa.2016.12.021>.
- [79] Goh GD, Yap YL, Agarwala S, Yeong WY. Recent progress in additive manufacturing of fiber reinforced polymer composite. *Adv Mater Technol* 2019;4:1800271.
- [80] Blok LG, Longana ML, Yu H, Woods BKS. An investigation into 3D printing of fibre reinforced thermoplastic composites. *Addit Manuf* 2018;22:176–86.
- [81] Aized T, Shirinzadeh B. Robotic fiber placement process analysis and optimization using response surface method. *Int J Adv Manuf Technol* 2011;55:393–404.
- [82] Chanteli A, Bandaru AK, Peeters D, O'Higgins RM, Weaver PM. Influence of repass treatment on carbon fibre-reinforced PEEK composites manufactured using laser-assisted automatic tape placement. *Compos Struct* 2020;248:112539.
- [83] Nguyen MH, Vijayachandran AA, Davidson P, Call D, Lee D, Waas AM. Effect of automated fiber placement (AFP) manufacturing signature on mechanical performance of composite structures. *Compos Struct* 2019;228:111335.
- [84] Lukaszewicz DH-JA, Ward C, Potter KD. The engineering aspects of automated prepreg layup: History, present and future. *Compos Part B Eng* 2012;43:997–1009. <https://doi.org/https://doi.org/10.1016/j.compositesb.2011.12.003>.
- [85] Gebart R, Strömbeck L. Principles of liquid composite molding. *Process Compos* 2000:358–87.
- [86] Petras A, Sutcliffe MPF. Failure mode maps for honeycomb sandwich panels. *Compos Struct* 1999;44:237–52.
- [87] Hertel H. *Struktur, Form, Bewegung* 1963.
- [88] Greene E. Marine composites: reducing weight, cost, and maintenance in the maritime environment. *Mar Technol* 2013.
- [89] Seo SI, Kim JS, Cho SH. Development of a hybrid composite bodyshell for tilting trains. *Proc Inst Mech Eng Part F J Rail Rapid Transit* 2008;222:1–13.
- [90] Hau E. *Windkraftanlagen: Grundlagen. Technik. Einsatz. Wirtschaftlichkeit*. Springer-Verlag;

- 2017.
- [91] Mathijssen D. Composite sandwich structures: The new milestone in bridge building. *Reinf Plast* 2013;57:17–23.
- [92] Zhang J, Ashby MF. Mechanical selection of foams and honeycombs used for packaging and energy absorption. *J Mater Sci* 1994;29:157–63. <https://doi.org/10.1007/BF00356587>.
- [93] Lamb AJ. Experimental investigation and numerical modelling of composite-honeycomb materials used in formula 1 crash structures 2007.
- [94] Pavlović A, Sintoni D, Minak G, Fragassa C. On the modal behaviour of ultralight composite sandwich automotive panels. *Compos Struct* 2020;248:112523.
- [95] Vinson JR. Sandwich structures: past, present, and future. *Sandw. Struct. 7 Adv. with Sandw. Struct. Mater.*, Springer; 2005, p. 3–12.
- [96] Vitale JP, Francucci G, Stocchi A. Thermal conductivity of sandwich panels made with synthetic and vegetable fiber vacuum-infused honeycomb cores. *J Sandw Struct Mater* 2017;19. <https://doi.org/10.1177/1099636216635630>.
- [97] Vitale JP, Francucci G, Xiong J, Stocchi A. Failure mode maps of natural and synthetic fiber reinforced composite sandwich panels. *Compos Part A Appl Sci Manuf* 2017;94. <https://doi.org/10.1016/j.compositesa.2016.12.021>.
- [98] Miravete A, Cuartero J, Compuestos AE de M. *Materiales compuestos*. Antonio Miravete; 2003.
- [99] Hertel H. *Leichtbau: Bauelemente, Bemessungen und Konstruktionen von Flugzeugen und anderen Leichtbauwerken*. Springer-Verlag; 2013.
- [100] Chatti S. *Production of profiles for lightweight structures*. BoD–Books on Demand; 2006.
- [101] Ashby MF, Brechet YJM. Designing hybrid materials. *Acta Mater* 2003;51:5801–21.
- [102] George T, Deshpande VS, Sharp K, Wadley HNG. Hybrid core carbon fiber composite sandwich panels: Fabrication and mechanical response. *Compos Struct* 2014;108:696–710. <https://doi.org/10.1016/J.COMPSTRUCT.2013.10.002>.
- [103] Xiong J, Ma L, Wu L, Wang B, Vaziri A. Fabrication and crushing behavior of low density carbon fiber composite pyramidal truss structures. *Compos Struct* 2010;92:2695–702.
- [104] Xiong J, Ma L, Vaziri A, Yang J, Wu L. Mechanical behavior of carbon fiber composite lattice core sandwich panels fabricated by laser cutting. *Acta Mater* 2012;60:5322–34.
- [105] Russell B, Deshpande VS, Wadley H. Quasi-Static Deformation and Failure Modes of Composite Square Honeycombs. *J Mech Mater Struct - J MECH MATER STRUCT* 2008;3:1315–40. <https://doi.org/10.2140/jomms.2008.3.1315>.
- [106] Herrmann AS, Zahlen PC, Zuardy I. Sandwich structures technology in commercial aviation. *Sandw. Struct. 7 Adv. with Sandw. Struct. Mater.*, Springer; 2005, p. 13–26.
- [107] Thomsen OT, Bozhevolnaya E, Lyckegaard A. *Sandwich Structures 7: Advancing with Sandwich Structures and Materials: Proceedings of the 7th International Conference on Sandwich Structures*, Aalborg University, Aalborg, Denmark, 29-31 August 2005. Springer Netherlands; 2006.
- [108] Fairbairn W. *An Account of the Construction of the Britannia and Conway Tubular Bridges: With a Complete History of Their Progress from the Conception of the Original Idea, to the Conclusion of the Elaborate Experiments which Determined the Exact Form and Mode of Cons.* J. Weale; 1849.
- [109] Savage G. Formula 1 composites engineering. *Eng Fail Anal* 2010;17:92–115.
- [110] Zenkert D. *The handbook of sandwich construction*. Engineering Materials Advisory Services; 1997.

- [111] Petras A. Design of sandwich structures 1999.
- [112] Birman V, Kardomateas GA. Review of current trends in research and applications of sandwich structures. *Compos Part B Eng* 2018;142:221–40. <https://doi.org/https://doi.org/10.1016/j.compositesb.2018.01.027>.
- [113] Allen HG. Analysis and design of structural sandwich panels: the commonwealth and international library: structures and solid body mechanics division. Elsevier; 2013.
- [114] Scheffler M, Colombo P. Cellular ceramics: structure, manufacturing, properties and applications. John Wiley & Sons; 2006.
- [115] Gibson LJ, Ashby MF. Cellular Solids: Structure and Properties. Cambridge University Press; 1999.
- [116] Gibson IJ, Ashby MF. The mechanics of three-dimensional cellular materials. *Proc R Soc London A Math Phys Sci* 1982;382:43–59.
- [117] Ashby MF, Evans T, Fleck NA, Hutchinson JW, Wadley HNG, Gibson LJ. Metal foams: a design guide. Elsevier; 2000.
- [118] Ashby M. Designing architected materials. *Scr Mater* 2013;68:4–7.
- [119] Wadley HNG. Multifunctional periodic cellular metals. *Philos Trans R Soc London A Math Phys Eng Sci* 2006;364:31–68.
- [120] Zhang P, Cheng Y, Liu J, Li Y, Zhang C, Hou H, et al. Experimental study on the dynamic response of foam-filled corrugated core sandwich panels subjected to air blast loading. *Compos Part B Eng* 2016;105:67–81.
- [121] Wadley HNG, Fleck NA, Evans AG. Fabrication and structural performance of periodic cellular metal sandwich structures. *Compos Sci Technol* 2003;63:2331–43.
- [122] Xiong J, Vaziri A, Ghosh R, Hu H, Ma L, Wu L. Compression behavior and energy absorption of carbon fiber reinforced composite sandwich panels made of three-dimensional honeycomb grid cores. *Extrem Mech Lett* 2016;7:114–20.
- [123] Wang B, Hu J, Li Y, Yao Y, Wang S, Ma L. Mechanical properties and failure behavior of the sandwich structures with carbon fiber-reinforced X-type lattice truss core. *Compos Struct* 2018;185:619–33. <https://doi.org/10.1016/J.COMPSTRUCT.2017.11.066>.
- [124] George T, Deshpande VS, Wadley HNG. Mechanical response of carbon fiber composite sandwich panels with pyramidal truss cores. *Compos Part A Appl Sci Manuf* 2013;47:31–40. <https://doi.org/10.1016/J.COMPOSITESA.2012.11.011>.
- [125] Kooistra GW, Wadley HNG. Lattice truss structures from expanded metal sheet. *Mater Des* 2007;28:507–14.
- [126] Zhu F, Lu G, Ruan D, Wang Z. Plastic deformation, failure and energy absorption of sandwich structures with metallic cellular cores. *Int J Prot Struct* 2010;1:507–41.
- [127] Sypeck DJ. Cellular Truss Core Sandwich Structures. *Appl Compos Mater* 2005;12:229–46. <https://doi.org/10.1007/s10443-005-1129-z>.
- [128] Gao L, Sun YG. Fluid flow and heat transfer characteristics of composite lattice core sandwich structures. *J Thermophys Heat Transf* 2014;28:258–69.
- [129] Mozafari H, Khatami S, Molatefi H, Crupi V, Epasto G, Guglielmino E. Finite element analysis of foam-filled honeycomb structures under impact loading and crashworthiness design. *Int J Crashworthiness* 2016;21:148–60.
- [130] Wicks N, Hutchinson JW. Sandwich plates actuated by a Kagome planar truss. *J Appl Mech* 2004;71:652–62.
- [131] Ho JY, Leong KC, Wong TN. Additively-manufactured metallic porous lattice heat exchangers for air-side heat transfer enhancement. *Int J Heat Mass Transf* 2020;150:119262.

- [132] Xiong J, Ma L, Stocchi A, Yang J, Wu L, Pan S. Bending response of carbon fiber composite sandwich beams with three dimensional honeycomb cores. *Compos Struct* 2014;108:234–42. <https://doi.org/http://dx.doi.org/10.1016/j.compstruct.2013.09.035>.
- [133] Smith M, Cantwell WJ, Guan Z, Tsopanos S, Theobald MD, Nurick GN, et al. The quasi-static and blast response of steel lattice structures. *J Sandw Struct Mater* 2011;13:479–501.
- [134] Al-Ketan O, Lee D-W, Rowshan R, Al-Rub RKA. Functionally graded and multi-morphology sheet TPMS lattices: Design, manufacturing, and mechanical properties. *J Mech Behav Biomed Mater* 2020;102:103520.
- [135] Evans AG, Hutchinson JW, Ashby MF. Multifunctionality of cellular metal systems. *Prog Mater Sci* 1998;43:171–221. [https://doi.org/10.1016/S0079-6425\(98\)00004-8](https://doi.org/10.1016/S0079-6425(98)00004-8).
- [136] Islam MA, Kader MA, Hazell PJ, Escobedo JP, Brown AD, Saadatfar M. Effects of impactor shape on the deformation and energy absorption of closed cell aluminium foams under low velocity impact. *Mater Des* 2020;191:108599.
- [137] Bonthu D, Bharath HS, Gururaja S, Prabhakar P, Doddamani M. 3D printing of syntactic foam cored sandwich composite. *Compos Part C Open Access* 2020;3:100068.
- [138] Wei X, Wu Q, Gao Y, Xiong J. Bending characteristics of all-composite hexagon honeycomb sandwich beams: experimental tests and a three-dimensional failure mechanism map. *Mech Mater* 2020;148:103401.
- [139] Feng L-J, Yang Z-T, Yu G-C, Chen X-J, Wu L-Z. Compressive and shear properties of carbon fiber composite square honeycombs with optimized high-modulus hierarchical phases. *Compos Struct* 2018;201:845–56. <https://doi.org/10.1016/J.COMPSTRUCT.2018.06.080>.
- [140] Eichenhofer M, Wong JCH, Ermanni P. Continuous lattice fabrication of ultra-lightweight composite structures. *Addit Manuf* 2017;18:48–57.
- [141] Karlsson KF, TomasÅström B. Manufacturing and applications of structural sandwich components. *Compos Part A Appl Sci Manuf* 1997;28:97–111.
- [142] Wu Q, Gao Y, Wei X, Mousanezhad D, Ma L, Vaziri A, et al. Mechanical properties and failure mechanisms of sandwich panels with ultra-lightweight three-dimensional hierarchical lattice cores. *Int J Solids Struct* 2018;132:171–87.
- [143] Schaedler TA, Jacobsen AJ, Torrents A, Sorensen AE, Lian J, Greer JR, et al. Ultralight metallic microlattices. *Science (80-)* 2011;334:962–5.
- [144] Triantafillou TC, Gibson LJ. Failure mode maps for foam core sandwich beams. *Mater Sci Eng* 1987;95:37–53.
- [145] Vinson J. *The behavior of sandwich structures of isotropic and composite materials*. Routledge; 2018.
- [146] Timoshenko S. *Strength of Materials: Elementary theory and problems*. R. E. Krieger Pub. Co.; 1976.
- [147] Wang CM, Reddy JN, Lee KH. *Shear Deformable Beams and Plates: Relationships with Classical Solutions*. Elsevier Science; 2000.
- [148] Frostig Y. Buckling of sandwich panels with a flexible core—high-order theory. *Int J Solids Struct* 1998;35:183–204.
- [149] Frostig Y, Baruch M. Localized load effects in high-order bending of sandwich panels with flexible core. *J Eng Mech* 1996;122:1069–76.
- [150] Vitale P, Francucci G, Rapp H, Stocchi A. Shear response of ultra-lightweight CFRP cores. *Compos Struct* 2020;238:111879. <https://doi.org/10.1016/j.compstruct.2020.111879>.
- [151] Xiong J, Ma L, Pan S, Wu L, Papadopoulos J, Vaziri A. Shear and bending performance of carbon fiber composite sandwich panels with pyramidal truss cores. *Acta Mater* 2012;60:1455–66. <https://doi.org/10.1016/J.ACTAMAT.2011.11.028>.

- [152] Heimbs S. Sandwichstrukturen mit Wabenkern: Experimentelle und numerische Analyse des Schädigungsverhaltens unter statischer und kurzzeitdynamischer Belastung 2008.
- [153] Cote F, Deshpande VS, Fleck NA, Evans AG. The out-of-plane compressive behavior of metallic honeycombs. *Mater Sci Eng A* 2004;380:272–80.
- [154] Côté F, Deshpande VS, Fleck NA, Evans AG. The compressive and shear responses of corrugated and diamond lattice materials. *Int J Solids Struct* 2006;43:6220–42. <https://doi.org/10.1016/J.IJSOLSTR.2005.07.045>.
- [155] Cote F, Deshpande V, Fleck N. The shear response of metallic square honeycombs. *J Mech Mater Struct* 2006;1:1281–99.
- [156] Zupan M, Chen C, Fleck NA. The plastic collapse and energy absorption capacity of egg-box panels. *Int J Mech Sci* 2003;45:851–71.
- [157] Chen B, Lang EJ, Chou T-W. Experimental and theoretical studies of fabric compaction behavior in resin transfer molding. *Mater Sci Eng A* 2001;317:188–96.
- [158] Kim J-K, Sham M-L. Impact and delamination failure of woven-fabric composites. *Compos Sci Technol* 2000;60:745–61.
- [159] Kim T, Hodson HP, Lu TJ. Fluid-flow and endwall heat-transfer characteristics of an ultralight lattice-frame material. *Int J Heat Mass Transf* 2004;47:1129–40.
- [160] Yang J-S, Ma L, Schmidt R, Qi G, Schröder K-U, Xiong J, et al. Hybrid lightweight composite pyramidal truss sandwich panels with high damping and stiffness efficiency. *Compos Struct* 2016;148:85–96.
- [161] Truesdell C. *Essays in the History of Mechanics*. Springer Science & Business Media; 2012.
- [162] Correia NC, Robitaille F, Long AC, Rudd CD, Šimáček P, Advani SG. Analysis of the vacuum infusion moulding process: I. Analytical formulation. *Compos Part A Appl Sci Manuf* 2005;36:1645–56.
- [163] Yenilmez B, Senan M, Sozer EM. Variation of part thickness and compaction pressure in vacuum infusion process. *Compos Sci Technol* 2009;69:1710–9.
- [164] Hammami A. Effect of reinforcement structure on compaction behavior in the vacuum infusion process. *Polym Compos* 2001;22:337–48.
- [165] Timoshenko SP, Gere JM. *Theory of elastic stability*. Courier Corporation; 2009.
- [166] Ericksen WS, March HW. Compressive buckling of sandwich panels having dissimilar facings of unequal thickness. *FPL Rep No 1583-B* 1950.
- [167] Standard A. C273, Standard Test Method for Shear Properties of Sandwich Core material 2000.
- [168] Hibbeler R. *Mechanics of materials*. Harlow: Pearson Education Limited; 2018.
- [169] Boresi AP, Schmidt RJ, Sidebottom OM. *Advanced mechanics of materials*. vol. 6. Wiley New York et al.; 1985.
- [170] Basan R. Untersuchung der intralaminaren Schubeigenschaften von Faserverbundwerkstoffen mit Epoxidharzmatrix unter Berücksichtigung nichtlinearer Effekte (in German). 2011.
- [171] Pflüger A. *Stabilitätsprobleme der Elastostatik*. Springer-Verlag; 2013.
- [172] Seydel E. Beitrag zur Frage des Ausbeulens von versteiften Platten bei Schubbeanspruchung. *Jahrb. 1930 der Dtsch. Versuchsanstalt für Luftfahrt, E. V.* (in German, Berlin: 1930, p. 235–54.
- [173] Johns DJ, Kirkpatrick DLI. *Shear buckling of isotropic and orthotropic plates: a review*. HM Stationery Office Richmond; 1971.
- [174] Leissa AW. *Buckling of laminated composite plates and shell panels*. Ohio State Univ Research Foundation Columbus; 1985.

- [175] Standard A. C365 (1994). Standard test method for flatwise compressive properties of sandwich cores. ASTM C365 n.d.;94.
- [176] Dong L, Wadley H. Shear response of carbon fiber composite octet-truss lattice structures. *Compos Part A Appl Sci Manuf* 2016;81:182–92. <https://doi.org/10.1016/J.COMPOSITESA.2015.11.015>.
- [177] Kooistra GW, Wadley HNG. Lattice truss structures from expanded metal sheet. *Mater Des* 2007;28:507–14. <https://doi.org/10.1016/J.MATDES.2005.08.013>.
- [178] Queheillalt DT, Wadley HNG. Titanium alloy lattice truss structures. *Mater Des* 2009;30:1966–75.
- [179] Kooistra GW, Deshpande VS, Wadley HNG. Compressive behavior of age hardenable tetrahedral lattice truss structures made from aluminium. *Acta Mater* 2004;52:4229–37.
- [180] Queheillalt DT, Wadley HNG. Pyramidal lattice truss structures with hollow trusses. *Mater Sci Eng A* 2005;397:132–7.
- [181] Lee Y-H, Lee B-K, Jeon I, Kang K-J. Wire-woven bulk Kagome truss cores. *Acta Mater* 2007;55:6084–94.
- [182] Lim J-H, Kang K-J. Mechanical behavior of sandwich panels with tetrahedral and Kagome truss cores fabricated from wires. *Int J Solids Struct* 2006;43:5228–46.
- [183] Mines RAW, Tsopanos S, Shen Y, Hasan R, McKown ST. Drop weight impact behaviour of sandwich panels with metallic micro lattice cores. *Int J Impact Eng* 2013;60:120–32.
- [184] Smith M, Guan Z, Cantwell WJ. Finite element modelling of the compressive response of lattice structures manufactured using the selective laser melting technique. *Int J Mech Sci* 2013;67:28–41.
- [185] Alwattar TA, Mian A. Development of an Elastic Material Model for BCC Lattice Cell Structures Using Finite Element Analysis and Neural Networks Approaches. *J Compos Sci* 2019;3:33.
- [186] Liu W, Song H, Wang Z, Wang J, Huang C. Improving mechanical performance of fused deposition modeling lattice structures by a snap-fitting method. *Mater Des* 2019;181:108065.
- [187] Dong L, Wadley H. Mechanical properties of carbon fiber composite octet-truss lattice structures. *Compos Sci Technol* 2015;119:26–33.
- [188] Swiss-Composite. Technical data sheet n.d. <https://www.swiss-composite.ch/pdf/t-carbon-profile.pdf>.
- [189] Wei K, Yang Q, Ling B, Xie H, Qu Z, Fang D. Mechanical responses of titanium 3D kagome lattice structure manufactured by selective laser melting. *Extrem Mech Lett* 2018;23:41–8.
- [190] Crupi V, Kara E, Epasto G, Guglielmino E, Aykul H. Static behavior of lattice structures produced via direct metal laser sintering technology. *Mater Des* 2017;135:246–56. <https://doi.org/https://doi.org/10.1016/j.matdes.2017.09.003>.
- [191] George T, Deshpande VS, Sharp K, Wadley HNG. Hybrid core carbon fiber composite sandwich panels: Fabrication and mechanical response. *Compos Struct* 2014;108:696–710. <https://doi.org/http://dx.doi.org/10.1016/j.compstruct.2013.10.002>.
- [192] Williams D, Leggett DMA, Hopkins HG. Flat sandwich panels under compressive end loads. HM Stationery Office; 1941.
- [193] Reissner E. On bending of elastic plates. *Q Appl Math* 1947;5:55–68.
- [194] Reissner E. Finite deflections of sandwich plates. *J Aeronaut Sci* 1948;15:435–40.
- [195] Hoff NJ. Bending and buckling of rectangular sandwich plates 1950.
- [196] Plantema FJ. Sandwich Construction: The Bending and Buckling of Sandwich Beams, Plates and Shells, 1966.

- [197] Jones RM. Buckling of bars, plates, and shells. Bull Ridge Corporation; 2006.
- [198] Sullins RT, Smith GW, Spier EE. Manual for Structural Stability Analysis of Sandwich Plates and Shells. GENERAL DYNAMICS CORP SAN DIEGO CA; 1969.
- [199] Fagerberg L. Wrinkling of sandwich panels for marine applications 2003.
- [200] Fagerberg L, Zenkert D. Imperfection-induced wrinkling material failure in sandwich panels. *J Sandw Struct Mater* 2005;7:195–219.
- [201] Hoff NJ, Mautner SE. The buckling of sandwich-type panels. *J Aeronaut Sci* 1945;12:285–97.
- [202] Fagerberg L, Zenkert D. Effects of anisotropy and multiaxial loading on the wrinkling of sandwich panels. *J Sandw Struct Mater* 2005;7:177–94.
- [203] Bartelds G, Astronautics SUD of A and, Mayers J, Laboratories USAAM. Unified Theory for the Bending and Buckling of Sandwich Shells - Application to Axially Compressed Circular Cylindrical Shells. Stanford University, Department of Aeronautics and Astronautics; 1966.
- [204] Norris CB. Short-column Compressive Strength of Sandwich Constructions as affected by Size of Cells of Honeycomb Core Materials. vol. 26. US Department of Agriculture, Forest Service, Forest Products Laboratory; 1964.
- [205] Wiedemann J. Leichtbau: Elemente und Konstruktion. Springer-Verlag; 2007.
- [206] Frolovs G, Rocens K, Sliseris J. Shear and tensile strength of narrow glued joint depending on the grain direction of plywood plies. *Procedia Eng* 2017;172:292–9.
- [207] Standard A. C393, Standard Test Method for Flexural Properties of Sandwich Constructions 2000.
- [208] Standard A. D7249, Standard Test Method for Facesheet Properties of Sandwich Constructions by Long Beam Flexure. ASTM Int West Conshohocken, PA 2012.
- [209] Tancogne-Dejean T, Diamantopoulou M, Gorji MB, Bonatti C, Mohr D. 3D Plate-Lattices: An Emerging Class of Low-Density Metamaterial Exhibiting Optimal Isotropic Stiffness. *Adv Mater* 2018;30:1803334.
- [210] Moongkhamklang P, Deshpande VS, Wadley HNG. The compressive and shear response of titanium matrix composite lattice structures. *Acta Mater* 2010;58:2822–35.
- [211] Crupi V, Kara E, Epasto G, Guglielmino E, Aykul H. Static behavior of lattice structures produced via direct metal laser sintering technology. *Mater Des* 2017;135:246–56. <https://doi.org/10.1016/J.MATDES.2017.09.003>.
- [212] Hou Y, Neville R, Scarpa F, Remillat C, Gu B, Ruzzene M. Graded conventional-auxetic Kirigami sandwich structures: Flatwise compression and edgewise loading. *Compos Part B Eng* 2014;59:33–42. <https://doi.org/https://doi.org/10.1016/j.compositesb.2013.10.084>.
- [213] Wierzbicki T. Crushing analysis of metal honeycombs. *Int J Impact Eng* 1983;1:157–74.
- [214] Corporation H. HexWeb™ Honeycomb Attributes and Properties. 1999.
- [215] Wang B, Hu J, Li Y, Yao Y, Wang S, Ma L. Mechanical properties and failure behavior of the sandwich structures with carbon fiber-reinforced X-type lattice truss core. *Compos Struct* 2018;185:619–33. <https://doi.org/10.1016/J.COMPSTRUCT.2017.11.066>.
- [216] Corporation H. HexWeb™ Honeycomb Attributes and Properties. 1999.
- [217] Zhao Z, Li L, Wang X, Zhang Q, Han B, Lu T. Strength optimization of ultralight corrugated-channel-core sandwich panels. *Sci China Technol Sci* 2019;62:1467–77.
- [218] Wicks N, Hutchinson JW. Optimal truss plates. *Int J Solids Struct* 2001;38:5165–83.
- [219] Valdevit L, Hutchinson JW, Evans AG. Structurally optimized sandwich panels with prismatic cores. *Int J Solids Struct* 2004;41:5105–24.

- [220] Ashby MF. Chapter 11 - Designing Hybrid Materials. In: Ashby MF, editor. *Mater. Sel. Mech. Des.* (Fourth Ed. Fourth Edi, Oxford: Butterworth-Heinemann; 2011, p. 299–340. <https://doi.org/https://doi.org/10.1016/B978-1-85617-663-7.00011-4>.
- [221] Carlin PS. Lightweight mirror systems for spacecraft-an overview of materials and manufacturing needs. *2000 IEEE Aerosp. Conf. Proc. (Cat. No. 00TH8484)*, vol. 4, IEEE; 2000, p. 169–82.
- [222] Wei L, Zhang L, Gong X. Design and optimization of the CFRP mirror components. *Photonic Sensors* 2017;7:270–7.
- [223] Sauer M, Kühnel M, Witten E. *Composites-Marktbericht 2017: marktentwicklungen, trends, ausblicke und herausforderungen, AVK–industrievereinigung Verstärkte Kunststoffe e. V. Carbon Compos EV* 2017.
- [224] Sauer M, Kühnel M, Witten E. *Composites Marktbericht 2018: Marktentwicklungen, Trends, Ausblicke und Herausforderungen. Carbon Compos EV* 2018:65.
- [225] Schüppe D. 18 EUROS/KG CFRP: The Leading-Edge Cluster MAI Carbon achieves cost goal. *Carbon Compos eV* 2018.
- [226] Gardiner G. Reducing manufacturing cost via RTM. *Compos World* 2015.
- [227] Sauer M. *Composites Market Report 2019. Carbon Compos e V* 2019:11.
- [228] *Composites World. Rear wall reboot: One-stop, tow to tape to CFRP part. Compos World Vol 4 No 6, p 48* 2018;4.
- [229] Chapetti MD. *Mecanica de materiales. First. La Plata, Bs. As.: Ediciones Al Margen; 2005.*